Transactions of the ASME, Journal of Heat Transfer (ISSN 0022-1481) is published monthly by The American Society of Mechanical Engineers, Three Park Avenue, New York, NY 10016. Periodicals postage paid at New York, NY and additional mailing offices. POSTMASTER: Send address changes to Transactions of the ASME, Journal of Heat Transfer, c/o THE AMERICAN SOCIETY OF MECHANICAL ENGINEERS, 22 Law Drive, Box 2300, Fairfield, NJ 07007-2300. **CHANGES OF ADDRESS** must be received at Society headquarters seven weeks before they are to be effective. Please send old label and new address. **STATEMENT from By-Laws.** The Society shall not be responsible for statements or opinions advanced in papers or ... printed in its publications (B7.1, Para. 3).

Journal of Heat Transfer

Published Monthly by ASME

VOLUME 127 • NUMBER 12 • DECEMBER 2005

RESEARCH PAPERS

TECHNICAL BRIEFS

(**Contents continued on inside back cover**)

This journal is printed on acid-free paper, which exceeds the ANSI Z39.48-1992 specification for permanence of paper and library materials. ♾™
♻ 85% recycled content, including 10% post-consumer fibers.

Journal of Heat Transfer **Volume 127, Number 12** **DECEMBER 2005**

ANNOUNCEMENT

The ASME Journal of Heat Transfer is abstracted and indexed in the following:

Applied Science and Technology Index, Chemical Abstracts, Chemical Engineering and Biotechnology Abstracts (Electronic equivalent of Process and Chemical Engineering), Civil Engineering Abstracts, Compendex (The electronic equivalent of Engineering Index), Corrosion Abstracts, Current Contents, E & P Health, Safety, and Environment, Ei EncompassLit, Engineered Materials Abstracts, Engineering Index, Enviroline (The electronic equivalent of Environment Abstracts), Environment Abstracts, Environmental Engineering Abstracts, Environmental Science and Pollution Management, Fluidex, Fuel and Energy Abstracts, Index to Scientific Reviews, INSPEC, International Building Services Abstracts, Mechanical & Transportation Engineering Abstracts, Mechanical Engineering Abstracts, METADEX (The electronic equivalent of Metals Abstracts and Alloys Index), Petroleum Abstracts, Process and Chemical Engineering, Referativnyi Zhurnal, Science Citation Index, SciSearch (The electronic equivalent of Science Citation Index), Theoretical Chemical Engineering

Neutral Instability and Optimum Convective Mode in a Fluid Layer with PCM Particles

Chuanshan Dai
e-mail: csdai@yahoo.com
College of Mechanical Engineering,
Tianjin University,
Tianjin 300072, People's Republic of China

Hideo Inaba
e-mail: inaba@mech.okayama-u.ac.jp
Department of Mechanical Engineering, Okayama University,
Okayama 700-8530, Japan

Linear stability analysis is performed to determine the critical Rayleigh number for the onset of convection in a fluid layer with phase-change-material particles. Sine and Gaussian functions are used for describing the large variation of apparent specific heat in a narrow phase changing temperature range. The critical conditions are numerically obtained using the fourth order Runge-Kutta-Gill finite difference method with Newton-Raphson iteration. The critical eigenfunctions of temperature and velocity perturbations are obtained. The results show that the critical Rayleigh number decreases monotonically with the amplitude of Sine or Gaussian function. There is a minimum critical Rayleigh number while the phase angle is between $\pi/2$ and π, which corresponds to the optimum experimental convective mode. [DOI: 10.1115/1.2060728]

1 Introduction

Natural convection in a horizontal fluid layer with variable fluid properties has attracted many researchers' interest in recent decades. The ongoing researches can be classified into several categories such as onset of convection, non-Boussinesq effects, re-evaluation of convection intensity (redefinition of Rayleigh number) and boundary effects. There are still some difficulties for an accurate estimation of critical conditions and the transition of flow patterns in a fluid layer with strong temperature-dependent fluid properties. For most of fluids, viscosity is more sensitive to temperature variations than specific heat and thermal conductivity. Therefore, most of previous investigations were focused on the influence of variable fluid viscosity on the onset of convection [1–5]. On the influence due to specific heat variation, however, the available literature is scarce. Generally, specific heat can be well represented by linear functions of the temperature for water, air and many other naturally existing fluids. The influence due to specific heat variations on the convective instability can be negligible for many cases. On the other hand, for some artificial fluids, the specific heat may undergo strong variations with temperature. In the last decade, some approaches using the phase-change-material (PCM) slurries as heat transfer fluids have been carried out [6,7]. These slurries produced by suspending many fine PCM particles in a carrying fluid, usually water, benefit from a number of special features. Experimental tests have shown their possibility for both energy transport and storage [8]. The up to date technology can make the diameter of suspended particle very small (<1 μm volumetric averaged), which is very important in order to make the slurry structural-stable and homogeneous. Paraffin wax, salt hydrate, for example, can be used as the PCM in particles. Paraffin wax consists of mixture of mostly straight-chain *n*-alkanes, $CH_3-(CH_2)_n-CH_3$. The crystallization of *n*-alkanes can release a large amount of latent heat. Both the melting point and heat of fusion increase with the chain length. Solidification or melting of multicomponent mixtures in microcapsules takes place over a range of temperature, whereas it occurs at a single temperature in pure materials [9,10]. For an example, the binary mixtures of tetradecane (30% mole fraction) and hexadecane start to crystallize while the temperature goes down to about 11°C, and end up at about 8.3°C [11]. The bulk specific heat of microencapsulated PCM slurry, which depends mainly on the selected phase-change-materials and their compositions, may vary strongly with temperature in the phase changing temperature range. The bulk specific heat is generally called the apparent specific heat or the effective specific heat. The effective specific heat could be increased up to 5 times and heat transfer coefficient of up to 2.8 times in flows of microcapsulated phase change material suspensions [6]. Recent investigations on natural convection in PCM slurry layers showed that PCMs also can enhance the heat transfer performance [12]. The maximum heat transfer coefficient can be achieved by controlling the bottom heating plate around a temperature where the PCM slurry has its maximum apparent specific heat. The numerical simulations on natural convection with a Rayleigh-Bénard configuration showed that convection starts earlier for the slurry with PCM than that without PCM [13]. Since the critical conditions observed in those experiments also involved other fluid property variations than specific heat, the influence due to specific heat variation alone were not clear, which needs to be clarified. Selak and Lebon [14] investigated the influences on the marginal stability due to the variations in viscosity, thermal conductivity and specific heat for Rayleigh-Marangoni convection. A linear temperature-dependent function of specific heat was used in their study. The results of their study showed that the instability threshold decreases with an increase in the constant of proportionality of the linear function used. In the present paper, we report the influence of nonlinear variation in specific heat with temperature on the neutral critical condition. Some results are compared with those of our experiments.

2 The Basic Equations and Boundary Conditions

Consider a horizontally infinite stationary fluid layer with thickness d and constant vertical temperature gradient γ. The upward vertical direction is taken as z_* coordinate, as shown in Fig. 1. The temperature difference between the lower hot and upper cold boundary is $\Delta T = T_h - T_c$. Since the basic state is stationary and thermal steady, the dimensional velocity, temperature and pressure in the fluid layer can respectively be expressed as $\vec{U}_* = 0$, $T_* = T_h - \gamma z_*$, and $P_* = p_0 - \rho_0 g\left(z_* + \frac{1}{2}\gamma\beta z_*^2\right)$, where γ is defined as $\Delta T/d$, β is the coefficient of thermal expansion, and the subscript $*$ indicates dimensional quantity. After introducing the Boussinesq approximation and ignoring the viscous dissipation, the dimensional governing equations of mass, momentum, and energy for a Newtonian fluid are, respectively,

$$\nabla \cdot \vec{u}_* = 0 \tag{2.1}$$

Contributed by the Heat Transfer Division of ASME for publication in the JOURNAL OF HEAT TRANSFER. Manuscript received by the Heat Transfer Division March 23, 2004; revision received June 10, 2005. Review conducted by: K. A. Thole.

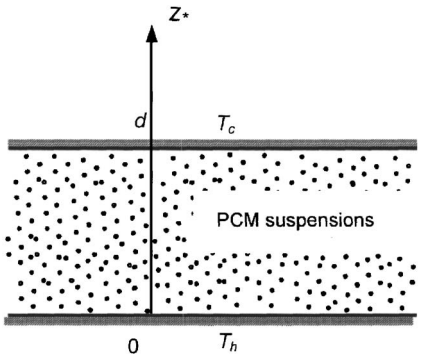

Fig. 1 Schematic diagram of a PCM fluid layer heated from below and cooled from above

$$\frac{\partial \vec{u}_*}{\partial t} + \vec{u}_* \cdot \nabla \vec{u}_* = -\nabla(p_*/\rho_0 + g z_*) + g\beta(T - T_0)\vec{k} + \nu \Delta \vec{u}_* \tag{2.2}$$

$$\rho C_p \left(\frac{\partial T}{\partial t} + \vec{u}_* \cdot \nabla T \right) = \lambda \nabla^2 T \tag{2.3}$$

where $\rho = \rho_0[1 - \beta(T - T_0)]$. The subscript "0" is for quantities at reference temperature T_0. The upper cooling plate temperature T_c is taken as the reference temperature in this analysis. The small disturbance quantities are as follows: velocity $\vec{u}'_* = \vec{u}_* - \vec{U}_*$; temperature $T' = T - T_*$; and pressure $p'_* = p_* - P_*$. After using the following scaling for the coordinates, time, velocity, pressure, and temperature,

$$\vec{x} = \frac{\vec{x}_*}{d}, \quad \tau = t\frac{\alpha_0}{d^2}, \quad \vec{u} = \vec{u}'_* \frac{d}{\alpha_0}, \quad p = p'_* \frac{d^2}{\rho_0 \alpha_0^2}, \quad \theta = \frac{T'}{\Delta T}$$

respectively, with

$$\mathrm{Ra} = \frac{g\beta_0(T_h - T_c)d^3}{\upsilon_0 \alpha_0},$$

$$\mathrm{Pr} = \frac{\nu_0}{\alpha_0},$$

$$Q = \frac{C_p}{C_{p0}},$$

$$\alpha_0 = \frac{\lambda_0}{\rho_0 C_{p0}},$$

and neglecting the second order perturbations. The dimensionless equations can be written as:

$$\nabla \cdot \vec{u} = 0 \tag{2.4}$$

$$\frac{\partial \vec{u}}{\partial \tau} = -\nabla p + \mathrm{Ra}\,\mathrm{Pr}\,\theta \vec{k} + \mathrm{Pr}\,\nabla^2 \vec{u} \tag{2.5}$$

$$Q\left(\frac{\partial \theta}{\partial \tau} - w \right) = \nabla^2 \theta \tag{2.6}$$

where the normalized apparent specific heat Q is given by C_p/C_{p0}. Note that except for the term of normalized specific heat Q in Eq. (2.6), Eqs. (2.5) and (2.6) are well known since the book written by Chandrasekhar [15].

2.1 Linear Stability Analysis. For simplicity, a linear stability analysis by using the normal mode technique has been carried out in the paper. The nondimensionalized perturbation quantities depending on x, y, and τ have the forms:

$$w = W(z) e^{i(k_x x + k_y y) + \sigma \tau} \tag{2.7}$$

$$\theta = \Theta(z) e^{i(k_x x + k_y y) + \sigma \tau} \tag{2.8}$$

where $k^2 = k_x^2 + k_y^2$. States of marginal or neutral stability are characterized by a zero growth rate σ. The forms of sinusoidal disturbances above satisfy the Helmholtz equation. They are used quite often for a linear stability analysis. However, a more sophisticated method, such as a weakly nonlinear stability analysis, is recommended for a strongly nonlinear hydrodynamic system. By twice taking curl of the momentum Eq. (2.5), we have

$$\frac{\partial(\nabla^2 \vec{u})}{\partial \tau} = \mathrm{Ra}\,\mathrm{Pr}\left(\nabla^2 \theta \vec{k} - \nabla \frac{\partial \theta}{\partial z} \right) + \mathrm{Pr}(\nabla^2 \vec{u})^2 \tag{2.9}$$

While σ in Eqs. (2.7) and (2.8) is equal to zero the stability problem is marginal or neutral, and the term related to the perturbation quantity growth with time can be eliminated. The vertical part of Eq. (2.9) is,

$$\mathrm{Ra}\,\Delta_1 \theta + (\nabla^2 w)^2 = 0 \tag{2.10}$$

where $\Delta_1 = \partial^2/\partial^2 x + \partial^2/\partial^2 y$, is the Laplacian operator. Substitute Eqs. (2.7) and (2.8) into Eqs. (2.10) and (2.6), we have

$$\mathrm{Ra}\,k^2 \Theta = (D^2 - k^2)^2 W \tag{2.11}$$

$$(D^2 - k^2)\Theta + QW = 0 \tag{2.12}$$

where $D = \partial/\partial Z$. Note that Eq. (2.10) is different from that derived by Stengel et al. [2] while only Q is considered.

For a rigid no-slip boundary with constant temperature, perturbed quantities for both velocity and temperature should vanish at the boundary. From the continuity equation it also follows that $DW = 0$. Therefore, we have

$$DW = 0, \quad W = \Theta = 0 \tag{2.13}$$

Using the same notation as given by Stengel et al. [2], the rigid boundary condition is denoted by R. In contrast, if the boundary is stress-free, one has

$$D^2 W = 0, \quad W = \Theta = 0, \tag{2.14}$$

and this boundary condition is denoted by F. Thus, R/F means a rigid top and a stress-free bottom.

2.2 Functions of Specific Heat With Temperature. Two types of normalized specific heat functions are investigated in the present study. One is a sine function and the other is a Gaussian function, which are written, respectively, as follows:

$$Q = 1 + b \sin(\Psi \tilde{T}) \tag{2.15}$$

$$Q = 1 + b\left\{ \exp\left[-c\left(\frac{\Psi}{\pi}\tilde{T} - \frac{1}{2} \right)^2 \right] - \exp\left(-\frac{c}{4} \right) \right\} \tag{2.16}$$

where

$$\psi = \left(\frac{T_h - T_s}{T_l - T_s} \right) \pi$$

and

$$\tilde{T} = \left(\frac{T - T_c}{T_h - T_c} \right) = 1 - z$$

while $\psi > \pi, Q(=C_p/C_{p0})$ is given by unity, which means that the apparent specific heat keeps constant with temperature except in the range of phase change temperature ($\psi \leqslant \pi$). T_s represents the temperature at which some PCM begins to melt, and T_l the temperature at which all of PCM changes into liquid phase. T_s and T_l can be determined through thermodynamic phase diagram for a given composition of mixtures of PCM and pressure. Equation (2.16) is a modified form of Gaussian distribution function of

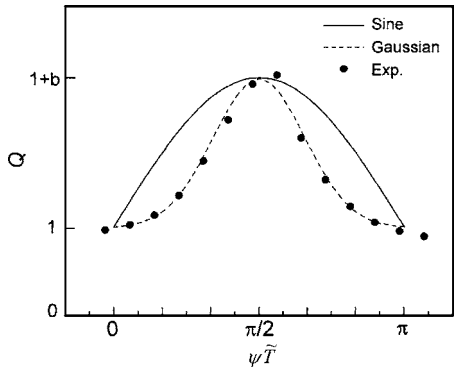

Fig. 2 Normalized specific heat models [Eqs. (2.15) and (2.16)]. The curves are for $b=1.688$ and $c=20$, the solid cycles are experimental data measured by DSC.

$$f(x) = f_0 + \frac{A}{\omega\sqrt{\pi/2}} e^{-2[(x-x_c)^2/\omega^2]} \tag{2.17}$$

where f_0, A, ω, and x_c are four constants. The two constants b and c in Eq. (2.16) are the reductions of these four constants. The approximation by giving the specific heat as a Gaussian function [Eq. (2.16)] is quite reasonable according to our measured data [12]. However, it has one more fitting constant of c than that of sine function. Figure 2 shows the two functions in the case of $\psi = \pi$. The solid points stand for experimental data. In order to make a comparison with our early experimental results [12], the theoretical analysis in this paper was performed by fixing the temperature of upper cooling plate at $T_c = T_s$. Therefore, that $\psi = \pi$ indicates the temperature from that of the upper cooling plate to that of lower heating plate covers exactly the range of phase change temperature. Figure 3 shows the three cases of $\psi < \pi$, $\psi = \pi$, and $\psi > \pi$. The case $\psi = \pi/2$ means that the lower heating plate is at a temperature the fluid having its local maximum specific heat.

2.3 The Numerical Procedure. To solve the boundary value problem of Eqs. (2.11)–(2.14), at first, we have tried two numerical methods to ensure the correctness for the output of calculation. One method is the numerical integration using the standard Simpson 1/3 rule. The other is the numerical differentiation using the fourth order Runge-Kuttta-Gill scheme with the shooting technique. The vertical coordinate z from 0 to 1 is uniformly divided into N parts, i.e., with $N+1$ grid points. The Simpson 1/3 rule requires an even number of N. It is convenient to combine Eqs. (2.11) and (2.12) into a single sixth order ordinary differential equation of W for this method, which is as follows:

$$(D^2 - k^2)^3 W + Q\,\mathrm{Ra}\,k^2 W = 0 \tag{2.18}$$

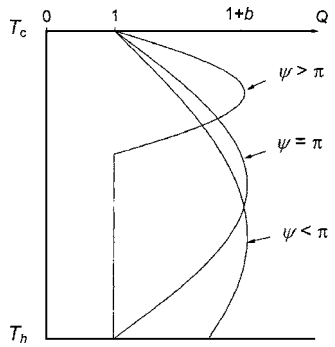

Fig. 3 Various modes of bottom heating for: a complete cycle of specific heat variation with temperature: $\psi = \pi$; less than a cycle: $\psi < \pi$; and over a cycle: $\psi > \pi$

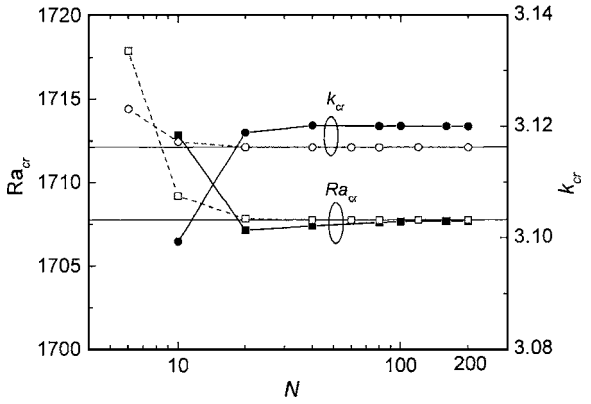

Fig. 4 Grid number dependence test for numerical integration (solid points) and numerical differentiation (open points) methods

Assuming the coefficients of $W^{(6)}(z_i)$ to be unity, where i is from 0 to N, $W^{(5)}(z_i)$ can be obtained by numerical integration using the Simpson 1/3 rule. But, an integration constant $W^{(5)}(z_0)$ has to be added. At the two boundaries, the trapezoidal rule was used instead of the Simpson 1/3 rule since only one side has the value. Using the same procedure, the other four derivatives from $W^{(4)}(z_i)$ to $W^{(1)}(z_i)$, and $W(z_i)$ can also be represented by $W^{(6)}(z_i)$. Substituting these derivatives into Eq. (2.18), we can get $N+1$ homogeneous equations with $N+7$ unknowns including the six integration constants. The boundary conditions [Eq. (2.13) or Eq. (2.14)] can provide the extra six equations that makes the set of equations complete. *QR* method is then applied to find the minimum real eigenvalue of the coefficient matrix [16]. In order to get a nontrivial solution, we have to make the determinant of the matrix equal to zero. Giving a wave number k, then we can find its corresponding Ra for satisfying the constraint above.

Generally, the numerical differentiation method is simpler and faster than the numerical integration method for solving ordinary differential equations. It is frequently used for solving initial value problems. Boundary value problems can also be solved using this method by properly selecting the values of one boundary. There are six initial values required to start the calculation, but three of them are already known according to the boundary conditions at $z=0$. In this analysis, Newton-Raphson iteration is applied to determine the other three initial values (one of which is given arbitrarily). The convergence criterion requires that the opposite boundary at $z=1$ also satisfy the boundary conditions. $W^{(2)}(0)$ is given by 10 for the rigid boundary (R) at $z=0$. For the stress-free boundary (F), $W^{(2)}(0)$ is equal to zero, and $W^{(1)}(0)$ given by 10.

For the F/F (pure Rayleigh problem) and R/R cases, the numerical results are consistent by using the two methods. Figure 4 shows the grid dependence test using the convectional R/R case for the two numerical methods. The numerical differentiation method is more accurate and converges faster than the numerical integration method. For the case of R/R, the critical Rayleigh number Ra_{cr} obtained by using numerical differentiation method with 80 uniform grid points is 1707.762 at critical wave number $k_{cr}=3.1163$, which is in good agreement with previous results [15]. In the following calculations, the numerical difference method is used. The grid number is taken as 80, because the accuracy of outputs is already enough according to Fig. 4. The calculated Ra_{cr} has three decimals accurate and k_{cr} four decimals for the particular case above. Further validation of the computation code has been carried out by running the program for a fluid layer with variable viscosity. For the exponential fluids, which the viscosity variation with temperature follows the exponential function, the critical thresholds at various viscosity ratios are calcu-

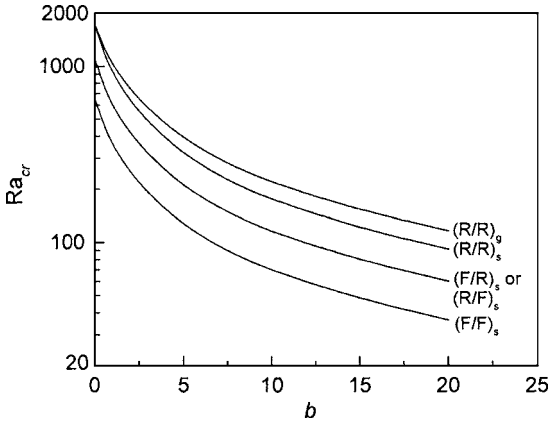

Fig. 5 Critical Rayleigh number versus the amplitude *b* of normalized specific heat at various boundary conditions, subscript "s" for a sine variation, and "g" a Gaussian variation

lated using the present computation code, and the results are in good accordance with those obtained by Stengel et al. [2].

3 Results and Discussion

3.1 Effect of Amplitude *b*. For a weak linear function of specific heat variation with temperature, the critical Rayleigh number and Marangoni number decreases linearly with its proportional coefficient for Rayleigh-Marangoni problem [14]. It is generally believed that an increase in specific heat, which results in a decrease in thermal diffusivity, promotes thermal inhomogeneities so that convection occurs more easily compared to fluids with constant specific heat. Figure 5 shows the critical Rayleigh number versus the amplitude b while the specific heat follows the sine function (four boundary cases) and the Gaussian function (the case R/R only). These curves in Fig. 5 are for the case of $\psi=\pi$. The coefficient c in Eq. (2.16) is given by 20 for the Gaussian function, which was obtained by fitting the experimental data as shown in Fig. 2. Although the other three boundary cases ($F/F, R/F, F/R$) for the Gaussian function are not shown in Fig. 5, it can be concluded that the critical Rayleigh number decreases monotonically with the amplitude b for all the four boundary cases ($R/R, F/F, R/F, F/R$). In the case of $\psi=\pi$, the critical wave numbers almost keep constants for all the boundary conditions, as shown in Fig. 4, i.e., R/R: 3.1163; R/F or F/R: 2.6826; and F/F: 2.2215. Note that the critical conditions for the cases of R/F and F/R are identical, which is probably due to the symmetrically distribution of specific heat with temperature in the fluid layer about the horizontal centerline. However, this is not necessarily the case while $\psi<\pi$ or $\psi>\pi$. For example, Ra_{cr} is 448.713 at $k_{cr}=2.6794$ in the case of R/F, but Ra_{cr} is 483.418 at $k_{cr}=2.6892$ in the case of F/R for $\psi=\pi/2$. The effect of phase angle ψ on the critical conditions is discussed in the next section.

3.2 Effect of Phase Angle ψ. Figures 6(a) and 6(b) show, respectively, the variations of critical Rayleigh number Ra_{cr} and critical wave number k_{cf} against phase angle ψ at a constant amplitude b in the case of R/R boundaries. The dashed lines show the cases that specific heat follows a sine function with temperature [Eq. (2.15)], and the solid lines a Gaussian function [Eq. (2.16)]. A minimum critical Rayleigh number exists while ψ is between $\pi/2$ and π. There are two interpretations for this. The first is that convection can be induced most easily if the lower heating plate is properly controlled at temperature $T_s+(T_l-T_s)\psi_{op}/\pi$, where ψ_{op} is the phase angle at which having the minimum critical Rayleigh number. The second is that the most enhanced heat transfer mode happens at a heating plate temperature larger than a point at which the fluid attains the largest specific heat. In the analysis models we used, specific heat has the largest value at temperature $(T_l+T_s)/2$. Increasing the amplitude b results in a lower value of the minimum critical Rayleigh number. It is shown that ψ_{op} seems to be independent of amplitude b for the two specific heat functions. It is about 0.905π if the specific heat follows a sine variation with temperature, and 0.895π for a Gaussian variation. Thus, $\psi_{op}=0.9\pi$ is adequate in accuracy for an industry use.

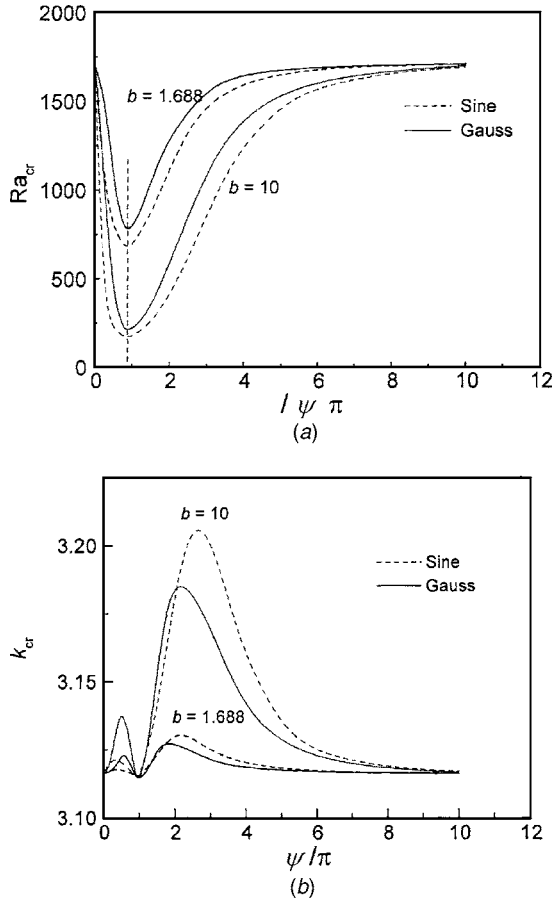

Fig. 6 Critical Rayleigh number (*a*) and wave number (*b*) versus phase angle ψ at constant amplitude *b* for Gaussian variations and for the case *R*/*R*

For a PCM slurry layer in practice, if it is already in a convective mode with a top cooling plate temperature of T_s, Rayleigh number increases with an increase in the bottom heating plate temperature T_h or the phase angle ψ. Since the critical Rayleigh number decreases with increasing ψ, and achieves the minimum at ψ_{op}, the difference between the real Rayleigh number and the calculated critical Rayleigh number $(\mathrm{Ra}-\mathrm{Ra}_{cr})$ becomes larger and larger. A maximum difference can be achieved at ψ_{op}, which means the convective mode gets relatively the farthest from the threshold. Therefore, it can be deduced that a maximum heat transfer coefficient can be achieved by controlling the heating plate temperature at $T_s+(T_l-T_s)\psi_{op}/\pi$.

A common tendency, which can be seen from Fig. 6(b), is that a big wave follows after ψ_{op}. k_{cr} increases rapidly with increasing ψ. This indicates that there will be a great change in flow pattern after ψ_{op}. The perturbed velocity and temperature at critical conditions for the case of R/R are summarized and shown in Fig. 7. The top two figures are for the cases of $b=1.688$, and the bottom two figures of $b=10$. The specific heat follows a Gaussian variation with temperature. The left column shows the velocity-perturbed quantity, and the right the temperature perturbed quan-

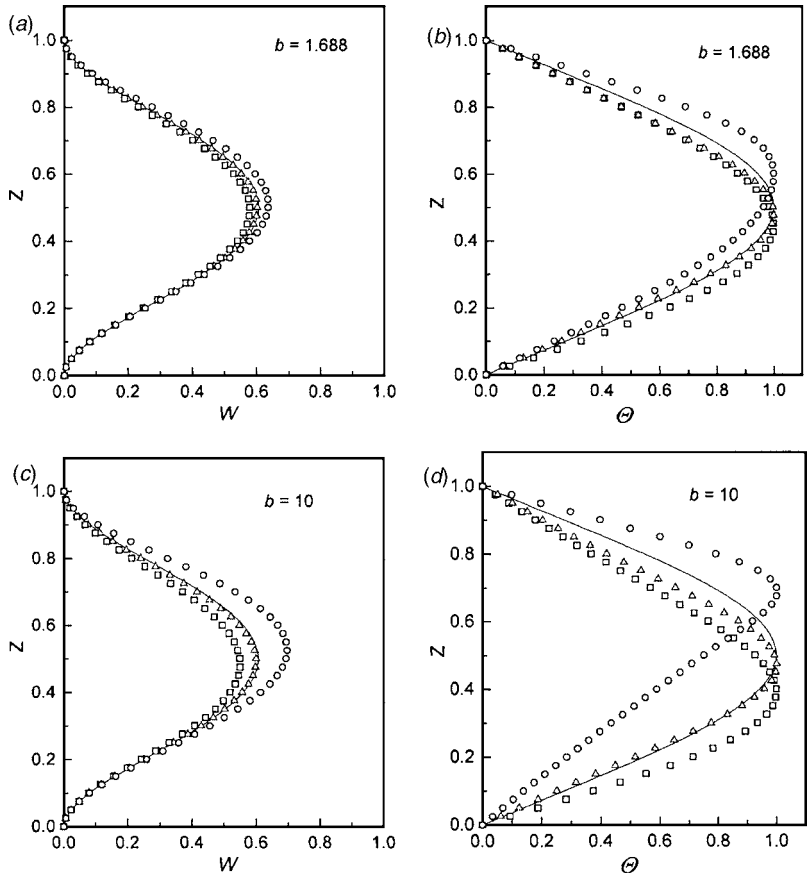

Fig. 7 Variation of the normalized vertical velocity (*a*) and (*c*), and temperature disturbance (*b*) and (*d*) with the normalized depth of the layer *z* for the case of *R*/*R* and the Gaussian variation of specific heat with temperature, the solid curve is for a fluid with constant specific heat, $\psi=\pi$ is denoted with □; $\psi=\pi/2$ with ○; and △ denotes the phase angle ψ_{op} at which has the minimum critical Rayleigh number

tity. It is worthy of note that in all the cases the open inverse triangles lie closest to the solid line of a fluid with a constant specific heat. As mentioned above, the maximum heat transfer coefficient can be obtained if the heating plate temperature is controlled at $\psi=0.9\pi$. Therefore, it can be concluded that the most optimum structures of perturbed velocity and temperature, at which the maximum heat transfer coefficient can be achieved, are much like those of fluids with constant specific heat.

3.3 Comparison With Experiments. The previous experimental results showed that the best convective heat transfer performance can be obtained by probably controlling the bottom heating plate temperature slightly larger than the melting point of major PCM component for the PCM slurry [8]. This is fairly in agreement with the present theoretical analysis. The PCM slurries used exposed a power-law non-Newtonian fluid behavior. They have other fluid property variations with temperature than the apparent specific heat. The experiments were done in a confined rectangular enclosure with a large aspect ratio (width/height) of 21.8. One of the results obtained is that the critical Rayleigh number for the most concentrated PCM slurry (30% mass) has the lowest critical Rayleigh number ($\mathrm{Ra}_{\mathrm{cr}}<700$), which is much lower than that of water. This is also in accordance with the calculated results of the present study. The best fitting curve of specific heat with temperature in the phase changing temperature range for the PCM slurry ($C_m=30\%$) is

$$C_p(T) = 4.464 + 7134e^{-0.162(T-46.02)^2} \tag{3.1}$$

In fact, Eq. (2.16) is derived from Eq. (3.1) by assigning the value of C_{p0}, T_s, and T_l to be 4.3, 40, and 52, respectively. However, it should be mentioned that the specific heat variation with temperature [Eq. (3.1)] was measured using the differential scanning calorimeter (DSC) technique, which is a transient measurement. The values of T_s, and T_l depend on the heating rate of the sample. Seven steps including two complete cycles were used in the measurement. The heating rate was 5°C/min. It is very interesting to make a comparison between the specific heat $C_p(T)$ and the thermal expansion coefficient $\beta(T)$, because $\beta(T)$ was measured by a volumetric expansion meter in relatively a thermal steady state. The two measured properties are shown in Fig. 8. The vertical coordinate has been linearly adjusted for their data matching. It is shown that the two properties match very well except for the rear part in the range of phase change temperature. According to this figure, the melting completion temperatures T_l for the two properties are different, but the melting start temperatures T_s are almost the same. Assuming $T_c=T_s=40$°C, and $T_l=52$°C [depending on $C_p(T)$ measured by DSC] or $T_l=49$°C [depending on $\beta(T)$ measured at thermal steady state], the optimum heating plate temperature, $T_s+(T_l-T_s)\psi_{\mathrm{op}}/\pi$, at which the maximum heat transfer coefficient can be achieved, can be predicted according to the present study. It is 50.8°C for the former and 48.1°C for the latter. Figure 9 shows the measured heat transfer coefficient with respect to temperature for the PCM slurries with

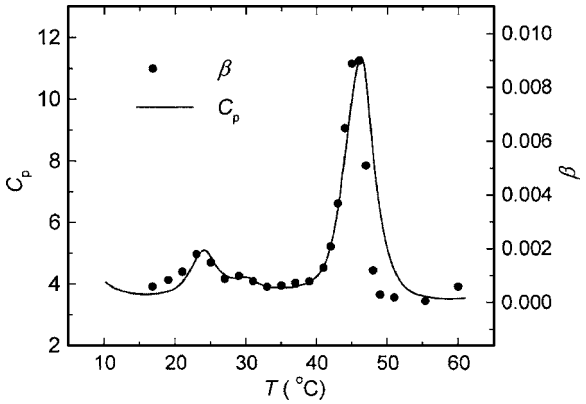

Fig. 8 Graph matching between the measured specific heat C_p by DSC and the coefficient of thermal expansion β by adjusting the vertical coordinate linearly

various concentrations. The optimum heating plate temperature of 48.1°C gives a more reasonable prediction comparing with experimental data.

In addition, according to our experiments, the most optimum heat transfer mode of convection is very unstable. By further increasing the heating flux through the microemulsion PCM slurry layer thereafter, a big jump in lower heating plate temperature has been observed. This is, to some extent, in accordance with the present theoretical results that the critical wave number increases rapidly.

4 Concluding Remarks

Sine and Gaussian functions were used for simulating the fluids with a large variation in apparent specific heat. By using the linear stability theory, the critical Rayleigh number and critical wave number were calculated for convection in an infinite horizontal fluid layer with variable specific heat. Results show that the critical Rayleigh number monotonically decreases as the amplitude b increases for either function. There is a minimum critical Rayleigh number with respect to phase angle ψ, where $\pi/2 < \psi_{op} < \pi$ for both sine and Gaussian functions and for any boundary condition. The theoretically calculated minimum critical mode is in good accordance with the experimental results in that at this point it has the maximum heat transfer coefficient. While the critical threshold is at the extreme case with respect to phase angle, the temperature and velocity perturbations are the most similar to those of the ideal fluids having constant thermal properties, and the convection mode can evolve into a different flow pattern by further increasing the phase angle thereafter, which corresponds to a rapid increase in critical wave number.

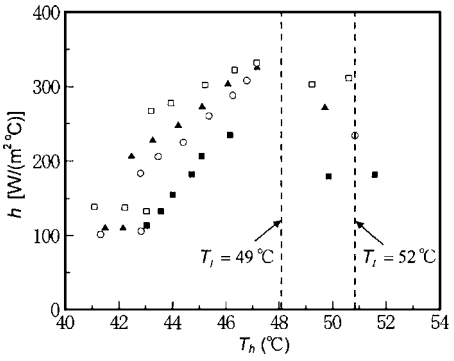

Fig. 9 Heat transfer coefficient h against the lower heating plate temperature T_h while the top cooling plate temperature T_c is fixed at 40°C. The vertical dashed lines are for the predicted temperatures at which a maximum heat transfer coefficient can be obtained. The data are from Inaba et al. [12]. The mass concentrations of the various PCM slurries are 30% (□), the amplitude b is approximately 1.688; 20%(▲), 10% (○), and 5% (■).

Acknowledgment

The project is sponsored by the Scientific Research Foundation for the Returned Overseas Chinese Scholars, State Education Ministry.

Nomenclature

A = constant defined in Eq. (2.17)
b = amplitude of nondimensionalized specific heat
c = curve fitting constant defined in Eq. (2.16)
C_m = mass concentration
C_p = specific heat, J/kg K
D = differentiation operator,
d = thickness of fluid layer, m
f = function symbol defined in Eq. (2.17)
g = gravitational constant, m/s^2
h = heat transfer coefficient, W/m^2 K
k, k_x, k_y = wave number, wave number vector in x and y direction, respectively
$\vec{k}$ = unit vector in z direction
N = mesh number
Nu = Nusselt number, $Nu = hd/\lambda$
P_*, p_*, p'_* = dimensional stationary, dynamic, and perturbed pressure, respectively, N/m^2
Pr = Prandtl number, $Pr = \nu/\alpha$
Q = nondimensionalized specific heat, $Q = C_p(T)/C_{p0}$
Ra = Raleigh number, $Ra = \beta g(T_h - T_c)d^3/\nu\alpha$
T, T_*, T' = real temperature, temperature at thermal steady state, and perturbed, respectively, K
$\tilde{T}$ = nondimensionalized temperature at thermal steady conduction state
t = time, s
$\vec{U}_*, \vec{u}_*, \vec{u}'_*$ = dimensional stationary, dynamic, and perturbed velocity vector, respectively, m
$\vec{u}$ = normalized velocity perturbation vector, (u, v, w)
W = amplitude of normalized velocity perturbation in z direction
w = normalized velocity perturbation in z direction
x, x_0 = dependent parameter and fitting constant, respectively, defined in Eq. (2.17)
z_*, z = dimensional and normalized coordinate in vertical direction, respectively

Greek

Δ_1 = Laplacian operator, $= \partial^2/\partial x^2 + \partial^2/\partial y^2$
∇ = vector operator, $\nabla = \vec{i}\partial/\partial x + \vec{j}\partial/\partial y + \vec{k}\partial/\partial z$
Θ = amplitude of nondimensionalized temperature perturbation
α = thermal diffusivity, m^2/s
β = volumetric expansion coefficient, l/K
γ = temperature gradient, K/m
λ = thermal conductivity, W/m K
ν = kinematic viscosity, m^2/s
θ = nondimensionalized temperature perturbation
ρ = density, kg/m^3
σ = growth rate of time
τ = nondimensionalized time
ω = curve fitting constant defined in Eq. (2.17)
ψ = phase angle, $\psi = (T_h - T_s)/(T_l - T_s)\pi$

Subscripts

0 = at reference temperature
$*$ = dimensional
c = upper cooling plate
cr = critical
h = lower heating plate
l = refer to PCM change completely into liquid
op = refer to the optimum convective mode
s = refer to PCM start to melting

References

[1] Booker, J. R., 1976, "Thermal Convection with Strongly Temperature-Dependent Viscosity," J. Fluid Mech., **76**, pp. 741–754.
[2] Stengel, K. C., Oliver, D. S., and Booker, J. R., 1982, "Onset of Convection in a Variable-Viscosity Fluid," J. Fluid Mech., **120**, pp. 411–431.
[3] Richer, F. M., Nataf, H. C., and Daly, S. F., 1983, "Heat Transfer and Horizontally Averaged Temperature of Convection With Large Viscosity Variations," J. Fluid Mech., **129**, pp. 173–192.
[4] Lu, J. W., and Chen, F., 1995, "Onset of Double-Diffusive Convection of Unidirectionally Solidifying Binary Solution with Variable Viscosity," J. Cryst. Growth, **149**, pp. 131–140.
[5] Char, M. I., and Chen, C. C., 1997, "Onset of Stationary Bénard-Marangoni Convection in a Fluid Layer with Variable Surface Tension and Viscosity," J. Phys. D, **30**, pp. 3286–3295.
[6] Goel, M., Roy, S. K., and Sengupta, S., 1994, "Laminar Forced Convection Heat Transfer in Microcapsulated Phase Change Material Suspensions," Int. J. Heat Mass Transfer, **37**(4), pp. 593–604.
[7] Inaba, H., Kim, M. J., and Horibe, A., 2004, "Melting Heat Transfer Characteristics of Microencapsulated Phase Change Material Slurries With Plural Microcapsules Having Different Diameters," ASME J. Heat Transfer, **126**(4), pp. 558–565.
[8] Inaba, H., 2000, "New Challenge in Advanced Thermal Energy Transportation Using Functionally Thermal Fluids," Int. J. Therm. Sci., **39**, pp. 991–1003.
[9] Naterer, G. F., *Heat Transfer in Single and Multiphase Systems*, CRC Press, Boca Raton, Chap. 5.
[10] Roy, S. K., and Sengupta, S., 1991, "An Evaluation of Phase Change Microcapsules for Use in Enhanced Heat Transfer Fluids, " Int. Commun. Heat Mass Transfer, **18**, pp. 495–507.
[11] Bo, H., Gustafsson, E. M., and Setterwall, F., 1999, "Tetradecane and Hexadecane Binary Mixtures as Phase Change Materials (PCMs) for Cool Storage in District Cooling Systems, " Energy, **24**, pp. 1015–1028.
[12] Inaba, H., Dai, C., and Horibe, A., 2003, "Natural Convection Heat Transfer of Microemulsion Phase-Change-Material Slurry in Rectangular Cavities Heated from Below and Cooled from Above, " Int. J. Heat Mass Transfer, **46**, pp. 4427–4438.
[13] Dai, C., 2003, "Natural Convection Heat Transfer and Heat Storage in Horizontal Rectangular Enclosures Filled With Microemulsion Phase Change Material Slurry, " Ph.D. thesis, Okayama University, Okayama, Japan.
[14] Selak, R., and Lebon, G., 1997, "Rayleigh-Marangoni Thermoconvective Instability With Non-Boussinesq Correction," Int. J. Heat Mass Transfer, **40**, pp. 785–798.
[15] Chandrasekhar, S., 1961, *Hydrodynamic and Hydromagnetic Stability*, Oxford University Press, UK.
[16] Gene, H. G., and James, M. O., 1992, *Scientific Computing and Differential Equations: An Introduction to Numerical Methods*, Cambridge University Press, Cambridge, UK.

Exchanger Performance Behavior Through Irreversibility Analysis for 1-2 TEMA G Heat Exchangers[1]

Ramesh K. Shah
e-mail: shahrk@asme.org
Subros Limited,
Noida, UP, India 201304

Teodor Skiepko
e-mail: tskiepko@pb.bialystok.pl
Department of Mechanical Engineering,
Bialystok Technical University,
Wiejska 45C, 15-351 Bialystok, Poland

*The objective of this paper is to illustrate, discuss, and explain the interrelationship between the temperature difference irreversibility and heat exchanger effectiveness to clarify the performance trends of exchangers with some complex flow arrangements. This is because there is no physical explanation provided for the following results presented by Shah and Skiepko (ASME J. Heat Transfer, **126**, pp. 994–1002, 2004): the heat exchanger effectiveness can be maximum, having an intermediate value or minimum at the maximum irreversibility operating point depending upon the flow arrangement of two fluids; similarly, the heat exchanger effectiveness can be minimum or maximum at the minimum irreversibility operating point. The analysis of such complex performance behavior is presented in this paper with an example of overall parallelflow and counterflow 1-2 TEMA G exchangers. This is accomplished by the decomposition of complex flow arrangements into simple subexchangers, and then the overall irreversibility trends for the exchangers are explained by irreversibilities produced due to temperature difference and fluid mixing in component subexchangers. It is shown for 1-2 TEMA G exchangers that the temperature difference irreversibility for a pure parallelflow subexchanger passes through a maximum at finite value of NTU_1, and then approaches 0 when $NTU_1 \rightarrow \infty$. On the contrary, the irreversibility for a pure counterflow subexchanger attains a minimum value at finite NTU_1 and then increases with NTU_1 and approaches maximum at $NTU_1 \rightarrow \infty$ for 1–2 TEMA G exchangers. This is because the temperatures at the inlet of the subexchangers are variable and dependent on the exit temperatures from the preceding subexchangers. Detailed exchanger effectivenesses and temperature ratios are presented as a function of NTU_1 for the explanation.* [DOI: 10.1115/1.2098827]

1 Introduction

Most of the published works on irreversibility analysis refer to estimation, presentation, and analysis of the overall irreversibilities for a heat exchanger under study. The flow arrangements taken into considerations have been rather quite simple, i.e., counterflow and parallelflow, as in Refs. [1–5] or in a few studies more complex [4,6], where the authors focus attention on the description of the overall irreversibility behavior. Kmecko [7] conducted a detailed analysis of 1–2 TEMA G and H exchangers with overall parallelflow, and 1–2 TEMA J and 1–4 TEMA J exchangers. He presented the exchanger total irreversibility in terms of $N_s = S^*/S^*_{\max}$ versus NTU_1, the segment (subexchanger) heat transfer rates, and hot and cold fluid temperature distributions. Kmecko's work is one of the most comprehensive works reported on the exchanger performance behavior. However, he did not determine the subexchanger irreversibilities and relating them to subexchanger overall effectivenesses as is done in this paper.

When comparing a variety of heat exchanger flow arrangements, lower irreversibility in a heat exchanger yields higher exchanger effectiveness for specified values of NTU, C^*, and the inlet temperature difference $(T_{h,i} - T_{c,i})$. This can be explained by a simple argument as follows. Finite temperature difference between heat exchanging fluids (within the exchanger of given NTU) is required to drive heat transfer. Efficiency of such heat transfer process, i.e., heat exchanger effectiveness, is estimated based on the 1st law. On the other hand, because heat flows at finite temperature difference, the process is inherently irreversible and its efficiency can be measured by the level of irreversibility produced within the exchanger, which is estimated based on the 2nd law. From this point of view, the reversible heat transfer process appears to be the most efficient and thus creates the upper limit for the effectiveness. Hence, one can expect higher effectiveness at lower irreversibility (and vice versa) for specified values of NTU, C^*, and $(T_{h,i} - T_{c,i})$, and the significance of irreversibility analysis for heat exchangers results from this interrelation.

The above simple trend may not be found in many heat exchangers with complex flow arrangements. The heat exchanger effectiveness may increase, then decrease and/or then increase/decrease asymptotically as one increases NTU from 0 to infinity. Similarly, the irreversibility versus NTU curves can have more than one maximum. In general, depending on the exchanger flow arrangement, the heat exchanger effectiveness can be maximum, having an intermediate value or minimum at the maximum irreversibility operating point depending on the flow arrangement; similarly, the heat exchanger effectiveness can be minimum or maximum at the minimum irreversibility operating point. These trends were summarized systematically for 18 different flow arrangements and explained the P_1-NTU_1, temperature cross and irreversibility $S^*/S^*_{\max}$ versus NTU_1 behaviors for these flow arrangements. However, no physical explanation or reasoning was provided for such behaviors. It is the subject of this paper to explain why we get such complicated performance behavior with exchangers of complex flow arrangement through an example of 1–2 TEMA G exchangers. This exchanger is divided into subexchangers having parallelflow and counterflow arrangements, and it is shown that the inlet temperature difference for different subexchangers is different depending on the performance of the preced-

[1]This paper is an updated version of the original paper: R. K. Shah and T. Skiepko, On the Relationship between Exchanger Effectiveness and Irreversibility for Complex Flow Arrangements, Paper No. HMT-2004-C127, Proc. ISHMT-ASME Heat and Mass Transfer Conference, Kalpakkam, India, 2004.

Contributed by the Heat Transfer Division of ASME for publication in the JOURNAL OF HEAT TRANSFER. Manuscript received February 27, 2004; final manuscript received June 22, 2005. Assoc. Editor: N. K. Anand.

ing subexchangers. This in turn results in complicated P_1-NTU_1 behavior. With an explanation of these unusual trends in the P_1-NTU_1, it should be clear why a variety of trends in P_1-NTU_1 can occur with many different flow arrangements discussed by Shah and Skiepko [6]. The present paper provides essentially new information on irreversibility for heat exchangers complex flow arrangements. On contrary to the former published papers [1–5], in this paper, we provide an explanation of unusual irreversibility versus NTU behavior that cannot be explained for a heat exchanger having various combinations of parallelflow and counterflow subexchangers.

We also wish to emphasize the application of irreversibility analysis into practical design of heat exchangers of complex flow arrangements with another viewpoint. A disadvantage of complex arrangements is reverse heat transfer that may occur within such exchangers [8]. We will call it an *internal temperature cross* (ITC) and beyond that point along the flow length $T_c > T_h$, and reverse heat transfer takes place (original cold fluid transferring heat to the original hot fluid). Hence, a designer has great practical interest in detection of the reverse heat transfer and thus avoids wasteful use of heat transfer surface if it can be managed. Based on the 1st law analysis, one can find the starting point of reverse heat transfer by the solution of differential energy transfer equations in terms of temperature distributions of both the fluids. Hence, finding the ITC for a heat exchanger with complex flow arrangement under consideration is not an easy task. However, if the irreversibility analysis is applied, the temperature cross phenomena can be easy detected [6] due to the peculiar behavior of irreversibility versus NTU (thermal size) curve going through minimum in between two maximum peaks due to reverse heat transfer in the exchanger.

The exchanger effectiveness definition and resultant formulas are derived based on assumption that the viscous fluid friction effects are negligible. Hence, we will evaluate $\dot{S}_{\rm irr}$ only due to heat transfer at finite temperature differences considering the fluids as pure simple single-phase compressible substances.

Our objectives in this paper are:

(1) to explain the overall irreversibility trends of complex flow arrangements of 1–2 TEMA G exchanger by irreversibilities produced in component subexchangers due to temperature difference or fluid mixing,
(2) to show that due to variable inlet temperatures, the dependency of irreversibility behavior on NTU_1 can be essentially different for a subexchanger of a complex flow arrangement when compared to such behavior of a standalone exchanger having the same flow arrangement (e.g., a counterflow exchanger),
(3) to explain the overall heat exchanger performance of complex flow arrangements by component performances, and
(4) to illustrate and discuss interrelationship between the overall exchanger and subexchanger behaviors with respect to temperature difference irreversibility and heat exchanger effectiveness.

We will present the analysis for two sets of flow arrangements: 1–2 TEMA G exchangers having both overall parallelflow and counterflow arrangements. Since these exchangers are made up of counterflow and parallelflow subexchangers, first we will summarize the irreversibility results for single-pass (standalone) parallelflow and counterflow exchangers, followed by those for the 1–2 TEMA G exchangers.

2 Single-Pass Counterflow and Parallelflow Exchangers

For heat exchangers with complex flow arrangements, we study their temperature difference irreversibility behavior considering them made of simple fundamental flow arrangements, i.e., counterflow and parallelflow. Hence, at first we illustrate here, as shown in Fig. 1, the temperature difference irreversibility, temperature effectiveness, and ratio of the outlet fluid temperatures for exchangers with these fundamental flow arrangements as a reference for further considerations. Refer to Shah and Skiepko [6] for the appropriate equations.

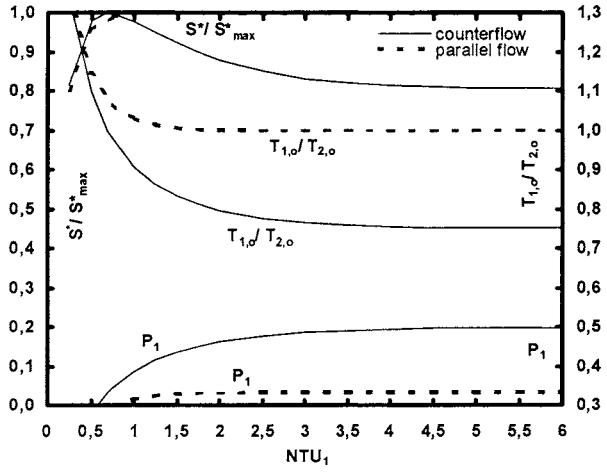

Fig. 1 Normalized temperature difference irreversibility $S^*/S^*_{\rm max}$, temperature effectiveness P_1 and ratio of the outlet fluid temperatures $T_{1,o}/T_{2,o}$ versus NTU_1 for pure counterflow and parallelflow arrangements, determined for $\vartheta=2$ at $R_1=2$

For standalone (single-pass) counterflow and parallelflow exchangers, we illustrate in Fig. 1 the normalized entropy generation rate $S^*/S^*_{\rm max}$ (where $S^*=\dot{S}_{\rm irr}/C_{\rm min}$) as a function of NTU_1. As NTU_1 increases for the counterflow, $S^*/S^*_{\rm max}$ passes through a maximum at finite values of NTU_1. In contrast, the curve $S^*/S^*_{\rm max}$ asymptotically approaches maximum at $NTU_1=\infty$ for the parallelflow exchanger. To explain why the maximums appear, let us consider a heat exchanger at any value of R_1 with inlet temperatures of two fluids specified. At $NTU_1=0$, the surface area of any heat exchanger approaches zero, and results in $dq=0$, hence, $\dot{S}_{\rm irr}=0$. Thus, increasing NTU_1 above zero must always increase in $\dot{S}_{\rm irr}$ because accordingly to the 2nd law of thermodynamics, $\dot{S}_{\rm irr}$ cannot be negative. This increase in $\dot{S}_{\rm irr}$ cannot continue to infinity as NTU_1 increases because $\dot{S}_{\rm irr}$ has a finite upper bound attainable for the case of two contiguous systems exchanging heat at spatially constant temperatures equal the inlet temperatures of the fluids for a heat exchanger. Such an upper limit for $\dot{S}_{\rm irr}$ is not attainable for a real heat exchanger because the fluid temperature difference (T_h-T_c) throughout the exchanger will be less than $(T_{h,i}-T_{c,i})$. As NTU_1 approaches infinity, the behavior of $\dot{S}_{\rm irr}$ becomes dependent on how fluid temperatures can differ, and $\dot{S}_{\rm irr}$ can be zero or a minimum value for all exchangers except for a parallelflow exchanger for which the initial increase is asymptotically continued to a maximum value. As an example, for a special case of the pure counterflow exchanger with $R_1=1$, the temperature difference (T_h-T_c) tends to zero throughout heat exchanger as $NTU_1\to\infty$ and $\dot{S}_{\rm irr}$ approaches zero. Hence, a non-negative function $\dot{S}_{\rm irr}$ possessing always a finite upper bound and with two minimum values (at $NTU_1=0$ and ∞) must have at least one maximum in between. In turn, existance of the maximum for the standalone heat exchanger is an intrinsic behavior of the temperature difference irreversibility function and it is the direct consequence of the 2nd law of thermodynamics. Existence of this maximum

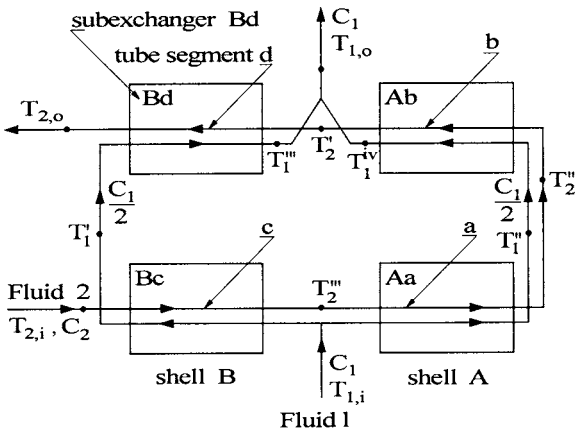

Fig. 2 Flow configuration for 1–2 TEMA G exchanger with overall parallelflow; two subexchangers have parallelflow (Aa and Ab) and the other two (Bc and Bd) have counterflow passes

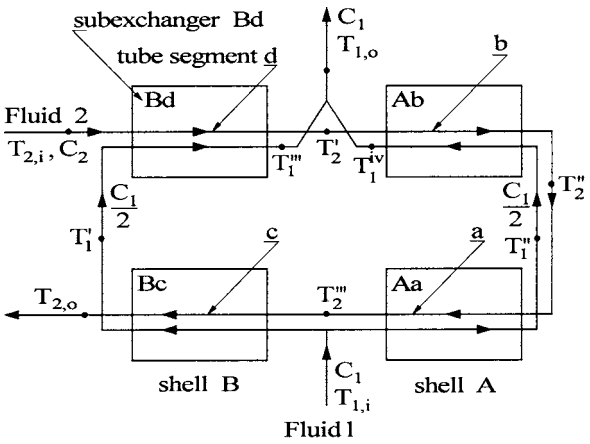

Fig. 3 Flow configuration for 1–2 TEMA G exchanger with overall counterflow; two subexchangers have parallelflow and the other two have counterflow passes

has been proven mathematically by Shah and Skiepko [6] where it is also shown that $T_{1,o}=T_{2,o}$ when $\dot{S}_{\rm irr}$ is at the maximum.

Hence, we have also shown the curves for the outlet temperature ratio $T_{1,o}/T_{2,o}$ in Fig. 1. When this ratio is unity (i.e., $T_{1,o}=T_{2,o}$), it represents the temperature cross (abbreviated as the TC) phenomenon at the exchanger outlet for the defined flow arrangements. Thus, for the counterflow, the TC occurs at a finite value of NTU_1, for $R_1=1$ at $\mathrm{NTU}_1=1$, and roughly at about 0.7 for the case $R_1=2$. However, for the parallelflow, the TC occurs when $\mathrm{NTU}_1 \rightarrow \infty$. Note also in Fig. 1 that maximum in $S^*/S^*_{\max}$ occurs at the TC point. The temperature effectiveness P_1 increases with an increase in NTU_1, approaching $P_1=0.5$ for the counterflow and $P_1=0.333$ for the parallelflow at $\mathrm{NTU}_1 \rightarrow \infty$ when $R_1=2$.

The results mentioned above are valid for specified constant inlet temperatures ($T_{h,i}$ and $T_{c,i}$) for standalone counterflow and parallelflow exchangers. In the exchangers to be discussed (overall parallelflow and counterflow 1–2 TEMA G exchangers), the subexchangers have counterflow and parallelflow passes, they are connected in series and the inlet temperatures of second and subsequent passes are a function of the exchanger total NTU_1 (i.e., they are not constant as in a standalone exchanger). It has been shown later in this paper that because of this variability in inlet temperatures, the performance and irreversibility behavior of a heat exchanger operating as an element of a complex flow system are different than the trends normally expected for standalone operating counterflow and parallelflow exchangers. This will be the key for explanation of the performance behavior of the 1–2 TEMA G exchangers. Hence, the results presented in the paper can be applied to heat exchanger design as well as minimization of irreversibility with appropriate operating NTU.

3 1–2 TEMA G Exchangers

In this section, we will provide a detailed analysis for two flow configurations for this exchanger: overall parallelflow and overall counterflow as shown in Figs. 2 and 3, respectively. In the case when overall flows are coupled in parallel configuration, one gets parallelflow 1–2 TEMA G, as in Fig. 2, where both fluids flow parallel from the bottom to the top (see the direction of two fluids in right most two parallel lines going from the exchanger Aa to Ab). If the overall flows are in opposite directions, we term this arrangement as counterflow 1–2 TEMA G as in Fig. 3.

3.1 Subexchanger Irreversibility for 1–2 TEMA G Exchanger with Overall Parallelflow. To derive expression of entropy generation rate, we assume the steady state operation of two-fluid exchanger having heat transfer only between fluids. Thus, based on entropy transport equation [2], one gets entropy generation rate as

$$\dot{S}_{\rm irr}=\dot{m}_1(s_{1,o}-s_{1,i})+\dot{m}_2(s_{2,o}-s_{2,i}) \tag{1}$$

We take into consideration only entropy generation rate or irreversibility rate due to single-phase heat transfer at finite temperature difference. Hence, for any flow arrangement, Eq. (1) can be expressed in terms of terminal temperatures and heat capacity rates as given by Shah and Sekulić [8]

$$\dot{S}_{\rm irr}=C_1\ln\frac{T_{1,o}}{T_{1,i}}+C_2\ln\frac{T_{2,o}}{T_{2,i}} \tag{2}$$

As shown in Fig. 2, the shell fluid 1 divides into two flow paths of ideally equal flow length and flow area. Hence, we will rewrite the first term on the right-hand side of Eq. (2) expressing temperature ratios $T_{1,o}/T_{1,i}$ and $T_{2,o}/T_{2,i}$ in terms of the inlet and outlet temperatures from the subexchangers as follows (see Fig. 2 for various temperatures)

$$\dot{S}_{\rm irr}=\frac{C_1}{2}\ln\frac{T_{1,o}}{T_{1,i}}+\frac{C_1}{2}\ln\frac{T_{1,o}}{T_{1,i}}+C_2\ln\frac{T_{2,o}}{T_{2,i}}=\frac{C_1}{2}\ln\left(\frac{T_{1,o}}{T_{1,i}}\frac{T_1'}{T_1'}\frac{T_1'''}{T_1'''}\right)+\frac{C_1}{2}\ln\left(\frac{T_{1,o}}{T_{1,i}}\frac{T_1''}{T_1''}\frac{T_1^{iv}}{T_1^{iv}}\right)+C_2\ln\left(\frac{T_{2,o}}{T_{2,i}}\frac{T_2'}{T_2'}\frac{T_2''}{T_2''}\frac{T_2'''}{T_2'''}\right) \tag{3}$$

Then using expressions equivalent to Eq. (1), subexchanger irreversibilities based on Eq. (2) are given by

$$\dot{S}_{\mathrm{irr}} = \underbrace{\frac{C_1}{2}\ln\left(\frac{T_1''}{T_{1,i}}\right) + C_2\ln\left(\frac{T_2''}{T_2'''}\right)}_{\dot{S}_{\mathrm{irr,Aa}}} + \underbrace{\frac{C_1}{2}\ln\left(\frac{T_1^{iv}}{T_1''}\right) + C_2\ln\left(\frac{T_2'}{T_2''}\right)}_{\dot{S}_{\mathrm{irr,Ab}}} + \underbrace{\frac{C_1}{2}\ln\left(\frac{T_1'}{T_{1,i}}\right) + C_2\ln\left(\frac{T_2'''}{T_{2,i}}\right)}_{\dot{S}_{\mathrm{irr,Bc}}} + \underbrace{\frac{C_1}{2}\ln\left(\frac{T_1'''}{T_1'}\right) + C_2\ln\left(\frac{T_{2,o}}{T_2'}\right)}_{\dot{S}_{\mathrm{irr,Bd}}} + \underbrace{\frac{C_1}{2}\ln\left(\frac{T_{1,o}}{T_1'''}\right) + \frac{C_1}{2}\ln\left(\frac{T_{1,o}}{T_1^{iv}}\right)}_{\dot{S}_{\mathrm{irr,mixing}}} \tag{4}$$

Thus the exchanger irreversibility is related to subexchanger irreversibilities as follows:

$$\dot{S}_{\mathrm{irr}} = \dot{S}_{\mathrm{irr,Aa}} + \dot{S}_{\mathrm{irr,Ab}} + \dot{S}_{\mathrm{irr,Bc}} + \dot{S}_{\mathrm{irr,Bd}} + \dot{S}_{\mathrm{irr,mixing}} \tag{5}$$

Note that the last term in this equation is due to mixing of two fluid 1 streams in the outlet header. Also, the exchanger effectiveness can be presented in terms of effectivenesses of particular subexchangers as follows:

$$\varepsilon = \frac{q}{q_{\max}} = \frac{\varepsilon_{\mathrm{Aa}} q_{\max,\mathrm{Aa}} + \varepsilon_{\mathrm{Ab}} q_{\max,\mathrm{Ab}} + \varepsilon_{\mathrm{Bc}} q_{\max,\mathrm{Bc}} + \varepsilon_{\mathrm{Bd}} q_{\max,\mathrm{Bd}}}{q_{\max}} \tag{6}$$

Equation (6) can be represented by

$$\varepsilon = \varepsilon_{\mathrm{Aa}} \underbrace{\frac{q_{\max,\mathrm{Aa}}}{q_{\max}}}_{f_{\mathrm{Aa}}} + \varepsilon_{\mathrm{Ab}} \underbrace{\frac{q_{\max,\mathrm{Ab}}}{q_{\max}}}_{f_{\mathrm{Ab}}} + \varepsilon_{\mathrm{Bc}} \underbrace{\frac{q_{\max,\mathrm{Bc}}}{q_{\max}}}_{f_{\mathrm{Bc}}} + \varepsilon_{\mathrm{Bd}} \underbrace{\frac{q_{\max,\mathrm{Bd}}}{q_{\max}}}_{f_{\mathrm{Bd}}} \tag{7}$$

Finally, we get the effectiveness of Eq. (6) as

$$\varepsilon = \varepsilon_{\mathrm{Aa}} f_{\mathrm{Aa}} + \varepsilon_{\mathrm{Ab}} f_{\mathrm{Ab}} + \varepsilon_{\mathrm{Bc}} f_{\mathrm{Bc}} + \varepsilon_{\mathrm{Bd}} f_{\mathrm{Bd}} \tag{8}$$

Thus, the overall exchanger effectiveness can be presented in terms of the subexchanger effectivenesses. Equation (8) can be interpreted differently as follows. Each term on the right-hand side ($\varepsilon_j f_j$) represents the ratio of actual heat transfer q_j in each subexchanger divided by $q_{\max} = C_{\min}(T_{1,i} - T_{2,i})$ for the overall exchanger.

We also define for later use the ratio of actual heat transfer rate in a subexchanger to that in the overall heat exchanger, designated as $X_{\varepsilon,j}$, and also relate it to $\varepsilon_j f_j$ as follows:

$$X_{\varepsilon,j} = \frac{q_{\text{sub-ex}}}{q_{\mathrm{ex}}} = \frac{\varepsilon_j f_j}{\varepsilon} \tag{9}$$

where subexchanger effectivenesses ε_j and multipliers f_j are defined by Eqs. (7) and (8). We express now ratio $X_{\varepsilon,j}$ in terms temperature effectiveness P_1 of fluid 1 as follows:

$$X_{\varepsilon,j} = \frac{q_{\text{sub-ex}}}{q_{\mathrm{ex}}} = \frac{\varepsilon_j f_j}{\varepsilon} = \frac{P_{1,j} R_{1,j} f_j}{P_1 R_1} = \frac{P_{1,j}(R_{1,j}/R_1) f_j}{P_1} = X_{P_{1,j}} \tag{10}$$

and thus $X_{\varepsilon,j} = X_{P_{1,j}}$. Note that $\Sigma_j X_{\varepsilon,j} = 1$, hence $\Sigma_j X_{P_{1,j}} = 1$ and we have used interchangeable the symbols $X_{\varepsilon,j}$ and $X_{P_{1,j}}$ where appropriate in the paper. Also note that $R_{1,j}/R_1 = 1/2$.

3.2 Subexchanger Irreversibility for 1–2 TEMA G Exchanger With Overall Counterflow. Now we analyze the case of Fig. 3. Equations (2) and (3) are the same for this case also. Using the appropriate temperatures from Fig. 3, Eq. (4) of the previous case will change as follows for this case:

$$\dot{S}_{\mathrm{irr}} = \underbrace{\frac{C_1}{2}\ln\left(\frac{T_1''}{T_{1,i}}\right) + C_2\ln\left(\frac{T_2'''}{T_2''}\right)}_{\dot{S}_{\mathrm{irr,Aa}}} + \underbrace{\frac{C_1}{2}\ln\left(\frac{T_1^{iv}}{T_1''}\right) + C_2\ln\left(\frac{T_2''}{T_2'}\right)}_{\dot{S}_{\mathrm{irr,Ab}}} + \underbrace{\frac{C_1}{2}\ln\left(\frac{T_1'}{T_{1,i}}\right) + C_2\ln\left(\frac{T_{2,o}}{T_2''''}\right)}_{\dot{S}_{\mathrm{irr,Bc}}} + \underbrace{\frac{C_1}{2}\ln\left(\frac{T_1'''}{T_1'}\right) + C_2\ln\left(\frac{T_2'}{T_{2,i}}\right)}_{\dot{S}_{\mathrm{irr,Bd}}} + \underbrace{\frac{C_1}{2}\ln\left(\frac{T_{1,o}}{T_1'''}\right) + \frac{C_1}{2}\ln\left(\frac{T_{1,o}}{T_1^{iv}}\right)}_{\dot{S}_{\mathrm{irr,mixing}}} \tag{11}$$

Finally entropy generation is represented by

$$\dot{S}_{\mathrm{irr}} = \dot{S}_{\mathrm{irr,Aa}} + \dot{S}_{\mathrm{irr,Ab}} + \dot{S}_{\mathrm{irr,Bc}} + \dot{S}_{\mathrm{irr,Bd}} + \dot{S}_{\mathrm{irr,mixing}} \tag{12}$$

Again note that the last term in this equation is the irreversibility due to mixing of two fluid 1 streams of different temperatures in the outlet header. As will be shown next, the mixing irreversibility for 1–2 TEMA G exchangers is small and negligible compared to the total irreversibility. The exchanger overall effectiveness relates to the subexchanger effectivenesses by Eq. (8) except that the values of ε_j and f_j (where the subscript j denotes the appropriate subscripts of ε and f of Eq. (8)) will be different from those for the overall parallelflow arrangement.

4 Irreversibility and Exchanger Effectiveness for 1–2 TEMA G Exchanger With Overall Parallelflow

The subexchanger and total exchanger dimensionless irreversibilities $S^*_{\text{sub-ex}}$ and S^*_{tot} for overall parallelflow 1-2 TEMA G exchanger are shown in Fig. 4 for a specific case of $\vartheta = 2.0$ and $R_1 = 2.0$. Contributions $X_{\varepsilon,j}$ of particular subexchangers to the overall exchanger ε are presented in Fig. 5. The ratios of temperatures at each end of four subexchangers are shown in Fig. 6.

The following observations for irreversibility trends for the overall parallelflow arrangement of 1–2 TEMA G exchanger can be made from Fig. 4 along with the results of Figs. 5 and 6.

- The overall irreversibility S^* increases with NTU_1, reaches maximum ($S^*_{\max} = 0.146$) at $\mathrm{NTU}_1 = 1.31$, and then starts decreasing with increasing values of NTU_1. The decrease in S^* with increasing NTU_1 is quite slower than that for a standalone counterflow exchanger shown in Fig. 1. For example at $\mathrm{NTU}_1 = 3$, the value of $S^*/S^*_{\max}$ is 0.834 and 0.979 for a standalone counterflow exchanger and 1–2 TEMA G exchanger with overall parallelflow, respectively. The reason for the slower decrease in S^* with an increase in NTU_1 will be clear after the subexchanger irreversibilities discussion.
- The irreversibility associated with the counterflow subex-

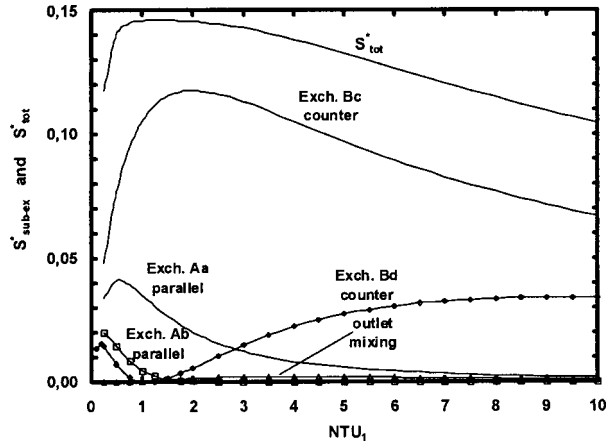

Fig. 4 S^*_{subex} and S^*_{tot}, as a function of NTU$_1$ for a 1–2 TEMA G with overall parallelflow exchanger determined for $\vartheta=2.0$ at $R_1=2$

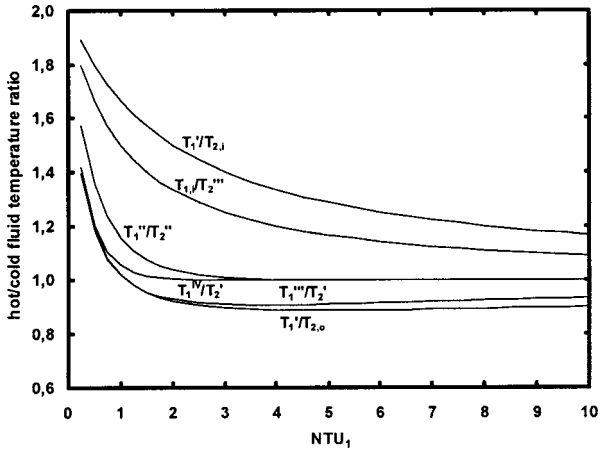

Fig. 6 Hot-to-cold fluid temperature ratios at the inlet and outlet of subexchangers as a function of NTU$_1$ for a 1–2 TEMA G with overall parallelflow determined for $\vartheta=2.0$ at $R_1=2$

changer Bc is the main contributor to the total irreversibility (see Fig. 4) and has the same trends with NTU$_1$ as the total irreversibility as well as that of a standalone single-pass counterflow exchanger (this last trend shown in Fig. 1) since both fluids from outside enter this subexchanger as in a standalone exchanger.

- The irreversibility S^* associated with the parallelflow subexchanger Aa is similar to that for a parallelflow exchanger for NTU$_1$ from 0 to about 0.5 (note that the subexchanger Aa has $R_1=1$ and should be compared only qualitatively with that in Fig. 1 having $R_1=2$). However, the temperature T_2''' of fluid 2 (see Fig. 2) coming out from the preceding counterflow subexchanger Bc continues to increase with NTU$_1$ (see the inverse value T_1/T_2''' in Fig. 6); the temperature difference $(T_{1,i}-T_2''')$ at the entrance of a parallelflow subexchanger Aa reduces with increasing exchanger NTU$_1$ from a maximum value at NTU$_1=0$; note that in general T_2''' is assumed to be constant when one performs irreversibility analysis for a standalone single-pass parallelflow exchanger, see, e.g., Refs. [8,9]. The lower is the inlet temperature difference, lower will be the subexchanger irreversibility, as is the case with increasing NTU$_1$. This temperature difference effect is stronger because the preceding subexchanger is a counterflow exchanger, hence, overpowers the initial major contribution to the irreversibility by increasing the surface area from zero (NTU$_1=0$) to a finite value for a parallelflow subexchanger. Thus for the particular case considered in Fig. 4 ($\vartheta=2.0, R_1=2.0$), the contribution of irreversibility by the subexchanger Aa continues to decrease with an increase in NTU$_1$ for NTU$_1$ greater than about 0.5 reaching zero value at NTU$_1\to\infty$.
- The subexchanger Ab is also a parallelflow exchanger, and its irreversibility contribution is very similar to that for the preceding subexchanger Aa, except that the inlet temperature difference is smaller to start with, and hence, its irreversibility contribution is also smaller as found in Fig. 4.
- The irreversibility behavior associated with the counterflow subexchanger Bd is somewhat unexpected. The expected behavior for a counterflow exchanger is that $\dot{S}_{irr}$ (or S^*/S^*_{max}) should first increase, reach a maximum value, and then start decreasing with a further increase in NTU$_1$ (e.g., see Fig. 1). In the present case, initially it behaves as expected: it starts increasing as shown in Fig. 4 and reaches a maximum at NTU$_1\approx 0.20$, and then decreases. The unexpected behavior refers to further variability of S^*_{bd} with increasing NTU$_1$ values so that it reaches a zero value at NTU$_1=1$, and then starts to increase approaching a maximum value at NTU$_1\to\infty$. When one reviews $T_1'/T_{2,o}$ (one-end temperature ratio of the exchanger) and T_1'''/T_2' (the other end temperature ratio) versus NTU$_1$ curves (the two bottom curves) in Fig. 6, it starts from about 1.42 at NTU$_1=0.25$ to 0.90–0.93 value as NTU$_1$ approaches a large value. Thus one can see that there is a temperature cross point (the aforementioned temperature ratio as unity) at NTU$_1$ of 1.12 of a special kind, having the ratio of temperatures at either end of this subexchanger equals unity simultaneously with q and S^* equal to zero, thus not contributing in the exchanger heat transfer. Beyond NTU$_1=1.12$, reverse heat transfer takes place with larger values of NTU$_1$. Thus increasing NTU$_1$, the temperature difference between the shell and tube fluid (at either end of the subexchanger) changes from positive to zero to a negative value. This in turn provides a peculiar performance behavior as shown in Fig. 5. When we add up the four subexchanger irreversibilities and the irreversibility due to mixing at outlet of fluid 1, we end up with the overall exchanger irreversibility curve S^*_{tot} versus NTU$_1$ shown in Fig. 4.
- Note that the outlet mixing irreversibility is negligibly small for smaller values of NTU$_1$ in the range $1\leqslant \text{NTU}_1\leqslant 2$. With

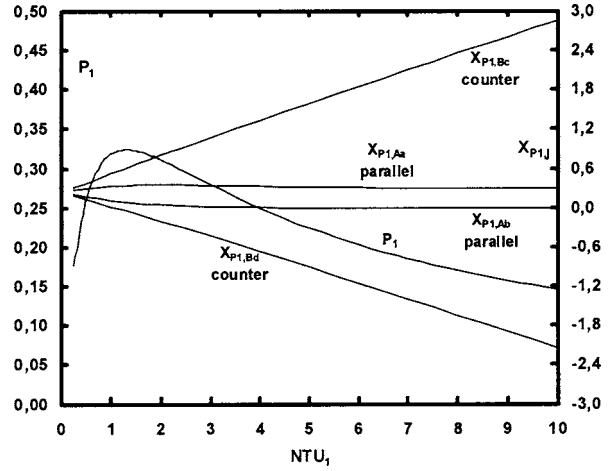

Fig. 5 Temperature effectiveness P_1 and contribution of particular subexchangers $X_{\varepsilon,j}$ in overall effectiveness ε as a function of NTU$_1$ for a 1–2 TEMA G with overall parallelflow for $\vartheta=2.0$ at $R_1=2$

increasing NTU_1, the mixing irreversibility increases, passes through maximum at $NTU_1 \approx 3.5$, and then asymptotically decreases to 0 at $NTU_1 \to \infty$. Note also in Fig. 4 that when $NTU_1 \geqslant 2$, the mixing irreversibility becomes higher than the temperature difference irreversibility for parallelflow subexchanger Ab.

Reviewing Fig. 5, the temperature effectiveness P_1 of the 1-2 TEMA G exchanger with overall parallelflow increases with NTU_1, reaches a maximum value at $NTU_1 = 1.31$ and starts decreasing with a further increase in NTU_1. Thus this flow arrangement has both S^*_{max} (see in Fig. 4) and P_{max} at the same NTU_1; and S^*_{min} and P_{min} (note that $P_{min} = 0$ if $R_1 = 2$) occur at $NTU_1 = \infty$. Contributions of the subexchanger heat transfer rate $X_{\varepsilon,j}$ (a ratio of the actual heat transfer rate by a subexchanger to that for the overall exchanger) in the overall exchanger effectiveness P_1 (see in Eq. (10)) are shown also in Fig. 5 to explain this peculiar behavior of $P_1 - NTU_1$ curve. As it can be observed in Fig. 5, two subexchangers of counterflow arrangement (Bc and Bd) have the most impact on the overall effectiveness and heat transfer; one contributes positive heat transfer and the other negative heat transfer for $NTU_1 > 1$. The subexchanger Aa of parallelflow arrangement contributes positive to P_1 but only slightly compared to the former counterflow subexchangers. The contribution of the subexchanger Ab is negligible. The surface area of the subexchanger Ab is practically wasted with no heat transfer beyond $NTU_1 = 1$. Summation of contributions by four subexchangers indicates this particular exchanger ($R_1 = 2$) has reasonable heat transfer rate (effectiveness) between NTU_1 of 1 and 2. When $NTU_1 \to \infty$, the overall effectiveness becomes 0 because contributions of Bc and Bd are then balanced but with opposite signs and contributions of Aa and Ab become 0.

Our results discussed above for the S^*_{tot}, $X_{\varepsilon,j}$ and the temperature ratios (Figs. 4–6) agree perfectly with those of Kmecko [6]. However, he did not present irreversibilities produced in particular subexchangers (what is shown here in Fig. 4). As we did with the discussion of Fig. 4, the behavior of the overall S^*_{tot} can be explained clearly by reviewing and adding up the subexchanger irreversibilities.

It should be emphasized that the review of Fig. 4 alone would indicate that the subexchanger Bc works very inefficiently compared to the subexchanger Bd because of a larger value of S^*/S^*_{max}. However, the results shown in Fig. 5 contradict this false conclusion. One can see in Fig. 5 that the truth is indeed opposite since subexchanger Bc contributes the most positive in the overall effectiveness (consequently in positive (from initially hot to cold fluid) heat transfer) and Bd provides negative (reverse heat transfer) contribution in overall effectiveness for $NTU_1 > 1$. This discrepancy between S^*/S^*_{max} and the effectiveness can be easily understood if one takes into account that in reality S^*/S^*_{max} is dependent on value of the finite temperature difference between the two fluids. Simply, a heat exchanger is inherently an irreversible device irrespectively of what heat flow direction may occur inside between initially hot and cold fluid—it generates entropy because it is forced to work at finite temperature difference. Hence, for a given NTU_1 value, one can see in Fig. 6 for subexchanger Bd (counterflow) that both the terminal temperature ratios $T'_1/T_{2,o}$ and T'''_1/T'_2 (initially hot to cold fluid) are bound in between approx. 0.9 and 1 for $NTU_1 > 1$. At the same time, the corresponding temperature ratios for subexchanger Bc (counterflow) are on overall essentially bigger. In turn, the fluid temperatures in Bd are different insignificantly (by approximately 10%) and the fluid temperatures in Bc are different essentially. In turn, subexchanger Bd must produce smaller irreversibility than Bc although it can be seen in Fig. 6 that simultaneously Bd yields reverse heat transfer. This fact can be explained also if in parallel with Fig. 4 one uses the actual temperature distributions of both the fluids and corresponding heat transfer rates presented in Ref. [8]. Hence, it must be emphasized that one needs information from both the first law (P_1, $X_{\varepsilon,j}$, q_j, terminal temperature ratios and temperature distributions) and from second law (irreversibility for both overall and subexchangers) to correctly interpret interrelation between heat exchanger entropy generation and the heat exchanger effectiveness. And overall entropy generation in a heat exchanger has the meaning for a system analysis.

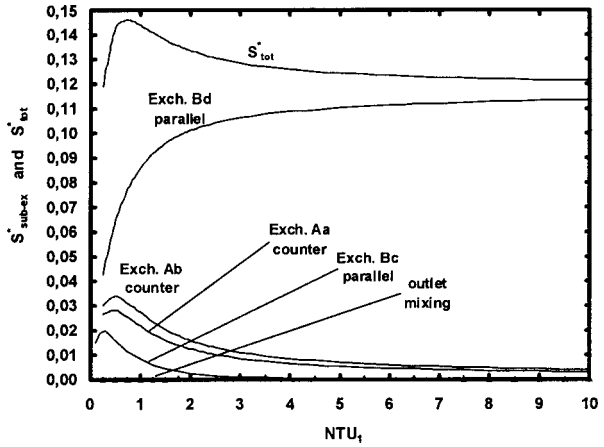

Fig. 7 $S^* = S_{irr}/C_{min}$, **as a function of** NTU_1 **for a 1–2 TEMA G with overall counterflow exchanger determined for** $\vartheta = 2.0$ **at** $R_1 = 2$

5 Irreversibility and Exchanger Effectiveness for 1–2 TEMA G Exchanger With Overall Counterflow

The subexchanger and total exchanger dimensionless irreversibilities S^*_{sub} and S^*_{tot} for this flow arrangement of 1–2 TEMA G exchanger are shown in Fig. 7 for a specific case of $\vartheta = 2.0$ and $R_1 = 2.0$. The $X_{\varepsilon,j}$ contributions to subexchanger effectivenesses ε_j are presented in Fig. 8. The ratios of temperatures at each end of four subexchangers are shown in Fig. 9. The following observations for irreversibility trends for the overall counterflow arrangement of 1–2 TEMA G exchanger can be made from Fig. 7 along with the results of Figs. 8 and 9. In this case, none of the subexchangers (shown in Fig. 3) represents the performance of a standalone exchanger because both fluids from outside do not enter directly in any subexchanger.

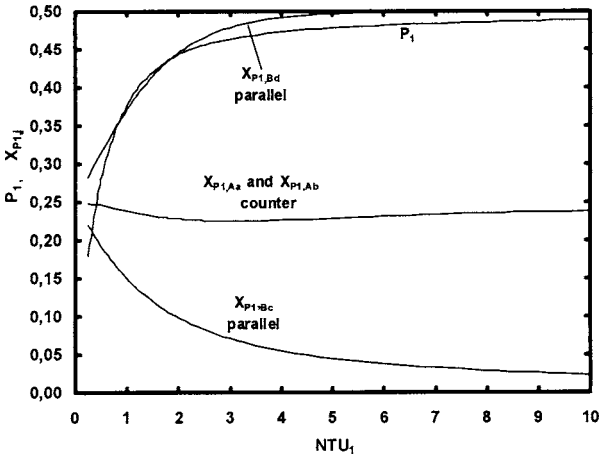

Fig. 8 Temperature effectiveness P_1 **and contribution of particular subexchangers** $X_{\varepsilon,j}$ **in overall effectiveness** ε **as a function of** NTU_1 **for a 1–2 TEMA G with overall counterflow determined for** $\vartheta = 2.0$ **at** $R_1 = 2$

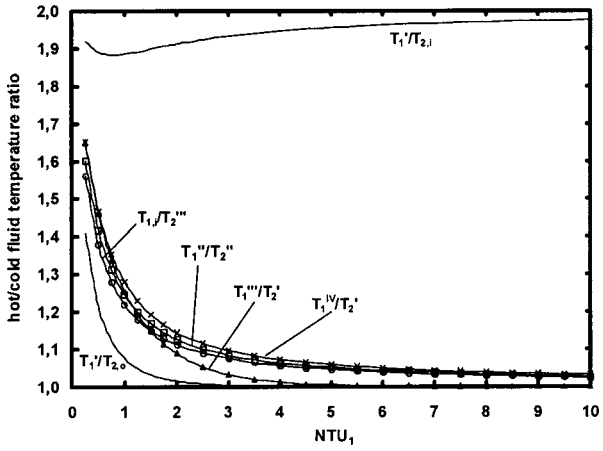

Fig. 9 Hot-to-cold fluid temperature ratios at the inlet and outlet of subexchangers as a function of NTU_1 for a 1–2 TEMA G with overall counterflow determined for $\vartheta=2.0$ at $R_1=2$

The exchanger total irreversibility S^* increases with NTU_1, reaches a maximum value at $NTU_1=0.72$, and then starts decreasing with increasing values of NTU_1, first fast and then slowly (see Fig. 7) reaching an asymptotic value higher than that for the previous case of the same exchanger with overall parallelflow (compare with Fig. 4). The reason for the slower decrease with an increase in NTU_1 will be clear after we discuss the subexchanger irreversibilities.

- The irreversibility associated with the parallelflow subexchanger Bd is the main contributor to the total irreversibility (see Fig. 7) and has similar trends with NTU_1 as that of a standalone single-pass parallelflow exchanger (this last trend shown in Fig. 1). This is because fluid 2 enters from outside (considering it as a cold fluid) and fluid 1 has experienced some temperature loss (considering it as a hot fluid) while flowing through sub-exchanger Bc (see Fig. 3), and represents almost highest inlet temperature difference ($T_h - T_c$) of the four subexchangers. The irreversibility increases asymptotically to a maximum value at $NTU_1=\infty$ for this parallelflow subexchanger.
- The lowest irreversibility of all subexchangers is produced in the subexchanger Bc of parallelflow arrangement. The trend for this case is unusual. It starts with zero at $NTU_1=0$, and then, as shown in Fig. 7, continues to increase, reaching maximum at $NTU_1=0.31$ and then decreases approaching 0 at $NTU_1\rightarrow\infty$. Such maximum S^* never occurs at finite value of NTU_1 or zero at$NTU_1\rightarrow\infty$ for a standalone parallelflow exchanger—see the trends in Fig. 1. When one compares values of $T_1'/T_{2,o}$ (one end temperature ratio of the subexchanger) with values of $T_{1,i}/T_2'''$ (the other end temperature ratio) in Fig. 9, it can be seen that the curves approach each other for values of $NTU_1<0.5$. Hence, the irreversibility can attain a maximum in this region without the TC because both end temperature ratios are simultaneously greater than 1. This is in turn a peculiar behavior of irreversibility for a parallelflow heat exchanger operating as an element of a complex flow arrangement.
- The subexchangers Aa and Ab are counterflow, and the irreversibility trends in Fig. 7 are similar to that for a counterflow exchanger except the magnitudes are low due to smaller inlet temperature differences. Note in Fig. 9 that the one end temperature ratio T_1^{iv}/T_2' for subexchanger Ab is higher than that $T_{1,i}/T_2'''$ for the subexchanger Aa while the other end temperature ratio T_1''/T_2'' is the same for both the subexchangers. Thus the subexchanger Ab has slightly higher irreversibility than that for the subexchanger Aa.
- Note that the contribution of irreversibility due to mixing of fluid 1 of two branches at the exchanger outlet is negligible for the complete range of NTU_1, at least one order of magnitude less than the lowest temperature difference irreversibility produced in the parallelflow subexchanger Bc.
- Like before, the irreversibility of the overall heat exchanger is the sum of the irreversibilities of four subexchangers and the irreversibility due to mixing at the outlet of fluid 1.

6 Irreversibility Comparison for 1–2 TEMA G Exchanger With Overall Parallelflow and Counterflow

A comparison of irreversibilities presented in Figs. 4 and 7 for these exchangers clearly indicates different performance behaviors for three of the four subexchangers (the fourth subexchanger Aa has similar behavior due to different reasons although the magnitudes are different). This translates into overall irreversibility behavior different for these two exchangers.

- The counterflow subexchanger Bc has the largest (controlling) irreversibility contribution for the 1–2 TEMA G exchanger with overall parallelflow (see Fig. 4). The parallelflow subexchanger Bd has the largest (controlling) irreversibility contribution for the 1–2 TEMA G exchanger with overall counterflow (see Fig. 7). Thus it is interesting to find that a counterflow subexchanger contributes the most to the irreversibility of the overall parallelflow, and just the reverse for the overall counterflow 1–2 TEMA G exchanger. Without the detailed analysis presented here, this would not have been an intuitive conclusion.
- For $1<NTU_1<6.5$, the total irreversibility for 1–2 TEMA G exchanger with overall parallelflow is larger than that for 1–2 TEMA G exchanger with overall counterflow (compare Figs. 4 and 7); and hence, we would expect lower effectiveness for overall parallelflow when compared to overall counterflow 1–2 TEMA G exchanger (compare Figs. 5 and 8).
- Above NTU_1 of about 6.5, the trends in irreversibilities and effectivenesses as a function of NTU_1 are just the opposite for these two exchangers. To explain these peculiar results, let us compare contributions of particular subexchangers in total irreversibility and overall effectiveness. For the case of overall parallelflow 1–2 TEMA G exchanger, the main contribution to the overall irreversibility is provided by subexchanger Bc of counterflow arrangement. As shown in Fig. 4, it behaves as a standalone counterflow heat exchanger with clear maximum and asymptotically decreasing irreversibility to 0 as $NTU_1\rightarrow\infty$. The other subexchangers for this flow arrangement contribute also decreasingly as well as the mixing (see for Aa and Ab, and mixing in Fig. 4). Note also that contribution of Bd approaches asymptotically a constant value as $NTU_1\rightarrow\infty$. Adding up all the irreversibilities for 1–2 TEMA G of parallelflow must result in decreasing trend when $NTU_1\rightarrow\infty$. The opposite situation is for overall counterflow 1–2 TEMA G exchanger in Fig. 7. Here, despite the overall flow as countercurrent, the main contributor in the irreversibility is subexchanger Bd of parallelflow arrangement that behaves as a standalone parallelflow with asymptotically increasing irreversibility to a maximum value at $NTU_1=\infty$. Because the effect of counterpart subexchangers Aa, Ab, and Bc is non-negligible only at small NTU_1 values where some maximums are present, and the mixing affects negligibly, the overall irreversibility after passing an initial maximum, goes asymptotically to a minimum of nonzero value when $NTU_1\rightarrow\infty$, as in Fig. 7. Regarding the overall effectivenesses, note in Fig. 5 that the main contributors in the overall effectiveness for the overall parallelflow 1–2 TEMA G are counterflow Bc (with positive contribution) and counterflow Bd (with negative contribution) subexchangers. When $NTU_1\rightarrow\infty$, the resultant overall effective-

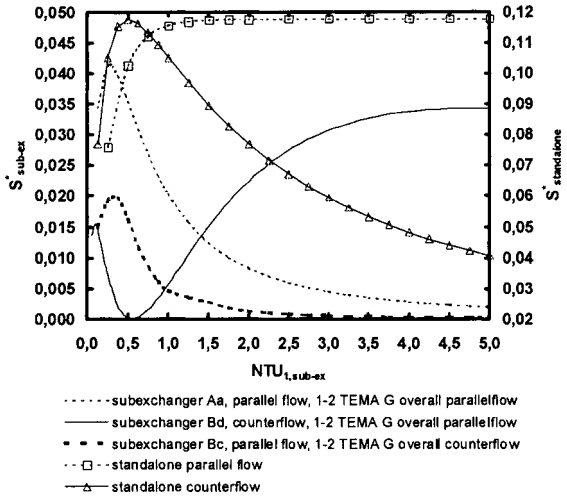

Fig. 10 Comparisons of irreversibility $S^*=S_{irr}/C_{min}$ peculiar behavior as a function of $NTU_{1,subex}$ for subexchangers operating as elements of complex flow arrangements and operating standalone for a 1–2 TEMA G with overall parallelflow and counterflow determined at $\vartheta=2.0$ at $R_1=2$

ness asymptotically approaches 0, because the other subexchangers (namely Aa and Ab) contribute insignificantly. The opposite picture is for the overall counterflow 1–2 TEMA G exchanger. Here, as in Fig. 8, although the overall exchanger is counterflow, the main contribution is brought about by subexchanger Bd of parallelflow arrangement. Its contribution is very similar to a standalone parallelflow exchanger for the case of $R_1=1$, i.e., asymptotically increases to a constant value of 0.5 with increase in $NTU_1\rightarrow\infty$. Because contributions of counterflow subexchangers Aa and Ab (both positive) go to a constant value (approximately 0.25) and contribution of the other parallelflow Bc decreases (also positive) asymptotically to 0, then the resultant effect is such that the effectiveness of overall counterflow 1–2 TEMA G exchanger increases up to 0.5 when $NTU_1\rightarrow\infty$, see in Fig. 8.

- At NTU_1 of about 1.31, the 1–2 TEMA G exchanger with overall parallelflow (see Fig. 2) has the maximum effectiveness of 0.32 (see Fig. 5), while the 1–2 TEMA G exchanger with overall counterflow (see Fig. 3) has the maximum effectiveness of about 0.5 at NTU_1 approaching infinity, as shown in Fig. 8.

7 Concluding Remarks

In a previous paper [6], for 18 different flow arrangements we have summarized systematically the extrema in the overall heat exchanger effectiveness and the overall irreversibility due to heat transfer at finite temperature difference and fluid mixing. In this paper, we analyzed and explained such complex behaviors by analyzing subexchangers of the 1-2 TEMA G exchangers with overall parallelflow and counterflow arrangements. To perform the study we have determined the subexchanger irreversibilities and related them to subexchanger effectivenesses.

We have shown the unusual irreversibility behavior for these heat exchangers because the dependency of the irreversibility on NTU_1 for a pure counterflow or parallelflow standalone heat exchanger is essentially different when compared to such behavior of the exchanger having the same flow arrangement and operating as an element of a heat exchanger of a complex flow arrangement. In open literature, this peculiar behavior is the first time noted in this paper and, hence, is shown in Sec. 7 and summarized in Fig. 10.

We have shown in Fig. 10 that the temperature difference irreversibility for a pure parallelflow subexchanger can pass through a maximum at finite NTU_1, and then approaches 0 when $NTU_1\rightarrow\infty$. On the contrary, the irreversibility for a pure counterflow subexchanger passes through a minimum at finite NTU_1 and then goes to maximum when $NTU_1\rightarrow\infty$. This is because the fluid inlet temperatures to subexchangers are changing with NTU_1 while they are considered constant in a standalone exchanger. Thus we demonstrated that the irreversibility curves for classical flow arrangements may not be applicable to study irreversibility behavior for complex flow arrangements. Regarding the overall exchanger effectiveness for complex flow arrangement under study, we explained the corresponding trends by component subexchanger performances. It appears from the analysis that pure counterflow subexchangers when operating in a complex flow arrangement can have significantly worse performance while pure parallelflow ones can improve the exchanger performance of complex flow arrangements.

It should be emphasized that in principle one may decompose readily a given complex flow arrangement into the elemental units. However, irreversibility analysis of complex flow arrangements cannot be done using the results obtained for subsequent elemental subexchangers when operating standalone. The only correct way to get readily the final results is to follow the approach presented in this paper that disregarding standalone behavior takes into account individual subexchanger flow arrangements and how the subexchangers are connected and what are consequences of the coupling for irreversibility and effectiveness behavior.

Acknowledgment

The authors are grateful to Dr. D. P. Sekulić of University of Kentucky for critically reviewing this paper and providing constructive suggestions.

Nomenclature

A = heat transfer surface area on which U is referred to, m^2

C = flow stream heat capacity rate with a subscript c or h, $\dot{m}c_p$ (where c_p is the specific heat at constant pressure), W/°C

C^* = heat capacity rate ratio, C_{min}/C_{max}, dimensionless

f_j = effectiveness multiplier for j^{th} sub-exchanger, $q_{max,j}/q_{max,ex}$, dimensionless

NTU = number of heat transfer units, $NTU=UA/C_{min}$, it represents the total number of transfer units in a multipass unit, $NTU_1=UA/C_1$, $NTU_2=UA/C_2$, dimensionless

N_s = irreversibility norm, S^*/S^*_{max}, dimensionless

P = temperature effectiveness for a fluid, $P_1=(T_{1,o}-T_{1,i})/(T_{2,i}-T_{1,i})$ for fluid 1, dimensionless

q = actual heat transfer rate in the exchanger, W

q_{max} = maximum heat transfer rate in the exchanger, $C_{min}(T_{h,i}-T_{c,i})$, W

R = heat capacity rate ratio, $R_1=C_1/C_2$, $R_2=C_2/C_1$, dimensionless

s = specific entropy, J/(kg K)

S^* = normalized entropy generation rate, $\dot{S}_{irr}/C_{min}$, dimensionless

$\dot{S}_{irr}$ = entropy generation rate, W/K

T = fluid temperature, K

TC = temperature cross at the exit of the exchanger

U = overall heat transfer coefficient, W/m^2 K

$X_{P_1,j}$ = contribution of jth subexchanger into temperature effectiveness P_1, dimensionless

$X_{\varepsilon,j}$ = contribution of jth subexchanger into overall exchanger effectiveness, $q_{\text{subex}}/q_{\text{ex}}$, dimensionless

ε = heat exchanger effectiveness, it represents an overall exchanger effectiveness for a multipass unit or for a subexchanger, dimensionless

ϑ = fluid inlet temperature ratio, $T_{1,i}/T_{2,i}$, dimensionless

Subscripts

Aa,Ab,Bc,Bd = refer to four subexchangers where A, B denote shells and a, b, c, d are tube segments as shown in Figs. 2 and 3

c = cold fluid side

cf = counterflow

ex = overall exchanger

h = hot fluid side

i = inlet to the exchanger

j = refer to jth subexchanger of four subexchangers as shown in Figs. 2 and 3

max = maximum

min = minimum

mixing = fluid mixing irreversibility

o = outlet to the exchanger when used as a second subscript with the temperature

pf = parallelflow

subex = subexchanger

tot = overall multipass exchanger irreversibility,

1 = fluid 1 (shell side); one section (inlet or outlet) of the exchanger

2 = fluid 2 (tube side); other section (outlet or inlet) of the exchanger

Superscripts

$'$, $''$, $'''$, iv = refer to Figs. 2 and 3 for fluid temperatures with these superscripts

References

[1] Bejan, A., 1977, "The Concept of Irreversibility in Heat Exchanger Design: Counterflow Heat Exchangers for Gas-to-Gas Applications," ASME J. Heat Transfer, **99**, pp. 374–380.

[2] Bejan, A., 1982, *Entropy Generation Through Heat and Fluid Flow*, Wiley, NY.

[3] Sekulić, D. P., 1986, "Entropy Generation in a Heat Exchanger," Heat Transfer Eng., **7**, pp. 83–88.

[4] Sekulić, D. P., 1990, "The Second Law Quality of Energy Transformation in a Heat Exchanger," ASME J. Heat Transfer, **112**, pp. 295–300.

[5] Hesselgreaves, J. E., 2000, "Rationalization of Second Law Analysis of Heat Exchangers," Int. J. Heat Mass Transfer, **43**, pp. 4189–4204.

[6] Shah, R. K., and Skiepko, T., 2004, "Entropy Generation Extrema and Their Relationship with Heat Exchanger Effectiveness—Number of Transfer Units Behavior for Complex Flow Arrangements," ASME J. Heat Transfer, **126**, pp. 994–1002.

[7] Kmecko, I., 1998, "Paradoxical Irreversibility of Enthalpy Exchange in Some Heat Exchangers," M.S. thesis, University of Novi Sad, Novi Sad, Yugoslavia.

[8] Shah, R. K., and Sekulić, D. P., 2003, *Fundamentals of Heat Exchanger Design*, Wiley, Hoboken, NJ.

[9] Sekulić, D. P., 1990, "A Reconsideration of the Definition of a Heat Exchanger," Int. J. Heat Mass Transfer, **33**, pp. 2748–2750.

Flow Boiling Heat Transfer of CO_2 at Low Temperatures in a Horizontal Smooth Tube

Chang Yong Park

Pega S. Hrnjak[1]
Phone: +1-217-244-6377
Fax: +1-217-333-1942
e-mail: pega@uiuc.edu

Department of Mechanical and Industrial Engineering,
University of Illinois at Urbana-Champaign,
1206 West Green Street, Urbana, Illinois 61801

Flow boiling heat transfer coefficients of CO_2 *are measured in a horizontal smooth tube with inner diameter* 6.1 mm. *The test tube is heated by a secondary fluid maintaining constant wall temperature conditions. Heat transfer coefficients are measured at evaporation temperatures of* −15 *and* −30°C, *mass flux from* 100 to 400 kg/m^2 s, *and heat flux from* 5 to 15 kW/m^2 *for qualities (vapor mass fractions) ranging from 0.1 to 0.8. The characteristics of* CO_2 *flow boiling are explained by* CO_2 *properties and flow patterns. The measured* CO_2 *heat transfer coefficients are compared to other published data. Experiments with R22 were also conducted in the same system and the results show that the heat transfer coefficients for* CO_2 *are 40 to 150% higher than for R22 at* −15°C *and low mass flux of* 200 kg/m^2 s *mostly due to the characteristics of* CO_2 *nucleate boiling. The presented* CO_2 *heat transfer coefficients indicate the reduction of heat transfer coefficient as mass flux increases at low quality regions and also show that dryout does not occur until the high quality region of 0.8, for mass fluxes of 200 and* 400 kg/m^2 s. *The Gungor and Winterton correlation gives a relatively good agreement with measured data; however it deviates more at lower evaporation temperature and high mass flux conditions.* [DOI: 10.1115/1.2098853]

1 Introduction

CO_2 has been seriously considered as an alternate refrigerant to those that raise environmental or operating concerns. Some commercial products using CO_2 as a working fluid are already on the market. As the application of CO_2 to real systems increases, accurate measurements of the flow boiling coefficient and a better understanding of the heat transfer mechanisms are required for good heat exchanger and system designs over wide ranges of operating conditions, for example, low temperature applications.

Recent studies of heat transfer in CO_2 are focused on evaporation temperatures from −4 to 25°C, which is the temperature range for air conditioners with tube inner diameters from 0.8 to 7.53 mm. Hihara and Tanaka [1], Koyama et al. [2], and Pettersen [3] measured flow boiling heat transfer coefficients for small diameter tubes of 1.0, 1.8, and 0.8 mm, respectively. Hihara and Tanaka [1] reported the heat transfer coefficients depended on heat flux but not on mass flux. Pettersen [3] presented the same relation as Hihara and Tanaka [1]. He also showed the evaporation temperature effect on the heat transfer change as the quality varied. Yun et al. [4] and Yoon et al. [5] studied a larger inner diameter tube, 6.0 and 7.53 mm, respectively. Yun et al. [4] explained the heat transfer trend with CO_2 properties and dryout effect at 5 and 10°C. Yoon et al. [5] proposed a correlation to predict the quality for the onset of dryout only for CO_2. Most of the studies concluded that the existing general correlations to predict flow boiling coefficients did not give a good agreement with their measurements. Thome and Hajal [6] released a correlation to estimate the flow boiling heat transfer coefficients only for CO_2 connected to flow patterns.

The boiling heat transfer coefficients for low evaporation temperature were measured by Bredesen et al. [7] and Høgaard Knudsen and Jensen [8]. Bredesen et al. [7] presented CO_2 boiling heat transfer coefficients in a 7.0-mm-i.d. tube for various mass fluxes, heat fluxes and evaporation temperatures of −25, −10, and 5°C. Their data showed that dryout occurred only at 5°C, and the heat transfer coefficients were almost independent of quality at −25°C. The measured results were influenced by heat flux change, whereas the effect of mass flux was minor at low evaporation temperatures. From these trends, they concluded that nucleate boiling is a more important mechanism of heat transfer for CO_2 than other refrigerants. Høgaard Knudsen and Jensen [8] measured heat transfer coefficients at −25 and −10°C. Their data also showed a similar relation between heat transfer coefficients and other parameters, which supports the former interpretation for the major contribution of nucleate boiling in flow boiling heat transfer. However, there is significant difference between the measured flow boiling heat transfer coefficients, about 40–80%, when comparing the two studies under similar test conditions. Also Bredesen et al.'s [7] data showed a wide range of the measured values for the same test conditions. Høgaard Knudsen and Jensen's [8] measurement was limited to qualities under 0.3 for low evaporation temperature, −25°C, and high mass flux, 175 kg/m^2 s.

This study is motivated by the discrepancies in the current results (Bredesen et al. show significantly higher heat transfer coefficients than Knudsen and Jensen). Additionally, this study presents the experimental verification of the superiority of flow boiling heat transfer for CO_2 versus R22 at low temperatures and a special feature of CO_2 boiling heat transfer which is the reduction of heat transfer coefficient with increasing mass flux at low quality regions.

2 Experimental Facility and Test Conditions

2.1 Experimental Facility. A schematic of the experiment facility is shown in Fig. 1. The test facility has two independent loops; one is for CO_2 and the other is for the secondary fluid, HFE7100. The CO_2 loop consists of a gear pump, mass flow meter, calorimeter, test section, control heater, receiver, and subcooler. Liquid CO_2 is pumped by the gear pump to the calorimeter. The calorimeter heats the subcooled liquid CO_2 to a desired quality at the inlet of the test section. The control heater adds heat to maintain a desired saturation temperature in the test section.

[1]Corresponding author.

Contributed by the Heat Transfer Division of ASME for publication in the JOURNAL OF HEAT TRANSFER. Manuscript received January 6, 2005; final manuscript received March 18, 2005. Review conducted by Satish G. Kandlikar.

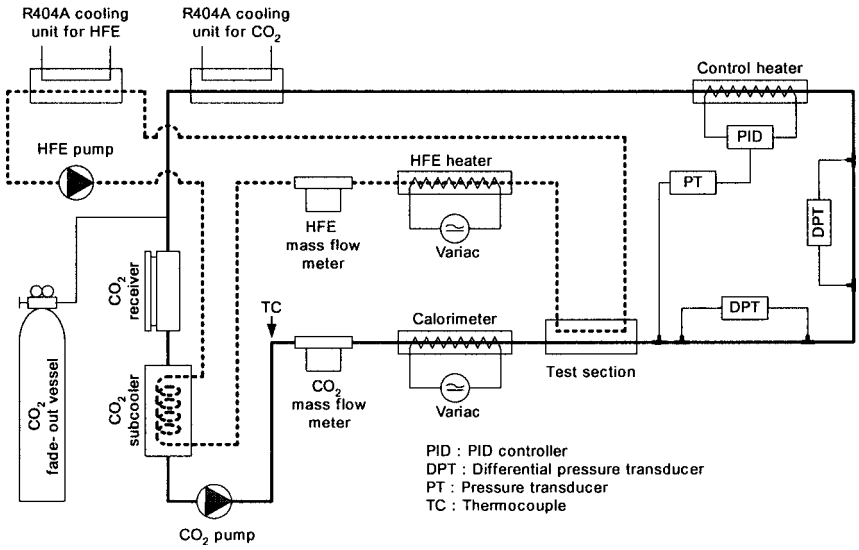

Fig. 1 Simplified schematic of the test facility

Then the CO_2 condenses in a plate heat exchanger connected to the R404A cooling unit. To avoid cavitation in the pump, the CO_2 passes through the receiver and enters the subcooler.

The other loop is for the single phase secondary fluid HFE. HFE first subcools the CO_2 in the subcooler and then adds heat in the test section. In order to perform both operations, HFE is chilled in a heat exchanger linked with the R404A cooling unit and is also heated to provide conditions for the test section.

2.2 Test Section. Figure 2 shows the test section schematically. The test section consists of the test tube, brass jacket, and tube circuit for HFE. The inside and outside diameters of the test tube are 6.1 and 9.6 mm, respectively. The test tube is made of copper with a heated length of 150 mm and the heated region is surrounded by a brass jacket which consists of two half-cylinder pieces. The secondary fluid, HFE, flows around this jacket in the tube circuit as shown in Fig. 2(*a*).

In order to provide the uniform temperature condition, two half-cylinder shaped brass pieces are located between the HFE circuit and the test tube as shown in Fig. 2(*b*). The HFE temperature glide is unified in the brass jacket. All gaps among the two brass pieces and the test tube are filled with high thermal conductivity paste to reduce the contact thermal resistance while the upper and lower parts of brass jackets are tightened with two metal band clamps. Thermocouples are placed at the top, bottom, and sides along three locations of test section. The thermocouples were attached in grooves carved on the tube surface with thin solder. The remaining portion of the grooves is filled with high thermal conductivity paste. The thermocouples are equally spaced along the axis of the test section at an interval of 50 mm starting 25 mm from the inlet of the heated section. As a result, the temperatures at 12 points on the tube surface are measured and their average values are used to calculate the heat transfer coefficient.

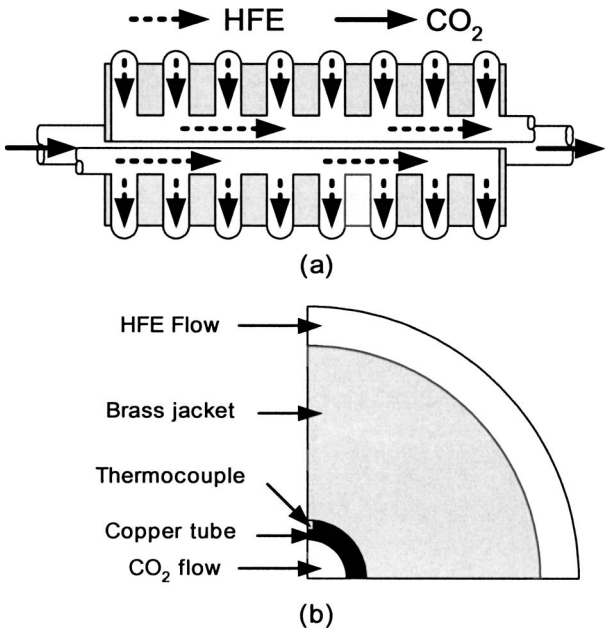

Fig. 2 Schematic of the test section

2.3 Instrumentation. T-type thermocouples with a calibrated accuracy of ±0.10°C are used to measure the refrigerant temperature and wall temperature on the test tube. The absolute pressure of CO_2 is determined by a pressure transducer with an uncertainty of ±3.4 kPa and the refrigerant mass flow rate is measured by a mass flow meter with an accuracy of ±0.1% of the reading. Electrical power inputs to the calorimeter and HFE heater are measured with watt transducers which have 0.2% reading accuracy.

2.4 Test Conditions. Flow boiling heat transfer coefficients are measured with a variation of saturation temperature, mass flux, heat flux, and quality. The evaporation temperature is set at −15 and −30°C, while the mass flux is varied at 100, 200, and 400 kg/m^2 s with the heat flux variation of 5, 10, and 15 kW/m^2. The CO_2 quality at the test section inlet is controlled from 0.1 to 0.8.

3 Data Reduction

In order to obtain an average heat transfer coefficient, the heat transfer rate to the CO_2 is determined as shown in the following

$$\dot{Q}_{CO_2} = (\dot{m}C_P)_{HFE} \cdot (T_{HFE,i} - T_{HFE,o}) + \dot{Q}_{Amb} - \dot{Q}_{Cond} \qquad (1)$$

The heat exchanged with the environment, $\dot{Q}_{Amb}$, was obtained in a calibration experiment at operating temperatures and presented as a function of the overall heat transfer coefficient of the test section and the log mean temperature difference between the HFE and the ambient air. The axially transferred conduction heat loss through the pipe, $\dot{Q}_{Cond}$, is estimated by a finite element code.

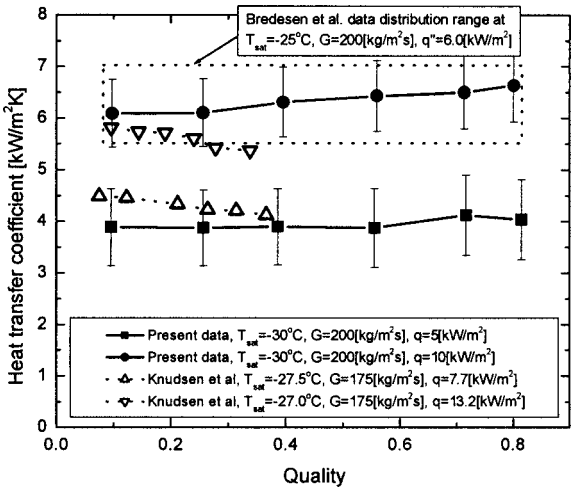

Fig. 3 Comparison of the data from this study to Bredesen et al. [7] and Knudsen and Jensen [8]

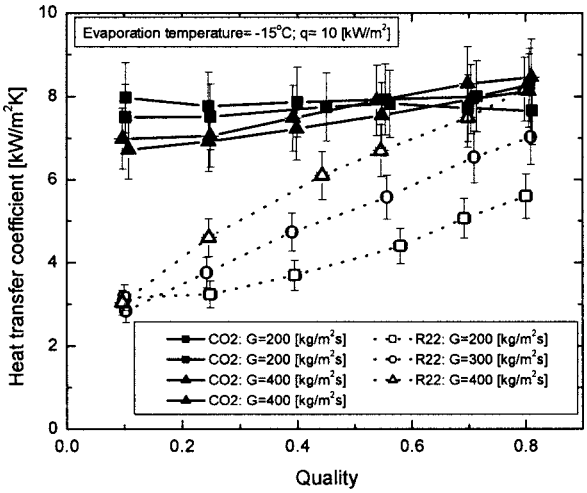

Fig. 4 Flow boiling heat transfer coefficient comparison for CO_2 and R22

As presented in Eq. (2), the average heat transfer coefficient, h, is determined from the calculated, $\dot{Q}_{CO_2}$, measured average tube wall temperature, the test tube geometry, and the CO_2 saturation temperature calculated from the measured saturation pressure. Data regression and determination of CO_2 properties are performed using Engineering Equation Solver [9] which uses the equation of state presented by Span and Wagner.

$$h = \frac{\dot{Q}_{CO_2}}{A_{surf} \cdot (T_W - T_{CO_2})} \tag{2}$$

The uncertainty of the heat transfer coefficient occurs due to the uncertainties of the independent measured parameters; temperature, pressure, mass flow, and electrical power input as shown earlier. The uncertainty propagation of heat transfer coefficient is done based on Moffat [10]. The uncertainty is within the range of 8–20% of the measured heat transfer coefficient. Each measurement uncertainty is shown as a vertical error bar in the figures.

4 Results and Discussion

4.1 Comparison With Other Data at Similar Test Conditions. Figure 3 shows the comparison of data in this study to Bredesen et al. [7] and Knudsen and Jensen [8] at similar test conditions. Knudsen and Jensen's [8] results are a little bit lower than the measured data in this study. The cause of this difference might be explained by the effect of geometry and flow rate. Knudsen and Jensen used 10 mm inside diameter tube, which is 64% larger than the tube in this study. Also mass flux is 12.5% lower. Although the effect of mass flux on CO_2 flow boiling heat transfer coefficient is known as not significant, low mass flux can cause insufficient liquid film on the upper part of tube for nucleate boiling. The other difference is that they used a stainless steel pipe in their experiment. Loebl and Kraus [11] experimentally showed that the pool boiling heat transfer of CO_2 for a stainless steel tube was about 30% less than that for a copper tube. Considering that the nucleate boiling heat transfer is the major heat transfer mechanism in CO_2 flow boiling, the use of stainless steel tube is most likely the cause of the lower heat transfer coefficient. In this study, the material of the test tube is copper.

The flow boiling heat transfer coefficients measured by Bredesen et al. [7] are higher than the determined coefficients in this study. Although the evaporation temperature in their experiment was higher than that in this study, their measured values are much larger considering the lower heat flux. Thome and Hajal [6] commented that Bredesen et al.'s [7] results were significantly larger than generally accepted correlations.

4.2 Comparison of Flow Boiling Heat Transfer Coefficients of CO_2 and R22 at Low Temperature. Figure 4 shows the heat transfer coefficient comparison for CO_2 and R22 at an evaporation temperature of $-15\,^{\circ}C$, a heat flux of 10 kW/m^2, and with a mass flux variation from 200 to 400 $kg/m^2\,s$. The presented data was obtained in the same test facility by replacing CO_2 with R22 under the same test conditions. The multiple points for the same operating conditions presented in the graph show repeatability of the measurements over a time period of several weeks. At low quality regions below 0.3, the heat transfer coefficient of CO_2 is about 100% higher than that of R22 for all mass fluxes, and as the quality and mass flux increase the improvement of the heat transfer coefficient decreases. Comparisons of the experimental R22 data with available correlations show the best agreement to Kandlikar [12] with −2.8% bias error for all measured flow boiling coefficients. Significantly higher heat transfer coefficients for CO_2, especially at low mass flux of 200 $kg/m^2\,s$, can be explained by the thermophysical properties and boiling characteristics of the two refrigerants. Since Chen [13] proposed the concept of combining the nucleate boiling and convective boiling contributions to estimate the heat transfer coefficient in flow boiling, many researchers have applied this concept to their correlations to predict the heat transfer coefficients. Generally, the nucleate boiling contribution can be calculated by the pool boiling heat transfer multiplied by a correction factor, like the correlation presented by Gungor and Winterton [14]. At an evaporation temperature of $-15\,^{\circ}C$ and heat flux of 10 kW/m^2, the calculated pool boiling coefficients with the Gorenflo [15] correlation gives 6650 and 1763 $W/m^2\,K$ for CO_2 and R22, respectively. For this calculation, standard surface roughness of 0.4 μm was applied. According to his correlation, a nucleate pool boiling coefficient is a function of heat flux, reduced pressure, and surface roughness. The difference of reduced pressure at $-15\,^{\circ}C$ (0.311 and 0.059 for CO_2 and R22, respectively) causes the higher pool boiling coefficient for CO_2 which contributes to the higher flow boiling heat transfer coefficient for CO_2.

As presented in Fig. 4, the heat transfer coefficient for CO_2 is nearly independent of vapor quality, whereas the heat transfer coefficient for R22 significantly increases as the quality and mass flux increase. This trend can be explained by the difference of the density ratio of vapor to liquid for CO_2 and R22. Convective boiling is usually enhanced by the increasing of the average ve-

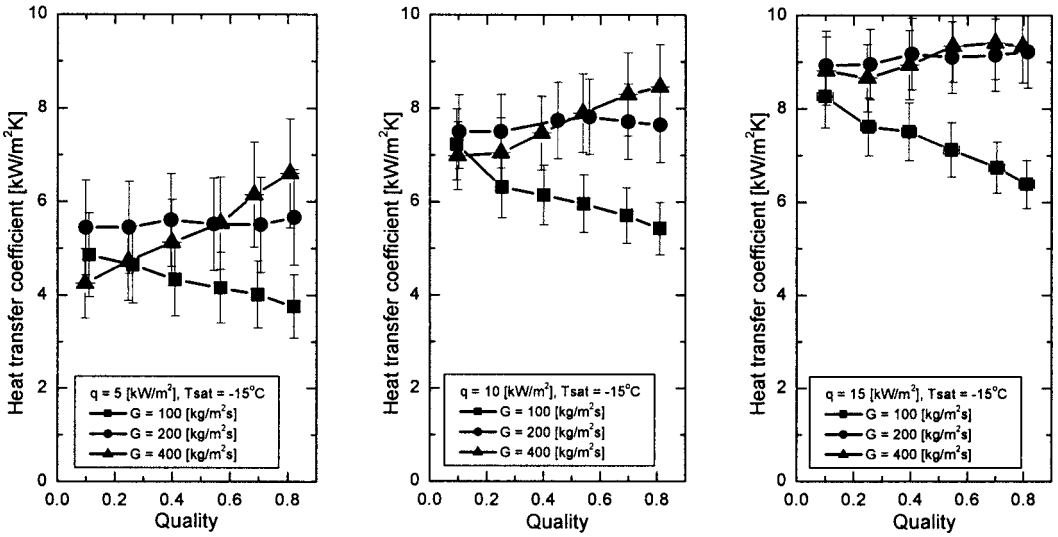

Fig. 5 Flow boiling heat transfer coefficient with respect to mass flux and heat flux at an evaporation temperature of −15°C

locities of liquid and vapor as the quality increases. As the density ratio of vapor to liquid increases, there is a smaller change in the convective boiling heat transfer coefficient as quality increases due to the smaller variation in the liquid and vapor average velocities. The density ratio of vapor to liquid for CO_2 is 0.0600, and that for R22 is 0.0097 at −15°C, which means CO_2 has about a six times larger value. Consequently, CO_2 flow boiling heat transfer coefficients are almost independent of quality due to the combination of relatively smaller change of convective heat transfer with respect to quality and high nucleate boiling values. However, CO_2 flow boiling heat transfer coefficients have a positive slope for a mass flux of 400 kg/m^2 s because of the increase of convective effect due to the increase in the mass flux.

In addition to the higher heat transfer coefficients for CO_2, another special trend for CO_2 heat transfer coefficients can be seen in Fig. 4. Generally, flow boiling heat transfer coefficients are augmented with increasing mass flux due to the enlarged convective heat transfer contribution; this behavior can be seen obviously in Fig. 4 for R22. However, heat transfer coefficients for CO_2 are lower for the higher mass flux of 400 kg/m^2 s than at 200 kg/m^2 s for low quality regions. In this study, this unexpected mass flux effect on the heat transfer coefficients was measured consistently at other test conditions for these two mass fluxes and the repeatability of this trend is shown in Fig. 4. Indication of similar mass flux effects could be seen in some data presented by Bredesen et al. [7] and Yun et al. [4], however it occurred at low qualities, less than 0.3, and the authors did not make any comment. Thome and Hajal [6] proposed a correlation predicting flow boiling heat transfer coefficients for CO_2 and they cited that the increase of mass flux does not always give a higher heat transfer coefficient based on their prediction results. These issues will be discussed later.

4.3 Effect of Mass Flux and Heat Flux on Flow Boiling Heat Transfer Coefficient. Figures 5 and 6 present the flow boiling heat transfer coefficient as the mass flux and heat flux varied at evaporation temperatures of −15 and −30°C, respectively. Unlike the heat transfer coefficients of conventional refrigerants, heat transfer coefficients for a higher mass flux, 400 kg/m^2 s, are lower than those for a lower mass flux, 200 kg/m^2 s, at low qual-

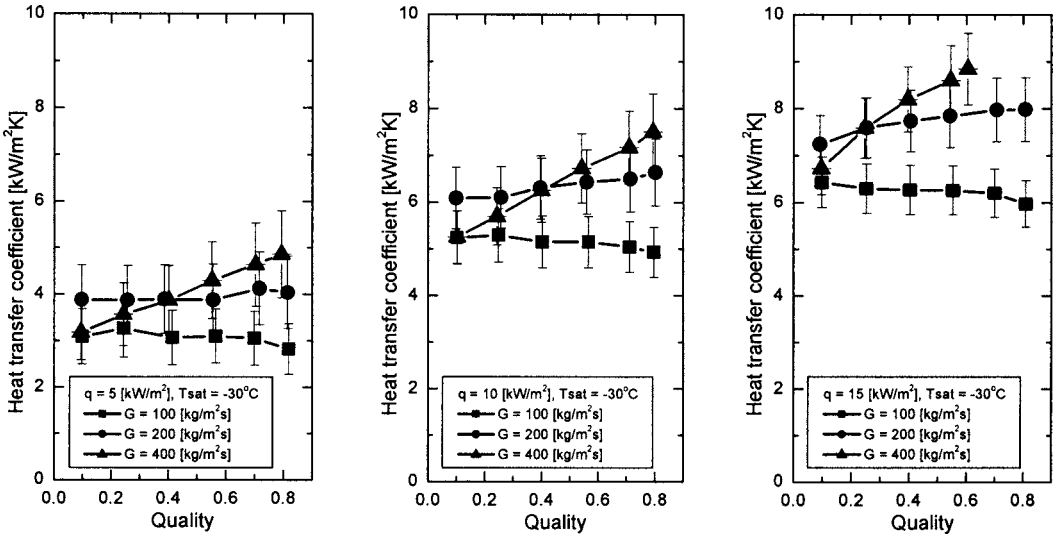

Fig. 6 Flow boiling heat transfer coefficient with respect to mass flux and heat flux at an evaporation temperature of −30°C

Table 1 Minimum heat flux to generate flow boiling based on Steiner and Taborek [16]

Mass flux [kg/m^2 s]	Evaporation Temperature −15°C	Evaporation Temperature −30°C
100	0.38 kW/m^2	0.67 kW/m^2
200	0.74 kW/m^2	1.36 kW/m^2
400	1.35 kW/m^2	2.50 kW/m^2

Table 2 Boiling suppression qualities for various test conditions based on Sato and Matsumura [19]

Evaporation Temperature [°C]	Mass flux [kg/m^2 s]	Heat flux 5 kW/m^2	Heat flux 10 kW/m^2	Heat flux 15 kW/m^2
-15	100	0.988	0.995	0.997
	200	0.961	0.982	0.988
	400	0.878	0.940	0.961
-30	100	0.945	0.988	0.992
	200	0.919	0.961	0.975
	400	0.768	0.877	0.918

ity regions. The unexpected decrease in heat transfer with increasing mass flux could be a result of a decrease in nucleate boiling due to partial obstruction of the bubble generation. This obstruction may be a consequence of the liquid and vapor dynamics which affects the thermal boundary layer needed to initiate nucleation.

However, the above-presented hypothesis will be strengthened by demonstrating that flow boiling occurs inside the test tube. Table 1 shows the minimum heat flux to generate flow boiling conditions and it can be concluded that the flow boiling occurs at all test conditions because the applied heat fluxes are above the required minimum values. The minimum heat fluxes were calculated from Eq. (3) presented by Steiner and Taborek [16] with the critical radius, $r=0.3$ μm, which is recommended for commercial tubes

$$q_{\mathrm{ONB}} = \frac{2\sigma T_{\mathrm{SAT}} h_{lo}}{r \rho_g h_{lv}} \tag{3}$$

where h_{lo} is calculated from the Gnielinski [17] correlation. Although the other properties should be considered to determine the minimum heat flux for the onset of boiling, it is obvious that the lower surface tension of a refrigerant results a lower minimum heat flux. In other words, a refrigerant with low surface tension easily boils. CO_2 has a much lower surface tension than other conventional refrigerants at low temperature; however this difference to other refrigerants gets smaller as the evaporation temperature decreases.

Jang and Hrnjak [18] visualized the flow patterns of CO_2 flowing adiabatically through a 6.1-mm-i.d. acrylic block placed after the condensing section. Visualization was performed at mass fluxes from 200 to 400 kg/m^2 s, at a saturation temperature of −15°C, and for qualities ranging from 0.1 to 0.9. In their visualization, slug flow occurred at a quality of 0.1 for mass fluxes of 200 and 400 kg/m^2 s. At a quality of 0.2, the slug flow pattern remained for a mass flux of 200 kg/m^2 s, whereas it changed to wavy flow for a mass flux of 400 kg/m^2 s. For a mass flux of 200 kg/m^2 s, wavy flow appeared at qualities of 0.3 and 0.4 and annular flow was seen after a quality of 0.5. For a mass flux of 400 kg/m^2 s, annular flow started at a quality 0.3. The interface between the liquid and the vapor for a mass flux of 400 kg/m^2 s became more unstable when it was compared with the interface for a mass flux of 200 kg/m^2 s in the quality range from 0.3 to 0.4. The instability may cause a strong interaction between the vapor bubble and the liquid in the liquid layer which could be an explanation for the obstruction of nucleation. As the quality increases, the heat transfer coefficients for a mass flux of 400 kg/m^2 s become higher than at 200 kg/m^2 s due to the increase of the convective heat transfer contribution to flow boiling heat transfer. This trend of the heat transfer coefficient is seen for both evaporation temperatures of −15 and −30°C.

For a mass flux of 200 kg/m^2 s, the visualization presented by Jang and Hrnjak [18] showed that liquid film existed on the tube wall even at high quality regions, which means that nucleate boiling heat transfer is still the major mechanism in this region. According to their visualization, a more stable interface between liquid and vapor could be seen for wavy flow for low mass flux, 200 kg/m^2 s, than that for a higher mass flux, 400 kg/m^2 s. From this visualization, it may be concluded that the boiling obstruction is not critical due to the less intense liquid and vapor dynamics, and convective boiling is not significant for the lower mass flux condition of 200 kg/m^2 s. These flow visualizations and two phase dynamics can explain the flow boiling heat transfer coefficient is nearly independent of quality.

Besides the visualization, the quality of nucleate boiling suppression can be used to prove the existence of a nucleate boiling heat transfer mechanism. The suppression quality is the quality at which nucleate boiling starts to cease due to the reduction of the temperature difference within the liquid film at a relatively high quality region. This boiling suppression is different from the partial boiling obstruction generated by liquid and vapor dynamic effects at low quality region. The nucleate boiling suppression quality is calculated by Eqs. (4) and (5) presented by Sato and Matsumura [19]

$$x_{\mathrm{sup}} = \frac{\gamma}{1+\gamma} \tag{4}$$

$$\gamma = \left(\frac{\rho_g}{\rho_l}\right)^{0.56} \left(\frac{\mu_l}{\mu_g}\right)^{0.11} \left(\frac{q'' k_l h_{lv} \rho_g}{98 \sigma T_{\mathrm{sat}} h_{lo}^2}\right)^{1.11} \tag{5}$$

Table 2 gives the boiling suppression qualities for the test conditions in this study. From the values in this table, it can be inferred that nucleate boiling occurs actively in almost every test condition because the flow boiling heat transfer coefficients are measured at qualities which are below the suppression qualities.

For a mass flux of 100 kg/m^2 s, flow boiling heat transfer coefficients have a different trend compared with those for 200 and 400 kg/m^2 s, especially for an evaporation temperature of −15°C. They are obviously lower heat transfer coefficients and show decreasing trend with respect to quality. In order to explain this trend, the flow pattern map presented by Thome and Hajal [6] was used because it shows the flow pattern for CO_2 in a 6 mm tube. According to their flow pattern map, the flow pattern for mass flux 100 kg/m^2 s is a stratified-wavy flow at every vapor quality for evaporation temperatures of −15 and −30°C. The stratified flow means that there is insufficient liquid film on the top part of tube. The insufficiency of a liquid film gets more severe as the quality increases. Under stratified flow conditions, nucleate boiling cannot be initiated on the top part of the tube wall, which results in the lower flow boiling heat transfer coefficients. Another noticeable trend of the heat transfer coefficient for 100 kg/m^2 s is the effect of the evaporation temperature.

CO_2 flow boiling heat transfer coefficients strongly depend on heat flux due to the active nucleate boiling mechanism for all test conditions. The significant effect of the heat flux is presented in Figs. 5 and 6.

4.4 Influence of Evaporation Temperature on Heat Transfer Coefficient. As shown in Figs. 5 and 6, the flow boiling heat transfer coefficients for −15°C are always higher than those for −30°C. Like in other fluids, this is mainly because the nucleate boiling heat transfer is reduced with decreasing evaporation temperature. The reduction of the nucleate boiling heat transfer is related to a decrease of the reduced pressure, which is a crucial parameter to determine the intensity of nucleate boiling in the Gorenflo [15] correlation. The reduced pressures for −15 and −30°C are 0.310 and 0.194, respectively.

The trend of the heat transfer coefficient change with respect to quality is similar for evaporation temperatures of −15 and −30°C for mass fluxes of 200 and 400 kg/m^2 s. However, for a mass flux of 100 kg/m^2 s, the reduction of the heat transfer coefficient with increasing quality is more apparent for −15 than −30°C.

Although the effect of evaporation temperature on the heat transfer is influenced by many thermophysical parameters of CO_2, surface tension could be the primary property to explain the temperature effect, especially for the liquid deficient region. For a mass flux of 100 kg/m^2 s, the flow seems to be stratified, and nucleate boiling could not occur on the top of the tube wall. CO_2 surface tension for −15°C is 70% of that for −30°C. A lower surface tension makes nucleate boiling in the liquid film occur easily, and this active nucleate boiling enhances the entrainment of liquid droplets through the mechanism of bubble bursting. Increasing the entrainment of liquid droplets helps to create dry regions on the tube wall [20]. As a result, the heat transfer coefficient decreases with increasing quality and this trend becomes more obvious for higher evaporation temperatures.

4.5 Comparison With General Correlations for Flow Boiling. Most of the correlations were generated without data for CO_2, and moreover the database, which was used to create correlations for conventional refrigerants, excluded evaporation at very low temperatures such as −30°C. Due to this limitation, some general correlations were known to underpredict the heat transfer coefficients for CO_2 [6,8]. They usually fail to evaluate the nucleate dominant mechanism in CO_2 flow boiling and the dryout effect on the heat transfer coefficient at relatively high evaporation temperatures. Recently, Thome and Hajal [6] proposed a correlation to calculate the flow boiling heat transfer coefficient for CO_2 only based on a heat transfer model linked to a flow pattern [21,22] with the correction of CO_2 nucleate boiling contribution. Based on simulation results with this model, one interesting phenomenon, the decreasing of the heat transfer coefficients with an increase in mass flux, was predicted. They insisted that an increasing in mass flux does not always result in a higher heat transfer coefficient due to the nucleation obstruction at low quality regions. The present study proves their assumption experimentally as shown in Fig. 7. However, their model overpredicts the coefficients at high quality regions, which was mentioned in their publication, and it is also unsuccessful in evaluating the effect of evaporation temperature on the heat transfer coefficient, especially for the low temperature of −30°C. Figure 8 shows the comparison of measured and predicted heat transfer coefficients with the Thome and Hajal [6] model. In this comparison, it is obvious that the deviation of the calculated coefficients becomes greater as the evaporation temperature decreases and quality increases. Their model predicts the special phenomenon of CO_2 flow boiling heat transfer; the reduction of heat transfer with increasing mass flux at low quality regions. However, it is still unable to predict the heat transfer coefficient at low evaporation temperature.

Although previous general correlations to predict flow boiling heat transfer coefficients have some obstacles, it is still valuable to apply them to predict the heat transfer coefficients for CO_2 at low evaporation temperatures because the thermophysical properties of CO_2 at this temperature range are similar to those of conventional refrigerants at their applicable temperature range, for example CO_2 at −30°C and R22 at 10°C. Table 3 presents the bias error and absolute average deviation of the predicted values with some general correlations [6,14,23–25] from the measured heat transfer coefficients in this study. Based on the results in the table, the Gungor and Winterton [14] correlation can predict the measured coefficients relatively well with a bias error and absolute average deviation of 1.7% and 14.5%, respectively. Yun et al. [4] also stated that this correlation yields good agreement with mea-

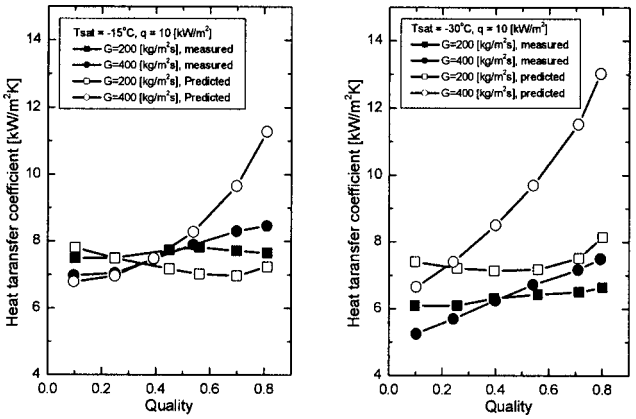

Fig. 7 Counterintuitive effect of a mass flux increase on heat transfer at low quality regions: prediction by Thome and Hajal [6] vs experimental data from this study

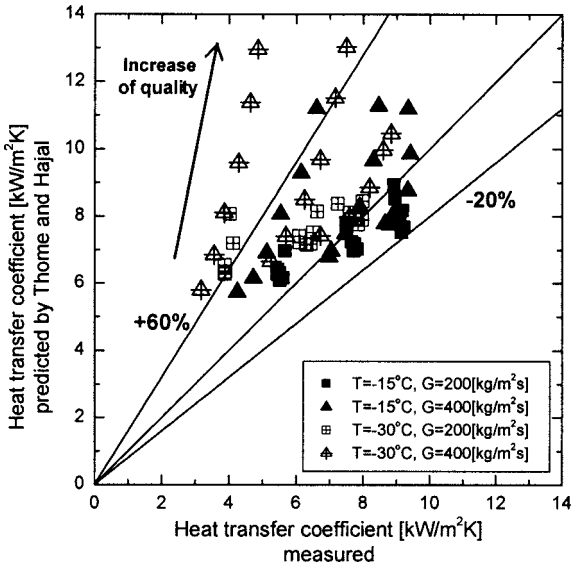

Fig. 8 Comparison of the measured and predicted heat transfer coefficients with Thome and Hajal [6] model

Table 3 Comparison of experimental data in this study with some general correlations

Correlations	Bias[a]	AAD[b]
Thome and Hajal [6]	27.0	30.9
Gungor and Winterton [14]	1.74	14.5
Gungor and Winterton [23]	–39.4	41.8
Shah [24]	–37.5	43.3
Wattelet et al. [25]	–6.15	18.4

[a]Bias error, %: $\frac{1}{N}\sum[(h_{predicted}-h_{measured})/h_{measured}]\times 100$

[b]Absolute average deviation (AAD) %: $\frac{1}{N}\sum\left|[(h_{predicted}-h_{measured})/h_{measured}]\right|\times 100$

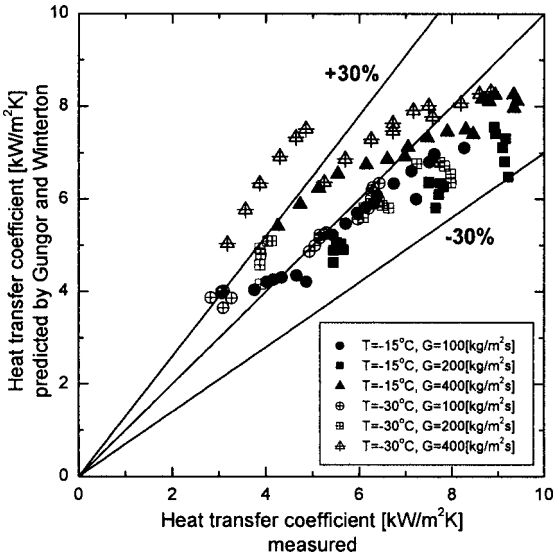

Fig. 9 Comparison of the measured and predicted heat transfer coefficients with the Gungor and Winterton [14] correlation

sured heat transfer coefficients at evaporation temperatures of 5 and 10°C for mass fluxes above 240 $kg/m^2 s$ which can make a stable annular flow as the dominant flow pattern. Also the Wattelet et al. [25] correlation gives moderate predictions with a bias error and absolute average deviation of −6.2% and 18.4%, respectively. Figure 9 shows the deviation of the Gungor and Winterton [14] prediction with respect to evaporation temperature and mass flux. In Fig. 9, the correlation tends to overpredict for a mass flux of 400 $kg/m^2 s$ and underpredict for 100 and 200 $kg/m^2 s$. This trend seems to be caused by an overestimation of the convective boiling contribution due to the fact that the convective heat transfer contribution for CO_2 is smaller than for conventional refrigerants.

5 Conclusions

The investigation of CO_2 flow boiling heat transfer coefficients is performed at low evaporation temperatures of −15 and −30°C for a horizontal tube with a variation of the mass flux, heat flux and vapor quality. The data indicate that CO_2 is a very attractive refrigerant from a heat transfer standpoint for evaporation at low temperatures. It is shown that the flow boiling heat transfer for CO_2 is much higher than that for conventional refrigerants due to the higher nucleate boiling heat transfer of CO_2 especially at a low mass flux of 200 $kg/m^2 s$ and low quality regions. The real advantage of CO_2 for low temperature applications is that dryout does not occur even at high quality regions because of the surface tension of CO_2 which is high enough to prevent dryout at low temperatures. As a result, the high heat transfer coefficient does not decrease until high quality regions.

The reduction of heat transfer coefficients with increasing mass flux in low quality regions is experimentally shown in this study. The flow boiling heat transfer coefficient at low temperature is not a strong function of mass flux due to the dominance of nucleate boiling in the heat transfer mechanism for mass fluxes of 200 and 400 $kg/m^2 s$. However, heat transfer is reduced when the mass flux is insufficient to wet the entire inner surface area of the tube at a mass flux of 100 $kg/m^2 s$. When designing the CO_2 heat exchangers for low temperature applications, the mass flux should be high enough to sufficiently wet the inside area of the tube. However, unnecessarily high mass flux does not enhance the heat transfer significantly and may even reduce it in low quality regions.

The CO_2 flow boiling heat transfer coefficient is very sensitive to heat flux whereas it is not strongly dependent on quality. Also, a decrease of evaporation temperature reduces the heat transfer coefficients for every test condition.

The Gungor and Winterton [14], and Wattelet et al. [25] correlations predict the heat transfer coefficients with relatively small deviation from measured values. However, the correlations need improvement, especially for lower temperature and high mass flux conditions.

Acknowledgments

This study is supported by Air-Conditioning and Refrigeration Center (Project 183) at University of Illinois at Urbana-Champaign. The authors are grateful to Wolverine Tube Co. for their support in building the facility and 3M Company for support in secondary refrigerant supply.

Nomenclature

A = area (m^2)
C_P = specific heat (J/kg K)
G = mass flux ($kg/m^2 s$)
h = heat transfer coefficient ($W/m^2 K$)
h_{lo} = heat transfer coefficient for only liquid flow ($W/m^2 K$)
h_{lv} = latent heat of vaporization (J/kg)
k = thermal conductivity (W/m K)
$\dot{m}$ = mass flow rate (kg/s)
N = number of data points
q = heat flux (W/m^2)
$\dot{Q}$ = heat transfer rate (W)
T = temperature (°C or K)

Greek symbols

γ = dimensionless number
μ = dynamic viscosity ($N s/m^2$)
ρ = density (kg/m^3)
σ = surface tension (N/m)

Subscripts

Amb = ambience
Cond = conduction
g = vapor
HFE = secondary fluid, HFE
i = inlet
l = liquid
o = outlet
ONB = onset of nucleate boiling
sat = saturation
sup = suppression
surf = surface
W = wall

References

[1] Hihara, E., and Tanaka, S., 2000, "Boiling Heat Transfer of Carbon Dioxide in Horizontal Tubes," *Proceedings of the Fourth IIR-Gustav Lorenzen Conference on Natural Working Fluids*, Purdue University, pp. 279–284.
[2] Koyama, S., Kuwahara, K., Shinmura, E., and Ikeda, S., 2001, "Experimental Study on Flow Boiling of Carbon Dioxide in a Horizontal Small Diameter Tube," *IIR Commission B1 Meeting*, Paderborn, Germany.
[3] Pettersen, J., 2004, "Flow Boiling of CO_2 in Microchannel Tubes," Exp. Therm. Fluid Sci., **28**, pp. 111–121.
[4] Yun, R., Kim, Y., Kim, M. S., and Choi, Y., 2003, "Boiling Heat Transfer and Dryout Phenomenon of CO_2 in a Horizontal Smooth Tube," Int. J. Heat Mass Transfer, **46**, pp. 2353–2361.
[5] Yoon, S. H., Cho, E. S., Hwang, Y. W., Kim, M. S., Min, K., and Kim, Y., 2004, "Characteristics of Evaporative Heat Transfer and Pressure Drop of Carbon Dioxide and Correlation Development," Int. J. Refrig., **27**, pp. 111–119.
[6] Thome, J. R., and Hajal, J. E., 2004, "Flow Boiling Heat Transfer to Carbon Dioxide: General Prediction Method," Int. J. Refrig., **27**, pp. 294–301.
[7] Bredesen, A. M., Hafner, A., Pettersen, J., Neksa, P., and Aflekt, P. K., 1997,

"Heat Transfer and Pressure Drop for In-tube Evaporation of CO_2," *Proceedings of the Internatioanl Conference on Heat Transfer Issues in Natural Refrigerants*, University of Maryland, pp. 1–15.
[8] Høgaard Knudsen, H. J., and Jensen, P. H., 1997, "Heat Transfer Coefficient for Boiling Carbon Dioxide," *Proceedings of the International R&D on Heat Pump, Air Conditioning and Refrigeration Systems*, Gatlinburg, Tennessee, pp. 113–122.
[9] Klein, S. A., 2004, Engineering Equation Solver, F-Chart Software, V7.205.
[10] Moffat, R. J., 1988, "Describing the Uncertainties in Experimental Results," Exp. Therm. Fluid Sci., **1**, pp. 3–17.
[11] Loebl, S., and Kraus, W. E., 2004, "Pool Boiling Heat Transfer of Carbon Dioxide on a Horizontal Tube," *Proceedings of the Sixth IIR Gustav-Lorentzen Conference on Natural Working Fluids*, IIR Commission A1 & A2 Meeting, Glasgow, UK.
[12] Kandlikar, S. G., 1990, "A General Correlation for Saturated Two-Phase Flow Boiling Heat Transfer Inside Horizontal and Vertical Tubes," J. Heat Transfer, **112**, pp. 219–228.
[13] Chen, J. C., 1966, "Correlations for Boiling Heat Transfer to Saturated Fluids in Convective Flow," Ind. Eng. Chem. Process Des. Dev., **5**, pp. 322–339.
[14] Gungor, K. E., and Winterton, R. H. S., 1986, "A General Correlation for Flow Boiling in Tubes and Annuli," Int. J. Heat Mass Transfer, **29**, pp. 351–358.
[15] Gorenflo, D., 1993, "Pool Boiling," VDI Gesellschaft Verfahrenstechnic und Chemiengenieurwesen, English translation of VDI, Dusseldorf, pp. Ha 4–Ha 18.
[16] Steiner, D., and Taborek, J., 1992, "Flow Boiling Heat Transfer in Vertical Tubes Correlated by Asymptotic Model," Heat Transfer Eng., **13**, pp. 43–69.
[17] Gnielinski, V., 1976, "New Correlations for Heat and Mass Transfer in Turbulent Pipe and Channel Flow," Int. Chem. Eng., **16**, pp. 359–368.
[18] Jang, J., and Hrnjak, P. S., 2003, "Flow Regimes and Heat Transfer in Condensation of Carbon Dioxide at Low Temperatures," *Proceedings of the Second International Conference on Heat Transfer, Fluid Mechanics and Thermodynamics*, Victoria Falls, Zambia, Paper number HP1.
[19] Sato, T., and Matsumura, H., 1964, "On the Conditions of Incipient Subcooled-boiling With Forced Convection," Bull. JSME, **7**, pp. 392–398.
[20] Fujita, T., and Ueda, T., 1978, "Heat Transfer to Falling Liquid Films and Film Breakdown II (Saturated Liquid Films With Nucleate Boiling)." Int. J. Heat Mass Transfer, **21**, pp. 109–118.
[21] Kattan, N., Thome, J. R., and Favrat, D., 1998, "Flow Boiling in Horizontal Tubes: Part 1—Development of a Diabatic Two-Phase Flow Pattern Map," J. Heat Transfer, **120**, pp. 140–147.
[22] Kattan, N., Thome, J. R., and Favrat, D., 1998, "Flow Boiling in Horizontal Tubes: Part 3—Development of a New Heat Transfer Model Based on Flow Pattern," J. Heat Transfer, **120**, pp. 156–165.
[23] Gungor, K. E., and Winterton, R. H. S., 1987, "Simplified General Correlation for Saturated Flow Boiling and Comparison of Correlations With Data," Chem. Eng. Res. Des., **65**, pp. 148–156.
[24] Shah, M. M., 1982, "Chart Correlation for Saturated Boiling Heat Transfer: Equations and Further Study," ASHRAE J., **88**, pp. 185–196.
[25] Wattelet, J. P., Chato, J. C., Christoffersen, B. R., Gaibel, J. A., Ponchner, M., Kenny, P. J., Shimon, R. L., Villaneuva, T. C., Rhines, N. L., Sweeney, K. A., Allen, D. G., and Heshberger, T. T., 1994, "Heat Transfer Flow Regimes of Refrigerants in a Horizontal-tube Evaporator," ACRC TR-55, University of Illinois at Urbana-Champaign.

Heat Transfer Enhancement by Acoustic Streaming in an Enclosure

Murat K. Aktas

Bakhtier Farouk[1]
e-mail: bfarouk@coe.drexel.edu

Yiqiang Lin

Department of Mechanical Engineering
and Mechanics,
Drexel University,
Philadelphia, Pennsylvania 19104

Thermal convection in a differentially heated shallow enclosure due to acoustic excitations induced by the vibration of a vertical side wall is investigated numerically. The fully compressible form of the Navier-Stokes equations is considered and an explicit time-marching algorithm is used to track the acoustic waves. Numerical solutions are obtained by employing a highly accurate flux corrected transport algorithm. The frequency of the wall vibration is chosen such that an acoustic standing wave forms in the enclosure. The interaction of the acoustic standing waves and the fluid properties trigger steady secondary streaming flows in the enclosure. Simulations were also carried out for "off-design" vibration frequency where no standing waves were formed. The effects of steady second order acoustic streaming structures are found to be more significant than the main oscillatory flow field on the heat transfer rates. The model developed can be used for the analysis of flow and temperature fields driven by acoustic transducers and in the design of high performance resonators for acoustic compressors. [DOI: 10.1115/1.2098858]

Introduction

Heat removal from power dissipating systems by acoustically driven oscillatory flow fields can be found in various industrial applications. A detailed understanding of thermal energy transport in these problems is challenging. Sound sources whose elements move essentially sinusoidally may generate a flow field in which the particle velocities are not simply sinusoidal but a pattern of steady vortices is often found in the body of the irradiated fluid. Sound at high intensity levels in gases and liquids is accompanied by these second order steady flow patterns known as acoustic streaming.

Acoustic streaming is often observed where a standing wave is formed in a resonator driven by vibrating surface. With suitable design, this steady vortex flow can be employed for cooling of electronic systems in micro-gravity environment where free convective flows in fluids are greatly reduced or completely eliminated. Such flows can also aid mixing processes in containers and augment heat and mass transfer from resonator walls. In the containerless processing of materials under reduced gravity conditions [1] alloy samples are acoustically levitated to avoid physical contact with the container walls. Acoustic levitation involves the creation of sufficiently strong and suitably shaped acoustic fields. However, the required high intensity level sound fields give rise to strong acoustic streaming flows around samples and on the walls of the test cells.

While various analytical models are available for describing acoustic streaming phenomena, they are usually based on substantial approximations and the solutions are often limited to idealized conditions. The study of acoustic streaming started with the theoretical work of Lord Rayleigh [2]. He considered vortex flows occurring in a long pipe (Kundt's tube) as a result of the presence of a longitudinal standing wave. Westervelt [3] obtained a general vorticity equation and developed a general procedure for evaluating the streaming velocity induced by acoustical disturbances. Nyborg [4] reviewed the theories for calculating steady streaming associated with sound fields. An approximate solution was also developed by Nyborg [5] for sonically induced steady flow near a fluid-solid interface subjected to the condition of known irrotational oscillatory velocity distribution in the vicinity of the interface. The effect of compressibility on acoustic streaming near a rigid boundary was investigated by Qi [6] with a theoretical study. Qi extended this study [6] to investigate acoustic streaming in a circular tube [7]. Vainshtein [8] combined the problems of Rayleigh streaming and Couette flow and investigated the effect of streaming on shear flows.

Hamilton et al. [9] derived an analytic solution for the average mass transport velocity generated by a standing wave confined by parallel plates. A standing planar pressure field is assumed to be present between two parallel plates and the viscous penetration depth is assumed to be very small compared to the acoustic wavelength. In this study both the outer, Rayleigh streaming vortices and the inner, boundary layer vortices were described. They found that as channel width is reduced, the inner vortices increase in size relative to the Rayleigh vortices and for sufficiently narrow channels the Rayleigh vortices disappear and only inner vortices exist. Hamilton et al. [10] extended this analysis to a gas in which heat conduction and dependence of viscosity on temperature are taken into account. Kawahashi and Arakawa [11] performed numerical analysis of acoustic streaming induced by finite-amplitude oscillation in a closed duct driven by a piston applying a fourth-order spatial difference method. Several research studies were conducted in order to achieve a better understanding of the physical mechanism of interaction between free convection and sound. Kawahashi et al. [12] studied the coupling of natural convective with acoustic streaming flows in a horizontal duct heated from below both experimentally and numerically. Mozurkewich [13] investigated the heat transfer from a cylinder in an acoustic standing wave, experimentally. Gopinath and Harder [14] presented the results of an experimental study on the convective heat transfer behavior from a cylinder in an intense acoustic field. The results of an experimental study on heat transport within a cylindrical resonance tube, mediated by acoustic streaming, were reported by Mozurkewich [15]. Richardson [16] analyzed the convection from a circular cylinder subjected to transverse oscillations relative to the fluid in which it is immersed. The analysis was based upon use of the acoustic streaming flow field and was carried out analytically. Gopinath and Mills [1] examined the convective heat transfer from a sphere due to acoustic streaming for large streaming Reynolds numbers. Analytical and numerical solution techniques were used to obtain Nusselt number correlations for a wide range

[1]Corresponding author.

Contributed by the Heat Transfer Division of ASME for publication in the JOURNAL OF HEAT TRANSFER. Manuscript received December 13, 2004; final manuscript received June 27, 2005. Assoc. Editor: G. Chen.

of Prandtl numbers with particular emphasis on the case of Pr ~ 1.0. An experiment was also performed to confirm some of the predictions. Convective heat transfer due to acoustic streaming across the ends of an air-filled tube modeling an acoustic levitation chamber and supporting an axial standing sound wave was investigated by Gopinath and Mills [17]. The focus was on determining the steady heat convection due to streaming generated on the walls of the levitation chamber in the absence of any samples. The flow was treated as incompressible. Analytic techniques were used along with a numerical solver for the solution of the equations governing the steady transport due to streaming motion. A parametric study of the effects of the controlling acoustic and geometric variables was conducted, and Nusselt number correlations were developed for air. Vainshtein et al. [18] considered a problem in which a steady-state sonic wave propagates in longitudinal direction in a fluid enclosed between two horizontal parallel plates. In this theoretical study, an acoustic Peclet number was defined. The results obtained demonstrated that acoustic streaming results in enhancement of heat transfer between the plates. Thermoacoustic streaming in a resonant channel (driven by a transducer) was studied theoretically by Gopinath et al. [19]. Mironov et al. [20] demonstrated that a differentially heated stack, the heart of all thermoacoustic devices, provides a source of streaming additional to those associated with Reynolds stresses in quasi-unidirectional gas flow.

The above-mentioned survey indicates that, in most of the analytical and numerical studies cited in the literature, the formation of acoustic streaming is analyzed with a simplified approach and the heat transfer effects of streaming flows are also based on simplified mathematical models. In most of these studies, a perfectly sinusoidal primary standing wave field in the domain of interest is assumed and hence the results are based on this idealized assumption. The sound field and streaming formation processes are not modeled in most of the studies given in the literature.

In the present study, we introduce a rigorous and robust approach for calculating the sound field in a resonator along with the associated transport processes. We do not employ any pre-defined sound field in the computational domain for the simulation of streaming formation. Instead, we compute and fully describe the formation of the standing wave field (if any) in the domain. With this model, we are able to simulate the physical processes including the compression/expansion of the fluid and wave generation, acoustic boundary layer development, the interaction of the wave field with viscous effects and finally formation of streaming structures and the associated thermal convection. The distinction between the present approach (direct numerical simulation of acoustically excited flows and acoustic streaming) and those available in the literature is thus significant. While the present method is general and can be applied to resonators driven at any frequencies, the existing analytical methods in the literature have restrictive assumptions. In general, an acoustic field is assumed to be present while in the present method, the generation and evolution of the acoustic field is computed explicitly. Non-resonant conditions can easily be investigated and the present method can be extended to full three dimensions for device design.

Problem Geometry

A two-dimensional rectangular enclosure filled with nitrogen is considered (Fig. 1). The left wall of the enclosure is modeled as a rigid boundary which vibrates harmonically and represents the motion of a loudspeaker diaphragm or the vibration of a commercial ultrasonic mixer probe. The vibrating boundary is the acoustic source in this geometry. Initially, the gas in the enclosure is quiescent and at $T_0=300$ K and at atmospheric pressure. The temperature of the vibrating wall was set to temperatures higher than the ambient for different cases studied. For all cases studied, the horizontal walls were considered insulated. The length and the height of the enclosure are $L=8.825$ mm and $H=0.316$ mm, respectively. The frequency of the wall vibration ($f=20$ kHz) is

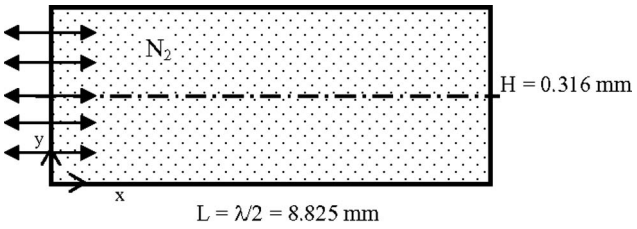

Fig. 1 Schematic of the problem

chosen such that an acoustic standing wave forms in the enclosure. Corresponding wavelength of the sound waves at this frequency is $\lambda=17.65$ mm based on the sonic speed in nitrogen ($c=353$ m/s). The length of the enclosure thus corresponds to a half wavelength. Nonlinear interaction of this wave field with the solid boundary and resulting acoustic boundary layer formation lead to the production of inner and outer acoustic streaming flow patterns in the enclosure. The thickness of the acoustic boundary layer (δ_{ac}) is given by $\delta_{ac}=(2\nu/2\pi f)^{1/2}$. Here f is the frequency of the wall vibration and ν is the kinematic viscosity of the fluid. For $f=20$ kHz, the ratio of the height of the enclosure (0.316 mm) to the acoustic boundary layer thickness (δ_{ac}) is twenty in the present configuration. Simulations were also carried out for "off-design" vibration frequency where no standing waves were formed.

Mathematical Model

Thermal convection in acoustic streaming flow fields is described by the full Navier-Stokes and energy equations for a compressible fluid. In two-dimensional Cartesian coordinate system these equations are expressed as

$$\frac{\partial \rho}{\partial t}+\frac{\partial(\rho u)}{\partial x}+\frac{\partial(\rho v)}{\partial y}=0 \tag{1}$$

$$\rho\frac{\partial u}{\partial t}+\rho u\frac{\partial u}{\partial x}+\rho v\frac{\partial u}{\partial y}=-\frac{\partial p}{\partial x}+\frac{\partial \tau_{xx}}{\partial x}+\frac{\partial \tau_{xy}}{\partial y} \tag{2}$$

$$\rho\frac{\partial v}{\partial t}+\rho u\frac{\partial v}{\partial x}+\rho v\frac{\partial v}{\partial y}=-\frac{\partial p}{\partial y}+\frac{\partial \tau_{yy}}{\partial y}+\frac{\partial \tau_{xy}}{\partial x} \tag{3}$$

$$\frac{\partial E}{\partial t}+\frac{\partial}{\partial x}[(E+p)u]+\frac{\partial}{\partial y}[(E+p)v]=\frac{\partial}{\partial x}[u\tau_{xx}+v\tau_{xy}]+\frac{\partial}{\partial y}[u\tau_{xy}+v\tau_{yy}]-\frac{\partial q_x}{\partial x}-\frac{\partial q_y}{\partial y} \tag{4}$$

Here t is time, x and y refer to the Cartesian coordinates, ρ is density, p is pressure, u and v are the velocity components, and E is the total energy given by

$$E=\rho c_v T+\tfrac{1}{2}\rho(u^2+v^2) \tag{5}$$

The components of the stress tensor τ are

$$\tau_{xx}=\frac{4}{3}\mu\frac{\partial u}{\partial x}-\frac{2}{3}\mu\frac{\partial v}{\partial y}\quad \tau_{yy}=\frac{4}{3}\mu\frac{\partial v}{\partial y}-\frac{2}{3}\mu\frac{\partial u}{\partial x}\quad \tau_{xy}=\mu\left(\frac{\partial u}{\partial y}+\frac{\partial v}{\partial x}\right) \tag{6}$$

where μ is the dynamic viscosity. The components of the heat-flux vector are written as

$$q_x=-k\frac{\partial T}{\partial x}\quad q_y=-k\frac{\partial T}{\partial y} \tag{7}$$

where k is thermal conductivity and T is temperature. The temperature dependence of the viscosity and thermal conductivity [21] are taken into account using the following polynomial expressions

$$\mu(T) = -1.253 \times 10^{-6} + 8.983 \times 10^{-8} T - 1.139 \times 10^{-10} T^2 + 9.101 \times 10^{-14} T^3 \quad (8)$$

$$k(T) = 1.494 \times 10^{-4} + 1.108 \times 10^{-4} T - 1.045 \times 10^{-7} T^2 + 6.958 \times 10^{-11} T^3 \quad (9)$$

The gravitational effects on the flow fields are neglected in this study as the effects are considered to be negligible when compared to the flow fields produced by the vibration of the left wall. The temperature is related to the density and pressure through the ideal-gas law

$$p = \rho R T \quad (10)$$

where R is the specific gas constant of the medium.

Numerical Scheme

The governing equations (except the diffusion terms) are discretized using a control-volume-based flux-corrected transport (FCT) algorithm. FCT is a high order, nonlinear, monotone, conservative and positivity-preserving scheme designed to solve a general one-dimensional continuity equation with appropriate source terms [22]. This scheme has fourth-order phase accuracy and is able to resolve steep gradients with minimum numerical diffusion. We have successfully used the algorithm in predicting the generation and propagation of thermoacoustic waves in gases [23,24] and liquid water [25]. In this algorithm, when a flow variable such as a density is initially positive, it remains positive during the computations and no new minimum or maximum are introduced due to numerical errors in the calculation process. To ensure positivity and stability, a minimum amount of numerical diffusion over the stability limit is added at each time step. Time-step splitting technique is used to solve the two-dimensional problem addressed here. Further details of the FCT algorithm used here are documented by Boris et al. [26]. The diffusion terms (the viscous term in the momentum equations and the conduction and viscous dissipation terms in the energy equation) were discretized using the central-difference approach and the time-step splitting technique was used to include the terms in the numerical scheme.

No-slip boundary conditions are used for all solid walls. A high-order non-dissipative algorithm such as FCT requires rigorous formulation of the boundary conditions. Otherwise, numerical solutions may show spurious wave reflections at the regions close to boundaries and nonphysical oscillations arising from instabilities. In the present computational method, the treatment proposed by Poinsot and Lele [27] is followed for implementing the boundary conditions for the density. This method avoids incorrect extrapolations and overspecified boundary conditions. Along any stationary solid wall, the density is calculated from

$$\left(\frac{\partial \rho}{\partial t}\right)_M + \frac{1}{c_M}\left(\frac{\partial p}{\partial n} + \rho c \frac{\partial u_n}{\partial n}\right)_M = 0 \quad (11)$$

where c is the acoustic speed, the subscript M indicates the location of the wall, and n is the direction normal to the wall. Since the current problem involves a moving boundary and a time dependent boundary velocity, a modification in this part of the scheme is required for the left boundary. Along the vibrating wall, the density is calculated from

$$\frac{\partial \rho}{\partial t} = \frac{\rho \gamma}{c_L}\frac{\partial u_W}{\partial t} + \frac{\rho \gamma (u_W - c_L)}{c_L}\frac{\partial u}{\partial x} - \frac{\gamma (u_W - c_L)}{c_L^2}\frac{\partial p}{\partial x} \quad (12)$$

where c_L is the acoustic speed at the left wall.

Acoustic streaming flows in high-intensity sound fields are characterized by two different types of circulatory steady flow structures. The circulations forming in the immediate vicinity of the viscous boundaries are referred as "inner" or Schlichting type of acoustic streaming. The inner streaming structures give rise to the second type of streaming called "outer" or Rayleigh streaming observed outside of the viscous layers. Inner and outer streaming motions have opposite rotational direction.

Since the formation of acoustic streaming structures results from the interaction between the wave field and the viscous boundary, resolving the acoustic boundary layer in the computational method is essential to accurately predict the inner acoustic streaming structures. For this reason, we employ a non-uniform grid structure with 121×111 computational cells for these simulations. The results of the grid independency tests are presented later in the manuscript. The computational cells are uniformly distributed in x direction and are found sufficient to capture wave propagation and reflection accurately. The grid has non-uniformly distributed cells in y direction with fine grids in the vicinity of the bottom and top walls of the enclosure. This grid has fine grids in the vicinity of the top and bottom walls of the enclosure and the grid quality gradually decreases with the increasing distance from the horizontal walls. In this grid structure, the variation of the left wall position and the size changes for the first column of cells were also taken into account since the problem involves the modeling of a vibrating wall.

Results and Discussion

The simulations were performed for three cases in this study. For each case, the calculations were started with the vibration of the left wall at $x=0$ and with uniform initial values of pressure, temperature, and density. For each cycle of the vibrating wall, about 25,000 time steps were used for the computations. This was primarily dictated by the requirements of the explicit time-marching scheme used and the tracking of the acoustic waves.

In the first case considered (Case 1), the heating is applied on the vibrating left wall ($f=20$ kHz, $T_L=310$ K) of the enclosure and the right wall of the enclosure is kept at ambient temperature $T_R=T_0=300$ K. The displacement of the vibrating wall is given by $s=s_m \sin(\omega t)$ where $\omega=2\pi f$. Here, s_m is the maximum displacement of the wall and $s_m\omega$ represents the maximum velocity of the wall. The maximum displacement of the wall is set to $s_m=10$ μm. In the second case (Case 2) the vibration frequency of the left wall is changed to $f=25$ kHz and $T_L=310$ K. In the last case considered (Case 3), the heating is applied on the stationary right wall of the enclosure ($T_R=310$ K). The vibration amplitude of the left wall is kept at the same value as in Case 1 and the temperature of the left wall is kept at ambient temperature $T_0=T_L=300$ K. The top and the bottom walls of the enclosure are thermally insulated for all cases.

The initial transients die out after a few cycles of the wall vibrations. The predicted u-velocity profiles for Case 1 are given in Fig. 2 for $\omega t=0$ and $\omega t=\pi/2$ (during cycle 101) along the horizontal mid-plane. The left wall velocity has non-zero value at $\omega t=0$ due to harmonic vibrations. The wall is stationary at $\omega t=\pi/2$. The u-velocity profiles at $\omega t=\pi$ and $\omega t=3\pi/2$ (not shown in Fig. 2) are nearly symmetric with the profiles given for $\omega t=0$ and $\omega t=\pi/2$, respectively. An oscillatory flow field is developed due to the vibrations of the left wall and the velocity distributions shown in Fig. 2 are repeated at subsequent cycles. The minimum and maximum velocity values are predicted approximately -12 m/s and 12 m/s in this primary flow field at $\omega t=0$ and $\omega t=\pi$, respectively. The results of a grid-independency study are also included in the figure. The figure contains predicted u-velocity values with three different grid structures (121×111, 101×101, and 81×101) for the same conditions. The results show that 121×111 grid structure is adequate for resolving the flow characteristics in the described configuration and the numerical predictions are grid independent.

The grid-independency study was extended by computing the cycle-averaged wall shear stress along the bottom horizontal wall for Case 1. Figure 3 shows the predicted wall shear values with three different grid structures (121×111, 101×101, and 81

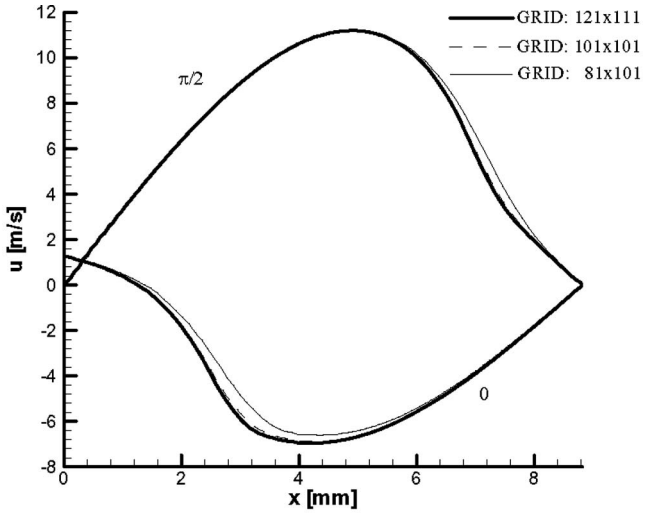

Fig. 2 Variation of *u* velocity along the horizontal mid-plane of the enclosure at two different instants ($\omega t=0, \pi/2$) during the acoustic cycle starting at $t=5$ ms (Case 1)

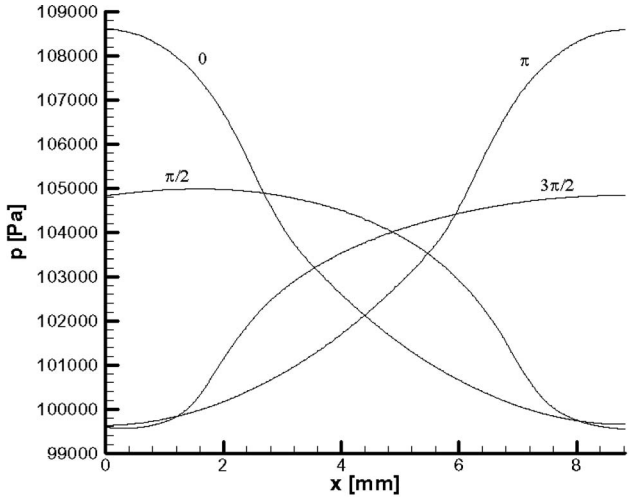

Fig. 4 Variation of pressure along the horizontal mid-plane of the enclosure at four different instant ($\omega t=0, \pi/2, \pi, 3\pi/2$) during the acoustic cycle starting at $t=5$ ms (Case 1)

$\times 101$) for the same conditions. The time averaging was applied during the 100th vibration cycle (between cycles 99 and 100). The results again show that 121×111 grid structure is adequate for resolving the flow characteristics in the described configuration and the numerical predictions are grid independent.

Figure 4 shows the pressure distribution along the horizontal mid-plane of the enclosure at $\omega t=0, \pi/2, \pi, 3\pi/2$ (during cycle 101) for Case 1. These pressure profiles remain essentially the same at any other horizontal plane away from the bottom and top walls and this indicates the near-one-dimensional character of the acoustic field in the bulk medium. The pressure distribution for $\omega t=2\pi$ (not shown here) is identical to the curve given for $\omega t=0$. At $\omega t=0$ and $\omega t=\pi$, the amplitude of the pressure waves reach a maximum and a minimum value at the ends of the enclosure value. At the beginning of the cycle ($\omega t=0$), the pressure is maximum on the vibrating (left) wall of the enclosure and decreases with increasing distance from the wall and reaches a minimum value at $x\cong L$. The behavior is quite opposite at $\omega t=\pi$ where the pressure is minimum on the vibrating (left) wall of the enclosure and increases with increasing distance from the wall

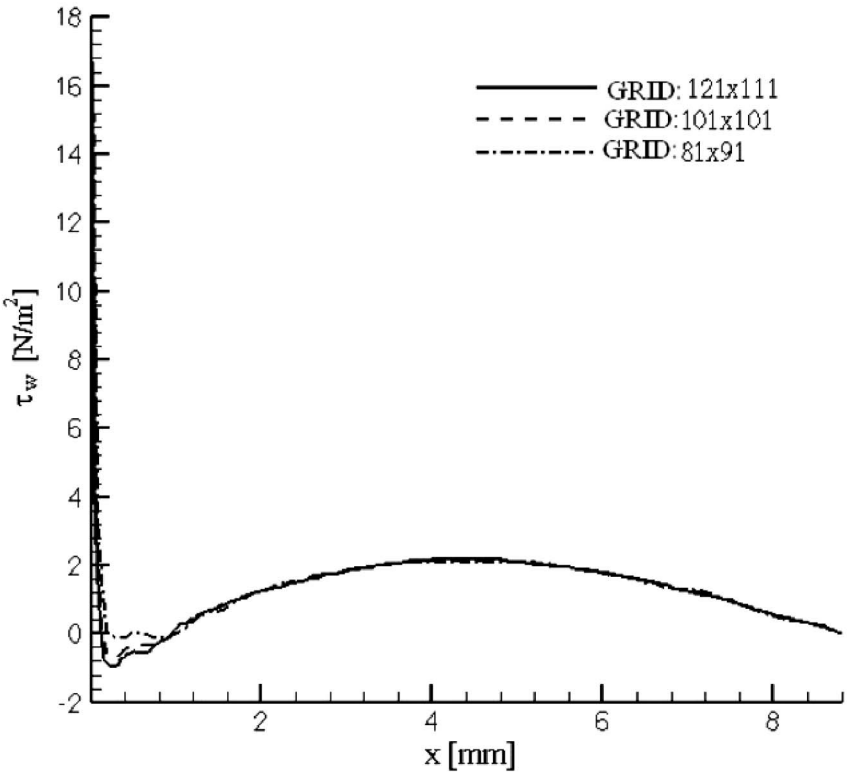

Fig. 3 Variation of wall shear stress along the bottom wall of the enclosure near $t=5.0$ ms (Case 1)

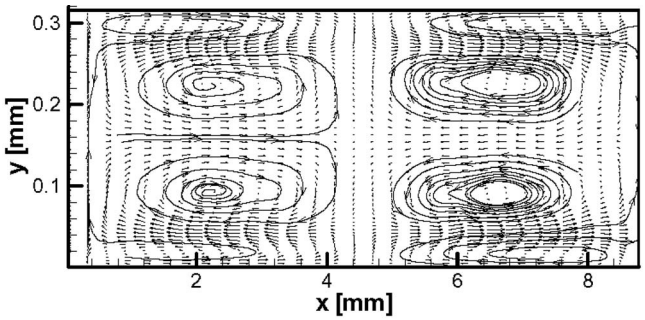

Fig. 5 Flow field in the enclosure based on the time averaged velocities at $t=5$ ms (Case 1)

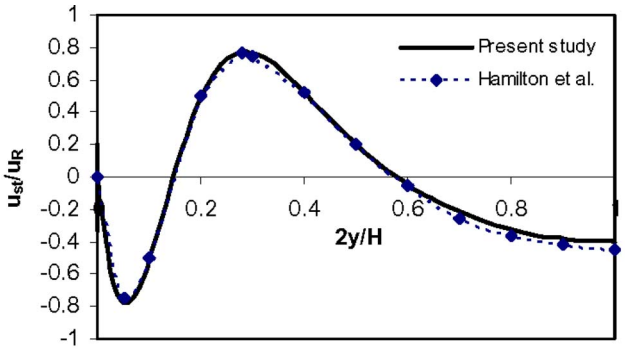

Fig. 6 Variation of the x component of the streaming velocity at $x=3L/4$ along the height of the enclosure

and reaches a maximum value at $x \cong L$. The pressure profiles given for $\omega t=0$, $\pi/2$, π, and $3\pi/2$ show that the pressure node is formed at approximately $x=L/2$.

For Case 1, the driving frequency of the left wall vibration is chosen such that $\lambda=L/2$. As expected, our simulations predict steady streaming flows in the enclosure for this case. The predicted steady streaming flow field is shown in Fig 5. This flow field is based on the average mass transport velocity values in the enclosure. The average mass transport velocity was given by

$$u_{st}=\frac{\langle \rho u\rangle}{\langle \rho\rangle} \quad v_{st}=\frac{\langle \rho v\rangle}{\langle \rho\rangle} \tag{13}$$

and describes the x and y components of the streaming velocities, respectively. Here $\langle\ \rangle$ indicates the time averaged quantities. The time averaging was applied during the 100th vibration cycle (between cycles 99 and 100) and gives the streaming velocity values near $t=5$ ms. The streaming velocities calculated based on the time averaging during 150th ($t=7.5$ ms) and 200th ($t=10$ ms) cycles do not differ significantly from the values computed at $t=5$ ms. Hence, the average mass transport velocities were assumed to be cycle-independent by this time ($t=5$ ms). The maximum streaming velocity value is found to be approximately 0.06 m/s while the maximum instantaneous velocities reach 12.0 m/s in the primary oscillatory flow field in the enclosure. Four clockwise and four counterclockwise circulations are observed in the enclosure. Inner streaming structures are formed at the vicinity of the bottom and the top walls. The height of the circulatory flow structures (inner streaming) observed in the vicinity of the horizontal walls is characterized by the thickness of the acoustic boundary layer. The streaming structures seen in the middle section of the enclosure (outer streaming) have larger sizes. The horizontal length of both the inner and the outer streaming vortices is characterized by quarter wavelength ($\lambda/4$). Predicted streaming structures are in good agreement with the results reported by Hamilton et al. [9,10].

Figure 6 shows the variation of the x component of the streaming velocity along the enclosure height at $x=3L/4$ for Case 1. In this figure, the vertical axis is the x component of the dimensionless streaming velocity (u_{st}/u_R) and u_R is the reference velocity given by $u_R=3u_0^2/16c_0$ where u_0 is the maximum oscillatory velocity. This reference velocity value represents the maximum streaming velocity in case of a perfect sinusoidal wave form obtained by Rayleigh. Results from Hamilton et al. [9] are also included in the same figure (dashed curve). The predictions of the current study compare well with the results from Hamilton et al. [9].

Figure 7 shows the instantaneous temperature profiles along the horizontal midplane for four different instants during the same acoustic cycle (101) in the enclosure. Far from the heated (left) wall, temperature profiles are also nearly periodic in nature. However, the temperature field is not characterized by diffusion dominated transport. Near the left wall, slightly higher temperatures are predicted than the prescribed wall temperature (310 K) at some instances due to compression effects. Since the right wall temperature in this case (Case 1) is the same as the enclosure gas initial temperature, the temperature variations observed near the right wall are primarily due to fluctuating velocity and pressure fields in the enclosure.

Figure 8 shows the time (cycle) averaged temperature profile along the horizontal midplane for Case 1 at $t=5$ ms. For comparison, an enclosure having identical geometry and temperature boundary conditions but without any acoustic excitation (stationary left wall) is also considered. The predicted temperature profile along the horizontal midplane for this problem is also included in the same figure. The case (with no wall vibration) is yet to reach steady-state conditions at this time, however, the acoustically excited case appeared to be quasi-steady from the streaming velocity field predictions. The steady streaming motion for this case was shown earlier in Fig. 5. For the case with the vibrating left wall, sharp temperature gradients are observed along the vertical walls and a local temperature peak appears in the center region of the geometry due to fluid motion (velocity antinode).

The heat transfer coefficient along a vertical wall is defined as

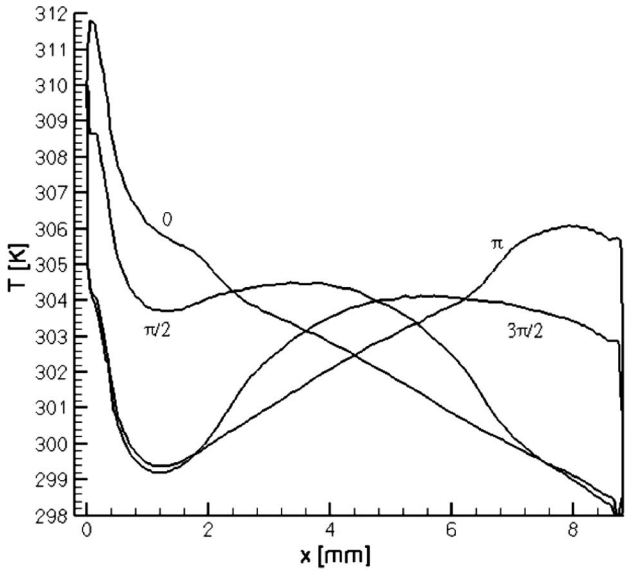

Fig. 7 Variation of temperature along the horizontal mid-plane of the enclosure at four different instants ($\omega t=0, \pi/2, \pi, 3\pi/2$) during the acoustic cycle starting at $t=5$ ms (Case 1)

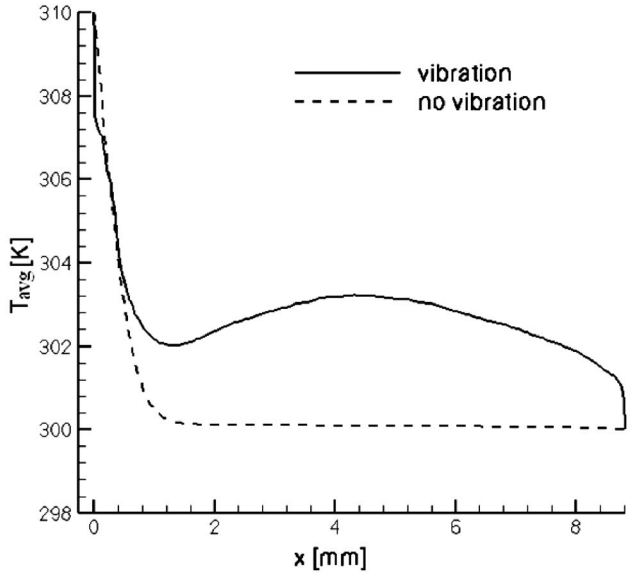

Fig. 8 Time (cycle) averaged temperature profile along the horizontal mid-plane of the enclosure at $t=5$ ms (Case 1)

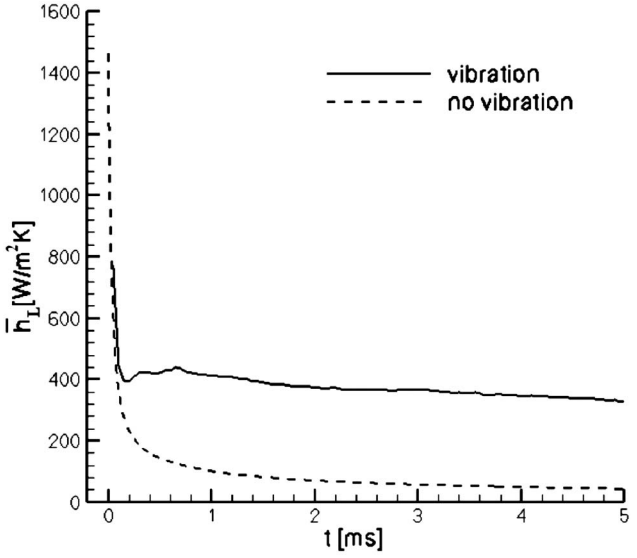

Fig. 10 Temporal variation of the cycle averaged left wall heat transfer coefficient (Case 1)

$$h = \frac{-k\dfrac{\partial T}{\partial x}}{|T_L - T_R|} \tag{14}$$

and the average heat transfer coefficient $\bar{h}$ is given as

$$\bar{h} = \frac{1}{H}\int_0^H h\,dy \tag{15}$$

Time variation of the average (spatial) heat transfer coefficient, $\bar{h}$, for the left wall during the first 100 cycle is given in Fig. 9 for Case 1. Initially heat transfer is high due to the large temperature difference between the wall and the gas. After approximately 10 cycles, the variation of the heat transfer coefficient is characterized by the oscillatory fluid motion in the enclosure.

Spatially and cycle averaged value of the left wall heat transfer coefficient is given in Fig. 10. The computed values of heat transfer coefficient for the case without the vibrating left wall are also included in the figure. The figure indicates that the overall heat transfer with streaming motion is higher compared to the case without oscillatory fluid motion. The left wall heat transfer coefficient reached a quasi-steady value of about 390 W/m^2 K. The cycle averaged power input to the enclosure by mechanical vibration is given by

$$P = \frac{1}{T}\int p(t)u(t)dt \tag{16}$$

where T is the period of wall oscillation. The power input from the left wall near $t=5$ ms was found to be about 2633 W/m^2. The heat transfer enhancement due to left wall vibration near $t=5$ ms was determined to be about 2451.35 W/m^2 (from Fig. 10). The ratio of mechanical energy addition to heat transfer enhancement was found to be about 1.07 for Case 1.

To further explore the physics of the heat transfer characteristics in enclosures with oscillatory flows we consider an "off-design" case (Case 2) where the wall vibration frequency is changed from 20 kHz to 25 kHz. The predicted time averaged flow field (cycle 101) is given in Fig. 11. A comparison with the similar time averaged flow field given for Case 1 (Fig. 5) clearly indicates that the regular clockwise and counterclockwise circulating acoustic streaming structures are not observed for the in-

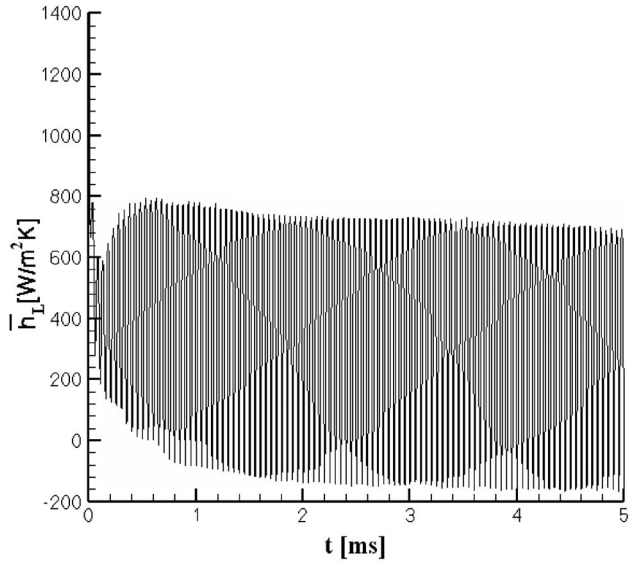

Fig. 9 Temporal variation of the left wall average heat transfer coefficient (Case 1)

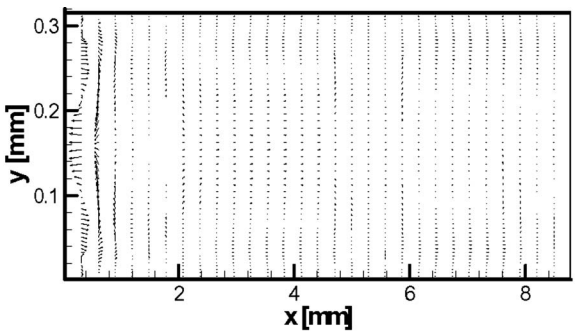

Fig. 11 Flow field in the enclosure based on the time averaged velocities at $t=5$ ms (Case 2)

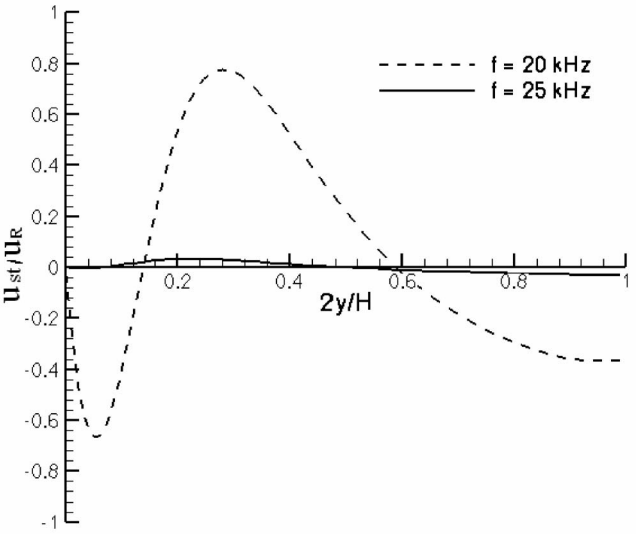

Fig. 12 Comparison of the *x* component of the time (cycle) averaged velocity values along the vertical plane (at $x=6.8$ mm) of the enclosure for Case 1 and Case 2

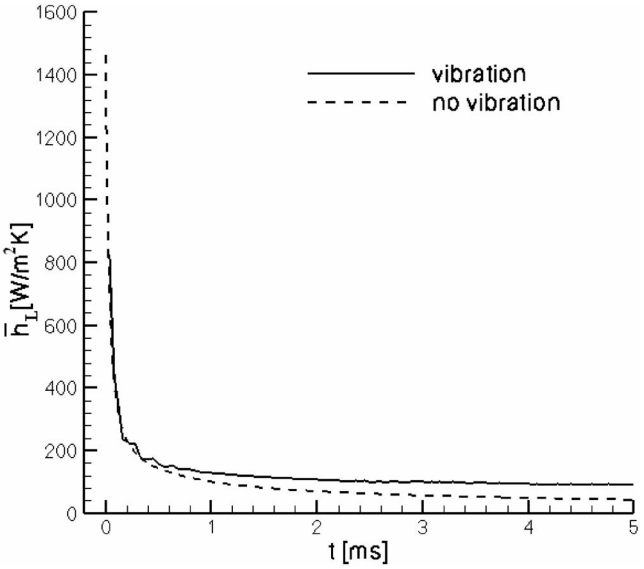

Fig. 14 Temporal variation of the time averaged left wall heat transfer coefficient (Case 2)

creased value of the vibration frequency. Since no standing waves are formed in this case, the steady streaming structures do not develop.

Figure 12 compares the x component of the time (cycle) averaged velocity values along the vertical plane at $x=6.8$ mm for Case 1 and Case 2. At $f=25$ kHz, predicted time averaged velocities are relatively weak and the streaming motion can be considered negligible. Figure 13 shows the time variation of the instantaneous values of the left wall heat transfer coefficient for Case 2. The effect of the primary oscillatory flow field is evident on the heat transfer characteristics of the enclosure. However, the time (cycle) averaged values of the heat transfer coefficient (Fig. 14) for the system with the left wall vibration frequency of 25 kHz are not very different from those given for the enclosure with a stationary left wall. No significant augmentation in the overall heat transfer rate was obtained with the addition of the vibrating boundary and the resulting oscillatory flow at an "off-design" frequency. Significant enhancement of the heat transfer coefficient

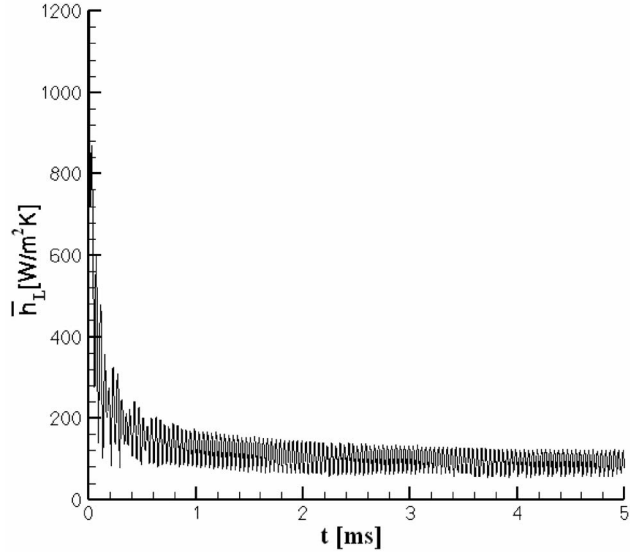

Fig. 13 Temporal variation of the left wall heat transfer coefficient (Case 2)

was reported earlier (Fig. 10) for the case with the left wall vibration frequency of 20 kHz. These results (Figs. 10 and 14) clearly demonstrate the significant effect of the steady second order streaming motion on the heat transfer characteristics of the system. Streaming structures introduce an additional circulatory motion that greatly contributes to the convective heat transfer in the system. Oscillatory primary flow fields (x directional) cannot provide the efficient cooling (along the vertical left wall) without streaming structures although the primary fluctuating flow velocities are about two orders of magnitude larger than the steady streaming velocities.

In the last case considered (Case 3), the heating is applied on the stationary right wall of the enclosure ($T_R=310$ K). The vibration frequency of the left wall is kept at the same value ($f=20$ kHz) as in Case 1 and the temperature of the left wall is kept at ambient temperature $T_0=T_L=300$ K. The top and the bottom walls of the enclosure are again thermally insulated. The predicted pressure amplitudes and primary flow field velocities for this case are quite similar (not shown here) to those given for Case 1. The wave field determined by the vibrating boundary and the heating condition has negligible effect on the secondary flow structures (not shown here).

Figure 15 shows the instantaneous temperature profiles along the horizontal midplane for four different instants during the same acoustic cycle (101) in the enclosure for Case 3. Far from the heated (right) wall and the cooled vibrating (left) wall, temperature profiles are also nearly periodic in nature. However, the temperature field is again not characterized by the diffusion dominated transport. Near the left vibrating wall, higher temperatures are predicted than the prescribed wall temperature (300 K) at some instances due to compression effects and lower temperatures are predicted at some instances due to expansion effects. Since the left wall temperature in this case (Case 3) is the same as the enclosure gas initial temperature, the temperature variations observed near the left wall are primarily due to fluctuating velocity and pressure fields in the enclosure.

Figure 16 shows the time (cycle) averaged temperature profile along the horizontal plane of the enclosure for Case 3 for cycle 101. The same figure also includes the predicted temperature profile for an enclosure (with the same heating conditions but) without vibrating wall. The temperature profile reveals a complicated heat transfer problem for Case 3. Since the heated wall is not vibrating in this case, quasi-steady conditions are not reached by

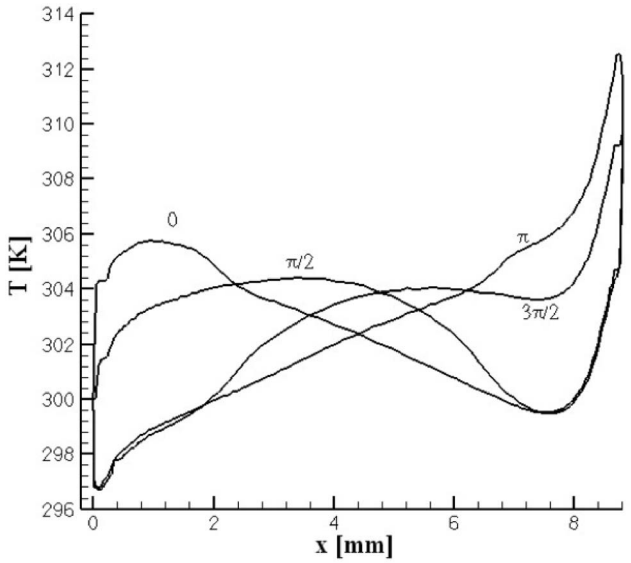

Fig. 15 Variation of temperature along the horizontal mid-plane of the enclosure at four different instants ($\omega t = 0, \pi/2, \pi, 3\pi/2$) during the acoustic cycle starting at $t = 5$ ms (Case 3)

cycle 101. The mechanical energy addition along the cooled right wall gives rise to the interesting temperature profile shown in Fig. 16. Longer time solutions are needed to predict the quasi-steady temperature field.

Time (cycle) averaged values of the right wall heat transfer coefficient at 5 ms are given in Fig. 17 for Case 3. Time (cycle) averaged values of the left wall heat transfer coefficient at 5 ms for Case 1 and the case with no vibration are also shown in the same figure. In Case 1, both thermal and mechanical energies are added along the left wall while for Case 3, mechanical energy is added along the left wall, but thermal energy is added along the right wall. For the case with no vibration, only thermal energy is added along the left wall. The figure indicates that the overall heat transfer with streaming motion is higher compared to the case without oscillatory fluid motion when the heated wall vibrates. The acoustic streaming causes vertical flow along the side walls

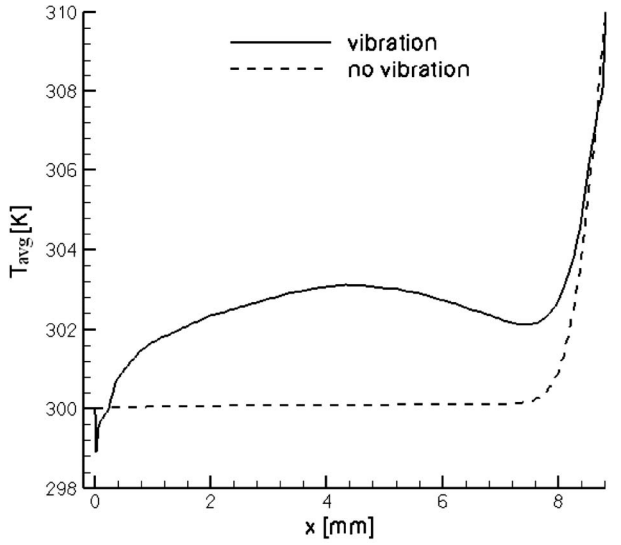

Fig. 16 Time averaged temperature profile along the horizontal mid-plane of the enclosure near $t = 5$ ms (Case 3)

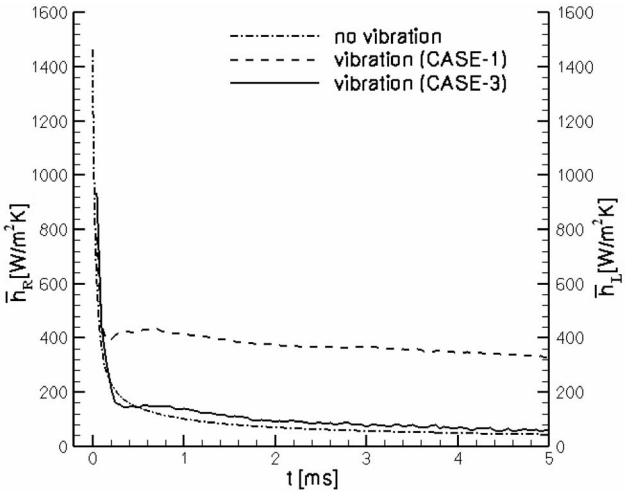

Fig. 17 Temporal variation of the time averaged right wall heat transfer coefficient (Case 3)

that is primarily responsible for the heat transfer enhancement. Heat transfer enhancement from the (heated) right wall is only marginal when the left (cooled) wall vibrates in the first 5 ms.

Discussion

The effects of the oscillatory primary flow field and the resulting steady second order acoustic streaming structures on developing thermal convection process in a nitrogen-filled shallow enclosure were studied computationally. The formation of pressure (acoustic) waves, acoustic-viscous boundary layer interactions and associated flows in a rectangular enclosure are studied along with convective heat transfer from vertical end walls of the enclosure by solving the unsteady compressible Navier-Stokes equations in two-dimensional Cartesian coordinate system. The acoustic field in the enclosure is created due to the harmonic vibration of the left wall. The effects of wall vibration on the wave field and the formed flow structures are determined by utilizing a highly accurate FCT algorithm. The mechanically induced periodic oscillations in the fluid are found to be insignificant on the heat transfer characteristics of the system (heated vertical wall), unless steady streaming flows are also present. Interesting effects were observed when the cooled wall vibrates instead of the heated wall.

Acoustic streaming introduces an additional convective heat transfer mode in to the systems in zero-gravity environment where it is assumed that conduction is the only heat transfer mode. The model developed can be a valuable tool in the optimized design of heat exchangers with acoustically enhanced performance.

Nomenclature

c = acoustic speed
c_v = specific heat
E = total energy
f = frequency of wall vibration
g = gravitational acceleration
h = heat transfer coefficient
k = thermal conductivity
L = width and height of the enclosure
p = pressure
q = heat flux
R = specific gas constant
t = time
T = temperature
u = velocity in the horizontal direction
v = velocity in the vertical direction
x = horizontal coordinate

y = vertical coordinate

Greek symbols

α = thermal diffusivity
γ = ratio of specific heats
μ = dynamic viscosity
ν = kinematic viscosity
ρ = density
τ = shear stress

Subscripts

0 = initial
L = left
M = wall location
n = direction normal to the wall
R = right

References

[1] Gopinath, A., and Mills, A. F., 1993, "Convective Heat Transfer From a Sphere Due to Acoustic Streaming," J. Heat Transfer, **115**, pp. 332–341.
[2] Lord Rayleigh, 1884, "On the Circulation of Air Observed in Kundt's Tubes," Philos. Trans. R. Soc. London, **A175**, pp. 1–21.
[3] Westervelt, P. J., 1953, "The Theory of Steady Rotational Flow Generated by a Sound Field," J. Acoust. Soc. Am., **25**, pp. 60–67.
[4] Nyborg, W. L., 1953, "Acoustic Streaming Due to Attenuated Plane Waves," J. Acoust. Soc. Am., **25**, pp. 68–75.
[5] Nyborg, W. L., 1958, "Acoustic Streaming Near a Boundary," J. Acoust. Soc. Am., **30**, pp. 329–339.
[6] Qi, Q., 1993, "The Effect of Compressibility on Acoustic Streaming Near a Rigid Boundary for a Plane Traveling Wave," J. Acoust. Soc. Am., **94**, pp. 1090–1098.
[7] Qi, Q., Johnson, R. E., and Harris, J. G., 1995, "Boundary Layer Attenuation and Acoustic Streaming Accompanying Plane-Wave Propagation in a Tube," J. Acoust. Soc. Am., **97**, pp. 1499–1509.
[8] Vainshtein, P., 1995, "Rayleigh Streaming at Large Reynolds Number and its Effect on Shear Flow," J. Fluid Mech., **285**, pp. 249–264.
[9] Hamilton, M. F., Ilinskii, Y. A., and Zabolotskaya, E. A., 2003, "Acoustic Streaming Generated by Standing Waves in Two-Dimensional Channels of Arbitrary Width," J. Acoust. Soc. Am., **113**, pp. 153–160.
[10] Hamilton, M. F., Ilinskii, Y. A., and Zabolotskaya, E. A., 2003, "Thermal Effects on Acoustic Streaming in Standing Waves," J. Acoust. Soc. Am., **114**, pp. 3092–3101.
[11] Kawahashi, M., and Arakawa, M., 1996, "Nonlinear Phenomena Induced by Finite-Amplitude Oscillation of Air Column in Closed Duct," JSME Int. J., **39**, pp. 280–286.
[12] Kawahashi, M., Tanahashi, M., Arakawa, M., and Hirahara, H., "Visualization and Measurement of Acoustic Streaming Coupling With Natural Convection." ASME/JSME Fluids Engineering and Laser Anemometry Conference and Exhibition, Hilton Head, SC, pp. 281–300.
[13] Mozurkewich, G., 1995, "Heat Transfer From a Cylinder in an Acoustic Standing Wave," J. Acoust. Soc. Am., **98**, pp. 2209–2216.
[14] Gopinath, A., and Harder, D. R., 2000, "An Experimental Study of Heat Transfer From a Cylinder in Low-Amplitude Zero-Mean Oscillatory Flows," Int. J. Heat Mass Transfer, **43**, pp. 505–520.
[15] Mozurkewich, G., 2002, "Heat Transport by Acoustic Streaming Within a Cylindrical Resonator," Appl. Acoust., **63**, pp. 713–735.
[16] Richardson, P. D., 1967, "Heat Transfer From a Circular Cylinder by Acoustic Streaming," J. Fluid Mech., **30**, pp. 337–355.
[17] Gopinath, A., and Mills, A. F., 1994, "Convective Heat Transfer Due to Acoustic Streaming Across the Ends of a Kundt Tube," J. Heat Transfer, **116**, pp. 47–53.
[18] Vainshtein, P., Fichman, M., and Gutfinger, C., 1995, "Acoustic Enhancement of Heat Transfer Between Two Parallel Plates," Int. J. Heat Mass Transfer, **38**, pp. 1893–1899.
[19] Gopinath, A., Tait, N. L., and Garrett, S. L., 1998, "Thermoacoustic Streaming in a Resonant Channel: The Time Averaged Temperature Distribution," J. Acoust. Soc. Am., **103**, pp. 1388–1405.
[20] Mironov, M., Gusev, V., Auregan, Y., Lotton, P., Bruneau, M., and Piatakov, P., 2002, "Acoustic Streaming Related to Minor Loss Phenomenon in Differentially Heated Elements of Thermoacoustic Devices," J. Acoust. Soc. Am., **112**, pp. 441–445.
[21] Kays, W. M., and Crawford, M. E., 1993, *Convective Heat and Mass Transfer* (McGraw-Hill, New York).
[22] Oran, E. S., and Boris, J. P., 2000, *Numerical Simulation of Reactive Flow* (Cambridge University Press, Cambridge).
[23] Farouk, B., Oran, E. S., and Fusegi, T., 2000, "Numerical Study of Thermoacoustic Waves in an Enclosure," Phys. Fluids, **12**, pp. 1052–1061.
[24] Aktas, M. K., and Farouk, B., 2003, "Numerical Simulation of Developing Natural Convection in an Enclosure Due to Rapid Heating," Int. J. Heat Mass Transfer, **46**, pp. 2253–2261.
[25] Aktas, M. K., Farouk, B., Narayan, P., and Weathley, M. A., 2004, "A Numerical Study of the Generation and Propagation of Thermoacoustic Waves in Water," Phys. Fluids, **16**, pp. 3786–3794.
[26] Boris, J. P., Landsberg, A. M., Oran, E. S., and Gardner, J. H., 1993, "LCPFCT-A Flux-Corrected Transport Algorithm for Solving Generalized Continuity Equations," NRL/MR/6410-93-7192, Naval Research Laboratory, Washington, DC.
[27] Poinsot, T. J., and Lele, S. K., 1992, "Boundary Conditions for Direct Simulations of Compressible Viscous Flows," J. Comput. Phys., **101**, pp. 104–129.

Energy and Exergy Balance in the Process of Pulverized Coal Combustion in a Tubular Combustor

S. K. Som[1]

S. S. Mondal

S. K. Dash

Department of Mechanical Engineering,
Indian Institute of Technology,
Kharagpur 721302, India

A theoretical model of exergy balance, based on availability transfer and flow availability, in the process of pulverized coal combustion in a tubular air-coal combustor has been developed to evaluate the total thermodynamic irreversibility and second law efficiency of the process at various operating conditions. The velocity, temperature, and concentration fields required for the evaluation of flow availability have been computed numerically from a two-phase separated flow model on a Eulerian-Lagrangian frame in the process of combustion of pulverized coal particles in air. The total thermodynamic irreversibility in the process has been determined from the difference in the flow availability at the inlet and outlet of the combustor. A comparative picture of the variations of combustion efficiency and second law efficiency at different operating conditions, such as inlet pressure and temperature of air, total air flow rate and inlet air swirl, initial mean particle diameter, and length of the combustor, has been provided to shed light on the trade-off between the effectiveness of combustion and the lost work in the process of pulverized coal combustion in a tubular combustor. [DOI: 10.1115/1.2101860]

Keywords: combustion, energy, exergy, heat transfer, pulverized coal, second law

Introduction

Coal is an important source of energy in generating electricity and also to meet its future demand, since coal reserves are much greater than those of other fossil fuels. Most of the coal-fired thermal power plants use pulverized coal for combustion. Coal is also used in the operation of a blast furnace, which employs pulverized coal injection along with blast air through its tuyere to reduce the coke feed rate. The pulverization of coal into fine particles is done to increase the specific surface area (the ratio of surface area to volume) to enhance the rate of heat and mass transfer between the coal particles and surrounding hot gas. An efficient and stable combustion of pulverized coal particles depends upon the physical and chemical properties of coal, the diameter of coal particles, and other operating conditions like temperature, pressure, and fluid-dynamic state of the surrounding gas.

The scope of coal combustion is very wide and well diversified. Research in the field of coal combustion has been going on for the last three decades. A host of articles, both experimental and numerical in nature, including the exhaustive reviews of Smoot [1,2] is available in the literature on the studies of pulverized coal combustion. However, all the works are centered around predicting the different aspects of combustion performance of pulverized coal. Important experimental studies are due to Flagan and Taylor [3], Mclean et al. [4], Seeker et al. [5], Neville et al. [6], Ragland et al. [7], Rees et al. [8], Kelly et al. [9], and Lester et al. [10]. These works pertain to the recognition of rate determining process and determination of the reaction rate constants at various stages of coal combustion process. Important numerical works, on the other hand, are due to Smith et al. [11], Williams et al. [12–14], Arenillas et al. [15], Görres et al. [16], Hurt et al. [17], Liakos et al. [18], Fan et al. [19], and Li et al. [20]. Most of these works deal with the modeling of reaction kinetics and chemistry of reactions of pulverized coal particles. Several computer codes are available to predict the rate of volatile release and the composition of key species during devolatilization of coal. A couple of works due to Akoi et al. [21], Guo et al. [22], and Gordon et al. [23] pertain to the modeling of pulverized coal combustion in a blowpipe, drop tube, and raceway zone of a blast furnace. The models are based on the solution of gas phase and particle phase conservation equations in either a Eulerian-Lagrangian or Eulerian-Eulerian frame, and depend on the empirical values of transport coefficients and coal reactivities at several stages of the physical process. The concept of mixture fraction along with PDF function for interaction of coal combustion with gas phase turbulence has been considered in the models based on a Eulerian-Lagrangian approach. The outcome of these models are the predictions of trajectories of burning coal particles, temperature histories in combustion zone, and the emission characteristics including the optimization of NO_x emission.

From the viewpoint of energy economy, an efficient process of coal combustion should be guided not only by the combustion efficiency of the process but also by its second law efficiency. While the combustion efficiency characterizes the effectiveness in converting the chemical energy of the fuel into thermal energy, following the principle of conservation of energy quantity, the second law efficiency characterizes the effectiveness in preservation of quality of energy defined as exergy. In principle, a high combustion efficiency implies a higher conversion or burnout of fuel into noncombustible products. On the other hand, rapid transport processes and chemical reactions increase process irreversibilities and result in a state of the system with a reduction in the work potential of the energy possessed by the system. This is conceived in the sense that there is every likelihood of obtaining a relatively smaller amount of useful work from the energy due to nonidealities in the process involved. Hence, the exergy analysis of a pulverized coal combustion process to evaluate the second law efficiency provides additional thermodynamic information about the lost work in the process through different kinds of dissipative effects due to transport processes and chemical reactions

[1]Corresponding author. E-mail: sksom@mech.iitkgp.ernet.in

Contributed by the Heat Transfer Division of ASME for publication in the JOURNAL OF HEAT TRANSFER. Manuscript received May 12, 2004; final manuscript received July 25, 2005. Assoc. Editor: Bakhtier Farouk.

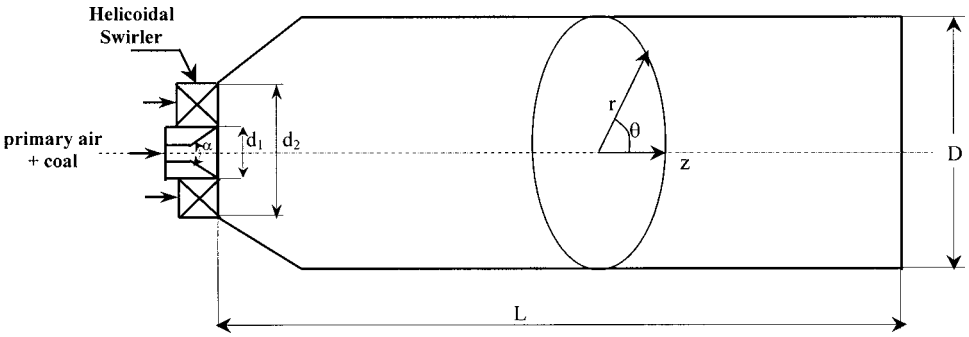

Fig. 1 Physical model

at various stages. A minimization of the losses by suitable choice of operating parameters leads to an optimum thermodynamic design of the process for an overall energy economy. In practice, the optimum design of the combustor is based on a trade-off between η_c and η_{II} for an overall energy economy. The relative weight of η_c and η_{II} to be assigned in the process of optimization depends on the relative saving in the cost of energy quantity over the energy quality for a specific application. This is a task of energy management, where the information being provided by the present paper will serve as the fundamental input.

Much less information is available in the literature regarding the thermodynamic irreversibilities and the exergy loss in the process of coal combustion. The work of Dash et al. [24] is perhaps the first one which provides the information on thermodynamic irreversibilities in the evaporation of a fuel droplet. Subsequently, the works of Dash and Som [25], Puri [26], and Hiwase et al. [27] provided similar information in the case of droplet combustion. Som and Dash [28] studied the second law analysis in the process of spray evaporation based on the exergy loss in the process. Dunbar and Lior [29] calculated the sources of combustion irreversibilities with hydrogen and methane flames, and found that approximately one-third of the useful energy of the fuel is destroyed during the combustion process. Based on the solution of field equations, Datta and Som [30] and Som and Sharma [31] reported the exergy destruction and second law efficiency of spray combustion in a gas turbine combustor. A comprehensive documentation on mathematical and modeling tools for calculating the irreversibilities in combustion, along with the reviews of some methods for reducing irreversibilities, is provided by Lior [32]. He also presented the results of exergy distribution in a low-NO_x pulverized coal combustor with reference to the earlier works of Kim and Lior [33,34]. However, a calculation of exergy destruction in a pulverized coal combustor to evaluate the relative roles of operating parameters on both combustion efficiency and second law efficiency has not yet been reported. The present paper makes an attempt towards this direction.

Theoretical Formulation

Physical Model. The physical model refers to the combustion of a continuously injected pulverized coal in a tubular combustor, as shown in Fig. 1. The primary air is supplied along with the coal particles through the small inner tube with a slanted divergent exit. The secondary air is supplied through the swirler at entry, as shown in Fig. 1. The slanted divergent exit of the inner tube has been made for a better radial dispersion of coal particles which are laden with the stream of parallel flow of primary air and are injected into the tubular combustor.

Flow and Combustion Modeling. A numerical model of pulverized coal combustion process within the combustor has been developed to determine the velocity, temperature, and species concentration fields, and finally the combustion efficiency.

The numerical model is based on a Eulerian-Lagrangian formulation of an axisymmetric two-phase (gas-particle) flow in which the coupling between the two phases is taken care of through interactive source terms. A Reynolds average k-ϵ model has been used for the gas phase turbulence. Body force and the buoyancy force on coal particles are neglected in the analysis because of the small diameter of the pulverized coal particles. Similarly, the virtual mass force and Bassett force on coal particles are also neglected due to the high density ratio between the two phases.

The standard k-ϵ model has been adopted despite the fact that many researchers observe some shortcomings in the ability of the k-ϵ model to predict a swirling flow field quantitatively. However, there is no conclusive information available in the literature regarding the accurate adaptability of a suitable modification of the k-ϵ model for a confined swirling flow. The models like ASM and RSM are either too complex or equally poor in predicting a strong swirling flow. Moreover, it is expected that the accuracy in predicting the gross flow parameters like combustion efficiency and second law efficiency will not be affected much with the adoption of a standard k-ϵ model. This is because the second law efficiency and combustion efficiency are evaluated through time mean values of field variables, and we are not interested in the variations in fluctuating components of the variables which determine the local turbulent properties. Therefore, the standard k-ϵ model has been considered for the solution in the present work. It has to be mentioned in the context that the prime objective of the present work is to develop an exergy model of a turbulent reacting flow with coal combustion and to establish mainly the qualitative trends of variation of second law efficiency with pertinent operating parameters. Therefore, simplified and popular models of chemical kinetics and turbulence have been used for the flow computation. A cylindrical coordinate system has been used for the present analysis.

Gas Phase Conservation Equations. The time average gas phase conservation equations are as follows:

Continuity.

$$\frac{\partial \rho}{\partial t} + \frac{\partial}{\partial x_i}(\rho U_i) = \dot{S} \tag{1}$$

Momentum.

$$\frac{\partial(\rho U_i)}{\partial t} + \frac{\partial}{\partial x_j}(\rho U_i U_j) = -\frac{\partial p'}{\partial x_i} + \frac{\partial}{\partial x_j}\left\{\mu_{\text{eff}}\left(\frac{\partial U_i}{\partial x_j} + \frac{\partial U_j}{\partial x_i}\right)\right\} + \dot{S}_{M_i} + \dot{S}U_i \tag{2}$$

where

$$\mu_{\text{eff}} = \mu + c_\mu \rho \frac{k^2}{\varepsilon} \tag{3}$$

$$p' = p + \frac{2}{3}\rho k + \frac{2}{3}\mu_{\text{eff}}\frac{\partial U_j}{\partial x_j} \tag{4}$$

Turbulent Kinetic Energy (k).

$$\frac{\partial(\rho k)}{\partial t} + \frac{\partial}{\partial x_i}(\rho U_i k) = \frac{\partial}{\partial x_i}\left(\frac{\mu_t}{\sigma_k}\frac{\partial k}{\partial x_i}\right) + P - \rho\varepsilon + \dot{S}k \tag{5}$$

where turbulent kinetic energy production rate P is given by

$$P = \mu_t\left(\frac{\partial U_i}{\partial x_j} + \frac{\partial U_j}{\partial x_i}\right)\frac{\partial U_i}{\partial x_j} - \frac{2}{3}\frac{\partial U_i}{\partial x_i}\left(\rho k + \mu_t\frac{\partial U_i}{\partial x_i}\right) \tag{6}$$

Turbulent Kinetic Energy Dissipation Rate (ε).

$$\frac{\partial(\rho\varepsilon)}{\partial t} + \frac{\partial}{\partial x_i}(\rho U_i\varepsilon) = \frac{\partial}{\partial x_i}\left(\frac{\mu_t}{\sigma_\varepsilon}\frac{\partial\varepsilon}{\partial x_i}\right) + c_{1\varepsilon}\frac{\varepsilon}{k}P - \rho c_{2\varepsilon}\frac{\varepsilon^2}{k} + \dot{S}\varepsilon \tag{7}$$

Constants for standard k-ε model are taken as

$$c_\mu = 0.09, \quad c_{1\varepsilon} = 1.44, \quad c_{2\varepsilon} = 1.92, \quad \sigma_k = 1.0, \quad \text{and } \sigma_\varepsilon = 1.3$$

Energy. The energy equation is written in terms of enthalpy as

$$\frac{\partial(\rho h)}{\partial t} + \frac{\partial}{\partial x_i}(\rho U_i h) = \frac{\partial}{\partial x_i}\left(\rho\alpha_t\frac{\partial h}{\partial x_i}\right) - \dot{S}_E - \frac{\partial q_i^r}{\partial x_i} + \dot{S}h \tag{8}$$

The term $\dot{S}_E$ accounts for the energy absorbed by the coal particles from the gas phase during their heating up period, and the term q_i^r represents the heat flux due to net radiation exchange between gas and particle phase.

The radiative energy exchange is evaluated in consideration of the gas phase to be gray, absorbing, and an emitting medium. The scattering is considered only for the particles. The radiative transfer equation is solved following a first-order moment method (Ozisik [35]) which reduces the integro-differential equation of radiative transfer into a differential equation as given below.

$$\frac{\partial q_i^r}{\partial x_i} = 4\pi\left[\kappa\frac{\sigma T^4}{\pi} + E_p\right] - [\kappa + \kappa_p]G \tag{9}$$

where the irradiation G is related to q_i^r as

$$q_i^r = -\frac{1}{3(\kappa + \kappa_p + \sigma_p)}\frac{\partial G}{\partial x_i} \tag{10}$$

where E_p is the equivalent emission of the particles; κ_p and σ_p are the equivalent absorption coefficient and scattering factor of the particle, respectively. The values of E_p, κ_p, and σ_p at any point in the gas phase are evaluated from the following relations:

$$E_p = \lim_{\forall\to 0}\sum_{i=1}^{n}\varepsilon_{pi}A_{pi}\frac{\sigma T_i^{p^4}}{\pi\forall} \tag{11a}$$

$$\kappa_p = \lim_{\forall\to 0}\sum_{i=1}^{n}\varepsilon_{pi}\frac{A_{pi}}{\forall} \tag{11b}$$

$$\sigma_p = \lim_{\forall\to 0}\sum_{i=1}^{n}(1 - f_{pi})(1 - \varepsilon_{pi})\frac{A_{pi}}{\forall} \tag{11c}$$

where ε_{pi} and f_{pi} are the emissivity and scattering factor for the ith particle, respectively. The dominant radiation intensity in the carrier phase is due to CO_2, H_2O, and CO. In light of the assumption of a gray gas radiation model, the absorption coefficient κ is replaced by Planck's mean absorption coefficient κ_m. The local value of κ_m is computed as

$$\kappa_m = C_{H_2O}\kappa_{m_{H_2O}}(T) + C_{CO_2}\kappa_{m_{CO_2}}(T) + C_{CO}\kappa_{m_{CO}}(T) \tag{12}$$

The values of $\kappa_m(T)$ as a function of temperature for CO_2, H_2O, and CO are taken from Sparrow and Cess [36].

Species Transport and Combustion Chemistry. The species concentration in gas phase is found from a conserved scalar formulation in consideration of a rapid chemical reaction for equilibrium to exist at the molecular level. The conservation equation of a scalar quantity, the mixture fraction ξ, is defined as

$$\xi = \frac{Z_i - Z_{io}}{Z_{if} - Z_{io}} \tag{13}$$

where Z_i is the element mass fraction for some element i. Subscripts o and f denote the values at the inlet oxidizer stream and inlet fuel stream, respectively.

A pdf approach (probability distribution of ξ) followed by Jones and Whitelaw [37] has been taken to account for the turbulent fluctuations of different scalar properties. A β function has been employed for the PDF in the present study as

$$p(\xi) = \frac{\xi^{\alpha-1}(1-\xi)^{\beta-1}}{\int \xi^{\alpha-1}(1-\xi)^{\beta-1}d\xi} \tag{14a}$$

where

$$\alpha = \overline{\xi}\left(\frac{\overline{\xi}(1-\overline{\xi})}{g} - 1\right) \tag{14b}$$

$$\beta = (1-\overline{\xi})\left(\frac{\overline{\xi}(1-\overline{\xi})}{g} - 1\right) \tag{14c}$$

$\overline{\xi}$, g are the mean and variance of the PDF function, respectively, and are defined as

$$\overline{\xi} = \int_0^1 \xi p(\xi)d\xi \tag{15}$$

$$g = \int_0^1 (\xi - \overline{\xi})^2 p(\xi)d\xi \tag{16}$$

The conservation equations, which are solved for $\overline{\xi}$ and g, are as follows:

$$\frac{\partial(\rho\overline{\xi})}{\partial t} + \frac{\partial}{\partial x_i}(\rho U_i\overline{\xi}) = \frac{\partial}{\partial x_i}\left(\frac{\mu_t}{\sigma_t}\frac{\partial\overline{\xi}}{\partial x_i}\right) + \dot{S} \tag{17}$$

$$\frac{\partial(\rho g)}{\partial t} + \frac{\partial}{\partial x_i}(\rho U_i g) = \frac{\partial}{\partial x_i}\left(\frac{\mu_t}{\sigma_t}\frac{\partial g}{\partial x_i}\right) + C_g\mu_t\left(\frac{\partial\overline{\xi}}{\partial x_i}\right)^2 - C_d\rho\frac{\varepsilon}{k}g \tag{18}$$

where $C_g = 2.86$, $C_d = 2.0$, and $\sigma_t = 0.7$.

The mean value of species concentration can be expressed as

$$\overline{C_i} = \int_0^1 p(\xi)C_i(\xi,h)d\xi \tag{19}$$

$$C_i = C_i(\xi,h) \tag{20}$$

where the instantaneous species concentration C_i for different species are found out from the principle of minimization of Gibbs' free energy following the algorithm given in Pratt and Smoot [38].

Generation of Particle Phase Information. The coal particles, injected continuously into the combustor, are considered to consist of a finite number of classes with definite size ranges. The initial particle size distribution of coal particle is assumed to follow a realistic four-parameter Rosin-Rammler distribution function, given by

$$G'(d_i) = \frac{\exp(-bd_i^n) - \exp(-bd_{\max\,i}^n)}{\exp(-bd_{\min\,i}^n) - \exp(-bd_{\max\,i}^n)} \tag{21}$$

where $G'(d_i)$ is the mass fraction of the spray having diameter above d_i. The dispersion parameter n is taken as 3, as recommended by Mugele and Evans [39].

The identity of each particle class is traced within the gas phase by tracking a representative particle of the class along its trajectory. The updated position, velocity, size, and temperature of the particles are determined from the solution of respective conservation equations on a Lagrangian frame.

Particle Velocity.

$$m^p \frac{dV_i^p}{dt} = \frac{\pi}{8}\rho d^{p^2} C_D |V_i^g - V_i^p|(V_i^g - V_i^p) \tag{22}$$

Drag coefficient C_D is computed by using the standard drag law from Clift et al. [40].

The effect of gas phase turbulence on the particle motion is simulated using a stochastic approach. The instantaneous gas phase velocity (V_i^g) is obtained by computing the fluctuating velocity component from the turbulent kinetic energy in consideration with isotropic turbulence and using a normally distributed random number, ζ, as

$$V_i^g = U_i + \varsigma\sqrt{\frac{2k}{3}} \tag{23}$$

The movement of the particles in gas phase is traced by updating their position from the equation

$$\frac{dx_i^p}{dt} = V_i^p \tag{24}$$

Particle Temperature.

$$m^p c_p^p \frac{dT^p}{dt} = hA_p(T^g - T^p) + \varepsilon_p A_p \sigma(\theta_R^4 - T^{p^4}) - \frac{dm_{\rm vol}}{dt}\Delta H_{\rm devolatilization} + \frac{dm_{\rm char}}{dt}\Delta H_{\rm char\ reaction} \tag{25}$$

The value of convective heat transfer coefficient h is found from the standard correlation by Ranz and Marshall [41] as

$$\mathrm{Nu} = 2.0 + 0.6\,\mathrm{Re}_p^{0.5}\mathrm{Pr}^{0.33} \tag{26}$$

In the initial period of particle heating, the contributions of devolatilization and char combustion at the particle surface (the third and fourth term in the right-hand side of Eq. (25)) are negligible as compared to the other two terms. Usually the processes of devolatilization and char combustion become prominent as the particle temperature rises above 500 K.

The rate of devolatilization is found following the well-established two competing-reactions kinetic model of Kobayashi et al. [42] as

$$\frac{dm_{\rm vol}}{dt} = \left[m_i^p(\alpha_1 R_1 + \alpha_2 R_2)\exp\left(-\int_0^t (R_1 + R_2)dt\right)\right] \tag{27a}$$

where

$$R_1 = A_{v1}\exp\left(-\frac{E_{v1}}{RT^p}\right) \tag{27b}$$

$$R_2 = A_{v2}\exp\left(-\frac{E_{v2}}{RT^p}\right) \tag{27c}$$

The char combustion reaction has been considered to be a single-step irreversible one, given by

$$\mathrm{C} + \frac{1}{2}\mathrm{O}_2 = \mathrm{CO} \tag{28}$$

The rate of char reaction is found following the models of Baum and Street [43] and Field [44] as

$$\frac{dm_{\rm char}}{dt} = \pi d^{p2}\rho R T^g \left(\frac{C_{\mathrm{O}_2}}{M_{\mathrm{O}_2}}\right)\frac{R_C R_D}{R_C + R_D} \tag{29a}$$

where

$$R_D = C_1 \frac{[(T^P + T^g)/2]^{0.75}}{d^p} \tag{29b}$$

$$R_C = A_c \exp\left(-\frac{E_C}{RT^P}\right) \tag{29c}$$

Interphase Source Interaction Terms. The source interaction terms $\dot{S}$, $\dot{S}_{M_i}$, and $\dot{S}_E$ appearing in the gas phase conservation equations (Eqs. (1), (2), and (8)) are determined as follows:

$$\dot{S} = \sum_{k=1}^{r} \frac{1}{\forall}\frac{d}{dt}(m^p(k))\dot{N}(k)\Delta t \tag{30}$$

$$\dot{S}_{M_i} = \sum_{k=1}^{r} \frac{1}{\forall}\frac{d}{dt}(m^p(k)V_i^p(k))\dot{N}(k)\Delta t \tag{31}$$

$$\dot{S}_E = \sum_{k=1}^{r} \frac{1}{\forall}\frac{d}{dt}(h\pi d^{p^2}(T^g - T^p) + \varepsilon_p \pi d^{p^2}\sigma(\theta_R^4 - T^{p^4}))\dot{N}(k)\Delta t \tag{32}$$

where $\forall$ is the volume of a computational cell which contains the particle class from 1 to r during a time interval of Δt. The rate of particle number (the number of particles flowing per unit time) of a given class is obtained as

$$\dot{N}(k) = \frac{\dot{m}_{f_{\rm in}} dG'\{d_i(k)\}}{m_i^p(k)} \tag{33}$$

Exergy Model of Pulverized Coal Combustion

The exergy analysis of the problem has been made on the basis of flow availability to the system comprising the entire combustor (Fig. 1), in consideration of the outer wall to be adiabatic. Since the words "availability" and "exergy" are synonymous in their thermodynamic implications, both of them will be used in the remaining part of the text, depending upon the appropriate uses in places following the general convention. It can be written for the conservation of exergy of the system that

$$\dot{A}_{\rm in} = \dot{A}_e + \dot{I} \tag{34}$$

where $\dot{A}_{\rm in}$ and $\dot{A}_e$ are the rates of flow availability coming in and going out of the system, respectively, and $\dot{I}$ is the rate of thermodynamic irreversibility within the system.

Determination of Flow Availabilities. The flow availabilities of different species at inlet and outlet of the combustor have been evaluated with respect to an exergy reference thermodynamic state of $P_r = 101.35$ kN/m^2, $T_r = 298.15$ K with mole fractions of the constituents as $x_r^{\mathrm{O}_2} = 0.2035$, $x_r^{\mathrm{CO}_2} = 0.0003$, and $x_r^{\mathrm{H}_2\mathrm{O}} = 0.0303$ as recommended by Moran and Shapiro [45].

The flow availability at the inlet is associated with the inflow of air and fuel to the system, and can be written as

$$\dot{A}_{\text{in}} = \dot{m}_{a_{\text{in}}} a^a_{\text{in}} + \dot{m}_{f_{\text{in}}} a^f_{\text{in}} \tag{35}$$

where $\dot{m}_{a_{\text{in}}}$ = mass flow rate of air in to the combustor, a^a_{in} = specific flow availability of air at inlet, $\dot{m}_{f_{\text{in}}}$ = mass flow rate of fuel into the combustor, and a^f_{in} = specific flow availability of fuel at inlet.

The specific flow availability of air is determined from the following equation:

$$a^a_{\text{in}} = (h^a_{\text{in}} - h_r) - T_r(s^a_{\text{in}} - s_r) \tag{36a}$$

where

$$(h^a_{\text{in}} - h_r) = \int_{T_r}^{T^a_{\text{in}}} c^a_p(T)dT \tag{36b}$$

$$(s^a_{\text{in}} - s_r) = \int_{T_r}^{T^a_{\text{in}}} \frac{c^a_p(T)}{T}dT - \frac{\overline{R}}{M_a}\int_{p_r}^{p^a_{\text{in}}} \frac{dp}{p} \tag{36c}$$

The fuel considered in the present analysis is coal, whose ultimate analysis is as follows:

70.2 % C, 5.7 % H, 13.4 % O, 1.9 % N, and 8.8 % ash

The flow availability of coal comprises both chemical and thermo-mechanical components, and is defined on the basis of a single-step irreversible reaction which can be represented in consideration of the ultimate analysis of coal as

$$\frac{70.2}{12}\text{C} + \left(\frac{5.7 - \frac{13.4}{8}}{2}\right)\text{H}_2 + 6.856\text{O}_2 = 5.85\text{CO}_2 + 2.0125\text{H}_2\text{O}$$

$$\text{or,}\quad \text{C} + 0.344\text{H}_2 + 1.172\text{O}_2 = \text{CO}_2 + 0.344\text{H}_2\text{O} \tag{37}$$

Therefore, the flow availability of coal per mole of carbon can be written as

$$\overline{a}^f_{\text{in}} = (\overline{h}^{\text{C}}_{\text{in}} + 0.344\overline{h}^{\text{H}_2}_{\text{in}} + 1.172\overline{h}^{\text{O}_2}_r - \overline{h}^{\text{CO}_2}_r - 0.344\overline{h}^{\text{H}_2\text{O}}_r) - T_r(\overline{s}^{\text{C}}_{\text{in}} + 0.344\overline{s}^{\text{H}_2}_{\text{in}} + 1.172\overline{s}^{\text{O}_2} - \overline{s}^{\text{CO}_2} - 0.344\overline{s}^{\text{H}_2\text{O}}) \tag{38}$$

where

$$\overline{h}^{\text{C}}_{\text{in}} = \Delta\overline{h}^{\text{C}}_f + \int_{T_r}^{T^f_{\text{in}}} \overline{c}_p(T)dT \tag{39a}$$

$$\overline{h}^{\text{H}_2}_{\text{in}} = \Delta\overline{h}^{\text{H}_2}_f + \int_{T_r}^{T^f_{\text{in}}} \overline{c}_p(T)dT \tag{39b}$$

$$\overline{h}^{\text{O}_2}_r = 0 \tag{39c}$$

$$\overline{h}^{\text{CO}_2}_r = \Delta\overline{h}^{\text{CO}_2}_f \tag{39d}$$

$$\overline{h}^{\text{H}_2\text{O}}_r = \Delta\overline{h}^{\text{H}_2\text{O}}_f \tag{39e}$$

$$\overline{s}^{\text{C}}_{\text{in}} = \overline{s}^{\text{C}}_r + \int_{T_r}^{T^f_{\text{in}}} \frac{\overline{c}_p(T)}{T}dT - \overline{R}\int_{p_r}^{p^f_{\text{in}}} \frac{dp}{p} \tag{39f}$$

$$\overline{s}^{\text{H}_2}_{\text{in}} = \overline{s}^{\text{H}_2}_r + \int_{T_r}^{T^f_{\text{in}}} \frac{\overline{c}_p(T)}{T}dT - \overline{R}\int_{p_r}^{p^f_{\text{in}}} \frac{dp}{p} \tag{39g}$$

$$\overline{s}^{\text{O}_2} = \overline{s}^{\text{O}_2}_r - \overline{R}\ln(x^{\text{O}_2}_r) \tag{39h}$$

$$\overline{s}^{\text{CO}_2} = \overline{s}^{\text{CO}_2}_r - \overline{R}\ln(x^{\text{CO}_2}_r) \tag{39i}$$

$$\overline{s}^{\text{H}_2\text{O}} = \overline{s}^{\text{H}_2\text{O}}_r - \overline{R}\ln(x^{\text{H}_2\text{O}}_r) \tag{39j}$$

The specific flow availability of the fuel (coal), i.e., the flow availability per unit mass of coal, is calculated from the molar availability as

$$a^f_{\text{in}} = n_C\frac{\overline{a}^f_{\text{in}}}{M_C} \tag{40}$$

where M_C is the molecular weight of carbon and n_C is the mass fraction of carbon, which is 0.702.

The flow availability at the combustor exit can be expressed as

$$\dot{A}_e = 2\pi\int_0^R \left(\sum_j C^j_e a^j_e\right)\rho^g_e U_{z_e} r\,dr \tag{41}$$

where C^j_e is the mass fraction of the jth species and U_{z_e} is the local axial gas velocity at the exit plane.

The specific flow availability a^j_e of a jth species at a point in the exit plane is calculated on the basis of local pressure and temperature in the similar fashion as done for an inlet. Both chemical and thermo-mechanical availabilities for reacting species (if any) and only thermo-mechanical availability for the nonreacting species are considered.

Second Law Efficiency. The second law efficiency of the combustor can be expressed as

$$\eta_{II} = \frac{\dot{A}_e}{\dot{A}_{\text{in}}} = 1 - \frac{\dot{I}}{\dot{A}_{\text{in}}} \tag{42}$$

Combustion Efficiency. The combustion efficiency, which can also be stated as first law efficiency, can be written as

$$\eta_c = \frac{(\dot{m}_f \,.\, \text{Calorific value of fuel}) - \sum_j \dot{m}_j|\Delta H_{\text{reaction},j}|}{\dot{m}_f \,.\, \text{Calorific value of fuel}} \tag{43}$$

where $\dot{m}_j$ is the mass flow rate of a reacting species (if any) at the exit plane and $\Delta H_{\text{reaction},j}$ is the enthalpy of reaction of that species for complete oxidation. The reactive species likely to be existent are CO, H_2, and C(s).

Method of Solution. The numerical code consisted of two different modules, one for gas phase computation and the other for calculation of the particle phase. The gas phase conservation equations (Eqs. (1), (2), (5), (7), (8), (17), and (18)) were solved following an implicit finite volume technique. A coupling between pressure and velocity was accomplished using the SIMPLE algorithm. The space derivatives of the diffusion terms were discretized by a central differencing scheme, while the advection terms were discretized by power law scheme. The conservation equations for the particle phase (Eqs. (22), (24), and (25)) were solved by the fourth-order Runge-Kutta method with appropriate initial conditions. The solution in this module continued until all the representative particles of different classes escaped from the domain of computation. The convergence criterion for all the equations such as, continuity, momentum, PDF variable, and turbulence was set to 10^{-3}, while for energy it was set to 10^{-6}. This means, when the whole field residual for all the above variables fell below 10^{-3} and 10^{-6} (for energy), the solution was said to have been converged. A variable size adaptive grid system was considered and the variations in the size of the grids were made smooth. A numerical mesh of 100×42 ($z\times r$) was used after several numerical experiments, which showed that further refinement in grids in either direction did not change the result (maximum change in velocity or any scalar variable in the carrier phase) by more than 2 percent.

Table 1 Operating parameters used for the present study

Mass flow rate of air	0.042kg/s, 0.068kg/s								
Mass ratio of secondary to primary air	6.5								
Inlet air temperature	600K, 1000K								
Inlet air Pressure	100 kPa, 500 kPa								
Mass flow rate of coal particle	0.004kg/s								
SMD of coal particle	50μm, 95μm, 145μm,								
Analysis of coal samples	Proximate analysis				Ultimate analysis (moisture-free)				
	Moisture	Volatile matter	Char	Ash	C	H	O	N	Ash
	2.4	45.4	43.6	8.6	70.2	5.7	13.4	1.9	8.8
Combustor Dimensions	Primary diameter (d_1)	0.016m							
	Secondary diameter (d_2)	0.054m							
	Combustor diameter (D)	0.2m							
	Length of Combustor (L)	0.75m, 1.0m, 1.5m							
	Divergent angle (α)	50^0							
Kinetic parameters Kobayashi Model: Eq(27) Baum and Street model: Eq(29)	$A_{v1}=2x10^5$,$E_{v1}=1.046x10^8$ (J/kmol), $A_{v2}=1.3x10^7$,$E_{V2}=1.67x10^8$ (J/kmol) $C_1=5x10^{-12}$, $A_e=0.002$, $Ec=7.9x10^7$ (J/kmol)								

A zero axial gradient was prescribed at the outlet for all the variables. Standard logarithmic law of wall was considered for the near-wall region. For radiation calculation, the end planes were assumed to be radiatively adiabatic, and the Marshak boundary condition was applied at the solid combustor wall. Symmetry boundary conditions (normal gradient to be zero) were applied at the axis with no-slip condition at the wall. The axial velocity distribution at both primary and secondary air inlet was considered to be uniform (a plug flow mode). For secondary air, a linear tangential velocity distribution was assumed at the inlet in consideration of a solid body-type rotation imparted by a helicoidal vane swirler. The temperature distribution of air at the inlet plane was considered to be uniform. The operating parameters used for the present work have been chosen from the typical values available in different literature and are given in Table 1.

Validation of Numerical Model. The accuracy of the quantitative and even the qualitative trends of the predicted results relating to combustion efficiency, process irreversibilities, and second law efficiency depends mainly on the accuracy with which the velocity, temperature, and species concentration fields in the process of pulverized coal combustion are determined from the numerical computation of the present model. The experimental results in identical situations of the present model are not available in the literature. However, a possible comparison of numerical results from the present model has been made with the available experimental data of Vu and Gouldin [46], in the case of a coaxial counter-swirling axisymmetric confined flow.

The physical model considered by Vu and Gouldin consisted of a primary or inner flow passage with a diameter of 0.0372 m and an outer or secondary flow passage of diameter of 0.145 m. The discharge from the swirl generator at the inner flow passage gave a swirl number of 0.49 and average axial velocity of 30.3 m/s. The counter-swirling air at the inlet to the secondary air passage had a swirl number of 0.51 and average velocity of 20.2 m/s. The comparison of experimental results of Vu and Gouldin with the present computational results is shown in Figs. 2(*a*)–2(*f*). Figures 2(*a*)–2(*c*) show a fair agreement of the predicted axial velocity distribution by the present model with the experimental values of Vu and Gouldin. The deviation is observed only near the axis at the upstream sections of the duct. This may be attributed due to the underprediction of the length of an on axis recirculation zone by the standard k-ε.

Figures 2(*d*)–2(*f*) show in a similar way a fair agreement of the tangential velocity distributions. In spite of some discrepancy observed between the predicted and experimental results in a certain zone, the calibrated accuracy of the present numerical model is quite acceptable for the purpose of predictions of gross engineering parameters like combustion efficiency and second law efficiency.

Results and Discussion

Influence of Air Pressure and Secondary Air Swirl at Inlet on Combustion Efficiency and Second Law Efficiency. It is observed from Table 2 that, for a given combustor length and for given values of other operating parameters, an increase in inlet

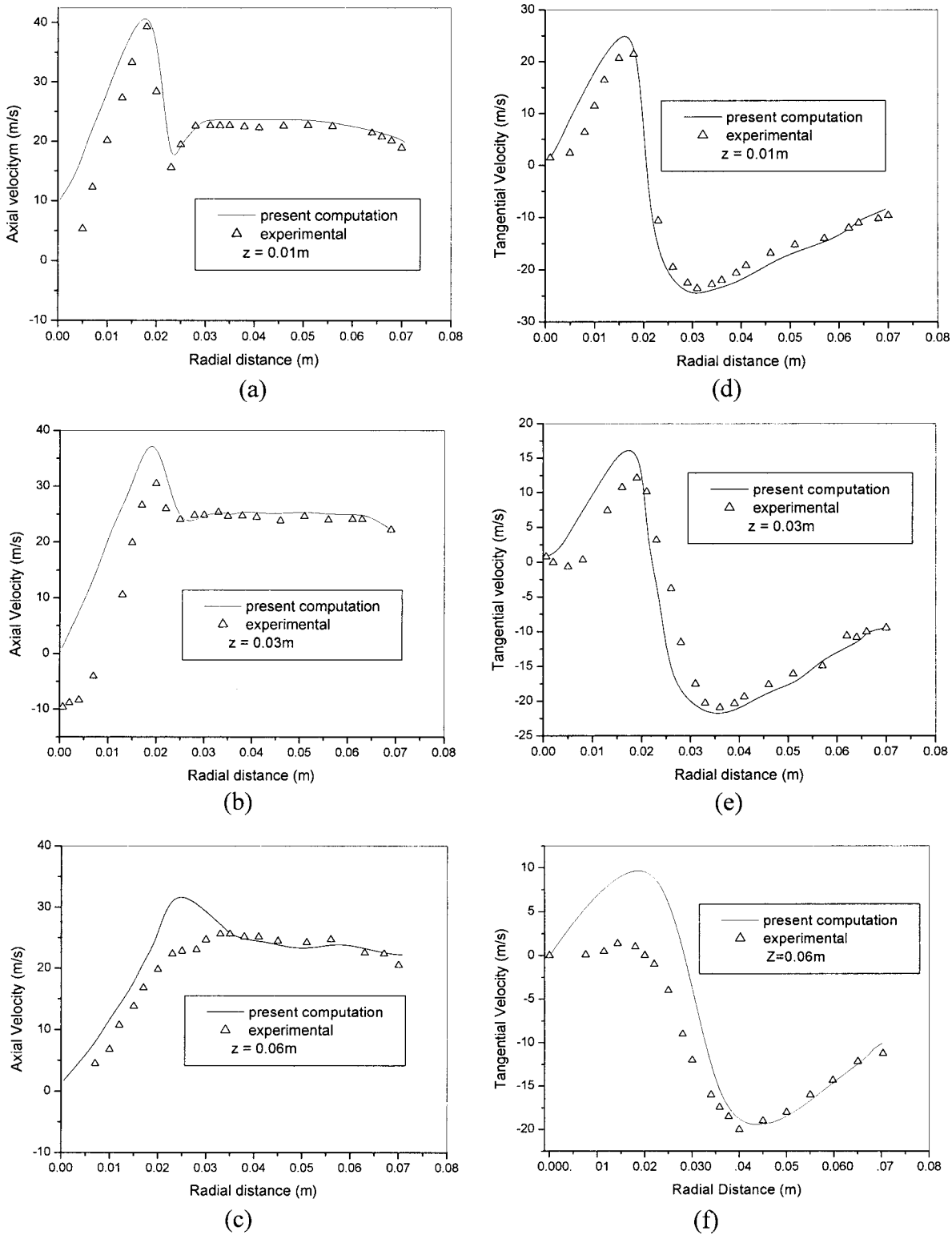

Fig. 2 Comparison of axial and tangential velocity components for a coaxial counter swirling axisymmetric confined flow with the experimental result of Vu and Gouldin [46]

pressure increases the combustion efficiency η_c and decreases the second law efficency η_{II} at all values of inlet swirl ($S=0.0$ to 0.77). The changes in η_c and η_{II} are drastic at zero-swirl condition. This trend of change in η_{II} can be attributed to an increase in total irreversibility due to an enhanced rate of char burning reaction at higher pressure and completion of burning process of coal particles because of their enhanced residence time in the combustor. At a higher pressure, but for a given temperature, the density of air becomes high, and hence for a given mass flow the air velocity is low. Under this situation, a coal particle, which is injected with a higher velocity, is quickly dragged to a relatively low velocity of air flowing through the combustor. Thus, the particle residence time is increased as observed from Figs. 3(*a*) and 3(*b*). The enhancement in the rate of burnout of coal particles with

Table 2 Influence of inlet air pressure and secondary air swirl on combustion efficiencies and second law efficiencies ($\dot{m}_{a_{in}}$=0.042 kg/s, $\dot{m}_{f_{in}}$=0.004 kg/s, T_{in}=600 K, SMD$_i$=50 μm)

Inlet air pressure (kPa)	Secondary Swirl number *(S)*	Second law efficiency			Combustion efficiency		
		0.75m	1.0m	1.5m	0.75m	1.0m	1.5m
100	0.0	81	78	59	79	85	98
	0.32	79	65	56	84	96	99
	0.77	84	67	57	82	93	97
500	0.0	59	56	55	99	99	99
	0.32	59	55	55	99	98	99
	0.77	65	61	56	91	95	97

air pressure is apparent from Figs. 4(*a*) and 4(*b*). It is observed from a comparison of Figs. 4(*a*) and 3(*a*) that at a lower pressure of 1 bar all particle classes except that of 150 μm leave the combustor without complete combustion because of their low residence time, as explained earlier. However, the particle class of 150 μm, because of its larger radial dispersion (Fig. 5), is trapped into the near-wall recirculating zone (Fig. 6) and hence stays for a relatively longer time in the combustor and undergoes almost complete combustion process before it leaves the combustor. On the other hand, at higher pressure, all coal particles undergo complete combustion much before they leave the combustor as ash particles, as observed from a comparison of Figs. 4(*b*) and 3(*b*).

As the length of the combustor increases, all reactions proceed near completion and hence combustion efficiency is increased. The loss in exergy increases as a consequence of complete chemical reaction, and prolongs gas phase transport processes, which results in a decrease in the second law efficiency.

It is found that an increase in swirl number *S*, from 0 to 0.32, increases the combustion efficiency in all situations. For a further increase in swirl number from 0.32 to 0.77, combustion efficiency is decreased. The purpose of imparting swirl to secondary air is to cause an off-axis recirculatory flow near the upstream region of

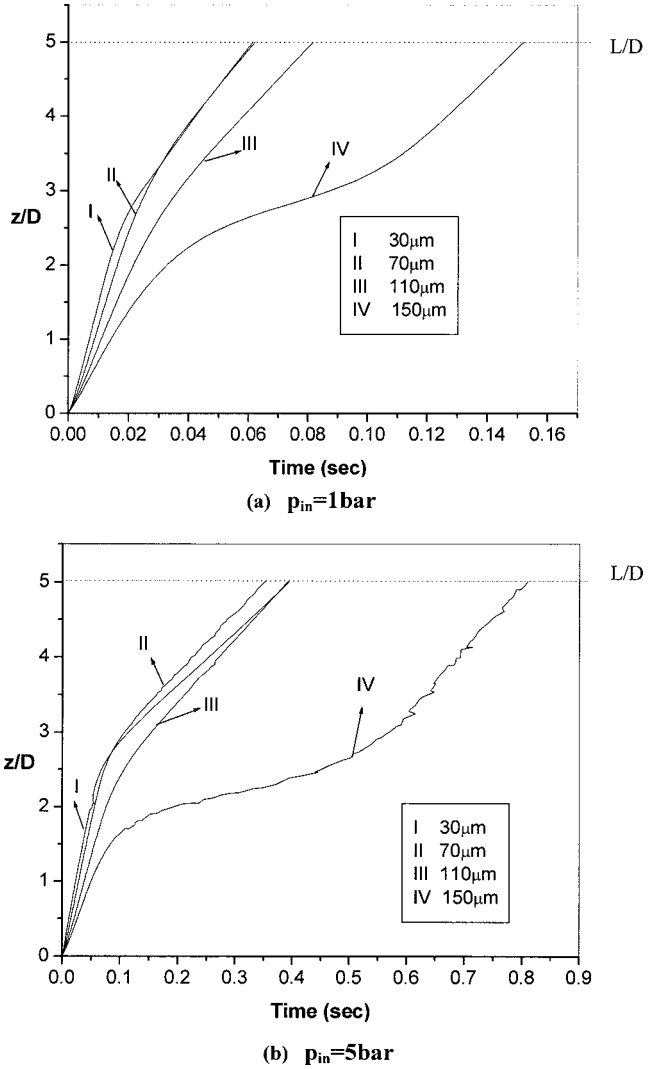

Fig. 3 Temporal histories of axial displacement of coal particles in the combustor at different inlet air pressure (S=0.0, T_{in}=600 K, $\dot{m}_{a_{in}}$=0.042 kg/s, $\dot{m}_{f_{in}}$=0.004 kg/s, SMD$_i$=50 μm)

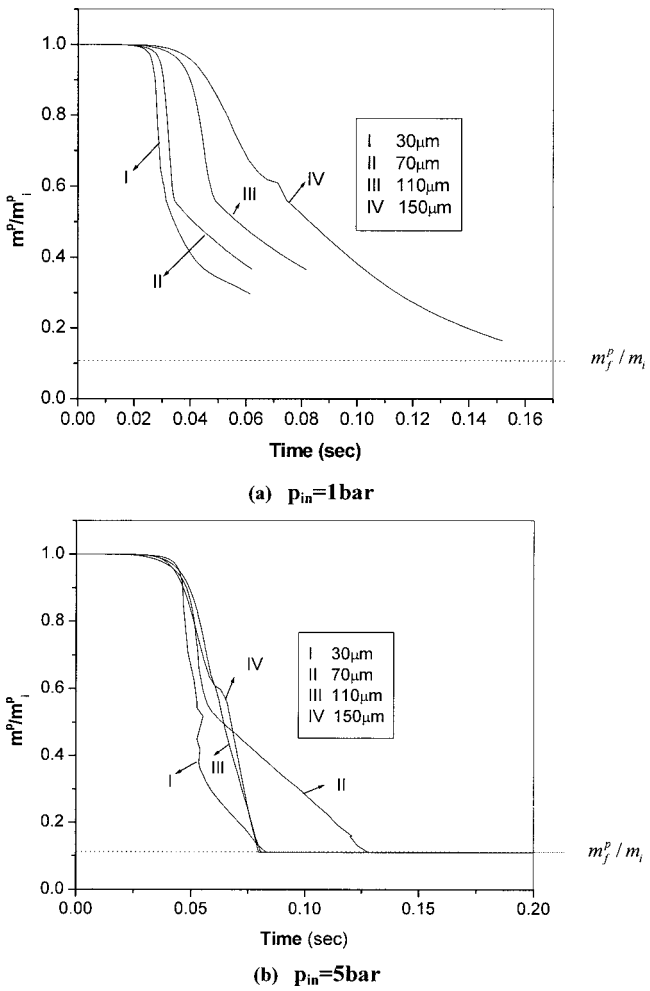

Fig. 4 Temporal mass depletion histories of coal particles in the combustor at different inlet air pressure (S=0.0, T_{in}=600 K, $\dot{m}_{a_{in}}$=0.042 kg/s, $\dot{m}_{f_{in}}$=0.004 kg/s, SMD$_i$=50 μm)

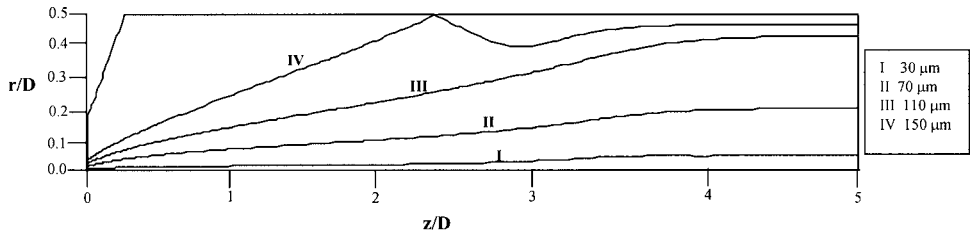

Fig. 5 Trajectories of pulverized coal particles in the combustor (p_{in}=1.0 bar, S=0.0, T_{in}=600 K, $\dot{m}_{a_{in}}$=0.042 kg/s, $\dot{m}_{f_{in}}$=0.004 kg/s, SMD$_i$=50 μm)

the primary zone (Fig. 7). This enhances the mixing of volatile gases in air and its subsequent combustion reaction. But, on the other hand, the recirculatory flow field in the inlet region of the combustor reduces the penetration of the coal particles to further downstream in the primary zone for a more effective interaction of the particles in hot air, for an enhanced release of volatile matter and char burning at particle surface. The relative role of these two counterweighing effects depends on the value of swirl number S. At a low swirl (S=0.32), the favorable effect of enhanced rates of transport processes becomes the dominant factor and increases the value of η_c, while at higher swirl (S=0.77), reduction in particle penetration counterweighs any favorable effect of enhanced mixing and transport in gas phase, and thus decreases the combustion efficiency η_c.

Swirl number, in the range of S=0 to 0.32, has almost negligible influence on second law efficiency. However, the second law efficiency increases with an increase in swirl number S from 0.32 to 0.77 (Table 2). Therefore, from the trends of variation of η_c and η_{II} with S, it can be concluded that, at a higher swirl number, the preservation of quality of energy is obtained at the cost of incomplete combustion of coal particles.

Influence of Inlet Air Temperature. An increase in inlet air temperature has two counterweighing effects on combustion efficiency and second law efficiency of the process. An increase in air temperature causes a higher flow velocity of air for a given mass flow rate, and thus decreases the residence time of coal particles in the combustor. An increase in particle penetration due to reduced air drag at higher inlet temperature of air is manifested by a relatively smaller radial dispersions of particles even at a larger axial displacement, as shown in Fig. 8. An increase in air temperature, on the other hand, increases the rate of gas phase and interphase transport processes, and also the rate of homogeneous and heterogeneous chemical reactions. For a shorter length of combustor of 0.75 m, the effect of less residence time of coal particles in the combustor becomes the dominant factor in reducing the combus-

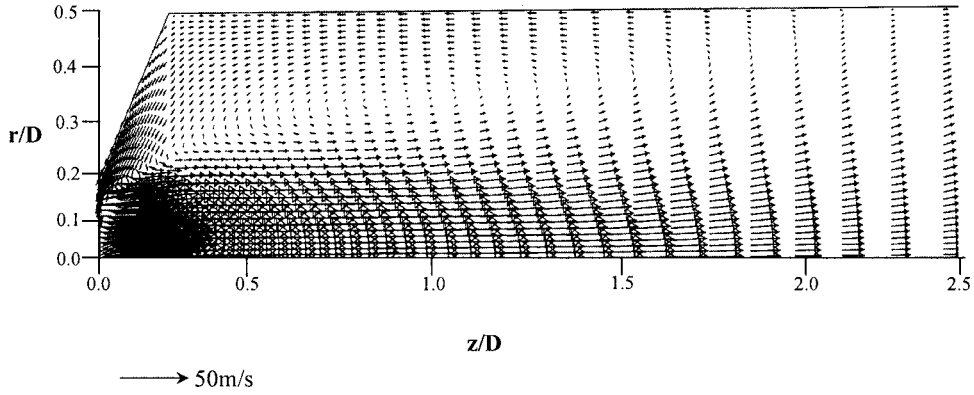

Fig. 6 Gas phase velocity field in the combustor (p_{in}=1.0 bar, S=0.0, T_{in}=600 K, $\dot{m}_{a_{in}}$=0.042 kg/s, $\dot{m}_{f_{in}}$=0.004 kg/s, SMD$_i$=50 μm)

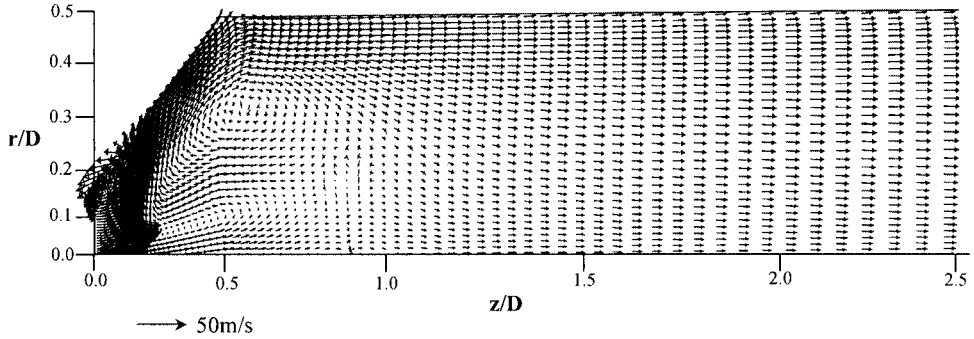

Fig. 7 Gas phase velocity field in the combustor with inlet air swirl (p_{in}=1.0 bar, S=0.77, T_{in}=600 K, $\dot{m}_{a_{in}}$=0.042 kg/s, $\dot{m}_{f_{in}}$=0.004 kg/s, SMD$_i$=50 μm)

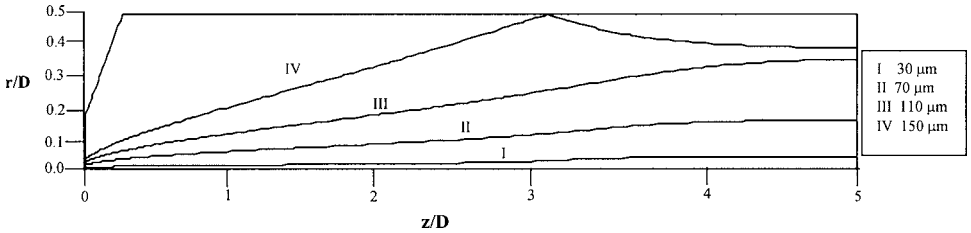

Fig. 8 Trajectories of pulverized coal particles at higher inlet air temperature ($S=0.0, p_{in}=1.0$ bar, $T_{in}=1000$ K, $\dot{m}_{a_{in}}=0.042$ kg/s, $\dot{m}_{f_{in}}=0.004$ kg/s, $SMD_i=50$ μm)

tion efficiency with temperature (Table 3). For an increased length of combustor (1.0 and 1.5 m), the enhanced rate of transport processes and chemical reactions with temperature counterweighs the adverse effect of short residence time of coal particles, and hence increases the combustion efficiency for an increase in air temperature (Table 3). The second law efficiency follows a trend which bears an inverse relationship to that in combustion efficiency under all situations (Table 3).

Influence of Total Airflow Rate. The influence of total air flow rate on combustion efficiency and second law efficiency is shown in Table 4. An increase in total air flow increases both the primary and secondary air flow proportionately, since the mass ratio of primary to secondary air remains the same. The two air flow rates for a given mass flow rate of coal have been used in the present study. The values of air flow rate, $\dot{m}_{a_{in}}=0.042$ kg/s, correspond to 5% more than the stoichiometric air, while the values of $\dot{m}_{a_{in}}=0.068$ kg/s correspond to 60% of excess air. It is observed that an increase in mass flow rate of air from 0.042 to 0.068 kg/s decreases the combustion efficiency drastically. Inlet air acts as a blast to drive out the coal particles before being burnt out completely in a combustor of short length. With an increase in the length of combustor, the air flow rate has little or negligible influence on combustion efficiency. However, it is observed from Table 4 that the second law efficiency has a monotonically inverse trend with an increase in air flow rate for combustor of different lengths. Moreover, the second law efficiency decreases with an increase in the length of combustor. For a combustion chamber of higher length, the coal particles undergo almost complete combustion, yielding a higher combustion efficiency which is less influenced by the air flow. The second law efficiency, on the other hand, increases with an increase in air flow rate due to the fact that the increase in the rate of irreversibility (loss in exergy) with air flow is less than the proportional increase in the rate of flow availability at the inlet associated with increased air flow rate.

Influence of Initial Particle Diameter. It is observed from Table 5 that an increase in initial mean diameter of coal particle decreases the combustion efficiency and increases the second law efficiency. This is probably due to a reduction in the rate of interphase transport processes and particle burning per unit mass of the particle with its initial diameter. The interesting feature to be mentioned in this context is that, at high secondary air swirl ($S=0.77$) the above trends are reversed. At $S=0.77$, combustion efficiency increases with an increase in SMD_i of coal particles from 50 μm to 95 μm and thereafter it decreases with a further increase in Sauter mean diameter (SMD_i) of coal particle from 95 μm to 145 μm, while second law efficiency, following the reverse trend, decreases with an increase in SMD_i of coal particles from 50 to 95 μm, and thereafter increases with a further increase in SMD_i of coal particle from 95 to 145 μm. However, this interesting feature is more prominent in a shorter length of combustor (0.75 m). This depicts a feature of the existence of an optimum particle diameter for maximum combustion efficiency and minimum second law efficiency at high inlet air swirl, similar to that reported in the case of spray combustion by Datta and Som [30]. The combustion efficiency depends upon the rate of interphase and gas phase transport processes, along with the rate of chemical reactions which, in turn, depend on the penetration of the incoming coal particles into the high temperature zone. The reason for the existence of an optimum particle diameter for maximum combustion efficiency can be attributed to the fact that, with an increase in particle diameter, a race takes place between the effective penetration of the particle and reduced rate of interphase transport processes per unit mass.

Conclusions

A comparative study on the variations in combustion efficiency and second law efficiency of a pulverized coal combustion process in a tubular combustor has been made for different operating

Table 3 Influence of inlet air temperature on combustion efficiencies and second law efficiencies ($\dot{m}_{a_{in}}=0.042$ kg/s, $\dot{m}_{f_{in}}=0.004$ kg/s, $S=0$, $SMD_i=50$ μm, $p_{in}=100$ kPa)

Inlet air temperature (K)	Second law efficiency			Combustion efficiency		
	0.75m	1.0m	1.5m	0.75m	1.0m	1.5m
600K	81	78	59	80	85	98
1000K	90	71	53	67	89	99

Table 4 Influence of inlet air flow rate on combustion efficiencies and second law efficiencies ($\dot{m}_{f_{in}}=0.004$ kg/s, $SMD_i=50$ μm, $S=0$, $T_{in}=600$ K, $p_{in}=100$ kPa)

Inlet air flowrate(kg/s) ($\dot{m}_{a_{in}}$)	Second law efficiency			Combustion efficiency		
	0.75m	1.0m	1.5m	0.75m	1.0m	1.5m
0.042	81	78	59	79	85	98
0.068	91	87	79	57	80	98

Table 5 Influence of initial particle diameter and secondary air swirl on combustion efficiencies and second law efficiencies ($\dot{m}_{a_{in}}$=0.042 kg/s, $\dot{m}_{f_{in}}$=0.004 kg/s, T_{in}=600 K, p_{in}=100 kPa)

SMD_i (μm)	Secondary Swirl number (*S*)	Second law efficiency			Combustion efficiency		
		0.75m	1.0m	1.5m	0.75m	1.0m	1.5m
50	0.0	81	78	59	79	85	98
	0.32	78	65	56	84	96	99
	0.77	84	67	57	82	93	97
95	0.0	90	83	77	52	68	81
	0.32	88	81	75	58	71	88
	0.77	74	67	55	88	93	97
145	0.0	98	92	89	45	66	80
	0.32	96	88	72	53	67	82
	0.77	95	86	70	54	69	84

conditions to shed light on the trade-off between the effectiveness of combustion and the lost work due to thermodynamic irreversibilities in the process of combustion. The major observations follow.

An increase in inlet air pressure increases the combustion efficiency and decreases the second law efficiency. The influences are more prominent in a shorter length of combustor and at a low value of inlet air swirl. An increase in swirl number from $S=0.0$ to 0.32 increases the combustion efficiency, whereas a further increase in swirl number from $S=0.32$ to 0.77 results in a decrease in the combustion efficiency. The second law efficiency is relatively lower for lower swirl number ($S=0.32$), where combustion efficiency is high, while it shows a relatively higher value at a high swirl number of $S=0.77$, where the combustion efficiency is low.

An increase in air temperature decreases the combustion efficiency for a shorter length of combustor, but increases the combustion efficiency for a higher length of combustor. The second law efficiency follows a trend which bears an inverse relationship to that in combustion efficiency with air temperature.

At low values of inlet air swirl ($S=0.0$ to 0.32), an increase in SMD_i of coal particle decreases the combustion efficiency. At a higher value of inlet air swirl ($S=0.77$) combustion efficiency increases with an increase in SMD_i from 50 to 95 μm, and thereafter decreases with a further increase in SMD_i of coal particle from 95 to 145 μm. The second law efficiency always increases with an increase in the particle diameter, whereas, at high swirl of $S=0.77$, this trend shows an optimum particle diameter with an initial decreasing trend of η_{II} followed by an increasing one with the particle diameter.

The optimum design of the combustor is based on a trade-off between η_c and η_{II} for an overall energy economy. The relative weight of η_c and η_{II} to be assigned in the process of optimization depends on the relative savings in the cost of energy quantity over the energy quality for a specific application. This is a task of energy management in practice, where the information provided by the present paper will serve as the fundamental input.

Nomenclature

$\dot{A}$ = rate of flow availability (W)
A = pre-exponential factor or particle surface area (1/s or m^2)
a = specific flow availability (J/kg)
b = size parameter of Rossin-Rammler function (m^{-n})
C_i = species mass fraction
c_p = specific heat at constant pressure (J/kg-K)
d = particle diameter (m)
d_i = particle diameter of *i*th class of particle (m)
$d_{\min i}$ = minimum diameter of *i*th class of particle (m)
$d_{\max i}$ = maximum diameter of *i*th class of particle (m)
D = combustor diameter (m)
E = activation energy (J/kmol)
G = irradiation (W/m^2)
$G'(d_i)$ = cumulative particle size distribution function
$\Delta H_{\text{volatilization}}$ = enthalpy of devolatilization during pyrolysis (J/kg)
$\Delta H_{\text{volatilization}}$ = enthalpy of char reaction (J/kg)
$\overline{h}$ = molar enthalpy (J/mole)
$\Delta \overline{h}_f$ = molar enthalpy of formation
M = molecular weight (kg/kmol)
$\dot{m}_f$ = mass flow rate of fuel (coal) (kg/s)
m = mass (kg)
$\dot{N}$ = number flow rate of particles (1/s)
Nu = Nusselt number
p = pressure (Pa)
P_r = Prandtl number
q_i^r = radiative heat flux in x_i direction (W/m^2)
R = radius of the combustor or universal gas constant (m or kJ/kmol K)
R_e = Reynolds number
r = radial location (m)
s = specific entropy (J/kg-K)
$\overline{s}$ = molar entropy (kJ/kmol-K)
S = swirl number
$\dot{S}$ = gas phase mass source term due to particles (kg/m^3 s)
$\dot{S}_E$ = gas phase energy source term due to energy exchange with particles (W/m^3)
$\dot{S}_{M_i}$ = gas phase momentum source term due to momentum exchange with particles ($kg/m^2\ s^2$)
SMD = Sauter mean diameter (m)
t = time (s)
T = temperature (K)
U_i = mean velocity in x_i direction (m/s)
U_z = mean axial velocity in x_i direction (m/s)
V_i = velocity in x_i direction (m/s)
x = mole fraction
z = axial location (m)

Greek Letters

θ_R = radiation temperature
α_t = turbulent thermal diffusivity
$\alpha_1\alpha_2$ = stoichiometric coefficients of two competing reactions
μ_{eff} = effective viscosity
μ_t = eddy viscosity
ρ = density
ξ = mixture fraction
κ = absorption coefficient
σ = Stefan-Boltzmann constant
$\forall$ = volume of a computational cell

Subscripts

char = char content in coal
i = initial/species/index of tensor notation
j = index of tensor notation
in = inlet
e = exit
r = reference quantity
p = particle phase
f = fuel (coal) or final state
vol = volatile matter in coal

Superscripts

f = fuel (coal)
g = gas phase
p = particle phase

References

[1] Smoot, L. D., 1997, "A Decade of Combustion Research," Prog. Energy Combust. Sci., **23**, pp. 203–232.
[2] Smoot, L. D., 1984, "Modeling of Coal Combustion Processes," Prog. Energy Combust. Sci., **10**, pp. 229–272.
[3] Flagan, R. C., and Taylor, D. D., 1981, "Laboratory Studies of Submicron Particles From Coal Combustion," *Eighteenth Symposium (International) on Combustion*, The Combustion Institute, pp. 1227–1237.
[4] McLean, W. J., Hardesty, D. R., and Pohl, J. H., 1981, "Direct Observations of Devolatilizing Pulverized Coal Particles in a Combustion Environment," *Eighteenth Symposium (International) on Combustion*, The Combustion Institute, pp. 1239–1248.
[5] Seeker, W. R., Samuelsen, G. S., Heap, M. P., and Trolinger, J. D., 1981, "The Thermal Decomposition of Pulverized Coal Particles," *Eighteenth Symposium (International) on Combustion*, The Combustion Institute, pp. 1213–1226.
[6] Neville, M., Quann, R. J., Haynes, B. S., and Sarofim, A. F., 1981, "Vaporization and Condensation of Mineral Matter during Pulverized Coal Combustion," *Eighteenth Symposium (International) on Combustion*, The Combustion Institute, pp. 1267–1274.
[7] Ragland, K. W., Jehn, T. C., and Yang, J. T., 1981, "Coal Combustion at High Reynolds Number," *Eighteenth Symposium (International) on Combustion*, The Combustion Institute, pp. 1295–1303.
[8] Rees, D. P., Smoot, L. D., and Hedman, P. O., 1981, "Nitrogen Oxide Formation Inside a Laboratory Pulverized Coal Combustor," *Eighteenth Symposium (International) on Combustion*, The Combustion Institute, pp. 1305–1311.
[9] Kelly, J. T., Brown, B. A., and Wightman, J. B., 1981, "Pilot-Scale Development of a Low-NO_x Coal-Fired Tangential System," *Eighteenth Symposium (International) on Combustion*, The Combustion Institute, pp. 1275–1283.
[10] Lester, T. W., Seeker, W. R., and Merklin, J. F., 1981, "The Influence of Oxygen and Total Pressure on the Surface Oxidation Rate of Bituminous Coal," *Eighteenth Symposium (International) on Combustion*, The Combustion Institute, pp. 1257–1265.
[11] Smith, P. J., Fletcher, T. H., and Smoot, L. D., 1981, "Model for Pulverized Coal-Fired Reactors," *Eighteenth Symposium (International) on Combustion*, The Combustion Institute, pp. 1285–1293.
[12] Williams, A., Pourkashanian, M., Jones, J. M., and Rowlands, L., 1997, "A Review of NO_x Formation and Reduction Mechanisms in Combustion Systems, With Particular Reference to Coal," J. Inst. Energy, **70**, pp. 102–113.
[13] Williams, A., Backreedy, R., Habib, R., Jones, J. M., and Pourkashanian, M., 2002, "Modelling Coal Combustion: The Current Position," Fuel, **81**, pp. 605–618.
[14] Williams, A., Pourkashanian, M., and Jones, J. M., 2001, "Combustion of Pulverized Coal and Biomass," Prog. Energy Combust. Sci., **27**, pp. 587–610.
[15] Arenillas, A., Bakreedy, R. I., Jones, J. M., Pis, J. J., Pourkashanian, M., Rubiera, F., and Williams, A., 2002, "Modelling of NO Formation in the Combustion of Coal Blends," Fuel, **81**, pp. 627–636.
[16] Görres, J., Schnell, U., and Hein, K. R. G., 1995, "Trajectories of Burning Coal Particles in Highly Swirling Reactive Flows," Int. J. Heat Fluid Flow, **16**, pp. 440–450.
[17] Hurt, R., Sun, J. K., and Lunden, M., 1998, "A Kinetic Model of Carbon Burnout in Pulverized Coal Combustion," Combust. Flame, **113**, pp. 181–197.
[18] Liakos, H. H., Theologos, K. N., Boudouvis, A. G., and Markatos, N. C., 1998, "Pulverized Coal Char Combustion: The Effect of Particle Size on Burner Performance," Appl. Therm. Eng., **18**, pp. 981–989.
[19] Fan, J., Qian, L., Ma, Y., Sun, P., and Cen, K., 2001, "Computational Modeling of Pulverized Coal Combustion Processes in Tangentially Fired Furnaces," Chem. Eng. J., **81**, pp. 261–269.
[20] Li, Z. Q., Wei, F., and Jin, Y., 2003, "Numerical Simulation of Pulverized Coal Combustion and NO Formation," Chem. Eng. Sci., **58**, pp. 5161–5171.
[21] Akoi, H., Nogami, H., Tsuge, H., Miura, T., and Furukawa, T., 1993, "Simulation of Transport Phenomena Around the Raceway Zone in the Blast Furnace With and Without Pulverized Coal Injection," ISIJ Int., **33**(6), pp. 646–654.
[22] Guo, Y. C., Chan, C. K., and Lau, K. S., 2003, "Numerical Studies of Pulverized Coal Combustion in a Tubular Coal Combustor With Slanted Oxygen Jet," Fuel, **82**, pp. 893–907.
[23] Gordon, Y., Shvidkiy, V., Yaroshenko, Y., Spirin, N., Lavrov, V., and Shvidkiy, D., 1998, "Blast Furnace Models to Analyze Raceway Zone Formation and to Predict Lining Life," *ICSTI/Ironmaking Conference Proceedings*, pp. 351–361.
[24] Dash, S. K., Sengupta, S. P., and Som, S. K., 1991, "Transport Processes and Associated Irreversibilities in Droplet Evaporation," J. Thermophys. Heat Transfer, **5**(3), 366–373.
[25] Dash, S. K., and Som, S. K., 1991, "Transport Processes and Associated Irreversibilities in Droplet Combustion in a Convective Medium," Int. J. Energy Res., **15**, pp. 603–619.
[26] Puri, I. K., 1992, "Second Law Analysis of Convective Droplet Burning," Int. J. Heat Mass Transfer, **35**, pp. 2571.
[27] Hiwase, S. D., Datta, A., and Som, S. K., 1998, "Entropy Balance and Exergy Analysis in the Process of Droplet Combustion," J. Phys. D, **31**, pp. 1601–1610.
[28] Som, S. K., and Dash, S. K., 1993, "Thermodynamics of Spray Evaporation," J. Phys. D, **26**, 574–584.
[29] Dunbar, W. R., and Lior, N., 1994, "Sources of Combustion Irreversibility," Combust. Sci. Technol., **103**, pp. 41.
[30] Datta, A., and Som, S. K., 1999, "Thermodynamic Irreversibilities and Second Law Analysis in a Spray Combustion Process," Combust. Sci. Technol., **142**, pp. 29–54.
[31] Som, S. K., and Sharma, N. Y., 2002, "Energy and Exergy Balance in the Process of Spray Combustion in a Gas Turbine Combustor," ASME J. Heat Transfer, **124**, pp. 828–836.
[32] Lior, N., 2001, "Irreversibility in Combustion, Invited Keynote Paper Proc. ECOS '01: Efficiency, Costs, Optimization, Simulation and Environmental Aspects of Energy Systems," Istanbul, Turkey, Vol. 1, pp. 39–48.
[33] Kim, C., and Lior, N., 1993, "Combined-Mode Conjugate Heat Transfer in a Radiatively/Conductively-Stabilized Pulverized Coal Combustor," ASME Paper 93-WA/HT-37, ASME Winter Annual Meeting, New Orleans, LA.
[34] Kim, C., and Lior, N., 1998, "A Numerical Analysis of NO_x Formation and Control in Radiatively/Conductively-Stabilized Pulverized Coal Combustors," Chem. Eng. J., **71**, pp. 221–231.
[35] Ozisik, M. N., 1973, *Radiative Transfer and Interactions with Conduction and Convection*, Wiley, New York.
[36] Sparrow, E. M., and Cess, R. D., 1978, *Radiation Heat Transfer*, Hemisphere, Washington, D.C.
[37] Jones, W. P., and Whitelaw, J. H., 1982, "Calculation Methods for Reacting Turbulent Flows: A Review," Combust. Flame, **48**, pp. 1–26.
[38] Smoot, L. D., and Pratt, D. T., 1979, *Pulverized Coal Combustion and Gasification*, Plenum Press, New York.
[39] Mugele, R. A., and Evans, H. D., 1951, "Droplet Size Distribution in Sprays," Ind. Eng. Chem., **43**, 1317–1324.
[40] Clift, R., Grace, J. R., and Weber, M. E., 1978, *Bubbles, Drops and Particles*, Academic Press, New York.
[41] Ranz, W. E., and Marshall, W. R., Jr., 1952, "Evaporation From Drops: Part II," Chem. Eng. Prog., **48**, pp. 173–180.
[42] Kobayashi, H., Howard, J. B., and Sarofim, A. F., 1976, "Coal Devolatilization at High Temperatures," *Sixteenth Symposium (International) on Combustion*, The Combustion Institute, pp. 411–425.
[43] Baum, M. M., and Street, P. J., 1971, "Predicting the Combustion Behavior of Coal Particles," Combust. Sci. Technol., **3**(5), pp. 231–243.
[44] Field, M. A., 1969, "Rate of Combustion of Size-Graded Fractions of Char From a Low Rank Coal Between 1200 K−2000 K," Combust. Flame, **13**, pp. 237–252.
[45] Moran, M. J., and Shapiro, H. N., 1988, *Fundamentals of Engineering Thermodynamics*, John Wiley, New York.
[46] Vu, B. T., and Gouldin, F. C., 1982, "Flow Measurements in a Model Swirl Combustor," AIAA J., **20**, pp. 642–651.

A Numerical Investigation of Mixing Processes in a Novel Combustor Application

Yeshayahou Levy[1]

Hui-Yuan Fan
Lady Davis Postdoctoral Research Fellow

Valery Sherbaum

Turbo and Jet Engine Laboratory,
Faculty of Aerospace Engineering,
Technion-Israel Institute of Technology,
Haifa 3200, Israel

A mixing process in a staggered toothed-indented shaped channel was investigated. It was studied in two steps: (1) numerical simulations for different sizes of the boundary-contour were performed by using a CFD code; (2) these results were used for simulation-data modeling for prediction of mixing performances across the whole field of changing geometric and the aerodynamic stream parameters. Support vector machine (SVM) technique, known as a new type of self learning machine, was selected to carry out this stage. The suitability of this application method was demonstrated in comparison with a neural network (NN) method. The established modeling system was then applied to some further studies of the prototype mixer, including observations of the mixing performance in three special cases and performing optimizations of the mixing processes for two conflicting objectives and hereby obtaining the Pareto optimum sets. [DOI: 10.1115/1.2103090]

1 Introduction

The development of efficient, low polluting combustion techniques is a major task for researchers and manufacturers of aircraft engines and industrial gas turbines. Nitrogen oxides (NOx) could be ranked as the most relevant pollutants from aircraft emissions because of their negative effects on the atmospheric environment. Within the past years, several new combustion techniques have been developed to reduce NOx emissions from combustion systems. Among these, the flameless oxidation technique seems promising [1]. The technique is characterized by a large recirculation of hot combustion products back into the combustion area. In this way, the maximal combustion temperature is decreased thus suppressing the thermal-NOx formation [2,3]. Though the flameless oxidation technique has already been applied to gas-fired industrial furnaces, its application to the combustors of aircraft engines and gas turbines is still in its infancy and shop-experimental stage. A feasibility study of such applications is currently being investigated by the authors within the framework of the FLOXCOM project supported by the European Commission [2,3].

As FLOXCOM is devoted to development of innovative combustors for aircraft engines and gas turbines, the recirculation, created to achieve flameless oxidation in a combustor, must be internal, and be carried out through proper design of the combustor chamber. From the flameless oxidation viewpoint, a well-designed combustor must provide for sufficient recirculation of burnt gases required to create the flameless-oxidation condition. As a part of the FLOXCOM project, the current study of the mixing process is intended to assist in augmenting the recirculation rate and internal mixing process to offer future practical design of flameless-oxidation combustors. Even though only the numerical simulation has been performed, this study opens the way to developing real combustors.

The prototype mixer studied in this paper, as shown in Fig. 1, is a geometrical design in which the mixing passage is simply taken as a "box" with given height and length, denoted as H and L, respectively. Though the passage width W (see Fig. 1) is assumed infinite, it can, however, be handled as a definite value within the toothed boundary feature of the mixing process. One of its open sides along the length is the inlet and the other is the exit. The inlet section is made up of two equal-area parts arranged up and down. The upper part is destined for cold air input, while the lower part is destined for hot air input. The former simulates the fresh air introduced into the combustors and the latter simulates the recirculating gas in the combustor chambers. The inlet of the designed mixer has a periodic and square tooth-indent shape, which can be determined in geometry by the height h and the width w. So, the effect of these two geometric parameters on the mixing process can be studied. In the present study, the height and length of the mixing passage were kept constant as $H=0.05$ m and $L=0.2$ m.

Two parameters are selected as the criteria (or, dependent parameters) to describe the studied mixing process. One is called temperature pattern factor (TPF), which is commonly used in gas turbines to describe the temperature uniformity of the gas entering the turbines. In the present study, the concept of TPF is adapted to measure the mixing degree attained at the exit cross section of the prototype mixer. In gas turbine design, TPF is usually defined as the peak local temperature minus the flow-weighted average temperature, all divided by the combustor temperature rise in the gas turbine system [4]. The cases in this study are assumed to be elementary imitations of mixing processes in an engine combustor, and there is no combustor temperature rise available at the moment. However, it is reasonable to take the temperature difference between the cold-air and hot-air streams to replace this quantity. Thus, in the present numerical analysis, TPF at the exit cross section can be defined by the following equation:

$$\mathrm{TPF} = (T_{\max} - \overline{T})/(T_2 - T_1) \tag{1}$$

where $T_{\max}$ is the peak (or maximal) temperature at the section, and $\overline{T}=\Sigma(c_{p_i}m_iT_i)/(\overline{c_p}\Sigma m_i)$ is the flow-weighted average temperature, in which T_i, m_i, and c_{p_i} are the local temperatures, mass rates, and constant-pressure specific heat obtained from computing cells at the exit cross section, and $\overline{c_p}$ is mean constant-pressure specific heat at the temperature $\overline{T}$; the temperatures T_1, T_2 relate to the cold-air stream (upper) and the hot-air stream (lower), respectively. The other representative parameter for the mixer is called total pressure loss factor (TPLF), which is used to record the kinetic-energy losses for the corresponding mixing process. TPLF is defined as percent flow-weighted average total pressure loss occurring between the inlet and exit. For a numerical analysis case it can be calculated from the flow inlet parameters and the param-

[1]To whom correspondence should be addressed.

Contributed by the Heat Transfer Division of ASME for publication in the JOURNAL OF HEAT TRANSFER. Manuscript received February 20, 2003; final manuscript received February 21, 2005. Assoc. Editor: A. F. Emery.

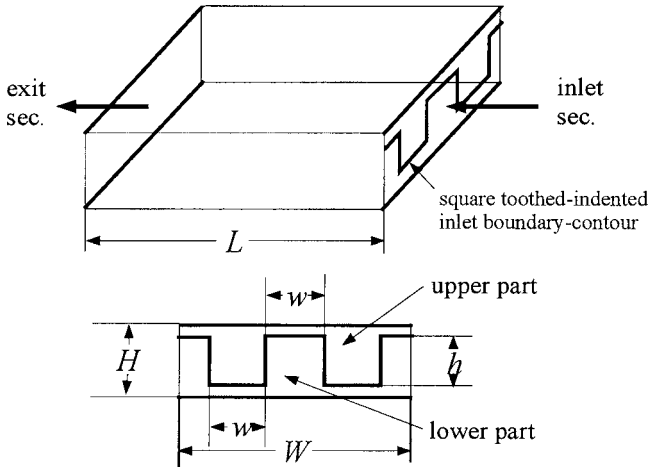

Fig. 1 Mixing domain and specifications

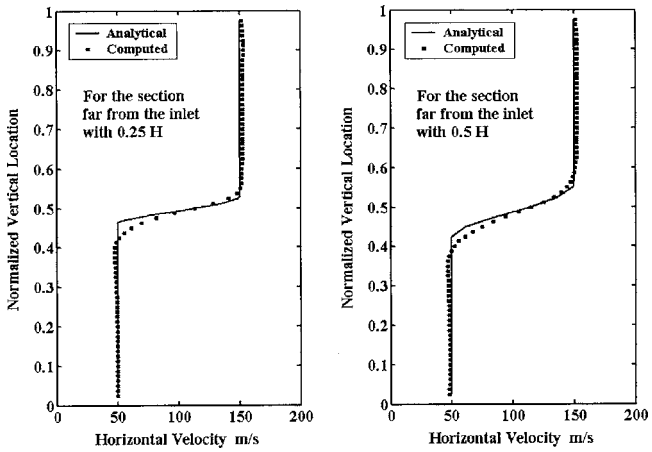

Fig. 2 Validation of the CFD code by some analytical results

eters obtained on the exit cross section. Hence the TPLF can be defined

$$\text{TPLF} = 1 - \overline{P}^*_{exit}/\overline{P}^*_{inlet} \tag{2}$$

where $\overline{P}^* = e^{\Sigma m_i \ln P_i^*/\Sigma m_i}$ is the flow-weighted average total pressure [5], and P_i^* is the local total pressure. The indices "inlet" and "exit" indicate the inlet section and exit section of the studied mixing passage.

This paper presents a detailed description of numerical simulation of the mixing process. A series of samples (i.e., simulation points) were obtained. These, we hope, may assist in obtaining a good physical representation of the studied process. Each simulation point included a CFD analysis for a given set of different inlet boundary contours and cold-air velocity. STAR-CD code was used to perform the simulations.

The present paper presents our work on modeling of the prototype mixer based on the obtained data. A new kind of learning machine called a support vector machine (SVM) was introduced to accomplish the modeling tasks. The suitability of SVMs for the modeling problem was proved by comparison with neural networks (NNs). Applying the established modeling system, the mixer was further studied in three specific cases, as well as optimization.

2 Numerical Simulations

2.1 Boundary Conditions and Simulation Points. For simplicity, it was assumed that cold and hot air streams under the same (atmospheric) pressure enter the mixing passage. The inlet conditions were the cold-air velocity, noted as V_1, and the temperature, T_1, and the hot-air velocity, noted as V_2, and temperature, T_2. In this study, the temperatures of cold and hot air were selected in accordance with common practical combustor design to be $T_1 = 500$ K and $T_2 = 1000$ K. The inlet hot-air velocity $V_2 = 50$ m/s and the cold-air velocity were allowed to vary in four values: 100 m/s, 150 m/s, 200 m/s, and 250 m/s. The inlet boundary parameters, i.e., the height and width, h and w, were selected to have different values: $h = 0, 0.015, 0.03, 0.04, 0.05$ m, and $w = 0.0025, 0.005, 0.01, 0.015, 0.02, 0.03, 0.05$ m. Consequently, from the above specifications, in total 140 numerical simulation points were required.

2.2 Simulation Tool: Description and Validation. The mixing process in the prototype mixer was described as a 3D steady viscous compressible turbulent flow problem that was governed by Navier-Stokes equations consisting of equations enforcing the principles of mass, momentum, and energy conservation. The simulations were done by repeatedly numerically solving the aforementioned partial differential equations under the given boundary conditions for the mixing process.

The commercial CFD code, STAR-CD version 3.15, was chosen for the simulations. As in the present problem the Reynolds number regarding the averaged inflow velocity and the total height of the mixing passage is greater than 10^4; the standard high Reynolds number *k-epsilon* turbulence model was applied. The model requires special algebraic formulas, often called "wall function," to present the distributions of velocity, temperature, turbulence energy, etc., within the boundary layers that form adjacent to the walls. The code is a finite-volume-based solver, and offers several differencing schemes such as central differencing (CD), upwind differencing (UD), QUICK, and others for selections. In this study, as is usual, the diffusive terms in the governing equations were treated by the CD scheme, and the convection terms by the UD scheme. A uniform grid system (40 grids in heightwise, regular hexahedron cells) was used for simplicity. The code solved the discretized transport equations for velocity components, temperature, plus the two turbulence quantities, k and ε. The well-known SIMPLE method was taken for handling the velocity-pressure linkage problems. The detailed settings of the described flow-field solver can be found in the STAR-CD manuals [6].

The selected code was validated by the analytical results that could be obtained from an extremely simple turbulent mixing case. When the boundary contour between the two inlet parts is taken as a straight line and the two inflow streams have the same temperature but different velocities, the mixing process evidently reduces to a 2D flow problem. In this case an analytical solution for velocity distribution at a section very close to the inlet can be obtained [7]. To validate the chosen code, we took the upper inflow with a velocity of 150 m/s and the lower with a velocity of 50 m/s and used the code to analyze the mixing process. The velocity distribution obtained by the CFD code at the sections apart from the inlet section with distances of a fourth and a half of the mixing-passage's height are compared with the corresponding analytical results in Fig. 2. It can be seen that the two results are quite consistent.

2.3 Simulation Results and Discussions. The mixing flowfields were solved by the STAR-CD code using the prescribed initial parameters and TPF and TPLF values were calculated.

Keeping the width w of the inlet boundary contour at given values ($w/H = 0.1$, 0.2, 0.3, and 0.4), the TPF and TPLF varying with the height h are shown in Fig. 3. Similarly, keeping the height h of the inlet boundary contour at a given value ($h/H = 0.3$, 0.6, 0.8, and 1.0), the TPF and TPLF varying with the width w are shown in Fig. 4.

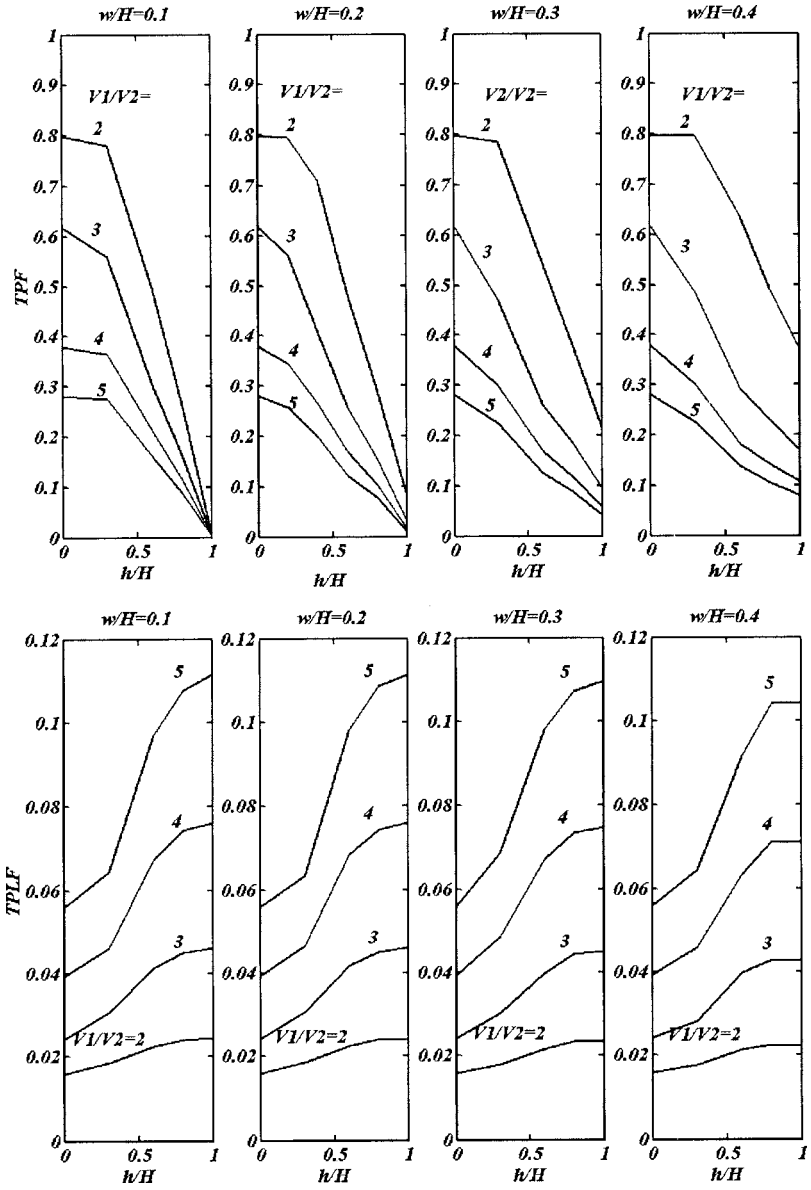

Fig. 3 Variations of TPF and TPLF with the height *h* for some given values of the width *w*

These two figures show the effect of geometry of the inlet boundary contour on the two dependent parameters. First, an increase of the height h can result in a decrease of TPF, and hereby to improve uniformity of the mixing process. This, however, simultaneously increases TPLF, with equivalent, kinetic-energy losses (see Fig. 3). Second, the influence of the width w on the mixing process is more complicated. As the width increases the TPF decreases until a certain value and then increases. The variations of the TPLF are roughly the opposite, i.e., as the width increases, TPLF slightly increases (or remains unchanged) and then decreases (see Fig. 4). Furthermore, for minimal TPF values, the extreme case of $h/H=1.0$ seems preferable. This fact can also be observed in Fig. 3 and Fig. 4: when $h/H=1.0$, each case of initial velocity obtains their minimal TPF value; the smaller the width w, the smaller the TPF value.

As for influences of the inlet cold-air velocity on the mixing results, it was found, as a general trend, that increasing the cold-air velocity will reduce TPF, and at the same time, will yield higher total pressure loss (i.e., with a large TPLF). This fact can be seen in Figs. 3 and 4, and is shown further in Fig. 5, in which both the width and height of the inlet boundary contour have a fixed value.

The simulation results verify a foreseeable fact in the prototypical mixing process that the two criteria for the mixing process, i.e., TPF and TPLF, are mutually contradictory. Hence, if a more uniform temperature distribution is needed, one needs to bear a larger total pressure loss, and vice versa. Compared with the above "no-free-lunch" principle between the two criteria in the mixing system, a phenomenon seen in Fig. 4 is remarkable and somehow exceeded our expectations. Originally, it was anticipated that, for a certain height h of the inlet boundary contour, the smaller the width w, the smaller the TPF value. But this is true only for the extreme cases in which the height h equals the mixing-passage height H. Besides those cases, for a given height h, within a certain small range of width w TPF does not decrease but increases as the width decreases closer to zero. Hence the TPF curves became not monotonic but basin-shaped. Here we offer a physical cause that may explain this phenomenon. For the given

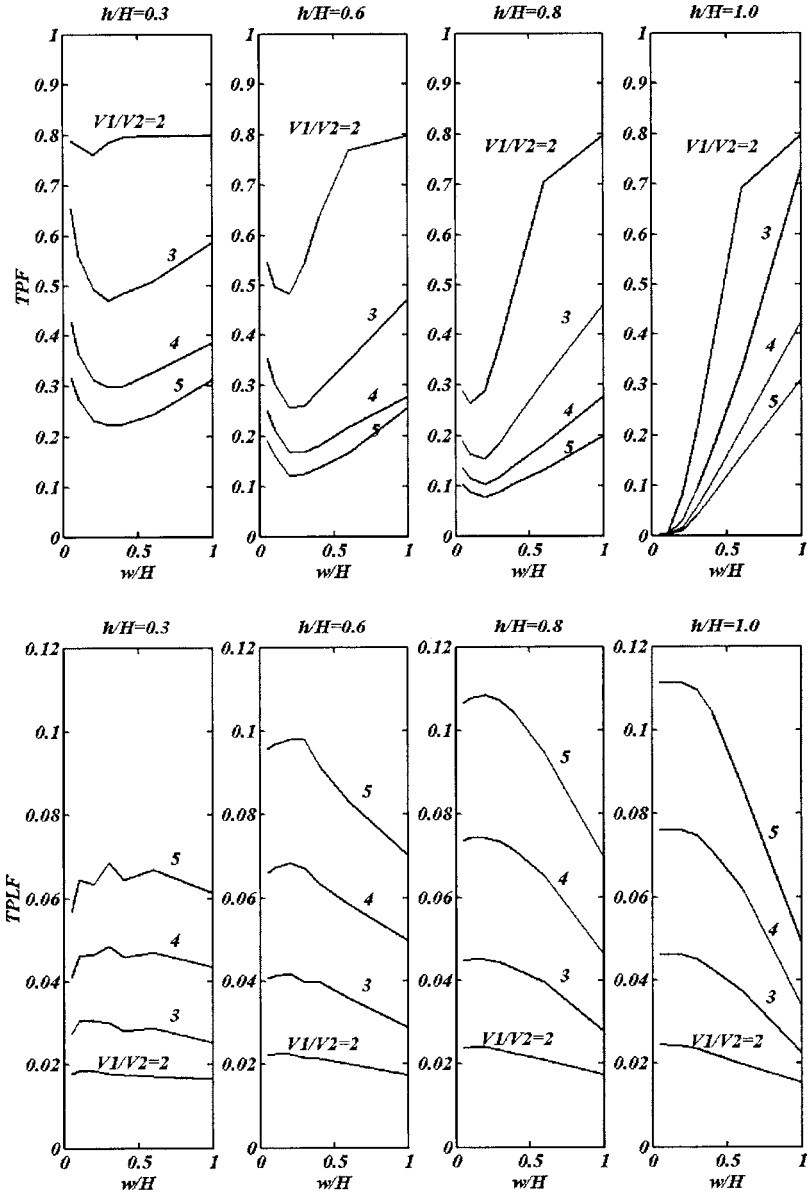

Fig. 4 Variations of TPF and TPLF with the width *w* for some given values of the height *h*

height *h* and small values of width *w*, the staggered area (see Fig. 6) may induce a zone where mixing of the two air streams may be of much greater intensity than outside this zone. In particular, the smaller the width, the stronger should be the mixing in the zone. Such a zone creates a "barrier" like a wall to resist the flow diffusion between the cold-air and the hot-air streams, and thereby results in an increase of TPF. On the other hand, when the width *w* is large enough, the mixing zone after the staggered area becomes too weak to affect the mixing process. Thus an increase of the width within that range can still result in a TPF increase.

3 Support-Vector-Machine Modeling

3.1 Background. We can define a data modeling problem for a physical system as establishment of a proper approximation of the system based on a given set of measurements of the system, which may be obtained by laboratory experiments, or, more recently, by numerical simulations. Accordingly, based on the data obtained from the simulations described previously, the numerical modeling process can be performed. The modeling task in our

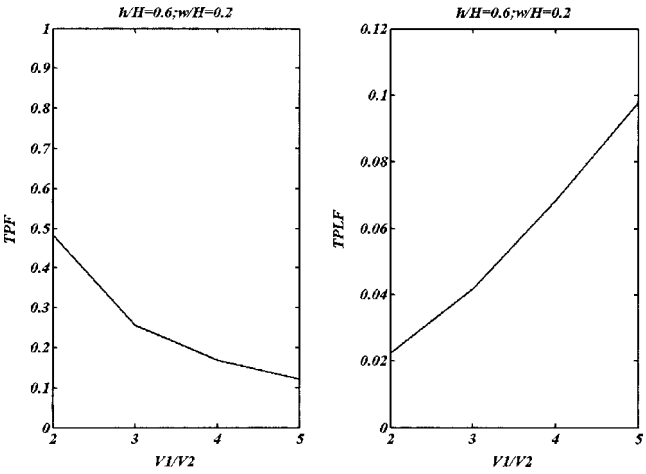

Fig. 5 Variations of TPF and TPLF with the fresh-air velocity for given values of the height *h* and width *w*

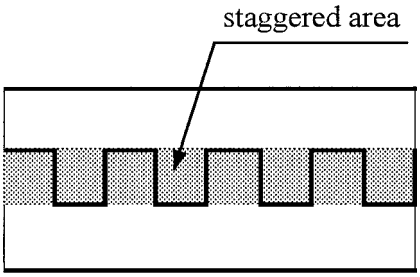

Fig. 6 The staggered area on the inlet section of the mixing domain

case is to find approximate relationships between the dependent parameters TPF and TPLF and the independent parameters such as height h, width w, and inlet cold-air velocity.

Data modeling may involve a variety of approaches. In recent years, the use of neural networks (NNs), and in particular multilayer feed-forward NNs, which can be trained to approximate virtually any smooth, measurable function, have become popular in many engineering fields, including fluid mechanics, and have produced promising results ([8,9], among many others). However, some inherent drawbacks, such as slow training convergence, low generalizing performance, etc., would make it difficult to put these models into practice. The classical radial basic function (RBF) network, as an effective algorithm for fast learning of feed-forward NNs, possesses good generalizing performance and, in the meantime, can avoid over-elaborated, lengthy computing like back propagation (BP) [10]. Nevertheless, like other NN models, local minimum and overfitting problems relating to the RBF neural network are critical issues as well. This usually leads to a poor level of generalization. As a result, for data modeling it is still worthwhile to seek superior approaches to conventional neural networks.

Support vector machines (SVMs), developed by Vapnik [11], provided an effective novel approach to improve the generalization performance of neural networks and to achieve global optimum. They are gaining popularity due to many attractive features and empirical performance (see, for example, [12–18]). SVMs embody the structural risk minimization (SRM) principle, which has been shown to be superior to the traditional empirical risk minimization (ERM) principle, employed by conventional neural networks. SRM minimizes an upper bound of the generalization error, as opposed to ERM, which minimizes the error on the training data. It is this difference that equips SVMs with greater ability to generalize, and to achieve global minimum, which are the goals in statistical learning. At the same time, SVMs can be theoretically analyzed and easily implemented. Real-world applications often mandate the use of more complex models and algorithms—such as NNs—which are much harder to analyze theoretically. SVMs construct models that are sufficiently complex, but simple enough to be analyzed mathematically. Although SVM is concerned with a high dimensional space, in practice, this does not involve any computations. By the use of *kernels*, all necessary computations are performed directly in the input space [13].

The basic idea of SVMs is to map the input variable into a high-dimensional feature space by nonlinear mapping and further to carry out linear operations in this space. This is the characteristic twist of SVMs—dealing with complex algorithms for nonlinear approximation problems, but for the sake of analysis and algorithms, it can pretend to work with a simple linear algorithm. Originally, SVMs were developed for pattern recognition problems. Recently, they have been successfully extended to nonlinear regression estimation. In the present work, SVMs were used to fulfill our modeling tasks.

3.2 SVM Regression. In regression formulation, the goal is typically to estimate an unknown continuous-valued function based on a finite number set of sample data $G=\{(x_i,d_i)\}_{i=1}^{l}$ (x_i is input vectors, d_i is the desired values). SVMs approximate the function by a linear regression

$$f(x)=\sum_{i=1}^{l} w_i\phi_i(x)+b \tag{3}$$

in a feature space F. Here, $\{\phi_i(x)\}_{1=1}^{l}$ denote a set of nonlinear transformations from input space x to feature space F, and $\{w_i\}_{i=1}^{l}$, b are coefficients.

Now the question is to determine $\{w_i\}_{i=1}^{l}$ and b from the sample data, G, by minimization of the regression risk, $R_{reg}(f)$, based on the empirical risk,

$$R_{reg}(f)=C\frac{1}{N}\sum_{i=1}^{N} L(d_i,f_i)+\frac{1}{2}\|w\|^2 \tag{4}$$

where C is a prespecified constant determining the tradeoff between the training error and the regression function flatness and $L(d,f(x))$ is a cost function that measures the empirical risk. The second term, $\frac{1}{2}\|w\|^2$, is used as a measure of function complexity. In general, the ε-insensitive loss function is used as the cost function [11,13]. For this function, when the data points are in the range of $\pm\varepsilon$, they do not contribute to the output error. The function is defined as

$$L(d,f(x))=\begin{cases}|d-f(x)|-\varepsilon & \text{if } |d-f(x)|\geqslant\varepsilon\\ 0 & \text{otherwise}\end{cases} \tag{5}$$

SVM regression performs linear regression in the high-dimensional feature space using ε-insensitive loss function and, at the same time, tries to reduce model complexity by minimizing the term, $\frac{1}{2}\|w\|^2$, in Eq. (4). This can be described by introducing (non-negative) slack variables ζ, ζ^* to measure the deviation of samples outside the ε-insensitive zone. Thus SVM regression is formulated as the following minimization problem:

$$\text{minimize } \frac{1}{2}\|w\|^2+C\sum_{i=1}^{n}(\zeta_i+\zeta_i^*) \tag{6}$$

$$\text{subject to } \begin{cases} w\phi(x_i)+b-d_i\leqslant\varepsilon+\zeta_i\\ d_i-w\phi(x_i)-b_i\leqslant\varepsilon+\zeta_i^*\\ \zeta_i,\zeta_i^*\geqslant 0\end{cases} \tag{7}$$

The solution of the above problem, Eq. (3), can be written:

$$f(x)=\sum_{i=1}^{l}(\alpha_i-\alpha_i^*)K(x,x_i)+b,\quad \text{subject to } 0\leqslant\alpha_i^*\leqslant C \text{ and } 0\leqslant\alpha_i\leqslant C \tag{8}$$

where α_i, α_i^* are Lagrange multipliers introduced to form a Lagrangian function. $K(x_i,x_j)$ is named as the kernel function. Its value is equal to the inner product of two vectors x_i and x_j in the feature space $\phi(x_i)$ and $\phi(x_j)$, i.e., $K(x_i,x_j)=\phi(x_i)\cdot\phi(x_j)$. Any symmetric function satisfying Mercer's condition [10] can be used as the kernel function. The commonly used kernel includes the linear kernel, the polynomial kernel, the Gaussian kernel, and the spline kernel [12].

These Lagrange multipliers in Eq. (8) can be determined by solving the following quadratic programming (QP) problem:

$$\text{maximize} \quad \phi(\alpha_i, \alpha_i^*) = \sum_{i=1}^{l} d_i(\alpha_i - \alpha_i^*) - \varepsilon \sum_{i=1}^{l} (\alpha_i + \alpha_i^*) - \frac{1}{2} \sum_{i=1}^{l} \sum_{j=1}^{l} (\alpha_i - \alpha_i^*)(\alpha_j - \alpha_j^*) K(\alpha_i, \alpha_j) \tag{9}$$

$$\text{subject to} \quad \begin{cases} \sum_{i=1}^{l} (\alpha_i - \alpha_i^*) = 0 \\ 0 \leqslant \alpha_i \leqslant C, \; i = 1, \ldots, l \\ 0 \leqslant \alpha_i^* \leqslant C \end{cases} \tag{10}$$

So far, the regression to the data can be completed by the SVM method. Based on the nature of the corresponding QP, in general, only a number of coefficients α_i, α_i^* will be assumed as nonzero, and the data points associated with the pair can be referred to as support vectors (SVs) (from which SVMs get the name).

3.3 Modeling Tasks. The simulation data are with respect to different inlet geometries, i.e., height h and width w, along with some different cold-air inflow velocities. Our attention was mainly focused on how the mixing process is affected by the inlet geometry for a fixed cold-air velocity. The numerical data were obtained for four different cold-air velocity values. Modeling may be done for each of these values. Nevertheless, for simplicity, only one case of the velocity value, namely, $V_1 = 150$ m/s, is considered herein. In the case under consideration there are only two independent variables, so we name it a 2-variable (2-V) modeling problem. Two SVMs were trained to approximate the parameters TPF and TPLF as the functions of the two geometric parameters h and w. There were 35 data points available for training the SVMs. Thereafter, for a wider study, our modeling work was also extended to include the cold-air velocity as an independent variable. This yielded a 3-variable (3-V) modeling problem. Again, two SVMs were trained for this modeling problem, among which one was for TPF and the other for TPLF. In total, 140 data points were available for training the SVMs in this case, which would constitute the whole simulation data space.

To train the SVMs, some options need to be decided a priori. The choice of kernel functions is very important for SVMs. In addition, the performance of SVM learning also depends on two prescribed control parameters, C and ε. In general, the above options are problem-specific and can be determined through a process of cross validation. In our case, a cross-validation process showed that as the three-order spline function was taken as the kernel function, and both the constants C and ε were chosen as 100 and 0.001, respectively, the best possible results could be produced for any of our modeling tasks. The training work was performed by a Matlab toolbox for SVMs, freely available in an Internet website (http://www.isis.ecs.soton.ac.uk).

3.4 Results and Assessment. In order to assess the performance of the constructed SVMs, some testing data were prepared in the same way as described in Sec. 2. The chosen testing points did not belong to the sets of points used for training the SVMs. For the 2-V problem, there were 12 testing points available, while for the 3-V problem, 48 testing points were available.

The BP-based multilayered feed-forward NNs were chosen as benchmarks for comparison. In our current work, four NNs were established to correspond with the four established SVMs, respectively. Each NN was specified as three-layered (i.e., one hidden layer besides the input and output layers) with a single-neuron-output layer to output the dependent TPF or TPLF parameter, and was trained by the same data used to construct the corresponding SVM. The training algorithm was the well-known BP algorithm. The target errors (mean square error (MSE)) were also given in the same values as in the SVM training. The number of neurons in the hidden layer of each NN was determined through a trial-and-error process so as to make for an optimal topological structure to the modeling task and hereby achieve maximal competitive ability with the counterpart, the SVM. The following statistical procedure was implemented for each NN to find the optimal number of neurons. Starting with a small neuron number in the layer, the NN was trained with the training data until a given target error was satisfied. It was then used to predict the testing data, and the relating MSE was recorded. These training-predicting coupling steps were repeated for the chosen neuron number with 100 differential initials of NN connection weights. The above steps were further repeated with progressively increasing neuron numbers from small to large numbers. Average errors over the 100 runs under each given neuron number were used to evaluate the NN structures. From the experiments, the four NNs get their optimal neuron number in the hidden layer as follows. For the 2-V modeling problem, the NN for TPF was with four neurons in the hidden layer, while the NN for TPLF was with 3 neurons in the layer. For the 3-V modeling problem, the NN for TPF was with 19 neurons in the hidden layer, for TPLF with 17 neurons in the layer. For all four NNs, the neurons in the hidden layer take the tansig transfer function, and the neuron in the second layer takes the simple linear transfer function. The training and testing of all the NNs are implemented by using the NN toolbox in Matlab 6.1.

Some comparison results for the 2-V and 3-V modeling problems are presented herein. As for each case the corresponding NN was trained with 100 different initials the established NNs had 100 different prediction outcomes. The results shown in the following for NNs were the averaged results over those 100 outcomes. For the 2-V problem, Fig. 7 shows the prediction results of the TPF and TPLF by SVMs and by NNs for the testing points, in which the target and predicted values of the two dependent parameters are compared together with the prediction performances presented in the form of error histograms. (The similar results for the 3-V problem are shown in Fig. 8.) In these cases, the target MSE value for training of SVMs and the MSE values recorded for the predictions of the testing data by SVMs and NNs are listed in Table 1. The time consumed for NN training and the above experimental decision, concerning the hidden neuron number for each case, is from 2 to 6 hours for training runs in a desk computer with P-III processor. In comparison, the training time taken by the SVMs for each of our application cases is a couple of seconds only. In summary, from these results one can conclude that statistically the SVMs introduced in this section for the modeling of the mixing process presented a better performance than the NN benchmark methods, the multilayer feed-forward NNs. This proves the advantages of SVMs for our problem.

It is worthwhile mentioning that for both modeling cases, the results from 100 NN different prediction times are quite random and vary within large ranges. This uncertainty phenomenon is of course unwelcome in any modeling, but it is an inherent drawback of NN-associated modeling. To further explain this, it is necessary to return to the principle of NN training. As is well known, NNs employ the ERM principle. So, training of an NN is to minimize an empirical risk function (in our case, a mean square error function) that is multimodal with many local minima. In the meantime, the training algorithms commonly used are gradient-based ones (e.g., BP algorithm in our cases). Using such algorithm with different initial weights of the connection, an NN training can attain different local minima and hereby obtain different results. This fact further supports our choice of SVMs because their training are deterministic and hence there is not the uncertainty encountered in the NN models.

3.5 Further Modeling-Based Studies.

3.5.1 Some Observations. Modeling predictions can realize different combinations of variables, for example the variations of the TPF and TPLF with the number of the vertical segments at the inlet. Three examples of such modeling predictions are shown in

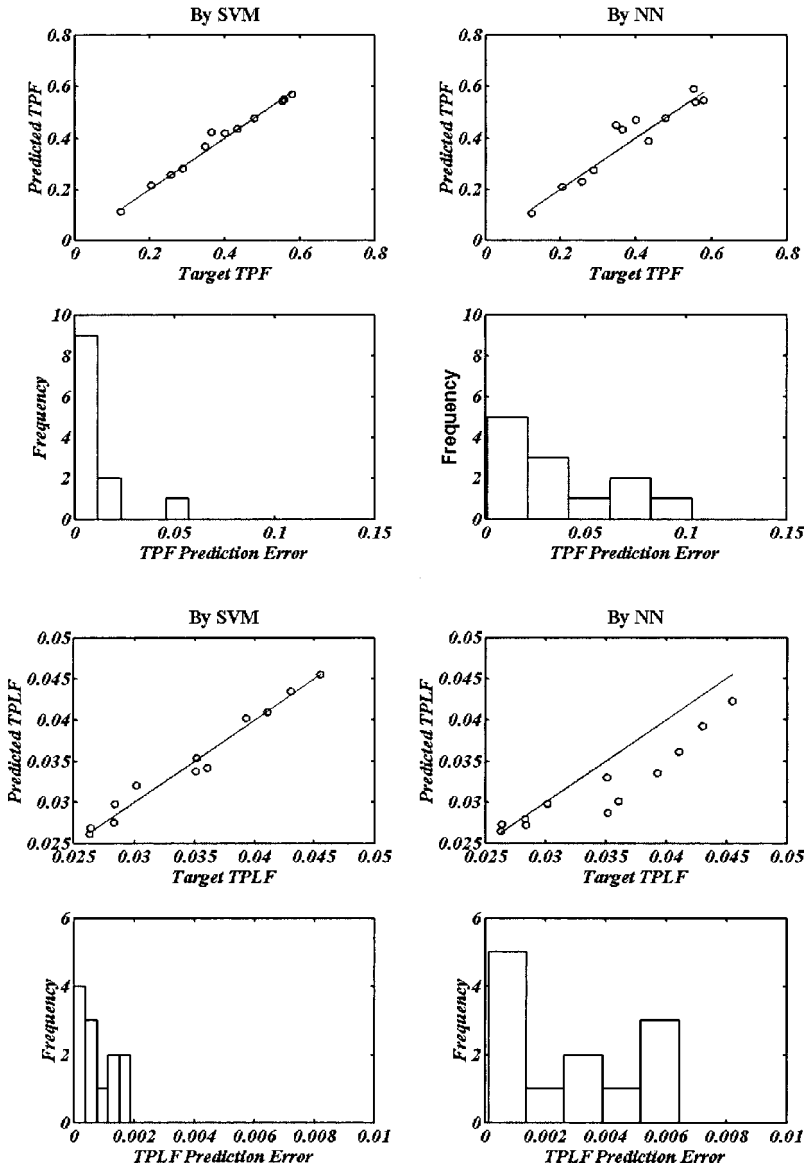

Fig. 7 Comparisons of the performances of SVMs and NNs for predicting the testing data in the 2-V modeling problem

the following. All examples were considered based on 2-V modeling (i.e., $V_1/V_2=3$) and on a fixed mixing passage width, namely, $W=H$.

(a) We denote the total length of the boundary contour within the given width, $W(=H)$, as S, and kept it at different constant values. The variations of the TPF and TPLF with respect to the number of vertical segments were predicted by the modeling system, and plotted in Fig. 9.

(b) Keeping the ratio of the height h to the width w at different constant values within the given width, $W(=H)$. The variations of the TPF and TPLF with the vertical segments were predicted by the modeling system, and plotted in Fig. 10.

(c) Keeping the height h at different constant values within the given width, $W(=H)$. The variations of the TPF and TPLF with the vertical segments were predicted by the modeling system, and plotted in Fig. 11.

The results from Fig. 9 and Fig. 10 show that in both situations the TPF increases as the number of vertical segments increases, while the TPLF performs contrary to the TPF. This fact is in agreement with the inferences from our simulation results (see Sec. 2), i.e., as the staggered area on the inlet section degrades toward a straight line, the TPF will increase, while the TPLF will decrease (see Figs. 3 and 4). The results from Fig. 11 again show the basin-shaped phenomenon depicted in Fig. 4 at a different angle.

3.5.2 Mixing Process Optimization. The modeling system enables one to optimize the described mixing process. Any of the two mixing criteria can be chosen as an optimized objective. In this example, both criteria were considered. The optimization problems are biobjective. Since our optimization problems are difficult to handle by conventional deterministic methods, e.g., the gradient-based methods, a populated stochastic optimization algorithm called differential evolution (DE) was selected. DE is one of the most promising and novel evolutionary algorithms. A more detailed description of DE can be found in [19]. Herein we adapt the DE version proposed by Lampinen [20] for multiobjective optimization.

A 2-V and a 3-V optimization problem were considered, respectively. The 2-V optimization problem is to find the most favorable two geometric parameters, the height h and the width w of

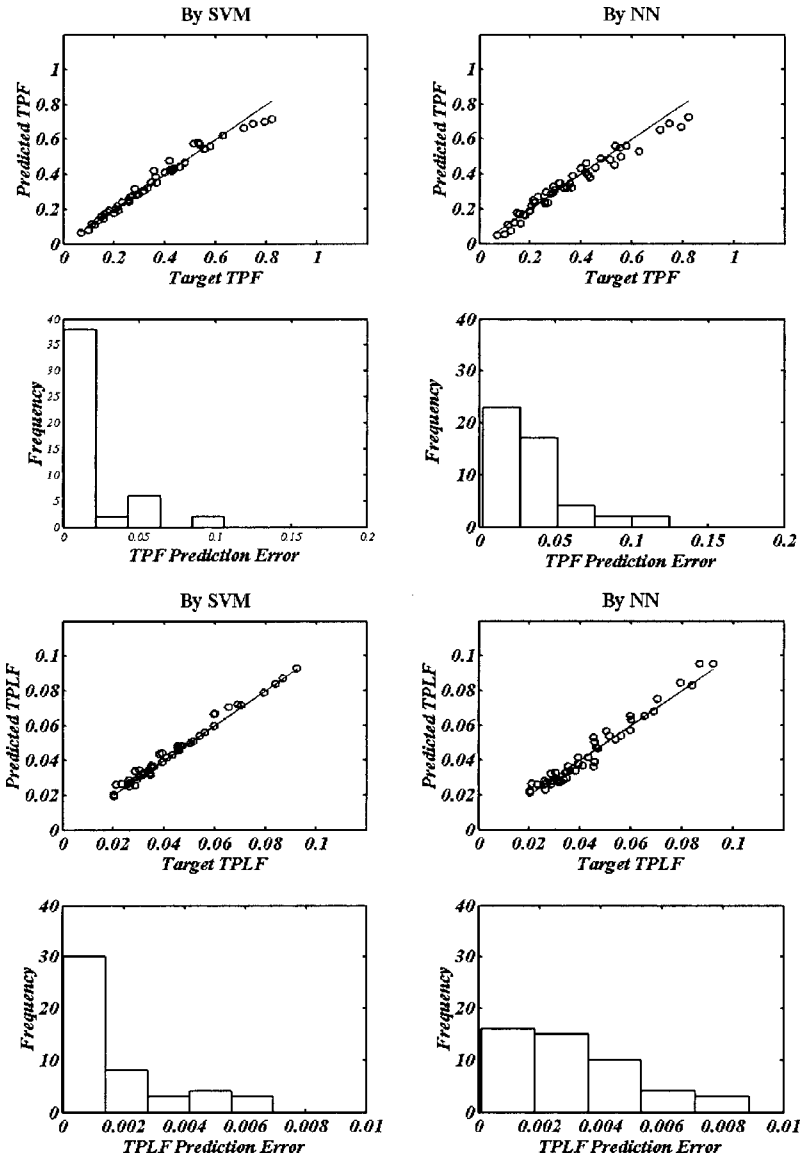

Fig. 8 Comparisons of the performances of SVMs and NNs for predicting the testing data in the 3-V modeling problem

the inlet boundary contour, under the fixed velocity ratio (given as $V_1/V_2=3$), while the 3-V optimization problem is to find the most favorable similar two geometric parameters together with the inlet velocity ratio.

Starting from a randomly produced initial population, DE was evolved to solve the two chosen optimization problems. Each evolving process was stopped at a given maximum number of generations (at 1000th generation). Both the evolving processes converged and the Pareto solutions were found. The obtained results are shown in Fig. 12 for the 2-V optimization problem, and in Fig. 13 for the 3-V one. In the figures, some examples of the solutions were indicated and the corresponding parameters were listed. Having the Pareto solutions, or more useful, the Pareto front, the user can now select any optimal point on this front.

It is worth mentioning that though the problems discussed herein were handled as biobjective optimizations, they can easily be reduced to one objective if the user requires only one of the

Table 1 The training target MSE values and the MSE values recorded for predictions of testing data

	2-V Problem: TPF/TPLF	3-V Problem: TPF/TPLF
Training Target:	$5.0\times10^{-4}/5.0\times10^{-6}$	$1.0\times10^{-3}/1.0\times10^{-5}$
SVM Predictions:	$6.2\times10^{-4}/7.9\times10^{-6}$	$1.3\times10^{-3}/9.2\times10^{-5}$
NN Predictions:	$2.0\times10^{-3}/5.9\times10^{-5}$	$5.2\times10^{-3}/1.2\times10^{-4}$

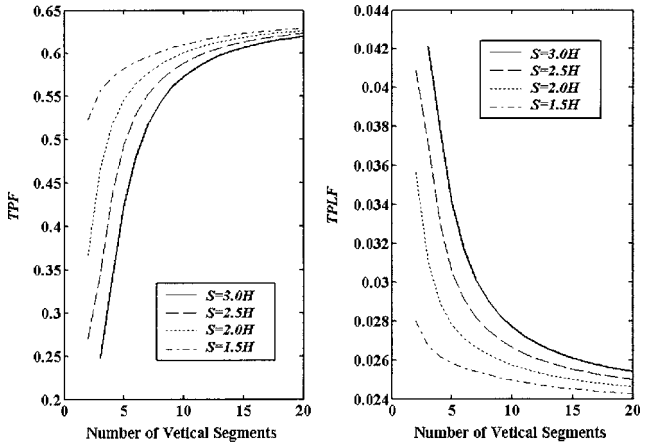

Fig. 9 Comparisons of the TPF and TPLF with the number of the vertical segments of the inlet boundary line in cases of fixed total length ($V_1/V_2=3$)

two objectives. The authors made a test run in which only the TPF is optimized. For the 2-V case, DE only needed about 50 generations to attain the optimum.

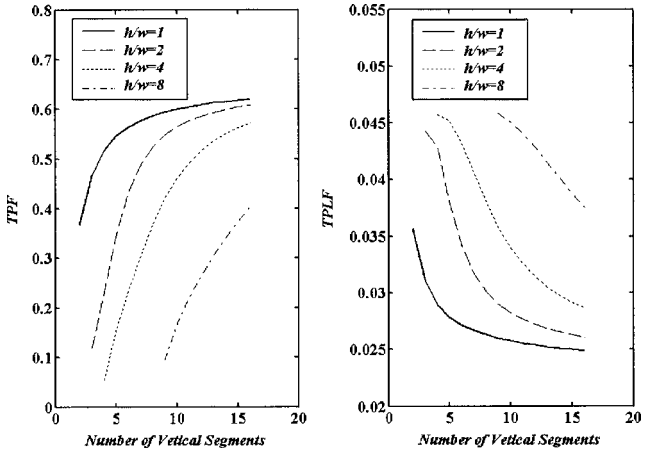

Fig. 10 The variations of TPF and TPLF with the number of the vertical segments of the inlet boundary line in cases of fixed ratio of the height h to the width w($V_1/V_2=3$)

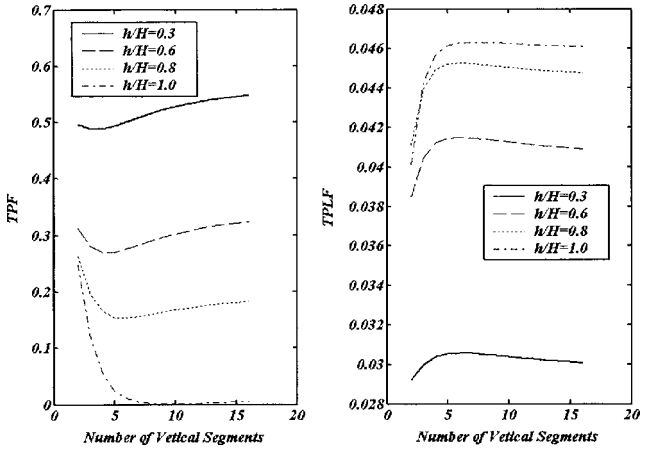

Fig. 11 The variations of TPF and TPLF with the number of the vertical segments of the inlet boundary line in cases of fixed height h($V_1/V_2=3$)

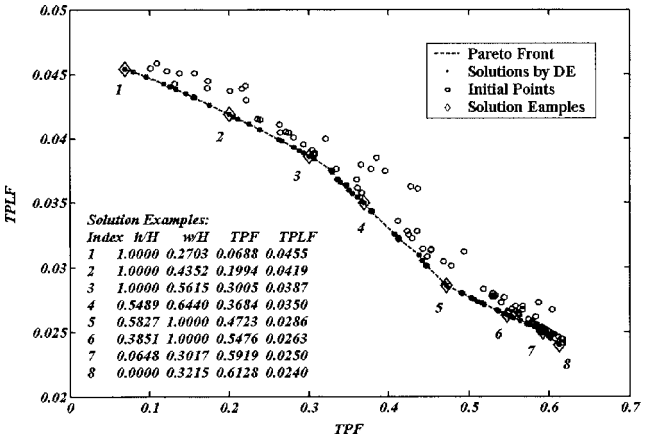

Fig. 12 The initial points and the results searched by DE after 1000 evolving generations for the 2-V optimization problem

4 Concluding Remarks

A prototype mixer, which has two air streams with different temperatures and equal pressure, was considered as a preliminary study of mixing in a combustor for flameless oxidation. Two parameters for mixing quality estimations, temperature pattern factor (TPF) and total pressure loss factor (TPLF), were defined. The process was analyzed by CFD and its main features were acquired. The dependence of TPF and TPLF on inlet geometry was found. Based on the obtained data, numerical modeling work of the mixing process was performed using a new learning machine technique—support vector machines (SVMs). It was shown that this approach models the studied process better than the well-known neural network (NN) methods. The mixing process was then further investigated through the modeling, including realizing observations of the mixing performance in three special cases of interest and performing optimizations of the mixing processes for two conflicting objectives and hereby obtaining the Pareto optimum sets.

Future work will concentrate on combustor design, its simulation and comparison with experimental study.

Nomenclature

b, w = coefficient

C, ε = positive specified constants

c_{p_i}, $\overline{c_p}$ = local constant-pressure specific heat, and mean constant-pressure specific heat

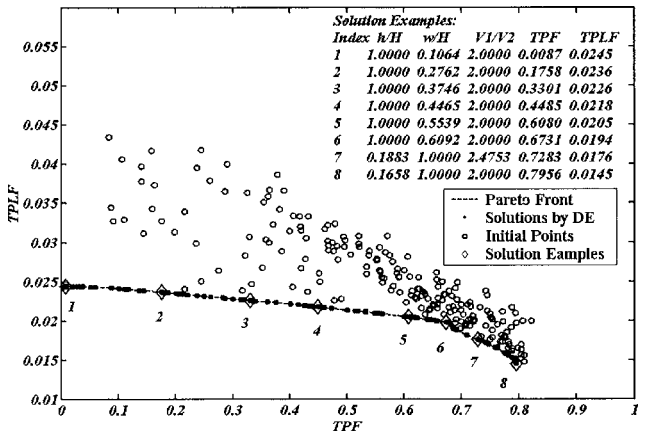

Fig. 13 The initial points and the results searched by DE after 1000 evolving generations for the 3-V optimization problem

d = desired value
F = feature space
f, ϕ = functions
G = data set
H, L, W = total height, length, and width of the mixing passage (m)
h, w = height and width of the boundary contour (m)
L_ε = ε-insensitive loss function
K = kernel function
k, *epsilon* = turbulence kinetic energy, dissipation rate
m_i = local mass rate (kg/s)
P_i^* = local total pressure (Pa)
$\overline{P_{inlet}^*}$, $\overline{P_{exit}^*}$ = inlet, exit flow weighted average total pressure (Pa)
R_{reg} = empirical risk function
S = total length of boundary contour (m)
T_1, T_2 = cold-, hot-air inflow temperature (K)
$\overline{T}$ = flow weighted average temperature (K)
T_i = local temperature (K)
$T_{\max}$ = maximal temperature (K)
TPF = temperature pattern factor
TPLF = total pressure loss factor
V_1, V_2 = cold-, hot-air inflow velocity (m/s)
x = input vector
α, α^* = Lagrange multipliers
ζ ζ^* = non-negative slack variables

Abbreviations:

BP = back-propagation algorithm
DE = differential evolution algorithm
NN = neural network
MSE = mean square error
RBF = radial basis function
QP = quadratic programming
SV = support vector
SVM = support vector machine

References

[1] Wunning, J. A., and Wunning, J. G., 1997, "Flameless Oxidation to Reduce Thermal NO-Formation," Prog. Energy Combust. Sci., **23**, pp. 81–94.
[2] Arfi, P., 2000, "Reduction of NOx Emissions From Gas Turbines Using Internal Exhaust Gas Recirculation," Ph.D. thesis, Technion-Israel Institute of Technology, Haifa, Israel.
[3] Levy, Y., 2000, Research Project: FLOXCOM, JTL001-09-2000, The Technion Turbo & Jet Laboratory, Israel (http://jet-engine-lab.technion.ac.il).
[4] Robert, E. D., 1967, in *Sawyer's Gas Turbine Engineering Handbook, Volume I, Theory & Design*, J. W. Sayer, ed., Gas Turbine Publications, Inc., Connecticut.
[5] Sedov, L. I., 1967, *Method of Similarity and Dimensions in Mechanics* (in Russian), Nauka, Moscow.
[6] Computational Dynamics Limited, 2001, STAR-CD Manuals (Version 3.15): Methodology, pp. 6.1–6.6.
[7] Abramovich, G. N., 1963, *The Theory of Turbulent Jets*, MIT, Cambridge, MA.
[8] Rediniotis, O. K., and Vijayagopal, R., 1999, "Miniature Multihole Pressure Probes and Their Neural-Network-Based Calibration," AIAA J., **37**(6), pp. 666–674.
[9] Krishna Kumar, K., Hachisako, Y., and Huang, Y., 2001, "Jet Engine Performance Estimation Using Intelligent System Technologies," AIAA paper no. 2001-1122.
[10] Papila, N., Shyy, W., Griffin, L., and Dorney, D. J., 2001, "Shape Optimization of Supersonic Turbines Using Response surface and Neural Network Methods," AIAA paper no. 2001-1065.
[11] Vapnik, V., 1995, *The Nature of Statistical Learning Theory*, Springer-Verlag, New York.
[12] Gunn, S. R., 1998, "Support Vector Machines for Classification and Regression," ISIS Technical Report, University of Southampton.
[13] Scholkopf, B., 1998, "SVMs—a Practical Consequence of Learning Theory," IEEE Intelligent System, July/August, 1998, pp. 19–21.
[14] Collobert, R., and Bengio, S., 2001, "SVM Torch: Support Vector Machines for Large-Scale Regression Problem," J. Mach. Learn. Res., **1**(2), pp. 143–160.
[15] Mangasarian, O. L., 2002, "Large Scale Kernel Regression via Linear Programming," Mach. Learn., **46**(1), pp. 255–269.
[16] Genton, M. G., 2002, "Classes of Kernels for Machine Learning: a Statistic Perspective," J. Mach. Learn. Res., **2**(2), pp. 299–312.
[17] Chuang, C. C., Su, S. F., Jeng, J. T., and Hsiao, C. C., 2002, "Robust Support Vector Regression Network for Function Approximation With Outliers," IEEE Trans. Neural Netw., **13**(6), pp. 1322–1330.
[18] Gestel, van Tony et al., 2004, "Benchmarking Least Square Support Vector Machine Classifiers," Mach. Learn., **54**(1), pp. 5–32.
[19] Price, K., 1999, in *New Ideas in Optimization*, D. Corne, D. Marco, and F. Glover, eds., McGraw-Hill, London, UK, pp. 78–108.
[20] Lampinen, J., 2001, "DE's Selection Rule for Multiobjective Optimization," Technical Report, Lappeenranta University of Technology, Finland.

Electrochemical and Transport Phenomena in Solid Oxide Fuel Cells

P. W. Li

M. K. Chyu
e-mail: mkchyu@engr.pitt.edu

Department of Mechanical Engineering,
University of Pittsburgh,
Pittsburgh, PA 15261

This paper begins with a brief review of the thermodynamic and electrochemical fundamentals of a solid oxide fuel cell (SOFC). Issues concerning energy budget and ideal energy conversion efficiency of the electrochemical processes in an SOFC are addressed. Chemical equilibrium is then discussed for the situations with internal reforming and shift reactions as an SOFC is fed with hydrocarbon fuel. Formulations accounting for electrical potential drops incurred by activation polarization, ohmic polarization, and concentration polarization are reviewed. This leads to a discussion on numerical modeling and simulation for predicting the terminal voltage and power output of SOFCs. Key features associated with numerical simulation include strong coupling of ion transfer rates, electricity conduction, flow fields of fuel and oxidizer, concentrations of gas species, and temperature distributions. Simulation results based primarily on authors' research are presented as demonstration. The article concludes with a discussion of technical challenges in SOFCs and potential issues for future research.
[DOI: 10.1115/1.2098828]

Keywords: solid oxide fuel cell, transport phenomenon, computational analysis

1 Introduction

Fuel cells are electrochemical devices that convert the energy from a chemical reaction directly into electrical energy. With advantages of high energy-conversion efficiency, less parasitic facilities and related noise and power consumption, ease of maintenance and flexibility for a distributed energy system, and reduced environmentally harmful emissions, including greenhouse gases, fuel cell technology has emerged as a new generation of power sources [1–4].

A fuel cell works very much like a battery. In both cases, two electrodes, an anode and a cathode, are separated by an electrolyte. The oxidation of fuel is separated into two steps performed on opposite sides of the electrolyte. The electrons involved in the oxidization reaction depart at the anode and return back to the cathode through an external load, and thus incur electrical potential and current flow for the external circuit. A battery contains all the substances for the electrochemical reaction and has a limited capacity. A fuel cell is supplied with reactants externally and operates continuously as long as it is supplied with fuel and oxidant.

Ideally the Gibbs free energy change in a chemical reaction can be directly converted into electrical energy in a fuel cell [5]. This is substantially different from the principle of a conventional thermal power plant, where the fuel is oxidized in a combustion process and a thermal-mechanical-electrical energy conversion process is employed, which is subjected to the limitation of Carnot cycle efficiency. The ideal energy conversion efficiency for a fuel cell (η_{FC}) operating at 1 atm (1.013×10^5 Pa) and for a heat engine (η_{Carnot}) is plotted as a function of the operating temperature in Fig. 1. Both these are assumed to utilize the chemical energy from the hydrogen oxidation reaction: $H_2(gas)+(1/2)O_2(gas)=H_2O(gas)$, and the heat engine is assumed a lowest heat rejection temperature of 373.15 K. The Carnot cycle efficiency is the asymptote of the heat engine's efficiency curve. If the operating pressure for a fuel cell can be increased, so can its efficiency [6–8]. The difference in the ideal efficiencies may not reflect the practical difference of the two kinds of energy conversion mechanisms involved in heat engines and fuel cells, but it does demonstrate the superiority of fuel cells for their much higher prospective power generation efficiencies. Fuel cells can work with high efficiency at relatively lower temperatures than heat engines; for example, a proton exchange membrane fuel cell works at temperatures ranging from room temperature to 100°C. However, a heat engine can only have the same level of ideal efficiency as a fuel cell when it works at temperature higher than 1000°C. On the other hand, when a fuel cell works at a higher temperature, around 1000°C, the waste gases can be introduced to a heat engine, such as a gas turbine, to produce even more power and a higher efficiency [9–13]. Among the various types of fuel cells, solid oxide fuel cells (SOFCs) must be operated at high temperatures, ranging from 600°C to 1000°C, and are feasible to combine with gas turbines to form hybrid systems. The review and study in the current work are focused on SOFCs.

The core component of a solid oxide fuel cell is a thin, gas-tight, ion conducting electrolyte layer sandwiched by a porous anode and cathode, as shown in Fig. 2. This electrolyte is a solid oxide material that only allows the passage of charge-carrying oxide ions. In the electrochemical process, oxygen, combining with electrons, is ionized at the cathode, and the oxide ions are driven across the electrolyte by the chemical potential difference between the two sides of the electrolyte due to the oxidation of fuel at the anode. Free electrons are released at the anode when the fuel (hydrogen, or carbon monoxide, or ammonia [14]) is oxidized, and they travel to the cathode through an external circuit because the electrolyte prevents electrons at the anode from returning back to the cathode. The difference in the chemical potential over the electrolyte reflects the electromotive force across the electrolyte, which sets up a terminal voltage towards the external load.

The output potential of an SOFC in practical operation is lower than the ideal values due to the overpotentials or potential losses induced from activation polarization, ohmic loss, and concentration polarization from the resistance of mass transport. The ion conductivity of the solid oxide electrolyte strongly depends on temperature and is only reasonably high when the temperature is above 600°C. Incidentally, high temperature operation could re-

Contributed by the Heat Transfer Division of ASME for publication in the JOURNAL OF HEAT TRANSFER. Manuscript received May 7, 2004; final manuscript received August 23, 2005. Review conducted by Jacob Chung.

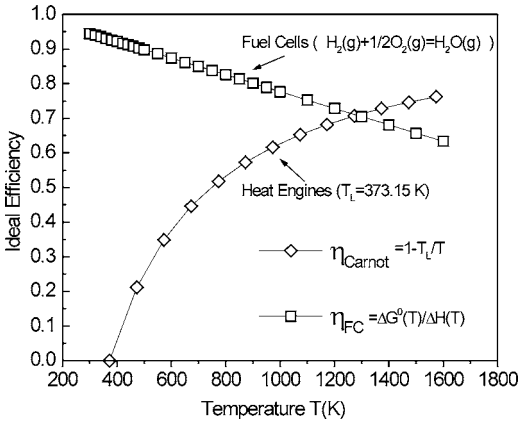

Fig. 1 The ideal efficiencies of fuel cells and heat engines

sult in issues of material safety. Since an SOFC operates via transport of oxide ions, in principle, an SOFC can be fueled with reforming gas containing a mix of CH_4, CO, H_2, CO_2, and H_2O, and reforming and shift reactions could occur because the high operating temperature ensures rapid fuel-side reaction kinetics without requiring extra catalyst. A review for the prediction of the voltage-current characteristics and a study of the impact of the above-mentioned issues on the SOFC performance will be helpful to the design and operation of an SOFC in order to have high electrical power density, efficiency, and safety.

2 Thermodynamics and Electrochemistry in SOFCs

The chemical potential and induced electromotive force across the electrolyte in a fuel cell involve the interrelation of thermodynamics and electrochemistry. Theoretically, the Gibbs free energy change in the fuel oxidation is what is to be converted into electrical energy in a fuel cell [15]. The systematical enthalpy change in an oxidation reaction of a fuel is composed of two parts, the Gibbs free energy change and the energy change due to entropy production in the process:

$$\Delta H = T\Delta S + \Delta G \tag{1}$$

While the Gibbs free energy change, $-\Delta G$, converts to electrical power, the entropy production, $-T\Delta S$, is released as heat or thermal energy in the electrochemical oxidation process. For a single gas species, if it is an ideal gas, the specific enthalpy h and standard Gibbs free energy g^0 are solely functions of temperature, and their values are available from the literature [16–22]. In practice, the gaseous reactants and products in solid oxide fuel cells can be treated as ideal gases, since their temperatures are generally higher than 600°C and their partial pressures are also relatively low. For an ideal gas at temperature T and pressure p, the chemical potential is expressed referring to the standard state value as

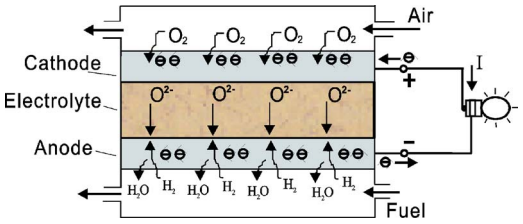

Fig. 2 Principle of an SOFC

$$g = g^0 + RT\ln\frac{p}{p^0} \tag{2}$$

where g represents the specific Gibbs free energy, R is the gas constant, and p^0 is the standard state pressure (=1 atm=1.015 $\times 10^5$ Pa). One may omit the p^0 in the denominator of the logarithm term in Eq. (2), when the pressure p is measured in the unit of atm.

2.1 Operation With Hydrogen Fuel. If pure hydrogen is the fuel for an SOFC, the oxidation of hydrogen is the only electrochemical reaction:

$$H_2 + \tfrac{1}{2}O_2 = H_2O(\text{gas}) \tag{3}$$

Based on the systematic Gibbs free energy change, the Nernst potential is expressed as

$$E_{(H_2+1/2O_2=H_2O)} = \frac{-\Delta G^0_{(H_2+1/2O_2=H_2O)}}{2F} + \frac{RT}{2F}[\ln(p_{H_2}/p^0)_{anode} + \ln(p_{O_2}/p^0)^{0.5}_{cathode} - \ln(p_{H_2O}/p^0)_{anode}] \tag{4}$$

where F(=96,486.7 C/mol) is Faraday's constant. The expression by Eq. (4) is commonly used for calculating the electromotive forces (EMFs) in fuel cells. The change of ideal chemical potentials $\Delta G^0_{(H_2+1/2O_2=H_2O)}$ at the temperature T can be calculated from the g^0 of the gas species involved.

An equivalent expression of the Nernst equation from the literature [23–25] is of the form

$$E_{(H_2+1/2O_2=H_2O)} = \frac{RT}{2F}[\ln(p_{O_2}/p^0)^{0.5}_{cathode} - \ln(p_{O_2}/p^0)^{0.5}_{anode}] \tag{5}$$

This expression is obtained by considering the equilibrium of the electrochemical reaction on the anode side which satisfies the condition of

$$\Delta G = 0 \tag{6}$$

Bringing the standard Gibbs free energy functions and partial pressures into Eq. (6), there is

$$-\Delta G^0_{(H_2+1/2O_2=H_2O)} + RT[\ln(p_{H_2}/p^0)_{anode} + \ln(p_{O_2}/p^0)^{0.5}_{anode} - \ln(p_{H_2O}/p^0)_{anode}] = 0 \tag{7}$$

Substituting Eq. (7) into Eq. (4), Eq. (5) is obtained. However, Eq. (5) is rarely used because of the inconvenience in obtaining the oxygen partial pressure on the anode side. In fact, the oxygen partial pressure at the anode is very low (on the order of 10^{-17} to 10^{-22} bar [5,25]) due to the anode reaction. It has no appreciable effect on the partial pressures of the major species in the anode flow. Therefore, when using Eq. (4), the partial pressures of gas species on the anode side are calculated without considering the oxygen in anodic gases.

In the electrochemical reaction of Eq. (3), one hydrogen molecule is deprived of two electrons, and one oxygen molecule acquires four electrons; therefore, the mole consumption rates of hydrogen and oxygen are related to current in the form of

$$m_{H_2} = \frac{I}{2F}; \quad m_{O_2} = \frac{I}{4F} \tag{8}$$

The mole generation rate of water from the electrochemical reaction is equal to the consumption rate of hydrogen according to the stoichiometric coefficients in Eq. (3).

2.2 Operation With Hydrocarbon Fuel. To obtain sufficient ionic conductivity, a solid oxide electrolyte has to be maintained at a high operating temperature. Therefore, an SOFC is favorable to accommodate for the reforming and shift reactions of hydrocarbon fuel, such as methane. In fact, the anode itself can serve as a catalyst, without the need of noble metals [26–29], for such chemical reactions at high temperatures. Moreover, an SOFC op-

erates based on the transport of oxide ions through the electrolyte layer; therefore, the reforming products, hydrogen and carbon monoxide, both can be oxidized to support electrochemical reactions. It is a common practice for SOFCs to directly utilize hydrocarbon fuels, such as methane or natural gas, which may be fully or partly pre-reformed before feeding them to the SOFC. In such a case, the fuel gas has components of CH_4, CO, CO_2, H_2, and H_2O, and further reforming and shift reactions will occur on the anode side simultaneously with the electrochemical reaction.

The electrochemical reaction will be affected by the coexistence of reforming and shift reactions. This is because the chemical equilibrium of the reforming and shift reactions affects the mole fractions of hydrogen gas. In the meantime, there is another electrochemical reaction

$$CO + 1/2O_2 = CO_2 \tag{9}$$

Because of the coexistence of two electrochemical reactions, one has to answer the question of how to determine the electromotive force. The following analysis verifies that the oxidation of CO and H_2 at the anode produces the same Nernst potential in an SOFC as long as the chemical equilibrium of the shift reaction is attained.

Consider the reforming and shift reactions

$$CH_4 + H_2O \leftrightarrow CO + 3H_2 \tag{10}$$

$$CO + H_2O \leftrightarrow CO_2 + H_2 \tag{11}$$

When both the two reactions attain chemical equilibrium, the partial pressures of the gas species involved must satisfy the condition of $\Delta G = 0$. This is expressed through the following two simultaneous equations [17]:

$$K_{PR} = \frac{(p_{H_2}/p^0)^3(p_{CO}/p^0)}{(p_{CH_4}/p^0)(p_{H_2O}/p^0)} = \exp\left(-\frac{\Delta G^0_{reforming}}{RT}\right) \tag{12}$$

$$K_{PS} = \frac{(p_{CO_2}/p^0)(p_{H_2}/p^0)}{(p_{CO}/p^0)(p_{H_2O}/p^0)} = \exp\left(-\frac{\Delta G^0_{shift}}{RT}\right) \tag{13}$$

Extending Eq. (13), there is

$$\left[g^0_{CO_2} + RT\ln\left(\frac{p_{CO_2}}{p^0}\right) + g^0_{H_2} + RT\ln\left(\frac{p_{H_2}}{p^0}\right)\right] - \left[g^0_{CO} + RT\ln\left(\frac{p_{CO}}{p^0}\right) + g^0_{H_2O} + RT\ln\left(\frac{p_{H_2O}}{p^0}\right)\right] = 0 \tag{14}$$

Rearranging this equation gives

$$g^0_{CO_2} + RT\ln\left(\frac{p_{CO_2}}{p^0}\right) - \left[g^0_{CO} + RT\ln\left(\frac{p_{CO}}{p^0}\right)\right] = g^0_{H_2O} + RT\ln\left(\frac{p_{H_2O}}{p^0}\right) - \left[g^0_{H_2} + RT\ln\left(\frac{p_{H_2}}{p^0}\right)\right] \tag{15}$$

Subtracting a term of $[(1/2)g^0_{O_2} + RT\ln(p_{O_2}/p^0)^{1/2}_{cathode}]$ from both sides of Eq. (15) results in

$$g^0_{CO_2} - g^0_{CO} - \frac{1}{2}g^0_{O_2} + RT\ln\left(\frac{p_{CO_2}}{p^0}\right) - RT\ln\left(\frac{p_{CO}}{p^0}\right) - RT\ln\left(\frac{p_{O_2}}{p^0}\right)^{1/2}_{cathode} = g^0_{H_2O} - g^0_{H_2} - \frac{1}{2}g^0_{O_2} + RT\ln\left(\frac{p_{H_2O}}{p^0}\right) - RT\ln\left(\frac{p_{H_2}}{p^0}\right) - RT\ln\left(\frac{p_{O_2}}{p^0}\right)^{1/2}_{cathode} \tag{16}$$

The left-hand side of Eq. (16) is the Gibbs free energy change in the electrochemical oxidation of CO, and the right-hand side is that for oxidation of H_2. Dividing both sides by $(2F)$, Eq. (16) is reduced to an expression in terms of electromotive forces,

$$E_{(H_2+1/2O_2=H_2O)} = E_{(CO+1/2O_2=CO_2)} \tag{17}$$

where $E_{(H_2+1/2O_2=H_2O)}$ is given in Eq. (4), while the Nernst potential for the electrochemical oxidation of CO is

$$E_{(CO+1/2O_2=CO_2)} = \frac{-\Delta G^0_{(CO+1/2O_2=CO_2)}}{2F} + \frac{RT}{2F}[\ln(p_{CO}/p^0)_{anode} + \ln(p_{O_2}/p^0)^{0.5}_{cathode} - \ln(p_{CO_2}/p^0)_{anode}] \tag{18}$$

Equation (17) is obtained at the equilibrium of the shift reaction. Studies of Peters et al. [27,30] and Achenbach and Riensche [31] show that the methane/steam reforming in the environment of an SOFC is very fast. Under a high temperature situation, the CO concentration is slightly higher than that given by the equilibrium composition. However, the operating temperature of an SOFC is high and the anode electrode can efficiently serve as a catalyst for the reforming and shift reactions to ensure rapid fuel reaction kinetics [32]. Therefore, the chemical equilibrium is a reasonable approximation to analyze the electromotive force and the species' variations [33–36]. Onuma et al. [37–39] also found that the dominant electrochemical reaction is the oxidation of H_2 when CO is in coexistence with H_2 in the fuel stream. They tested an SOFC with gas mixtures of CO and CO_2 and found that the electrochemical oxidation of CO is an order of magnitude slower than that of hydrogen. However, the above analyses also suggested that it is unnecessary to distinguish if the electrochemical oxidation process involves H_2 or CO in formulating the electromotive force, because the oxidation of both H_2 and CO yields the same electromotive force from equilibrium gas compositions. This is also supported by the experimental studies by Eguchi et al. [40,41].

Based on the discussion above, the electrochemical reaction can be considered to only be attributed to hydrogen; the electrochemical fuel value of CO is readily exchanged for hydrogen by the shift reaction at chemical equilibrium. In other words, CO is considered to only take part in the shift reaction. Whereas the EMF of an internal reforming SOFC is calculated according to the electrochemical oxidation of H_2, the species' consumption and production is determined collectively from the reactions by Eqs. (3), (10), and (11).

Recently, researchers have attempted to develop low temperature SOFCs [42], to a range of 500–800°C. As a result, the equilibrium assumption for reforming reaction may be inapplicable and reaction kinetics has to be applied [41]. The methane reaction rate is then expressed as a function of the load of catalyst, partial pressure, and temperature [43,44]:

$$R_{st} = 1.75\left(\frac{P_{CH_4}}{101325}\right)^{1.2} W_{cat}\exp\left(\frac{-57840}{RT}\right) \tag{19}$$

where R_{st} [mol/(cm^3·s)] is reaction rate of steam reforming and W_{cat} (g/cm^3) is the density of catalyst load. The method of determining the species' variation for an SOFC with internal reforming and shift reactions will be discussed later in the SOFC modeling.

3 Potential Losses in an SOFC

The actual efficiency in the operation of any fuel cell is always lower than the ideal efficiency. Understanding of the overpotentials, or polarizations, is essential for predicting the operational output parameters. In general, there are three overpotentials, caused by different mechanisms. These are reflected from the nature of the fuel cell voltage in response to a loading condition, as shown in Fig. 3. The drop of potential due to activation resistance or activation polarization is associated with the electrochemical reactions in the system. The second drop of potential comes from the ohmic resistance in the fuel cell components when the ions and electrons conduct in the electrolyte and electrodes, respectively. The third drop, which could be significant at high current densities, attributes to the mass transport resistance, or concentration polarization, in the flow of the fuel and oxidant. It is known

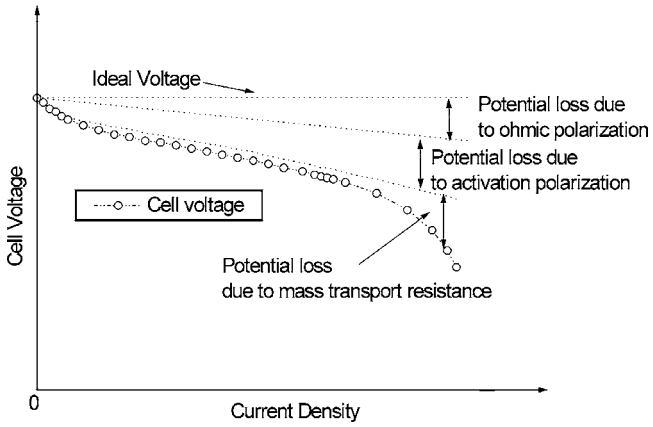

Fig. 3 Schematic view of the over-potentials in an SOFC

from the Nernst equation that the electromotive force of a fuel cell is a function of the temperature and the gas species' partial pressures at the electrolyte/electrode interface. The gas species' partial pressures are directly proportional to their mole fractions. Along with the fuel and air streams, the consumption of reactants or generation of products will make the mole fractions of the reactants decrease and those of the products increase. Due to the resistance in the mass transport process, the feeding of reactants and removing of products to/from the reaction site proceed at a large concentration gradient between the bulk flow and the electrode surface when the current density is high. This will induce a significant drop in the fuel cell potential. As a consequence of all the drop of potential, extra thermal energy will be released together with the entropy production heat ($-T\Delta S$). The heat transfer issues will be discussed later.

3.1 Activation Polarization. The activation polarization is the electronic barrier that must be overcome prior to current and ion flow in the fuel cell. Processes involving absorption of reactant species, transfer of electrons across the electrolyte layer, desorption of product species, and the nature of the electrode surface can all contribute to activation polarization. Chemical reactions, including electrochemical reactions, also involve energy barriers, which must be overcome by the reacting species. The activation polarization may also be perceived as the extra potential necessary to overcome the energy barrier of the rate-determining step of the reaction to a value that allows the electrode reaction to proceed at a desired rate [45,46].

The expression and relevant coefficients for activation polarization are generally derived from the well-known Butler-Volmer equation

$$i = i_0\left[\exp\left(\beta\frac{n_eF\eta_{Act}}{RT}\right) - \exp\left(-(1-\beta)\frac{n_eF\eta_{Act}}{RT}\right)\right] \tag{20}$$

where η_{Act} is the activation polarization, i is the actual current density in the fuel cell, and i_0 is the exchange current density, which is the forward and reverse electrode reaction rate at the equilibrium potential. A high exchange current density means that a high electrochemical reaction rate and good fuel cell performance can be expected. The β in Eq. (20) is the transfer coefficient, which is the fraction of the change in polarization that leads to a change in the reaction-rate constant. The n_e is the electrons transferred per electrochemical reaction, which is 2 for the reaction of Eq. (3). However, there are different derivative expressions from Eq. (20) by different researchers [44,45,47].

Chan et al. [45] suggested that β is 0.5 for the fuel cell application. Substituting the value of β=0.5 into Eq. (20), a new expression is

$$i = 2i_0\sinh\left(\frac{n_eF\eta_{Act}}{2RT}\right) \tag{21}$$

which can result in an explicit expression for the activation polarization:

$$\eta_{Act} = \frac{2RT}{n_eF}\sinh^{-1}\left(\frac{i}{2i_0}\right) \quad \text{or}$$
$$\eta_{Act} = \frac{2RT}{n_eF}\ln\left[\left(\frac{i}{2i_0}\right) + \sqrt{\left(\frac{i}{2i_0}\right)^2 + 1}\right] \tag{22}$$

For a high activation polarization, Eq. (22) can be approximated as the simple and well-known Tafel equation:

$$\eta_{Act} = \frac{2RT}{n_eF}\ln\left(\frac{i}{i_0}\right) \tag{23}$$

On the other hand, if the activation polarization is small, Eq. (20) can be approximated as the linear current-potential expression:

$$\eta_{Act} = \frac{2RT}{n_eF}\frac{i}{i_0} \tag{24}$$

Chan et al. [45] suggested an i_0 of 5300 A/m^2 for the anode and 2000 A/m^2 for the cathode for an SOFC, yet no comment was made on how the i_0 was determined in their work.

In the above formulations, the difference in activation polarization for the anode and cathode depends only on the different exchange current densities in the same type of equation. However, Iwata et al. [47] argued that the expressions of activation polarization between the two electrodes are different, i.e.,

$$i = \frac{RT}{3F}S^a\left[\exp\left(\frac{2F\eta^a_{Act}}{RT}\right) - \exp\left(\frac{-F\eta^a_{Act}}{RT}\right)\right] \tag{25}$$

for the anode, and

$$i = \frac{RT}{4F}S^c\left[\exp\left(\frac{2F\eta^c_{Act}}{RT}\right) - \exp\left(\frac{-2F\eta^c_{Act}}{RT}\right)\right] \tag{26}$$

for the cathode. The S^a and S^c are the electrode/electrolyte interface conductivity $[1/(\Omega\cdot m^2)]$ for the anode and the cathode, respectively, and they are expressed as

$$S^a = 125.6\times10^{10}\exp[-138{,}000/(RT)]p^{0.15}_{O_2,anode} \tag{27}$$

$$S^c = 62.7\times10^{6}\exp[-136{,}000/(RT)]p^{0.5}_{O_2,cathode} \tag{28}$$

The partial pressure of oxygen at the anode, $p_{O_2,anode}$, satisfies the chemical equilibrium in the fuel side, and thus it can be determined by using Eq. (5) or using the equilibrium equation of the electrochemical reaction in the form of

$$\frac{(p_{H_2O}/p^0)_{anode}}{(p_{H_2}/p^0)_{anode}(p_{O_2}/p^0)^{0.5}_{anode}} = \exp\left(-\frac{\Delta G^0_{(H_2+1/2O_2=H_2O)}}{RT}\right) \tag{29}$$

For an explicit expression of the activation polarization, Eq. (26) can be further reduced to

$$\eta^c_{Act} = \frac{RT}{2F}\sinh^{-1}\left(i\frac{4F}{RTS^c}\right) \tag{30}$$

Nagata et al. [44] showed different but similar expressions for S^a and S^c to that given by Iwata et al. [47]

$$S^a = 10^{7.79}\exp[-120{,}000/(RT)](p_{O_2}/p^0)^{0.133}_{anode} \tag{31}$$

$$S^c = 10^{6.02}\exp[-130{,}000/(RT)](p_{O_2}/p^0)^{0.5}_{cathode} \tag{32}$$

Prediction of activation polarization based on the three different sources discussed above also shows discrepancy. The expressions by Iwata et al. [47] and Nagata et al. [44] show less deviation. Due partly to the semi-empirical adjustment of the exchange cur-

Table 1 Data and equations for resistivity of SOFC components

	Cathode $\Omega \cdot cm$	Electrolyte $\Omega \cdot cm$	Anode $\Omega \cdot cm$	Interconnect $\Omega \cdot cm$
Bessette et al. [53]	$0.008114e^{500/T}$	$0.00294e^{10350/T}$	$0.00298e^{-1392/T}$	--
Ahmed et al. [54]	*0.0014	$0.3685+0.002838e^{10300/T}$	*0.0186	*0.5
Nagata et al. [44], and Hirano et al. [55]	*0.1	$10.0e^{[10092(1/T-1/1273)}$	*0.013	*0.5
Ferguson et al. [56]	$\frac{T}{4.2\times10^5}e^{1200/T}$	$\frac{1}{3.34\times10^2}e^{10300/T}$	$\frac{T}{9.5\times10^5}e^{1150/T}$	$\frac{T}{9.3\times10^4}e^{1100/T}$

* At temperature of 1000 °C.

rent densities i_0 for both the anode and cathode in the expression by Chan et al. [45], it may predict the activation polarization with greater discrepancy. For example, using the values suggested by Chan et al. [45] leads to a nearly 50 percent higher activation polarization than that calculated by the other two expressions when the cell current density is above 5000 A/m^2. The present authors in an earlier study [48] used higher exchange current densities i_0, i.e. 6300 and 3000 A/m^2 for the anode and cathode, respectively, to avoid overprediction of the activation polarizations. Their simulated results for three different tubular SOFCs agreed well with the experimental data. Because the expressions by Chan et al. [45] explicitly give the activation polarization, Eq. (22) is somewhat popular and has been used frequently [49–52]. The exchange current densities in these studies, however, were adjusted so as to make simulated cell voltage to fit with experimental measurements. The present authors suggested in [48] that the adequate values for the exchange current densities i_0 of SOFCs is 6000–6500 A/m^2 for the anode and 2500–3500 A/m^2 for the cathode when using Eq. (22). For predictions involving less empirical coefficients, Eqs. (25)–(32) are recommended.

3.2 Ohmic Resistance and Joule Heating. The ohmic loss comes from the ionic conduction resistance of the electrolyte layer as well as the electric resistances of the electrodes and the current collection components. Therefore, the conductivity of cell components and the current collecting pathway are the two factors most influential to the overall ohmic loss of an SOFC. In modern-day SOFCs, lanthanum manganite, suitably doped with alkaline and rare earth elements, is used for the cathode (air electrode) [8], yttria stabilized zirconia (YSZ) has been most successfully employed for the electrolyte, and nickel/YSZ is applied over the electrolyte to form the anode. Temperature is the major influence that could significantly affect the conductivity of SOFC materials. With regards to the electrolyte, the resistivity could be two orders of magnitude smaller if the temperature increases from 700°C to 1000°C. The equations quantifying resistivity for SOFC components reported in literature are compiled in Table 1.

The predicted values of resistivity using the different equations listed in Table 1 were compared. The expressions by Bessette et al. [53] were found to be favorable, which yielded nearly identical predictions to those by Ahmed et al. [54], Nagata et al. [44], and Hirano et al. [55]. On the other hand, the equation by Ferguson et al. [56] exhibits a higher predicted resistivity for the anode and lower prediction for the cathode compared to other expressions. Recently the effects of material aging on the resistivity or ion conductivity of the electrolyte Y_2O_3–ZrO_2 (YSZ) were reported [57]. However, the aging effect is insignificant when an optimum 9.5 mol % of Y_2O_3 is doped in ZrO_2.

The ohmic losses from current and ion conduction depend on the current collection pathway, which varies with the different structures of fuel cells. There are three major types of structures, including tubular, flat-tube, and planar for SOFCs [54,58–60]. For the analysis of the internal ohmic loss in fuel cells, the Kirchhoff's loop rule is applicable. Analysis of the internal circuit in fuel cells with differential formulations was presented earlier in 1973 by Sverdrup et al. [61]. In a planar type SOFC, as shown in Fig. 4, the current collects through the channel walls, also called ribs, and oxide ions move perpendicularly across the electrolyte layer. Before the current reaches the channel walls, it must travel in the in-plane direction of the electrodes, resulting in more ohmic loss. A network circuit for current flow modeled by Iwata et al. [47] considers the channel walls as current collection pathways in a planar SOFC. Generally speaking, the height and the width of the gas channels are relatively small, and the electric resistance through the channel wall might be negligible, as was assumed in the study of Ahmed et al. [54]. This assumption leads to a simplification that the current is almost perpendicularly collected, which means that the current flows normally through the tri-layer consisting of cathode, electrolyte, and anode.

To determine the ohmic loss, one may start to formulate the local current in the following way [62]:

$$I = \Delta A \cdot \frac{(E - \eta^a_{Act} - \eta^c_{Act}) - V_{cell}}{(\delta^a \rho^a_e + \delta^e \rho^e_e + \delta^c \rho^c_e)} \tag{33}$$

where ΔA is a finite area on the anode/electrolyte/cathode tri-layer, through which the current I passes; δ is the thickness of the individual layers; ρ_e is the resistivity of the electrodes and electrolyte; V_{cell} is the cell terminal voltage; and the denominator of the right-hand side term is the summation of the resistance of the tri-layer. The volumetric Joule heating in the volume of $\Delta A \times \delta$ in the anode can be expressed as

$$\dot{q}^a_{Ohmic} = I^2 \cdot (\rho^a_e / \Delta A^2) \tag{34}$$

This is also applicable to the electrolyte and cathode by replacing the thickness and resistivity accordingly. The volumetric heating due to the activation polarization is expressed as

$$\dot{q}^a_{Act} = I \cdot \eta^a_{Act} / (\Delta A \cdot \delta^a) \text{ for the anode} \tag{35}$$

$$\dot{q}^c_{Act} = I \cdot \eta^c_{Act} / (\Delta A \cdot \delta^c) \text{ for the cathode} \tag{36}$$

The thermodynamic heat generation in the area of ΔA at the anode/electrolyte interface is

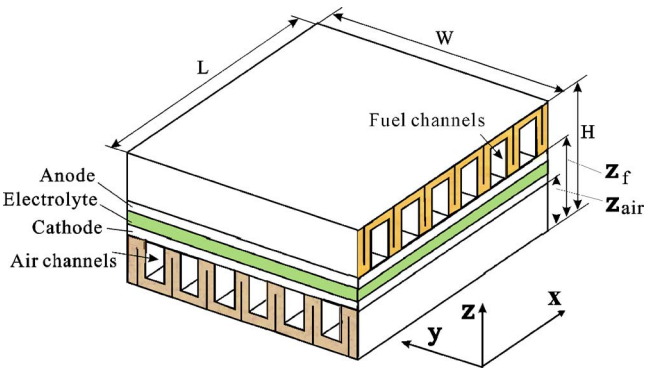

Fig. 4 Structure of a planar SOFC

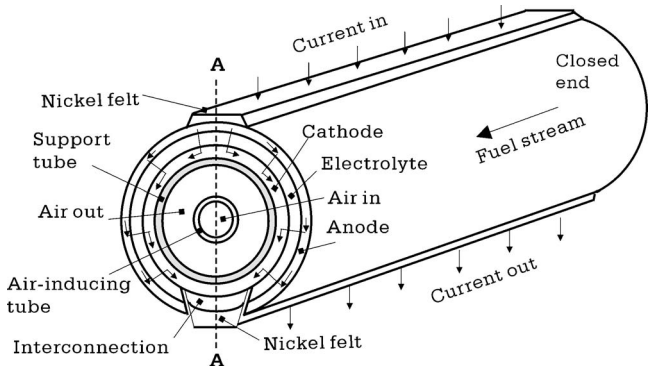

Fig. 5 Structure of a tubular SOFC

$$Q^R = (\Delta H - \Delta G)\left(\frac{I}{2F}\right) \tag{37}$$

The current pathway in a tubular type SOFC, as shown in Fig. 5, is relatively longer than its planar counterpart, as the current has to flow circumferentially around the tube [58]. To account for the ohmic loss and Joule heating along a circumferential pathway, various network circuit models [48,55,61,63], such as the one demonstrated in Fig. 6, may be adopted. Because the current collection in the peripheral direction is symmetric, only half of the tube shell needs to be considered in an analysis. The local current routing from the anode to the cathode through electrolyte can be obtained based on the local electromotive force, E, the local potentials in the anode and cathode, and the ionic resistance of the electrolyte layer:

$$I = \frac{E - \eta^a_{Act} - \eta^c_{Act} - (V^c - V^a)}{R^e} \tag{38}$$

where V^a and V^c are the potentials in the anode and cathode, respectively, and R^e is the ionic resistance of the electrolyte layer. Given a thickness of δ^e and a unit area of ΔA,

$$R^e = \rho^e_e \cdot \delta^e / \Delta A \tag{39}$$

where the ρ^e_e is the ionic resistivity of the electrolyte.

To obtain the local current across the electrolyte by using Eq. (38), supplemental information or equations for V^a and V^c are necessary. Applying Kirchhoff's loop rule to a grid located in the anode, the equation linking the potentials of the central grid point P and its neighboring points (east, west, north, south) as well as the corresponding grid P in the cathode can be obtained as

$$\left(\frac{V^a_E - V^a_P}{R^a_e} + \frac{V^a_W - V^a_P}{R^a_w}\right) + \left(\frac{V^a_N - V^a_P}{R^a_n} + \frac{V^a_S - V^a_P}{R^a_s}\right) + \left[\frac{V^c_P - V^a_P - (E_P - \eta^P_{Act})}{R^e_P}\right] = 0 \tag{40}$$

Similarly, for a grid point P in the cathode,

$$\left(\frac{V^c_E - V^c_P}{R^c_e} + \frac{V^c_W - V^c_P}{R^c_w}\right) + \left(\frac{V^c_N - V^c_P}{R^c_n} + \frac{V^c_S - V^c_P}{R^c_s}\right) + \left[\frac{V^a_P - V^c_P + (E_P - \eta^P_{Act})}{R^e_P}\right] = 0 \tag{41}$$

where R^a and R^c are the discretized resistances in the anode and cathode, respectively. Each term is determined according to the resistivity, the length of the current path, and the area upon which the current acts. The η^P_{Act} is the total activation polarization, encompassing the anode side and the cathode side.

With all of the equations for the discretized grids in both the cathode and the anode given, a matrix representing the pair of Eqs. (40) and (41) can be created. When finding a solution from such a matrix equation for the potentials, the following approximations are useful:

1. At the two ends of the cell tube, longitudinal current flow is absent, and, therefore, an insulation condition is applicable.
2. At the symmetric plane *A-A*, as shown in Figs. 5 and 6, peripheral current in the cathode and anode is absent, unless either electrode is in contact with the current collecting nickel felt through which the current flows in or out of the cell.
3. The potentials of the nickel felts are assumed to be uniform due to their high electric conductivities.
4. Since the potential difference between the two nickel-felts is the cell terminal voltage and the potential at the nickel felt in contact with the anode layer can be assumed to be zero. The potential at the nickel felt in contact with the cathode will be the terminal voltage of the fuel cell.

Once all the local electromotive forces are obtained, the only unknown condition for the equation matrix is either the total current flowing out of the cell or the potential at the nickel felt in contact with the cathode. To proceed further, two approaches may be adopted. If the total current out of the cell is prescribed, the terminal voltage can be predicted. On the other hand, one can prescribe the terminal voltage and predict the total current, which is the summation of the local current I across the electrolyte layer.

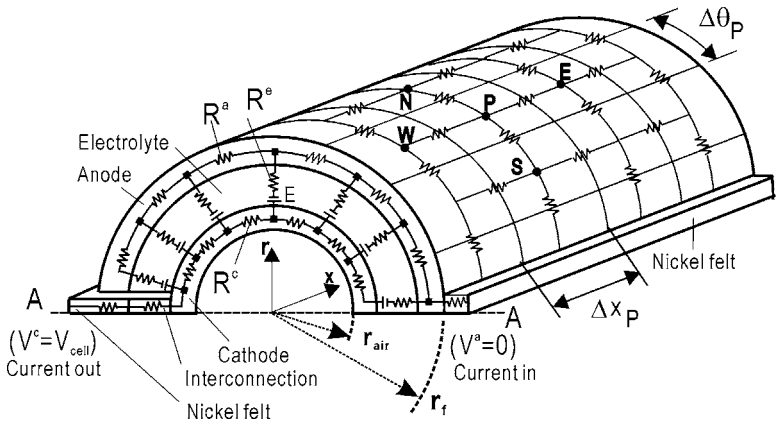

Fig. 6 Discretization of current conduction in electrodes for a tubular SOFC

With the potentials being obtained in the electrode layers, the discretized volumetric Joule heating in the electrode for a volume centered at P can be given as

$$\dot{q}_P^a = \frac{1}{2}\left(\frac{(V_E^a - V_P^a)^2}{R_e^a} + \frac{(V_W^a - V_P^a)^2}{R_w^a} + \frac{(V_N^a - V_P^a)^2}{R_n^a} + \frac{(V_S^a - V_P^a)^2}{R_s^a} \right) / (\Delta x_P \cdot r^a \cdot \Delta\theta_P \cdot \delta^a) \quad (42)$$

$$\dot{q}_P^c = \frac{1}{2}\left(\frac{(V_E^c - V_P^c)^2}{R_e^c} + \frac{(V_W^c - V_P^c)^2}{R_w^c} + \frac{(V_N^c - V_P^c)^2}{R_n^c} + \frac{(V_S^c - V_P^c)^2}{R_s^c} \right) / (\Delta x_P \cdot r^c \cdot \Delta\theta_P \cdot \delta^c) \quad (43)$$

$$\dot{q}_P^e = \left(\frac{(E_P - \eta_{Act}^P - V_P^c + V_P^a)^2}{R_P^e} \right) / (\Delta x_P \cdot r^e \cdot \Delta\theta_P \cdot \delta^e) \quad (44)$$

where r and δ with the corresponding superscripts of a, c and e are the average radius and thickness, respectively, for the anode, cathode, and electrolyte, and Δx_P and $\Delta\theta_P$ are the P-controlled mesh sizes in the axial and peripheral directions, as shown in Fig. 6. The magnitudes of volumetric heating induced by the activation polarization in the anode and cathode are

$$\dot{q}_{Act}^{P,a} = I_P \cdot \eta_{Act}^{P,a} / (\Delta x_P \cdot r^a \cdot \Delta\theta_P \cdot \delta^a) \quad (45)$$

$$\dot{q}_{Act}^{P,c} = I_P \cdot \eta_{Act}^{P,c} / (\Delta x_P \cdot r^c \cdot \Delta\theta_P \cdot \delta^c) \quad (46)$$

The thermodynamic heat generated at the anode-electrolyte interface in the area controlled by mesh point P is

$$Q_P^R = (\Delta H - \Delta G) \cdot I_P / (2F) \quad (47)$$

The network circuit model discussed above is also applicable to the flat-tube type SOFCs [64,65]. However, formulation details are expected to vary, due to differences in geometry and possibly complexity in layer structure.

3.3 Concentration Polarization. The fraction of reactants and oxidant respectively in fuel and air streams decreases along with the gradual consumption of these species. This will cause the electromotive force to decrease gradually along the flow streams. On the other hand, due to the mass transport resistance, the concentration of the gas species will encounter polarization between the core flow region and the electrode surface, resulting in lower partial pressures for the reactants and higher partial pressures for the products at the electrode surfaces. At high cell current density, the increased requirements for the feed of the reactants and removal of the products can significantly enhance the concentration polarization, and the cell output potential will drop accordingly.

To take account of the concentration polarization when calculating the electromotive force, the local partial pressures of the reactants and products at the electrode surface must be known. However, this requires a solution for the concentration fields for the gas species in the fuel and oxidant channels, which may be based on a one-dimensional solution [66,67], or on a rather complex two- or three-dimensional solution for the mass conservation governing equations [36,48,63,68–70].

Some researchers, such as Ahmed et al. [54], Hirano et al. [55], and Ferguson et al. [56], considered the mass transfer resistance in both electrode layers as part of the loss contributing to activation polarization. This can be done, for example, by decreasing the exchange current density, thus the level of activation polarization is increased. In fact, the ionization of oxygen occurs in the cathode layer and the formation of water occurs in the anode layer; neither process proceeds exactly at the electrode-electrolyte interface. Therefore, such an approximation is not unreasonable and is applied to the models introduced in this paper. More rigorous but sophisticated models for mass transfer in the electrodes may be found in a report by Suwanwarangkul [71].

4 Survey of Experimental Studies for SOFCs

Due mainly to the high operating temperature and difficulty in gas sealing, extensive experimental tests for solid oxide fuel cells are rather costly. Most test data for tubular type SOFCs presently available are mainly from researchers associated with the SOFC projects conducted by Siemens-Westinghouse Power Corporation and its collaborators.

Hagiwara et al. [72] reported test data of cell voltage versus current density for four single tubular SOFCs with diameters of 16 mm and lengths of 500 mm. The test was conducted using a fuel comprised of hydrogen and a small amount of water vapor. The utilization percentage of hydrogen and oxygen for all test runs were set at 85% and 17%, respectively. They observed that when the temperature of the fuel cell was controlled at around 1000 °C, the degradation of cell performance was rather insignificant. However, when the fuel cell was operated at a temperature around 1050 °C, the degradation of performance increased modestly. They concluded that the formation of porosity when temperature exceeds 1050°C is responsible for the performance degradation. It is evident that temperature control for an SOFC is important for a reliable and efficient performance.

Tomlins and Jaszcar [6] reported test data for a single SOFC with a diameter of 22 mm and length of 1500 mm. They used humidified hydrogen as fuel and set the utilization percentage of hydrogen at 85% and that of oxygen at 17%. More than 5% higher cell voltages were observed for the same current density when the SOFC was pressurized to 5 atm compared to the atmospheric (1.0 atm) operation. More test data for pressurized operation (from 1 to 15 atm) were also reported by Singhal [8]. Another experimental study carried out in Japan was reported by Watanabe [73], where SOFC performance degradation and pressurized operation were discussed. He suggested a 12% increment of cell voltage by increasing the operation pressure from 1 to 7 atm.

With regard to planer-type SOFCs, Keegan et al. [51] reported experimental data using an anode-supported unit, with an electrolyte layer 10 μm thick and an active area of 3.8 cm^2. The cell operation was based on a fuel composed of hydrogen, water vapor, and a fraction of nitrogen adjusted to dilute the concentration of hydrogen. While there was no description of other structural dimensions in the article, their results showed a high operational current density when the hydrogen fraction was above 50%. Elangovan et al. [74] performed a test of two electrolyte-supported planar SOFCs. The electrolyte for each cell was 180 μm thick, and the active areas were 10.2×10.2 and 5×5 cm^2, respectively. Their results showed that the current density is limited to 600 mA/cm^2, which is much lower than that of the anode-supported SOFC studied by Keegan et al. [51]. It is generally understood that a thinner electrolyte layer is critical for an SOFC to produce high current density at a reasonable voltage.

5 Modeling and Simulations

An operation curve for an SOFC that characterizes the average current density versus the terminal voltage is important when designing a power system. Transport information, such as temperature and concentration fields, is also of significant concern for proper operation of both SOFC itself and associated facilities in a hybrid power generation system. As mentioned earlier, experimental testing for an SOFC is rather difficult and costly, due largely to its high operating temperature. Therefore, numerical modeling is a viable way to study SOFCs.

A computer simulation for an SOFC must be capable of predicting the operational characteristics in terms of the average current density versus the cell terminal voltage under various operating conditions. The operating condition of an SOFC is determined

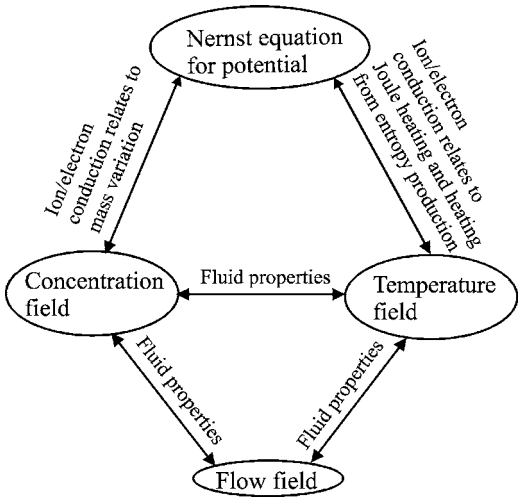

Fig. 7 Multi-physics coupling for SOFC modeling

when the flow rates and the thermodynamic states of the fuel and oxidant are prescribed and one of the load conditions, terminal voltage, current, or external load, is given [48]. The flow rates and thermodynamic conditions of the fuel and oxidant may be referred to as internal conditions, whereas the terminal voltage, the output current, and the external load are designated as external conditions. Similar to a battery, the external load condition of an SOFC dictates the consumption rates of the fuel and oxidant, as well as the generation rate of products, in the electrochemical reaction.

5.1 Multi-Physics Coupling and Challenges. The physics and transport of flow, heat and mass transfer, conduction of ions and electrons, and chemical reactions are strongly coupled in fuel cells. First, the gas species' concentration field and temperature distribution determine the electromotive forces. Then, the ion/electron conduction driven by the electromotive force determines the mass variation and heat generation in the fuel cell. On the other hand, the gas species' mole/mass fractions determine the gas properties in the flow fields; the flow fields affect the gas species' concentration and temperature distributions. Figure 7 illustrates such coupling of all the parameters in fuel cells. Given below is a discussion for every specific process.

5.2 Species Variation and Charge Transfer Rate. If pure hydrogen is the fuel in an SOFC, the determination of species' variation is relatively straightforward, as is given by Eq. (8). When hydrocarbon fuel, such as natural gas or methane, is fed to an SOFC, reforming, shift, and electrochemical reactions may proceed simultaneously. The chemical equilibrium expressions in Eqs. (12) and (13) can be used to determine the variations of gas species. Assume that $\overline{x}$, $\overline{y}$, and $\overline{z}$ are the mole consumption rates for CH_4, CO, and H_2, in the three reactions given by Eqs. (10), (11), and (3), respectively. The coupled variations of the five participating species between the inlet and outlet of a domain in a fuel channel are

$$\mathrm{CH}_4^{out} = \mathrm{CH}_4^{in} - \overline{x} \tag{48}$$

$$\mathrm{CO}^{out} = \mathrm{CO}^{in} + \overline{x} - \overline{y} \tag{49}$$

$$\mathrm{CO}_2^{out} = \mathrm{CO}_2^{in} + \overline{y} \tag{50}$$

$$\mathrm{H}_2^{out} = \mathrm{H}_2^{in} + 3\overline{x} + \overline{y} - \overline{z} \tag{51}$$

$$\mathrm{H}_2\mathrm{O}^{out} = \mathrm{H}_2\mathrm{O}^{in} - \overline{x} - \overline{y} + \overline{z} \tag{52}$$

The overall mole flow rate of the fuel, denoted by M_f, will vary from the inlet to the outlet in the form of

$$M_f^{out} = M_f^{in} + 2\overline{x} \tag{53}$$

In addition, according to the chemical equilibrium assumption for reforming and shift reactions, the partial pressures of the species, proportional to the mole fractions, must satisfy Eqs. (12) and (13) at the domain outlet. Substituting Eqs. (48)–(53) into Eqs. (12) and (13), there is

$$K_{PR} = \frac{\left(\dfrac{\mathrm{CO}^{in} + \overline{x} - \overline{y}}{M_f^{in} + 2\overline{x}}\right)\left(\dfrac{\mathrm{H}_2^{in} + 3\overline{x} + \overline{y} - \overline{z}}{M_f^{in} + 2\overline{x}}\right)^3\left(\dfrac{p}{p^0}\right)^2}{\left(\dfrac{\mathrm{CH}_4^{in} - \overline{x}}{M_f^{in} + 2\overline{x}}\right)\left(\dfrac{\mathrm{H}_2\mathrm{O}^{in} - \overline{x} - \overline{y} + \overline{z}}{M_f^{in} + 2\overline{x}}\right)} \tag{54}$$

$$K_{PS} = \frac{\left(\dfrac{\mathrm{H}_2^{in} + 3\overline{x} + \overline{y} - \overline{z}}{M_f^{in} + 2\overline{x}}\right)\left(\dfrac{\mathrm{CO}_2^{in} + \overline{y}}{M_f^{in} + 2\overline{x}}\right)}{\left(\dfrac{\mathrm{CO}^{in} + \overline{x} - \overline{y}}{M_f^{in} + 2\overline{x}}\right)\left(\dfrac{\mathrm{H}_2\mathrm{O}^{in} - \overline{x} - \overline{y} + \overline{z}}{M_f^{in} + 2\overline{x}}\right)} \tag{55}$$

where p is the overall pressure of the fuel flow in the domain of interest, and K_{PR} and K_{PS}, as given by Eqs. (12) and (13), are chemical equilibrium constants, which are functions of the temperature at which the chemical reactions proceed.

If the assumption of chemical equilibrium for the reforming reactions is invalid, such as the case for low or intermediate temperature (500–800°C) SOFCs, the reaction rate of methane needs to be considered as a function of catalyst loading density, partial pressure of methane, and reaction temperature [43,44], i.e.,

$$\overline{x} = \Delta V R_{st} = \Delta V\left[1.75\left(\frac{P_{\mathrm{CH}_4}}{101{,}325}\right)^{1.2} W_{cat}\exp\left(\frac{-57{,}840}{RT}\right)\right] \tag{56}$$

where R_{st} (mol/cm^3·s) is the reaction rate of steam reforming, ΔV (cm^3) is the finite volume of the anode layer of interest, which is loaded with catalyst, and W_{cat} (g/cm^3) is the catalyst loading density.

Since oxidation of H_2 is the main feature of the electrochemical reaction in a fuel cell, the consumption of hydrogen is directly related to the charge transfer rate or current I across the electrolyte layer, i.e., from Eq. (8)

$$\overline{z} = I/(2F) \tag{57}$$

Here $\overline{z}$ directly relates to the current density, which has to be obtained from the solution of the circuit network in a fuel cell based on the prescribed condition of either current density or cell voltage. Solution of the species mole consumption rates $\overline{x}$, $\overline{y}$, and $\overline{z}$ must be pursued simultaneously [75], and the variations of the five participating species in the domain of interest can be determined from Eqs. (48)–(52). However, the local electric current of the fuel cell must be known before solving for the species consumption rates. This demonstrates that the processes in an SOFC feature a strong coupling of the species' mole variation, the electromotive force, and the ion conduction and current flow. When the reacted mole numbers of CH_4 and CO are determined, the heat absorbed in the reforming reaction and the heat released from the shift reaction can be obtained:

$$Q^{Reforming} = \Delta H^{Reforming}\cdot\overline{x} \tag{58}$$

$$Q^{Shift} = \Delta H^{Shift}\cdot\overline{y} \tag{59}$$

5.3 Flow and Heat/Mass Transfer. The determination of local electromotive forces in a fuel cell relies on the local temperature and species' concentration fields. Therefore, one of the important tasks in fuel cell modeling is to solve the governing equations for the temperature and concentration fields. In addition, fuel cells are generally stacked to achieve a higher and more desirable overall voltage and power output. Single-cell analysis of

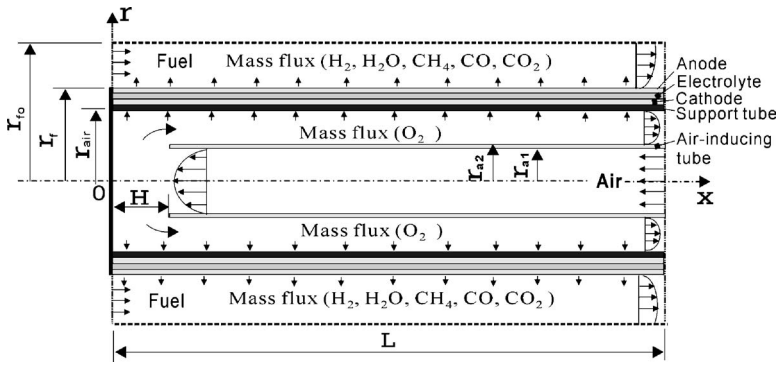

Fig. 8 Illustration of the computation domain for a tubular SOFC

the heat/mass transfer and the chemical/electrochemical performance over its controlled domain can be extended for evaluating the stack performance of multiple fuel cells. The present authors introduced a modeling process to apply the studies from a single SOFC fuel cell to the cells in a stack [48].

5.3.1 Tubular Type SOFCs. Figure 8 shows the flow arrangement and computational domain for a single tubular SOFC [48]. Geometrically, the problem can be modeled in a two-dimensional and axi-symmetric manner. Two flow streams and solid area of the cell tube and air-inducing tube are included in the computation domain.

Since mass fractions of the participating species vary in the flow field, all of the thermal and transport properties of the fluids are local functions of the species concentration, temperature, and pressure. As a result, the governing equations [36,48,63] for momentum, energy, and species mass fractions use nonuniformly distributed thermal and transport properties. These equations are applicable over the entire computational domain, and zero velocities are prescribed to the solid area in the numerical computation. In the energy equation, the thermal energy and Joule heating, calculated from Eqs. (58), (59), and (42)–(47), must be circumferentially averaged and reduced to a volumetric heating source, denoted by $\dot{q}$, and introduced as a source term in the proper locations in the fuel cell. Source terms arise as energy diffusion driven by the concentration diffusion of the gas species are deemed to be small in magnitude and negligible [76,77]. The boundary conditions for the momentum, heat, and mass conservation equations are as follows:

1. On the symmetrical axis, at $r=0$, $v=0$ and $\partial\phi/\partial r=0$, where ϕ represents general variables except for v.
2. At the outmost boundary, where $r=r_{fo}$, it is thermally adiabatic, nonchemically reactive, and species impermeable. This leads to $v=0$ and $\partial\phi/\partial r=0$, where ϕ represents general variables except for v.
3. At $x=0$, the fuel inlet has a prescribed uniform velocity, temperature, and species mass fraction, and the solid part has $u=0$, $v=0$, $\partial T/\partial x=0$, and $\partial Y_J/\partial x=0$.
4. At $x=L$, the air inlet has a prescribed uniform velocity, temperature, and species mass fraction, and the gas exit has $v=0$, $\partial u/\partial x=0$, $\partial T/\partial x=0$, and $\partial Y_J/\partial x=0$; the tube-end solid part has $u=0$, $v=0$, $\partial T/\partial x=0$, and $\partial Y_J/\partial x=0$.
5. At the interfaces of the air/solid, at $r=r_{air}$, and fuel/solid, at $r=r_f$, $u=0$ is assumed.

In the fuel flow channel, the mass flow rate increases along the x direction due to the influx of oxide ions. Similarly, a reduction of the flow rate occurs in the air flow channel due to the ionization of oxygen and efflux of oxide ions to the fuel side. This mass transfer induces the following two radial velocities at $r=r_{air}$ and $r=r_f$, respectively:

$$v_f = \left.\frac{\sum \dot{m}_x^{fuel,species}}{\rho_x^{fuel}}\right|_{r=r_f} \tag{60}$$

$$v_{air} = \left.\frac{\sum \dot{m}_x^{air,species}}{\rho_x^{air}}\right|_{r=r_{air}} \tag{61}$$

where $\dot{m}[\mathrm{kg}/(\mathrm{m}^2\mathrm{s})]$ is the mass flux of the gas species at the interface of the electrodes and the fluid, which arises from the electrochemical reaction in the fuel cell. The mass fractions of all participating chemical components at the boundaries of $r=r_{air}$ and $r=r_f$ are calculated considering both diffusion and convection effects [78,79]:

$$\dot{m}_x^{J,air} = -D_{J,air}\rho_x^{air}\frac{\partial Y_J}{\partial r} + \rho_x^{air}Y_J v_{air} \tag{62}$$

$$\dot{m}_x^{J,fuel} = -D_{J,fuel}\rho_x^{fuel}\frac{\partial Y_J}{\partial r} + \rho_x^{fuel}Y_J v_f \tag{63}$$

Note that the mass fluxes for the species in Eqs. (60)–(63) are strongly related to the ion/electron conduction. The determination of mass variation and mass flux that arises from the electrochemical reaction has been discussed in preceding sections. As a result, the mass fraction at the solid/fluid interface, derived from Eqs. (62) and (63), will be used to calculate the partial pressures and the local electromotive forces by Eq. (4).

5.3.2 Planar Type SOFCs. For a planar SOFC as shown in Fig. 4, the governing equations of flow and heat/mass transfer are three-dimensional in nature [62]. At the fluid-electrode interfaces in the Z direction the velocities induced by mass fluxes from the consumption and production of gas species are

$$w_{x,y}^{air} = \left.\frac{\sum \dot{m}_{x,y}^{air,species}}{\rho_{x,y}^{air}}\right|_{z=z_{air}} \tag{64}$$

$$w_{x,y}^{fuel} = \left.\frac{\sum \dot{m}_{x,y}^{fuel,species}}{\rho_{x,y}^{fuel}}\right|_{z=z_f} \tag{65}$$

The mass fractions of all participating chemical species at the internal boundaries of $z=z_{air}$ and $z=z_f$ can be formulated similar to Eqs. (62) and (63), including both diffusion and convection effects:

$$\dot{m}_{x,y}^{J,air} = -D_{J,air}\rho_{x,y}^{air}\frac{\partial Y_J}{\partial z} + \rho_{x,y}^{air}Y_J \cdot w_{x,y}^{air} \tag{66}$$

Table 2 Properties of SOFC materials

	Thermal conductivity W/(m K)	Cp J/(kg K)	Density kg/m^3
Cathode	[d]11; [c]2.0; [b]2.0	[b] 623	[a] 4930
Electrolyte	[d]2.7; [c]2.7; [b]2.0	[b] 623	[a] 5710
Anode	[c]11.0; [d]6.0; [b]2.0	[b] 623	[a] 4460
Support tube	[c]1.0		
Air-inducing tube	[c]1.0		
Interconnector	[b]13; [c]2.0; [d]6.0	[b] 800	[a] 6320; [b]7700

[a]Ahmed et al. [54]; [b]Recknagle et al. [69]; [c]Nagata et al. [44]; [d]Iwata et al.[47]

$$\dot{m}_{x,y}^{J,fuel} = -D_{J,fuel}\rho_{x,y}^{fuel}\frac{\partial Y_J}{\partial z} + \rho_{x,y}^{fuel}Y_J \cdot w_{x,y}^{fuel} \tag{67}$$

It is reasonable to assume that the overall flow of fuel is evenly distributed into the multiple fuel channels. Therefore, the inlet conditions for all fuel channels are the same. This assumption is also applicable for airflow and the air channels.

The entire area, except the fuel inlet, at the surface of $y=0$ has zero velocity and adiabatic/impermeable boundary conditions for the temperature and mass fraction equations. The same situation is representative for the surface at $x=0$, where the inlets of the air channels are located. The adiabatic/insulation condition of $\partial\phi/\partial n=0$ is valid for equations of temperature and mass fractions at the surfaces of $x=L$ and $y=W$, as well as for the equations of velocities of fuel and air at their outflow boundaries. Zero velocity is applicable for the surfaces of $y=W$ and $x=L$, except for the areas of fuel and air outflow. For the energy equation, thermal energy from the electrochemical reaction and the Joule heating (Eqs. (34)–(37), (58), and (59)) must be reduced to a volumetric heating source, as denoted by $\dot{q}$, and introduced as source terms in the proper locations in the fuel cell. Again, source terms related to energy diffusion driven by concentration diffusion of the gas species are small in magnitude and negligible [76,77].

In a planar cell stack, one fuel cell unit must have its anode channel-plate in contact with the cathode channel-plate of the neighboring unit, while the cathode channel-plate of the cell must contact the anode channel-plate of the other-side neighboring unit. If every fuel cell unit operates at the same conditions in a stack, it is reasonable to assume that the outside surface temperature of the cathode and anode plates for one unit must comply with the condition of a consecutive heat flux given by:

$$q\,(x,y)|_{z=0} = q\,(x,y)|_{z=H} \tag{68}$$

The thermal properties of solid materials in an SOFC are not well documented in the literature. Table 2 shows some compiled data which have some discrepancies from different literary sources. The single gas properties are available from Refs. [18,80]. The mixing rules for the thermal and transport properties of a gas mixture are available from Refs. [18,81].

5.4 Numerical Scheme and Computation. To perform a numerical simulation for flow, temperature, and concentration fields in an SOFC, the finite volume approach is probably the most common for discretizing the governing equations [63,64,69]. For the momentum equations, the SIMPLE algorithm or its derivatives can be used to treat the coupling of the velocity and pressure fields [82]. In a tubular SOFC, the temperature difference between the cell tube and the air-inducing tube might be sufficiently large and radiation heat transfer could be significant. Numerical treatments of heat radiation with finite-volume formulation are abundant in the literature, such as [83].

A computation is based on the states of fuel and air and either the cell current or cell voltage. As a consequence of the simulation, one of the unknown electrical properties, either cell voltage or current, will be given along with other operational details. Depending on the specific way of prescribing the external parameters, the following three schemes are designated to predict other unknown parameters when constructing a numerical model for an SOFC: (1) use the internal conditions and cell voltage to predict the cell current, (2) use the internal conditions and cell current to predict the cell voltage, and (3) use the internal conditions and external load to predict the cell voltage and current density. As expected, the computational time and effort among the three schemes are quite different. In the first scheme, the cell voltage is known, and the local current can be obtained by using Eq. (33) and Eqs. (38)–(41) for a planar- and tubular-type SOFC, respectively. The integrated value from the local current is the total current from the SOFC. The second scheme is basically a trial-and-error solution, in which the cell voltage is recorrected iteratively to ensure that the total current integrated from local current agrees with the prescribed value. The third scheme resembles the second scheme in that one needs to assume a terminal voltage and to find the total current. The computation converges only when the voltage-current ratio equals to the prescribed external load. Figure 9 shows the flowchart of numerical computation, where two routes, varying with the prescribed conditions, are indicated.

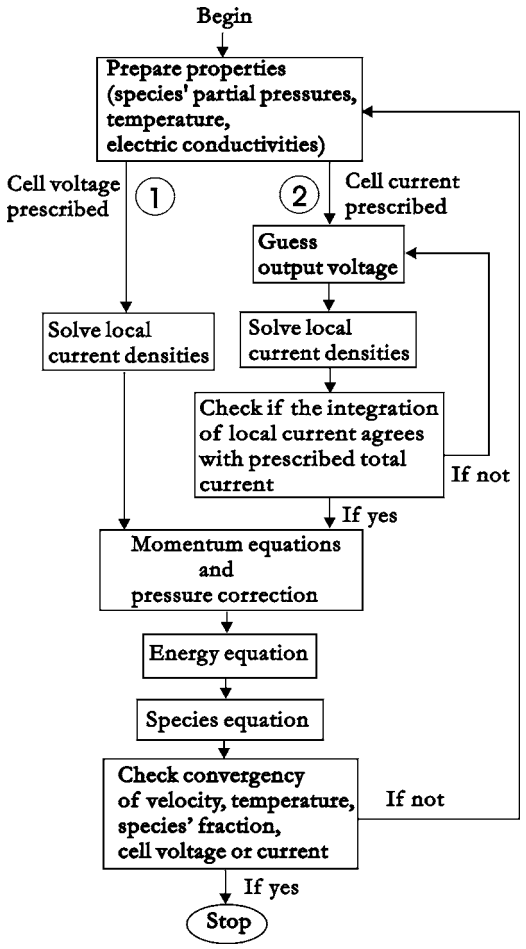

Fig. 9 Computation flow chart for simulation of SOFCs

The current-carrying characteristic of a fuel cell is generally expressed in terms of the average current density of the fuel cell. Also, instead of specifying the flow rates of fuel and air, the stoichiometric data represented by the utilization percentages of hydrogen and oxygen are prescribed typically for practical applications. This way of characterizing operating conditions facilitates direct and sensible comparisons of fuel cell performance based on the same levels of average current density and hydrogen and oxygen utilization percentages. The utilization percentages for both fuel and air can be related to the inlet velocities of the flow channels:

Table 3 Example SOFCs with test data available

Data sequence: Outer diameter (mm) / Thickness (mm) / Length (mm)			
	Hagiwara et al. [72]	Hirano et al. [55]	Singhal [8] Tomlins et al. [6]
Air-inducing tube	7.00 /1.00 /485	6.00 /1.00/290	12.00/1.00/1450
Support tube	-	13.00/1.50/300	-
Cathode	15.72/2.20/500	14.40/0.70/300	21.72/2.20/1500
Electrolyte	15.80/0.04/500	14.48/0.04/300	21.80/0.04/1500
Anode	16.00/0.10/500	14.68/0.10/300	22.00/0.10/1500
Fuel boundary	18.10/ - /500	16.61/ - /300	24.87/ - /1500
Grid number ($r$xx)	66x602	66x602	66x1602

$$u_{fuel} = \left(\frac{A_{cell} i_{cell}}{2F U_{H_2} X_{H_2} A_{fuel}} \right) \frac{RT_f}{P_f} \tag{69}$$

$$u_{air} = \left(\frac{A_{cell} i_{cell}}{4F U_{O_2} X_{O_2} A_{air}} \right) \frac{RT_{air}}{P_{air}} \tag{70}$$

where i_{cell} is the cell average current density, A_{cell} is the surface area of the electrolyte layer, A_{fuel} and A_{air} are the inlet flow areas of the fuel and air, P_f, P_{air}, T_f, and T_{air} are the inlet pressures and temperatures of the fuel and air, respectively, X_{H_2} and X_{O_2} are the mole fractions of hydrogen in the fuel and oxygen in the air, respectively, and U_{H_2} and U_{O_2} are the utilization percentages for hydrogen and oxygen, respectively.

6 Features of Cell Performance Studied From Simulations

6.1 Fuel Cell Terminal Parameters. The present authors have performed numerical simulations of three tubular SOFCs [48,63,70], which have been experimentally investigated by Hagiwara et al. [72], Hirano et al. [55], Singhal [8], and Tomlins et al. [6]. The fuel used in the SOFC tested by Hirano et al. [55] had components of H_2, H_2O, CO and CO_2; therefore, there was water-shift reaction of the carbon monoxide as well as the electrochemical reaction in the fuel cell. The fuel used by the other researchers [6,8,72] had components of H_2 and H_2O, in which case there is no chemical reaction except the electrochemical reaction in the fuel channel. The dimensions of the three different SOFCs tested in their studies are summarized in Table 3, along with the mesh size adopted in our numerical computation. Table 4 lists the species' mole fractions and temperatures in those tests, which are also used as prescribed conditions for the numerical computation. In the experimental work by Singhal [8], a test of the effect of pressure was also conducted by varying the fuel and air pressure from 1 to 15 atm. The experimental data for these SOFCs in different dimensions and operating conditions can serve as a benchmark for validation of the numerical modeling work.

Figure 10 shows the comparison among the calculated and experimentally obtained cell terminal voltages under different cell current densities. The relative deviation of the modeling-predicted data from the experimental data is less than 1.0% for the SOFC tested by Hirano et al. [55], 5.6% for that by Hagiwara et al. [72], or 6.0% for that by Tomlins et al. [6]. Figure 11 shows the effects of pressure on SOFC performance comparatively among the computational and measured results for current density 300 mA/cm^2. While the general trend that cell voltage and power increase with rising operating pressure is evident, our numerical results agree favorably with the experimental data by Singhal [8], with a maximum 7.4% deviation at a low operating pressure. When the operating pressure is raised from 1 to 5 atm, the cell output power shows a 9% improvement. However, further raising the operating pressure becomes less effective, as the gain of cell output power reduces to an increase of only 6% when the operating pressure increases from 5 to 15 atm. This is due to the fact that operating pressure contributes to the cell voltage output in a logarithmic manner. Overall, when the operating pressure increases from 1 to 15 atm, the cell output power can have a gain of nearly 16%.

Because the measurement of temperature in an SOFC could be difficult, only three experimental data points, the temperatures at the two ends and near the mid-point of a cell tube, were available from the work by Hirano et al. [55]. Figure 12 shows the simulated cell temperature distribution in comparison with the data of Hirano et al. [55]. The agreement of the simulated results and the experimental data is reasonably good near the mid-point of the cell where the hotspot is located, but a relatively larger deviation between the predicted and experimental values appears at the two ends of the cell.

Table 4 Species' mole fractions, utilization percentages, and temperatures

	Air O_2 %–U_{O_2} / N_2 %/T(°C)	Fuel H_2 %–U_{H_2} /H_2O%/CH_4 %/CO%/CO_2% /T(°C)
I	21.00-17.00/79.00/600.0	98.64-85.00/1.36 /0/ 0 / 0 / 900.0
II	*21.00-25.00/79.00/600.0	55.70-80.00/27.70/0/10.80/5.80/800.0
	**21.00-25.00/79.00/400.0	55.70-80.00/27.70/0/10.80/5.80/800.0
III	21.00-17.00/79.00/600.0	98.64-85.00/1.36 /0/ 0 / 0 / 800.0

*Current density= 185 mA/cm^2; ** Current density= 370 mA/cm^2.
I- Tested by Hagiwara et al. [72]
II- Tested by Hirano et al. [55]
III- Tested by Singhal [8] and Tomlins et al. [6]

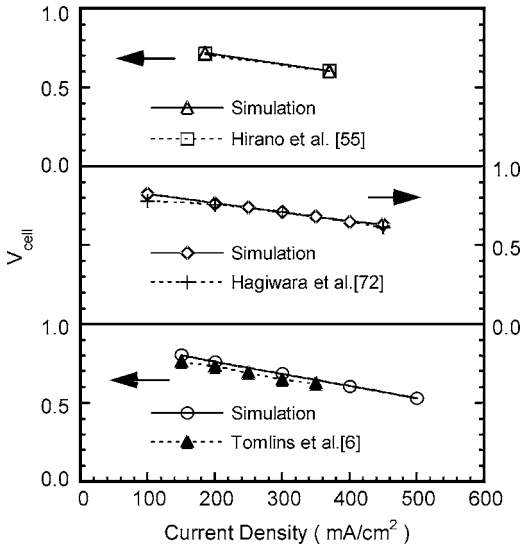

Fig. 10 Results of prediction and test for cell voltage versus current density. (Operating pressures of the cells tested by Hagiwara et al. [72] and Hirano et al. [55] are 1.0 atm, and that by Tomlins et al. [6] is 5 atm.)

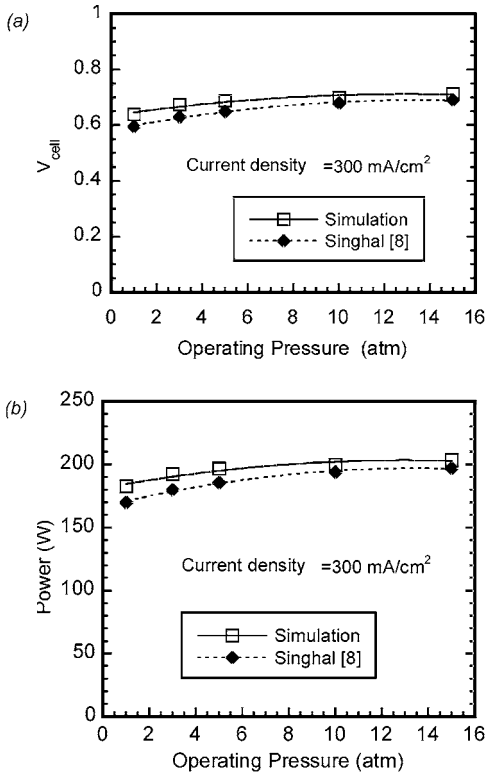

Fig. 11 Effect of operating pressure on the cell voltage and power: (*a*) cell voltage and (*b*) cell power

6.2 Effects of Diameter of Tubular SOFC. It is understandable that a larger tube diameter leads to a longer pathway for the electrons or current to travel toward the current collector in a tubular SOFC. Table 5 gives the diameters of three different SOFCs that were numerically simulated. In this simulation, the species in the fuel flow were hydrogen (98.64% in mole fraction) and water vapor, and there were no internal reforming and shift reactions. The fuel flow rate was based on a hydrogen utilization percentage of 85% and an oxygen (in mole fraction of 21% in air) utilization percentage of 17% at an average cell current density of 600 mA/cm^2. This is intended to simulate the situation that occurs when the flow rates of fuel and air are constant, in which case the SOFC can be controlled to have a decreased cell voltage at an increased current or vice versa. The actual percentages of hydrogen and oxygen utilization, shown in Fig. 13, are predicted in the simulation according to the different cell voltages and current densities.

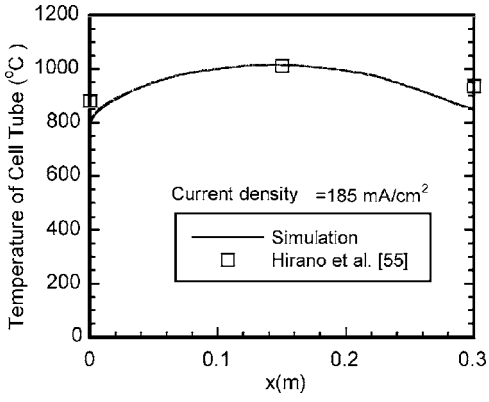

Fig. 12 Longitudinal temperature distribution in a fuel cell

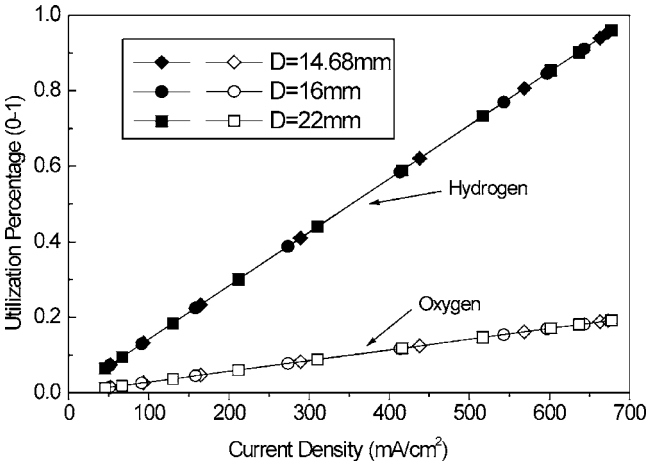

Fig. 13 Utilization percentages of species versus current density for SOFCs of different diameters ($p_{air}=p_f=1.013\times10^5$ Pa; $T_f=900°C$; $T_{air}=600°C$; flow rates are set constant at an average current density of 600 mA/cm^2; U_{H_2} of 85% and U_{O_2} of 17% for each SOFC)

Figure 14 shows the curves of cell voltage and output power varying with the actual current density for the three SOFCs of different diameters but with the same length. The SOFC with a smaller diameter has a higher cell voltage under the same current density. As suggested earlier, this is attributable to the shorter circumferential current pathway in the electrodes when the cell diameter is small. The activation polarization and concentration polarization appears to be less dependent on the cell tube diameter. The maximum electrical power drawn from the cell is also exhibited in the figure. Because of its high cell voltage, the maximum electrical power occurs at a higher current density for the SOFC with smallest diameter. Although the SOFC of larger diameter appears to produce higher electrical power, due to greater reaction area, the one with a smaller diameter, in fact, gives higher specific electrical power (W/m^3).

Figure 15 shows the average, maximum, and minimum cell tube temperatures as functions of current density for the three SOFCs of different diameters. These representative temperatures apparently are rather insensitive to the variation of tube diameter. An increase in tube diameter extends the pathway length of current collection, and ohmic heating rises accordingly. On the other

Table 5 Dimensions of the three SOFCs in different diameters

Data sequence: Outer diameter (mm) / Thickness (mm) / Length (mm)			
	D14	D16	D22
Air-inducing tube	6.00 /1.00/485	7.00 /1.00 /485	12.00/1.00/485
Support tube	-	-	-
Cathode	14.40/2.2 /500	15.72/2.20/500	21.72/2.20/500
Electrolyte	14.48/0.04/500	15.80/0.04/500	21.80/0.04/500
Anode	14.68/0.10/500	16.00/0.10/500	22.00/0.10/500
Fuel boundary	16.61/ - /500	18.10/ - /500	24.87/ - /500
Grid number (*r*x*x*)	66x602	66x602	66x602

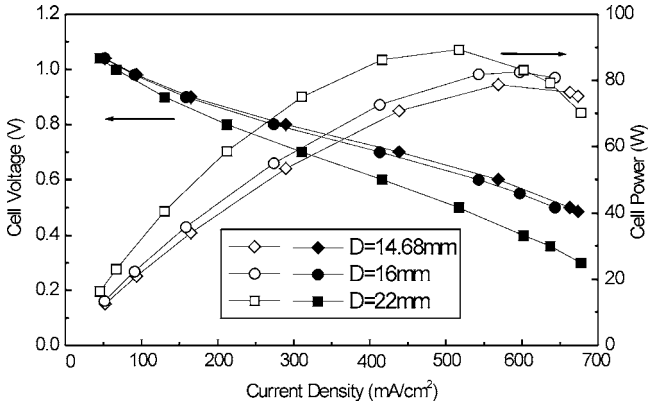

Fig. 14 Cell voltage and power versus current density for SOFCs of different diameters ($p_{air}=p_f=1.013\times10^5$ Pa; $T_f=900°C$; $T_{air}=600°C$; flow rates are set constant at an average current density of 600 mA/cm^2, U_{H_2} of 85% and U_{O_2} of 17% for each SOFC)

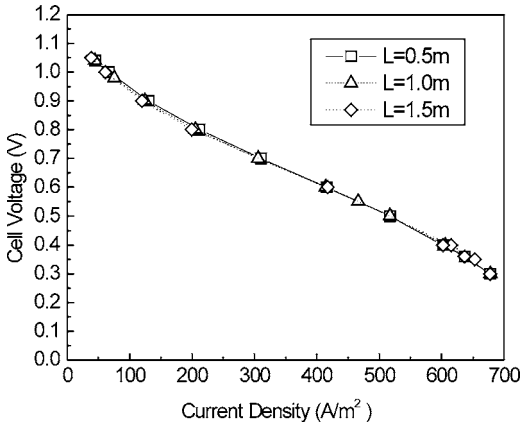

Fig. 16 Cell voltage versus current density at different lengths of the cell tube ($p_{air}=p_f=1.013\times10^5$ Pa; $T_f=900°C$; $T_{air}=600°C$; flow rates are set constant at an average current density of 600 mA/cm^2; U_{H_2} of 85% and U_{O_2} of 17% for each SOFC)

hand, the flow rates of fuel and air, which are responsible for the convective heat transfer in the cell, also increase with the tube diameter. As a result of these two competing effects, the tube diameter posts little influence on the SOFC's temperature characteristics. This supports the judgment that the differences in electrical output are caused primarily by the change in circumferential pathway length for current collection.

Also revealed in Fig. 15 is the difference between the maximum and minimum temperatures for a given cell tube. A large difference is an indication of the high nonuniformity of the temperature distribution over a tubular SOFC. At low current densities the average temperature is closer to the lowest temperature, while at higher current densities the average temperature is closer to the highest temperature. The increase in average temperature is an indication that there is more heat generated in the fuel cell. Near the mid-range of current densities, say around 400 mA/cm^2, the average, maximum, and minimum temperatures are fairly close, implying a more uniform temperature distribution. Such information is useful for better control of the temperature fields and thermal stresses in SOFCs.

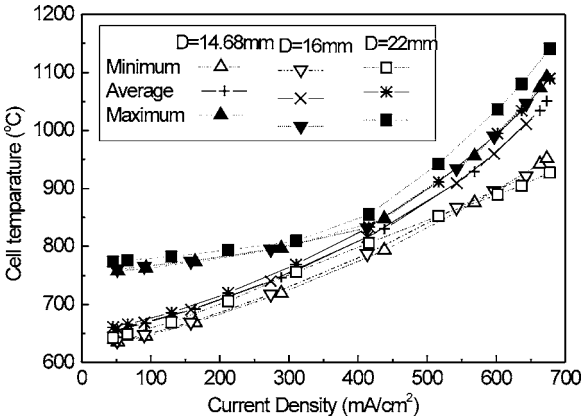

Fig. 15 Variation of cell temperature with current density for SOFCs of different diameters ($p_{air}=p_f=1.013\times10^5$ Pa; $T_f=900°C$; $T_{air}=600°C$; flow rates are set constant at an average current density of 600 mA/cm^2; U_{H_2} of 85% and U_{O_2} of 17% for each SOFC)

6.3 Effects of Length of Tubular SOFC. Figure 16 shows the relation of cell voltage versus current density for tubular SOFCs with the same diameter but different tube lengths as given in Table 6. It is evident that the cell length has virtually no effect on the voltage-current density relation in the situation whereby fuel and air are fed proportionally with the tube length. This is in a sharp contrast to the corresponding effects by diameter, as evidenced in Fig. 14. A plausible explanation is that unlike diameter, tube length is by no means along the principal pathway of current collection. On the other hand, the representative temperatures, i.e., the maximum, minimum, and average temperatures over a cell tube, as shown in Fig. 17, are more sensitive to tube length than the diameter. The effect is particularly evident for the longest case, $L=1.5$ m, whereas the other two cases, $L=0.5$ m and $L=1.0$ m, exhibit less difference.

Further examining Fig. 17 reveals that, at low current densities, the average temperature of the fuel cell is closer to the lowest temperature, which reflects an overall low level of cell temperature. At high current densities, the average temperature of the fuel cell is closer to the maximum temperature, which implies an overall high level of cell temperature. Meanwhile, the difference between the maximum and minimum temperatures is relatively higher for the longer cell, suggesting the deteriorated uniformity of cell temperature. For low current density cases, the temperature uniformity for the shorter cells is worse, because a relatively larger difference between the maximum temperature and mini-

Table 6 Dimensions of the three SOFCs in different length

Data sequence: Outer diameter (mm) / Thickness (mm) / Length (mm)			
	L-0.5	L-1.0	L-1.5
Air-inducing tube	12.00/1.00 /485	12.00/1.00/970	12.00/1.00/1450
Support tube	-	-	-
Cathode	21.72/2.20/500	21.72/2.20/1000	21.72/2.20/1500
Electrolyte	21.80/0.04/500	21.80/0.04/1000	21.80/0.04/1500
Anode	22.00/0.10/500	22.00/0.10/1000	22.00/0.10/1500
Fuel boundary	24.87/ - /500	24.87/ - /1000	24.87/ - /1500
Grid number (rxx)	66x602	66x1202	66x1602

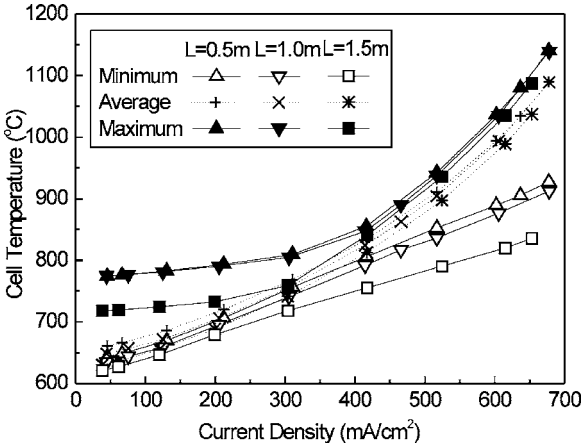

Fig. 17 Cell temperature versus current density at different lengths of the cell tube ($p_{air}=p_f=1.013\times10^5$ Pa; $T_f=900°C$; $T_{air}=600°C$; flow rates are set constant at an average current density of 600 mA/cm^2; U_{H_2} of 85% and U_{O_2} of 17% for each SOFC)

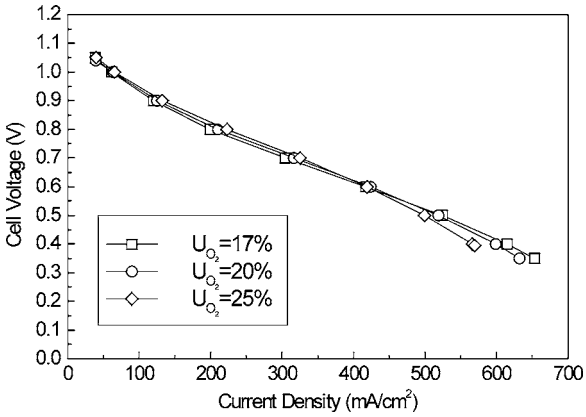

Fig. 19 Cell voltage versus current density at different oxygen stoichiometries (the cell in Table 6 with a length of 1500 mm; $p_{air}=p_f=1.013\times10^5$ Pa; $T_f=900°C$; $T_{air}=600°C$; flow rates are set constant at an average current density of 600 mA/cm^2; U_{H_2} of 85% and U_{O_2} of interest)

mum temperature exists. Similar to the finding shown in Fig. 15 concerning the diameter effects, all cells exhibit the best temperature uniformity in the mid-range of current density, about 300–500 mA/cm^2.

The longitudinal temperature distribution, as a function of cell voltage, for the longest cell, $L=1.5$ m, is shown in Fig. 18. This simulates the situation that occurs when the flow rates of fuel and air are constant, in which case the variation of the cell voltage, as well as the current density, results in varying cell temperatures. At a high cell voltage, the cell current density is low, so the heat released in the cell tube is relatively low. The heat transfer in fuel cell in this situation is closer to a co-flow heat transfer between the high temperature fuel and the low temperature air streams. When the cell voltage decreases, the current density of the fuel cell increases, and the heat generation in the fuel cell also increases, raising the temperature of the fuel cell. To eliminate excessive heating in the cell tube, the cell voltage should be kept above 0.35 V in the present situation.

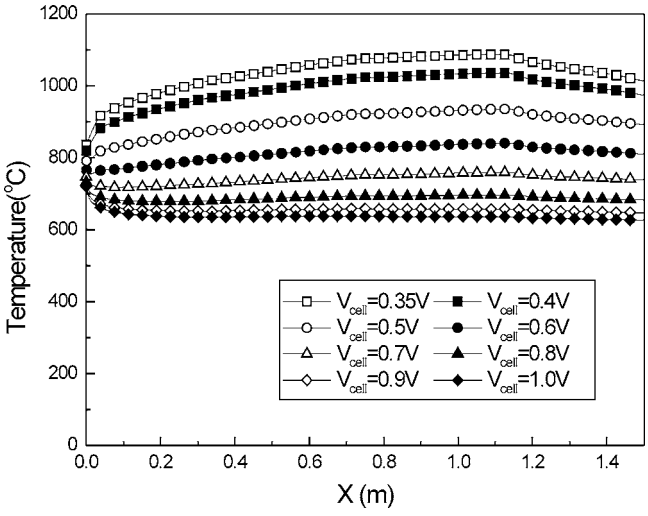

Fig. 18 Cell tube temperature distribution with variation of cell voltage (the cell in Table 6 with a length of 1500 mm; $p_{air}=p_f=1.013\times10^5$ Pa; $T_f=900°C$; $T_{air}=600°C$; flow rates are set constant at an average current density of 600 mA/cm^2; U_{H_2} of 85% and U_{O_2} of 17%)

6.4 Effects of Stoichiometries of Oxygen in Tubular SOFC. To determine the feeding flow rate of the fuel for a desired level of current density, the acceptable fuel utilization percentage is generally around 80%–85%. This is also confirmed in the present study that, as shown in Figs. 13 and 14, the maximum output power prevails at fuel utilization percentages ranging from 80% to 85%. The variation of the air flow rate could influence the average oxygen concentration and affects the fuel cell temperature significantly. Note that air stream fed into an SOFC essentially is the convective coolant for the system. Figure 19 shows the results of cell voltage versus current density for the longest fuel cell given in Table 6. The flow rate of fuel is based on a hydrogen utilization percentage (U_{H2}) of 85%, and that of air is based on an oxygen utilization percentage (U_{O2}) ranging from 17% to 25% at an average cell current density of 600 mA/cm^2. At a high current density, the cell voltage is slightly higher for the case with $U_{O2}=17\%$, corresponding to a higher air flow rate than that of 20% and 25% utilization of oxygen. This agrees with the general notion that the concentration polarization is significant when the current density is high. When the current density is low, the high flow rate of air makes the cell temperature relatively lower than that of the cases with low air flow rates. Hence, the ionic conductivity of the electrolyte will be slightly reduced, which, in turn, lowers the cell voltage output.

Figure 20 shows the maximum, minimum, and average cell tube temperatures for different oxygen utilization percentages. As expected, the different magnitude of air flow rate resulting from a change of U_{O2} can have substantial influence on the temperature characteristics of an SOFC. In the cases with low air flow rates, the cell temperature may be very high, especially when the current density level is high. In general, hotspots in a cell tube should be kept below 1050°C for better operation and durability control. More parametric studies based on the models presently discussed are available in the authors' other works [36,48,63].

6.5 Species Concentrations in Fuel and Air Flows for Tubular SOFCs. The streamwise distributed flow rates and concentration of participating gas species are strongly dependent on the nature of chemical and electrochemical reactions taking place in the cell. Figure 21 shows the simulated streamwise variations of flow rates for hydrogen, oxygen, and water in a tubular SOFC, for which Singhal [8] and Tomlins [6] have done experimental studies. Tables 3 and 4 give the cell tube dimensions and conditions, while the current density was maintained at 300 mA/cm^2 for all the cases. The result shows a rapid reduction of hydrogen and

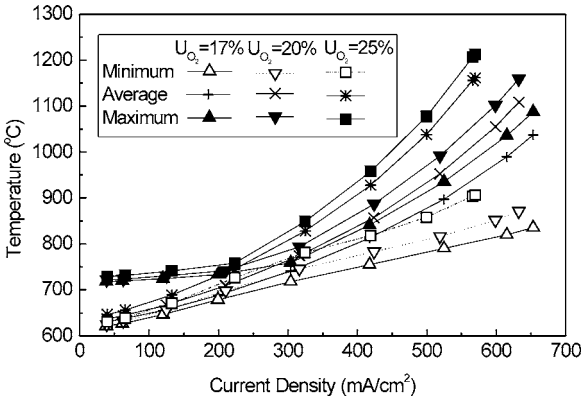

Fig. 20 Variation of cell temperature with current density at different oxygen stoichiometries (the cell in Table 6 with a length of 1500 mm; $p_{air}=p_f=1.013\times10^5$ Pa; $T_f=900°C$; $T_{air}=600°C$; flow rates are set constant at an average current density of 600 mA/cm^2; U_{H_2} of 85% and U_{O_2} of interest)

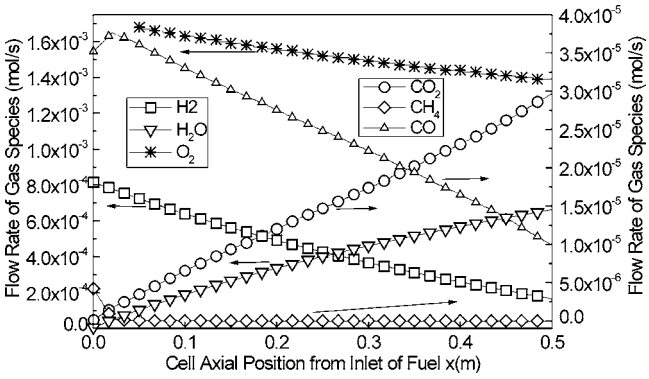

Fig. 22 Variation of flow rate in a tubular SOFC with reforming (the cell and operating conditions in Table 9; current density =450 mA/cm^2)

increase of water in mole flow rates immediately downstream of the inlet region. This reflects that strong electrochemical reaction occurred and high local current density resulted in this region.

When internal reforming and shift reactions are involved, the variation of hydrogen is collectively determined by its consumption by the electrochemical reaction and generation by the reforming and water-shift reactions. Figure 22 shows the streamwise variation of gas species in a tubular SOFC with reforming and shift reactions. The dimensions and operating conditions of this SOFC are given in Table 7. Since hydrogen is consumed continuously throughout the entire fuel channel, the hydrogen mole fraction decreasing along the fuel stream is evidently seen in Fig. 22. Water vapor, as a product of the hydrogen consumption and also a consumed reactant for both the reforming and water-shift reactions, induces a somewhat modest increase in mole fraction along the fuel stream. The water-shift of CO proceeds rather gradually in the fuel steam. Collectively, the mole fraction of CO decreases and that of CO_2 increases. Due mainly to the fast kinetics of the reforming reaction proceeding with high temperature, the CH_4 is readily consumed in the inlet region.

Figure 23 shows the local distributions of gas species' mass fractions for the above discussed tubular SOFC. The contours representing oxygen concentration in the air channel are in a parabolic shape, which reflects a significant concentration gradient existing between the bulk airflow and the air/cathode interface. The contours of species' concentrations in the fuel path are relatively flat from the anode surface to the bulk flow. This is an indication that the mass diffusion of hydrogen in the fuel channel is more effective than that of oxygen in the airflow.

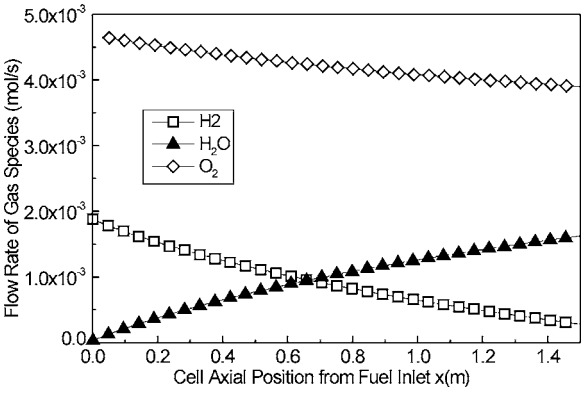

Fig. 21 Variation of flow rate in a tubular SOFC without reforming (the cell in Table 6 with a length of 1500 mm; $p_{air}=p_f=1.013\times10^5$ Pa; $T_f=800°C$; $T_{air}=600°C$; current density of 300 mA/cm^2; U_{H_2} of 85% and U_{O_2} of 17%)

6.6 Solid Oxide Fuel Cells in Planar Structure. Electrical outputs and transport phenomena in planar SOFCs have also been numerically simulated based on the same modeling approach as that for tubular SOFCs. The discretized governing equations are in three-dimensional, rectangular-coordinate formulation. One of the key objectives of this effort is to compare the performance and transport characteristics between the anode-supported and electrolyte-supported planar SOFCs. Dimensions for both cells are listed in Table 8 and the operating conditions are given in Table 9. While these two SOFCs are of distinctly different layer thicknesses, their designs are primarily driven by structural concerns and thermo-mechanical compatibility among participating layers. To illustrate the modeling of internal reforming, a small proportion of CH_4 is part of the fuel inflow supplied through the fuel channels.

Figure 24 shows the cell voltage and power versus the cell current density for the two types of planar SOFCs studied. Very evident is the anode-supported cell having a much higher output voltage than the electrolyte-supported cell. This observation agrees favorably with the experimental findings discussed earlier in Sec. 4. The ion conduction resistance in the thick electrolyte layer in the electrolyte-supported SOFC apparently dominates the polarization and loss in the cell. Therefore, the electrolyte-supported planar-type SOFC is an unfavorable structure from the standpoint of cell power output compared to the anode-supported SOFC at the same current density.

For the planar-type SOFC discussed above, the hydrogen and

Table 7 Dimensions and operating condition of a tubular SOFC with internal reforming

Data sequence: Outer diameter (mm)/Thickness (mm)/Length (mm)	
Air-inducing tube	9.00 /0.5/450
Support tube	16.80/1.50/500
Cathode	18.80/1.00/500
Electrolyte	18.90/0.05/500
Anode	19.20/0.15/500
Fuel boundary	29.20/ - /500
Grid number (rxx)	66x602
Fuel (1.013×10^5 Pa, U_{H_2}=85%, T_f=900 °C)	
Mole fractions of H_2, H_2O, CO_2, CO, and CH_4 are: 0.949, 0.0049, 0.0001, 0.041, 0.005	
Air (1.013×10^5 Pa, U_{O_2}=20%, T_{air}=800 °C)	
Mole fractions of O_2, and N_2 are: 0.21, 0.79	

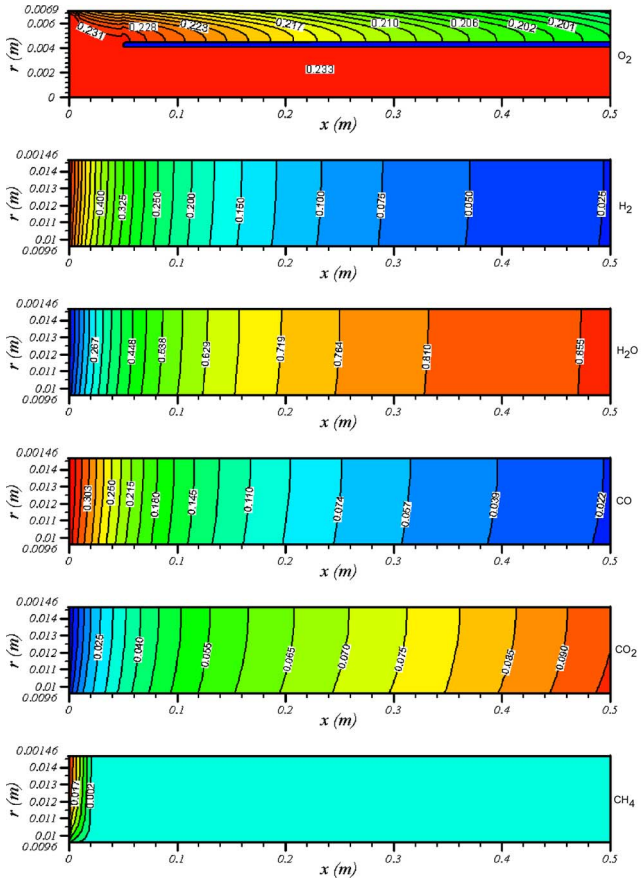

Fig. 23 Local mass fraction distributions of gases in a tubular SOFC with internal reforming (the cell and operating conditions in Table 9; current density=450 mA/cm^2)

oxygen mass fraction contours on the *x-y* plane at the mid-height of the supply channels for both fuel and air are shown in Fig. 25. Note that the fuel channels and the air channels are aligned orthogonally and overall in a cross-flow type of arrangement, as shown earlier in Fig. 4. The hydrogen diffusion is strong in the fuel stream, so the contour shape is rather flat. Meanwhile, the

Table 8 Dimensions of a planar single cell unit

Full size (L×W×H)	100×100×5.80 mm	
Channel width	7.804 mm	
Top and bottom plate thickness	0.59 mm	
Wall thickness	1.18 mm	
	Anode-supported	**Electrolyte-supported**
Anode	700 μm	37 μm
Electrolyte	10 μm	165 μm
Cathode	50 μm	28 μm
Channel height	1.57 mm	1.83 mm

Table 9 Inlet species and mole fractions for planar SOFC

Fuel (1.013×10^5 Pa, U_{H_2}=85%,)			
H_2 :	0.949	H_2O :	0.0049
CO_2 :	0.0001	CO :	0.041
CH_4 :	0.005		
T_f=900 °C for anode-supported SOFC			
T_f=1000 °C for electrolyte-supported SOFC			
Air (1.013×10^5 Pa, U_{O_2}=20%)			
O_2 :	0.21	N_2 :	0.79
T_{air}=800 °C			

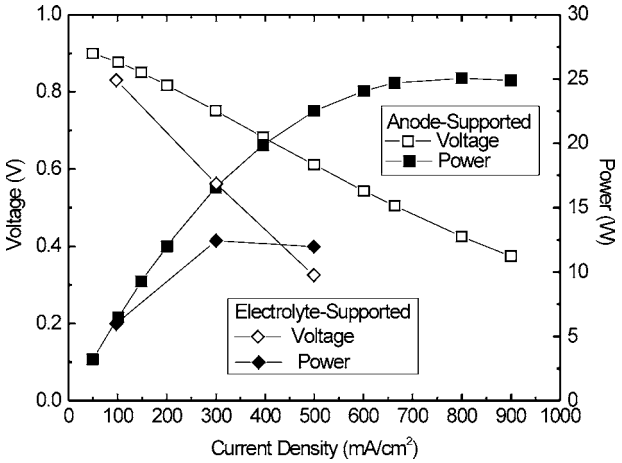

Fig. 24 Voltage and power of a planar type SOFC (with dimensions and operating conditions given in Tables 7 and 8; flow rate of fuel and air vary with the current density at U_{H_2} of 85% and U_{O_2} of 20%)

mass fraction of hydrogen decreases along the fuel flow direction. However, the variation, in terms of hydrogen concentration, from one fuel channel to another is rather insignificant. This is due mainly to the fact that hydrogen depletion is rather strong in the region near the fuel inlet. On the other hand, the oxygen mass fraction contour shows significant variation among the air supply channels. In the air channels near the fuel inlet region, more oxygen is consumed, and thus the contours display a more significant mass fraction difference of oxygen from the air inlet to the outlet.

7 Concluding Remarks

Solid oxide fuel cells and their hybrids have been emerging as one of the key components for future clean energy generation. However, to mature the SOFC technology, it requires substantial advances in developing much more reliable and cost-effective manufacturing processes [84]. High-temperature gas sealing has long been a challenging issue for planar SOFCs. On the other hand, developments of highly efficient SOFCs operated in a relatively lower temperature range, say around 600–800°C, has emerged as one the major research thrusts in the SOFC community.

For SOFC's performance evaluation or design improvements, direct measurements under a high-temperature environment are difficult, and thus numerical simulation embedded with proper physical models is a viable resolution. An intention to demonstrate this notion is one of the main scopes of this article. Summarized below are significant findings drawn from the present simulation efforts.

1. Assumption of chemical equilibrium for the methane reforming and water-shift reactions in an internal reforming SOFC significantly simplifies the solution of the coupled variation of gas species. With this assumption, it is unnecessary to account for the possible electrochemical oxidation of CO, instead of H_2, because CO is readily substituted for hydrogen by the shift reaction at chemical equilibrium. However, this assumption may be invalid for intermediate- and low-temperature SOFCs,
2. To facilitate a simulation for a fuel cell terminal performance, one of the two procedures may be adopted, i.e., either the cell voltage or cell current/current density is prescribed. The computational time, however, is significantly longer for the latter approach.
3. The circumferential current collection pathway, depending on the cell tube diameter, can significantly affect the cell

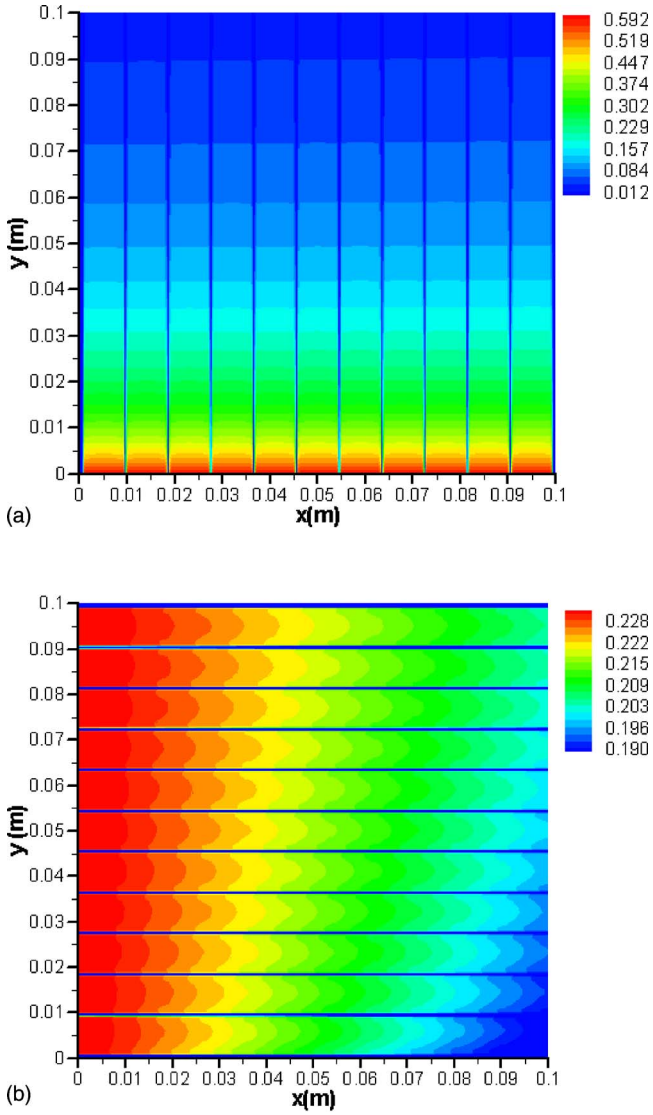

Fig. 25 Local mass fraction distributions of gases in a planar SOFC with internal reforming: (*a*) Hydrogen and (*b*) Oxygen (with dimensions and operating conditions given in Tables 7 and 8; current density=600 mA/cm^2)

voltage output and the power density. For a given current density, the cell terminal output voltage increases with a decrease in tube diameter.

4. The local temperature distribution in a tubular SOFC varies significantly with the operating conditions. However, there exist optimal operating conditions in current density where the cell temperature is quite uniformly distributed. This implies that SOFCs may be optimally designed and operated for enhanced current carrying capacity with reduced thermal stresses in the system.
5. The endothermic reforming reaction in an internal reforming SOFC proceeds very rapidly and may only take place in the fuel inlet region. This could result in excessive heat absorption at the fuel inlet and induce higher thermal stress. More studies in control of thermal and species transport for various reaction processes in SOFCs are recommended.
6. Planar SOFC promises higher power density output than its tubular counterpart, because of shorter current collection pathway. However, a comparative study between an electrolyte-supported and an anode-supported planar SOFC suggests that an electrolyte presents the greatest electron/ion resistance in the cell and its thickness must be minimized for enhanced power output.

Nomenclature

A = area, m^2
A_{cell} = surface area of electrolyte layer, m^2
A_{air}, A_{fuel} = inlet flow area of air and fuel, respectively, m^2
Cp = specific heat capacity at constant pressure, J/(kg K)
$D_{J,m}$ = diffusion coefficient of jth species into the left gases in a mixture, m^2/s
E = electromotive force or electric potential, V
F = Faraday's constant, 96486.7 C/mol
g = Gibbs free energy, J/mol
h = enthalpy, kJ/kmol or J/mol
H = height, m
i = current density, A/m^2
i_0 = exchange current density, A/m^2
I = current, A
k = thermal conductivity, W/m K
K_{PR}, K_{PS} = chemical equilibrium constant for reforming and shift reactions, respectively
L = length, m
m = mass transfer rate or mass consumption/production rate, mol/s
$\dot{m}$ = mass flux, mol/(m^2 s)
n_e = number of electrons transferred per electrochemical reaction
M_f = total mole flow rate of fuel, mol/s
p, P = pressure (Pa) or position
$\dot{q}$ = volumetric heat source, W/m^3
Q = heat, W
r = radial coordinate, m
r^a, r^c, r^e = average radius of anode, cathode, and electrolyte layers of a tubular SOFC, m
R = universal gas constant, 8.31434 J/(mol K)
R_{st} = reaction rate of CH_4 in steam reforming, mol/(cm^3·s)
R^a, R^c, R^e = discretized resistance in anode, cathode, and electrolyte, Ω
S^a, S^c = interface conductivity for anode/electrolyte and cathode/electrolyte, (1/(Ω·m^2)
T = temperature, K
u = velocity in axial direction, m/s
U = utilization percentage, 0-1
v = velocity in r or y direction, m/s
V_{cell} = cell terminal voltage, V
V^a, V^c = potentials in anode and cathode, respectively, V
w = coordinate, m
W = width, m
W_{cat} = catalyst loading density, g/cm^3
x = axial coordinate, m
$\overline{x}$, $\overline{y}$, $\overline{z}$ = reacted mole rate of CH_4, CO, and H_2, respectively, in a section of interest in flow channel, mol/s
y = coordinate, m
Y = mass fraction
z = coordinate, m

Greek Symbols

θ, $\Delta\theta$ = circumferential position, angle
δ = thickness of electrodes and electrolyte layers, m
ΔG = Gibbs free energy change of a chemical reaction, J/mol

ΔG^0 = standard state Gibbs free energy change of a chemical reaction, J/mol
ΔH = enthalpy change of a chemical reaction, J/mol
ΔS = entropy production, J/(mol K)
ΔV = volume, cm^3
Δx = one axial section of flow channel centered at x position, m
λ = thermal conductivity, $W/(m\,^\circ C)$
μ = dynamic viscosity, Pa s
ρ = density, $kg\,m^{-3}$
ρ_e^a, ρ_e^c = electronic resistivity of anode and cathode, respectively, $\Omega \cdot cm$
ρ_e^e = ionic resistivity of electrolyte, $\Omega \cdot cm$
η_{Act} = activation polarization, V
η_{Carnot}, η_{FC} = energy conversion efficiencies by heat engines and fuel cells, respectively

Subscripts

a = anode
c = cathode
$cell$ = overall parameter of fuel cell
e,w,n,s = east, west, north, and south interfaces between grid P and it neighboring grids
E,W,N,S = east, west, north, and south neighboring grids of grid P
f = fuel
J = gas species
P = variables at grid P
R = electrochemical reaction
x,y,z = axial position

Superscripts

a = anode
c = cathode
e = electrolyte
in = inlet of a section of channel of interest
out = outlet of a section of channel of interest
P = variables at grid P
R = reaction
u,v,w = variable related to velocities of U, V, W

References

[1] Carrette, L., Friedrich, K. A., and Stimming, U., 2001, "Fuel Cells—Fundamentals and Applications," Fuel Cells, **1**(1), pp. 5–39.
[2] Laughton, M. A., 2002, "Fuel Cells," Eng. Sci. Educ. J., **11**, No. 1, pp. 7–16.
[3] Srinivasan, S., Mosdale, R., Stevens, P., and Yang, C., 1999, "Fuel Cells: Reaching the Era of Clear and Efficient Power Generation in the Twenty-First Century," Annu. Rev. Energy Environment, **24**, pp. 281–328.
[4] Ellis, M. W., Von Spakovsky, M. R., and Nelson, D. J., 2001, "Fuel Cell Systems: Efficient, Flexible Energy Conversion for the 21st Century," Proc. IEEE, **89**(12), pp. 1808–1818.
[5] Gardner, F. J., 1997, "Thermodynamic Processes in Solid Oxide and Other Fuel Cells," Proc. Inst. Mech. Eng., Part A, **211**, pp. 367–380.
[6] Tomlins, G. W., and Jaszcar, M. P., 1999, "Elevated Pressure Testing of the Simens Westinghouse Tubular Solid Oxide Fuel Cell," *Proceedings of the Third International Fuel Cell Conference*, Nagoya, Japan, 369–372.
[7] Palsson, J., Selimovic, A., and Sjunnesson, L., 2000, "Combined Solid Oxide Fuel Cell and Gas Turbine Systems for Efficient Power and Heat Generation," J. Power Sources, **86**, pp. 442–448.
[8] Singhal, S. C., 2000, "Advances in Solid Oxide Fuel Cell Technology," Solid State Ionics, **135**, pp. 305–313.
[9] Suzuki, K., Iwai, H., Kim, J. H., Li, P. W., and Teshima, K., 2003, "Solid Oxide Fuel Cell and Micro Gas Turbine Hybrid Cycle and Related Fluid Flow and Heat Transfer," *The 12th International Heat Transfer Conference*, Grenoble, August 18–23, Vol. 1, pp. 403–414.
[10] Kuchonthara, P., Bhattacharya, S., and Tsutsumi, A., 2003, "Combination of Solid Oxide Fuel Cells and Several Enhanced Gas Turbine Cycles," J. Power Sources, **124**, pp. 65–75.
[11] Harvey, S. P., and Richter, H. J., 1994, "Gas Turbine Cycles With Solid Oxide Fuel Cells, Part I: Improved Gas Turbine Power Plant Efficiency by Use of Recycled Exhaust Gases and Fuel Cell Technology," ASME J. Energy Resour. Technol., **116**, pp. 305–311.
[12] Bevc, F., 1997, "Advances in Solid Oxide Fuel Cells and Integrated Power Plants," Proc. Inst. Mech. Eng., Part A, **211**, pp. 359–366.
[13] Singhal, S. C., 2002, "Solid Oxide Fuel Cells for Stationary, Mobile, and Military Applications," Solid State Ionics, **152–153**, pp. 405–410.
[14] Wojcik, A., Middleton, H., Damopoulos, I., and Herle, J. V., 2003, "Ammonia as a Fuel in Solid Oxide Fuel Cells," J. Power Sources, **118**, pp. 342–348.
[15] Cengel, Y. A., and Boles, M. A., 1994, *Thermodynamics: An Engineering Approach*, 2nd Ed., McGraw-Hill, New York, pp. 762–763.
[16] Wark, K., 1971, *Thermodynamics*, 2nd Edition, McGraw-Hill Book Company, New York, pp. 536–561.
[17] Wood, R. E., 1970, *Introduction to Chemical Thermodynamics*, Meredith Corporation, New York.
[18] Perry, R. H., and Green, D. W., 1986, *Perry's Chemical Engineer's Handbook*, 7th Ed. McGraw-Hill, New York.
[19] Li, P. W., and Chyu, M. K., 2005, "Multiple Processes in Solid Oxide Fuel Cells," in *Transport Phenomena in Fuel Cells*, edited by B. Sunden and M. Fahgri, WIT Press, Southampton, UK.
[20] Douvartzides, S. L., Coutelieris, F. A., Demin, A. K., and Tsiakaras, P. E., 2003, "Fuel Options for Solid Oxide Fuel Cells: A Thermodynamic Analysis," AIChE J., **49**(1), pp. 248–257.
[21] Chopey, N. P., and Hicks, T. G., 1984, *Handbook of Chemical Engineering Calculations*, McGraw Hill Book Co., New York.
[22] Chase, Jr., M. W., Davies, C. A., Downey, Jr., J. R., Frurip, D. J., McDonald, R. A., and Syverud, A. N., 1986, *JANAF Thermochemical Tables*, 3rd Edition, American Institute of Physics for the National Bureau of Standards, New York.
[23] Gopalan, S., and DiGiuseppe, G., 2004, "Fuel Sensitivity Test in Tubular Solid Oxide Fuel Cells," J. Power Sources, **125**, pp. 183–188.
[24] Coutelieris, F. A., Douvartzides, S., and Tsiakaras, P., 2003, "The Importance of the Fuel Choice on the Efficiency of a Solid Oxide Fuel Cell System," J. Power Sources, **123**, pp. 200–205.
[25] Brown, J. T., 1988, "Solid Oxide Fuel Cell Technology," IEEE Trans. Energy Convers., **3**(2), pp. 193–198.
[26] Dicks, A. L., 1998, "Advances in Catalysts for Internal Reforming in High Temperature Fuel Cells," J. Power Sources, **71**, pp. 111–122.
[27] Peters, R., Dahl, R., Kluttgen, U., Palm, C., and Stolten, D., 2002, "Internal Reforming of Methane in Solid Oxide Fuel Cell Systems," J. Power Sources, **106**, pp. 238–244.
[28] Finnerty, C. M., and Ormerod, R. M., 2000, "Internal Reforming Over Nickel/Zirconia Anodes in SOFCS Operating on Methane: Influence of Anode Formulation, Pre-Treatment And Operating Conditions," J. Power Sources, **86**, pp. 390–394.
[29] Finnerty, C., Tompsett, G. A., Kendall, K., and Ormerod, R. M., 2002, "SOFC System With Integrated Catalytic Fuel Processing," J. Power Sources, **86**, pp. 459–463.
[30] Peters, R., Riensche, E., and Cremer, P., 2000, "Pre-Reforming of Natural Gas in Solid Oxide Fuel-Cell Systems," J. Power Sources, **86**, pp. 432–441.
[31] Achenbach, E., and Riensche, E., 1994, "Methane/Steam Reforming Kinetics for Solid Oxide Fuel Cells," J. Power Sources, **52**, pp. 283–288.
[32] Takeguchi, T., Kani, Y., Yano, T., Kikuchi, R., Eguchi, K., Tsujimoto, K., Ychida, Y., Ueno, A., Omoshiki, K., and Aizawa, M., 2002, "Study on Steam Reforming of CH_4 and C_2 Hydrocarbons and Carbon Deposition on Ni-YSZ cermets," J. Power Sources, **112**, pp. 588–595.
[33] Aguiar, P., Chadwick, D., and Kershenbaum, L., 2002, "Modeling of an Indirect Internal Reforming Solid Oxide Fuel Cell," Chem. Eng. Sci., **57**, pp. 1665–1677.
[34] Massardo, A. F., and Lubelli, F., 1998, "Internal Reforming Solid Oxide Fuel Cell-Gas Turbine Combined Cycles (IRSOFC-GT), Part A: Cell Model and Cycle Thermodynamic Analysis," *International Gas Turbine & Aeroengine Congress & Exhibition*, Stockholm, Sweden, No. 98-GT-577.
[35] Costamagna, P., Arato, E., Antonucci, P. L., and Antonucci, V., 1996, "Partial Oxidation of CH_4 in Solid Oxide Fuel Cells: Simulation Model of the Electrochemical Reactor and Experimental Validation," Chem. Eng. Sci., **51**(11), pp. 3013–3018.
[36] Li, P. W., Schaefer, L., and Chyu, M. K., 2004, "A Numerical Model Coupling the Heat and Gas Species' Transport Processes an a Tubular SOFC," ASME J. Heat Transfer, **126**, pp. 219–229.
[37] Onuma, S., Kaimai, A., Kawamura, K., Nigara, Y., Kawada, T., Mizusaki, J., and Tagawa, H., 2000, "Influence of the Coexisting Gases on the Electrochemical Reaction Rates Between 873 and 1173 K in a CH_4–H_2O/Pt/YSZ System," Solid State Ionics, **132**, pp. 309–331.
[38] Onuma, S., Kaimai, A., Kawamura, K., Nigara, Y., Kawada, T., Mizusaki, J., Inaba, H., and Tagawa, H., 1998, "Electrochemical Oxidation in a CH_4–H_2O System at the Interface of a Pt Electrolyte and Y_2O_2-Stabilized ZrO_2 Electrolyte—I: Determination of the Predominant Reaction Processes," J. Electrochem. Soc., **145**(3), pp. 920–925.
[39] Onuma, S., Kaimai, A., Kawamura, K., Nigara, Y., Kawada, T., Mizusaki, J., Inaba, H., and Tagawa, H., 1998, "Electrochemical Oxidation in a CH_4–H_2O System at the Interface of a Pt Electrolyte and Y_2O_2-Stabilized ZrO_2 Electrolyte—II: The Rates of Electrochemical Reactions Taking Place in Parallel," J. Electrochem. Soc., **145**(9), pp. 3117–3122.
[40] Eguchi, E., Kojo, H., Takeguchi, T., Kikichi, R., and Sasaki, K., 2002, "Fuel Flexibility in Power Generation by Solid Oxide Fuel Cells," Solid State Ionics, **152–153**, pp. 411–416.
[41] Eguchi, K., and Kikuchi, R., 2004, "Development of Solid Oxide Fuel Cells and the Component Materials," Second ASME International Conference on Fuel Cell Science, Engineering and Technology, June 14–16, Rochester, NY, edited by R. K. Shah and S. G. Kandlikar, SOFC Keynote, pp. 419–425.
[42] Zhu, B., 2004, "Advanced Ceramic Fuel cell R&D," Second ASME International Conference on Fuel Cell Science, Engineering and Technology, June

14–16, Rochester, NY, edited by R. K. Shah and S. G. Kandlikar, SOFC Keynote, pp. 409–417.
[43] Nishino, T., Iwai, H., and Suzuki, K., 2004, "Numerical Investigation of the Strategies for Reducing the Cell Temperature Gradient of an Indirect Internal Reforming Tubular SOFC," Second ASME International Conference on Fuel Cell Science, Engineering and Technology, June 14–16, Rochester, NY, edited by R. K. Shah and S. G. Kandlikar, pp. 353–360.
[44] Nagata, S., Momma, A., Kato, T., and Kasuga, Y., 2001, "Numerical Analysis of Output Characteristics of Tubular SOFC With Internal Reformer," J. Power Sources, **101**, pp. 60–71.
[45] Chan, S. H., Khor, K. A., and Xia, Z. T., 2001, "A Complete Polarization Model of a Solid Oxide Fuel Cell and its Sensitivity to the Change of Cell Component Thickness," J. Power Sources, **93**, pp. 130–140.
[46] Minh, N. Q., and Takahashi, T., 1995, *Science and Technology of Ceramic Fuel Cells*, Elsevier, New York.
[47] Iwata, M., Hikosaka, T., Morita, M., Iwanari, T., Ito, K., Onda, K., Esaki, Y., Sakaki, Y., and Nagata, S., 2000, "Performance Analysis of Planar-Type Unit SOFC Considering Current and Temperature Distributions," Solid State Ionics, **132**, pp. 297–308.
[48] Li, P. W., and Chyu, M. K., 2003, "Simulation of the Chemical/Electrochemical Reaction and Heat/Mass Transfer for a Tubular SOFC Working in a Stack," J. Power Sources, **124**, pp. 487–498.
[49] Ota, T., Koyama, M., Wen, C. J., Yamada, K., and Takahashi, H., 2003, "Object-Based Modeling of SOFC System: Dynamic Behavior of Micro-Tube SOFC," J. Power Sources, **118**, pp. 430–439.
[50] Burt, A. C., Celik, I. B., Gemmen, R. S., and Smirnov, A. V., 2004, "A Numerical Study of Cell-to-Cell Variations in a SOFC Stack," J. Power Sources, **126**, pp. 76–87.
[51] Keegan, K., Khaleel, M., Chick, L., Recknagle, K., Simner, S., and Deibler, J., 2002, "Analysis of a Planar Solid Oxide Fuel Cell Based Automotive Auxiliary Power Unit," *SAE 2002 World Congress*, Detroit, MI, No. 2002–01–0413.
[52] Srikar, V. T., Turner, K. T., Andrew Ie, T. Y., and Spearing, S. M., 2004, "Structural Design Considerations for Micromachined Solid-Oxide Fuel Cells," J. Power Sources, **125**, pp. 62–69.
[53] Bessette, N. F., 1994, "Modeling and Simulation for Solid Oxide Fuel Cell Power System," Ph.D. thesis, Georgia Institute of Technology.
[54] Ahmed, S., McPheeters, C., and Kumar, R., 1991, "Thermal-Hydraulic Model of a Monolithic Solid Oxide Fuel Cell," J. Electrochem. Soc., **138**, pp. 2712–2718.
[55] Hirano, A., Suzuki, M., and Ippommatsu, M., 1992, "Evaluation of a New Solid Oxide Fuel Cell System by Non-Isothermal Modeling," J. Electrochem. Soc., **139**(10), pp. 2744–2751.
[56] Ferguson, J. R., Fiard, J. M., and Herbin, R., 1996, "Three-Dimensional Numerical Simulation for Various Geometries of Solid Oxide Fuel Cells," J. Power Sources, **58**, pp. 109–122.
[57] Ohara, S., Mukai, K., Lee, J. H., and Fukui, T., 2004, "Effect of Aging on Conductivity of Yttria Stabilized Zirconia," J. Power Sources, **126**, pp. 23–27.
[58] Singhal, S. C., 2001, "Progress in Tubular Solid Oxide Fuel Cell Technology," Proc.-Electrochem. Soc., **99**(19), pp. 40–50.
[59] George, R. A., and Bessette, N. F., 1998, "Reducing the Manufacturing Cost of Tubular SOFC Technology," J. Power Sources, **71**, pp. 131–137.
[60] Kim, J. H., Song, R. H., Song, K. S., Hyun, S. H., Shin, D. R., and Yokokawa, H., 2003, "Fabrication and Characteristics of Anode-Supported Flat-Tube Solid Oxide Fuel Cell," J. Power Sources, **122**, pp. 138–143.
[61] Sverdrup, E. F., Warde, C. J., and Eback, R. L., 1973, "Design of High Temperature Solid-Electrolyte Fuel Cell Batteries for Maximum Power Output Per Unit Volume," Energy Convers., **13**, pp. 129–136.
[62] Li, P.-W., Schaefer, L., and Chyu, M. K., 2003, "Three-Dimensional Model for the Conjugate Processes of Heat and Gas Species Transportation in a Flat Plate Solid Oxide Fuel Cell," *14th International Symposium of Transport Phenomenon*, Bali, Indonesia, June 6–9, pp. 305–312.
[63] Li, P.-W., and Suzuki, K., 2004, "Numerical Modeling and Performance Study of a Tubular Solid Oxide Fuel Cell," J. Electrochem. Soc., **151**(4), pp. A548–A557.
[64] Bharadwaj, A., Archer, D. H., and Rubin, E. S., 2005, "Modeling the Performance of Flattened Tubular Solid Oxide Fuel Cell," ASME J. Fuel Cell Sci. Technol., **2**, pp. 52–59.
[65] Lu, Y. X., Schaefer, L., and Li, P. W., 2005, "Numerical Simulation of Heat Transfer and Fluid Flow of a Flat-Tube High Power Density Solid Oxide Fuel Cell," ASME J. Fuel Cell Sci. Technol., **2**, pp. 65–69.
[66] Bessette, N. F., and Wepfer, W. J., 1995, "A Mathematical Model of a Tubular Solid Oxide Fuel Cell," ASME J. Energy Resour. Technol., **117**, pp. 43–49.
[67] Campanari, S., 2001, "Thermodynamic Model and Parametric Analysis of a Tubular SOFC Module," J. Power Sources, **92**, pp. 26–34.
[68] Haynes, C., and Wepfer, W. J., 2001, "Characterizing Heat Transfer Within a Commercial-Grade Tubular Solid Oxide Fuel Cell for Enhanced Thermal Management," Int. J. Hydrogen Energy, **26**, pp. 369–379.
[69] Recknagle, K. P., Williford, R. E., Chick, L. A., Rector, D. R., and Khaleel, M. A., 2003, "Three-Dimensional Thermo-Fluid Electrochemical Modeling of Planar SOFC Stacks," J. Power Sources, **113**, pp. 109–114.
[70] Li, P. W., Schaefer, L., and Chyu, M. K., 2003, "Investigation of the Energy Budget in an Internal Reforming Tubular Type Solid Oxide Fuel Cell Through Numerical Computation," *Proceedings of the International Joint Power Conference*, June 16–19, Atlanta, GA, USA, Paper No. IJPGC2003–40126.
[71] Suwanwarangkul, R., Croiset, E., Fowler, M. W., Gouglas, P. L., Entchev, E., and Douglas, M. A., 2003, "Performance Comparison of Fick's Dusty-Gas and Stefan-Maxwell Models to Predict the Concentration Overpotential of a SOFC Anode," J. Power Sources, **122**, pp. 9–18.
[72] Hagiwara, A., Michibata, H., Kimura, A., Jaszcar, M. P., Tomlins, G. W., and Veyo, S. E., 1999, "Tubular Solid Oxide Fuel Cell Life Tests," *Proceedings of the Third International Fuel Cell Conference*, Nagoya, Japan, pp. 365–368.
[73] Watanabe, T., 1997, "Fuel Cell Power System Applications in Japan," Proc. Inst. Mech. Eng., Part A, **211**, pp. 113–119.
[74] Elangovan, S., Hartvigsen, J., Khandkar, A., Privette, R. M., Kneidel, K. E., Perna, M. A., and Rowley, D. R., 1998, "Planar Solid Oxide Fuel Cell Integrated System Technology Development," J. Power Sources, **71**, pp. 354–360.
[75] Smith, W. R., and Missen, R. W., 1982, *Chemical Reaction Equilibrium Analysis*, John Wiley & Sons, Inc., New York.
[76] Bird, R. B., Stewart, W. E., and Lightfoot, E. N., 1960, *Transport Phenomena*, John Wiley & Sons, New York.
[77] Williams, F. A., 1985, *Combustion Theory*, Benjamin/Cummings Publishing Co., New York.
[78] Eckert, E. R. G., and Drake, R. M., 1966, *Heat and Mass Transfer*, 2nd edition of *Introduction to the Transfer of Heat and Mass*, McGraw-Hill Book Company, Inc., New York.
[79] Turns, S. R., 1999, *Introduction to Combustion: Concept and Application*, 2nd Ed., McGraw-Hill Higher Education, New York.
[80] Incropera, F. P., and DeWitt, D. P., 1996, *Introduction to Heat Transfer*, 3rd Ed., John Wiley & Sons, New York.
[81] Todd, B., and Young, J. B., 2002, "Thermodynamic and Transport Properties of Gases for Use in Solid Oxide Fuel Cell Modeling," J. Power Sources, **110**, pp. 186–200.
[82] Patankar, S. V., 1980, *Numerical Heat Transfer and Fluid Flow*, McGraw-Hill, New York.
[83] Beckermann, C., and Smith, T. F., 1993, "Incorporation of Internal Surface Radiation Exchange in the Finite-Volume Method," Numer. Heat Transfer, Part B, **23**, pp. 127–133.
[84] Li, P. W., Chen, S. P., and Chyu, M. K., 2005, "Novel Gas Distributors and Optimization for High Power Density in Fuel Cells," J. Power Sources, **140**, pp. 311–318.

Transport Phenomena Analysis in Proton Exchange Membrane Fuel Cells

Hongtan Liu

Tianhong Zhou

Department of Mechanical Engineering,
University of Miami,
Coral Gables, Florida 33124

Ping Cheng

School of Mechanical & Power Engineering,
Shanghai Jiaotong University,
Shanghai 200030, People's Republic of China

The objective of this review is to provide a summary of modeling and experimental research efforts on transport phenomena in proton exchange membrane fuel cells (PEMFCs). Several representative PEMFC models and experimental studies in macro and micro PEMFCs are selected for discussion. No attempt is made to examine all the models or experimental studies, but rather the focus is to elucidate the macro-homogeneous modeling methodologies and representative experimental results. Since the transport phenomena are different in different regions of a fuel cell, fundamental phenomena in each region are first reviewed. This is followed by the presentation of various theoretical models on these transport processes in PEMFCs. Finally, experimental investigation on the cell performance of macro and micro PEMFC and DMFC is briefly presented.
[DOI: 10.1115/1.2098830]

1 Introduction

The proton exchange membrane fuel cell (PEMFC) is also called the "polymer electrolyte membrane fuel cell" since a proton conducting polymer is used as the electrolyte in this type of fuel cell. Thanks to the intrinsic nature of the membrane, the PEMFC can have high power densities when operating at low temperatures (usually less than 120°C). It could be argued that PEMFC exceeds all other electrical energy generating technologies in the breadth of scope for possible applications.

PEMFC was first developed by General Electric in the 1960s for use in the NASA Gemini spacecraft. The problem that deferred the PEMFC from subsequent development was mainly due to its high cost and low power output. The catalyst technology at that time was such that 28 mg of platinum were needed for each square centimeter of electrode as compared to 0.2 mg/cm^2 or less today [1]. Recent developments have brought the current densities up to around 1 A/cm^2 or more, while at the same time reducing the platinum loading by a factor of over 100. The drastic reduction in cost and significant improvement in power density have made PEMFC the most promising future vehicle and portable power sources for a wide range of applications. Research activities in this field have experienced accelerated growth in recent years. Figure 1 shows the number of papers published on fuel cells since 1994 as listed by Science Citation, the majority of which are on PEMFC.

Although enormous progress has been made in recent years, there still exist many obstacles to near term market entry by the PEM fuel cells. The problems include high cost, durability, cold-start, operation control, thermal and water management, design optimization, etc., which call for further research on various transport and electrochemical processes occurring in fuel cells.

This review focuses on the current research status on the transport phenomenon during PEM fuel cell operation. It is organized as follows: Section 2 reviews the transport phenomenon in different layers of PEM fuel cell; Section 3 discusses various fuel cell models; Section 4 summarizes experimental investigation on the performance of marco and micro fuel cells.

Contributed by the Heat Transfer Division of ASME for publication in the JOURNAL OF HEAT TRANSFER. Manuscript received May 11, 2004; final manuscript received April 8, 2005. Review conducted by Jacob Chung.

2 Transport Phenomena in a PEMFC

Figure 2 shows the geometry of a single fuel cell, which consists of a membrane, two catalyst layers, two gas diffusion layers, two gas channels, and two collector plates. The major functions and characteristics of these components are: collector plates with flow channels are used for reactants and products transport, electron conduction and heat removal; gas diffusion layers are for reactant distributions, electron conduction, and liquid water removal; catalyst layers are used to promote electrochemical reactions where reactants are consumed, and products and heat are generated; and the membrane is used to conduct protons from the anode catalysts layer to the cathode catalyst layer.

The electrochemical reaction occurring in the PEMFC is illustrated in Fig. 3. At the anode catalyst layer, hydrogen is consumed to produce protons and electrons, i.e.,

$$2H_2 \rightarrow 4H^+ + 4e^- \tag{1}$$

Electrons pass through an external circuit to the cathode thus providing electrical power, while the protons transport through the membrane to the cathode. At the cathode catalyst layer, oxygen combines with the protons and electrons to produce water, i.e.,

$$O_2 + 4e^- + 4H^+ \rightarrow 2H_2O \tag{2}$$

Although chemical reaction principles are rather simple, the transport processes inside a fuel cell are quite complex. First, the reactant species (O_2, H_2) must be able to effectively transfer to different parts of the catalyst layers. Second, the electrical resistance to both protons and electrons must be low. And third, the product water and heat must be removed out of the fuel cell from the catalyst layers through the gas diffusion layers and other cell components. Further complications come from the duel effects of temperature and water.

The influence of temperature on fuel cell operation has two important consequences. On one hand, higher temperature is favorable for electrochemical reactions. On the other hand, higher temperature also leads to a reduction in reactant partial pressure, cell open circuit voltage, and water activity, which results in an increase of membrane ionic resistance. In addition, nonuniform temperature distributions cause transient effects and create hot spots that may lead to cell failures. If the temperature or temperature gradient is too high, the fragile membrane could be damaged. The heat produced by a PEMFC is comparable to its power output. Heat generation inside the PEMFC includes entropic heat of reactions, irreversible reaction heat, and ohmic heating (from both

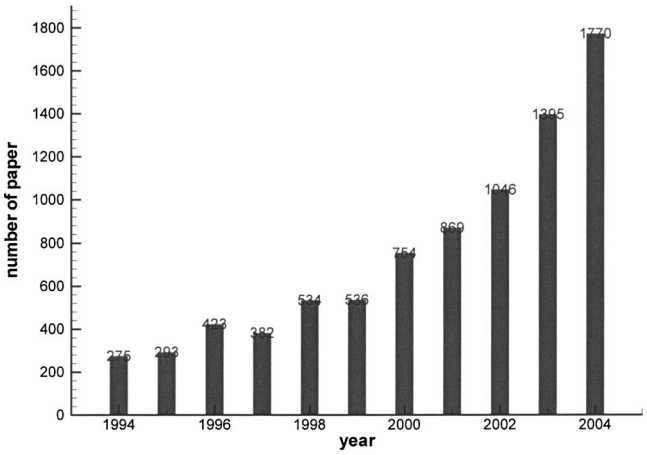

Fig. 1 Number of papers published on fuel cells since 1994

proton current and electron current), etc. The present commercially available membranes cannot sustain high temperature and it is difficult for the membranes to maintain high degree of hydration at a temperature much higher than the local saturation temperature.

Water plays a very special role in PEM fuel cells. On one hand, the polymer membrane must be kept hydrated to maintain high proton conductivity. On the other hand, excess water can fill the pores in the catalyst layers and the gas diffusion layers (GDL), thus blocking the transfer of reactants to the reaction sites, which is often referred to as flooding. A good water management is to keep the membrane hydrated while avoiding flooding of the electrodes and the GDL. In practice, humidification of anode fuels and/or cathode oxidants (air or oxygen) is often used to provide sufficient membrane hydration. This common practice ensures a highly hydrated ionomer with high ionic conductivity and thus low ohmic loss. However, as water is produced in the cathode catalyst layer and water also tends to migrate from the anode side to cathode side under the electro-osmotic drag, flooding in the cathode becomes a key issue in PEMFC. In addition, humidification of the gas streams requires additional equipment and power in the energy system. An ideal PEMFC should be able to operate at low humidity conditions while still maintaining high ionic conductivity. Adoption of the humidifying strategy depends strongly on the understanding of the water transfer processes within a PEMFC.

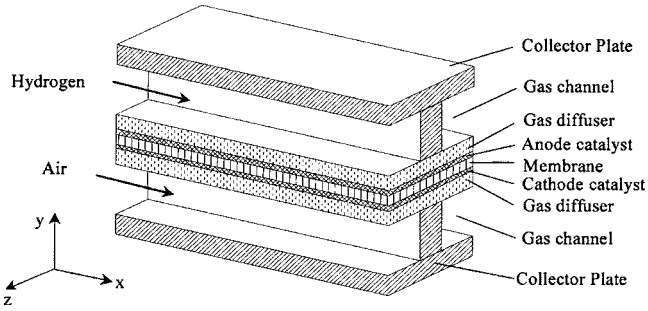

Fig. 2 A single fuel cell

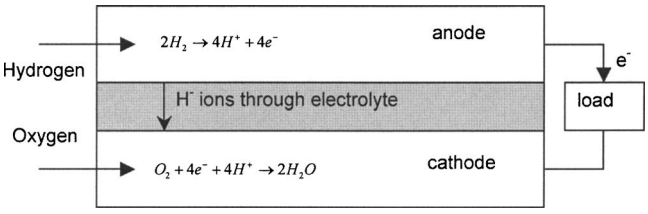

Fig. 3 The chemical reaction in the PEMFC

2.1 Transport Phenomena in Gas Channels. As mentioned earlier, gas channels are used to distribute reactants to the whole fuel cell and also remove product water and heat from the fuel cell. The velocity and flow characteristics have significant effects on mass transfer from the channel to the diffusion layer, and thus to the catalyst layer. Currently, there are many kinds of complex transport pathways with different manifold of multiple bends and branches being investigated, such as interdigitated flow field, etc. The objective is to maximize the reaction surface area exposed to the oxygen and hydrogen gas streams, while providing the pathway for liquid water to leave the fuel cell. As individual cells have to be combined in a series, or a stack, in order to obtain the desired voltage, oxygen and fuel are provided to the individual cells of the stack through a manifold. It is critical to the performance of the fuel cell stack that the flows of reactants distribution be as uniform as possible in the stack and that water is effectively removed from all cells.

In modeling practice, the conventional mass conservation, the Navier-Stokes, energy and species conservation equations are used in the numerical modeling of heat and mass transfer in the gas channels.

2.2 Transport Phenomen in Gas Diffusion Layers. The GDL is the porous backing between the gas channel and the catalyst layer. It is often composed of either a single or multiple layers of highly porous and hydrophobic material. For example, carbon fiber papers or clothes, treated with a hydrophobic solution (commonly polytetrafluoroethylene, or Teflon®), are often used as gas diffusion layers. The main functions of the diffusion layer are to distribute reactants and remove product water to and from the area under the lands (or shoulders) of the collector plates, to conduct electrons to/from the lands of the collector plates from/to everywhere in the catalyst layer, and to remove heat.

Although diffusion is the predominant mode of mass transfer in the diffusion layer, convection may not be neglected under many conditions, and the Darcy law

$$v = -\frac{k_p}{\mu}\nabla p \tag{3}$$

may be used as the momentum equation in numerical models. Other numerical models used the modified Brinkman equation [2] as the momentum equation, which is given by

$$\rho \mathbf{V}\cdot(\nabla \mathbf{V}) = -\nabla \mathbf{P} + r^{(2)}\mu\nabla^2\mathbf{V} - \varepsilon\mu/k_p\mathbf{V} \tag{4}$$

where the porous media correction factor $r^{(2)}$ given by Dagan [2] is

$$r^{(2)} = 2.25\frac{(1-\varepsilon)^2}{\varepsilon^2} \tag{5}$$

The gas phase transport within the porous diffusion layer is usually modeled with the Stefan-Maxwell equation

$$\nabla X_i = \sum_{j\neq i}\frac{X_iN_j - X_jN_i}{cD_{i,j}^{\text{eff}}} \tag{6}$$

where c is the total concentration of the gas species, X the mole fraction of species i, N the molar flux, and $D_{i,j}^{\text{eff}}$ the effective binary diffusivity where $D_{i,j}=D_{j,i}$. To take into consideration the porous structure, an effective diffusivity is usually used. Bernardi and Verbrugge [3] and Gurau et al. [4] used the following expression for the effective diffusivity

$$D_{i,j}^{\text{eff}} = \varepsilon^{\tau}D_{i,j} \tag{7}$$

where ε and τ are the porosity and tortuosity, respectively.

The gas mixtures in the diffusion layer may contain a substantial amount of water vapor, especially at the cathode where water

Table 1 Electrical conductivity of carbon and carbon fiber paper

Properties	Values (S/m)	Source
Graphite conductivity	1.28×10^5	http://www.ndt-ed.org/GeneralResources/MaterialProperties/ET/ET_matlprop_Misc_Matls.htm
Graphite conductivity		http://www.phy.mtu.edu/~jaszczak/graphprop.html
perpendicular	1.03×10^5	
parallel	7.09×10^5	
natural	8.33×10^5	
Fine carbon	$1.11-1.18\times10^5$	http://www.tokaicarbon.co.jp/en/products/semicon03.shtml
GDL conductivity		Toray Industries, Inc.
through plane	1.25×10^3	
in plane	$1.72-2.13\times10^4$	

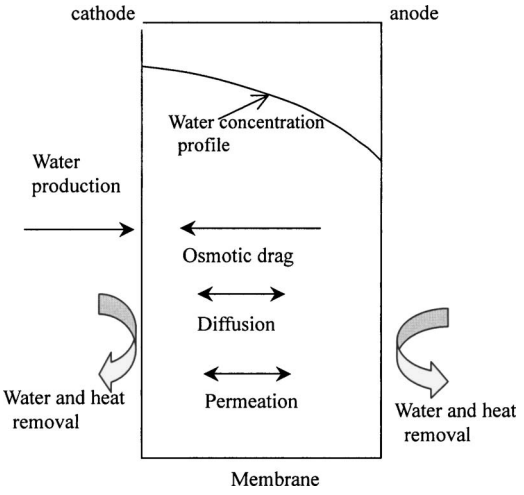

Fig. 4 Water movement within the membrane

is generated from chemical reaction. Depending on the partial pressure of water vapor, condensation/evaporation may occur in the diffusion layer. When liquid water is present, the effective porosity is given by

$$\varepsilon = (1-s)\varepsilon_{\text{dry}} \tag{8}$$

where s is the liquid water saturation in the porous media which is defined as

$$s = \frac{\text{volume of liquid in the pores}}{\text{total volume of pores}} \tag{9}$$

More in-depth discussions about the effective diffusivity and liquid water saturation inside the PEMFC diffusion layer are given by Nam and Kaviany [5].

In addition to the function of distributing reactants and removing product water, GDL also serves as a media to conduct electrons. Table 1 lists values of electrical conductivity of carbon and carbon fiber paper. From these values, it is seen that the electric conductivities differ greatly between the through-plane and in-plain directions. In the through-plane direction, the electric conductivity can be 5–10 times smaller than that of the in-plane direction. Although the collector plate has electric conductivity on the order of 10^4 S/m for graphite plates, the effective electric conductivities of GDL and catalyst layers are much lower ranging from 300 to 500 S/m in the through-plane direction [6].

If the resistance in the in-plane direction can be neglected, the electric resistance of GDL is given by

$$R = \int_{\text{GDL}} dy/\sigma_e \approx L/\sigma_e \tag{10}$$

where σ_e is the electron conductivity.

The heat generation rate in the GDL due to electron current can be calculated from

$$Q_{\text{ohmic heating}} = \int_{\text{GDL}} \frac{i^2}{\sigma_e} dV \tag{11}$$

2.3 Transport Phenomena in the Membrane. As mentioned earlier, the major function of the membrane is to transfer protons from anode to cathode. As the protonic conductivity of the membrane depends strongly on its water content, the polymer electrolyte must be kept hydrated during operation. However, on the other hand, flooding of the porous electrodes and GDL should be avoided so that reactants can be transported effectively to the reaction sites in the catalyst layer. As indicated in Fig. 4, there are three mechanisms of water transport in the membrane: electro-osmotic drag, diffusion, and hydraulic permeation. A good water management is to balance the three water fluxes so that the membrane is kept well-hydrated while avoid flooding.

2.3.1 Water Transfer by Electro-Osmosis. The electro-osmotic drag occurs when H^+ ions move from anode to cathode pulling water molecules with them. There are two approaches in the literature to model water transfer due to electro-osmosis in the membrane.

(i) Using an empirical drag coefficient. Springer et al. [7] were one of the first to use the drag coefficient approach in modeling of water transfer due to electro-osmosis in the membrane. The drag coefficient n_d is defined as the number of water molecules per proton dragged from the anode to the cathode. Using this approach the water flux due to electro-osmosis is

$$\text{N}_{w,\text{drag}} = n_d \cdot \frac{i}{F} \tag{12}$$

where i is current density and F is Faraday constant. Studies indicate that the drag coefficient n_d depends not only on the chemical structure of the membrane and the fixed charge concentration within the membrane but also on the water content of the membrane, which is defined as the number of moles of water per mole of sulfonic sites, i.e.,

$$\lambda = \frac{\text{number of water molecules}}{\text{number of sulfonic sites}} \tag{13}$$

LaConti and co-workers [8] reported drag coefficients with the value of 2–3 water molecules per proton for water content in the range $15<\lambda<25$. They concluded that the drag coefficient decreases linearly with water content for immersed membranes, and that the electro-osmotic drag drops slightly with a decrease in equivalent weight. Zawodzinski et al. [9] reported that for fully hydrated and (immersed) Nafion® 110 membranes, a drag coefficient of 2.5 was measured. For immersed Nafion 117 at a low water content of $\lambda=11$, the drag coefficient was determined to be 0.9. Zawodzinski et al. [9] presented electro-osmotic water drag data for several different membranes. The data suggested that there is a substantial difference in the drag coefficient observed for vapor and liquid equilibrated membranes (1.0 for vapor equilibrated membranes versus 2.5 for liquid equilibrated membranes). It is generally believed that for fully hydrated membrane, the drag coefficient is a little less than 3, while for dry membranes this value is practically zero. The lack of knowledge on the accurate value of the electro-osmotic drag coefficient is one of the major

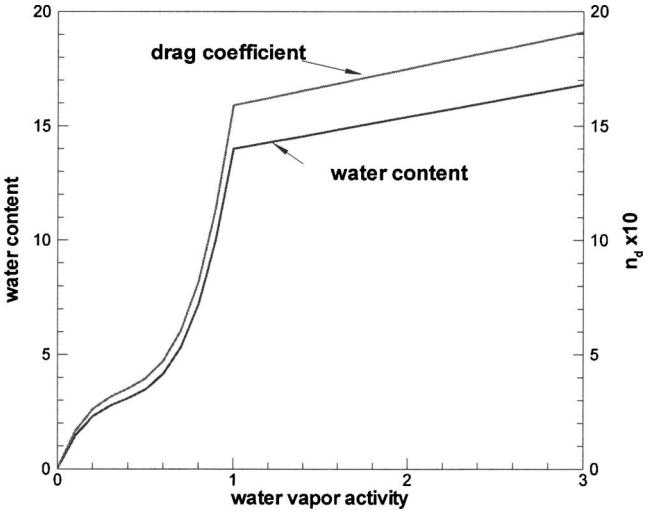

Fig. 5 The relationship of water content and the drag coefficient versus water vapor activity given by Eqs. (15) and (17) [7]

problems in water transport modeling in PEMFCs.

Based on experimental data, Springer et al. [7] proposed that the drag coefficient for Nafion 177 membrane at 80°C as

$$n_d = 2.5\frac{\lambda}{22} \tag{14}$$

with

$$\lambda = \begin{cases} 0.043 + 17.81a_w - 39.85a_w^2 + 36.0a_w^3 & 0 \leqslant a_w \leqslant 1 \\ 14 + 1.4(a_w - 1) & 1 \leqslant a_w \leqslant 3 \end{cases} \tag{15}$$

where a_w is the water-vapor activity which is defined as

$$a_w = \frac{x_w}{p_{\text{sat}}/p} \tag{16}$$

with x_w being the mole fraction of water vapor, p_{sat} the water saturation pressure at the give temperature, and p the total pressure. Substituting Eq. (15) into Eq. (14) gives [7,10]

$$n_d = \begin{cases} 0.0049 + 2.20a_w - 4.53a_w^2 + 4.09a_w^3 & 0 \leqslant a_w \leqslant 1 \\ 1.59 + 0.159(a_w - 1) & 1 \leqslant a_w \leqslant 3 \end{cases} \tag{17}$$

The relationships between water content λ and drag coefficient n_d as functions of the water vapor activity a_w, given by Eqs. (15) and (17), are illustrated in Fig. 5. It is seen that the drag coefficient is between 0 and 2. The empirical equations given by Eqs. (15)–(17) were used by many subsequent researchers including Dutta et al. [11], Wang et al. [12], and Zhou and Liu [13] for numerical modeling work.

(ii) Using Schögl's equation. Bernardi and Verbrugge [3,14] were the first to use Schögl's equation to account for electro-osmosis in PEM fuel cell modeling. Even though water molecule is electrically neutral, the electrical force acting on protons are considered to be acting on the water molecules, since they are considered to cluster around the protons. Thus, the velocity of water transfer through the membrane due to electro-osmosis is given by the Schögl's equation

$$v = \frac{k_\phi}{\mu} z_f c_f F \frac{d\phi}{dy} \tag{18}$$

where c_f is mole concentration of sulfonic groups, μ is the dynamic viscosity of water, z_f is the charge number of each sulfonic group, k_ϕ is the electronic permeability, ϕ is the electrical potential, and F is the Faraday constant. Equation (18) and its modified forms were used by Gurau et al. [15], Zhou and Liu [16–18], Singh et al. [19], Berning et al. [20], and Um et al. [21] for water transfer due to electro-osmosis in the membrane.

2.3.2 Water Transfer by Diffusion. Water transfer by diffusion through the membrane is given by the standard diffusion equation

$$N_{w,\text{diffusion}} = -D_w \frac{\partial c_w}{\partial y} \tag{19}$$

where c_w is mole concentration of water and D_w is the diffusion coefficient. The diffusion coefficient D_w depends on the water content of the membrane. Zawodzinski et al. [22] have reported self-diffusion coefficients of water in Nafion 117 and Dow membranes equilibrated with water vapor at 303 K. The data on the self-diffusion coefficient of Nafion 117 equilibrated with water vapor decreased by more than an order of magnitude, from roughly 8×10^{-6} cm^2/s down to 5×10^{-7} cm^2/s as water content in the membrane decreased from $\lambda=14$ to $\lambda=2$. In his modeling work, Springer et al. [7] estimated the diffusion coefficient to be

$$D_w = 10^{-10}\exp\left[2416\left(\frac{1}{303} - \frac{1}{273+T}\right)\right](2.563 - 0.33\lambda + 0.0264\lambda^2 - 0.000671\lambda^3) \tag{20}$$

Several other empirical equations for the diffusion coefficients have been proposed by Fuller and Newman [23], Nguyen and White [10], Yi and Nguyen [24], etc. However, the values of these coefficients vary greatly.

The mole concentration of water can be calculated from the water activity as [7,10]

$$c_w = \begin{cases} \frac{\rho_m}{M_m}[0.043 + 17.8a_w - 39.85a_w^2 + 36.0a_w^3] & 0 \leqslant a_w \leqslant 1 \\ \frac{\rho_m}{M_m}[14. + 1.4(a_w - 1)] & 1 \leqslant a_w \leqslant 3 \end{cases} \tag{21}$$

where ρ_m and M_m are the density and equivalent weight of the membrane when it is dry. Equation (19) together with Eqs. (20) and (21) have been used in many subsequent numerical models to compute water transfer by diffusion.

2.3.3 Water Transfer by Hydraulic Permeation. The membrane is a porous media and water can transfer through it by pressure difference which is called hydraulic permeation. The water flux in the membrane due to pressure difference is given by

$$N_{w,\text{permeation}} = -c_w \frac{k_p}{\mu}\frac{\partial p_w}{\partial y} \tag{22}$$

where k_p is the hydraulic permeability of the membrane to water, μ is the dynamic viscosity of water, and c_w is the mole concentration of water in the membrane.

2.3.4 The Net Water Transfer. The net water transfer through the membrane is the combined result of water transfer due to all three mechanisms discussed in Secs. 2.3.1, 2.3.2, and 2.3.3. If we define α as the net water transfer coefficient, i.e., the net number of moles of water flux per mole of proton transfer, the net water flux is given by

$$N_{w,a} = \frac{\alpha i}{F} \tag{23}$$

where i is the current density. If the drag coefficient approach is used, α can be determined by

$$\alpha = n_d - D_w \frac{\partial c_w}{\partial y}\frac{F}{i} - c_w \frac{k_p}{\mu}\frac{F}{i}\frac{\partial p_w}{\partial y} \tag{24}$$

Note that Springer et al. [7] did not include the last term (the hydraulic permeation term) in their paper. On the other hand, if Schögl's equation is used for water transfer due to electro-osmosis in the membrane, α is determined by

$$\alpha = \frac{F}{i}\frac{k_\phi}{\mu} z_f c_f F \frac{\partial \phi}{\partial y} - D_w \frac{\partial c_w}{\partial y}\frac{F}{i} - c_w \frac{k_p}{\mu}\frac{F}{i}\frac{\partial p_w}{\partial y} \tag{25}$$

Note that Bernardi and Verbrugge [3,14] did not include the second term (the diffusion term).

2.3.5 Membrane Proton Conductivity. The conductivity of a membrane to proton is a critical parameter in determining PEM fuel cell performances. The very name of this type of fuel cell, proton exchange membrane (PEM) fuel cell, is derived from the membrane and this special property. Higher conductivity is always desired since higher conductivity means lower ohmic loss. Thus, reducing the ionic resistance of the membrane is one of the main objectives of membrane research. The membrane resistance R_m can be calculated from

$$R_m = \int_{\text{membrane}} \frac{dy}{\sigma(\lambda)} \tag{26}$$

while the heat generation rate in the membrane due to proton current can be calculated from

$$Q_{\text{ohmic heating}} = \int_{\text{membrane}} \frac{i^2}{\sigma} dV \tag{27}$$

where σ is the ionic conductivity.

The ionic conductivity σ depends on many factors such as the type of membrane and its equivalent weight, methods of pretreatment, temperature, as well as other external variables, and the amount of water uptake, etc. Its values can vary between 1 and 10 S/m for a Nafion membrane [25]. The experimental results of Zawodzinski et al. [9] show that the proton conductivity decreases roughly linearly with decreasing water content. Springer et al. [7] obtained the following correlation equation for the ionic conductivity σ as a function of temperature and water content λ

$$\sigma(T) = (0.005139\lambda - 0.00326)\exp\left[1268\left(\frac{1}{303} - \frac{1}{273+T}\right)\right] \quad \text{for } \lambda > 1 \tag{28}$$

which has been used in many modeling works.

2.4 Transport Phenomena in Catalyst Layers. Transport phenomena in the catalyst layer (CTL) are complicated because of the electro-chemical reactions. The catalyst layer usually consists of platinum, carbon, membrane material, and Teflon®. Catalyst layers are made highly porous, so that their active surface areas are orders of magnitudes greater than their geometrical ones. The requirements of a catalyst layer are: high intrinsic activity, large active surface area, high ionic and electric conductivities, highly porous for reactant access and product removal, and stability.

As seen from the chemical reaction given by Eq. (1), two electrons pass round the external circuit for each molecule of hydrogen reacted. Thus, for one mole of hydrogen consumed, two moles of electrons pass through the external circuit. If e is the charge of one electron, then the charge flow is

$$\text{charge} = 2N \cdot e = 2F \text{ C} \tag{29}$$

where N is the Avagadro's number and F is the Faraday constant. In other words,

$$1 \text{ mol } H_2 \rightarrow 2F \text{ C charge} \tag{30}$$

Since the current density is defined as

$$i = \frac{\text{charge}}{\text{time} \cdot \text{area}} \tag{31}$$

therefore the relationship between hydrogen flux and current density is

$$N_{H_2} = \frac{i}{2F} \tag{32}$$

According to Eq. (1), for each mole of hydrogen consumed, 1/2 mole of oxygen is consumed and one mole of water is produced. Thus the oxygen and water fluxes are

$$N_{O_2} = \frac{i}{4F} \quad N_w = \frac{i}{2F} \tag{33}$$

Since

$$\nabla \cdot i = j \tag{34}$$

thus, the source (or sink) of these species are, respectively,

$$\nabla \cdot N_{O_2} = \frac{\nabla \cdot i}{4F} = \frac{j_c}{4F} \quad \nabla \cdot N_{H_2} = \frac{\nabla \cdot i}{2F} = \frac{j_a}{2F} \quad \nabla \cdot N_w = \frac{\nabla \cdot i}{2F} = \frac{j_a}{2F} \tag{35}$$

where j_a and j_c are the transfer current density at anode and cathode, which represent the reaction rates. Note that the value of j_c is negative and j_a is positive. The relationships between j_a, j_c and the species concentration are given by the Butler-Volmer equation

$$j_a = (a i_0^{\text{ref}})_a \left(\frac{X_{H_2}}{X_{H_2 \text{ref}}}\right)^{1/2} \left[\exp\left(\frac{\alpha_a^a F}{RT}\eta_a\right) - \exp\left(-\frac{\alpha_c^a F}{RT}\eta_a\right)\right] \tag{36}$$

$$j_c = (a i_0^{\text{ref}})_c \left(\frac{X_{O_2}}{X_{O_2 \text{ref}}}\right) \left[\exp\left(\frac{\alpha_a^c F}{RT}\eta_c\right) - \exp\left(-\frac{\alpha_c^c F}{RT}\eta_c\right)\right] \tag{37}$$

where a is the active catalyst surface area per unit volume of the catalyst layer, and i_0^{ref} is the exchange current density under the reference conditions.

Because chemical reaction occurs in the catalyst layer, heat is also generated in the catalyst layer and it is related to the current density j and the overpotential η as

$$Q_{\text{reaction}} = \int_{\text{catalyst layer}} j\eta dV \tag{38}$$

where j is related to the current density i by Eq. (34) and η is given by Eq. (36) or (37), depending on whether it is in the anode or cathode catalyst layer. The overpotential η is an "extra" potential required for a given current to flow through the electrode. The amount of energy due to overpotential is converted to heat. When an ionic current flows through a catalyst layer, ohmic loss occurs and the rate of heat generation is given by

$$Q_{\text{ohmic heating}} = \int_{\text{catalyst layer}} \frac{i^2}{\sigma_{\text{ct}}} dV \tag{39}$$

where σ_{ct} is the effective ionic conductivity of the catalyst layer. Since only a fraction of the catalyst layer is made of membrane material, σ_{ct} is lower than the conductivity of the membrane σ in Eq. (27). Boyer et al. [26] conducted experiments to measure the ionic conductivity of the catalyst layer as a function of the weight percent platinum on carbon support and the amount of perfluorosulfonic ionomer (PFSI) electrolyte. They reported that the specific conductivity of Nafion dispersed with platinum supported catalyst was found to be proportional to the volume fraction of Nafion in the catalyst layer as

$$\sigma_{ct} \approx 0.078\varepsilon_{\text{Nafion}} + 0.004 \text{ S/cm} \quad (40)$$

where $\varepsilon_{\text{Nafion}}$ is the volume fraction of Nafion (membrane material) in the catalyst layer. When no experimental data are available, Eq. (40) may be used to estimate the effective ionic conductivity of the catalyst layer.

Besides transferring protons, CTL must also conduct electrons. The electric conductance of CTL depends on the amount of carbon and platinum in the catalyst layer. The electric conductance of CTL can be calculated as

$$\sigma_{e,\text{ct}} = \sigma_e \varepsilon_s \quad (41)$$

where ε_s is the volume fraction of solid(carbon and platinum) in the catalyst layer, σ_e is the electron conductivity.

As CTL is extremely thin, the influence of the electric resistance is mainly in the direction of through plane. So the electric resistance of CTL can be determined by

$$R = \int_{\text{CTL}} dy/\sigma_{e,\text{ct}} \approx L/\sigma_{e,\text{ct}} \quad (42)$$

The heat generation rate in the CTL due to electron current can be calculated from

$$Q_{\text{ohmic heating}} = \int_{\text{CTL}} \frac{i^2}{\sigma_{e,\text{ct}}} dV \quad (43)$$

3 Theoretical Modeling

Fuel cell modeling is a broad term that refers to a wide range of analytical/numerical studies. One easy way to classify the enormous number of fuel cell models is to separate them into two groups: the macroscopic models and the microscopic models. The microscopic models simulate the transport phenomena on a pore or microscopic level, whereas the macroscopic ones study the fuel cell operation using averaged parameters. Among the existing PEMFC models, most of them are macroscopic, and only a few microscopic models are published, e.g., Cwirko and Carbonell [27]; Din and Michaelides [28]; Eikerling and Kornyshev [29]. This is due to the fact that although the microscopic models may be more realistic, they require more detailed information of the microstructures which are not readily available. Also, the computation time is much longer for the microscopic models. In a macroscopic model, the exact geometric details of the modeling domain are neglected. Instead, the domain is treated as a randomly arranged porous structure that can be described by a small number of variables such as porosity, permeability, and surface area per unit volume, etc. The transport properties within the domain are averaged over an elementary volume, which is small compared to the size of the electrode, but large compared to the microstructure. Thus, all variables are defined at all positions within the domain. For modeling fuel cells, macroscopic models are more common and appropriate, and some microscopic details can be incorporated into them [30].

The macroscopic models can also be classified according to the object of study. The objects include a single-fuel-cell unit, stack and systems. The single-fuel-cell unit usually contains a cathode, a membrane assembly, and an anode. A stack contains a number of fuel cells arranged in a matrix so as to produce the desired power output. A system is a power production unit which includes not only the fuel cell stack, but also the peripherals such as gas supply systems, heat exchangers, power controls, etc. This review focuses mainly on macroscopic models for a single fuel cell. Although many papers on PEMFC models have been published to investigate different aspects of the heat and mass transport processes in the fuel cells, the fundamental approaches can be traced back to several pioneering papers. In this review, the discussion will be focused only on representative work. To unify the symbols for discussion of these models, the coordinates as shown in Fig. 2 are used: x represents the direction of gas flow, y represents the direction across the fuel cell from cathode to anode, and z represents the direction across the gas channels, passing through the collector plate shoulders.

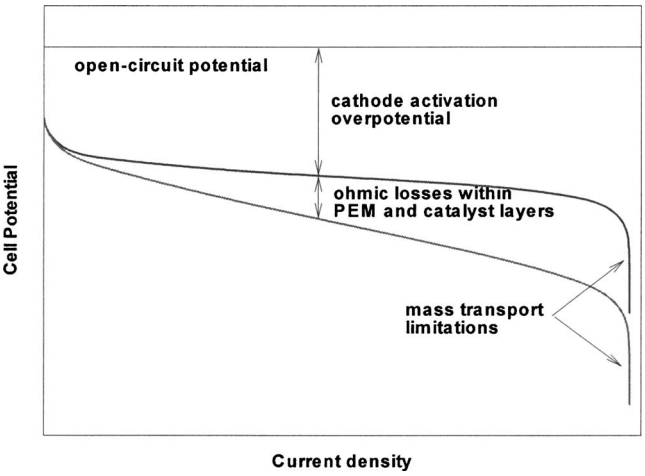

Fig. 6 A typical polarization curve

3.1 Zero-Dimensional Models. A plot of cell output voltage E versus cell current density i is called the polarization curve, which is the most commonly used reference for the PEMFC performance. The zero-dimensional models are mainly empirical models which fit the polarization curve with a simple empirical equation. It is very useful in experimental data analyses, kinetic parameters determination, as well as comparison of various types of losses ([25,30,31], etc.). The PEM fuel cell polarization curve (excluding the high-current density region) can be described with only three parameters: exchange current density i_0, Tafel slop b, and the area specific resistance R that lumps together all the effects of ionic and electronic resistance plus all the different mass-transport losses. A typical expression of this type of model is

$$E = U - b \log i - iR \quad (44)$$

where E and iR are the cell voltage and the overall ohmic loss, respectively, and U is given by

$$U = E_0 + b \log i_0 \quad (45)$$

where i_0 is the exchange current density and E_0 is the open circuit voltage. Substituting Eq. (45) into Eq. (44) gives

$$E = E_0 - b \log \frac{i}{i_0} - iR \quad (46)$$

A more general form of Eq. (46) is often expressed as

$$E = E_0 - \eta - iR \quad (47)$$

while η is the overall overpotential. If the absolute value of η is large, one of the exponential terms in Eq. (36) or Eq. (37) can be neglected, then the Tafel equation is obtained

$$\eta = b \log(i/i_0) \quad (48)$$

where b is the Tafel slop and it represents a proper combination of various parameters.

A typical polarization curve of the voltage of the fuel cell E versus the current density i is shown in Fig. 6, where it can be roughly broken down into the following three main regions: low current density region where kinetic losses due to activation overpotential dominate; medium current density region where ohmic loss is increasing rapidly; and the high current density region where concentration overpotential increase drastically due to mass-transport limitations.

(1) The initial drop in the polarization curve is due to the slow-

ness of kinetics of the oxygen reduction reaction (ORR). Usually the hydrogen-oxidation reaction (HOR) at the anode is very fast and the anode overpotential can be omitted [1].

(2) As the current is increased, ohmic losses become important in reducing the overall cell potential. These ohmic losses stem from ionic and electronic losses in the membrane electrode assembly (MEA) and other components. In this region, the potential varies linearly with the current density. Thus, the change in the cell potential ΔE may be calculated from the Ohm's law to give

$$\Delta E = iR \tag{49}$$

where R is the overall cell resistance.

(3) At high currents, mass-transport limitations become an increasingly important factor in limiting the fuel cell performance. These mass-transport losses mainly stem from the fact that the reactants cannot reach the reaction sites fast enough. This is mainly due to the inefficiency of the mass transport process through the GDL and CTL and the flooding of the electrodes where liquid water blocks the reactants from reaching the reaction sites. Again, these mass-transport limitations are dominated at the cathode where air rather than pure oxygen is usually used and the diffusivity of oxygen is much lower than that of hydrogen. Due to water production at cathode catalyst layer and water transport from the anode to the cathode by the electro-osmosis, flooding tends to occur at the cathode.

By examining the polarization curve obtained from experiments with model equations such as Eqs. (44)–(48) or their extended forms, some parameters such as open cell voltage, exchange current density, Tafel slop, and the overall resistance of the fuel cell can be determined. However, this procedure cannot be used for optimization, prediction, or in-depth examination of the underlying phenomena such as drying and flooding of a membrane, mass-transport limitation, or temperature variation within a fuel cell. Also, this approach cannot yield detailed information on the nature of these losses.

3.2 One-Dimensional Models. In contrast to the zero-dimensional approach with emphasis on the polarization curves that involve only a few effective parameters, one-dimensional models treat the fuel cell sandwich with varying degrees of complexity. The early one-dimensional models, given by Verbrugge and Hill [32,33], Bernardi [34], Bernardi and Verbrugge [3,14], Springer et al. [7], Springer et al. [35], and Amphlett et al. [30], described different regions within the fuel cell in varying details. These one-dimensional models have laid the foundation for subsequent development of multi-dimensional models.

Early one-dimensional models usually consider the variation in the direction across the fuel cell from cathode to anode (i.e., y direction in Fig. 2). This approach has the advantage of simultaneous treatment of all possible sources of loss in a PEM fuel cell. According to the treatment of water movement in the membrane, these early works can be roughly divided into two groups as discussed in Sec. 2.3: the water-drag-coefficient approach by Springer et al. [7], and the approach using Schögl's equation by Verbrugge and Hill [32,33] and Bernardi and Verbrugge [3,14].

Since only the direction across the MEA sandwich was considered, Springer et al. [7] omitted the variation of the gas composition along the gas channel. The fluid composition in the anode and cathode flow channel is assumed to be constant. The mass diffusion is assumed to follow the Stefan-Maxwell equation with a Bruggemann correction to take into account the electrode porosity. Equilibrium of water activity is assumed at the electrode/membrane interface and it determines the local water content at the membrane surface. Figure 7 shows the computed water profiles across the Nafion 117 membrane for four current densities. The net water flux moves from anode (right) to cathode (left), i.e., in the direction of increasing water content. At higher current density, the net water flux is higher even though the ratio of net water flux per proton is lower.

Bernardi and Verbrugge's one-dimensional model [3,14] includes the cathode diffusion layer, cathode catalyst layer, the membrane, and the anode catalyst layer. The governing equations include the species (oxygen, hydrogen, and nitrogen) conservation equations, Bulter-Volmer expression to account for the current density generation/consumption, and other supporting relationships. The numerical results from these works gave valuable information regarding the chemical reactions inside the fuel cell. For example, Fig. 8 gives the reaction rate distributions throughout the catalyst layer for three operating current densities. For lower current densities, the reaction rate is distributed almost uniformly throughout the catalyst layer, while at higher current densities, the distribution changes rapidly and only a thin layer immediately near the diffusion layer is utilized.

Gurau et al. [4] developed a one-dimensional model that included not only the diffusion layer, the catalyst layer, and the membrane, but also the channel. The governing equations included transport equations for the oxygen mass fraction in the channel, diffusion layer, and the catalyst layer, as well as Ohm's

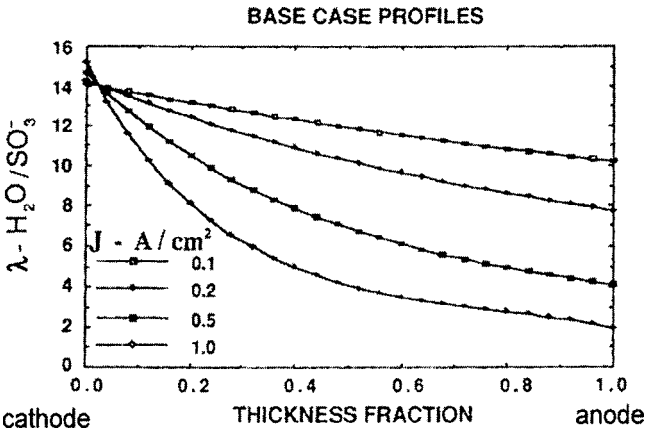

Fig. 7 Predicted water profiles across the Nafion® 117 membrane for four current densities [7]

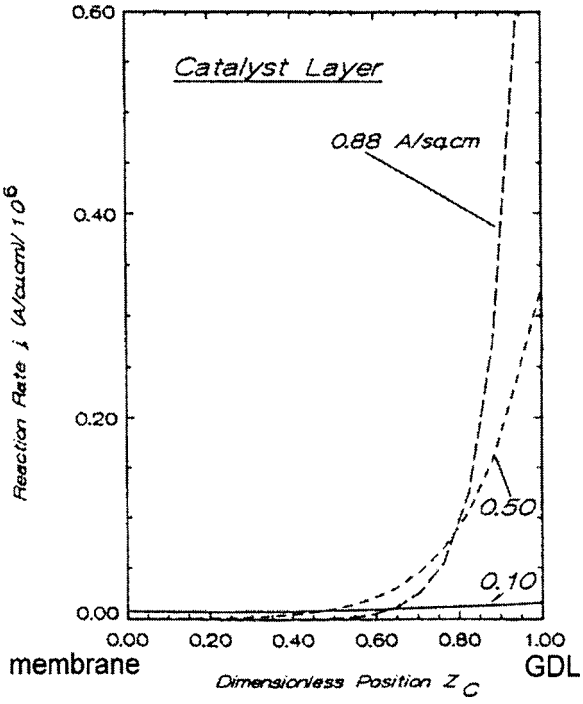

Fig. 8 Modeling results for spatial variation of reaction rate j through active catalyst layer for various current densities [3]

law. With appropriate boundary conditions, the governing equations were solved analytically. The profiles of current density and oxygen concentrations obtained from the analytical solutions were similar to those given numerically by Bernardi and Verbrugge [3,14], but the analytical solutions reveal more underlying physics and permit the use of functional analysis to identify trends. Polarization curves can be easily obtained from the analytical solution.

3.3 Two-Dimensional Models. The shortcoming of one-dimensional models is that they cannot take into consideration the effects of reactants consumption and product generation along the channel direction, or the effects of different reactants concentrations due to the blockage of the collector plate shoulders. Two-dimensional models have been developed to remedy these deficiencies. Two-dimensional models can be divided into two categories: along the channel (x,y directions) and across the shoulder (y,z directions).

3.3.1 Two-Dimensional Along-Channel Models. Along-channel models have incorporated the directions of x and y (see Fig. 2). The variations across the shoulder are neglected and only the changes in the sandwich direction and along the flow direction are considered. The earlier two-dimensional (2D) models, given by Fuller and Newman [23], Nguyen and White [10], Amphlett et al. [30], Singh et al. [36], and Yi and Nguyen [24,37], etc., are pseudo two-dimensional. These models generally only contain the MEA and do not include the channel. It is also assumed that diffusion is the only mechanism for oxygen transport. The coupling between the flow and the species field in the channel and the diffusion layer was not considered. To account for the changes of the species along the channel direction, some concentration boundary conditions were prescribed at the channel/diffusion-layer interface, or at the catalyst-layer/diffusion-layer interface. For example, Singh et al. [36] assumed linear variations of the chemical species at the channel/diffusion layer interfaces, and the modeling domain was limited to the membrane, catalyst layers, and diffusion layers. Fuller and Newman [23] obtained numerical solutions for the transport across the fuel cell sandwich at certain locations along the channel and thereafter integrated in the second direction, while the gas outside the diffusion layer was assumed to be of uniform composition in the direction across the cell. Nguyen and White [10] used algebraic expressions for the concentrations along the electrodes while Amphlett et al. [30] assumed averaged partial pressures along the channels. However, these arbitrary prescribed boundary conditions may not represent the variations of the reactants correctly.

Gurau et al. [15] developed the first true two-dimensional PEMFC model, which included the channel in the computation domain and eliminated the necessity of using artificial boundary conditions as discussed above. Other CFD-based 2D models using a similar approach are given by Singh et al. [19] and Um et al. [21]. In the work of Gurau et al. [15], they divided a single fuel cell domain into five sub-layers: cathode channel, cathode diffusion layer, cathode catalyst layer, membrane, anode catalyst layer, anode diffusion layer, and anode channel. The flow and transport equations are coupled with chemical reaction kinematics. The general form of convection-diffusion-source equation is

$$\rho\mathbf{V}\cdot(\nabla\psi)=\nabla(\Gamma\Delta\psi)+S \tag{50}$$

where Ψ is the general variable, V is the velocity factor, Γ is the diffusion coefficient, and S is the source term.

Rewriting the equations in vector notations, the governing equations given by Gurau et al. [15] are

Continuity equation

$$\nabla\cdot(\rho\mathbf{V})=0 \tag{51}$$

Momentum equation

$$\rho\mathbf{V}\cdot(\nabla\mathbf{V})=-\nabla\mathbf{P}+\begin{cases}\mu\nabla^2\mathbf{V} & \text{channel}\\ r^{(2)}\mu\nabla^2\mathbf{V}-\varepsilon\mu/k_p\mathbf{V} & \text{diffuson layer}\\ r^{(2)}\mu\nabla^2\mathbf{V}-\varepsilon\mu/k_p\mathbf{V}+\varepsilon z_f c_f F k_\phi(\nabla\phi)/k_p & \text{catalyst layer and membrane}\end{cases} \tag{52}$$

where the porous media correction factor $r^{(2)}$ is given by Eq. (5).

Species equation

$$\rho\mathbf{V}\cdot(\nabla\mathbf{X_k})=\varepsilon\rho D_k^{\text{eff}}\nabla^2\mathbf{X}_k+\begin{cases}0 & \text{channel and diffusion layers}\\ \varepsilon\rho S_k & \text{catalyst layer}\end{cases} \tag{53}$$

where D_k^{eff} is the effective diffusivity of the kth component in the gas mixture, which is given by

$$D_k^{\text{eff}}=\begin{cases}D_k & \text{channel}\\ D_k\varepsilon^{1.5} & \text{porous media}\end{cases} \tag{54}$$

At the cathode, the mass generation source term S_k for oxygen, water and protons are $j_c/(2Fc)-j_c/(2Fc)$ and $j_c/(Fc)$, respectively. At the anode, the source terms for hydrogen molecules and protons are $-j_a/(2Fc)$, and j_a/Fc, respectively. The reaction rates j_a and j_c are calculated from Butler-Volmer expression Eqs. (36) and (37).

Energy equation

$$\rho c_p\mathbf{V}\cdot(\nabla T)=k_{\text{eff}}\nabla^2T+\begin{cases}0 & \text{channels and diffusion layers}\\ Q & \text{catalyst layer and membrane}\end{cases} \tag{55}$$

with

$$k_{\text{eff}}=\begin{cases}k_g & \text{channels}\\ -2k_s+\dfrac{1}{\dfrac{\varepsilon}{2k_s+k_g}+\dfrac{1-\varepsilon}{3k_s}} & \text{porous media}\end{cases} \tag{56}$$

where k_g is the thermal conductivity of the gas while k_s is the thermal conductivity of the solid matrix of the porous media. The heat generation rates Q in different regions are given by

$$Q=\begin{cases}i\eta_a/\ell_{cl} & \text{anode catalyst layer}\\ i^2/\sigma_m & \text{membrane}\\ i\eta_c/\ell_{cl} & \text{cathode catalyst layer}\end{cases} \tag{57}$$

where ℓ_{cl} is the thickness of the catalyst layer. Note that j is implicitly assumed to be constant in the catalyst layer in the above equation.

The phase potential satisfies

$$\nabla\cdot(\sigma\nabla\phi)=\begin{cases}j_c & \text{cathode catalyst layer}\\ 0 & \text{membrane}\\ j_a & \text{anode catalyst layer}\end{cases} \tag{58}$$

where ϕ is the phase potential. The current density is given by

$$\mathbf{i}=\sigma\nabla\phi \tag{59}$$

After numerical results for $\mathbf{i}$ are obtained, then, the cell voltage can be determined by Eq. (47).

If the gas is considered compressible, the perfect gas equation of state $p=\rho RT$ is also needed. With appropriate boundary conditions, Eqs. (51)–(59) and Eq. (6) are solved with the SIMPLE-family algorithms of Patankar [38]. Figure 9 presents the computed oxygen mole fraction distributions at the interface between the cathode channel and gas diffusion layer for different operating

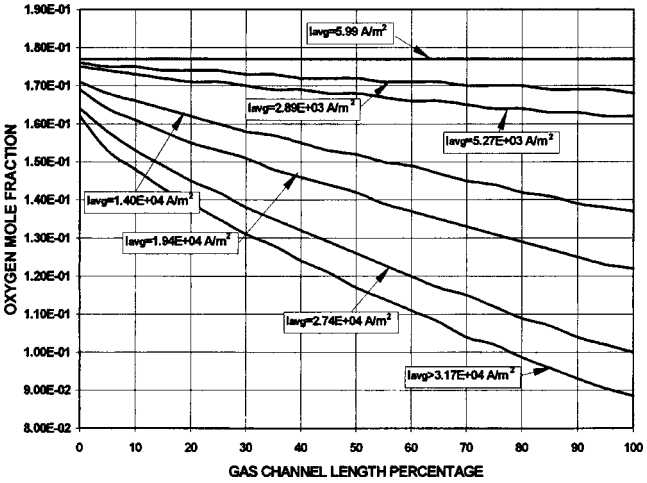

Fig. 9 The oxygen mole fraction distribution along the channel/diffusion layer interface [15]

current densities. For higher operating current densities, the oxygen mole fraction distributions near the entrance of the channel are clearly nonlinear. This nonlinear behavior is different from previous linear assumption in pseudo-two-dimensional models given by Nguyen and White [10]. Other numerical results obtained from this model include species concentrations, membrane liquid flow field, local current density distributions, etc.

3.3.2 Two-Dimensional Across-Shoulder Models. The across-shoulder models, including the direction across the MEA (*y* direction) and the direction across the shoulder (*z* direction), are given by Kulikovsky et al. [39], Kazim et al. [40], Nguyen [41], Yi and Nguyen [37], as well as by Natarajan and Nguyen [42], etc. The objectives of these models are to study the blockage effects of the solid shoulder of the collector plates. Obviously, these shoulders hinder the mass diffusion to the region immediately under them, causing a decreased current generation rate. In a conventional fuel cell system as shown in Fig. 10(*a*), gas (air or hydrogen) passes through the open channels. Because of the concentration gradient, oxygen or hydrogen diffuses through the porous gas diffusion layer to reach the chemical reaction sites in the catalyst layer. Since the mechanism of mass transfer is diffusion, this results in a low limiting current density due to the low mass transfer rates. To overcome such mass-transport limitation, the interdigitated flow field as shown in Fig. 10(*b*) was proposed, which consists of dead-ended channels. Because the inlet channel is blocked at the end, the gas stream is then forced to flow through the porous GDL before it is released through the adjacent open-ended channel. Through such a forced convection process, mass transfer is enhanced and the reaction rate within the catalyst layer can be increased. Similarly, heat generated by the reaction can be transferred out more effectively and thus provide better thermal management during fuel cell operations.

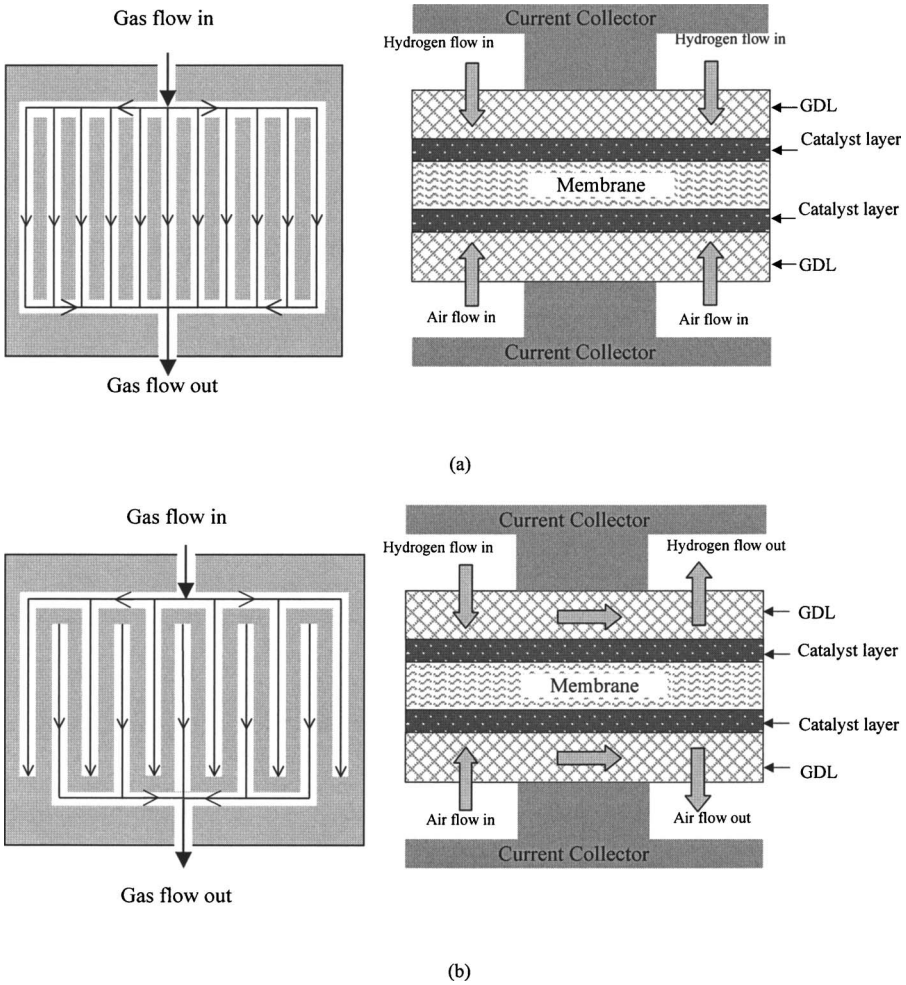

Fig. 10 The geometry of flow fields: (*a*) conventional flow field and (*b*) interdigitated flow field [40]

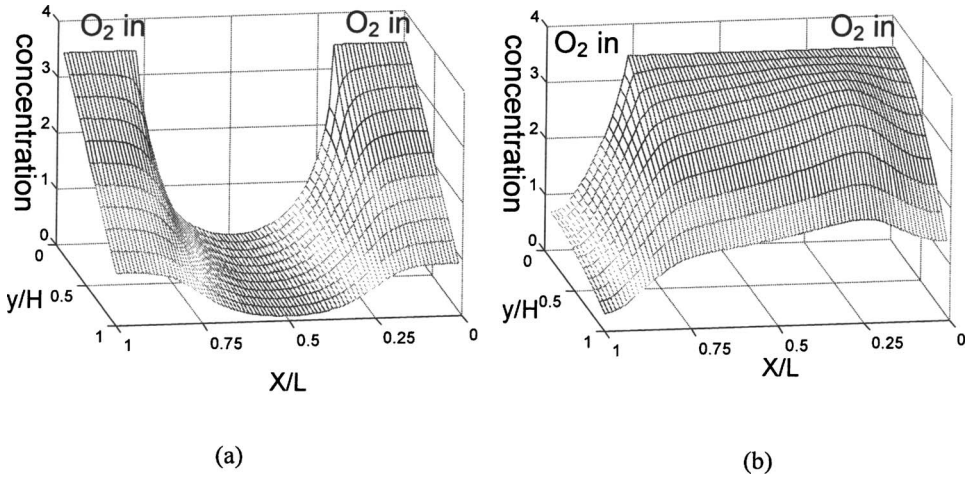

Fig. 11 Oxygen concentration distribution in the gas diffusion layer (*a*) with conventional flow field and (*b*) with interdigitated flow field at different values of over-potential η at $P=5$ atm and $T=85°C$ [40]

To compare the conventional flow field and the interdigitated flow field, Kazim et al. [40] used Darcy's law to study the flow through the porous gas diffusion layer and utilized Butler-Volmer expression as the prescribed boundary conditions along the interface between the gas diffusion layer and the catalyst layer. The computation domain was restricted to the diffusion layer only, with the channel and the catalyst layer treated as boundary conditions. The flow inside the porous media was simulated by Darcy's law. In the channel, pressure and the oxygen concentration are assumed to be constant. The computational results gave oxygen concentration, current density distribution, and polarization curves. Figure 11(*a*) shows the oxygen concentration distribution in the diffusion layer with conventional flow field at the over-potential $\eta=0.12$ V. Since diffusion is the only mass transfer mechanism, oxygen concentration decreases linearly in the direction toward the reaction surface. Furthermore, as expected, low concentrations are obtained at locations far from the source of O_2 and on the reaction surface where oxygen is consumed. Figure 11(*b*) shows the oxygen concentration distribution in the gas diffusion layer of the interdigitated flow field at the same over-potential $\eta=0.12$ V. A comparison between Figs. 10(*a*) and 10(*b*) clearly indicates the superiority of mass transfer mechanism by the interdigitated flow field design. The computational results show that, if the pressure-drop penalty is omitted, the interdigitated flow field can provide better mass transfer and thus better fuel cell performance.

Other 2D across-shoulder models (including *y* and *z* directions) are given by Yi and Nguyen [43], Natarajan and Nguyen [42], and Wang et al. [44]. Instead of assuming incompressible flow, Yi and Nguyen [37] assumed the mixture flow to be an ideal gas. The numerical results were similar to those obtained by Kazim et al. [40], showing superiority of the interdigitated flow field design if the penalty of additional pressure drop is neglected.

3.4 Three-Dimensional Models. The three-dimensional (3D) models including all three dimensions are shown in Fig. 2. The governing equations for 3D models are basically the same as the 2D models, with only the third dimension added. CFD-based 3D models are given by Dutta et al. [11,45], Shimpalee et al. [46], Natarajan and Nguyen [47], Berning et al. [20], as well as by Zhou and Liu [13,17]. The 3D model by Dutta et al. [11,45] used the popular CFD software FLUENT, and the drag-coefficient approach was adopted for water transfer in the membrane.

Zhou and Liu's 3D model [13,17] was an extension of the 2D model given by Gurau et al. [15], with the ohmic heating in the catalyst layers taken into consideration and better treatment and resolution in the catalyst layer. In this 3D model, in addition to the five sub-domains accounted for in 2D model by Gurau et al. [15], the collector plates are also included. Liu and Zhou [13] took into consideration the variations of overpotential and volumetric current density *j* across the catalyst layers. Thus, the heat generation terms in Eq. (57) are modified to be

$$Q=\begin{cases} j\cdot\eta_a+\dfrac{i^2}{\sigma_{cl}} & \text{anode catalyst layer} \\ \dfrac{i^2}{\sigma_m} & \text{membrane} \\ j\cdot\eta_c+\dfrac{i^2}{\sigma_{cl}} & \text{cathode catalyst layer} \end{cases} \tag{60}$$

Note that Eq. (60) differs from Eq. (57) in the heat generation in the catalyst layers on two different aspects: (1) the ohmic heating terms in the catalyst layers have been added. (2) i/ℓ_{ct} is used in Eq. (57) which indicates that *j* is assumed to be constant across the catalyst layers, but no such assumption for *j* is used in Eq. (60). After the governing equations are solved, the cell voltage is determined by,

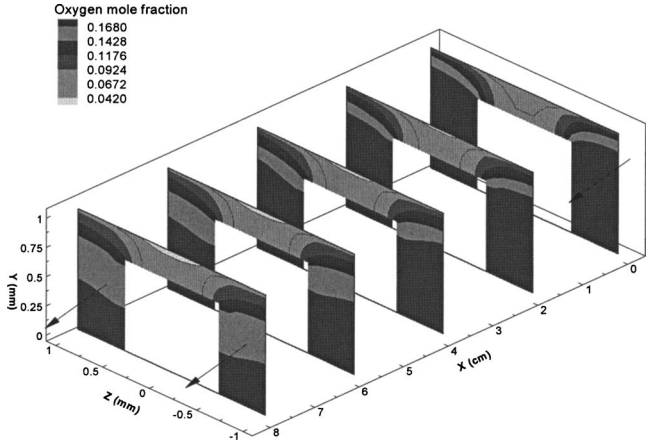

Fig. 12 Typical oxygen mole fractions along the flow direction [17]

$$E = E_0 - \eta_a + \eta_c - \int_m i/\sigma_m dV - \int_{\mathrm{ct},c} i/\sigma_{\mathrm{ct}} dV - \int_{\mathrm{ct},a} i/\sigma_{\mathrm{ct}} dV \tag{61}$$

where E_0 is the open circuit potential. Comparing this equation with Eq. (48), it is clear that the ohmic loss term (iR) in Eq. (48) is separated into three terms, each representing the ohmic loss in the membrane, cathode catalyst layer, and the anode catalyst layer, respectively.

Unlike the domain-dividing approach which binds sub-domains through boundary continuity, Zhou and Liu [16–18,48,49] utilized the similarity between the governing equations in different domains to expand the computation to the whole fuel cell. In this way, iteration time was reduced and a more smooth concentration contour could be achieved.

Zhou and Liu [13,17] obtained a numerical solution for detailed 3D distributions of species concentrations, current density, overpotential, temperature, water content and reaction rates in a PEMFC, as well as polarization curves. Some representative computation results are presented in Figs. 12–15. The oxygen concentration contours in Fig. 12 clearly display the oxygen concentration gradient due to chemical consumption and the blockage effect of the collector plate shoulder. Due to the variations of oxygen concentrations, the local current density of the fuel cell varies as shown in Fig. 13. Figure 14 shows the water distribution at the cathode and anode. Figure 15 is the temperature distribution across the fuel cell sandwich and across the shoulder plate. Heat is generated inside the catalyst layer and the membrane, which is transferred out to the channel walls, where cooling is provided. In this specific example, the channel wall temperature is kept constant, approximating effective liquid cooling or phase-change cooling. Across the fuel cell from cathode to anode, the highest temperature is located at the cathode catalyst layer due to the large activation overpotential. Across the z direction, the highest temperature occurs directly under the gas channel where the reaction rate is high and heat removal rate is low.

3.5 Two-Phase Models. All of the multi-dimensional models discussed earlier are based on single-phase flow, and assumes that the gas inside the fuel cell chamber is a perfect gas, even if some water droplets are present. In reality, liquid water exists, especially at the cathode, where water is accumulated because of the water production as well as water transport from the anode due to electro-osmosis. Thus, two-phase mixture can at least exist in the cathode.

To accurately model transport phenomena in a PEM fuel cell, two-phase models are required. There are essentially two approaches dealing with the two phase phenomenon in PEM fuel cell. The first approach considers the water vapor and water liquid as two different species, and assuming that there is no influence by the condensation/evaporation on the gas mixture flow field. This simplified approach was used by Bernardi and Verbrugge [3,14], Nguyen and White [10], He et al. [50], Yi and Nguyen [24], as well as by Natarajan and Nguyen [42,47]. In addition to the single-phase governing equations, the water-drag-coefficient given by Eqs. (14)–(17) are also needed.

Another popular approach to study phase change phenomenon is based on the concept of "multiphase mixture." Such an approach was proposed by Wang and Cheng [51] for multiphase flow in porous media. The key idea in the multiphase mixture model is to focus on the level of a multiphase mixture, rather than on the separate phases. Thus, the multiphase flow is described by a mass-averaged mixture velocity and a diffusive flux representing the difference between the mixture velocity and individual phase velocities. In this definition, phases are assumed to be distinct and separable components with nonzero interfacial areas, and their mixture represents a single fluid with smoothly varying phase composition. Using the multiphase mixture model, the governing equations are ([52–54], etc.):

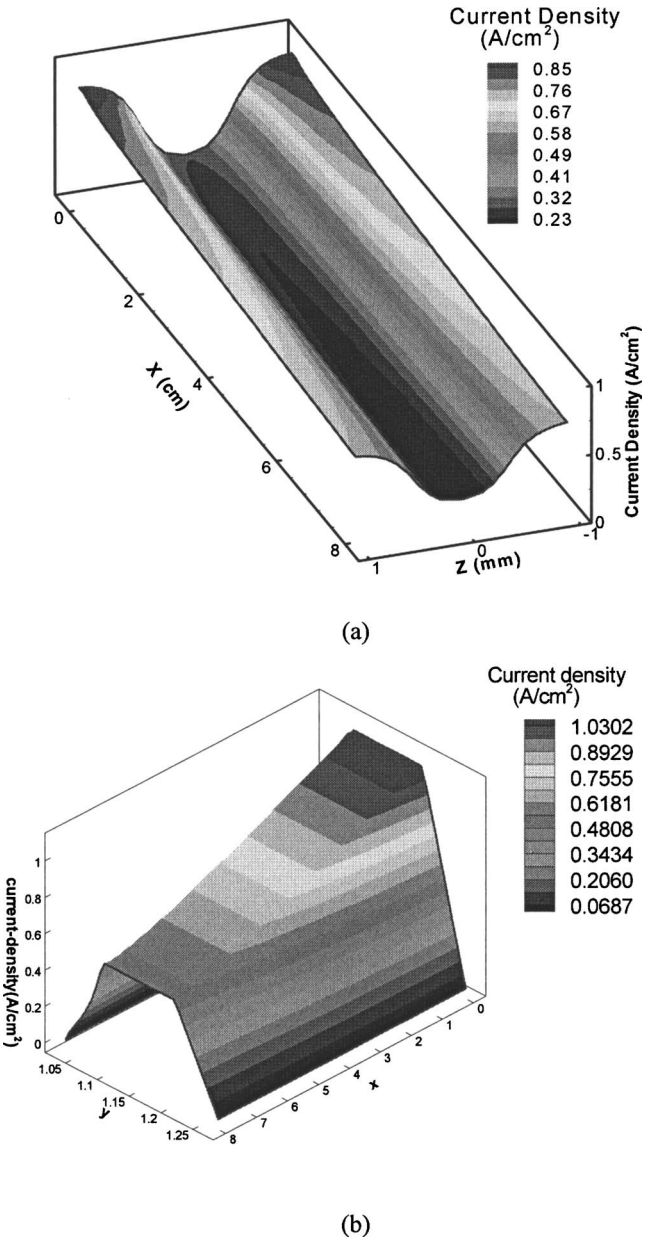

Fig. 13 Typical current density distribution (*a*) along *oxz* section and (*b*) across the fuel cell from cathode to anode [17]

$$\varepsilon \frac{\partial \rho}{\partial t} + \nabla \cdot (\rho \mathbf{u}) = 0 \tag{62}$$

$$\frac{\partial (\rho \mathbf{u})}{\partial t} + \nabla \cdot (\rho \mathbf{u}\mathbf{u}) = -\nabla p + \nabla \cdot (\nabla \mu \mathbf{u}) + \begin{cases} 0 & \text{channel} \\ -\dfrac{\mu}{k_p}(\varepsilon \mathbf{u}) & \text{porous media} \end{cases} \tag{63}$$

For the specific system in PEM fuel cell cathode, the oxygen mass fraction equation can be simplified as

$$\varepsilon \frac{\partial}{\partial t}(\rho c_{\mathrm{O}_2}) + \nabla \cdot (\gamma_{\mathrm{O}_2} \rho \mathbf{u} c_{\mathrm{O}_2}) = \nabla \cdot (\varepsilon \rho D_{\mathrm{O}_2} \nabla c_{\mathrm{O}_2}) - \nabla \cdot \left(\frac{\rho}{\rho_g s_g} c_{\mathrm{O}_2} \mathbf{j}_g \right) \tag{64}$$

For nitrogen

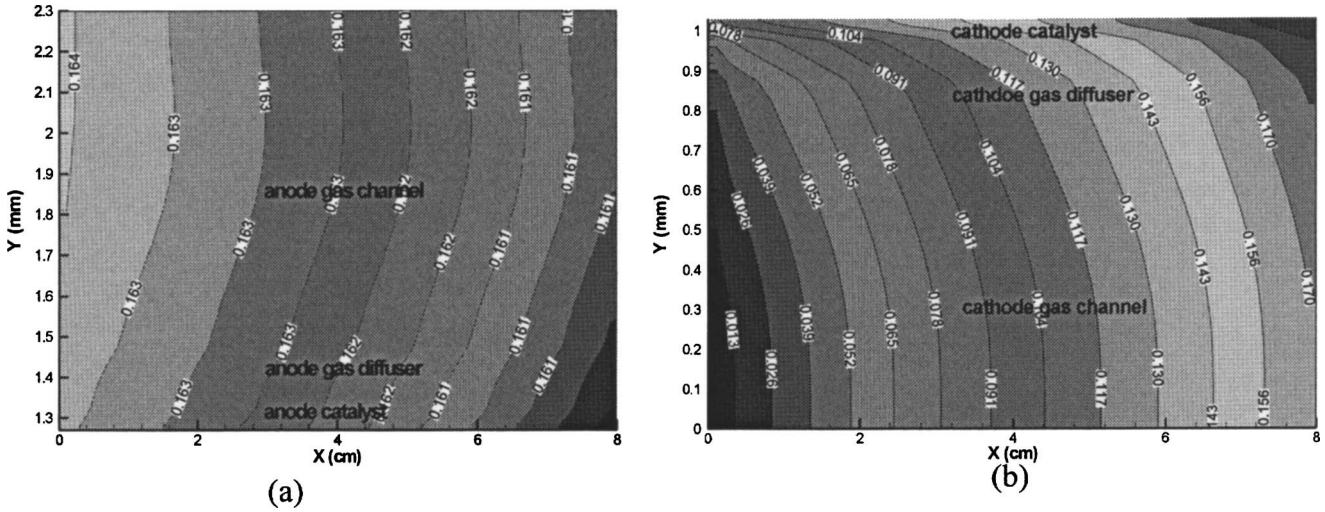

Fig. 14 Typical water mole concentration contours (*a*) at anode, (*b*) at cathode [17]

$$\varepsilon\frac{\partial}{\partial t}(\rho c_{N_2}) + \nabla\cdot(\gamma_{N_2}\rho\mathbf{u}c_{N_2}) = \nabla\cdot(\varepsilon\rho D_{N_2}\nabla c_{N_2}) - \nabla\cdot\left(\frac{\rho}{\rho_g s_g}c_{N_2}\mathbf{j}_g\right) \tag{65}$$

For water

$$\varepsilon\frac{\partial}{\partial t}(\rho c_w) + \nabla\cdot(\gamma_{H_2O}\rho\mathbf{u}c_w) = \nabla\cdot(\varepsilon\rho D_w\nabla c_w) - \nabla\cdot[\varepsilon\rho_l D_w\nabla s_l] - \nabla\cdot\left[\left(\frac{\rho_w^v}{\rho_g} - 1\right)\mathbf{j}_g\right] \tag{66}$$

where γ is the multiphase correction factor, c is the species mass fraction, s is the saturation whose definition is given by Eq. (9), and J_g is the diffusive mass flux (kg/m^2 s). The density ρ, concentration c, velocity v, diffusivity and other parameters are mixture variables and are calculated from the compositions of the liquid and gas. For example, the concentration of water is determined by

$$\rho c_w = \rho_l c_w^l s + \rho_g c_w^g (1-s) \tag{67}$$

where c_w^l and c_w^g are the mass fraction of liquid water and water vapor. Wang et al. [52] used the above-mentioned model, and classified four regimes of water transport and distribution in the PEM fuel cell air cathode and presented some interesting two-phase flow and transport results. However, their model did not include the catalyst layer, the membrane and the anode side.

Instead of assuming two-phase throughout the fuel cell, You and Liu [53,54] assumed that the anode side will remain single phase due to the electro-osmosis water transfer from anode to cathode. The governing equations in the anode side also include the continuity equation, the momentum equation and the species equation. The continuity equation and the momentum equation are similar to those at the cathode side. The species governing equation is

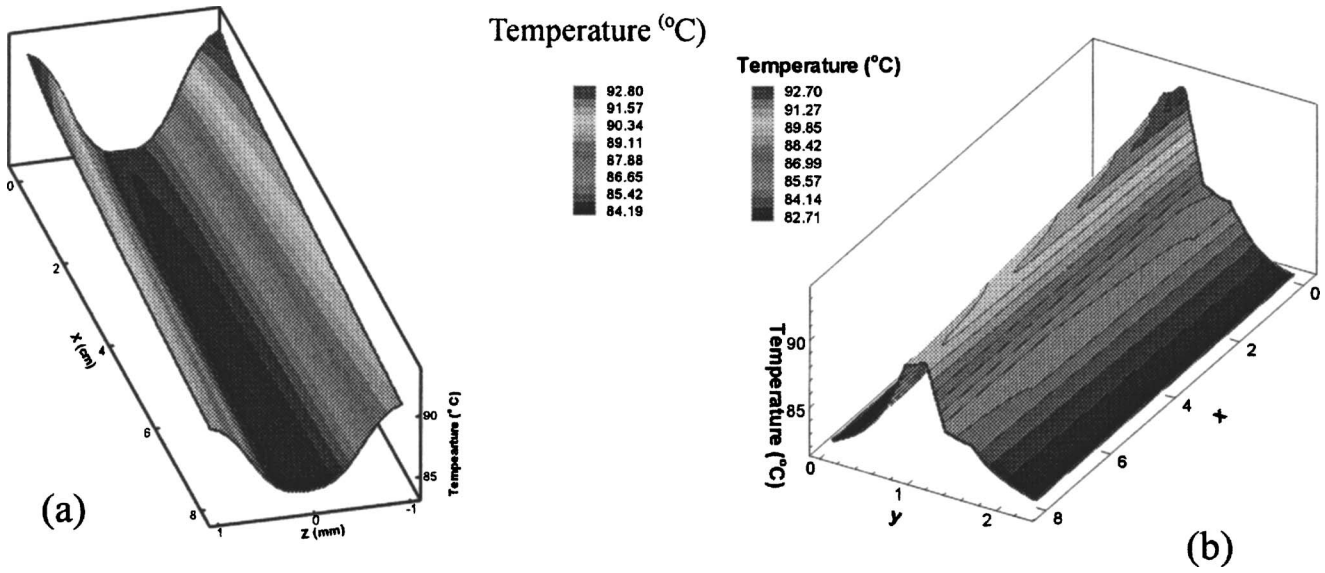

Fig. 15 Temperature distributions (*a*) across section *oxz* and (*b*) across the section *oxy* [17]

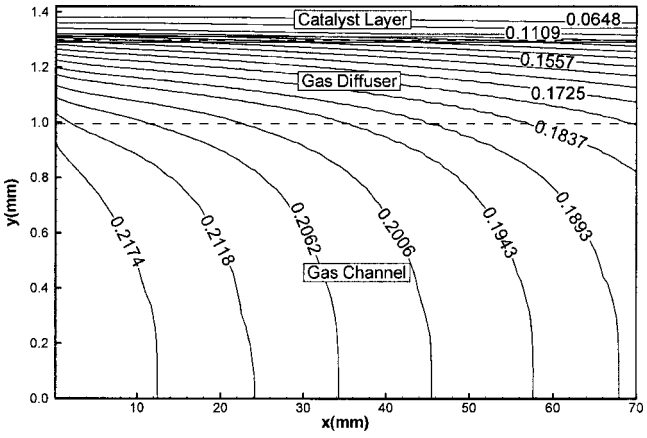

Fig. 16 Oxygen mass fraction in the "two-phase" mixture in the cathode channel, diffusion layer and catalyst layer for the base case with I_{avg}=1.09 A/cm^2 [54]

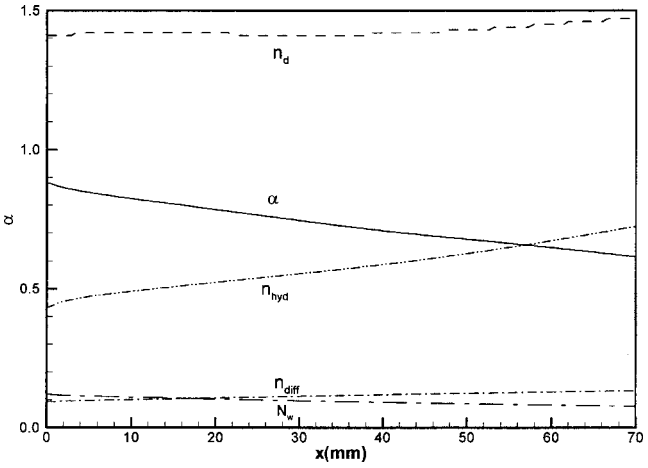

Fig. 18 The net water transfer coefficient α, as well as electro-osmotic, diffusion and hydraulic permeation water transport coefficients across the membrane along the flow direction [54]

$$\varepsilon\frac{\partial}{\partial t}(\rho c_k) + \nabla\cdot(\rho\mathbf{u}c_k) = \nabla\cdot(\varepsilon\rho D_k\nabla c_k) \tag{68}$$

where k denotes species that include hydrogen, water vapor, and other gases such as nitrogen and carbon dioxide.

The governing equations in the cathode side, anode side, catalyst layer, and membrane are solved simultaneously to ensure the coupling of the flow, species, potential and current density distribution in the cathode and anode fluid channel, diffusion layer, catalyst layer, and membrane. Figure 16 shows the concentration contours of oxygen while Fig. 17 presents the water mass fraction in the "two-phase" mixture in the cathode. The net water transfer coefficient, α, as well as the water transfer coefficients due to electro-osmosis, diffusion, and hydraulic permeation across the membrane along the flow direction are shown in Fig. 18.

4 Cell Performance

4.1 Macro Fuel Cells. The performance of PEM fuel cells is known to be influenced by many parameters, such as operating temperature, pressure, and humidification of the gas streams. In order to improve fuel cell performances, it is necessary to understand these parametric effects on fuel cell operations. Systematic experimental data are very valuable for the optimization of fuel cell operating conditions according to their specific fuel cell designs and operation requirements.

In recent years, experiments on PEM fuel cell performances, focusing on different aspects, have been published. Rho et al. [55] carried out performance experiments using different mixtures of oxygen and other inert gases. Jordan et al. [56] studied the effects of diffusion layer parameters on fuel cell performances. Sridhar et al. [57] conducted humidification studies on PEM fuel cell performances.

Wang et al. [58] carried out a series of systematic experiments on a single PEM fuel cell. Polarization curves with different fuel cell temperatures, humidification temperatures, and back pressures were obtained. These polarization curves show the trend of the PEM fuel cell performance with different parameters. Figure 19 shows that the performance of the fuel cell improves with the increasing of the cell temperature and humidification temperatures from 50 to 90°C. As the humidification temperature is equal to the fuel cell temperature, the reactant gases are well humidified. So the main factor affecting the cell performance is fuel cell tem-

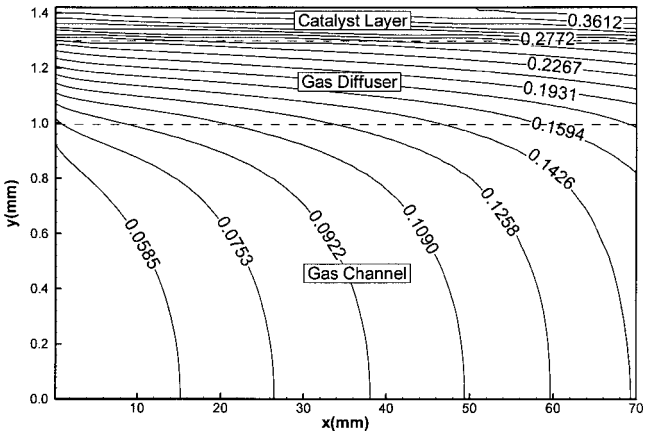

Fig. 17 Water mass fractions in the "two-phase" mixture in the cathode channel, diffusion layer and catalyst layer [54]

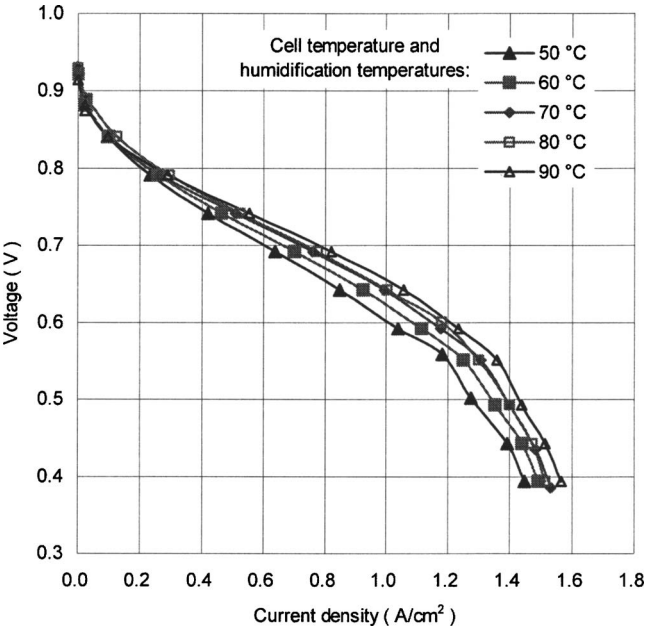

Fig. 19 Polarization curves for different fuel cell temperatures. The anode and cathode humidification temperature are equal to the fuel cell temperature, back pressures are 3 atm on both the anode and cathode sides and flow rates are 1200 sccm on the anode side and 2200 sccm on the cathode side [58]

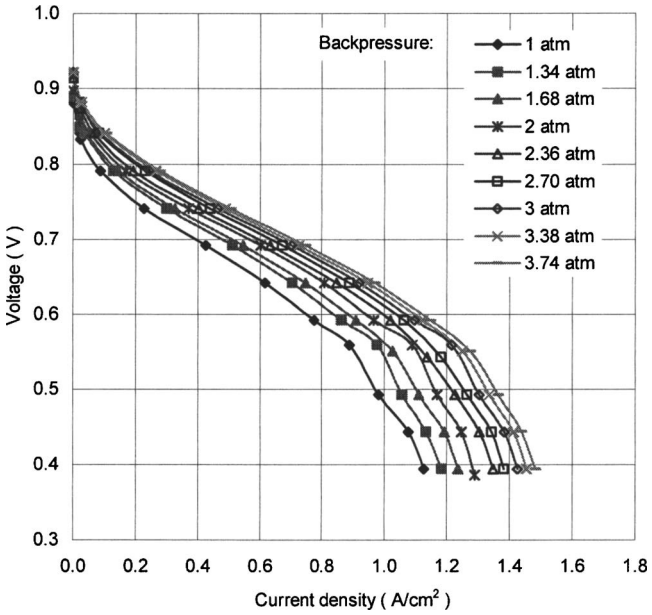

Fig. 20 Polarization curves for different backpressures. The fuel cell temperature and humidification temperatures on both the anode and cathode sides are 70°C, flow rates are 1200 sccm on the anode side and 2200 sccm on the cathode side [58].

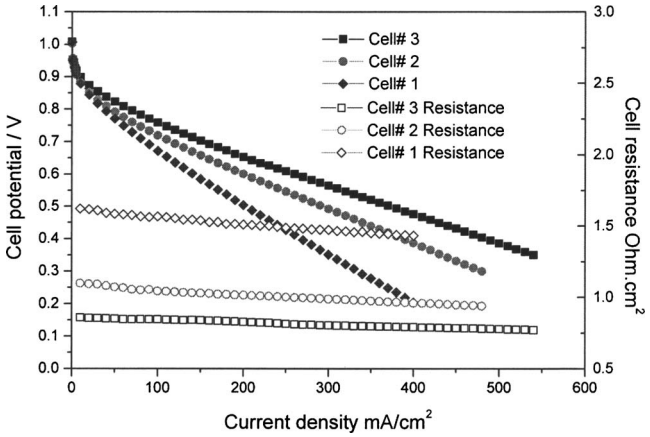

Fig. 21 Effect of current collector's thickness on cell performance [62]

perature. The slope of the linear portion of the curve decreases as fuel cell temperature increases. This is due to the increase of the proton conductivity and the exchange current density with the increase of the cell temperature. The limit current density increases with the increase of the fuel cell temperature as well, due to the improvement of mass transport. Figure 20 shows polarization curves with different operating pressures ranging from 1 to 3.74 atm. It is shown that the performance of the fuel cell improves with the increase of pressure. Based on the experimental studies, Wang et al. [58] concluded that when enough humidification is provided, the performance of the PEM fuel cell improves with the increase of operation temperature; when fuel cell operating temperature is higher than the gas stream humidification temperature, the performance of the fuel cell can decrease, and this is especially true in the low current density region; the anode humidification temperature has considerable effects on fuel cell performances: in the low current density region, the lower the degree of humidification, the lower the fuel cell performances while at high current densities, the effect of anode humidification temperature is not significant; the cathode humidification temperature has no significant effects on fuel cell performances, especially at high current densities; the performance of the fuel cell increases with the increase of pressure due to the increase of the exchange current density and the reactant gas partial pressures.

It must be stressed that some of the above-noted results may not be universally applicable. Results from different fuel cell designs may very well be different. For instance, if a thicker membrane is used, the diffusive water transport will be low and the difference in water content across the membrane will be high due to the predominant role of electro-osmosis, especially at high current densities. On the other hand, for very thin membranes, the water diffusion may become dominant and humidification in the anode side may not be as critical.

4.2 Micro Fuel Cells. In recent years, there has been a great deal of interest in the development of micro fuel cells to replace batteries as the portable power source. Micro fuel cells differ from the macro fuel cells in the materials used for the bi-polar plates. While a macro fuel cell uses graphite as polar plates which are relatively thick (about 5 mm), a micro fuel cell uses silicon substrates (about 0.5 mm thick) as its polar plates. The microchannels in the silicon wafer are fabricated by MEMS technologies. There are two types of micro fuel cells that operate at room temperature: the μPEMFC that uses H_2 as fuel and air (or O_2) as oxidant while the μDMFC (the micro direct methanol fuel cell) that uses diluted methanol as fuel and air (or O_2) as oxidant.

4.2.1 Single Cells. Kelley et al. [59] found that the cell performance of their 0.25 cm^2 μDMFC was slightly lower than that of their 25 cm^2 macro DMFC with graphite as polar plates. Meyers et al. [60] suggested that the higher resistance in the polar plates of the micro fuel cells was responsible for their lower cell performance. Since the electrical current in the micro fuel cell is derived from the gold layer acting as a current collector in the silicon wafer, it is beneficial to reduce the resistance of the current collector. For this purpose, Yu et al. [61–63] sputtered a Cu/Au composite layer on the silicon substrates as the current collector. The reason for choosing the Cu/Au composite material to replace Au as the current collector is not only because the resistivity of Cu is lower than that of Au, but also because it would reduce cost. In this design, the current generated by the micro fuel cell was derived from lateral contact pads, which have the same thickness as that of the current collector. Figure 21 shows the effects of material and thickness of the current collector on cell performance of a μPEMFC. The thickness and materials of the current collectors for Cells 1, 2, and 3 are: (a) 0.5 μm Au, (b) 1.4 μm Cu/0.2 μm Au, and (c) 1.5 μm Cu/0.9 μm Au, respectively. As shown in the figure, the thicker the current collector, the better its cell performance. This is because the thicker the current collector the thicker the thickness of the lateral contact pads, and the smaller the cell resistance thus resulting in better performance. The improved cell performance by increasing the thickness of the current collector can also be seen from the power density versus current density curves presented in Figure 22.

Figure 23 is a comparison of performance between micro and macro PEM fuel cells [61], where the same MEA was used. The only difference between these two fuel cells was the materials used in the polar plates and the size of the flow channels. A micro fuel cell used a silicon wafer with a smaller channel size (1/9 of that of macro fuel cell) covered with a thin composite layer of 1.5 μm Cu/0.9 μm Au sputtered on its surface (Cell 3 in Fig. 21). As seen from Fig. 23, although the micro fuel cell had a cell resistance slightly higher than that of a macro fuel cell, the cell performance of the micro fuel cell (with smaller channels) was higher than that of a macro fuel cell for the whole current density range, especially at the diffusion-limiting range. One explanation is that the higher flow velocity in the smaller size of the microchannels facilitates reactant diffusion into the catalyst layer and

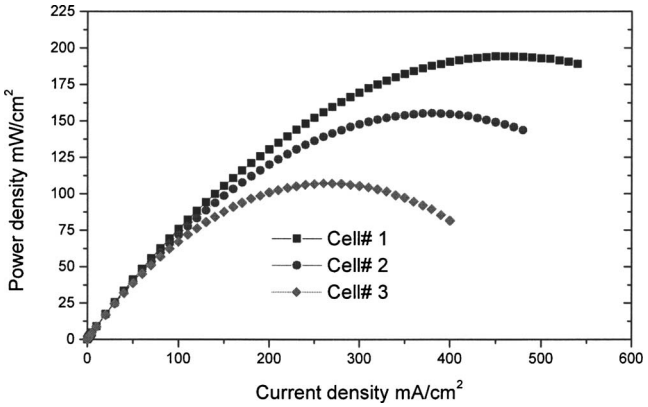

Fig. 22 Power density versus current density curves of Cells 1, 2, and 3, respectively [62]

convective removal of the water at the cathode side, both of which enhance the mass transfer process [61,64]. Another reason as given by Cha et al. [64] is that smaller microchannels make the reactant concentration more uniformly distributed across the whole diffusion layer, eliminating inefficiency that would normally be caused by obstructed "dead-zones" behind the dividing ribs. The numerical results with similar trend were also presented by Cha et al. [64], who showed that the cell performance (with pure H_2 and O_2) increased as the channel size was decreased from 500 to 5 μm. It is also interesting to note that smaller channels not only extend the gas diffusion limit, but also affect the so-called linear IR region, and thereby increase the voltage levels in that region. In the same paper, Cha et al. [64] obtained experimental data for cell performance using microchannels with two different hydraulic diameters of 20 and 100 μm. The data showed that the cell with smaller channels had higher limiting current and peak power. Most recently, Yen et al. [65] and Lu et al. [66] also used the Cu/Au (3.0 μm Cu and 0.5 μm Au) composite current collector on the silicon wafer with microchannels (750 $\times$400 μm) in their μDMFC operating with methanol/air at ambient pressure. They also observed an improvement in ohmic polarization and cell performance of their μDMFC.

4.2.2 Fuel Cell Stack. A single micro fuel cell usually produces a voltage lower than 1.0 V. Therefore, several cells are connected in series in order to achieve a higher voltage output for practical applications. Instead of a vertical *back-to-back* stack assembly as in a conventional fuel cell stack, Cohen [67] arranged micro fuel cells in a *side-by-side* configuration in which cells are

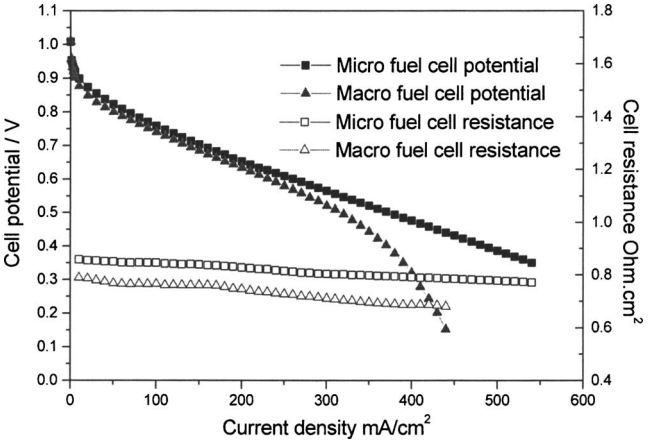

Fig. 23 Polarization and cell resistance curves of micro and macro fuel cells [62]

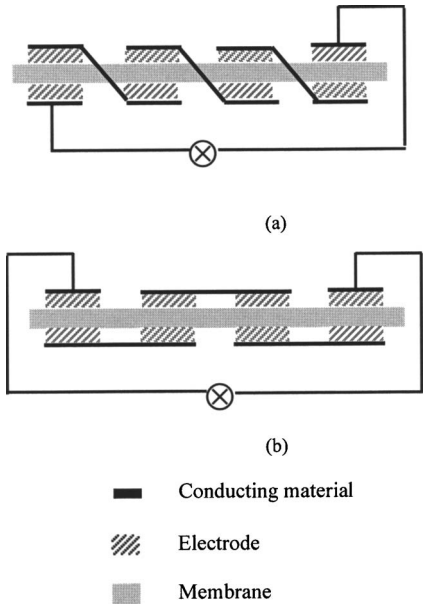

Fig. 24 Fuel cell stack of banded and flip-flop configuration

connected on the same plane, forming a planar array of fuel cells. A planar array of micro fuel cells with banded structure connector was used by Heinzel et al. [68]. This three-dimensional banded structure connects from upside of one cell to downside of the adjacent cell (see Fig. 24(*a*)). An improved method with flip-flop configuration for connecting several cells in series in a planar array was proposed by Lee et al. [69], which was later used by Yu et al. [61,62]. In the flip-flop configuration, the connection from the cathode of one cell to the anode of the next cell was located on the same plane (see Fig. 24(*b*)), which does not need additional wiring. The flip-flop structure is better than the banded structure from the points of view of simpler construction, lower electrical resistance, and less local sealing problems. However, the fuel and oxidant must be alternately supplied in a flip-flop configuration, which presents a challenging design problem. The best design of a fuel cell stack should be based on cost and reliability issues.

5 Concluding Remarks

In this review, the fundamental transport phenomena in the different regions of a fuel cell were examined first. Representative PEMFC models together with some experimental studies were then discussed. The focus of the theoretical modeling is placed on the macroscopic approaches. The merits of these models cannot be directly compared to each other, since most of the models would compare well with experimental polarization data through adjustment of some parameters used in the calculation. In general, it can be assumed that the more complex models, based on fundamental physical laws with fewer simplifying assumptions, may be closer to the reality. However, this may not always be true due to the uncertainties of the larger number of parameters involved, especially the effective physical properties in different components. Models with different complexities have different applications. For instance, for a fuel cell energy system study, the simplest models, such as the zero-dimensional models, may be the best choice; while for detailed optimization study of the MEA, one may need a more sophisticated model. Hopefully, this review provides the readers with a systematic overview of the transport phenomena in different regions of a PEMFC, how they have been modeled, and what remains to be done. In recent years, fuel cell modeling and prediction have played a key role in the understanding of transport phenomena in PEMFC and will remain to be an essential tool in fuel cell research and development.

Nomenclature

a = effective catalyst area per unit volume, m^2/m^3
a_w = water activity
$(ai_0^{ref})_a$ = reference exchange current density times area at anode, A/m^3
$(ai_0^{ref})_c$ = reference exchange current density times area at cathode, A/m^3
b = Tafel slop
c = mole concentration of the gas mixture, mol/m^3
$c_{O,ref}$ = reference mole concentration of oxygen
c_p = specific heat at constant pressure, J/(kg K)
c_w = mole concentration of water at anode, mol/m^3
D = diffusivity, m^2/s, cm^2/s
D_w = capillary diffusivity of water, m^2/s, cm^2/s
E = fuel cell voltage, V
E_0 = thermodynamic open circuit potential, V
F = Faraday constant, 96487 C/mol
I, i = current density, A/m^2
i_0 = exchange current density, A/m^2
j = transfer current density, A/m^3
$\mathbf{j_g}$ = diffusive mass flux (kg/m^2 s)
k = thermal conductivity, W/(m K)
k_m = mass transfer rate through condensation or evaporation
k_φ = electrokinetic permeability, m^2
k_p = hydraulic permeability of the porous medium, m^2
M = molecular weigh, g/mol, kg/mol
M_m = molecular weigh of membrane, g/mol, kg/mol
N = mass flux, mol/m^2 s
n_d = osmosis drag coefficient
p = pressure, partial pressure, Pa
p_{sat} = saturation pressure, Pa
R = universal gas constant, 8314 J/(mol K)
R = Resistance
$r^{(2)}$ = coefficient in the generalized Darcy's equation
S_h = heat generation term of the energy equation
q = specific discharge
Q = heat generation
S = source term of the transport equations
s = phase saturation
T = temperature, K
U = cell voltage, V
$\mathbf{V}, \mathbf{u}$ = velocity vector, m/s
V = volume
u, v, w = velocity components, m/s
w_c = water content
x = dimension along gas flow direction
y = dimension along the direction from cathode to anode
z = dimension along the direction across the gas channel and shoulder
z_i = charge number of species i
X = mole fraction

Greek Symbols

ρ = density, kg/m^3
η = electrode overpotential, V
σ = ionic/electric conductivity, $1/\Omega m$
γ = multiphase correction factor
α = net water flux per proton flux
ε = porosity
μ = viscosity, kg/(m s)
λ = water content in ionomer, kmol H_2O $kmol^{-1}$ SO_3
α_a = anodic transfer coefficient
α_c = cathodic transfer coefficient
ϕ = potential, V
Γ = diffusion coefficient for general transport equation
τ = tortuosity
Ψ = general variable for transportation Eq. (50)

Subscripts and Superscripts

a = anode, anodic
avg = averages
c = cathode, cathodic
ct = catalyst layer
dry = dry membrane
e = electron
eff = effective, accounting for porous medium
g = gas phase
gr = graphite
h = hydrogen
H^+ = proton
H_2 = hydrogen
ion = ionomer
k = kth component
l = liquid phase
m = membrane
N_2 = nitrogen
O_2 = oxygen
p = porous media
ref = reference
s = solid
sat = saturated condition
v = vapor
w = water

References

[1] Larmine, A. B., and Dicks, A., 2003, *Fuel Cell Systems Explained*, John Wiley, New York.
[2] Dagan, G., 1989, *Flow and Transport in Porous Formations*, Springer, Berlin.
[3] Bernardi, D. M., and Verbrugge, M. W., 1991, "Mathematical-Model of a Gas-Diffusion Electrode Bonded to a Polymer Electrolyte," AIChE J., **37**, pp. 1151–1163.
[4] Gurau, V., Barbir, F., and Liu, H. T., 2000, "An Analytical Solution of a Half-Cell Model for PEM Fuel Cells," J. Electrochem. Soc., **147**, pp. 2468–2477.
[5] Nam, J. H., and Kaviany, M., 2003, "Effective Diffusivity and Water-Saturation Distribution in Single- and Two-Layer PEMFC Diffusion Medium," Int. J. Heat Mass Transfer, **46**, pp. 4595–4611.
[6] Meng, H., and Wang, C. Y., 2004, "Electron Transport in PEFCs," J. Electrochem. Soc., **151**, pp. A358–A367.
[7] Springer, T. E., Zawodzinski, T. A., and Gottesfeld, S., 1991, "Polymer Electrolyte Fuel-Cell Model," J. Electrochem. Soc., **138**(8), pp. 2334–2342.
[8] Laconti, A. B., Fragala, A. R., and Boyack, J. R., 1977, "Electrode Materials and Processes for Energy Conversion and Storage," in *ECS Processing*, Pennington, NJ.
[9] Zawodzinski, T. A. et al., 1993, "Water Transport-Properties of Various Fuel-Cell Ionomers," *Abstracts of Papers of The American Chemical Society*, American Chemical Society, Washington, D.C., Vol. 205.
[10] Nguyen, T. V., and White, R. E., 1993, "A Water and Heat Management Model for Proton-Exchange-Membrane Fuel-Cells," J. Electrochem. Soc., **140**, pp. 2178–2186.
[11] Dutta, S., Shimpalee, S., and Van Zee, J. W., 2000, "Three-Dimensional Numerical Simulation of Straight Channel PEM Fuel Cells," J. Appl. Electrochem., **30**, pp. 135–146.
[12] Wang, G. G., and Dong, Z. M., 2000, "Design Optimization of a Complex Mechanical System Using Adaptive Response Surface Method," Trans. Can. Soc. Mech. Eng., **24**, pp. 295–306.
[13] Zhou, T., and Liu, H. T., 2000, "3-D Model of Proton Exchange Membrane Fuel Cells," in ASME 2000, Heat Transfer Division, Orlando, Florida.
[14] Bernardi, D. M., and Verbrugge, M. W., 1992, "A Mathematical-Model of the Solid-Polymer-Electrolyte Fuel-Cell," J. Electrochem. Soc., **139**, pp. 2477–2491.
[15] Gurau, V., Liu, H. T., and Kakac, S., 1998, "Two-Dimensional Model for Proton Exchange Membrane Fuel Cells," AIChE J., **44**, pp. 2410–2422.
[16] Zhou, T., and Liu, H. T., 2003, "Performance Modeling of PEM Fuel Cell Operated on Reformate," in Fuel Cell Science, Engineering And Technology., pp. 233–240.
[17] Zhou, T., and Liu, H. T., 2001, "A General Three-Dimensional Model for Proton Exchange Membrane Fuel Cells," Int. J. Transp. Phenom., **3**, pp. 177–198.
[18] Zhou, T., and Liu, H. T., 2002, "Heat Transfer Enhancement in Fuel Cells With

Interdigitated Flow Field Design," Progress Computational Fluid Dynamics, **2**, pp. 97–105.
[19] Singh, D., Lu, D. M., and Djilali, N., 1999, "A Two-Dimensional Analysis of Mass Transport in Proton Exchange Membrane Fuel Cells," Int. J. Eng. Sci., **37**, pp. 431–452.
[20] Berning, T., Lu, M. D., and Djilali, N., 2002, "Three-Dimensional Computational Analysis of Transport Phenomena in a PEM Fuel Cell," J. Power Sources, **106**, pp. 284–294.
[21] Um, S., Wang, C. Y., and Chen, C. S., 2000, "Computational Fluid Dynamics Modeling of Proton Exchange Membrane Fuel Cells," J. Electrochem. Soc., **147**, pp. 4485–4493.
[22] Zawodzinski, T. A. et al., 1993, "Water-Uptake by and Transport Through Nafion® 117 Membranes," J. Electrochem. Soc., **140**, pp. 1041–1047.
[23] Fuller, T. F., and Newman, J., 1993, "Water and Thermal Management in Solid-Polymer-Electrolyte Fuel-Cells," J. Electrochem. Soc., **140**(5), pp. 1218–1225.
[24] Yi, J. S., and Nguyen, T. V., 1998, "An Along-The-Channel Model for Proton Exchange Membrane Fuel Cells," J. Electrochem. Soc., **145**, pp. 1149–1159.
[25] Parthasarathy, A. et al., 1992, "Pressure-Dependence of the Oxygen Reduction Reaction at the Platinum Microelectrode Nafion Interface—Electrode-Kinetics and Mass-Transport," J. Electrochem. Soc., **139**, pp. 2856–2862.
[26] Boyer, C. et al., 1998, "Measurements of Proton Conductivity in the Active Layer of PEM Fuel Cell Gas Diffusion Electrodes," Electrochim. Acta, **43**, pp. 3703–3709.
[27] Cwirko, E. H., and Carbonell, R. G., 1992, "Interpretation of Transport-Coefficients in Nafion Using a Parallel Pore Model," J. Membr. Sci., **67**, pp. 227–247.
[28] Din, X. D., and Michaelides, E. E., 1998, "Transport Processes of Water and Protons Through Micropores," AIChE J., **44**, pp. 35–47.
[29] Eikerling, M., and Kornyshev, A. A., 2001, "Proton Transfer in a Single Pore of a Polymer Electrolyte Membrane," J. Electroanal. Chem., **502**, pp. 1–14.
[30] Weber, A. Z., and Newman, J., 2004, "Modeling Transport in Polymer-Electrolyte Fuel Cells," Chem. Rev., **104**, pp. 4679–4726.
[31] Amphlett, J. C. et al., 1995, "Performance Modeling of the Ballard-Mark-IV Solid Polymer Electrolyte Fuel-Cell.2. Empirical-Model Development," J. Electrochem. Soc., **142**, pp. 9–15.
[32] Verbrugge, M. W., and Hill, R. F., 1990, "Analysis of Promising Perfluorosulfonic Acid Membranes for Fuel-Cell Electrolytes," J. Electrochem. Soc., **137**, pp. 3770–3777.
[33] Verbrugge, M. W., and Hill, R. F., 1990, "Ion and Solvent Transport in Ion-Exchange Membranes.1. A Macrohomogeneous Mathematical-Model," J. Electrochem. Soc., **137**, pp. 886–893.
[34] Bernardi, D. M., 1990, "Water-Balance Calculations for Solid-Polymer-Electrolyte Fuel-Cells," J. Electrochem. Soc., **137**, pp. 3344–3350.
[35] Springer, T. E., Wilson, M. S., and Gottesfeld, S., 1993, "Modeling and Experimental Diagnostics in Polymer Electrolyte Fuel-Cells," J. Electrochem. Soc., **140**, pp. 3513–3526.
[36] Singh, D., Lu, D. M., and Djilali, N., 1996, "Numerical Analysis of Transport Processes in Proton Exchange Membrane Fuel Cells," in 1st International Energy and Environment Symposium, Karadeniz Technical University, Trabzon, Turkey.
[37] Yi, J. S., and Nguyen, T. V., 1999, "Multicomponent Transport in Porous Electrodes of Proton Exchange Membrane Fuel Cells Using the Interdigitated Gas Distributors," J. Electrochem. Soc., **146**, pp. 38–46.
[38] Patankar, S. V., 1980, *Numerical Heat Transfer and Fluid Flow*, Hemisphere, New York.
[39] Kulikovsky, A. A., Divisek, J., and Kornyshev, A. A., 1999, "Modeling the Cathode Compartment of Polymer Electrolyte Fuel Cells: Dead and Active Reaction Zones," J. Electrochem. Soc., **146**, pp. 3981–3991.
[40] Kazim, A., Liu, H. T., and Forges, P., 1999, "Modelling of Performance of PEM Fuel Cells With Conventional and Interdigitated Flow Fields," J. Appl. Electrochem., **29**, pp. 1409–1416.
[41] Nguyen, T. V., 1996, "A Gas Distributor Design for Proton-Exchange-Membrane Fuel Cells," J. Electrochem. Soc., **143**, pp. L103–L105.
[42] Natarajan, D., and Van Nguyen, T., 2001, "A Two-Dimensional, Two-Phase, Multicomponent, Transient Model for the Cathode of a Proton Exchange Membrane Fuel Cell Using Conventional Gas Distributors," J. Electrochem. Soc., **148**, pp. A1324–A1335.
[43] Yi, J. S., and Van Nguyen, T., 1999, "Multicomponent Transport in Porous Electrodes of Proton Exchange Membrane Fuel Cells Using the Interdigitated Gas Distributors," J. Electrochem. Soc., **146**, pp. 38–45.
[44] Wang, Z. H., Wang, C. Y., and Chen, K. S., 2000, "A Pseudo-Homogeneous Model for Cathode Catalyst Layer in PEM Fuel Cells," in ASME HTD, Orlando, Florida.
[45] Dutta, S., Shimpalee, S., and Van Zee, W. J., 2001, "Numerical Prediction of Mass-Exchange Between Cathode and Anode Channels in a PEM Fuel Cell," Int. J. Heat Mass Transfer, **44**, pp. 2029–2042.
[46] Shimpalee, S., and Dutta, S., 2000, "Numerical Prediction of Temperature Distribution in PEM Fuel Cells," Numer. Heat Transfer, Part A, **38**, pp. 111–128.
[47] Natarajan, D., and Nguyen, T. V., 2001, "A Two-Dimensional, Two-Phase, Multicomponent, Transient Model for the Cathode of a Proton Exchange Membrane Fuel Cell Using Conventional Gas Distributors," J. Electrochem. Soc., **148**, A1324–A1335.
[48] Zhou, T. H., and Liu, H. T., 2004, "A 3D Model for PEM Fuel Cells Operated on Reformate," J. Power Sources, **138**, pp. 101–110.
[49] Zhou, T., and Liu, H. T., 2002, "Development and Simplification of a Three-Dimentional PEM Fuel Cell Model," in ESDA 2002, 6th Biennial Conference on engineering Systems Design and Analysis, Istanbul, Turkey.
[50] He, W. S., Yi, J. S., and Van Nguyen, T., 2000, "Two-Phase Flow Model of the Cathode of PEM Fuel Cells Using Interdigitated Flow Fields," AIChE J., **46**, pp. 2053–2064.
[51] Wang, C. Y., and Cheng, P., 1996, "A Multiphase Mixture Model for Multiphase, Multicomponent Transport in Capillary Porous Media, 1. Model Development," Int. J. Heat Mass Transfer, **39**, pp. 3607–3618.
[52] Wang, Z. H., Wang, C. Y., and Chen, K. S., 2001, "Two-Phase Flow and Transport in the Air Cathode of Proton Exchange Membrane Fuel Cells," J. Power Sources, **94**, pp. 40–50.
[53] You, L. X., and Liu, H. T., 2000, "A Pseudo-Homogeneous Model for Cathode Catalyst Layer in PEM Fuel Cells," in ASME 2000, Orlando, Florida.
[54] You, L. X., and Liu, H. T., 2002, "A Two-Phase Flow and Transport Model for the Cathode of PEM Fuel Cells," Int. J. Heat Mass Transfer, **45**, pp. 2277–2287.
[55] Rho, Y. W., Srinivasan, S., and Kho, Y. T., 1994, "Mass-Transport Phenomena in Proton-Exchange Membrane Fuel-Cells Using O_2/He, O_2/Ar, And O_2/N_2 Mixtures.2. Theoretical-Analysis," J. Electrochem. Soc., **141**, pp. 2089–2096.
[56] Jordan, L. R. et al., 2000, "Diffusion Layer Parameters Influencing Optimal Fuel Cell Performance," J. Power Sources, **86**, pp. 250–254.
[57] Sridhar, P. et al., 2001, "Humidification Studies on Polymer Electrolyte Membrane Fuel Cell," J. Power Sources, **101**, pp. 72–78.
[58] Wang, L., Husar, A., Zhou, T., and Liu, H. T., 2003, "A Parametric Study of PEM Fuel Cell Performances," Int. J. Hydrogen Energy, **28**, pp. 1263–1272.
[59] Kelley, S. C., Deluga, G. A., and Smyrl, W. H., 2000, "A Miniature Methanol/Air Polymer Electrolyte Fuel Cell," Electrochem. Solid-State Lett., **3**, pp. 407–409.
[60] Meyers, J. P., and Maynard, H. L., 2002, "Design Considerations for Numaturized PEM Fuel Cells," J. Power Sources, **109**, pp. 76–88.
[61] Yu, J. R. et al., 2003, "Fabrication of a Miniature Twin-Fuel-Cell on Silicon Wafer," Electrochim. Acta, **48**, pp. 1537–1541.
[62] Yu, J. R., Cheng, P., Ma., Z. Q., and Yi, B. L., 2003, "Fabrication of Miniature Silicon Wafer Fuel Cells With Improved Performance," J. Power Sources, **124**, pp. 40–46.
[63] Yu, J. R., Cheng, P., Ma, Z. Q., and Yi, B. L., 2003, "Fabrication of Miniature Silicon Wafer Fuel Cells Using Micro Fabrication Technologies," 1st International Conference on Fuel Cell Science, Engineering and Technology, Rochester, New York, April 21–23.
[64] Cha, S. W., Lee, S. J., Park, Y. I., and Prinz, F. B., 2003, "Investigation of Transport Phenomena in Micro Flow Channels for Miniature Fuel Cells," in Ist International Conference on Fuel Cell Science, Engineering and Technology, Rochester, New York.
[65] Yen, T. J., Fang, N., Zhang, X., Lu, G. Q., and Wang, C. Y., 2003, "A Micro Methanol Fuel Cell Operating at Near Room Temperature," Appl. Phys. Lett., **38**, pp. 4056–4058.
[66] Lu, C. et al., 2002, "Development of Solid Oxide Fuel Cells for the Direct Oxidation of Hydrocarbon Fuels," Solid State Ionics, **152**, pp. 393–397.
[67] Cohen, R., 1991, Plaque fuel cell stack, United States.
[68] Heinzel, A. et al., 1998, "Membrane Fuel Cells-Concepts and System Design," Electrochim. Acta, **43**, pp. 3817–3820.
[69] Lee, S. J. et al., 2002, "Design and Fabrication of a Micro Fuel Cell Array With 'Flip-Flop' Interconnection," J. Power Sources, **112**, pp. 410–418.

Analysis of Intermediate Temperature Solid Oxide Fuel Cell Transport Processes and Performance

Jinliang Yuan

Bengt Sundén

Division of Heat Transfer,
Lund Institute of Technology (LTH),
Box 118,
22100 Lund, Sweden

A new trend in recent years is to reduce the solid oxide fuel cell (SOFC) operating temperature to an intermediate range by employing either a thin electrolyte, or new materials for the electrolyte and electrodes. In this paper, a numerical investigation is presented with focus on modeling and analysis of transport processes in planar intermediate temperature (IT, between 600 and 800°C) SOFCs. Various transport phenomena occurring in an anode duct of an ITSOFC have been analyzed by a fully three-dimensional calculation method. In addition, a general model to evaluate the stack performance has been developed for the purpose of optimal design and/or configuration based on specified electrical power or fuel supply rate. [DOI: 10.1115/1.2098847]

1 Introduction and Motivation

One of the main factors that have influenced the development of fuel cells has been the increasing concern about the environmental consequences of fossil fuel utilization in the production of electricity and for the propulsion of vehicles. An increased global awareness of various advance impacts on the environment from various industries and the need for sustainable energy conversion devices have also contributed to the recent focus on fuel cells. Various types of fuel cells have been actively developed for different applications. In general, high temperature fuel cells (e.g., solid oxide fuel cells—SOFCs hereafter) can employ both hydrogen and hydrocarbon as fuels, because hydrocarbon fuels can be directly introduced with internal reforming, and integrated thermal management to achieve high system efficiencies.

An important component in a planar SOFC stack is the interconnect (or impermeable bipolar plate in the literature). It is designed to distribute fuel and oxidant to anodes and cathodes, respectively, and to provide electrical contacts between adjacent cells as well. In general, the operating temperature of SOFCs is affected by the specific application (stationary, mobile, and transportation), type of fuels and properties of electrolytes. If SOFCs are used in an integrated power generation system with a gas turbine, the exhaust gas from the stack should be higher than 850°C to achieve higher efficiency, based on system requirements [1]. For this case, more expensive materials should be employed for the interconnect and other relevant components/sub-systems (e.g., recuperators) in the integrated system, which result in significant difficulties for cost reduction at present.

As a general requirement, the combined area specific resistivity (ASR) of the cell components (anode-electrolyte-cathode) for all fuel cells should be below $0.5\ \Omega\,\mathrm{cm}^2$ (ideally approach $0.1\ \Omega\,\mathrm{cm}^2$) to ensure high power density and minimize the amount of material per kW of power supply [1]. For a certain material, electrolyte ASR depends on its thickness, specific ionic conductivity, and operating temperature. Most important, the contribution of the electrolyte to the total combined ASR ($=\delta/\sigma$ where δ is electrolyte thickness and σ specific ionic conductivity) is typically required to be less than $0.15\ \Omega\,\mathrm{cm}^2$. To meet this requirement, the maximum thickness of the electrolyte is about 150 μm when conventional yttria-stabilized zirconia (YSZ) electrolyte is self-supported and operating temperature is about 950°C [1].

To reduce the cost and increase life expectency, many efforts have been performed to reduce the SOFC operating temperatures to intermediate range (between 600 and 800°C, ITSOFC hereafter). Two technical routes for ITSOFCs have emerged, as shown in Table 1.

The first case in Table 1 shows a design in which thin film technology is employed with conventional YSZ for the electrolyte. When the working temperature is reduced to around 700°C, the specific ionic conductivity σ is about 0.01 S/cm [1], and then maximum thickness allowed for conventional YSZ electrolyte is 8–15 μm. The electrode-supported (e.g., anode-supported) configuration is usually employed for this thin electrolyte structure [2,3]. The second case employs new materials with very high ionic conductivity ($\sigma=1.0$ S/cm at 700°C). If a thick layer electrolyte (around 500 μm thick) is adopted, the contribution to the total ASR is only about $0.05\ \Omega\,\mathrm{cm}^2$, which is still lower than that of the conventional high temperature SOFCs (HTSOFCs hereafter).

In this study, a fully three-dimensional numerical investigation is presented for gas flow and heat transfer in an anode duct of the first design (anode-supported ITSOFC). The duct under investigation includes the porous layer, gas flow duct, and the solid interconnects. By calculating fuel gas species, the electrochemical reactions related mass generation and consumption have been identified and applied. Moreover, the variable thermal-physical properties of the fuel mixture (H_2+H_2O) have also been taken into account. The unique thermal boundary conditions of the fuel cell are employed in the investigation as well. The emphasis is put on the interesting parameters such as pressure drop and Nusselt number, as well as the species convection and diffusion in the porous layer. In addition, a general model to evaluate the performance of ITSOFC stack with new materials is developed for the purpose of optimal design and/or configuration based on specified electrical power or fuel supply rate.

2 Problem Statement

For the case of small SOFC stacks without a gas turbine integration, the operating temperature should be at a level where the electrode kinetics and internal resistance of the stack are not affected. These small stacks can be used as combined heat and

Contributed by the Heat Transfer Division of ASME for publication in the JOURNAL OF HEAT TRANSFER. Manuscript received June 7, 2004; final manuscript received March 2, 2005. Review conducted by Stefan Thynell.

Table 1 Various technical routes for planar design ITSOFCs

Case	Electrolyte Material	Specific Ionic Conductivity at 700 °C (*S/cm*)	Electrolyte Thickness allowed (μm)	Proposed Design
1	Conventional YSZ	0.01	8-15	Electrode-supported
2	Composite ceramics	1.0	500	Electrolyte-supported

power units for a stand-by power supply, and/or auxiliary power unit for additional power requirements in vehicles. As expected, ITSOFCs may offer advantages over HTSOFCs, such as mechanical robustness against fast thermal cycles and thermal stresses, lower material and manufacturing costs, system compactness as a result of less critical requirement on the associated components (e.g., heat exchangers).

2.1 The Fundamentals of Various Processes in New Material ITSOFCs. For new material ITSOFCs, commercial $Gd_{0.1}Ce_{0.9}O_{1.95}$ (GDC) powder is used as the electrolytes, while platinum and silver pastes are used for the fuel cell anode and cathode, respectively. As mentioned earlier, new material ITSOFC offers higher Nernst voltage and allows the use of less expensive stainless steels (replacing expensive super-alloys used in HTSOFC) for the interconnect, gaskets, and associated components/sub-systems. For this case, it may avoid the high cost in conventional HTSOFCs [4]. Moreover, new material ITSOFC may possess wide fuel flexibilities, such as pure hydrogen, hydrocarbons, natural gas, biogas, and gas derived from coal [4].

2.1.1 Internal Reforming Reactions. With the high heat generation in the new material ITSOFC stack, it is possible to have internal reforming of bio fuels at the anode of the cells with water/steam. Internal reforming can be considered to occur at the anode and be separated from the fuel cell reaction. Because the section of the anode where reforming occurs is adjacent to the place where the electrochemical reaction occurs, the heat from the fuel cell electrochemical reaction is supplied for the reforming reaction by internal heat transfer with minimal losses.

Methane and carbon monoxide from biomass production can be reformed into H_2 by the following reactions [5]

$$CH_4 + H_2O \rightarrow CO + 3H_2 \quad \Delta H = 206 \text{ kJ/mol} \tag{1}$$

$$CO + H_2O \rightarrow CO_2 + H_2 \quad \Delta H = -41 \text{ kJ/mol} \tag{2}$$

Equation (2) is usually referred to as water-gas shift reaction. The overall reforming reaction is

$$CH_4 + 2H_2O \rightarrow CO_2 + 4H_2 \tag{3}$$

It should be mentioned that the above-noted process in Eq. (1) is endothermic and the overall balance of the reaction requires external heat input. Excess steam and heat are required to shift the reaction equilibrium to the right and maximize the hydrogen generation from bio fuels.

2.1.2 Electrochemical Reactions. Electrochemical reactions in new material ITSOFCs are by either H^+ or O^{2-} ionic transmission through the electrolyte, while only by O^{2-} ionic transmission in conventional SOFCs. The half reactions at the electrodes of ITSOFCs are as follows:

$$\text{Anode:} \quad H_2 + O^{2-} \rightarrow H_2O + 2e^-$$

$$2H_2 \rightarrow 4H^+ + 4e^-$$

$$\text{Cathode:} \quad O_2 + 2e^- \rightarrow O^{2-}$$

$$O_2 + 4e^- + 4H^+ \rightarrow 2H_2O$$

The overall reaction is

$$\tfrac{1}{2}O_2 + H_2 \rightarrow H_2O \tag{4}$$

The above-noted reactions produce a significant amount of water at both the anode and cathode during operation, which is confirmed experimentally. This is an indication of combined ion conduction of proton and oxygen ions through the electrolyte. The combined ion transport processes correspond to new electrochemical processes. Furthermore, the combined ion conduction with higher ion concentrations/flows can enhance the fuel cell performance characteristics.

As revealed in [4], oxygen ion and proton conduction can take place at the same time due to the two phases involved in the composite electrolyte, i.e., oxygen ion transport through one phase and proton conduction through another phase. In addition, there is also the interfacial conduction, so-called "composite effect" in [4], between two phases. It is a new concept to combine the advantages of proton and oxygen ion conductors to form new material ITSOFCs.

2.2 Gas Flow and Heat/Mass Transfer in Anode-Supported ITSOFCs. For anode-supported planar ITSOFCs, the thickness and width of the porous layer is larger than that of the flow duct. The transport rate of fuel gases to active sites for reactions is controlled by various parameters, such as porous microstructure (e.g., pore size, permeability, volume percent porosity), pressure gradient between the flow duct and porous layer, gas composition and inlet conditions, etc.

In an ITSOFC anode duct, part of the fuel (e.g., H_2) is consumed while water vapor (H_2O) is generated during the electrochemical reactions. This can be simulated as a mass suction and injection with velocity V_m (or $\mathrm{Re}_m = V_m D_h/\nu$), respectively, at the permeable wall on the anode side [6]. Fundamental studies of forced convective heat transfer and gas flow, where porous media appear in SOFCs, have been considered by various investigators in recent years [7–16]. These studies have been driven by the need for a better understanding of flow and heat transfer in porous media. Because of the simplicity and reasonable performance within a certain range of applications, the Darcy model has been used for the majority of existing studies on gas flow and heat transfer in porous media. It is clear that part of the gas flow penetrates into the porous layer and the remaining gas flows downstream at reduced rates. The static pressure in such a duct then changes along the main flow due to the following reasons: the friction between the gas flow and the internal surfaces of the duct creates a pressure loss, and the mass permeation across the interface between the flow duct and the porous layer implies that mass and momentum are transferred from/into the porous layer. The latter one complicates the transport processes further even in a simple duct flow, because it is a mass changing process and depends on the pressure difference between the flow duct and porous layer. However, this process is usually considered as an overall mass transport with a constant permeability. Another factor should be considered, because part of the fuel (e.g., H_2) is consumed and water (H_2O) is generated in the electrochemical reaction [17].

As in this study, the fuel gas in the anode is a binary mixture (H_2+H_2O). Fick's law is then used to determine the mass diffusion flux. There is usually an energy flux associated with the mass diffusion in the energy balance. For the specific case investigated, Lewis numbers $\mathrm{Le} = k_{\mathrm{eff}}/(\rho_{\mathrm{eff}} c_{p,\mathrm{eff}} D_{\mathrm{eff}})$ are likely to be different from unity in some regions, but nonetheless assumed. Future work will address nonunity Le numbers.

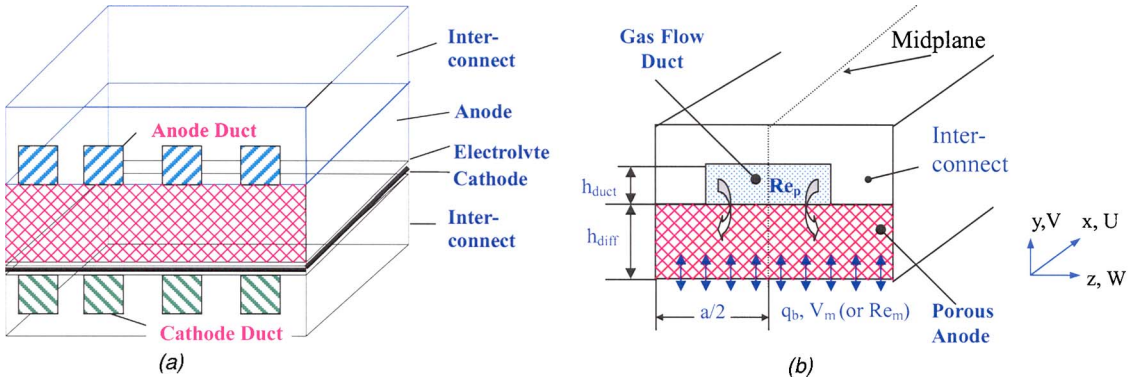

Fig. 1 (*a*) Structure of a unit cell; (*b*) schematic drawing of a composite anode duct

In this study, a three-dimensional CFD (computational fluid dynamics) approach is employed to solve the Navier-Stokes equations, mass conservation equation, and energy equation for an anode duct of a typical planar anode-supported ITSOFC, see Fig. 1(*a*). Figure 1(*b*) shows the schematic structure of the anode duct. The duct consists of a thick porous anode layer, the gas flow duct, and solid current inter-connector. The porous anode layer is assumed to be homogeneous and characterized by effective parameters, such as porosity, permeability, and thermal conductivity, and the fluid in the porous layer is in local thermal equilibrium with the solid matrix. A chemical reaction occurs at the porous surface in contact with the electrolyte (bottom surface in Fig. 1(*b*)). A constant flow rate $U=U_{in}$ with a mass fraction of the mixed fuel ($H_2/H_2O=80/20$) is specified at the inlet of the gas flow duct, while $U=0$ is specified at the inlet for the inter-connector and porous anode layer. Only the right half of the duct is considered by imposing symmetry conditions on the mid-plane.

2.2.1 Governing Equations. The governing equations to be solved are the continuity, momentum, energy, and fuel gas species equations, which are written as

$$\nabla \cdot (\rho_{\text{eff}} \mathbf{V}) = S_m \tag{5}$$

$$\nabla \cdot (\rho_{\text{eff}} \mathbf{V}\mathbf{V}) = -\nabla P + \nabla \cdot (\mu_{\text{eff}} \nabla \mathbf{V}) + S_{\text{di}} \tag{6}$$

$$\nabla \cdot (\rho_{\text{eff}} c_{p\,\text{eff}} \mathbf{V} T) = \nabla \cdot (k_{\text{eff}} \nabla T) \tag{7}$$

$$\nabla \cdot (\rho_{\text{eff}} \mathbf{V} y_{H_2}) = \nabla \cdot (\rho_{\text{eff}} D_{H_2,\text{eff}} \nabla y_{H_2}) \tag{8}$$

2.2.2 Source Terms. A source term S_m in the mass conservation equation accounts for the mass transfer caused by the electrochemical reaction from/to the porous anode layer (bottom surface A_{active}). It reads

$$S_m = J_{H_2} + J_{H_2O} \tag{9}$$

where J_{H_2} and J_{H_2O} are calculated as follows

$$J_{H_2} = -\frac{i(x,y,z)}{2F} M_{H_2} A_{\text{active}}/V \tag{10}$$

$$J_{H_2O} = \frac{i(x,y,z)}{2F} M_{H_2O} A_{\text{active}}/V \tag{11}$$

It is well known that the Darcy model has some limitations. It cannot predict the viscous effects and the flow development. It also breaks down due to the increasing role of inertial forces, where the interstitial flow velocity is not small based on pore Reynolds number [7]. Studies are available that have addressed these limitations. For example, a term accounting for friction due to macroscopic shear was included in the model to account for the transition from Darcy flow to highly viscous flow (without porous matrix, i.e., extremely high permeability). This model is usually referred to as the Brinkman-extended Darcy model, because the term was introduced first by Brinkman. A term representing the inertial energy of the fluid has been suggested and is often referred as the Forchheimer-extended Darcy model, see [7,11].

For the case of transition from porous medium flow to the pure duct flow, the permeability increases, and none of the above-mentioned models adequately address this transition. This is due to the fact that, in the high permeability limit, the terms in the momentum conservation equation can only survive for the highly viscous flows in which the effects of fluid inertia are negligible relative to pressure and friction forces [12]. A fully extended model is obtained by combining the Forchheimer-extended Darcy model and the Navier-Stokes equations. This combined model accounts for the boundary-layer development, shear stress, and microscopic inertial force as well. In this paper, the model is formulated for both porous medium flow and pure duct flow without the limitation of high viscosity, and it is called the generalized Brinkman-Forschheimer-Darcy model in the literature [12], or generalized BFD model in some cases. The generalized BFD model has gained tremendous popularity partly because it enables a porous/fluid composite region to be treated as a single domain. By considering the regular fluid as a porous medium with large permeability, only one set of conservation equations needs to be solved for the entire domain. The model has been employed in fundamental studies of fluid flow and heat transfer in various porous media applications, e.g., [8,9]. A more important reason for its success lies in the fact that numerically predicted results using this formulation together with conventional boundary conditions at the interface agree well with experimental results [13].

Equation (6) has been modified to be valid for both the porous layer and the flow duct, by including a source term S_{di} [12]

$$S_{\text{di}} = -(\mu_{\text{eff}} \mathbf{V}/\beta) - \rho_{\text{eff}} B V_i |\mathbf{V}| \tag{12}$$

In Eq. (12), β is the porous layer permeability and $\mathbf{V}$ represents the volume-averaged velocity vector of the species mixture. As an example, the volume-averaged superficial velocity component U in the x direction is equal to εU, in which ε is the porosity, U the average pore velocity (or interstitial velocity in the literature). The inertial coefficient B in Eq. (12) depends very much on the microstructure of the porous medium, and theoretical determination of it is not easy. In fact, the value of B reported often varies between investigators and the porous medium tested. As an example, two models from the literature for B are given in Table 2.

Table 2 The inertial coefficient *B* in Eq. (12)

Model	The inertial coefficient	References
1	$B = \varepsilon F/(\beta)^{0.5}$	[12, 13, 14, 15]
2	$B = 1.75(1-\varepsilon)/(\varepsilon^3 d)$	[16]

Table 3 The Forchheimer coefficient *F* in the model

Model	The Forchheimer coefficient	References
1a	$F = 1.8/(180\varepsilon^5)^{0.5}$	[12]
1b	$F = 0.143\varepsilon^{-1.5}$	[15]

It is clear that model 2 in Table 2 needs more detailed information about the porous medium microstructure (d—sphere diameter) in SOFC, which is not available presently. Only model 1 is then used in the present study. Table 3 shows methods to determine the Forchheimer coefficient F in model 1.

The source term S_{di} accounts for the linear relationship between the pressure gradient and flow rate by the Darcy law. It should be noted that Eqs. (5)–(8) are formulated to be generally valid for both the flow duct and the porous layer. The source term in Eq. (6) is zero in the flow duct.

The species transport Eq. (8) is solved for the mass flow rate of the hydrogen based on the fuel mixture (H_2+H_2O) velocities and variable thermal-physical properties, while the concentration of H_2O is determined by a summation of the mass fractions in the duct, i.e.,

$$y_{H_2O} = 1 - y_{H_2} \tag{13}$$

In the above equations, all parameters with subscript eff are the effective ones, and reduce to the values of the fuel gas mixture in the flow duct based on the composition and temperature. As an example, the effective specific heat capacity $c_{p\,\text{eff}}$ in the flow duct is the one of the fuel gas mixture c_{pg}, i.e., $c_{p\,\text{eff}}=c_{pg}=y_{H_2}c_{p,H_2}+(1-y_{H_2})c_{p,H_2O}$. In the porous anode, the effective density ρ_{eff} is the fuel gas mixture ρ_g. For the effective transport properties, there are several methods to estimate the effects of the microstructure parameters, such as the porosity, pore size, particle size, and tortuosity. For example, a large portion of the correction is made using the ratio of porosity to tortuosity, although in some cases, the Bruggeman correction ($\varepsilon^{1.5}$) is used. It should be noted that in this study the simplified approach in [9] is employed. The effective conductivity k_{eff} and H_2 effective binary diffusion coefficient are estimated by employing various values for the ratios to consider the porous layer effects [9], i.e.,

$$k_r = k_{\text{eff}}/k_{fg} \tag{14}$$

$$D_r = D_{H_2,\text{eff}}/D_{H_2} \tag{15}$$

where D_r is the species binary diffusion coefficient ratio, D_{H_2} is the H_2 diffusion coefficient in the fuel gas mixture. By varying the property ratio, the corresponding effective property in the porous layer sub-domain can be different from that of the species mixture, if the property ratio is not equal to 1. Future work will address the various methods to obtain the effective properties, particularly for the multi-component species mixture in the porous layer involving internal steam reforming reactions.

2.2.3 Additional Equations. To characterize the overall pressure difference between inlet and outlet, either a pressure coefficient C_p or an apparent friction factor f_{app} of the gas flow in a duct can be employed as

$$C_p = \frac{(P_{\text{in}} - P)}{(\rho U_{\text{bulk}}^2/2)} \tag{16a}$$

$$4f_{\text{app}} = \frac{D_h}{(\rho U_{\text{bulk}}^2/2)}\frac{dP}{dx} \tag{16b}$$

where U_{bulk} is the mean velocity of the main flow, D_h is the hydraulic diameter defined in the conventional manner, dP/dx the pressure gradient along the main flow direction. As mentioned earlier, the mass permeation across the interface between the flow duct and the porous anode layer contributes to the pressure change along the main flow direction. Consequently, the apparent Fanning friction factor f_{app} is employed. Based on the fact that the mass permeation is small, the deduced pressure change can be written as

$$\left(\frac{dP}{dx}\right)_p = -\rho U_{\text{bulk}}\left(\frac{\partial U_{\text{bulk}}}{\partial x}\right) \tag{17}$$

The Nusselt number Nu_b at the heated wall is

$$\overline{\text{Nu}_b} = \frac{\overline{h_b}D_h}{k_{\text{eff}}} = \frac{q_b D_h}{k_{\text{eff}}(\overline{T_b} - T_{\text{bulk}})} \tag{18}$$

$\overline{T_b}$ is the heated wall spanwise average temperature, T_{bulk} the mean stream-wise flow temperature in the cross section

$$T_{\text{bulk}} = \frac{\int T|U|dA}{\int |U|dA} \tag{19}$$

while the heat flux q_b at the bottom wall in Eq. (18) is calculated as follows [18]

$$q_b = -\frac{i(x,y,z)}{2F}\Delta H_{H_2O}M_{H_2O} - i(x,y,z)V_{\text{cell}} \tag{20}$$

where ΔH is the enthalpy change of water vapor formation. The first term in Eq. (20) accounts for the quantity of water, and the second term takes care of the current density generated by the electrochemical reaction.

2.2.4 Boundary and Interfacial Conditions. Based on the fuel cell function, the unique thermal and fuel gas mass concentration/flux boundary conditions at the walls are as follows

$$U = V - V_m = W = 0, \quad -k_{\text{eff}}\frac{\partial T}{\partial y} = q_b,$$

$$-\rho_{\text{eff}}D_{H_2,\text{eff}}\frac{\partial y_{H_2}}{\partial y} = J_{H_2} \quad \text{at the bottom wall } (y=0) \tag{21}$$

$$U = V = W = 0, \quad q = 0, \quad J_{H_2} = 0 \quad \text{at the top and side walls} \tag{22}$$

$$\frac{\partial U}{\partial z} = \frac{\partial V}{\partial z} = W = \frac{\partial T}{\partial z} = \frac{\partial y_{H_2}}{\partial z} = 0 \quad \text{at the mid-plane } (z = a/2) \tag{23}$$

In the present investigation, the interfacial boundary conditions, commonly employed in the literature and including the continuity of velocity, shear stress, temperature, heat flux, mass fraction and flux are applied as follows

$$U_- = U_+ \quad (\mu_{\text{eff}}\partial U/\partial y)_- = (\mu_f \partial U/\partial y)_+ \tag{24}$$

$$T_- = T_+ \quad (k_{\text{eff}}\partial T/\partial y)_- = (k_f \partial T/\partial y)_+ \tag{25}$$

$$y_{H_{2-}} = y_{H_{2+}}, \quad (\rho_{\text{eff}}D_{H_2,\text{eff}}\partial y_{H_2}/\partial y)_- = (\rho_f D_{H_2}\partial y_{H_2}/\partial y)_+ \tag{26}$$

Here subscript + (plus) stands for fluid side, − (minus) for porous layer side. Moreover, the thermal interfacial condition, Eq. (25), is also applied at an interface between the porous media and the solid current inter-connector with k_s instead of k_g

3 Modeling Approaches and Numerical Procedures

3.1 New Material ITSOFC Stack Models. The stack modeling is based on the fundamental thermodynamics and electrochemical reactions with aims to evaluate the ITSOFC stack performance. Various processes are included in the separate sub-

modules, such as internal reforming reactions, electrochemical reactions. Fuel cell performance is estimated by voltage-current characteristics, output of electricity/heat and fuel consumption. The optimal design and/or configuration of an ITSOFC stack may be achieved based on the specified electrical power or fuel supply rate.

3.1.1 Reforming Reactions. Reforming of the fuels to provide pure hydrogen for the fuel cell reaction consumes a significant portion of the heat produced by fuel cells. The energy absorbed is calculated by the reforming reaction, including that in the water gas shift reaction. The molar and mass balance for the reforming reaction and calculation of the theoretical mass ratio of fuel to hydrogen are based on the unit of hydrogen supplied to the fuel cell. For internal reforming of bio fuels as in this study, the internal reforming factor (or efficiency) based on mass flow rate is used to measure the equilibrium position. The definition of η_R is the ratio between the theoretical fuel flow required and actual fuel flow rate to yield a unit flow of hydrogen. The fuel flow rate reads

$$m_{f,\text{in}} = m_{\text{H}_2} \times R_{\text{fuel\_H}_2}/\eta_R \tag{27}$$

In the above equation, $m_{f,\text{in}}$ is the inlet fuel flow rate required, m_{H_2} hydrogen flow rate generated from the reforming, $R_{\text{fuel\_H}_2}$ ratio of molecular weights between fuel and hydrogen which will depend on the fuels employed. As an example when pure methane is the fuel, the ratio is calculated as

$$R_{\text{fuel\_H}_2} = M_{\text{CH}_4}/M_{\text{H}_2} \tag{28}$$

Heat is required by the reforming process

$$Q_R = m_{\text{H}_2} \times \Delta H_{\text{reformation}} \tag{29}$$

Here, $\Delta H_{\text{reformation}}$ is enthalpy change of the reforming, m_{H_2} the hydrogen flow rate (kg/s). If the biomass generated syngas is used as fuel, mass ratio of fuel to hydrogen can be applied by the compositions of the components in the syngas. For example, water consumption needed the reformation of CH_4 is

$$m_{\text{H}_2\text{O\_}R} = m_{\text{H}_2} \times (2M_{\text{H}_2\text{O}})/(4M_{\text{H}_2}) \tag{30}$$

3.1.2 Electrochemical Reactions. The maximum theoretical electrical power from the Gibbs free energy at any operating temperature and pressure is calculated by

$$W_{\text{stack,max}} = -m_{\text{H}_2}\Delta G^o = -m_{\text{H}_2}\Delta G^T + RTm_{\text{H}_2}\ln\left[\frac{P_{\text{H}_2}P_{\text{O}_2}^{1/2}}{P_{\text{H}_2\text{O}}}\right] \tag{31}$$

where $\Delta G^T = RT\ln(K_p)$ represents the Gibbs energy change in the overall cell reaction. The open circuit voltage is calculated as

$$V_{\text{oc}} = V_\infty^o + \frac{RT}{nF}\ln\left[\frac{P_{\text{H}_2}P_{\text{O}_2}^{1/2}}{P_{\text{H}_2\text{O}}}\right] \tag{32}$$

The above-noted equation is well known as the Nernst equation, and provides a relationship between the ideal potential for the cell reaction (given by the first term of the equation on the right-hand side) and the ideal equilibrium potential at other partial pressure and temperature of reactants and products. F is the Faraday constant, V_∞^0 ideal fuel cell electromotive force, P the partial pressure in bar. V_∞^o is given as

$$V_\infty^o = -\frac{\Delta G^o}{nF} = -\frac{\Delta H^o - T\Delta S^o}{nF} \tag{33}$$

in which ΔG^o is free Gibbs energy change, ΔS^o entropy change in the electrochemical reaction. It should be noted that the ideal fuel cell electromotive force V_∞^o (at one bar) depends only on the temperature.

3.1.3 Fuel Cell Characteristics. The voltage-current characteristic of fuel cells derives from: voltage losses due to internal resistance to current flow in the cell components and electrode activation potentials; and voltage losses due to the effect of gas flows and concentrations on the utilization ratio of the fuel. Internal resistance losses dominate except at high current densities or high fuel utilization ratios ($>85\%$), when mass transfer effects or low concentrations/partial pressures of fuel cause a decrease in voltage. These effects are dependent upon the detailed design of the fuel cell and the gas flow channels, and are difficult to model theoretically. However, they may be derived empirically. Given ITSOFC operating characteristics, the target operating current density and voltage can be specified to give a good combination of power output, voltage efficiency, and fuel utilization. Cell voltage is given by [18]

$$V_{\text{cell}} = V_{\text{oc}} - iR - (a + b\ln(i)) \tag{34}$$

in which i is the current density, R represents internal resistance (ohmic) of the cell, a and b are Tafel constants. The first term on the right-hand side of Eq. (34) is the open-circuit voltage from Eq. (32), the second term represents the internal ohmic resistance loss, while the last one accounts for the activation loss. It should be noted that there exists several approximations to the activation loss, derived from the Butler-Volmer equation. Under certain conditions, such as low-activation polarization, the linear relation is often employed as well in the literature.

3.1.4 Electricity, Heat Output, and Fuel Consumption. Two options are available: calculation of the heat output and fuel consumed for a given electrical power output; calculation of the electricity and heat output for a given supply of fuel. For the first option, the calculation procedures are as follows:

- add ancillary loads referred to ac supply, and add converter efficiency factor to give dc output required from fuel cell stack;
- determine sum of currents through all cells in stack

$$I = W_{\text{stack}}/V_{\text{stack}} \tag{35}$$

- hence hydrogen utilized in stack is

$$m_{\text{H}_2} = I/(\alpha nF) \tag{36}$$

while for the second one, the following methods are employed:

- define hydrogen flow available from the reforming by reformer efficiency and hydrogen to fuel mass ratio;
- hence calculate hydrogen utilized in fuel cell stack by considering fuel cell utilization factor;
- calculate stack current

$$I = m_{\text{H}_2}\alpha nF \tag{37}$$

and stack power

$$W_{\text{stack}} = V_{\text{stack}} \times I \tag{38}$$

Stack heat is balanced as

$$\Delta Q = \Delta H_{\text{stack}} = m_{\text{H}_2}(\Delta G^o - \Delta H_{\text{reaction}} - \Delta H_{\text{reformation}}) \tag{39}$$

in which ΔH_{stack} is enthalpy change of the stack, while ΔG^o Gibbs free energy, $\Delta H_{\text{reaction}}$ enthalpy change of the fuel cell reaction, $\Delta H_{\text{reformation}}$ enthalpy change of the fuel reformation.

As mentioned earlier, there are voltage losses connected to the activation, gas transport, and current resistance. Assuming that a portion (represented by F_{rec}) of the voltage losses within the fuel cell stack are recovered as heat, and by correcting for fuel utilization α, one has

$$\Delta Q = m_{\text{H}_2}\alpha(\Delta G^o - \Delta H_{\text{reaction}}) + m_{\text{H}_2}\alpha F_{\text{rec}}\Delta G^o - m_{\text{H}_2}\Delta H_{\text{reformation}} \tag{40}$$

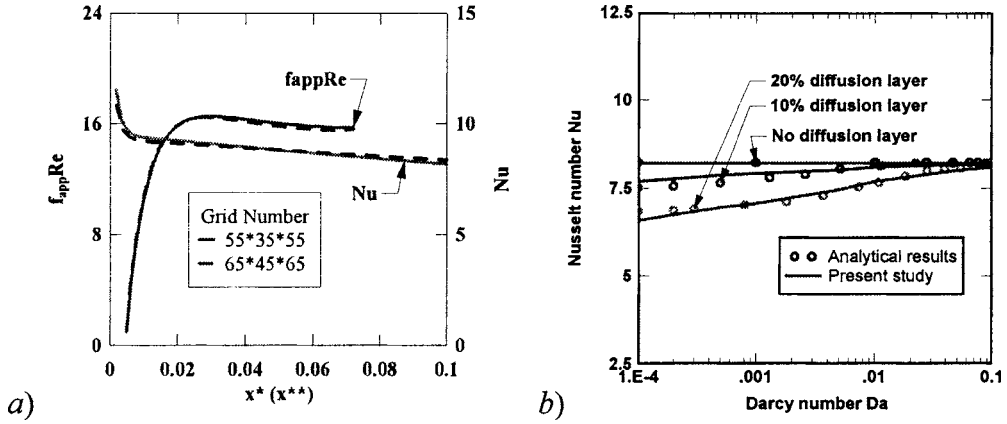

Fig. 2 (*a*) **Influence of grid size on f_{app}Re and Nu; and (*b*) fully developed Nu variation in a parallel plate duct with Darcy number (Da=β/h^2), compared with the analytical ones from [9]**

If unutilized fuel is recirculated and burnt to preheat the fuel, one has

$$\Delta Q = m_{H_2}\alpha(\Delta G^o - \Delta H_{reaction}) + m_{H_2}\alpha F_{rec}\Delta G^o - m_{H_2}\Delta H_{reformation} + m_{H_2}(1-\alpha)\Delta H_{comb} \quad (41)$$

where $\Delta H_{comb}=\Delta H_{formation\_H_2O}$ is based on the activated temperatures. The first term on the right-hand side of Eq. (41) represents heat generation by the electrochemical reaction, the second one voltage losses recovery, the third one reforming related heat, while the last one comes from the combustion of unused fuel. Water generation from the electrochemical reaction in the stack is given by

$$m_{H_2O\_generation} = m_{H_2}\alpha M_{H_2O}/M_{H_2} \quad (42)$$

3.1.5 Fuel Cell Stack Configuration. Two calculation options are available: specify the number of cells in series and active areas of a unit cell to determine fuel cell stack voltage and power supply; and specify desired fuel cell stack operating voltage and power to determine number of cells required in series and cell active area needed.

The present approach is totally integrated in the *Microsoft EXCEL®* environment. This enables the user to easily interact with input data, monitor the simulation results in terms of a stack performance graph or data. Most of the input parameters and simulation results with overall performance, such as *V-I* and *W-I* curves, are shown in user sheet (or interface). Users are required to modify the input data in various sub-sheets. Input parameters can be divided into various categories:

- stack material properties and dimensions (e.g., cell active area/electrolyte thickness);
- stack operating conditions (operating temperature, °C; operating pressure, MPa; reforming efficiency; reforming preheat, kW; and fuel utilization ratio as well). Depending on modeling strategy, either electrical power required or fuel flow rate supplied to stack should be given. One should specify target operating stack voltage, and adjust actual number of cells based on estimation; or specify number of cells and cell active area, and estimate the operating point of the stack.
- adjustable parameters (Tafel coefficients *a*, *b* and internal ohmic resistance *R* of the cell) used in calibrating the model to fit experimental data, such as the parameters connecting to over-potentials and ohmic potentials.

3.2 Numerical Procedures for Anode-Supported ITSOFC. A three-dimensional CFD code was used to solve the governing Eqs. (5)–(8), together with the boundary conditions (21)–(23) and interfacial conditions (24)–(26). The code is a general purpose one and based on the finite-volume technique with boundary fitted coordinates for solving the differential equations. The Cartesian coordinate system in the physical space is replaced by a general non-orthogonal coordinate system. The momentum equations are solved for the velocity components on a non-staggered grid arrangement. The Rhie-Chow interpolation method is used to compute the velocity components at the control volume faces. Algorithms based on the TDMA (tridiagonal matrix method) and a modified SIP (strong implicit procedure) are employed for solving the algebraic equations. In this study, the convective terms are treated by the QUICK (quadratic upwind interpolation of convective kinematics) scheme, while the diffusive terms are treated by the central difference scheme. The SIMPLEC (semi-implicit method for pressure linked equations consistent) algorithm handles the linkage between velocities and pressure.

As shown earlier, the equations needed for the calculation are coupled by current density, temperature, partial pressure / concentration of gas species via source terms and thermal-physical properties. It should be noted that the source term in Eq. (6) is zero in most of the regions, and non-zero only in the regions neighboring boundaries, where mass transfer caused by the electrochemical reaction occurs (bottom wall in Fig. 1(*b*)). It is clear that no gas flow is present in the solid interconnect. Equations (5), (6), and (8) are then blocked out and only the heat conduction equation, derived from the energy Eq. (7), is solved for this domain. As mentioned earlier, the thermal-physical properties of the fuel gas mixture vary. These parameters depend on the position in the duct, and the species mass fraction and/or temperature as well. Fuel gas mixture density, viscosity and specific heat capacity are then calculated and updated during the calculation.

In this investigation, a uniform grid point distribution in the cross section is applied. To obtain finer meshes in the entrance region of the duct, a non-uniform distribution of grid points with an expansion factor is implemented for the main flow direction. Various values of the expansion factor have been checked and 1.01 was found to be sufficient to achieve grid independent solutions.

In order to evaluate the performance of the numerical method and code, test calculations considering grid sensitivity, code performance, and validation were carried out. It is clear that the calculated *f*Re and Nu do not change significantly when the number of grid points is increased beyond $55\times35\times55$ (55×35 for the cross section, 55 for the main flow direction), see Fig. 2(*a*). Calculations have been carried out for fully developed conditions in a parallel plate duct for various thickness of the porous layer and the same boundary conditions of constant heat flux on the walls. The comparison in Fig. 2(*b*) shows that the computed Nu values agree well with the analytical ones.

Table 4 Input parameters and values of the ITSOFC stack at the base conditions

Input Parameters	Value
Electrolyte thickness, μm	500
Temperature T, ^oC	700
Pressure P, MPa	0.1
Fuel utilization ratio α, %	85
Internal reforming efficiency η_R, %	100
Effectiveness of heat recovery from voltage losses F_{rec}, %	50
Heat exchanger effectiveness $\varepsilon_{heatexchanger}$	0.8

4 Applications and Discussion

4.1 Analysis of a New Material ITSOFC Stack. Table 4 shows the input parameters and values used as the base case condition for the investigated stack. Figure 3 shows a predicted cell performance characteristics in terms of voltage V and power density w vs current density i, with comparison to the measured one [4]. The results demonstrate rather a high-power output with a level between 200 and 600 mW/cm^2 corresponding to the current density of 400–2000 mA/cm^2. From the figure, it is found that the agreement between calculations and experimental results is good in terms of V-i curve.

Figure 4 shows the predicted ITSOFC stack performance. The designed stack should supply 1 kW ac electrical power at 24 V. Based on Fig. 3, it is clear that the unit cell voltage should be 0.5–0.7 V when the current density is within 200–950 mA/cm^2. If 0.6 V (corresponding to a current density 600 mA/cm^2) is chosen as operating voltage, the stack then contains 40 cells and 0.008 m^2 active working area per cell for the required electricity power. The designed operation points are shown in Fig. 4 as well in terms of stack parameters in Table 4.

A bio-fuel with a composition of CO (30%)+CO_2(10%)+H_2(50%)+CH_4 (10%) is supplied to the stack. The cell/stack operating parameters and predicted performance are listed in Table 5. Because the voltage loss is related to the current density, the electrical power density supplied by the fuel cell has a trade-off to achieve a maximum value. It is clear from Fig. 3 that a maximum power density (w_{max}=650 mW/cm^2) is approached when V_{cell}=0.32 V and i=2000 mA/cm^2. It should be mentioned

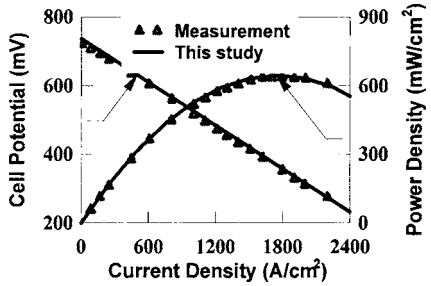

Fig. 3 ITSOFC performance (*V-i* curve) for gas composition of CO(28%)+CO_2(17%)+H_2(55%) [4] at the base condition

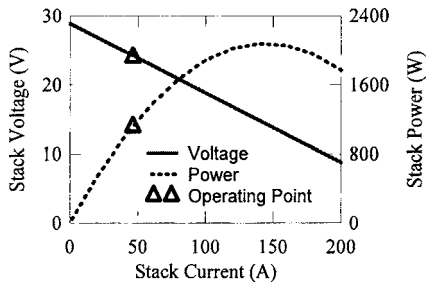

Fig. 4 ITSOFC stack performance at the base condition

Table 5 The ITSOFC stack operating parameters and predicted performance

Parameters	Values
Stack nominal electrical power, kW	1
Fuel composition	CO (30%) + CO_2 (10%) + H_2 (50%)+ CH_4 (10%)
Stack nominal voltage, V	24
Stack current, A	46.3
Stack temperature, ^oC	700
Pressure, MPa	0.1
Cell power density, mW/cm^2	364
Cell current density, mA/cm^2	606
Stack fuel consumed, kg/s	1.22×10^{-4}

that the operating point should be well balanced and optimized in terms of power density, energy conversion efficiency, and required power supply /current/voltage. Such optimization is possible when further information concerning the stack requirements is available.

4.2 Transport Processes in an Anode Duct of ITSOFCs. The following geometries are employed [17]: length of the duct L=20 mm; width of the porous layer a=2 mm, and its thickness h_p=2 mm; while the width of the flowing duct b=1 mm, and its height h_d=1 mm. The fuel gas has 0.80 mass fraction of H_2, and 0.20 of water vapor with an inlet temperature T_{in}=700°C; thermal conductivity ratio $k_r(=k_{eff}/k_f)$=1, effective dynamic viscosity $\mu_{eff}=\mu_f$; porosity ε=0.5 and permeability $\beta=1.7\times10^{-10}$ m^2; Re_{in}=100, Re_m=1.0, $D_{H_2}=3\times10^{-4}$ m^2/s.

Based on the mass average velocity, Fig. 5 shows the permeation Reynolds number Re_p, the apparent friction factor times the Reynolds number $f_{app}Re$, and the Nusselt number Nu along the main flow direction of an anode-supported ITSOFC duct. Similar to the wall Reynolds number Re_m (for mass transfer across the bottom wall), the permeation Reynolds number is defined for gas permeation across the interface. It is found that Re_p has a large negative value (i.e., permeation into the porous anode layer) at the inlet region, see Fig. 5(a). Due to the decreasing pressure gradient along the duct, permeation into the porous layer becomes smaller. On the other hand, H_2O generation caused by the electrochemical reaction at the bottom wall, together with back permeation described earlier, contributes to a mass injection into the flow duct. This is confirmed by a small but positive (i.e., back flow into the flow duct) Re_p shortly downstream the inlet in Fig. 4(a).

It should be noted that the boundary conditions employed are mass consumption of H_2, generation of H_2O due to the electrochemical reactions at the active surface (represented by the wall velocity V_m at the bottom surface in Fig. 1(b)), as well as the uniform velocity U_{in} specified at the flow duct inlet. It is a fact that the above-mentioned boundary conditions affect the gas flow and species distribution in the anode. However, the net contribution of the electrochemical reaction is a mass injection to the porous anode and further to the flow duct. Consequently the negative permeation Re_p in the entrance region is not from the electrochemical reaction related wall mass transfer. As a sensitive study, a fully developed velocity (parabolic profile) is employed at the inlet, i.e., imposing the uniform velocity boundary condition further away from the cell. The tested results show a similar trend, i.e., a negative Re_p appears in the entrance region. However, the maximum value of Re_p is smaller than that with a uniform entrance velocity (max Re_p=−4 vs −24). It is revealed that this strong mass permeation to the porous anode is dominated by the pressure gradient between the flow duct and the porous layer.

For a pure flow duct with impermeable walls, $f_{app}Re$ decays rapidly from the inlet, and reduces to a constant value as the convective gas flow becomes fully developed (see Fig. 5(b)). For the anode duct with a porous layer, the apparent friction factor, $f_{app}Re$, starts at a small value at the inlet region but increases rapidly at the entrance region and also reaches a near-constant value shortly downstream along the main flow direction. Similar

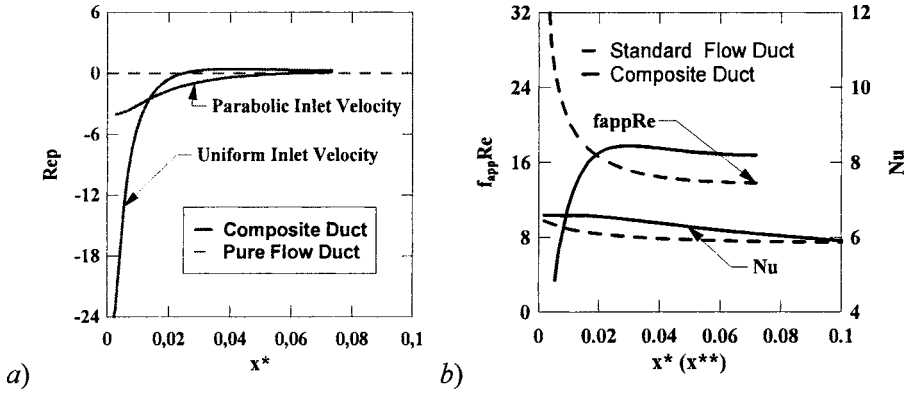

Fig. 5 (*a*) Permeation Reynolds number Re_p; (*b*) $f_{app}Re$ and Nu along the main flow direction

to a suction flow from a duct, there is certainly a decrease in the apparent friction factor from that of the pure forced convection, as mentioned before. For increasing x^*, the Re_p becomes smaller and its contribution to the decrease of $f_{app}Re$ is less significant. This contribution will be zero when $Re_p=0$. Along the flow direction beyond this position, the gas flow is possibly affected by the following mechanisms: secondary flow and back permeation to increase $f_{app}Re$, convective flow to decrease $f_{app}Re$. It can be clearly observed that $f_{app}Re$ in Fig. 5(*b*) is nearly constant downstream the entrance region. Further down the flow duct, the secondary flow and back permeation balance each other and the effects on the main flow fades away. The Nu for the composite duct has a similar behavior as that of the pure forced flow duct. However, a slightly bigger Nu can be observed for the composite duct (see Fig. 5(*b*)), due to the mass permeation into the porous layer. From the discussion above, it is clear that mass permeation across the interface has more significant effects on the gas flow than on heat transfer, both at the entrance region and further downstream.

Axial velocity contours (U/U_{in}) are presented and discussed for an ITSOFC anode duct in Fig. 6. As mentioned earlier, gas flow and heat transfer in the composite ducts are affected by the porous layer and the electrochemical reaction. Due to the permeation and mass injection/suction effects, the uniform distribution and the symmetry of the axial velocity associated with a pure forced duct flow no longer exist, and the position of the maximum contour values shifts away from the central plane ($y/h=0.625$ in Fig. 6). More mass is permeated into the porous anode layer in the entrance area because of the biggest pressure difference between the flow duct and the porous layer is found there. As a consequence, part of the boundary is shifted into the porous anode layer, which can be verified by a change of the boundary layer thickness close to the interface in Fig. 6. Because the pressure in the flow duct will fall, a decreased pressure difference along the flow direction is expected. Consequently, gas permeation decreases and becomes weaker. It is confirmed that the hydrodynamic boundary layer moves back into the flow duct from the porous anode layer. However, it is clear that the axial velocity magnitude of the gas decreases rapidly in the porous layer.

It is clear that the temperature increases monotonically along the main flow direction as shown in Fig. 7. The variation in the vertical direction of the temperature can also be observed with a slightly larger variation close to the active surface. This is due to the heat generation by the electrochemical reactions close to the active surface.

H_2 and H_2O concentration profiles along the main flow direction are shown in Figs. 8(*a*) and 8(*b*), respectively. It is found that the H_2 concentration decreases, while the H_2O concentration increases continuously along the main flow direction in the porous layer and the flow duct. This is due to the consumption of H_2 and generation of H_2O during the electrochemical reaction. Moreover, the gradients of the H_2 and H_2O concentrations in the direction normal to the active surface (the bottom surface in Fig. 8) are larger close to the interface areas of both the porous layer and flow duct compared to those close to the reaction sites.

It is clear that the fuel gas species is transported to the active sites for the reaction by both convection and diffusion in the po-

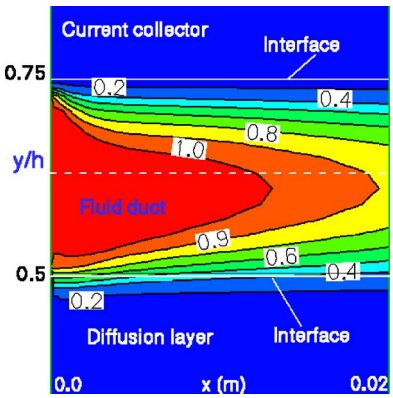

Fig. 6 Dimensionless axial velocity contours (U/U_{in}) along the main flow stream of an ITSOFC anode duct

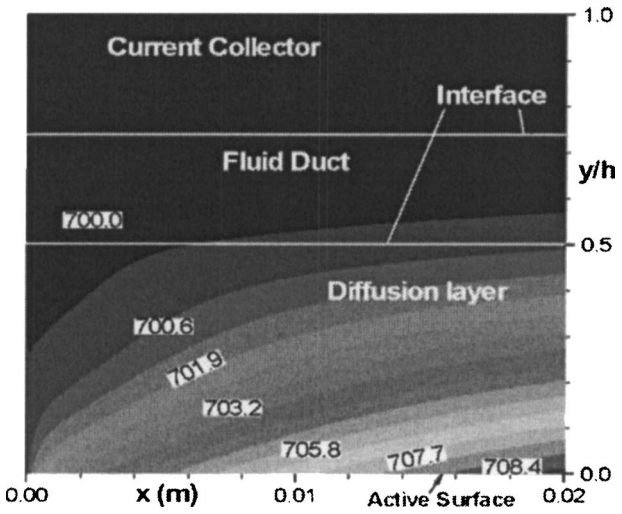

Fig. 7 Dimensionless temperature contours along the main flow stream of an ITSOFC anode duct

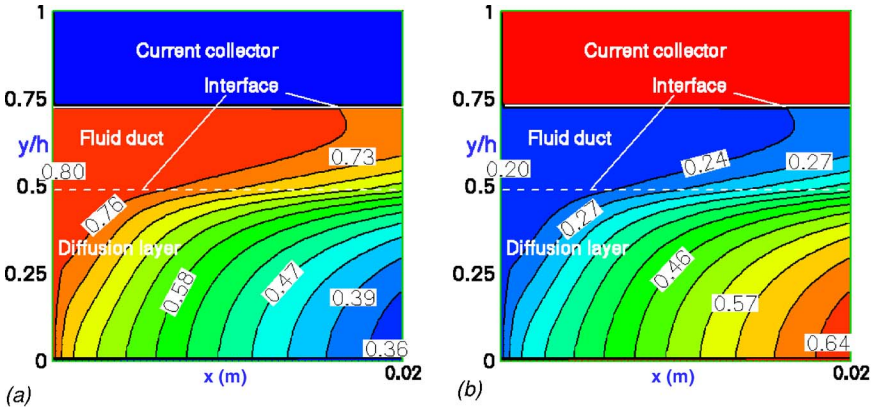

Fig. 8 (*a*) H_2; and (*b*) H_2O mass concentration distribution along the main flow direction of an ITSOFC anode duct

rous layer. Similarly, the generated water is transported from the active sites. However, the species transport rate in the porous layer is smaller than in the flow duct, which can be verified by a flat mass fraction profile close to the interface areas in the porous layer. It is also clear from the figures that the H_2 concentration is large while H_2O is small in the porous layer in the entrance region, due to the significant mass permeation across the interface from the flow duct.

Hydrogen mass fraction profiles are plotted in Fig. 9 for the cross section at the stations of the half-length from the inlet and the exit of the duct. It is found that, in a cross section, the hydrogen mass fraction has minimum values close to the bottom active surface, which is caused by the electrochemical reaction mentioned earlier. Almost uniformly distributed mass concentration is found in both the flow duct and the porous layer. However, a larger value has been predicted in the porous layer close to the side wall.

In this study, the performance of the ITSOFC anode duct is also analyzed using the vertical component of the total hydrogen mass flux vector at the active site (bottom surface), which is proportional to the local current density produced. It is given by

$$(J_{H_2,y})_b = \left(\rho_{\text{eff}} y_{H_2} V - \rho_{\text{eff}} D_{H_2,\text{eff}} \frac{\partial y_{H_2}}{\partial y} \right)_b \tag{43}$$

It should be noted that the first part on the right-hand side represents the convection effects, while the second part is the contribution by the diffusion. Figure 10 shows a comparison of the hydrogen mass fluxes by convection, diffusion, and the total value. It can be seen that the convection mass flux has a large negative value (i.e., fuel species transport is to the reaction sites) at the inlet region. Due to the decreasing pressure difference along the duct, this convection becomes weaker. On the other hand, water generation caused by the electrochemical reaction at the active sites, together with back permeation clarified in [3], contributes to species flowing back to the flow duct. This is confirmed by a small positive value of the convection flux. It is also clear that the hydrogen diffusion flux maintains an almost constant value. By comparing the absolute values of convection and diffusion fluxes, it is found that the convection is stronger in the entrance region; however, the diffusion dominates the species transport further downstreams. The position, where this change occurs, is about 1/6 length from the inlet for this specific case. Consequently the total flux from Eq. (43) is controlled by the convection in the entrance region, and dominated by the diffusion for the rest of the duct, see Fig. 10.

Figure 11 shows the predicted values of the cross-sectional hydrogen mass flux for various stations along the main flow direction. It is found that the total hydrogen mass flux has almost uniform values for the cross sections, except for the case of the inlet. A stronger transport (i.e., larger negative values) to the reaction site is predicted for the entrance region, and particularly for the site below the flow duct. This large mass transport is due to the strong permeation caused by the pressure difference between the flow duct and the porous layer. However, all other stations have similar characteristics dominated by the diffusion.

As revealed in both [3] and the above discussion, the duct con-

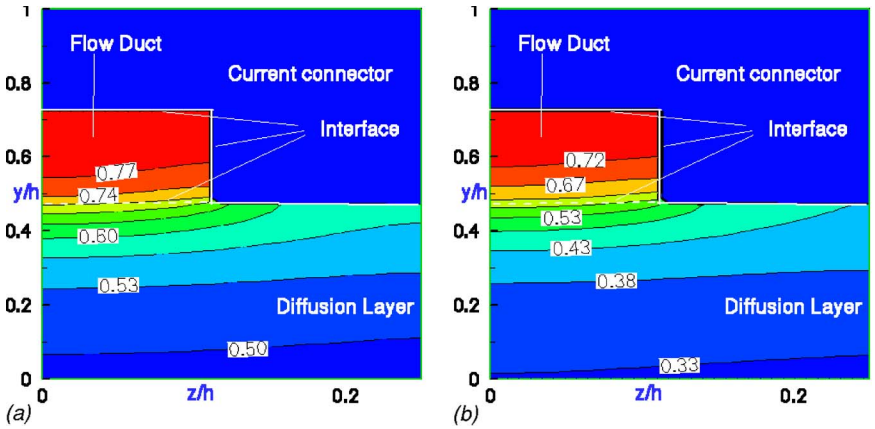

Fig. 9 Cross-sectional hydrogen mass concentration distribution at: (*a*) $\frac{1}{2}$ length from the inlet; (*b*) the exit of ITSOFC anode duct

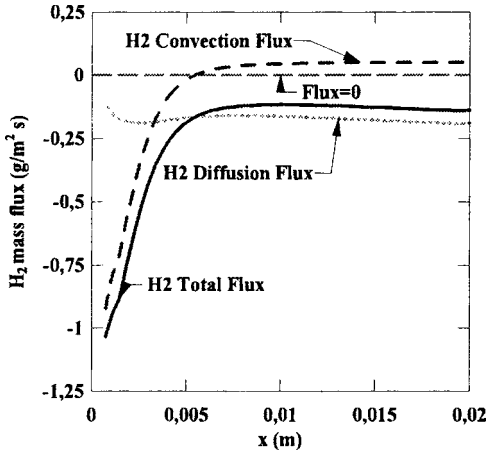

Fig. 10 Various contributions to hydrogen flux at the bottom wall at the base case condition

figuration and properties of the porous layer have significant effects on both gas flow and heat transfer in anode-supported ITSOFC ducts. The large thickness of the porous layer produces transport processes that are controlled by diffusion. However, in a conventional HTSOFC duct, where the size of the porous layers is small, the convection is expected to be a significant process.

5 Conclusions

The characteristics of ITSOFC with thin electrolyte design and new materials are studied using mathematical models. The models are based on the fundamental thermodynamics, gas flow, heat/mass transfer and electrochemical reactions with aims to evaluate the role of various transport processes and/or thermal/gas balances. It has been revealed that the impact of the thick porous anode is significant on the gas flow and heat transfer in an anode duct of ITSOFCs. The axial velocity is no longer uniformly distributed and the boundary layer is shifted into the porous layer in the entrance region; gas species transport from/to the reaction site is mainly dominated by mass convection in the entrance region and by species mass concentration associated diffusion after a certain distance downstream the inlet. Consequently, f_{app}Re has a low value due to the large mass permeation to the porous layer in the entrance; the secondary flow and mass transfer increase f_{app}Re from a certain position in the main flow direction. On the other hand, the stack model presented can be applied as a stand alone assessment/design tool, or implemented into an overall energy system modeling approach for the purpose of system studies.

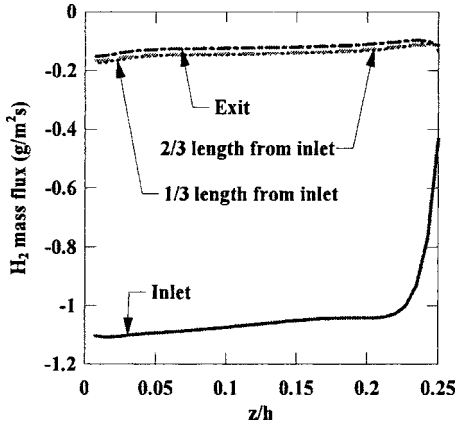

Fig. 11 Variations of hydrogen mass flux of the bottom wall at the base case condition

Acknowledgment

The National Fuel Cell Programme by the Swedish Energy Agency (*STEM*) financially supports the current research.

Nomenclature

- ASR = area specific resistivity, $\Omega\,cm^2$
- A_{active} = surface area of control volume at active site, m^2
- B = inertial coefficient
- a = width of porous layer, m; Tafel constant
- b = width of flow duct, m; Tafel constant
- c_p = specific heat capacity, J/(kg K)
- D_h = hydraulic diameter, m
- D_{H_2} = H_2 diffusion coefficient, m^2/s
- D_r = H_2 diffusion coefficient ratio
- F = Faraday constant, 96 487 A/(s mol); Forchheimer coefficient
- F_{rec} = effectiveness of heat recovery from voltage losses in fuel cell stack
- f_{app} = apparent Fanning friction factor
- G = Gibbs free energy, kJ/mol
- H = enthalpy, kJ/mol
- h_d = height of the duct, m
- h_p = thickness of porous layer, m
- I = stack current, A
- i = local current density, A/m^2
- J = unit area mass flux of species, $kg/(m^2\,s)$
- k = thermal conductivity, W/(m K)
- k_r = thermal conductivity ratio (k_{eff}/k_f)
- M = molecular weight of species (hydrogen or water vapor), kg/mol
- $m_{f,in}$ = inlet fuel flow rate, mol/s
- n = electrons released at anode per mole of H_2
- P = pressure, bar or Pa
- Q = heat, kW
- q_b = heat flux, $W/(m^2)$
- R = specific internal ohmic resistance, $\Omega\,cm^2$
- Re = Reynolds number (UD_h/ν), dimensionless
- $R_{fuel\text{-}H_2}$ = ratio of molecular weight between fuel and hydrogen
- T = temperature, °C
- $\mathbf{V}$ = velocity vector, m/s
- V_i = velocity components in x, y, and z directions, respectively, m/s
- V_{cell} = cell voltage, V
- V_m = mass transfer velocity at bottom wall, m/s
- V_p = permeation velocity across interface, m/s
- W_{stack} = stack electrical power, W
- W_{max} = maximum theoretical electrical power, W
- w = power density, W/m^2
- x, y, z = Cartesian coordinates
- x^* = hydrodynamic dimensionless axial distance ($x/(D_h Re)$), dimensionless
- x^{**} = thermal dimensionless axial distance (x^*/Pr), dimensionless
- y_{H_2} = hydrogen mass fraction, dimensionless

Greek Symbols

- α = fuel utilization,%
- β = permeability of diffusion layer, m^2
- δ = electrolyte thickness, m
- ε = porosity, dimensionless
- η_R = internal reforming factor
- μ = dynamic viscosity, kg/(m s)
- ν = kinematic viscosity, m^2/s

ρ = density, kg/m^3
σ = specific ionic conductivity, S/cm

Subscripts

a = anode
b = bottom wall
bulk = bulk fluid condition
cell = cell
di = diffusion
eff = effective parameter
g = gas mixture
H_2 = hydrogen
H_2O = water vapor
in = inlet
m = mass transfer
p = permeation
s = solid current connector

References

[1] Steele, B. C. H., and Heinzel, A., 2001, "Materials for Fuel-Cell Technologies," Nature (London), **414**, pp. 345–352.
[2] Yuan, J., Rokni, M., and Sundén, B., 2003, "Gas Flow and Heat Transfer Analysis for an Anode Duct in Reduced Temperature SOFCs," FUELCELL2003–1721, *Fuel Cell Science, Engineering and Technology*, R. K. Shah and S. G. Kandlikar (eds) (ASME, New York), pp. 209–216.
[3] Yuan, J., Rokni, M., and Sundén, B., 2003, "Three-Dimensional Computational Analysis of Gas and Heat Transport Phenomena in Ducts Relevant for Anode-Supported Solid Oxide Fuel Cells," Int. J. Heat Mass Transfer, **46**, pp. 809–821.
[4] Zhu, B., Bai, X. Y., Chen, G. X., and Buesell, M., 2002, "Fundamental Study on Biomass Fuelled Ceramic Fuel Cells," Int. J. Energy Res., **26**, pp. 57–66.
[5] Brchewitz, L., and Palsson, J., 2000, "Design of an SOFC System Combined to the Gasification of Biomass," Proc. the 4th European SOFC Forum, A. J. McEvoy, ed., Lucerne, Switzerland, Vol. 1, pp. 59–68.
[6] Yuan, J., Rokni, M., and Sundén, B., 2001, "Simulation of Fully Developed Laminar Heat and Mass Transfer in Fuel Cell Ducts with Different Cross Sections," Int. J. Heat Mass Transfer, **44**, pp. 4047–4058.
[7] Teng, H., and Zhao, T. S., 2000, "An Extension of Darcy's Law to Non-Stokes Flow in Porous Media," Chem. Eng. Sci., **55**, pp. 2727–2735.
[8] Alkam, M. K., Al-Nimr, M. A., and Hamdan, M. O., 2001, "Enhancing Heat Transfer in Parallel-Plate Channels by Using Porous Inserts," Int. J. Heat Mass Transfer, **44**, pp. 931–938.
[9] Alazmi, B., and Vafai, K., 2001, "Analysis of Fluid Flow and Heat Transfer Interfacial Conditions between a Porous Medium and a Fluid Layer," Int. J. Heat Mass Transfer, **44**, pp. 1735–1749.
[10] Wang, J., Gao, Z., Gan, G., and Wu, D., 2001, "Analytical Solution of Flow Coefficients for a Uniformly Distributed Porous Channel," Chem. Eng. J., **84**, pp. 1–6.
[11] Comiti, J., Sabiri, N. E., and Montillet, A., 2000, "Experimental Characterization of Flow Regimes in Various Porous Media-III: Limit of Darcy's or Creeping Flow Regime for Newtonian and Purely Viscous Non-Newtonian Fluids," Chem. Eng. Sci., **55**, pp. 3057–3061.
[12] Bejan, A., 1987, Convective Heat Transfer in Porous Media, in *Handbook of Single-phase Convective Heat Transfer*, Kakac, S., Shah, R. K., and Aung, W., eds. (J. Wiley & Sons, New York).
[13] Vafai, K., and Kim, S. J., 1994, "On the Limitations of the Brinkman-Forchheimer-Extended Darcy Equation," Int. J. Heat Fluid Flow, **16**, pp. 11–15.
[14] Chikh, S., Bounedien, A., and Bouhadef, K., 1995, "Non-Darcian Forced Convection Analysis in an Annulus Partially Filled with a Porous Material," Numer. Heat Transfer, Part A, **28**, pp. 707–722.
[15] Marafie, A., and Vafai, K., 2001, "Analysis of Non-Darcian Effects on Temperature Differentials in Porous Media," Int. J. Heat Mass Transfer, **44**, pp. 4401–4411.
[16] Vafai, K., and Kim, S. J., 1990, "Fluid Mechanics of the Interface Region between a Porous Medium and a Fluid Layer—An Exact Solution," Int. J. Heat Fluid Flow, **11**, pp. 254–256.
[17] Yakabe, H., Hishinuma, M., Uratani, M., Matsuzaki, Y., and Yasuda, I., 2000, "Evaluation and Modeling of Performance of Anode-supported Solid Oxide Fuel Cell," J. Power Sources, **86**, pp. 423–431.
[18] Iwaa, M., Hikosaka, T., Morita, M., Iwanari, T., Ito, K., Onda, K., Esaki, Y., Sakaki, Y., and Nagata, S., 2000, "Performance Analysis of Planar-type Unit SOFC Considering Current and Temperature Distributions," Solid State Ionics, **132**, pp. 297–308.

A Review of Heat Transfer Issues in Hydrogen Storage Technologies

Jinsong Zhang

Timothy S. Fisher[1]

Energy Center at Discovery Park and
School of Mechanical Engineering,
Purdue University,
West Lafayette, IN 47907-2088

P. Veeraraghavan Ramachandran
Energy Center at Discovery Park and
Department of Chemistry,
Purdue University,
West Lafayette, IN 47907-2084

Jay P. Gore

Issam Mudawar

Energy Center at Discovery Park and
School of Mechanical Engineering,
Purdue University,
West Lafayette, IN 47907-2084

Significant heat transfer issues associated with four alternative hydrogen storage methods are identified and discussed, with particular emphasis on technologies for vehicle applications. For compressed hydrogen storage, efficient heat transfer during compression and intercooling decreases compression work. In addition, enhanced heat transfer inside the tank during the fueling process can minimize additional compression work. For liquid hydrogen storage, improved thermal insulation of cryogenic tanks can significantly reduce energy loss caused by liquid boil-off. For storage systems using metal hydrides, enhanced heat transfer is essential because of the low effective thermal conductivity of particle beds. Enhanced heat transfer is also necessary to ensure that both hydriding and dehydriding processes achieve completion and to prevent hydride bed meltdown. For hydrogen storage in the form of chemical hydrides, innovative vehicle cooling design will be needed to enable their acceptance. [DOI: 10.1115/1.2098875]

Keywords: hydrogen storage, heat transfer, compressed hydrogen, liquid hydrogen, metal hydrides, chemical hydrides

Introduction

Hydrogen has been recognized as the likely energy carrier for future energy systems because it may enable the use of a diverse array of primary energy sources, including fossil fuels as well as sustainable long-term energy sources, such as hydropower, biomass, wind, and solar. As an energy carrier, hydrogen offers the advantage of clean and complete conversion to water, which has generally benign environmental impacts. The development of a hydrogen-based energy economy with the use of sustainable energy sources promises to alleviate numerous current problems facing our nation and the world—such as air pollution, greenhouse gas production, and global security. Recent reports [1–4] have identified many critical technical challenges that remain to be addressed before a hydrogen-based energy economy can become viable. While much contemporary research has focused on the conversion of hydrogen-carried energy to electrical form using fuel cells, upstream issues involving production, distribution, and storage of hydrogen are also critically important. Of these, on-board hydrogen storage for vehicle applications involves many technical challenges and opportunities. This review summarizes the technical characteristics and requirements of the most promising hydrogen storage approaches, particularly for fuel-cell-powered vehicles, while identifying significant heat transfer issues associated with each.

To realize the full potential of the hydrogen economy, the challenges of storage and distribution must be addressed, particularly for the transportation sector. Vehicle-based hydrogen storage systems must meet stringent requirements of gravimetric and volumetric energy densities. According to the U.S. Department of Energy's Freedom Car Program targets, the gravimetric density should be at least 6 wt.% (i.e., 6 kg H_2 in a 100 kg tank), and the volumetric density should be at least 45 g H_2/L by 2010 [3], while even more aggressive targets have been set for future years. In addition, fast hydrogen fueling processes are needed to meet the ingrained expectations of consumers, with a targeted fueling rate of 1.5–2.0 kg H_2/min [3].

Hydrogen storage and distribution systems must be energy efficient in order to retain the inherent efficiency advantages of fuel cells. The energy efficiency of hydrogen storage is typically measured by comparing the lower heating value (LHV) of hydrogen (approximately 120,000 kJ/kg or 240 kJ/mol) to the total energy input during a complete use cycle. Current hydrogen storage methods include compression, liquefaction, absorption, and chemical binding as the four potential processes for increasing energy density. Each of these processes involves exothermic and endothermic operations and requires thermal management for controlling process temperatures and enhancing process efficiencies. For the entire system to be practical, on-board thermal management devices for hydrogen storage must be designed to be as compact and lightweight as possible while minimizing parasitic losses. In this respect, passive cooling systems, such as thermosyphons [5,6], which do not require pumping power, may be highly attractive. Nevertheless, thermal management will surely involve a trade-off between energy efficiency gains from improved thermal management and efficiency losses from additional weight and the energy consumption of the thermal management system itself.

Recently, several review articles have addressed various aspects of hydrogen storage technologies [7–12], but none has specifically considered heat transfer and related energy-efficiency issues, which are the focus of this review. The storage methods considered here include compressed hydrogen, liquid hydrogen, metal hydrides (including complex hydrides), and chemical hydrides. (Nanostructured carbon for hydrogen storage is not discussed because of inconsistent experimental results [13].) This review describes each of these technologies with an emphasis on thermal management and heat transfer issues. Throughout the text, opportunities for heat transfer research are highlighted.

Compressed Hydrogen

Compressed hydrogen storage is one of the few commercially available hydrogen storage technologies. Because of hydrogen's relatively low energy density, it must be compressed to high pressure to store a sufficient amount of hydrogen for vehicle use. At room temperature, the density of compressed hydrogen at 350 bar (~5000 psi) is approximately 22.9 g/L, and at 700 bar (~10,000 psi) it is approximately 39.6 g/L. Industry standards

[1]Corresponding author: tsfisher@purdue.edu; phone: 765-494-5627.

Contributed by the Heat Transfer Division of ASME for publication in the JOURNAL OF HEAT TRANSFER. Manuscript received September 30, 2004; final manuscript received August 25, 2005. Assoc. Editor: Jacob Chung.

for compressed hydrogen storage have been set at 350 bar, with a future target of 700 bar [7,14–16]. High-strength, carbon-fiber composite pressure vessels rated to 700 bar may achieve a gravimetric storage density of 6 wt.% and a volumetric storage density of 30 g/L [14], which falls short of the Freedom Car Program's goal for volumetric density.

One of the main advantages of compressed hydrogen storage is that it is relatively simple and filling of a vehicle tank can be completed in a short time. Because of these advantages, compressed hydrogen has been adopted in many prototype fuel-cell vehicles. The main disadvantages are its low volumetric and gravimetric densities compared to other storage methods. Another shortcoming of compressed hydrogen is the public's perception of safety concerns associated with extremely high-pressure hydrogen tanks. However, recent test results have indicated that 700 bar composite vessels may actually be safer than their low pressure counterparts widely used in industry, primarily because of thicker tank walls [17].

The process of compressing hydrogen from atmospheric pressure to 700 bar consumes a large amount of energy. Thermodynamically, isothermal reversible compression consumes the least work [18], which can be calculated as (assuming ideal gas behavior)

$$w = RT_1 \ln\left(\frac{P_2}{P_1}\right) = 4.157 \cdot 300 \cdot \ln\left(\frac{700}{1}\right) = 8170 \text{ kJ/kg} \quad (1)$$

In reality, the temperature rise of hydrogen during compression is substantial even with multi-stage intercooling technology. Therefore, the compression process is better described by a polytropic process [18]. The energy consumption for such a process can be calculated as

$$w = \frac{n}{n-1} RT_1 \left[\left(\frac{P_2}{P_1}\right)^{(n-1)/n} - 1 \right] \quad (2)$$

Because the pressure ratio for each stage is limited to approximately 7.0 for diaphragm compressors and much less for other types [19], at least four compression stages would be necessary to obtain a pressure of 700 bar. Assuming perfect intercooling (i.e., gas cooled to the initial temperature before the next stage begins), the minimum compression work is 10,161 kJ/kg ($n=1.36$ [19]), which is still 24% greater than that of the isothermal process. Consequently, significant potential and interest exist in achieving energy savings by means of enhanced heat transfer during the compression process [20].

Two types of compressors are widely used in industry to boost hydrogen pressure to at least 150 bar: reciprocating piston compressors and diaphragm compressors. Reciprocating piston compressors can be used for both large-scale applications (e.g., pipelines [21]) and small-scale applications (e.g., fueling stations), while diaphragm compressors are mainly used for small-scale applications due to their limited flow rates imposed by the size of the diaphragm [20]. Improvements in energy efficiency for both compressor types are still possible by enhancing heat transfer.

In general, diaphragm compressors remove heat more effectively than piston compressors because of the relatively large surface area of the compression chamber, the presence of the cooled compression oil near the diaphragm, and the ability to include a cooling system in the cover of the compressor [19]. Nevertheless, the compression ratio for diaphragm compressors remains limited by the gas temperature increase during compression. Most existing diaphragm compressors employ a simple one-loop cooling system in the cover of the compressor, which can be improved significantly by increasing the number of cooling loops, implementing micro- or mini-channels, and/or coupling to a refrigeration loop.

For piston compressors, the high speed and cyclic nature of the compression process make heat transfer modeling and design quite challenging [22–24]. Traditionally, such compressors are cooled by lubricant oil, but this approach may not be feasible for hydrogen because high-purity hydrogen is required by the fuel cell. Yong [25] developed a cooling approach that employed a water spray inside a compressed-gas cylinder to reduce gas temperature via evaporation. Because PEM fuel cells require a humidified hydrogen stream, this method may be used to boost hydrogen from pipeline pressure to final charging pressure. A new approach in the design of piston compressors involves the use of a long, slow stroke in conjunction with a water-cooled gas cylinder to improve cooling performance [26]. However, the flow rates for this type of compressor are small because of the slow motion of the piston.

Equations (1) and (2) indicated that reducing the inlet hydrogen temperature decreases compression work proportionally [27]. Intercooling techniques have been designed to compensate for insufficient cooling during the compression process, and water sprays have been proposed for intercooling of air compressors [28] and may be useful for hydrogen compressors as well.

Another important heat-transfer issue for compressed hydrogen storage is the temperature increase during fast tank-filling processes [4,15]. Hydrogen exhibits a reverse Joule-Thomson effect at room temperature, i.e., throttling processes from a high-pressure stationary tank to a tank being filled cause heating of the gas instead of cooling [29,30]. During rapid filling (>1 kg H_2/min), the temperature rise inside the tank can be as high as 50°C [29], and overheating can adversely affect the integrity of the composite tank [31]. Further, with increasing temperature, the tank carries less hydrogen at a given pressure. If this temperature rise is compensated by transient overpressurization, the extra compression work, typically more than 10% of the nominal work, is wasted. Another possible remedy to overheating is precooling of the filling gas [31], but such an approach would require additional energy for refrigeration. An energy-efficient solution may be to enhance both internal and external heat transfer during the filling process and to optimize the pressure throttling process. The former approach would likely require cylinder frames made of materials with high thermal conductivities or installing heat pipes to transfer heat from inside the vehicle tank to an external heat sink, such as the vehicle frame. We note that hydrogen has a much higher thermal conductivity than most industrial gases [32], and this property may enable innovative heat transfer design.

To minimize throttling losses and resulting overheating during filling processes, multi-bank cascade systems can be employed. For example, to fill a vehicle tank to 350 bar, three banks at 450, 300, and 160 bar could be employed. The 160 bar bank would fill the vehicle tank to 130 bar, and then the 300 bar bank would fill the tank to 270 bar. Ultimately, the 450 bar bank would fill the tank to 350 bar (or higher to account for overheating). The overall temperature rise and the total fueling time in such a process can be optimized by using thermodynamic and heat transfer principles [33].

Liquid Hydrogen

Liquid hydrogen (LH_2) storage is another commercially available technology [34]. LH_2 is stored at atmospheric pressure in cryogenic tanks (20.3 K) with a density of 70.8 g/L—almost twice that of compressed hydrogen at 700 bar (39.6 g/L). An 18 gal (68 L inner vessel) cryogenic tank can carry approximately 5 kg LH_2, which is sufficient to power a fuel-cell passenger vehicle approximately 300 miles (480 km). LH_2 tanks can be filled in a relatively short time and are perceptually much safer at appropriate cryogenic temperatures than high-pressure hydrogen tanks. The main disadvantages with LH_2 are the high energy consumption associated with liquefaction processes and continuous boil-off during storage [7,35].

The simplest liquefaction cycle is the Joule-Thompson cycle [36] in which hydrogen gas is first compressed to a high pressure

(e.g., $P=100$ bar) and then cooled in a heat exchanger before passing through a throttling valve, where it undergoes isenthalpic Joule-Thomson expansion and produces some liquid. The cooled gas is separated from the liquid and returned to the compressor through a heat exchanger. Because the inversion temperature (i.e., the temperature below which throttling produces a cooling effect) of hydrogen is only approximately 200 K, expansion at room temperature will not induce a cooling effect, and liquid nitrogen ($T=77$ K) is often used to precool hydrogen before expansion [37,38].

Thermodynamically, liquefying hydrogen involves three heat transfer stages. The first stage extracts sensible heat (4000 kJ/kg) to reduce the temperature from 300 K to 20.3 K [32]. In the second stage, latent heat (450 kJ/kg) is extracted to condense hydrogen at 20.3 K [32]. The third stage is called ortho-para conversion, which requires heat extraction of 703 kJ/kg [39]. The entire liquefaction process requires heat removal of 5153 kJ/kg that must be provided by a liquefaction cycle. The minimum theoretical work to liquefy normal hydrogen to 99.79% para form is 14,280 kJ/kg (~12% H_2 LHV) [39]. In comparison, the minimum theoretical work to liquefy nitrogen is only 6% that of liquid hydrogen. The actual energy consumption for hydrogen liquefaction is usually at least 2.5 times the theoretical minimum, depending on the capacity of the liquefaction plant [40].

The storage of LH_2 requires highly insulated cryogenic tanks. To minimize heat ingress, the three basic mechanisms of heat transfer should be considered. The rate of radiation heat transfer is proportional to the emissivity of the shields between the warm and cold surfaces and inversely proportional to the number of these shields. To minimize radiation heat transfer, multilayer insulation (MLI), also called superinsulation, is often used. The apparent thermal conductivity of MLI is $1-8\times10^{-5}$ W/m-K, which is approximately three orders of magnitude lower than the thermal conductivity of fiberglass building insulation [41]. MLI consists of 30–80 layers of low-emissivity radiation shields, e.g., aluminum foil ($\varepsilon=0.05$), separated by low-conductivity spacers, e.g., fiberglass paper. When placed against each other, the shields touch at only a few discrete points to minimize heat conduction. For MLI, the apparent thermal conductivity parallel to the radiation shields is typically three to six orders of magnitude higher than that normal to the layers [36]. Such a large disparity in directional thermal conductivity presents considerable challenges in thermal insulation design for systems where structural supports and feedlines penetrate the insulation. An alternative to MLI is to use microsphere insulation, which exhibits isotropic thermal conductivity and can tolerate significantly higher compression; nevertheless, the apparent thermal conductivity of microsphere insulation is one order of magnitude higher than that of MLI [42].

A critical design variable for MLI-insulated vessels is the optimal number of insulation layers per unit thickness. If the layer density is too high, the increase in conductive heat loss through the spacers can outweigh the decrease in radiative heat flux provided by more insulation layers. A typical dependence of the apparent thermal conductivity on layer density for MLI is shown in Fig. 1 [42]. To minimize convection, the volume between the inner vessel and the outer vessel is typically evacuated to high vacuum, e.g., 1.3×10^{-8} bar [41]. The vacuum is maintained by gas-adsorbing getter materials such as activated carbon [36]. Under such high vacuum conditions, free molecular conduction can occur because the molecular mean free path is large relative to the distance between the boundaries, and, typically, heat flux by free-molecular conduction varies linearly with pressure, as shown in Fig. 2 [42].

To accelerate the time required for cooling and to reduce evaporation losses during the cool-down process of the vessel, the thickness of the inner shell is usually designed to be as thin as needed to withstand the maximum internal pressure and bending forces. The outer shell is designed to keep the vessel wall from collapsing due to the difference between atmospheric pressure on the outside and vacuum pressure on the inside [43]. Support members are installed within the outer shell to buttress the inner shell and must balance the competing needs for adequate mechanical support and minimal heat conduction. Further research on materials with appropriate combinations of mechanical and thermal properties is warranted.

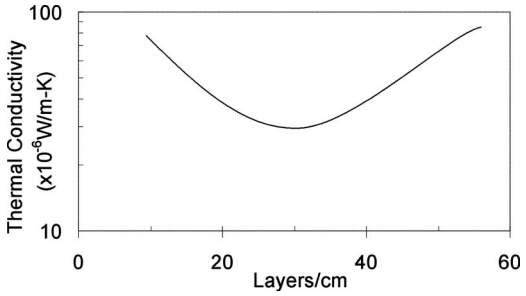

Fig. 1 Typical variation of thermal conductivity with layer density for a typical MLI with boundary temperatures of 294 and 78 K, adapted from Ref. [42]

Heat flow from the ambient to the tank's cryogenic interior will inevitably cause evaporation, or "boil-off," and the vessel's pressure will increase. When the pressure increases to a prescribed level, hydrogen vapor must be vented through a pressure relief valve. Cryogenic storage vessels are generally designed for a vapor volume of 10% to extend the dormancy time—the time that the inner vessel can be sealed before the pressure level reaches a critical value [36]. Because of heat ingress, LH_2 can stratify inside the vessel, and this phenomenon increases the boil-off rate because the segregated warmer fluid vaporizes more readily, thus raising the tank pressure to the saturation pressure of the warm layer. This pressure rise shortens the storage period between successive ventings and is especially severe with large vessels. For small-sized vehicle tanks, metal conducting rods can be used to redistribute heat from the top to the bottom portions of the inner vessel [36].

To reduce boil-off rates, liquid or vapor shields can be employed. Vapor shields take advantage of the cold vent gas from the liquid hydrogen vessel. The escaping vent gas is routed through a vapor shield and sensibly absorbs some of the heat that would otherwise warm the LH_2 [42]. A patented recooling system using a similar principle can extend the dormancy time of a 68 L vehicle vessel to more than 12 days before evaporation losses occur [44,45]. Liquid shields use a similar process to absorb latent heat in an inexpensive cryogenic liquid such as nitrogen. Nevertheless, the addition of liquid or vapor shielding adds extra volume and weight to the storage system.

Another source of boil-off is sloshing—the motion of liquid inside a vessel caused by acceleration and deceleration—which

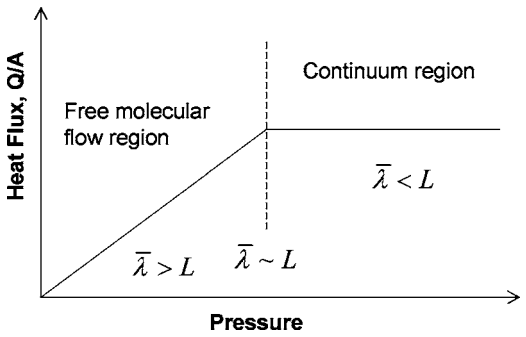

Fig. 2 Heat transfer as a function of pressure for vacuum insulation, adapted from Ref. [42]

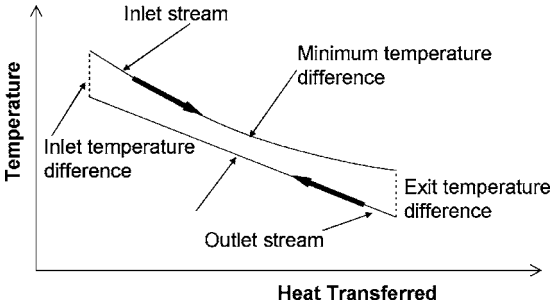

Fig. 3 Temperature profile in a countercurrent hydrogen heat exchanger, adapted from Ref. [36]

transforms some of the liquid's kinetic energy and impact energy to thermal energy [46]. Sloshing can be significant for vehicles in a city driving environment. A potential solution is to insert traverse or antislosh baffles to restrain the motion of the liquid [46], but this approach will reduce the system's gravimetric storage density.

To appreciate the challenges in designing LH_2 tanks for vehicle applications, a sample design is given here. Assuming a 68 L inner vessel design volume, 300 K ambient temperature, and 4% daily boil-off rate, the allowable heat ingress rate is 1 W for a full tank. A vessel wall thickness of 10 cm would require an apparent thermal conductivity of 3.2×10^{-5} W/m-K with a resulting exterior volume of 185 L (assuming a spherical vessel structure). A wall thickness of 5 cm would require an apparent thermal conductivity of 1.9×10^{-5} W/m-K with an exterior volume of 117 L, and the resulting volumetric density would be approximately 37 g H_2/L, which is slightly below the DOE target of 45 g H_2/L.

The design of liquid hydrogen transfer lines also involves many heat transfer issues. Two-phase flow is common in the transfer of liquid hydrogen as a result of heat transfer to the fluid, particularly during the start-up transient of the filling process. The existence of vapor in a transfer line can critically reduce its carrying capacity; therefore, evaporation must be minimized by insulation. The insulation strategies for the transfer line are similar to those for the storage vessel. Additional issues, such as severe contractions and expansions of the transfer piping in station filling cycles, need to be addressed through the analysis and design of expansion joints, bellows, and U-bends [36].

Heat exchangers are used extensively in LH_2 production. Because of the low operating temperature, cryogenic liquefiers cannot produce liquid if the heat exchanger effectiveness is less than approximately 85% [41]. Several measures can be utilized to improve heat exchanger effectiveness, including small temperature differences between inlet and outlet streams, large surface area-to-volume ratios, and high heat transfer coefficients [36,41]. Because of the variation of the specific heat of hydrogen during heat transfer processes, an unusual situation can occur in which the minimum temperature difference between the heat exchanging streams occurs in the middle of the flow path, as shown in Fig. 3 [36]. This phenomenon should be considered when attempting to improve heat exchanger efficiency by minimizing temperature differences between inlet and outlet streams.

A new method of storage involves cryo-compressed hydrogen [47,48]. In this process, medium-pressure hydrogen (e.g., 150 bar) is adsorbed by activated carbon inside a tank that is maintained at 77 K by a liquid nitrogen jacket, which must be replenished approximately once per week [47]. The advantage of this method is that it does not require the direct input energy associated with hydrogen liquefaction, yet its storage capacity is similar to that of a high-pressure hydrogen tank at 700 bar [47]. Nevertheless, the overall energy consumption may not be favorable because of the work involved with compression and nitrogen liquefaction.

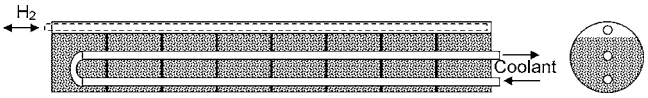

Fig. 4 Schematic of a patented metal-hydride hydrogen storage bed, adapted from Ref. [52]

Metal Hydrides

The broad family of metal hydrides comprises an alternative to the previously discussed storage approaches, which do not involve chemical reactions. Thousands of metals and alloys can react reversibly with hydrogen to form hydrides [10]. Such a reversible process from a metal M and hydrogen to a metal hydride can be expressed as

$$M + 0.5x\mathrm{H}_2 \rightleftarrows M\mathrm{H}_x + \text{heat} \tag{3}$$

The charging, or hydriding, process releases heat, while the discharging, or dehydriding, process requires heat input. Most prior research has focused on conventional metal hydrides—hydrides of alloys and intermetallic compounds in which a strong hydride forming metal element (A) combines with a weak hydriding metal element (B) to achieve desired intermediate thermodynamic affinities for hydrogen [49]. The intermetallic compounds used in conventional metal-hydride systems can be generally classified into four categories: AB_5, AB_2, AB, and A_2B [49]. Some typical intermetallic compounds are $LaNi_5$, ZrV_2, $ZrMn_2$, TiFe, ZrNi, Mg_2Ni, and Ti_2Ni [7]. To promote better information exchange and to encourage discovery, a public hydride database has been established by the U.S. Department of Energy [50].

Conventional metal hydrides are commercially available [51,52] and are perceptually much safer than compressed hydrogen, as evidenced by their application in fuel-cell-powered mining locomotives [53]. Their material volumetric densities are comparable to that of liquid hydrogen [7], but the main disadvantage of metal hydrides is low gravimetric density, which is currently less than 2.0 wt.% [51]. Another serious drawback is associated with low hydriding and dehydriding rates, which are limited in part by thermal properties. Hydriding processes release large amounts of heat, as dictated by the heat of reaction, while the hydride expands in volume. If the heat is not removed efficiently, the temperature rise can be so large that the process will stall. Furthermore, metal hydrides may sinter at high internal temperatures [54] and lose hydrogen storage capacity. The dehydriding process requires heating at a specific temperature, dictated by chemical thermodynamics, to proceed. Without sufficient heat supply, the release of hydrogen will cease because of the reduced temperature in the hydride bed. Therefore, enhanced internal heat transfer is essential to improve system performance and to maintain system reliability [55]. Utilizing the waste heat from a fuel cell to dehydrogenate the metal-hydride bed could improve overall energy efficiency and, consequently, metal-hydride research [7] has focused on materials that can release hydrogen near 80°C, the normal operating temperature of a PEM fuel cell. The coupling of fuel cells with metal-hydride beds would not only enable higher energy efficiencies but also save scarce on-board space [56].

Metal-hydride powder has a typical grain size of 50–100 μm. After approximately 10 to 100 hydriding/dehydriding cycles, the powder decomposes to an equilibrium grain size approximately 1 μm [57]. Such fine metal-hydride powders typically have low effective thermal conductivities of the order of 0.1 W/m-K [58]. Heat and mass transfer enhancement methods suggested for metal-hydride beds can be broadly classified into two categories: extended areas in the forms of fins, foams, or meshes, and binding metal hydrides into a solid matrix formed by high-conductivity materials such as copper, aluminum, or nickel [59].

Figure 4 illustrates the design of a developmental metal-hydride hydrogen storage vessel using metal foams [60]. The vessel is

divided into compartments by metal plates, and each compartment is filled with a metal foam and fitted with a porous metal filter and U-shape coolant tube. The foam material, normally aluminum, provides support for the metal-hydride powders and enhances internal heat transfer [60]. The foam generally occupies approximately 6% of the volume. Metal-hydride powders occupy approximately 80% of the open space, while the remainder is left for expansion [60].

Expanded natural graphite/metal-hydride compacts have recently been proposed to enhance heat transfer and have exhibited promising results [57,58,61]. To make such compacts, commercially available expandable graphite is heated in order to expand in volume, and the expanded graphite is then homogeneously mixed with metal-hydride particles. The mixture is then pressed into small cylindrical blocks to make compacts [57]. Compacts with 2.1% mass fraction of expanded graphite can increase the effective thermal conductivity of metal-hydride powders from 0.1 W/m-K to above 3 W/m-K [57].

The effective thermal conductivity of a powder bed depends strongly on the thermal contact resistance among particles. When particles are pressed against each other, the contact area and effective thermal conductivity increase. Consequently, particle beds under high internal stress have much higher thermal conductivities than those that are loosely packed [62,63]. However, particles that are pressed too tightly against each other suffer from significantly reduced hydrogen storage capacity. For example, highly compacted alanates (discussed in detail below) exhibit 67% lower reversible hydrogen storage capacities than unconstrained samples [64]. In addition, the containing vessel may rupture at high internal stresses [51]. A potential design that can take advantage of this phenomenon would involve a piston-type structure for the containing vessel. The piston would be preset to a certain pressure by springs or other mechanisms. Once the internal stress of metal-hydride bed exceeds the preset pressure, the piston would move outward to allow for expansion of the metal-hydride bed and maintain an appropriate stress level to achieve adequate internal heat transfer.

To illustrate more quantitatively the issues involved with metal hydrides, we consider sodium alanate (sodium aluminum hydride), which can reversibly absorb and desorb hydrogen in the presence of titanium catalyst, as reported by Bogdanovic [65,66] in 1997. This discovery has stimulated much recent research in complex hydrides, such as sodium aluminum hydride (sodium alanate), lithium aluminum hydride (lithium alanate), ammonia borane, and magnesium-modified lithium-amide compound [11,64,67–72]. The absorption (desorption) of hydrogen to (from) sodium alanate proceeds in two stages as follows:

$$NaAlH_4 \rightleftarrows \tfrac{1}{3}Na_3AlH_6 + \tfrac{2}{3}Al + H_2 \rightleftarrows NaH + Al + \tfrac{3}{2}H_2 \qquad (4)$$

The first step releases 3.7 wt.% H_2, while the second step releases additional 1.9 wt.% H_2 for a total theoretical gravimetric storage capacity of 5.6 wt.% H_2. The heats of formation for the two steps are 37 kJ/mol (15% of the H_2 LHV) and 47 kJ/mol (20% of the H_2 LHV), respectively [66]. Though research on $NaAlH_4$ may not provide an ultimate solution to hydrogen storage because of its limited gravimetric density, developments in catalysis could produce true reversibility with related borohydride and transition metal complexes [73]. The weighted average heat of formation of sodium alanate is 40.3 kJ/mol H_2. For a hydride bed with a capacity of 5 kg H_2 and a fueling rate of 1.5 kg/min (750 mol/min), the average heat dissipation rate is an astounding 0.50 MW during the fueling process.

Because of the extremely high required heat transfer rates and stringent space and weight requirements, on-board regeneration of metal-hydride beds may not be practical. One alternative is to develop cartridge-type metal-hydride beds that can be inserted and removed at fueling stations. Then, in an off-board process at the station, the heat transfer rate for the charging process could be significantly reduced by extending the charging time. However, this solution presents other practical challenges because the cartridge's mass will be of the order of 100 kg, and active heat transfer measures will likely be required even for off-board regeneration. Another possibility is to transfer charged metal-hydride powder from the fueling station to the vehicle tank and to transfer the discharged metal-hydride powder from the vehicle tank back to the fueling station for recharging. The viability of this powder-based method will depend largely on thermal hardware required for on-board heat exchange processes. Plate-fin heat exchangers with wide plate spacing could allow relatively simple powder injection and removal processes. However, if compact heat-exchangers are needed, then powder transfer processes could become excessively unreliable and time consuming. One benefit of any off-board charging process would be the possibility of using waste heat for domestic or commercial processes, such as water and space heating.

Another issue with the sodium alanate system is that the final discharged products consist of sodium hydride and aluminum. For the hydriding process to reach completion, all reactants (sodium hydride, aluminum, and hydrogen) must exist in close proximity to each other. This requirement applies to other promising complex hydrides as well and suggests that partial chemical immobilization could be used to enhance system performance. To this end, glass microspheres have been proposed to confine the metal-hydride particles [74] in a shell that is gas-permeable at higher temperatures and gas-tight at room temperature [75]. The advantage of this method is that the shell dramatically reduces diffusion of the metal hydride, thus inhibiting separation of the dehydrogenation products inside the bed. The disadvantage of this method is a decrease in volumetric storage density (weight is not a serious issue because glass microspheres are extremely light-weight). Another challenge lies in reduced heat conduction caused by the shells. Because of the low thermal conductivity of glass and the large number of material interfaces, improved heat exchange processes as well as fundamental studies of thermal conductivity and heat capacity are needed, such as those that employ the transient hot-wire method [76].

With ongoing research on potential complex hydrides [7,67], characterization of their thermal properties will be an essential step in developing well engineered systems [1]. Most of the potential complex hydrides are extremely moisture sensitive and readily react with air-borne water vapor, generating highly flammable and explosive hydrogen gas [55]. Therefore, experiments must be conducted under inert environments. To make matters more difficult, critical thermal properties vary significantly from the hydrogenated and dehydrogenated states and also can depend strongly on particle diameter and density. Therefore, the thermal properties of partially and fully dehydrogenated tanks will differ significantly, and the heat transfer systems must be flexible enough to accommodate all such conditions [64].

Most prior modeling work has involved conventional metal hydrides. Metal-hydride beds are usually modeled as porous media, and Darcy's law is used to calculate the gas velocity [77]. The chemical kinetics of the hydriding and dehydriding processes may be described by an Arrhenius equation [78]. The shrinking core model, which describes a chemical reaction progressing from outside a spherical reactant to the inside, has been used to model hydriding and dehydriding processes [79]. The pressure inside the hydride bed can be related to temperature by van't Hoff's equation [77]:

$$\ln(P_{eq}) = \frac{\Delta H}{RT} - \frac{\Delta S}{R} \qquad (5)$$

Klein et al. [61] calculated effective thermal conductivity based on a model assuming two half-spherical particles in contact and using a deformation factor to account for the change in shape under stress. A homogenization method that is capable of considering microscopic behaviors, such as pulverization, changes of void fraction, and contact area, has been proposed to calculate the

effective thermal conductivities of metal-hydride beds [63,79,80]. Gadre et al. [60] explored the possibility of using a simple numerical model to predict the discharging behavior of a practical metal hydride bed and obtained relatively good agreement with experimental data. Askri et al. [78] examined the validity of ignoring radiation heat transfer for $LaNi_5$ and magnesium hydride systems and also examined hydrogen flow and heat transfer in the expansion section of the metal-hydride bed. Guo et al. [81] examined the importance of considering conjugate heat transfer between gas-phase convection and solid-phase conduction. Given the early state of the field and the limited amount of prior work, a significant need exists for combined modeling and experimental studies [82] of metal-hydride systems to include conjugate heat and mass transfer, stress analysis, and thermo-mechanical effects on thermal conductivities and mass transfer coefficients.

Chemical Hydrides

Chemical compounds that release hydrogen when they react with water or other substances are classified as chemical hydrides. Unlike metal hydrides, chemical hydrides generally do not hydrogenate and dehydrogenate reversibly. The dehydrogenated products are not easily converted back to chemical hydrides, and central recycling facilities would likely be needed to provide such conversion. The recycling process usually involves a significant number of chemical reactions; therefore, the overall energy efficiency of chemical-hydride systems must account for the following factors: energy consumption to transport chemical hydrides from recycling facilities to fueling stations, energy consumption to transfer reaction products from fueling stations to recycling facilities, energy efficiency of the hydrogen release reaction, and energy efficiencies of all the physical treatments and chemical reactions involved in a complete recycling process.

Many chemical hydrides such as sodium hydride (NaH), magnesium hydride (MgH_2), and sodium borohydride ($NaBH_4$) are under investigation [83–86]. Sodium borohydride is the most developed among chemical hydrides for hydrogen storage applications, as evidenced by its use in Daimler-Chrysler's fuel-cell-powered Natrium™ minivan [87]. Because sodium borohydride reacts very slowly with water at room temperature except in the presence of catalysts such as $RuCl_3$ and $CoCl_3$ [88], it can be stored stably in aqueous solution containing a few percent NaOH as a stabilizer [89]. The solution can be pumped through a chamber to interact with a catalyst bed to produce hydrogen [90,91] according to the following reaction [89–92]:

$$NaBH_4 + 2H_2O \xrightarrow{\text{Catalyst}} NaBO_2 + 4H_2 + \text{Heat} \qquad (6)$$

The exothermic reaction releases approximately 55 kJ of heat per mole of H_2 [92] (23% of the H_2 LHV). Assuming a PEM fuel-cell efficiency of 50%, heat generation from a sodium borohydride storage system represents an additional 46% increase above the heat rejection from the fuel cell alone. Given that thermal management of PEM fuel cells is already a serious issue [93], this extra heat load will only intensify the need for innovative, vehicle-scale heat transfer systems, as discussed below.

One of the main advantages of sodium borohydride is its intrinsic safety. Accidental spillage of the solution will not cause severe problems because the uncatalyzed reaction rate is very low. Sodium borohydride systems exhibit fast response to fuel demand and potentially high gravimetric (up to 21 wt.%) and volumetric densities, and the use of aqueous solution is generally compatible with current gasoline-based fueling facilities. Therefore, commercial conversion could be relatively straightforward. Furthermore, hydrogen produced from the catalyst chamber is inherently humidified and, with appropriate system design [94], can be fed directly to PEM fuel cells without extra humidification processing.

A major challenge of sodium borohydride involves the cost and energetics of recycling. The current price of sodium borohydride is approximately 50 times higher than the energy-equivalent price of gasoline. The high cost is inherent to the current industrial process, called the Schlesinger-Brown process [95], in which one mole of $NaBH_4$ requires four moles of metallic sodium produced by sodium chloride (NaCl) electrolysis, which a very energy-intensive process. Several ongoing projects are addressing these recycling issues [92,96–98]. Even if the overall cost cannot match that of gasoline, sodium borohydride systems may be useful in less cost-sensitive applications, such as powering portable electronics [92].

Another impediment to the adoption of sodium borohydride or other chemical hydrides, which typically have similar heats of reaction, involves the cooling requirements. Though fuel-cell vehicles need to dissipate approximately the same amount of the waste heat as internal-combustion (IC) engines [99], the low operational temperature of the PEM fuel cell, approximately 80°C, makes vehicle cooling design particularly challenging. The coolant temperature for an IC engine can reach as high as 120°C, while that for a PEM fuel cell can be only 60–65°C. Given a maximum design ambient temperature of 38°C [100], the temperature difference from the radiator to ambient in IC engine vehicles is two to four times that of fuel-cell vehicles. Furthermore, because of the extremely low electrical conductivity required of the fuel-cell coolant, the fuel cell is normally cooled directly by deionized water, which then transfers heat to an antifreeze loop through a heat exchanger, reducing the operating temperature of the radiator even further [101]. To satisfy all heat rejection requirements, larger radiator surface areas and much higher coolant and air flow rates are needed. These requirements will contribute to significant increases in parasitic power consumption and vehicle volume for the cooling systems in fuel-cell vehicles.

Because most on-board waste heat is eventually dissipated to the ambient through the radiator, innovative radiator designs must be adopted to address the cooling challenges faced by chemical-hydride storage systems. Because of the inefficiency of air as a heat transfer medium, the air-side heat transfer coefficient is considerably smaller than that of the coolant side [99]. In most existing vehicle designs, the flow field around the radiator is generally not optimized for heat transfer. With such a high on-board cooling load, a great need exists to integrate cooling system design with aerodynamic vehicle design. A prior study on the interaction of cooling air flow and aerodynamic performance suggests that aerodynamic improvements need not necessarily interfere with cooling requirements [102], and recent back-end radiator designs have demonstrated simultaneous improvements in cooling performance and aerodynamic performance [101]. In addition to air-side improvements, adoption of multiple-pass crossflow heat exchangers may also improve radiator performance [103]. Other heat transfer enhancement techniques (e.g., variable-roughness exchanger tube inserts, interrupted and wavy fins) could also provide significant performance improvements [104].

Summary and Conclusions

The foregoing review indicates that each potential hydrogen storage method for vehicle applications involves substantial heat transfer challenges. In some cases, heat transfer issues could become the determining factor in the feasibility of a given storage method, and heat transfer research is needed for each of the four identified hydrogen storage methods. Enhanced cooling during compression processes is not only important for compressed hydrogen systems, but also essential for hydrogen storage approaches involving liquid hydrogen and metal hydrides. Many opportunities for improved thermal insulation exist for liquid hydrogen systems because of the need to maintain extremely low temperatures over long time periods. Enhanced heat transfer for metal-hydride systems is essential in allowing rapid hydrogen uptake (i.e., tank filling) and sufficiently fast kinetics for hydrogen

release. Innovative vehicle radiator designs will be needed for chemical-hydride systems, which require very high rates of heat dissipation during vehicle operation.

In the near term, compressed hydrogen systems will likely remain dominant for fuel-cell demonstration vehicles. Liquid hydrogen systems may soon gain in popularity because most existing hydrogen fueling stations are already supplied by liquid hydrogen tankers. Metal- and chemical-hydride systems are currently less developed, but each offers both significant advantages and disadvantages relative to the alternatives. Much of the uncertainty surrounding their feasibility involves technical issues that require the attention of the heat transfer research community, particularly in the areas of thermophysical properties and on-board vehicle thermal management systems.

Acknowledgment

The authors thank Dr. Scott Jorgensen and Dr. Florian Mertens of General Motors and William Liss of the Gas Technology Institute for useful discussions. P.V.R thanks General Atomics and the Purdue Research Foundation for financial support.

Nomenclature

ΔH = enthalpy change, kJ/kg
L = distance between two surfaces, m
LH_2 = liquid hydrogen
LHV = lower heating value, kJ/kg
n = polytropic constant, 1.41 for isentropic process for hydrogen
P = pressure, bar
P_1 = initial pressure, bar
P_2 = final pressure, bar
P_{eq} = equilibrium pressure, Pa
R = gas constant for hydrogen, 4.157 kJ/kg-K
ΔS = entropy change, kJ/kg-K
T = temperature, K
T_1 = initial temperature, K
w = specific compression work, kJ/kg
ε = emissivity
λ = mean free path, m

References

[1] U.S. Department of Energy, Office of Basic Energy Sciences, 2003, *Basic Research Needs for the Hydrogen Economy*, http://www.sc.doe.gov/bes/hydrogen.pdf
[2] U.S. Department of Energy, Basic Energy Sciences Advisory Committee, 2003, *Basic Research Needs to Assure a Secure Energy Future*, http://www.sc.doe.gov/bes/BESAC/Basic_Research_Needs_To_Assure_A_Secure_Energy_Future_FEB2003.pdf
[3] U.S. Department of Energy, Office of Hydrogen, Fuel Cells, and Infrastructure Technologies, 2003, *Multi-Year Research, Development and Demonstration Plan*, http://www.eere.energy.gov/hydrogenandfuelcells/mypp/
[4] National Research Council and National Academy of Engineering, 2004, *The Hydrogen Economy: Opportunities, Costs, Barriers, and R&D Needs*, The National Academies Press, Washington, DC.
[5] Mukherjee, S., and Mudawar, I., 2003, "Pumpless Loop for Narrow Channel and Micro-Channel Boiling From Vertical Surfaces," ASME J. Electron. Packag., **125**, pp. 431–441.
[6] Mukherjee, S., and Mudawar, I., 2003, "Smart, Low-Cost, Pumpless Loop for Micro-Channel Electronic Cooling using Flat and Enhanced Surfaces," IEEE Trans. Compon. Packag. Technol., **26**, pp. 99–109.
[7] Zuttel, A., 2003, "Materials for Hydrogen Storage," Mater. Today, **6**(9), pp. 24–33.
[8] Zhou, L., 2005, "Progress and Problems in Hydrogen Storage Methods," Renewable Sustainable Energy Rev., **9**(4), pp. 395–408.
[9] Sarkar, A., and Banerjee, R., 2005, "Net Energy Analysis of Hydrogen Storage Options," Int. J. Hydrogen Energy, **30**(8), pp. 867–877.
[10] Grochala, W., and Edwards, P. P., 2004, "Thermal Decomposition of the Non-Interstitial Hydrides for the Storage and Production of Hydrogen," Chem. Rev. (Washington, D.C.), **104**(3), pp. 1283–1315.
[11] Ritter, J. A., Ebner, A. D., Wang, J., and Zidan, R., 2003, "Implementing a Hydrogen Economy," Mater. Today, **6**(9), pp. 18–23.
[12] Fakioglu, E., Yurum, Y., and Nejat Veziroglu, T., 2004, "A Review of Hydrogen Storage Systems Based on Boron and Its Compounds," Int. J. Hydrogen Energy, **29**(13), pp. 1371–1376.
[13] Hirscher, M., Becher, M., Haluska, M., Zeppelin, F. V., Chen, X. H., Dettlaff-Weglikowska, U., and Roth, S., 2003, "Are Carbon Nanostructures an Efficient Hydrogen Storage Medium?" J. Alloys Compd., **356–357**, pp. 433–437.
[14] Irani, R. S., 2002, "Hydrogen Storage: High-Pressure Gas Containment," MRS Bull., **27**(9), pp. 680–682.
[15] Newell, K., 2004, "Low Cost, High Efficiency, High Pressure Hydrogen Storage," *Proc. 2004 Annual U.S. DOE Hydrogen Program Review*, http://www.eere.energy.gov/hydrogenandfuelcells/2004_annual_review.html
[16] Funck, R., 2003, "High Pressure Storage," *Handbook of Fuel Cells—Fundamentals, Technology and Applications*, Vielstich, W., Gasteiger, H. A., and Lamm, A. Eds., John Wiley & Sons, Hoboken, NJ, Vol. 3, pp. 83–88.
[17] Gambone, L., and Herr, M., 2005, "Performance Testing of 700 bar Hydrogen Vehicle Fuel System Components," Proc. National Hydrogen Association Annual Conference, Washington, DC.
[18] Çengel, Y. A., and Boles, M. A., 2002, *Thermodynamics: An Engineering Approach*, McGraw-Hill Higher Education, New York, pp. 337–338.
[19] PPI, Inc. *Data Sheet for 4LX Diaphragm Compressor*, http://www.gotoppi.com/
[20] Tzimas, E., Filiou, C., Peteves, S. D., and Veyret, J. B., *Hydrogen Storage: State-of-the-art and Future Perspective*, Institute for Energy, Directorate General Joint Research Centre, The Netherlands, http://www.jrc.nl/publ/P2003-181=EUR20995EN.pdf
[21] Venki, R., 2003, "The Hydrogen Fuel Infrastructure for Fuel Cell Vehicles," *Energy and Transportation: Challenges for the Chemical Sciences in the 21st Century*, The National Academies Press, Washington, DC.
[22] Hsieh, W. H., and Wu, T. T., 1996, "Experimental Investigation of Heat Transfer in a High-Pressure Reciprocating Gas Compressor," Exp. Therm. Fluid Sci., **13**, pp. 44–54.
[23] Recktenwald, G. W., Ramsey, J. W., and Patankar, S. V., 1986, "Predictions of Heat Transfer in Compressor Cylinders," Proceedings of the 1986 International Compressor Engineering Conference, Purdue, West Lafayette, IN, Vol. 1, pp. 159–174.
[24] Keribar, R., and Morel, T., 1988, "Heat Transfer and Component Temperature Prediction in Reciprocating Compressors," Proceedings of the 1988 International Compressor Engineering Conference, Purdue, West Lafayette, IN, Vol. 2, pp. 454–463.
[25] Yong, K., 1988, "Calculation of the Heat and Mass Transfer in Reciprocating Compressor With Spraying Water Into Cylinders," Proceedings of the 1988 International Compressor Engineering Conference, Purdue, West Lafayette, IN, Vol. 2, pp. 472–476.
[26] Hydro-Pac, Inc., *High-Pressure Hydrogen Compressor Data Sheet*, http://www.hydropac.com/
[27] Bailyn, M., 1994, *A Survey of Thermodynamics*, AIP Press, New York.
[28] Yong, K., 1986, "The Intercooler With Spraying Water for Air Compressors," Proceedings of the 1986 International Compressor Engineering Conference, Purdue, West Lafayette, IN, Vol. 1, pp. 153–158.
[29] Richards, M. E., Liss, W., and Kountz, K., 2002, "Natural Gas Reformer-Based Hydrogen Fueling Station Modeling," *Proceedings of the 8th International Conference of Natural Gas Vehicles*, Washington, DC.
[30] Campbell, K., Cohen, J., Eichelberger, D., and Hansel, J., 2003, "Hydrogen Fueling Safety Advances," *The 20th International Electric Vehicle Symposium and Exposition*, Long Beach, CA.
[31] Schneider, J., Suckow, T., Lynch, F., Ward, J., Caldwell, M., Tillman, J., Mathison, S., Stephanian, G., Richards, M., Liss, B, Quong, S., Durán, A., Friedlmeier, G., Maus, S., King, J., Canteen Walla, Z., Moorhead, B., Adler, R., Chernicoff, W., Sloane, C., Steele, M., and Cherry, J., 2005, "Optimizing Hydrogen Vehicle Fueling," Proceedings of the National Hydrogen Association Annual Conference, Washington, DC.
[32] Jacobsen, R. T., Penoncello, S. G., and Lemmon, E. W., 1997, *Thermodynamic Properties of Cryogenic Fluids*, Plenum Press, New York.
[33] Nilsen, S., Andersen, S. H., Haugom, G. P., and Rikheim, H., 2003, "Risk Assessments of Hydrogen Refueling Station Concepts Based on Onsite Production," *The 1st European Hydrogen Energy Conference & Exhibition (EHEC)*, Grenoble, France.
[34] Taylor, J. B., Alderson, J. E. A., Kalyanam, K. M., Lyle, A. B., and Phillips, L. A., 1986, "Technical and Economic Assessment of Methods for the Storage of Large Quantities of Hydrogen," Int. J. Hydrogen Energy, **11**(1), pp. 5–22.
[35] Amos, W. A., 1998, *Costs of Storing and Transporting Hydrogen*, National Renewable Energy Laboratory Report, NREL/TP-570–25106.
[36] Timmerhaus, K. D., and Flynn, T. M., 1989, *Cryogenic Process Engineering*, Plenum Press, New York.
[37] Newton, C. L., 1967, "Hydrogen Production, Liquefaction and Use," Cryogen. Eng. News, **2**(8), pp. 50–60.
[38] Newton, C. L., 1967, "Hydrogen Production, Liquefaction and Use," Cryogen. Eng. News, **2**(9), pp. 24–30.
[39] Baker, C. R., and Shaner, R. L., 1978, "A Study of the Efficiency of Hydrogen Liquefaction," Int. J. Hydrogen Energy, **3**(3), pp. 321–334.
[40] Bossel, U., Eliasson, B., and Taylor, G., 2003, "The Future of the Hydrogen Economy: Bright or Bleak?" *2003 European Fuel Cell Forum*, Lucerne, Switzerland, http://www.efcf.com/reports/E08.pdf
[41] Barron, R. F., 1999, *Cryogenic Heat Transfer*, Taylor & Francis, Philadelphia, PA.
[42] Flynn, T. M., 1997, *Cryogenic Engineering*, Marcel Dekker, Inc., New York.
[43] Reijerkerk, J., 2005, "Potential of Cryogenic Hydrogen Storage in Vehicles," Proc. National Hydrogen Association Annual Conference, Washington, DC.
[44] Wolf, J., 2002, "Liquid-Hydrogen Technology for Vehicles," MRS Bull., **27**(9), pp. 684–687.

[45] Wolf, J., 2003, "Liquid Hydrogen Technology for Vehicles," *Handbook of Fuel Cells—Fundamentals, Technology and Applications*, Vielstich, W., Gasteiger, H. A., and Lamm, A. Eds., John Wiley & Sons, Hoboken, NJ, Vol. 3, pp. 89–100.
[46] Sherif, S. A., Zeytinoglu, N., and Veziroğlu, T. N., 1997, "Liquid Hydrogen: Potential, Problems, and a Proposed Research Program," Int. J. Hydrogen Energy, **22**(7), pp. 683–688.
[47] Zhou, L., Zhou, Y., and Sun, Y., 2004, "Enhanced Storage of Hydrogen at the Temperature of Liquid Nitrogen," Int. J. Hydrogen Energy, **29**(3), pp. 319–322.
[48] Perfect, S., Weisberg, A., and Aceves, S. M., 2004, "Optimum Utilization of Available Space in a Vehicle Through Conformable Hydrogen Tanks," *Proceedings of the 2004 Annual U.S. DOE Hydrogen Program Review*.
[49] Sandrock, G., 2003, "Hydride Storage," *Handbook of Fuel Cells—Fundamentals, Technology and Applications*, Vielstich, W., Gasteiger, H. A., and Lamm, A. Eds., John Wiley & Sons, Hoboken, NJ, Vol. 3, pp. 101–112.
[50] Sandrock, G., and Thomas, G., *Hydride Information Center*, http://hydpark.ca.sandia.gov
[51] Heung, L. K., 2003, *Using Metal Hydride to Store Hydrogen*, DOE report: WSRC-MS-2003-00172.
[52] Chen, Y., Sequeira, C. A. C., Chen, C., Wang, X., and Wang, Q., 2003, "Metal Hydride Beds and Hydrogen Supply Tanks as Minitype PEMFC Hydrogen Sources," Int. J. Hydrogen Energy, **28**(3), pp. 329–333.
[53] Story, G. C., 2000, "Hydride Bed/Fuelcell Project," *Proceedings of the 2000 Hydrogen Program Review*, NREL/CP-570–28890, http://www.eere.energy.gov/hydrogenandfuelcells/annual_review2000.html
[54] Sandrock, G., Gross, K., Thomas, G., Jensen, C., Meeker, D., and Takara, S., 2002, "Engineering Considerations in the Use of Catalyzed Sodium Alanates for Hydrogen Storage," J. Alloys Compd., **330–332**, pp. 696–701.
[55] Anton, D. L., Mosher, D. A., and Opalka, S. M., 2004, "High Density Hydrogen Storage System Demonstration Using NaAlH4 Complex Compound Hydrides," *Proceedings of the 2004 Annual U.S. DOE Hydrogen Program Review*.
[56] Ahluwalia, R., and Kumar, R., 2005, "Metal-Hydride Hydrogen Storage for Automotive Fuel Cell Systems," *Proceedings of the National Hydrogen Association Annual Conference*, Washington, DC.
[57] Rodriguez Sanchez, A., Klein, H.-P., and Groll, M., 2003, "Expanded Graphite as Heat Transfer Matrix in Metal Hydride Beds," Int. J. Hydrogen Energy, **28**(5), pp. 515–527.
[58] Kim, K. J., Montoya, B., Razani, A., and Lee, K.-H., 2001, "Metal Hydride Compacts of Improved Thermal Conductivity," Int. J. Hydrogen Energy, **26**(6), pp. 609–613.
[59] Oi, T., Maki, K., and Sakaki, Y., 2004, "Heat Transfer Characteristics of the Metal Hydride Vessel Based on the Plate-Fin Type Heat Exchanger," J. Power Sources, **125**(1), pp. 52–61.
[60] Gadre, S. A., Ebner, A. D., Al-Muhtaseb, S. A., and Ritter, J. A., 2003, "Practical Modeling of Metal Hydride Hydrogen Storage Systems," Ind. Eng. Chem. Res., **42**(8), pp. 1713–1722.
[61] Klein, H.-P., and Groll, M., 2004, "Heat Transfer Characteristics of Expanded Graphite Matrices in Metal Hydride Beds," Int. J. Hydrogen Energy, **29**(14), pp. 1503–1511.
[62] Kaviany, K., 1995, *Principles of Heat Transfer in Porous Media*, Springer, New York.
[63] Asakuma, Y., Miyauchi, S., Yamamoto, T., Aoki, H., and Miura, T., 2004, "Homogenization Method for Effective Thermal Conductivity of Metal Hydride Bed," Int. J. Hydrogen Energy, **29**(2), pp. 209–216.
[64] Wang, J., 2004, "Hydride Development for Hydrogen Storage," *Proceedings of the 2004 Annual U.S. DOE Hydrogen Program Review*.
[65] Bogdanović, B., and Schwickardi, M., 1997, "Ti-Doped Alkali Metal Aluminum Hydrides as Potential Novel Reversible Hydrogen Storage Materials," J. Alloys Compd., **253–254**, pp. 1–9.
[66] Bogdanović, B., Brand, R. A., Marjanović, A., Schwickardi, M., and Tölle, J., 2000, "Metal-Doped Sodium Aluminum Hydrides as Potential New Hydrogen Storage Materials," J. Alloys Compd., **302**, pp. 36–58.
[67] Anton, D. L., Opalka, S. M., Tang, X., Mosher, D. A., Zidan, R., Motyka, T., Hauback, B., Brinks, H., Lovvik, O. M., Strickler, J., Wu, F.-J. R., and Boone, J. E., 2004, "Complex Hydride Compounds With Enhanced Hydrogen Storage Capacity," *Proceedings of the 2004 Annual U.S. DOE Hydrogen Program Review*.
[68] Ritter, J. A., Ebner, A. D., Gadre, S. A., Prozorov, T., and Wang, J., 2004, "Development of Complex Hydride Hydrogen Storage Materials and Engineering Systems," *Proceedings of the 2004 Annual U.S. DOE Hydrogen Program Review*.
[69] Sachtler, J. W. A., 2004, "Discovery of Novel Complex Metal Hydrides for Hydrogen Storage Through Molecular Modeling and Combinatorial Methods," *Proceedings of the 2004 Annual U.S. DOE Hydrogen Program Review*.
[70] Baitalow, F., Baumann, J., Wolf, G., Jaenicke-Robler, K., and Leitner, G., 2002, "Thermal Decomposition of B-N-H Compounds Investigated by Using Combined Thermoanalytical Methods," Thermochim. Acta, **391**(1–2), pp. 159–168.
[71] Autrey, T., Gutowska, A., Li, L., Gutowski, M., and Linehan, J., 2004, "Chemical Hydrogen Storage: Control of H2 Release From Release From Ammonia Ammonia Borane," *Proceedings of the 2004 Annual U.S. DOE Hydrogen Program Review*.
[72] Luo, W. F., Gross, K., Ronnebro, E., and Wang, J., 2005, "Metal-N-H New Promising Hydrogen Storage Materials," Proceedings of the National Hydrogen Association Annual Conference, Washington, DC.
[73] Jensen, C. M., Srinivasan, S., Sun, D., Wang, P., Sulic, M., and Kuba, M., 2004, "Doped Sodium Aluminum Hydride: Fundamental Studies and Development of Related Hydrogen Storage Materials," *Proceedings of the 2004 Annual U.S. DOE Hydrogen Program Review*.
[74] Danko, E., 2005, "Hydrogen Technology at the Savannah River National Laboratory," Proceedings of the National Hydrogen Association Annual Conference, Washington, DC.
[75] Hall, M. M., and Shelby, J. E., 2005, "Hollow Glass Microspheres for Hydrogen Gas Storage," Proceedings of the National Hydrogen Association Annual Conference, Washington, DC.
[76] Hahne, E., and Kallweit, J., 1998, "Thermal Conductivity of Metal Hydride Materials for Storage of Hydrogen: Experimental Investigation," Int. J. Hydrogen Energy, **23**(2), pp. 107–114.
[77] Askri, F., Jemni, A., and Ben Nasrallah, S., 2003, "Study of Two-Dimensional and Dynamic Heat and Mass Transfer in a Metal-Hydrogen Reactor," Int. J. Hydrogen Energy, **28**(5), pp. 537–557.
[78] Askri, F., Jemni, A., and Nasrallah, S. B., 2004, "Prediction of Transient Heat and Mass Transfer in a Closed Metal-Hydrogen Reactor," Int. J. Hydrogen Energy, **29**(2), pp. 195–208.
[79] Asakum, Y., Miyauchi, S., Yamamoto, T., Aoki, H., and Miura, T., 2003, "Numerical Analysis of Absorbing and Desorbing Mechanism for the Metal Hydride by Homogenization Method," Int. J. Hydrogen Energy, **28**(5), pp. 529–536.
[80] Nakagawa, T., Inomata, A., Aoki, H., and Miura, T., 2000, "Numerical Analysis of Heat and Mass Transfer Characteristics in the Metal Hydride Bed," Int. J. Hydrogen Energy, **25**(4), pp. 339–350.
[81] Guo, Z., and Sung, H. J., 1999, "Technical Note Conjugate Heat and Mass Transfer in Metal Hydride Beds in the Hydriding Process," Int. J. Heat Mass Transfer, **42**(2), pp. 379–382.
[82] Georgiadis, J. G., 1990, "Future Research Needs in Convective Heat and Mass Transport in Porous Media," *Convective Heat and Mass Transfer in Porous Media*, Kakac, S., Kilkis, B., Kulacki, F. A., and Arinc, F., Eds., Kluwer Academic Publishers, Boston, pp. 1073–1088.
[83] James, B. D., 2003, "An Overview of Chemical Hydrides," *ORNL Hydrogen Storage Workshop*, http://www.ms.ornl.gov/hsw/presentation/May7/BJAMES1.PPT
[84] Cooper, A. C., and Pez, G. P., 2004, "Hydrogen Storage by the Reversible Hydrogenation of Liquid and Solid Substrates," *Proceedings of the 2004 Annual U.S. DOE Hydrogen Program Review*.
[85] McClaine, A. W., 2004, "Chemical Hydride Slurry for Hydrogen Production and Storage," *Proceedings of the 2004 Annual U.S. DOE Hydrogen Program Review*.
[86] Dipietro, J. P., and Skolnik, E. G., 2000, "Analysis of Sodium-Hydride-Based Hydrogen Storage System," *Proceedings of the the 2000 DOE Hydrogen Program Review*, NREL/CP-570–28890.
[87] Hyde, J., 2001, "Chrysler Offers Fuel Cell Van With Soapy Twist," Reuters World Environment News, http://www.planetark.org/dailynewsstory.cfm/newsid/13671/story.htm, December 12.
[88] Brown, H. C., and Brown, C. A., 1962, "New, Highly Active Metal Catalysts for the Hydrolysis of Borohydride," J. Am. Chem. Soc., **84**, pp. 1493–1494.
[89] Schlesinger, H. I., Brown, H. C., Finholt, A. E., Gilbreath, J. R., Hoekstra, H. R., and Hyde, E. K., 1953, "Sodium Borohydride, Its Hydrolysis and Its Use as a Reducing Agent and in the Generation of Hydrogen," J. Am. Chem. Soc., **75**, pp. 215–219.
[90] Amendola, S. C., Sharp-Goldman, S. L., Janjua, M. S., Spencer, N. C., Kelly, M. T., Petillo, P. J., and Binder, M., 2000, "An Ultrasafe Hydrogen Generator: Aqueous, Alkaline Borohydride Solutions and Ru Catalyst," J. Power Sources, **85**(2), pp. 186–189.
[91] Amendola, S. C., Sharp-Goldman, S. L., Janjua, M. S., Spencer, N. C., Kelly, M. T., Petillo, P. J., and Binder, M., 2000, "A Safe, Portable, Hydrogen Gas Generator Using Aqueous Borohydride Solution and Ru Catalyst," Int. J. Hydrogen Energy, **25**(10), pp. 969–975.
[92] Suda, S., 2003, "Aqueous Borohydride Solutions," *Handbook of Fuel Cells—Fundamentals, Technology and Applications*, Vielstich, W., Gasteiger, H. A., and Lamm, A., Eds., John Wiley & Sons, Hoboken, NJ, Vol. 3, pp. 115–120.
[93] Ju, H., Meng, H., and Wang, C. Y., 2004, "A Single-Phase, Non-Isothermal Model for PEM Fuel Cells," Int. J. Heat Mass Transfer, **48**(7), pp. 1303–1315.
[94] Hovland, V., Pesaran, A., Mohring, R. M., Eason, I. A., Smith, G. M., Tran, D., Schaller, R., and Smith, T., 2003, "Water and Heat Balance in a Fuel Cell Vehicle With Sodium Borohydride Hydrogen Fuel Processor," SAE Paper No. 2003–01–2271.
[95] Schlesinger, H. I., Brown, H. C., and Finholt, A. E., 1953, "The Preparation of Sodium Borohydride by the High Temperature Reaction of Sodium Hydride With Borate Esters," J. Am. Chem. Soc., **75**, pp. 215–209.
[96] Kojima, Y., and Haga, T., 2003, "Recycling Process of Sodium Metaborate to Sodium Borohydride," Int. J. Hydrogen Energy, **28**(9), pp. 989–993.
[97] Bingham, D., Wendt, K., and Wilding, B., 2004, "Radiolysis Process for the Regeneration of Sodium Borate to Sodium Borohydride," *Proceedings of the 2004 Annual U.S. DOE Hydrogen Program Review*.
[98] Wu, Y., 2004, "Low Cost, Off-Board Regeneration of Sodium Borohydride," *Proceedings of the 2004 Annual U.S. DOE Hydrogen Program Review*.
[99] Gehres, E., 1963, "An Analysis of Engine Cooling in Modern Passenger Cars," SAE Paper No. 660c.
[100] Fronk, M. H., Wetter, D. L., Masten, D. A., and Bosco, A. D., 2000, "PEM Fuel Cell System Solutions for Transportation," SAE Paper No. 2000–01–0373.
[101] Masten, D. A., and Bosco, A. D., 2003, "System Design for Vehicle Appli-

cations: GM/Opel," *Handbook of Fuel Cells—Fundamentals, Technology and Applications*, Vielstich, W., Gasteiger, H. A., and Lamm, A., Eds., John Wiley & Sons, Hoboken, NJ, Vol. 4, pp. 714–724.
[102] Renn, V., and Gilhaus, A., 1986, "Aerodynamics of Vehicle Cooling Systems," J. Wind. Eng. Ind. Aerodyn., **22**(2–3), pp. 339–346.
[103] Komatubara, T., 1995, "A Study for Improving Thermal Effectiveness in Automotive Radiators," JSAE Rev., **16**(1), p. 111.
[104] Goldstein, R. J., Eckert, E. R. G., Ibele, W. E., Patankar, S. V., Simon, T. W., Kuehn, T. H., Strykowski, P. J., Tamma, K. K., Heberlein, J. V. R., Davidson, J. H., Bischof, J., Kulacki, F. A., Kortshagen, U., and Garrick, S., 2003, "Heat Transfer—a Review of 2001 Literature," Int. J. Heat Mass Transfer, **46**, pp. 1887–1992.

Journal of Heat Transfer

Technical Briefs

Impact of Nonequilibrium Between Electrons and Phonons on Heat Transfer in Metallic Nanoparticles Suspended in Dielectric Media

Y. Sungtaek Ju
Department of Mechanical and Aerospace Engineering and Biomedical Engineering IDP,
University of California, Los Angeles, CA 90095-1597
e-mail: just@seas.ucla.edu

Controlled heating of nanoparticles is a key enabling technology for various nanomanufacturing and biomedical applications. A theoretical study of energy transport in nanoparticles is conducted to elucidate the role of electron-phonon spatial nonequilibrium in heat conduction across metal-dielectric interfaces. The continuum two-temperature heat conduction model is shown to capture the apparent size dependence of the thermal interface resistance of Au nanoparticle suspensions. Consideration of coupling between electrons and atomic vibrations is important in understanding energy transport in nanoscale metallic structures suspended in a dielectric medium. [DOI: 10.1115/1.1929779]

Heat transfer across interfaces is a critical consideration in a wide variety of scientific and engineering applications. This is especially true for nanoscale devices and structures, where interface phenomena often dominate their overall thermal behavior. One example is metallic nanoparticles suspended in dielectric media. Pulsed laser heating of suspended nanoparticles allows control of their size and shape [1]. Targeted heating of biological molecules or cells bound to nanoparticles opens intriguing biomimetic as well as therapeutic applications [2]. Liquids containing nanoparticles, often referred to as nanofluids, also have received a great deal of attention following experimental demonstration of their improved energy transport properties [3].

Previous experimental work studied energy transport phenomena in metallic nanoparticles during ultrafast pulsed laser heating experiments [4]. Most of these studies focused on electron-electron and electron-phonon relaxation processes within nanoparticles that take place on pico- or subpicosecond timescales. Energy transfer between nanoparticles and their surroundings at longer timescales is of more direct relevance to practical applications but has only begun to receive attention. A recent experimental study [5] observed systematic size dependence in the cooling time constant of gold nanoparticles suspended in water. Although the qualitative trend was consistent with the continuum heat diffusion theory predictions, the measured time constants were substantially greater than the predicted values.

The present paper reports a theoretical study of energy transport in metallic nanoparticles and the surrounding medium after pulsed laser heating. We take into account nonequilibrium between electrons and phonons by employing the two-fluid heat-diffusion model. The prediction of the present model agrees well with the previous experimental data on Au nanoparticles and suggests that spatial nonequilibrium between electrons and phonons has significant impact on energy transport in nanostructures even on time scales greater than the electron-phonon coupling time.

The pump-probe technique has been widely used to study energy transport phenomena in nanoparticles. Very briefly, a solution containing nanoparticles is illuminated with short-duration laser pulses and a time-delayed probe beam is used to monitor temporal changes in optical properties of the solution, such as the absorbtance, which are functions of temperature. Hu and Hartland [5] applied the pump-probe technique to gold nanoparticles suspended in water. They found that the temporal electron temperature decay profiles can be fitted using a stretched exponential function $A\exp[-(t/\tau)^{\beta}]$. The characteristic cooling time constant τ was found to increase approximately in proportion to the square of the particle diameter. The qualitative behavior can be understood using scaling analysis based on the conventional heat conduction equation as first described by Wilson et al. [6]. When the interface resistance is negligible, the characteristic cooling time can be estimated by equating the heat capacity of the particle C_p to the heat capacity of a layer of the surrounding liquid defined by the thermal diffusion length. This procedure yields a scaling relation $\tau \sim D^2 C_p^2 / Ck$, where D is the particle diameter, C is the heat capacity, and k is the thermal conductivity of the liquid.

Despite such qualitative agreement, the fit parameters, τ and β, obtained from numerical solutions to the conventional heat conduction equation deviated considerably from the parameters obtained from the experimental data. Figure 1 compares the experimental data (squares) to the prediction (diamonds) by Hu and Hartland [5]. One possible explanation for the discrepancy is that finite thermal resistance at the interface between nanoparticles and liquid water impedes heat conduction cooling. It is well established that a mismatch in atomic vibrational properties gives rise to the thermal resistance at interfaces between dissimilar materials [7], including liquid-solid interfaces. Wilson et al. [6] also suggested the impact of the thermal interface resistance in nanoparticle solutions, although spurious electronic effects on optical properties of nanoparticle solutions and other experimental uncertainties made it difficult to analyze their data.

We are not aware of theoretical studies of the thermal boundary resistance for Au-water interfaces. Existing data for solid-solid interfaces are typically of the order of 10^{-8} m^2 K/W near room temperature and do not exhibit significant variations among different material combinations. Since water may approximately be considered as an amorphous dielectric solid from a heat conduction point of view, we anticipate that thermal resistance of similar magnitude exists at Au-water interfaces.

Contributed by the Heat Transfer Division of ASME for publication in the JOURNAL OF HEAT TRANSFER. Manuscript received October 5, 2004; final manuscript received March 28, 2005. Review conducted by C. P. Grigoropoulos.

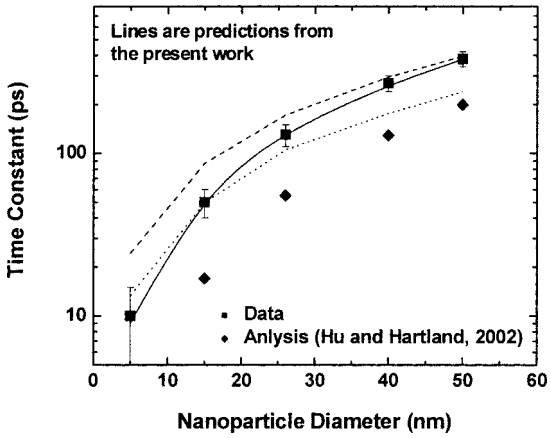

Fig. 1 Characteristic time constants of electron cooling in Au nanoparticles as a function of particle size. The data and prediction from Ref. [5] are shown as the square and diamond symbols, respectively. The dashed and dotted lines are predictions of the continuum heat diffusion equation with two different values of the thermal interface resistance (0.5 and 1 $\times 10^{-8}$ m^2 K/W). The solid line corresponds to predictions of the two-temperature heat-diffusion model that takes into account nonequilibrium between electrons and phonons.

To test whether the thermal interface resistance can fully explain the experimental data, we numerically solve the continuum heat diffusion equation. The dashed and dotted lines in Fig. 1 represent the time constants τ predicted using two different values for the thermal interface resistance, 0.5 and 1×10^{-8} m^2 K/W. The smaller value results in reasonable agreement for the smallest diameter particles, whereas bigger values are needed to explain data for the larger particles. We note that the thermal interface resistance does lead to an increase in the predicted time constants, but the overall agreement with the data is still poor.

To explain the data over the entire particle size range studied, one may need to assume that the apparent thermal interface resistance increases with increasing particle size. Since the mean-free path of electrons in Au is approximately 40 nm at room temperature, the thermal conductivity of Au nanoparticles can be smaller than its bulk value due to the size effect. This would increase the thermal resistance for smaller particles, a trend opposite to the experimental data. Another possibility is the effects of molecular layering, where an ordered layer of liquid molecules is formed near interfaces with solids [8] and affects energy transport. Molecular dynamics simulations of heat conduction in van der Waals liquid-solid interfaces [9], however, showed no appreciable impact of molecular layering.

We propose an alternative explanation for the apparent size dependence of the thermal interface resistance. The analysis using the conventional heat conduction equation implicitly assumes that electrons and phonons within Au nanoparticles are in equilibrium with each other. This assumption may be deemed valid because electron-phonon coupling time, which is of the order of 1 ps, is a lot shorter than the measured cooling time constants.

If heat transfer to the surrounding media is significant, however, there can be significant *spatial* as opposed to temporal nonequilibrium between electrons and phonons near the interface. This is because electrons interact indirectly with atomic vibrations in the adjacent dielectric medium in the absence of strong inelastic scattering at the interface. Energy transfer across the interface is achieved primarily through coupling of phonons in the nanoparticles with atomic vibrations in the surrounding medium.

To study the possible impact of such electron-phonon spatial nonequilibrium on nanoparticle cooling, we employ the two-temperature heat conduction model [10] that has been used widely to analyze pump-probe experiments

$$C_e\frac{\partial T_e}{\partial t} = \nabla\,(k_e\nabla T_e) - G(T_e - T_{ph}) + q''' \tag{1}$$

$$C_{ph}\frac{\partial T_{ph}}{\partial t} = \nabla\,(k_{ph}\nabla T_{ph}) + G(T_e - T_{ph}) \tag{2}$$

where subscripts *e* and *ph* are used to label quantities relevant to electrons and phonons, respectively. The temperature is denoted by T and the electron-phonon coupling constant by G. The time-dependent volumetric heat source q''' models energy gained by electrons through absorption of laser irradiation. The conventional continuum heat diffusion equation is used for water. The boundary conditions are

$$\left.\frac{dT_e}{dr}\right|_{r=0,D/2} = 0$$

$$\left.\frac{dT_{ph}}{dr}\right|_{r=0} = 0,$$

$$-k_{ph}\left.\frac{\partial T_{ph}}{\partial r}\right|_{r=D/2} = \frac{T_{ph}|_{r=D/2} - T_w|_{r=D/2}}{R_B''} = -k_w\left.\frac{\partial T_w}{\partial r}\right|_{r=D/2}, \tag{3}$$

$$T_w|_{r=\infty} = T_0.$$

The subscript w is used to label quantities pertaining to water. The intrinsic thermal boundary resistance R_B'', which may arise, for example, from a mismatch in atomic vibrational properties, is specified at the particle surface $r=D/2$. We introduce the electron-phonon coupling length δ as the characteristic length of a region near the interface over which electrons and phonons remain out of equilibrium. A functional form for δ is obtained from an analytic solution in planar one-dimensional geometry as $\delta=[k_e k_{ph}/(k_e+k_{ph})G]^{1/2}$.

In the limit $D \gg \delta$, the electron-phonon nonequilibrium results in extra thermal resistance R_{NE}'' of magnitude given approximately by δ/k_{ph} on top of the intrinsic thermal interface resistance. Note that the phonon thermal conductivity rather than the total thermal conductivity appears in the denominator. This is understandable because, over distance δ from the interface, electrons and phonons are decoupled from each other and only phonons contribute to heat conduction across the interface. When the particle size is smaller than δ, the spatial extent of the nonequilibrium region is determined by the particle diameter D instead of δ. The size dependence of the apparent thermal interface resistance can therefore be observed when the particle diameter is comparable to or smaller than the electron-phonon coupling length. An independent work used the electron-phonon nonequilibrium to explain the discrepancy between the diffuse mismatch theory and the experimental data on the resistance at interfaces between TiN films and sapphire substrates [11].

Au and other noble metals have weak electron-phonon coupling compared to other metals and, therefore, the impact of phonon-electron nonequilibrium is expected to be most pronounced. The electron-phonon coupling constant used in the present calculations is an average of existing data from bulk (2.9×10^{16} W/m^3 K) [12] and nanoshell (2.2×10^{16} W/m^3 K) samples [13]. Reduced phonon density of states was suggested as one possible reason for smaller coupling constants in nanoshells with dimensions of only a few nanometers. Experimental and theoretical studies [5] showed that electron-boundary scattering [14] does not have a strong effect on the coupling constant of Au.

The phonon heat conduction in pure metals near room temperature is believed to strongly limited by phonon-phonon Umklapp scattering as well as electron-phonon scattering [15]. Direct measurement of the phonon thermal conductivity is difficult, but estimates can be made from a thermal conductivity model using the atomic mass M, Debye temperature θ, unit cell size a, number of

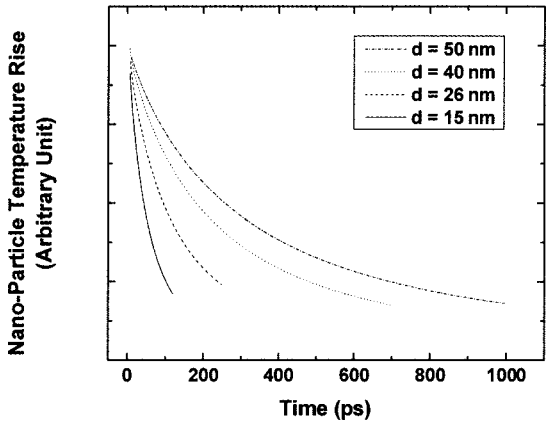

Fig. 2 Predicted electron temperature decay profiles for Au nanoparticles subjected to a subpicosecond pulsed laser heating.

atoms ν, and Grüneisen constant γ as input parameters: $k_{ph}=3\times10^{-5}\, M\, a\theta/T\gamma^2\nu^{2/3}$. The lattice thermal conductivity of metals is typically much smaller than that of crystalline dielectric materials. Experiments yielded the lattice thermal conductivity of $\sim$5 W/m K at 300 K for Cu and Pt, which agreed reasonably well with the model prediction [15]. The lattice thermal conductivity of Au is expected to be even smaller because it has a much lower Debye temperature and much larger Grüneisen constant. Using the same model, we predict the phonon thermal conductivity in Au to be $\sim$1 W/m K.

Strictly speaking, we need to distinguish between phonon modes that can and those that cannot directly interact with atomic vibrations in water. We expect the thermal conductivity of the former modes to be smaller than the total lattice thermal conductivity since only low-frequency longitudinal vibrations are believed to be wavelike in water. We take the model prediction discussed above as a first-order estimate recognizing that the extra thermal resistance R''_{NE} is a relatively weak function of k_{ph}, being inversely proportional to the square root of k_{ph}.

Equations (1)–(3) are solved numerically to predict the time evolution of electron and phonon temperature in Au nanoparticles suspended in water as shown in Fig. 2. The predicted electron cooling curves are once again fitted using the stretched exponential function. The time constants predicted using the two-fluid model are plotted as the solid line in Fig. 1. The intrinsic thermal interface resistance is fixed at 5×10^{-9} m^2 K/W, which is comparable to the total thermal interface resistance estimated for Pt-water interface [6]. The electron-phonon nonequilibrium is expected to play a smaller role for Pt. The nonequilibrium prediction agrees well with the data over the entire particle size range studied and captures the apparent size dependence of the interface resistance. The agreement, however, may not be viewed as the definitive proof of the proposed theory. Surfactants used to prevent aggregation of nanoparticles as well as surface morphology of nanoparticles may also influence heat conduction. It is not immediately clear how such effects can lead to the systematic size dependence discussed here, but further theoretical as well as experimental studies are needed to reach a definite conclusion.

In summary we report a theoretical study of heat transfer in metallic nanoparticles suspended in a dielectric medium following pulsed laser heating. The two-temperature heat conduction model is shown to capture the apparent size dependence of the thermal interface resistance observed for Au particles suspended in water. The present analysis suggests that nonequilibrium between electrons and phonons has significant impact on energy transport of metallic nanostructures even on times cales greater than the electron-phonon coupling time.

Nomenclature

a = unit cell size, m
C = heat capacity per unit volume, J/m^3 K
D = particle diameter, m
G = electron-phonon coupling constant, W/m^3 K
k = thermal conductivity, W/m K
M = atomic mass, kg/kmol
r = radial coordinate, m
T = temperature, K

Greek symbols

β = exponent in the fitting function
δ = electron-phonon coupling length, m
γ = Grüneisen constant
ν = number of atoms in a unit cell
θ = Debye temperature, K
τ = cooling time constant, s

Subscripts

e = quantities pertaining to electron
ph = quantities pertaining to phonon
w = quantities pertaining to water

Acknowledgment

This material is based upon work supported by the National Science Foundation under Grant No. CTS-0422789.

References

[1] Kurita, H., Takami, A., and Koda, S., 1998, "Size Reduction of Gold Particles in Aqueous Solutions by Pulsed Laser Irradiation," Appl. Phys. Lett., **72**, pp. 789–791.
[2] Hamad-Schifferli, K., Schwartz, J. J., Santos, A. T., Zhang, S., and Jacobson, J. M., 2002, "Remote Electronic Control of DNA Hybridization through Inductive Coupling to an Attached Metal Nanocrystal Antenna," Nature (London), **415**, pp. 152–155.
[3] Eastman, J. A., Choi, S. U. S., Li, S., Yu, W., and Thompson, L. J., 2001, "Anomalously Increased Effective Thermal Conductivities of Ethylene Glycol-Based Nanofluids Containing Copper Nanoparticles," Appl. Phys. Lett., **78**, pp. 718–720.
[4] Link, S., and El-Sayed, M. A., 2003, "Optical Properties and Ultra-Fast Dynamics of Metallic Nanocrystals," Annu. Rev. Phys. Chem., **54**, pp. 331–366.
[5] Hu, M., and Hartland, G. V., 2002, "Heat Dissipation for Au Particles in Aqueous Solution: Relaxation Time Versus Size," J. Phys. Chem. B, **106**(28), pp. 7029–7033.
[6] Wilson, O. M., Hu, X. Y., Cahill, D. G., and Braun, P. V., 2002, "Colloidal Metal Particles as Probes of Nanoscale Thermal Transport in Fluids," Phys. Rev. B, **66**, p. 224301.
[7] Swartz, E. T., and Pohl, R. O., 1989, "Thermal-Boundary Resistance," Rev. Mod. Phys., **61**(3), pp. 605–668.
[8] Yu, C. J., Richter, A. G., Datta, A., Durbin, M. K., and Dutta, P., 2000, "Molecular Layering in a Liquid on a Solid Substrate: An X-Ray Reflectivity Study," Physica B, **283**, pp. 27–31.
[9] Xue, L., Keblinski, P., Philpot, S. R., Choi, S. U. S., and Eastman, J. A., 2003, "Two Regimes of Thermal Resistance at a Liquid-Solid Interface," J. Chem. Phys., **118**, pp. 337–339.
[10] Anisimov, S. I., Kapeliovich, B. L., and Perelman, T. L., 1974, "Emission of Electrons From the Surface of Metals Induced by Ultrashort Laser Pulses," Zh. Eksp. Teor. Fiz., **66**(2), pp. 776–81.
[11] Majumar, A., and Reddy, P., 2004, "Role of Electron-Phonon Coupling in Thermal Conductance of Metal-Nonmetal Interfaces," Appl. Phys. Lett., **84**, pp. 4768–4770.
[12] Hostetler, J. L., Smith, A. N., Czajkowsky, D. M., and Norris, P. M., 1999, "Measurement of the Electron-Phonon Coupling Factor Dependence on Film Thickness and Grain Size in Au, Cr, and Al," Appl. Opt., **38**(16), pp. 3614–3620.
[13] Averitt, R. D., Westcott, S. L., and Halas, N. J., 1998, "Ultrafast Electron Dynamics in Gold Nanoshells," Phys. Rev. B, **58**(16), pp. R10203–R10206.
[14] Qiu, T. Q., and Tien, C. L., 1993, "Size Effects on Nonequilibrium Laser-Heating of Metal-Films," ASME J. Heat Transfer, **115**(4), pp. 842–847.
[15] Berman, R., 1976, *Thermal Conduction in Solids*, Clarendon Press, Oxford.

An Inverse Solution for Determining Arbitrary Boundary-Conditions using a Least-Squares Approach

A. E. Segall
Associate Professor
Mem. ASME
Engineering Science and Mechanics,
The Pennsylvania State University,
University Park, PA 16802

Introduction

Despite the versatility of numerical approaches to the inverse problem (Beck et al. [1] and Xue et al. [2]), there is still a strong need for analytical solutions. In fact, many numerical simulations require a starting point and must be verified and bounded to help ensure the validity of the solution. In addition to bounding the problem, there is always a need for closed-form solutions or first-order approximations that can be quickly used to highlight the significance of various parameters and their often complicated interrelationships. Even with this enduring importance, significant limitations remain including a reliance on higher-order derivatives that magnify data errors, restrictions to small time frames, or the inability to handle arbitrary boundary-conditions. Fortunately, many of these limitations can be avoided and the inverse-solution found for a variety of geometries by using a generalized direct-solution combined with a least-squares approach.

Inverse Solution

It has long been established that the response $v(\xi,t)$ of a structure of coordinate, ξ subjected to an arbitrary temperature-history, $\Delta T(t)$ can be expressed by Duhamel's form of the convolution integral using the unit response, $\Phi(\zeta,t)$:

$$v(\xi,t)=\int_0^t \frac{\partial \Delta T(\tau)}{\partial \tau}\Phi(\xi,t-\tau)d\tau=\frac{\partial \Delta T}{\partial t}*\Phi(\xi,t) \tag{1}$$

While Eq. (1) is clearly a direct solution of the problem, its form can also be used for the corresponding inverse problem by employing a polynomial with coefficients a_n to represent the unknown temperature boundary-condition,

$$\Delta T(t)=a_1 t^{1/2}+a_2 t+a_3 t^{3/2}+\cdots=\sum_{n=1}^{N} a_n t^{n/2} \tag{2}$$

A generalized inverse solution is then possible by fitting temperatures obtained at location, ξ to Eq. (1) with the polynomial coefficients now satisfying the following linear equations in a least-squares sense,

$$\begin{bmatrix} \frac{\partial \Delta T_n}{\partial t}*\Phi(\xi,t_1) & \frac{\partial \Delta T_{n+1}}{\partial t}*\Phi(\xi,t_1) & \cdots & \frac{\partial \Delta T_N}{\partial t}*\Phi(\xi,t_1) \\ \frac{\partial \Delta T_n}{\partial t}*\Phi(\xi,t_2) & \frac{\partial \Delta T_{n+1}}{\partial t}*\Phi(\xi,t_2) & \cdots & \frac{\partial \Delta T_N}{\partial t}*\Phi(\xi,t_2) \\ \vdots & \vdots & & \vdots \\ \frac{\partial \Delta T_n}{\partial t}*\Phi(\xi,t_N) & \frac{\partial \Delta T_{n+1}}{\partial t}*\Phi(\xi,t_N) & \cdots & \frac{\partial \Delta T_N}{\partial t}*\Phi(\xi,t_N) \end{bmatrix} \times \begin{bmatrix} a_1 \\ a_2 \\ \vdots \\ a_N \end{bmatrix} = \begin{bmatrix} v(\xi,t_1) \\ v(\xi,t_2) \\ \vdots \\ v(\xi,t_N) \end{bmatrix} \tag{3}$$

Provided the unit-response, $\Phi(\xi,t)$ can be derived analytically or numerically, the inverse problem for any combination of geometry and boundary conditions can be solved with the determination of the coefficients and the use of Eq. (2). Once the coefficients are determined, the direct solution obtained via Eq. (1) can then be used to determine the temperature distribution throughout the solid.

Generalized Response

A generalized inverse-solution for both slabs ($\xi=x$) and cylinders ($\xi=r$) is possible by recognizing a common form to their unit response:

$$\Phi(\xi,t)=\psi+\varepsilon\sum_{k=1}^{\infty} Z_k e^{-b_k^2 t} \tag{4}$$

where ε, ψ, and Z reflect geometry, thermal diffusivity (κ), and known boundary-conditions. Given this generalized form, the direct response to a system can be shown to be (Segall [3]):

$$v(\xi,t)=\sum_{j=1}^{N} a_j\left[\psi t^{j/2}+\varepsilon\frac{j}{2}\delta_j(\xi,t)\right] \tag{5}$$

where the response functions for even $(2j)$ and odd $(2j-1)$ terms are defined as follows and all other terms have been previously defined (Segall [3,4], Austin [5], and Vedula et al. [6]):

$$\delta_{2j}(\xi,t)=(-1)^j\chi(j-1,j-1)\sum_{k=1}^{\infty}\frac{Z_k e^{-b_k^2 t}}{b_k^{2j}}+\sum_{i=0}^{j-1}\left[(-1)^i t^{j-i-1}\chi(i,j-1)\sum_{k=1}^{\infty}\frac{Z_k}{b_k^{2(i+1)}}\right] \tag{6a}$$

$$\delta_{2j-1}(\xi,t)=\frac{(-1)^{j+1}}{2^{j-1}}\zeta(j-1,2j-3)\sum_{k=1}^{\infty}\frac{Z_k\Omega_k}{b_k^{2j-2}}+\cdots+\frac{2}{\pi}\tan^{-1}[e^{10}(j-1)]\sum_{i=0}^{j-2}\left[(-1)^i\frac{t^{\frac{2(j-i)-3}{2}}}{2^i}\zeta(i,2j-3)\sum_{k=1}^{\infty}\frac{Z_k}{b_k^{2(i+1)}}\right] \tag{6b}$$

For a semi-infinite solid, a relationship has already been expressed in a form suitable for the least-squares approach by Carslaw and Jaeger [7]:

$$v(\xi,t)=\sum_{n=1}^{N} a_n 2^n\Gamma(j+1)t^{n/2}i^n\,\mathrm{erfc}\left(\frac{\xi}{2\sqrt{\kappa t}}\right) \tag{7}$$

Hence, when using Eq. (5) for slabs and cylinders or Eq. (7) for a semi-infinite solid, the coefficients, a_n are determined by Eq. (3) in a least-squares sense with Eq. (2) then providing the inverse solution.

Contributed by the Heat Transfer Division of ASME for publication in the JOURNAL OF HEAT TRANSFER. Manuscript received June 30, 2004; final manuscript received May 24, 2005. Review conducted by A. F. Emery.

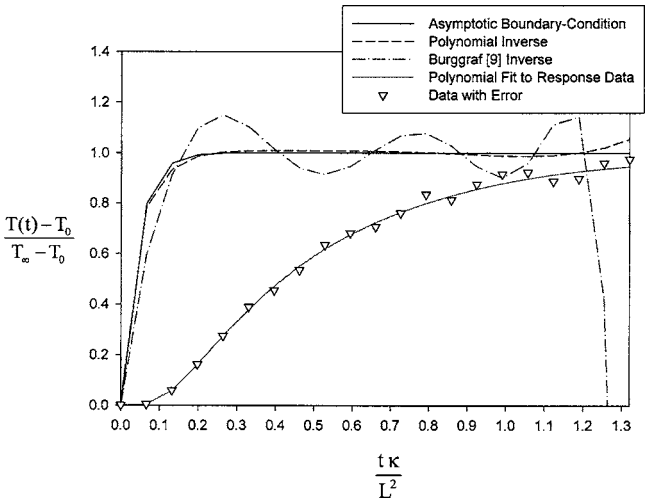

Fig. 1 Comparison of inverse predictions and asymptotic boundary-condition of a semi-infinite slab as a function of nondimensional time

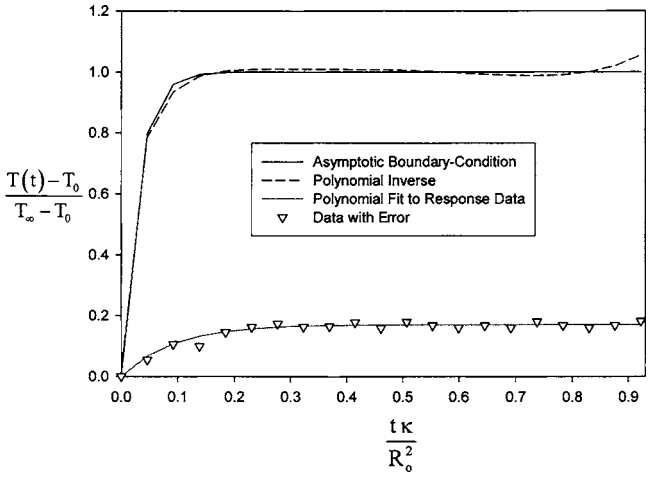

Fig. 3 Comparison of inverse predictions and asymptotic boundary-condition of an infinitely long and hollow cylinder as a function of nondimensional time

Results

Confirmatory calculations were conducted for a semi-infinite slab (thickness $L=0.05$ m and $\kappa=0.085$ cm^2/s) under an asymptotic boundary-condition, $\Delta T(t)=1\cdot(1-e^{-0.5t})$ at $x/L=0$ and adiabatic at $x/L=1$. A solution derived by Austin [5] was then used to generate the response at the adiabatic boundary with a random number generator used to simulate experimental errors as high as ±10%. The error-laden data was then fit to a polynomial of the form of Eq. (5) and the unknown polynomial coefficients determined via a least-squares algorithm. As shown in Fig. 1, the resulting inverse solution via Eq. (5) gives excellent agreement with the applied boundary-condition. As shown by Fig. 2, excellent agreement was also seen with a triangular temperature-history except at the apex. The flattening of the apex by the curve-fit does highlight a shortcoming of continuous functions including polynomials, as well as some numerical approaches (Frankel and Keyhani [8]) in that they cannot reflect abrupt changes; the use of more sophisticated piecewise relationships such as B-splines or radial basis functions might solve this problem. Similar calculations were also performed for an infinitely long cylinder ($R_i/R_o=0.667$) subjected to the same asymptotic temperature-history on the i.d. with convection on the o.d. (Bi=1200). Again using existing relationships (Vedula et al. [6]) with artificial error to generate a response, the least-squares approach determined the inverse solution as shown in Fig. 3. For both the slab and cylinder, the late upswing in the results reflects the typical breakdown of the polynomial near the end of the defining time-interval.

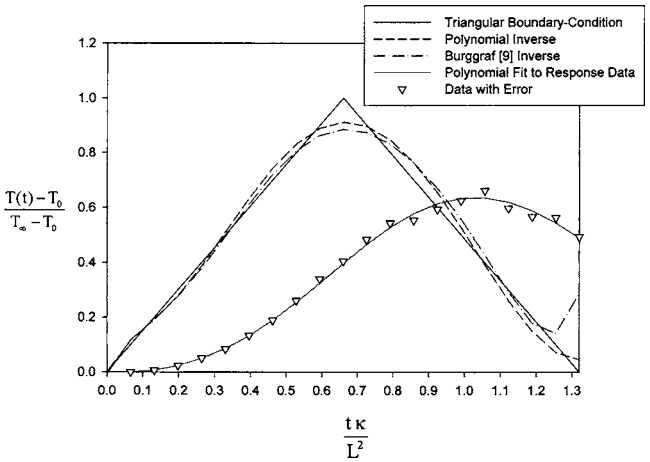

Fig. 2 Comparison of inverse predictions and triangular boundary-condition of a semi-infinite slab as a function of nondimensional time

In order to further validate the proposed method, as well as highlight two interrelated advantages with respect to generalized polynomials, a comparison was also made to the seminal solution derived by Burggraf [9] for a plate:

$$\Delta T(t) = T_s(t,\xi) + \sum_{n=1}^{\infty} \frac{1}{2n!}\left(\frac{\xi^2}{\kappa}\right)^n \frac{d^n T_s(t,\xi)}{dt^n} \tag{8}$$

where $T_s(\xi,t)$ represents the known temperature history and all other terms are as previously defined. As discussed in Burggraf [9], there is a limiting requirement of Eq. (8) in that the function $T_s(\xi,t)$ must be infinitely-differentiable to allow sufficient terms for convergence and a uniform temperature-distributions at $t=0$. Since a uniform initial-temperature was desired and a truncated polynomial in the form of Eq. (2) is not infinitely-differentiable, a new polynomial capable of matching the remote responses was required. Therefore, instead of using Eq. (2) with its limited number of derivatives, a new polynomial containing integral orders of time and the complimentary error function was derived for this study:

$$T_s(\xi,t) = \sum_{m=1}^{N} t^m \operatorname{erfc}(\omega) \tag{9}$$

where

$$\omega = \frac{m\xi}{2L\sqrt{\kappa t}} \tag{10}$$

By using a polynomial in this form, the nth order derivative for each term in Eq. (9) can be determined by

$$\frac{d^n}{dt^n} t^m \operatorname{erfc}(\omega) = \sum_{i=0}^{\substack{n \text{ if } n<m \\ m \text{ if } n>m}} \binom{n}{i} \frac{\Gamma(m+1)}{\Gamma(m+1-i)} t^{m-1} \left\{ \sum_{p=1}^{n} \frac{U_p}{p!} F^{(p)}(\omega) \right\} \tag{11}$$

The following terms used in Eq. (11) are defined as

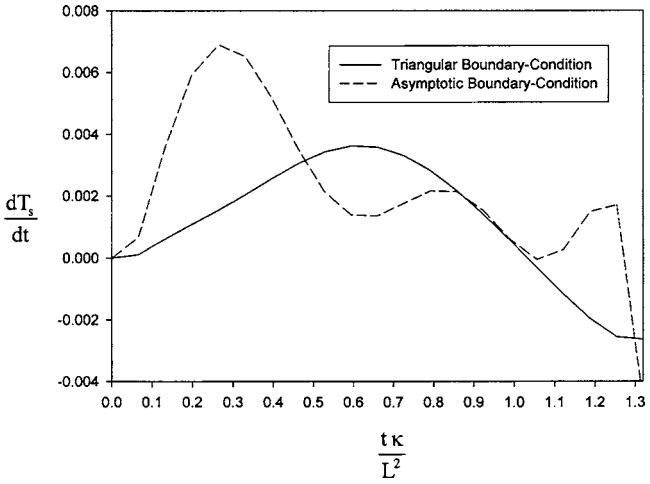

Fig. 4 Comparison of the dominant first-derivatives of the asymptotic and triangular boundary-conditions as fit by Eq. (9) and used in the Burggraf [9] solution

$$F^{(p)}(\omega) = \frac{2}{\sqrt{\pi}}(-1)^n e^{-(y)^2} H_{n-1}(\omega) \tag{12}$$

with H_n representing a Hermite polynomial of nth order

$$H_n(\omega) = n!\left[\sum_{j=0}^{\text{integer}(n/2)} (-1)^{-1}\frac{(2\omega)^{n-2m}}{m!(n-2m)!}\right] \tag{13}$$

and

$$U_p = \sum_{j=0}^{p-1}(-1)^j \frac{\Gamma(p+1)}{\Gamma(p+1-j)}\frac{\omega^j}{j!}\left[\left\{\prod_{i=0}^{n-1}\left(\frac{j-p}{2}-i\right)\right\} a^{p-j} t^{[(j-p)/2]-n}\right] \tag{14}$$

As shown in Fig. 1, the polynomial given by Eq. (8) does a relatively poor job of predicting the asymptotic boundary-condition when the data with artificial errors was introduced. In contrast, a relatively smooth estimation of the triangular boundary-condition was made with the same polynomial as shown in Fig. 2. This seemingly contradictory performance can be ascribed to the dependence on derivatives and their tendency to magnify errors in the underlying data (Rowlands et al. [10]) as shown by the oscillations of temperature and first derivative in Figs. 1 and 4, respectively. In terms of the asymptotic boundary-condition, the first derivative is clearly dominating the solution with the oscillations reflecting a greater polynomial "wiggle" about the original data points relative to the triangular input; the observed oscillations probably originate in the term U_p since it contains various powers of time. Higher-order derivatives also displayed similar tendencies, but were always at least one order-of-magnitude lower than the proceeding order and did not appear to influence the solution. The least-squares method advocated in this paper avoids these problems altogether.

Discussion

The results shown in Figs. 1–3 indicate the versatility and reasonable accuracy of the proposed method without the need for derivatives and the potential errors contained within. Additional or combinations of functions including piecewise polynomials could also be used with Eq. (1) as long as they are reasonably capable of describing the excitation over the known time interval and not used beyond. Provided the thermophysical properties are independent of temperature, the least-squares method can be used for any geometry and boundary conditions as long as a unit response is known in closed-form or determined numerically. When temperature dependent properties are warranted, the iterated-polynomials advocated by Imber [11] could be used in Eq. (2) instead of the convolution terms with the resulting coefficients again determining the inverse solution. However, it is probably more prudent to simply use the current least-squares approach with minimum and maximum values of diffusivity to help bound the inverse solution.

Conclusions

A least-squares methodology based on a generalized direct-solution has been developed to solve the inverse problem for common geometries without the need for higher order derivatives. Good agreement was seen between the current study and earlier results for various test cases including triangular and asymptotic boundary conditions. While the mixed-order polynomials used in this study are clearly versatile, they do have limitations in that they cannot readily model abrupt temperature changes. Nevertheless, the method appears well suited for estimating boundary conditions provided the analysis is restricted to the time interval used to determine the polynomial and the thermophysical properties do not vary with temperature. Methods for handling different geometries and temperature dependent properties are suggested.

References

[1] Beck, J. V., Blackwell, B., and Clair, C. R., 1985, *Inverse Heat Conduction-Ill Posed Problems*, Wiley-Interscience, New York.
[2] Xue, X., Luck, R., and Berry, J. T., 2005, "Comparisons and Improvements Concerning the Accuracy and Robustness of Inverse Heat Conduction Algorithms," Inverse Probl., **13**, pp. 177–199.
[3] Segall, A. E., 2003, "Thermal Stresses in an Infinite Slab under an Arbitrary Thermal Shock," ASME J. Appl. Mech., **70**, pp. 779–782.
[4] Segall, A. E., 2001, "Relationships for the Approximation of Direct and Inverse Problems With Asymptotic Kernels," Inverse Probl., **9**, pp. 127–140.
[5] Austin, J. B., 1932, "Temperature Distribution in Solid Bodies during Heating or Cooling," J. Appl. Phys., **3**, pp. 179–184.
[6] Vedula, V. R., Segall, A. E., and Rangarazan, S. K., 1998, "Transient Analysis of Internally Heated Tubular Components With Exponential Thermal Loading and External Convection," Int. J. Heat Mass Transfer, **41**, pp. 3675–3678.
[7] Carslaw, H. S., and Jaeger, J. C., 1959, *Conduction of Heat in Solids*, Oxford University Press, Great Britain.
[8] Frankel, J. I., and Keyhani, M., 1997, "A Global Time Treatment for Inverse Heat Conduction Problems," J. Heat Transfer, **119**, pp. 673–383.
[9] Burggraf, O. R., 1964, "An Exact Solution of the Inverse Problem in Heat Conduction Theory and Applications," J. Heat Transfer, **86C**, pp. 373–382.
[10] Rowlands, R. E., Libor, T., Daniel, I. M., and Rose, P. G., 1973, "Higher Order Numerical Differentiations of Experimental Information," Exp. Mech., **14**, pp. 105–112.
[11] Imber, M., 1979, "Nonlinear Heat Transfer in Planar Solids: Direct and Inverse Applications," AIAA J., **17**, pp. 204–213.

Steady Laminar Convective Flow with Variable Properties Due to a Porous Rotating Disk

Kh. Abdul Maleque
American International University-Bangladesh,
House-54/B, 21 Kemal Ataturk Avenue,
Banani, Dhaka-1213, Bangladesh
e-mail: khmaleque@yahoo.com

Md. Abdus Sattar
North South University,
Department of C S E,
12 Kemal Ataturk Avenue,
Banani, Dhaka-1213, Bangladesh
e-mail: asattar@northsouth.edu

The present paper investigates the effects of variable properties (density (ρ), viscosity (μ), and thermal conductivity (κ)) on steady laminar flow and heat transfer for a viscous fluid due to an impulsively started rotating porous infinite disk. These properties ρ, μ and κ are taken to be the functions of temperature. The system of axisymmetric nonlinear partial differential equations governing the steady flow and heat transfer are written in cylindrical polar coordinates and are reduced to nonlinear ordinary differential equations by introducing suitable similarity parameters. The resulting steady equations are solved numerically by using Runge-Kutta and Shooting methods, and the effects of the relative temperature difference and suction/injection parameters are examined. [DOI: 10.1115/1.2098860]

1 Introduction

The problem of the flow over a rotating disk has a long history, in particular rotating disk flow with heat transfer is one of the classical problems of fluid mechanics that has both theoretical and practical values. The importance of heat transfer from a rotating body can be ascertained in cases of various types of machinery, for example computer disk drives (see Herrero et al. [1]) and gas turbine rotors (see Owen and Rogers [2]).

The first solution to the classical problem of rotating disk flow was obtained by von-Karman (see Schlichting [3]). His results were further improved by Cochran [4]. Benton [5] and Roger and Lance [6] extended this problem to the flow starting impulsively from rest. Considering the importance of suction/blowing, their effects on the surface of a rotating disk were studied by Stuart [7], Ockendon [8], Kuiken [9], and Kelson and Desseaux [10]. Kelson and Desseaux re-examined the flow, motivated by the view that the problem can serve as a prototype for practical swirl flows.

In all the above-mentioned studies the density (ρ), viscosity (μ), and thermal conductivity (κ) of the fluid were assumed to be constants. However, it is known that these physical properties may change significantly with temperature of the flow. To predict the flow behavior accurately, it may be necessary to take into account these variable properties. In light of this concept, Herwig [11] analyzed the influence of variable properties on laminar fully developed pipe flow with constant heat flux across the wall. It was shown how the exponent in the property ratio method depends on the fluid properties. The influence of temperature dependent fluid properties on laminar boundary layers was further examined by Herwig and Wickern [12] for wedge flows. In case of fully developed laminar flow in concentric annuli, the effect of the variable properties has been studied by Herwig and Klemp [13].

The present investigation is concerned with the effects of variable properties (density (ρ), viscosity (μ), and thermal conductivity (κ)) on a steady laminar forced convection system along a porous rotating disk with uniform temperature. Such a study is relevant to that of Gokuglu and Rosner [14]. Here we have considered that the fluid properties are strongly functions of temperature. The resulting similarity equations are solved numerically by Runge-Kutta and Shooting methods. The results are mainly focused on the effects of the relative temperature difference and suction/injection parameters.

2 Governing Equations

In a non-rotating cylindrical polar coordinates (r,ϕ,z), the disk which is placed at $z=0$ is assumed to rotate with a constant angular velocity Ω. The fluid occupies the region $z>0$. Here z is the vertical axis in the cylindrical coordinates system and r and ϕ are the radial and tangential axes, respectively. The components of the flow velocity $\mathbf{q}$ are (u,v,w) in the directions of increasing (r,ϕ,z), respectively, the pressure is P and the density of the fluid is ρ. T is the fluid temperature and the surface of the rotating disk is maintained at a uniform temperature T_w. Far away from the wall, the free stream is kept at a constant temperature T_∞ and at a constant pressure P_∞.

We assume that the dependency of the fluid properties, viscosity (μ) and thermal conductivity (κ) coefficients and density (ρ) are functions of temperature alone and obey the following laws (see Jayaraj [15])

$$\mu=\mu_\infty[T/T_\infty]^a \quad \kappa=\kappa_\infty[T/T_\infty]^b \quad \rho=\rho_\infty[T/T_\infty]^c \tag{1}$$

where the a, b, and c are arbitrary exponents, κ_∞ is a uniform thermal conductivity of heat, and μ_∞ is a uniform viscosity of the fluid. For the present analysis the fluid is considered to be flue gas. For flue gases the values of the exponents a, b, and c are taken as $a=0.7$, $b=0.83$, and $c=-1.0$. Here $c=-1.0$ implies an ideal gas.

The physical model and geometrical coordinates are shown in Fig. 1. Due to steady axially symmetric, compressible laminar flow of a homogeneous fluid the continuity, Navier-Stokes and energy equations for the present problem take the following form

$$\frac{\partial}{\partial r}(\rho r u)+\frac{\partial}{\partial z}(\rho r w)=0 \tag{2}$$

$$\rho\left(u\frac{\partial u}{\partial r}-\frac{v^2}{r}+w\frac{\partial u}{\partial z}\right)+\frac{\partial P}{\partial r}=\frac{\partial}{\partial r}\left(\mu\frac{\partial u}{\partial r}\right)+\frac{\partial}{\partial r}\left(\mu\frac{u}{r}\right)+\frac{\partial}{\partial z}\left(\mu\frac{\partial u}{\partial z}\right) \tag{3}$$

$$\rho\left(u\frac{\partial v}{\partial r}+\frac{uv}{r}+w\frac{\partial v}{\partial z}\right)=\frac{\partial}{\partial r}\left(\mu\frac{\partial v}{\partial r}\right)+\frac{\partial}{\partial r}\left(\mu\frac{v}{r}\right)+\frac{\partial}{\partial z}\left(\mu\frac{\partial v}{\partial z}\right) \tag{4}$$

$$\rho\left(u\frac{\partial w}{\partial r}+w\frac{\partial w}{\partial z}\right)+\frac{\partial P}{\partial z}=\frac{\partial}{\partial r}\left(\mu\frac{\partial w}{\partial r}\right)+\frac{1}{r}\frac{\partial}{\partial r}(\mu w)+\frac{\partial}{\partial z}\left(\mu\frac{\partial w}{\partial z}\right) \tag{5}$$

$$\rho C_p\left(u\frac{\partial T}{\partial r}+w\frac{\partial T}{\partial z}\right)=\frac{\partial}{\partial r}\left(\kappa\frac{\partial T}{\partial r}\right)+\frac{\kappa}{r}\frac{\partial T}{\partial r}+\frac{\partial}{\partial z}\left(\kappa\frac{\partial T}{\partial z}\right) \tag{6}$$

where C_p is the specific heat at constant pressure.

Appropriate boundary conditions for the flow induced by an infinite disk ($z=0$) which is started impulsively into steady rotation with constant angular velocity Ω and with a uniform suction/injection w_w through the disk are given by

Contributed by the Heat Transfer Division of ASME for publication in the JOURNAL OF HEAT TRANSFER. Manuscript received June 16, 2004; final manuscript received July 18, 2005. Assoc. Editor: Jay M. Khodadadi.

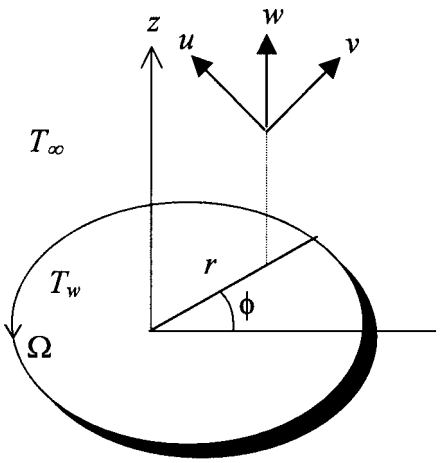

Fig. 1 The flow configuration and the coordinate system

$$u = 0, \quad v = \Omega r, \quad w = w_w, \quad T = T_w \text{ at } z = 0$$

$$u \to 0, \quad v \to 0, \quad T \to T_\infty \quad P \to P_\infty \text{ as } z \to \infty \tag{7}$$

3 Similarity Transformations

To obtain the solutions of the governing equations, following von Karman, a dimensionless normal distance from the disk, $\eta = z(\Omega/\nu_\infty)^{1/2}$, is introduced along with the following representations for the radial and tangential velocities, pressure and temperature distributions

$$u = \Omega r F(\eta), \quad v = \Omega r G(\eta), \quad w = (\Omega \nu_\infty)^{1/2} H(\eta),$$

$$P - P_\infty = 2\mu_\infty \Omega p(\eta) \text{ and } T - T_\infty = \Delta T \theta(\eta), \tag{8}$$

where ν_∞ is a uniform kinematic viscosity of the fluid and $\Delta T = T_w - T_\infty$.

Equations (2)–(4) and (6) in this case with the use of Eq. (8) reduce to

$$H' + 2F + cH\theta'(1 + \gamma\theta)^{-1}\gamma = 0 \tag{9}$$

$$F'' + a\gamma(1 + \gamma\theta)^{-1}\theta' F' - [F^2 - G^2 + HF'](1 + \gamma\theta)^{c-a} = 0 \tag{10}$$

$$G'' + a\gamma(1 + \gamma\theta)^{-1}\theta' G' - [2FG + HG'](1 + \gamma\theta)^{c-a} = 0 \tag{11}$$

$$\theta'' + b\gamma(1 + \gamma\theta)^{-1}\theta'^2 - \Pr H\theta'(1 + \gamma\theta)^{c-b} = 0 \tag{12}$$

where $\Pr = \mu_\infty C_p/\kappa_\infty$ is the Prandtl number and $\gamma = \Delta T/T_\infty$ is the relative temperature difference parameter, which is positive for a heated surface, negative for a cooled surface, and zero for uniform properties. The boundary conditions (7) then transform to

$$F(0) = 0 \quad G(0) = 1 \quad H(0) = W_S \quad \theta(0) = 1$$

$$F(\infty) = G(\infty) = \theta(\infty) = p(\infty) = 0 \tag{13}$$

where $W_S = w_w/\sqrt{\nu_\infty \Omega}$, which is obtained from Eq. (8). Here W_S represents a uniform suction ($W_S < 0$) or injection ($W_S > 0$) at the surface (see Kelson and Desseaux [10]).

The skin friction coefficients and the rate of heat transfer to the surface, which are of chief physical interest, are also calculated out. The action of the viscosity in the fluid adjacent to the disk sets up a tangential shear stress, which opposes the rotation of the disk. As a consequence, it is necessary to provide a torque at the shaft to maintain a steady rotation. To find the tangential shear stress τ_t and surface (radial) stress τ_r, we apply the Newtonian formulas

Table 1 Numerical values of the radial and tangential skin-friction coefficients and the rate of heat transfer coefficient obtained for Pr=0.71 and γ=0

	Present			Kelson & Desseaux [10]		
W_S	$F'(0)$	$-G'(0)$	$-\theta'(0)$	$F'(0)$	$-G'(0)$	$-\theta'(0)$
6	.1656631	.910681e-2	.14012e-9	.165663	.910681e-2	.139705e-9
5	.1975659	.154706e-1	.67521e-7	.197566	.154706e-1	.672820e-7
4	.2430438	.289211e-1	.10756e-4	.243044	.289211e-1	.107326e-4
2	.3989332	.1359517	.110523e-1	.398934	.135952	.110135e-1
0	.5101519	.6159631	.325769	.510233	.615922	.325856
-2	.2425126	2.0391123	1.442129	.242421	2.038527	1.437782
-4	.1247762	4.0053780	2.844701	.124742	4.005180	2.842381
-5	.0999689	5.0029754	3.554116	.099918	5.002661	3.551223
-10	.0505964	10.0015690	7.102015	.050002	10.00033	7.100153

$$\tau_t = \left[\mu\left(\frac{\partial v}{\partial z} + \frac{1}{r}\frac{\partial w}{\partial \phi}\right)\right]_{z=0} = \mu_\infty (1+\gamma)^a R_e^{1/2} \Omega G'(0),$$

$$\tau_r = \left[\mu\left(\frac{\partial u}{\partial z} + \frac{\partial w}{\partial r}\right)\right]_{z=0} = \mu_\infty (1+\gamma)^a R_e^{1/2} \Omega F'(0)$$

Hence the tangential and radial skin-frictions are, respectively, given by

$$(1+\gamma)^{-a} R_e^{1/2} C_{f_t} = G'(0) \tag{14}$$

$$(1+\gamma)^{-a} R_e^{1/2} C_{f_r} = F'(0). \tag{15}$$

The rate of heat transfer from the disk surface to the fluid is computed by the application of Fourier's law as given in the following

$$q = -\left(\kappa \frac{\partial T}{\partial z}\right)_{z=0} = -\kappa_\infty \Delta T (1+\gamma)^b \left(\frac{\Omega}{\nu_\infty}\right)^{1/2} \theta'(0).$$

Hence the Nusselt number (Nu) is obtained as

$$(1+\gamma)^{-b} R_e^{-1/2} \mathrm{Nu} = -\theta'(0), \tag{16}$$

where $R_e (= \Omega r^2/\nu_\infty)$ is the local rotational Reynolds number.

In Eqs. (14)–(16), the gradient values of G, F, and θ at the surface are evaluated when the corresponding differential equations are solved satisfying the convergence criteria.

4 Numerical Solutions

The set of coupled, non-linear differential equations (9)–(12) are solved numerically using a standard initial value solver called the Shooting method. For this purpose Nachtsheim and Swigert [16] iteration technique has been employed. Thus adopting this numerical technique, a computer program was set up for the solutions of the basic non-linear differential equations of our problem where the integration technique was adopted as a six ordered Range-Kutta method of integration. Various groups of the parameters W_s and γ were considered in different phases.

In all the computations the step size $\Delta\eta = 0.001$ was selected that satisfied a convergence criterion of 10^{-6} in almost all phases mentioned above. The value of η_∞ was found to each iteration loop by setting $\eta_\infty = \eta_\infty + \Delta\eta$. Thus $(\eta_\infty)_{\max}$, to each group of parameters, has been determined when the value of the unknown boundary conditions at $\eta = 0$ (that arise in the Shooting method) not change to successful loop with error less than 10^{-6}. Since we are not aware of any paper that deals with porous rotating disk flow and heat transfer with variable properties, to establish the validity of our code we have made some numerical calculations with constant properties taking $\Pr = 0.71$ (air). A comparison of these calculated results are made with those of Kelson and Desseaux [10] in Table 1. This shows excellent agreement between both the results.

5 Results and Discussion

As a result of the numerical calculations, the velocity and temperature distributions for the flow are obtained from Eqs. (9)–(12) and are displayed in Figs. 2 and 3 for different values of γ (relative temperature difference parameter) and W_S (suction/injection parameter), respectively. In the present analysis the fluid considered is flue gas (Pr=0.64).

The effects of suction and injection for $\gamma=0.05$ and Pr=0.64 on the radial velocity profiles and temperature profiles are shown in Figs. 2(*a*) and 2(*b*). From Fig. 2(*a*) it is observed that for strong suction the radial velocity is very small while for injection ($W_S > 0$) the boundary layer is increasingly blown away from the disk to form an interlayer between the injection and the outer flow regions. Figure 2(*a*) also depicts that for high values of injection parameter ($W_S=4$), the radial velocity near the disk (for small values of η) is lower than that for smaller values of W_S. This is

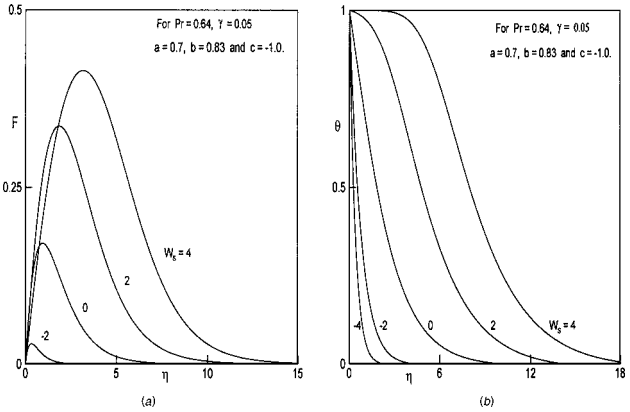

Fig. 2 (*a*) Effect of W_S on the radial velocity profiles, and (*b*) effect of W_S on the temperature profiles

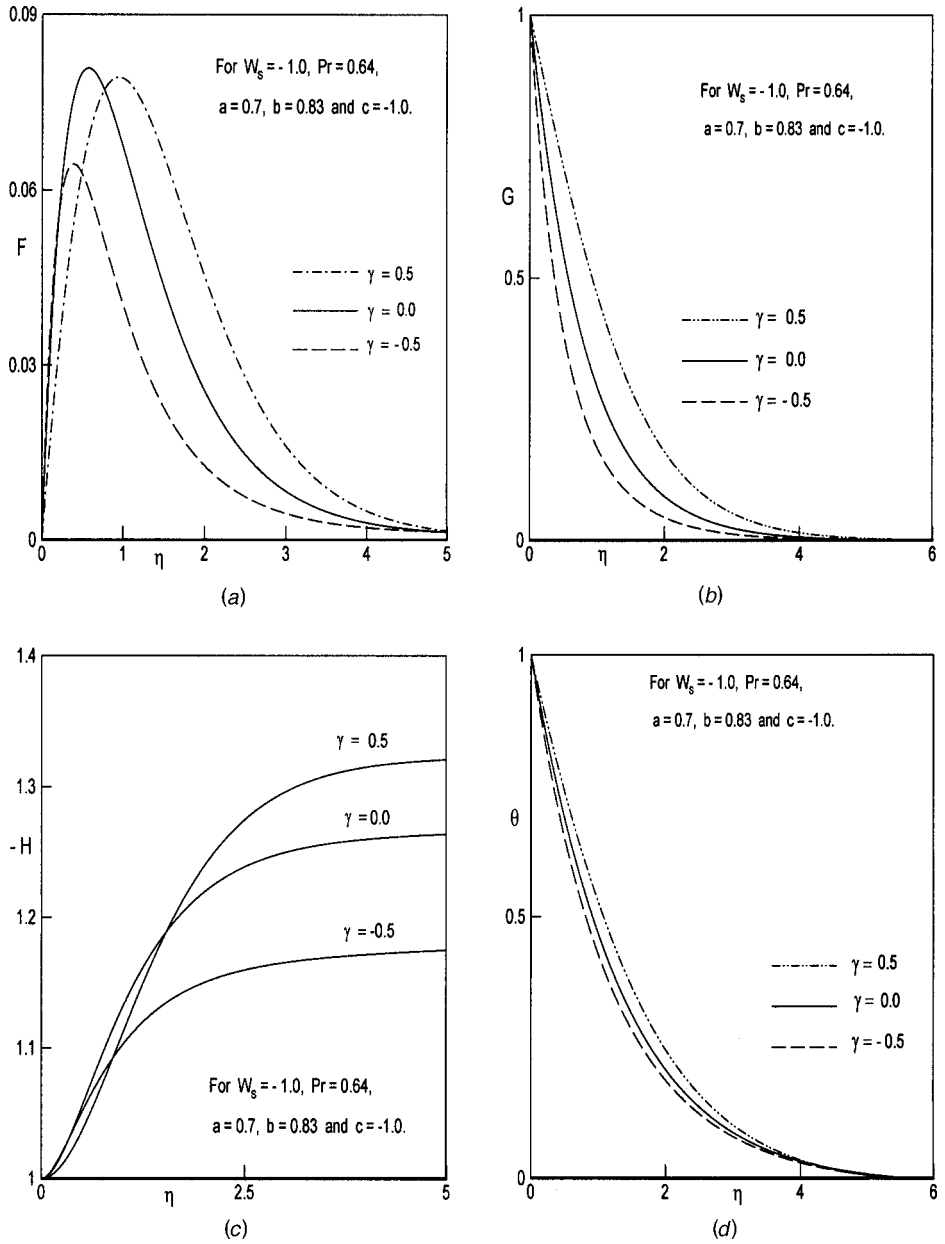

Fig. 3 (*a*) Effect of γ on the radial velocity profiles; (*b*) effect of γ on the tangential velocity profiles; (*c*) effect of γ on the axial velocity profiles; and (*d*) effect of γ on the temperature profiles.

Table 2 Numerical values of the radial and tangential skin-friction coefficients and the rate of heat transfer coefficient obtained for Pr=0.64

	$W_S=-1.0$			$W_S=1.0$		
γ	$F'(0)$	$-G'(0)$	$-\theta'(0)$	$F'(0)$	$-G'(0)$	$-\theta'(0)$
-0.50	0.50548	2.00221	1.31859	0.62691	0.31956	0.07716
-0.25	0.45483	1.54634	0.97469	0.56634	0.31410	0.08217
0.00	0.38962	1.17586	0.72634	0.48947	0.30218	0.08975
0.25	0.29993	0.85453	0.53218	0.38520	0.27800	0.09960
0.50	0.16839	0.55557	0.36352	0.22250	0.22963	0.10990

due to the fact that, with increasing values of W_s, the injected flow can sustain axial motion to greater distances from the wall. Then, near the wall, the radial flow which is fed by the axial flow is expected to decrease as the injected parameter increases. Figure 2(*b*) shows the usual decay of temperature for strong suction while the thermal boundary layer increases rapidly for strong injection.

The effects of γ on the velocity (radial, tangential and axial) and temperature profiles are shown in Figs. 3(*a*)–3(*d*). In these figures comparison is made between the constant property and variable property solutions. In Fig. 3(*a*), it is observed that for all values of γ the radial velocity attains a maximum value close to the surface of the disk and then decreases monotonically with the increase of the boundary layer. This effect near the surface of the disk is due to the existence of the centrifugal forces. The above maximum value is, however, larger in case of constant property ($\gamma=0$) compared to those values in cases of variable property ($\gamma=-0.5$ and $\gamma=0.5$). Figure 3(*a*) also shows that very close to the disk surface an increase in the values of γ leads to the decrease in the values of the radial velocity while for most part of the boundary layer at a fixed η position radial velocity increases with the increase of the relative temperature difference parameter γ. Similar effects of γ are also observed in case of axial velocity profile (Fig. 3(*c*)). From Fig. 3(*c*), it is also observed that close to the disk surface the positive values of γ have a tendency to gives rise to the familiar inflection point profile, which indicates that variable property with highly heated surface may lead to the destabilization of the laminar flow resulting in the development of the viscous sub-layer. The tangential velocity, as observed in Fig. 3(*b*), is found to increase with increasing values of γ at a fixed point of the boundary layer. From Fig. 3(*d*), it may be observed that the non-dimensional temperature increases with the increasing values of γ, but this rate of increase is very small and hence the thermal boundary layer does not vary much for solutions with the consideration of the property variations. The above results pertain to the suction case $W_s=-1$. However, calculations were also made for $W_s=1$ (injection) and it was observed that the results follow the same trend as in the case of suction.

Finally, the values of the radial and tangential skin friction coefficients and the rate of heat transfer coefficient have been presented in Table 2. The above coefficients are found to decrease with the increasing values of temperature parameter γ in case of suction ($W_s=-1$). But in case of injection ($W_s=1$) the heat transfer shows an opposite trend.

6 Conclusions

In this paper, the effects of variable properties and transpiration on the physical problem of a steady laminar flow with heat transfer, due to an impulsively started rotating porous disk in a three dimensional cylindrical coordinate system, has been investigated. The Nachtsheim and Swigert [16] iteration technique based on sixth-order Range-Kutta and Shooting method has been employed to complete the integration of the resulting similarity equations.

From the above investigation, we can draw the following conclusions:

1. Due to the existence of the centrifugal forces, the radial velocity reaches a maximum value close to the surface of the disk. The largest maximum value is attained for constant property ($\gamma=0$).
2. Close to the disk surface positive values of γ give rise to the familiar inflection point profile leading to the destabilization of the laminar flow. This destabilization effect is also apparent in case of strong injection.
3. For fixed values of the suction parameter and the Prandtl number, momentum boundary layer is found to increase considerably while the thermal boundary layer is found to vary little with variable properties.
4. Increasing the values of γ (-0.5 to 0.5) lead to the decrease in radial and tangential skin-friction coefficients and the rate of heat transfer coefficient in case of suction whereas in case of injection the rate of heat transfer coefficient shows an opposite trend.

References

[1] Herrero, J., Humphrey, J. A. C., and Giralt, F., 1994, "Comparative Analysis of Coupled Flow and Heat Transfer between Co-rotating Discs in Rotating and Fixed Cylindrical Enclosures," ASME J. Heat Transfer, **300**, pp. 111–121.

[2] Owen, J. M., and Rogers, R. H., 1989, *Flow and Heat Transfer in Rotating Disc System*, Rotor-stator Systems Vol. 1 (Research Studies, Taunton, UK and Wiley, New York).

[3] Schlichting, H., 1968, *Boundary Layer Theory*, 6th ed. (McGraw Hill, New York), pp. 93–98.

[4] Cochran, W. G., 1934, "The Flow due to a Rotating Disc," Proc. Cambridge Philos. Soc., **40**, pp. 465–475.

[5] Benton, E. R., 1966, "On the Flow due to a Rotating Disc," J. Fluid Mech., **24**, pp. 781–800.

[6] Roger, M. G., and Lance, G. N., 1960, "The Rotationally Symmetric Flow of a Viscous Fluid in Presence of Infinite Rotating Disc," J. Fluid Mech., **7**, pp. 617–631.

[7] Stuart, J. T., 1954, "On the Effect of Uniform Suction on the Steady Flow due to a Rotating Disc," Q. J. Mech. Appl. Math., **7**, pp. 446–457.

[8] Ockendon, H., 1972, "An Asymptotic Solution for Steady Flow Above an Infinite Rotating Disc with Suction," Q. J. Mech. Appl. Math., **25**, pp. 291–301.

[9] Kuiken, H. K., 1971, "The Effect of Normal Blowing on the Flow Near a Rotating Disk of Infinite Extent," J. Fluid Mech., **47**, pp. 789–798.

[10] Kelson, N., and Desseaux, A., 2000, "Note on Porous Rotating Disk Flow," ANZIAM J., **42(E)**, pp. C847–C855.

[11] Herwig, H., 1985, "The Effect of Variable Properties on Momentum and Heat Transfer in a Tube with Constant Heat Flux Across the Wall," Int. J. Heat Mass Transfer, **28**, pp. 424–441.

[12] Herwig, H., and Wickern, G., 1986, "The Effect of Variable Properties on Laminar Boundary Layer Flow," Warme und Stoffubertragung, **20**, pp. 47–57.

[13] Herwig, H., and Klemp, K., 1988, "Variable Property Effects of Fully Developed Laminar Flow in Concentric Annuli," ASME J. Heat Transfer, **110**, pp. 314–320.

[14] Gokoglu, S. A., and Rosner, D. E., 1984, "Correlation of Thermophoretically Modified Small Particle Diffusional Deposition Rates in Forced Convection Systems with Variable Properties," Int. J. Heat Fluid Flow, **6**, pp. 37–41.

[15] Jayaraj, S., 1995, "Thermophoresis in Laminar Flow Over Cold Inclined Plates with Variable Properties," Heat Mass Transfer, **40**, pp. 167–174.

[16] Nachtsheim, P. R., and Swigert, P., 1965, "Satisfaction of Asymptotic Boundary Conditions in Numerical Solution of System of Nonlinear of Boundary Layer Type," NASA TN-D3004.

Correlations for the Onset of Instabilities of Spherical Laminar Premixed Flames

M. Z. Haq
Department of Mechanical Engineering,
Bangladesh University of Engineering and Technology,
Dhaka-1000, Bangladesh
Phone: (8802) 9665636
Fax: (8802) 8613046
e-mail: zahurul@me.buet.ac.bd

A spherically expanding flame in a quiescent premixture is a bifurcation phenomenon, in which the flame becomes unstable at a radius, greater than some critical value, while remaining stable below that critical radius. Beyond this critical radius, developing instabilities are initiated by propagating cracks to form a coherent structure covering the entire flame surface and the flame accelerates. The present paper reports a Schlieren photographic study of spherical flame propagation in methane—air, iso-octane—air and n-heptane—air premixtures at different initial conditions where the onset of instability and the flame acceleration are clearly perceived. Critical size and corresponding elapsed time for the development of such instability are measured and these values are correlated with the appropriate flame parameter.
[DOI: 10.1115/1.2098867]

Introduction

The development of flame instabilities in the form of cells and ridges of characteristic sizes over the flame surface have been attributed as "perhaps one of the most beautiful and fascinating phenomena in the flame dynamics" [1]. Instability can cause or enhance turbulence in the premixture and significant acceleration of the flame front [2]. The resulting enhanced burning rate has positive implications for most practical applications. However, spills in case of the storage and transportation of large quantities of fuels pose a potential hazard from large-scale gaseous explosions because of the flame acceleration associated with such instability [3], and therefore demand comprehensive probing into the development of such instability.

The seminal stability analyses of Darrieus and Landau, reviewed in [4], treated the flame as a gasdynamic surface of discontinuity in density that propagates normal to itself at a constant speed and formulated the problem of "hydrodynamic instability" of a plane flame front. The analysis did not consider any length scale and a flame has been shown to be unstable to perturbations of all wavelengths that is not observed experimentally [5]. In real flames, instability condition is modified significantly by gravity forces and also by the fact that the premixed flames have finite thickness and a laminar burning velocity that is sensitive to the flame stretching. Effect of gravity is straightforward in the situation in which a fluid is stratified vertically where the buoyancy force will destabilize the flame if the direction of the flow is such as to place the low-density combustion products below the high-density unburned mixture, and vice versa [6]. The effects of flame thickness and stretch, however, are somewhat more complex in nature.

Contributed by the Heat Transfer Division of ASME for publication in the JOURNAL OF HEAT TRANSFER. Manuscript received April 1, 2004; final manuscript received January 25, 2005. Assoc. Editor: Bakhtier Farouk.

It has been experimentally observed that intrinsic flame instability primarily occurs in fuel-oxidizer mixtures where the Lewis number of the deficient species is smaller than some critical value. In other words, rich mixtures of heavy fuels or lean mixtures of light fuels exhibit "cellular instability" [5]. Sivashinsky [5] has reviewed the flame instability mechanism, and identified the source of cellular instability as "preferential diffusion." Simply stated the thermal gradients in the preheat zone have a stabilizing effect because a convex section of the flame would be expected to propagate more slowly than a concave section if thermal diffusion only are operating in the region of the flame, and vice versa. Therefore, when any sufficiently light species of the fuel-oxidant pair is sufficiently deficient, any concave perturbation of a flat flame shape would grow to become a deep trough, because preferential diffusion of the light and deficient species toward the reaction zone will deplete that species in the neighborhood of the perturbation and can cause the local burning velocity to be reduced, and vice versa. Accordingly, such flame instability primarily occurs in fuel-oxidizer mixtures that are deficient in the light reactants (e.g., rich mixtures of heavy fuels or lean mixtures of light fuels) [5]. However, increasing the pressure leads to an increase in flame instability [7]. Therefore, the concept of preferential diffusion of species fails to explain the flame instability developed at high pressure for the fuel-air premixture with same stoichiometry, and invokes the use of the concept of flame stretch.

Practical flames do not conform to the idealized planar steady configuration; instead these can be wrinkled and can propagate in flow fields that are non-uniform and unsteady. Therefore, a propagating flame front is subjected to strain and curvature effects, which together constitute flame stretch and change the flame frontal area. Hence, the flame stretch rate, α, at any point on the flame surface is defined as the Lagrangian time derivative of the logarithm of the area, A, of an infinitesimal element of the surface surrounding the point [4],

$$\alpha = \frac{d \ln A}{dt} = \frac{1}{A}\frac{dA}{dt} \tag{1}$$

Flames stretch can increase or decrease the flame speed significantly [8–12]. A linear relationship between the flame speed, S_n, and the stretch rate, α, has been reported in theoretical analysis [11], numerical computation [12], and experiments [8–10]. A burned gas Markstein length, L_b, is defined in [11] to account for the sensitivity of S_n to α such that

$$S_n = S_s - L_b\alpha \tag{2}$$

where S_s is the unstretched flame speed, and is obtained as the intercept of S_n at $\alpha=0$, in the plot of S_n against α. Markstein length, L_b, is expressed in dimensionless form, as Markstein number, Ma_b, by normalizing the L_b by laminar flame thickness, δ_l. Laminar flame thickness, δ_l, is given by, $\delta_l = \nu/u_l$ [10], in which ν is the kinematic viscosity of the unburned mixture.

Incorporation of Markstein number, Ma_b, into the linear stability analysis showed that, for positive values of Ma_b, the flame remains hydrodynamically unstable in the absence of buoyancy forces only to the long-wavelength perturbation [13]. For a negative value of Ma_b, the burning velocity is decreased where the flame is concave to the unburned mixture and that the instability of the flame is therefore increased. The use of the Markstein number as a measure of the susceptibility to instability, as in the present work, overcomes the confusion between the two types of instability because, based on experimental data, it is an indicator of the resultant effect, not the cause. Further instability analysis using Markstein number yields an inner cut-off of wavelength, where a planar flame is stable to perturbations of shorter wavelength and unstable to those of long-wave length [3]. This approach results in the stabilization of short-wave length perturbations only when the value of the Markstein number is positive. When the sign is reversed, the short-wave perturbations could provide an additional destabilizing factor [1].

From theoretical and experimental considerations, a spherical flame originated from a point ignition source and propagating in a premixture provides a convenient means of studying the development of flame instability as the size of the flame sphere limits the perturbation wavelength range that is also growing in time, and this sets definable limits to the critical wavelengths associated with the instability [13]. Hence, if the absolute magnitudes of perturbation amplitudes rise in time more slowly than the flame front itself, the flame surface becomes smoother. The flame front wrinkling and flame acceleration are observed only if the flame front perturbations grow faster than the flame front propagation [14]. Hence, the first stage of a developing instability in the spherical flame is the propagation of surface "cracks" across the flame surface [15]. The onsets of these correspond with the onset of instabilities as predicted by the linear theory of flame instability [16]. However, experiments show a further delay to occur before the transition to a fully developed cellular flame [7–10]. The flame speed increases continuously as a consequence of the increasing wrinkled flame surface area and for unconfined large-scale explosions an eventual transition to a turbulent flame is observed [17–19].

In the present paper, the transition to the fully developed cellular flame regime has been investigated using Schlieren photography. Analyses of flame images, obtained from spherical flame propagation in methane—air, iso-octane—air, and heptane—air premixture, clearly show the flames to accelerate as the instability develops, giving rise to cellular flame structure. Critical conditions for the transition to the cellular flames are estimated and correlated with the appropriate flame parameter.

Experimental and Measurement Techniques

In the present study, images of spherical flames propagating in quiescent premixtures are captured using high-speed Schlieren photography at, typically, 6000 frames per second at different initial conditions of pressures, temperatures and stoichiometry where the onset of flame instability and associated flame acceleration are clearly perceived. The experimental conditions and the summarized results are presented in Table 1. A 380-mm-diam, spherical, stainless steel vessel has been employed that is capable of withstanding the temperatures and pressures generated from explosions with initial pressures up to 1.5 MPa and initial temperatures up to 600 K. It has extensive optical access through three pairs of orthogonal windows of 150 mm diameter. A Spectra-Physics 10 mW He–Ne laser, model 106-1, with a beam diameter of 0.65 mm and wavelength of 632.8 nm has been used as a light source. Other aspects of the equipment and experimental technique are reported in [7].

Shown in Fig. 1 are the flame images obtained from an explosion of stoichiometric methane-air premixture. Flame propagation is essentially spherical, and the smooth flame front is easily identifiable from these images. Shown in Fig. 2 are the images of a flame propagating in a lean premixture at 300 K and 0.5 MPa. These images reveal the grainy appearance of cell formation and the formation of dimples along the flame front. The contrast in appearance between a cellular and non-cellular flame is emphasized in Fig. 3. The cellular flame, in Fig. 2, shows the distribution of cells of different sizes like a "web" of cracks and cells. The transition to instability exhibits some delay in which the cells continue to grow and divide during flame growth. Using the flame images, the flame speed, S_n, is calculated from the flame front radius against time by

$$S_n = \frac{dr_u}{dt} \tag{3}$$

Here, r_u is the cold front radius of the flame. In [10], r_u has been shown to be very close to the flame front radius observed by Schlieren photography, r_{Sch}; and therefore values of r_{Sch} are used instead of r_u for simplicity. Hence, for spherical flame propagation, flame stretch, α, is given by

$$\alpha = \frac{1}{A}\frac{dA}{dt} = \frac{2}{r_u}\frac{dr_u}{dt} \cong \frac{2}{r_{\mathrm{Sch}}}\frac{dr_{\mathrm{Sch}}}{dt} = \frac{2}{r_{\mathrm{Sch}}}S_n \tag{4}$$

Shown in Fig. 4 are the variations of flame speed with total stretch rate for stoichiometric methane-air premixtures at an initial temperature of 300 K. At small flame radius the flame stretch is high. For methane-air flames at 0.1 MPa, flame stretch has an adverse effect on the flame stretch that is an indicative of a positive Markstein length. However, the effect of stretch on the flame speed is reversed for methane-air flames at 0.5 MPa where the flame speed is reduced with the flame expansion and the reduction of flame stretch. As stretch is further reduced, a point is reached where the flame becomes unstable and cellular flame develops, and this is associated with an increase in flame speed. The point at which the flame speed begins to accelerate rapidly with decreasing stretch defines a critical Peclet number, $\mathrm{Pe}_{\mathrm{cl}}$, given by the critical flame radius, r_{cl}, at the onset of flame acceleration, normalized by the flame thickness, δ_l. A linear relationship between the S_n and α exists over a wide range of flame radii that excludes cellular flame regime. The gradient of the best fit straight line to the experimental data, presented in Fig. 4, gives L_b, and the intercept of the plot at zero stretch gives the value of unstretched flame speed, S_s. The unstretched laminar burning velocity, u_l, is deduced from S_s using

$$u_l = S_s\left(\frac{\rho_b}{\rho_u}\right) \tag{5}$$

Here, ρ_u is the density of unburned and ρ_b is the density of burned gas at the adiabatic flame temperature, and the value of ρ_b is found from the calculated properties of the equilibrated adiabatic products, computed using thermodynamic database by Burcat and McBride [20].

Results and Correlations

Shown in Fig. 5 are the variations of Ma_b as a function of ϕ for flame propagation in methane-air and iso-octane-air premixtures at initial temperatures of 300 and 358 K, respectively. At all measured conditions, the values of Ma_b's increase with ϕ for methane-air premixtures, and the trend is reversed for iso-octane-air premixtures. These trends are persistent with the generalized trends of the Markstein numbers to increase monotonically with equivalence ratio for lighter than air fuel and to decrease for the heavy hydrocarbon-air mixtures [21]. The effects of temperature on Markstein numbers are reported to be small [10]. Also shown in Fig. 5 are the variations of Ma_b's for methane-air premixtures at 0.5 MPa. Significant decrease in the Markstein numbers from the corresponding 0.1 MPa values are observed, and in case of lean and stoichiometric mixtures these flame have negative Markstein numbers. Flame instability and cellularity are observed with flames having lower values of Markstein numbers [22].

Shown in Fig. 6 are the variations of critical Peclet numbers as a function of Markstein numbers, for initial conditions presented in Table 1. Critical Peclet numbers for the onsets of flame instability are found to increase with Markstein numbers. A straight-line fit describes them well with a correlation of 0.84, and the correlation between $\mathrm{Pe}_{\mathrm{cl}}$ and Ma_b can be written as

$$\mathrm{Pe}_{\mathrm{cl}} = 2331 + 34.67\mathrm{Ma}_b \tag{6}$$

For a large-scale explosion of initially quiescent propane-air premixture ($\phi = 1.06$) at atmospheric pressure, the experimental value of $\mathrm{Pe}_{\mathrm{cl}}$ is reported in [23] as 3150 with $\mathrm{Ma}_b = 28.1$; and the estimated value of $\mathrm{Pe}_{\mathrm{cl}}$, using Eq. (6), is 3305 with only 5% deviation form the experimental result.

In the present study, dimensionless critical time for onset of flame instability, $\overline{\tau_{\mathrm{cl}}}$, is defined as the elapsed time for onset of instability, t_{cl}, normalized by the chemical time of the laminar

Table 1 Experimental conditions and summary of results of the present study

Symbol	Fuel	P [MPa]	T [K]	ϕ	ρ_u/ρ_b	u_l [m/s]	δ [mm]	τ_c [ms]	Ma_b	Pe_{cl}	$\overline{\tau_{cl}}$
1	Methane	0.50	302	0.8	6.71	0.12	0.027	0.23	-22.25	1078	137
2	Methane	0.51	306	0.8	6.71	0.12	0.026	0.21	-24.50	1115	139
3	Methane	0.51	358	0.8	5.73	0.15	0.028	0.19	-8.95	1662	268
4	Methane	0.51	360	0.8	5.73	0.16	0.027	0.17	-7.26	1081	170
5	Methane	0.50	401	0.8	5.20	0.22	0.024	0.11	-16.08	937	155
6	Methane	0.50	301	1.0	7.58	0.19	0.017	0.09	-23.38	1096	119
7	Methane	0.50	301	1.0	7.58	0.20	0.016	0.08	-15.20	1734	204
8	Methane	0.51	350	1.0	6.44	0.26	0.016	0.06	-16.92	1427	193
9	Methane	0.51	359	1.0	6.44	0.27	0.016	0.06	-20.75	1927	270
10	Methane	0.50	404	1.0	5.82	0.32	0.016	0.05	-30.75	1455	216
11	Methane	0.50	397	1.0	5.82	0.31	0.017	0.05	-10.57	1929	318
12	Methane	1.02	310	0.8	6.73	0.09	0.018	0.20	-27.76	1104	129
13	Methane	1.02	311	0.8	6.73	0.08	0.019	0.23	-35.20	872	95
14	Methane	1.02	358	0.8	5.73	0.12	0.018	0.15	-33.08	1599	232
15	Methane	1.01	359	0.8	5.73	0.12	0.018	0.14	-23.85	1615	244
16	Methane	1.02	404	0.8	5.20	0.16	0.017	0.11	-3.49	1813	319
17	Methane	1.01	404	0.8	5.20	0.15	0.017	0.12	-16.38	1681	283
18	Methane	1.00	297	1.0	7.63	0.14	0.011	0.08	-34.09	1507	162
19	Methane	1.00	302	1.0	7.63	0.15	0.011	0.07	-24.02	1797	207
20	Methane	1.00	356	1.0	6.47	0.21	0.011	0.05	-27.72	2263	296
21	Methane	1.01	359	1.0	6.47	0.21	0.011	0.05	-30.17	2292	313
22	Methane	1.02	401	1.0	5.84	0.24	0.011	0.05	-3.54	2517	399
23	Methane	1.02	402	1.0	5.84	0.23	0.011	0.05	-18.38	1988	301
A	Iso-Octane	1.01	356	1.0	7.05	0.26	0.007	0.03	40.84	4095	645
B	Iso-Octane	1.01	350	1.0	7.16	0.25	0.007	0.03	26.91	4273	684
C	Iso-Octane	0.49	362	1.0	6.90	0.32	0.013	0.04	19.25	3395	502
D	Iso-Octane	0.50	361	1.0	6.92	0.32	0.012	0.04	35.17	3924	582
E	Iso-Octane	0.24	363	1.2	6.91	0.35	0.023	0.07	-1.74	1400	192
F	Iso-Octane	0.25	362	1.2	6.93	0.33	0.023	0.07	-3.86	1071	147
G	Iso-Octane	0.75	400	1.0	5.69	0.34	0.012	0.03	11.30	2340	409
H	Iso-Octane	0.75	452	1.0	5.67	0.32	0.012	0.04	-2.07	2337	414
I	Iso-Octane	0.75	451	1.0	5.67	0.31	0.013	0.04	2.20	2321	413
J	Iso-Octane	0.75	363	1.0	6.91	0.28	0.010	0.04	-23.56	2205	287
K	Iso-Octane	1.00	454	0.8	5.00	0.25	0.012	0.05	34.67	3407	694
a	n-Heptane	0.50	361	1.0	6.92	0.32	0.012	0.04	30.94	3102	460
b	n-Heptane	0.49	455	1.0	5.61	0.48	0.013	0.03	-2.50	2051	349
c	n-Heptane	0.52	452	1.0	5.65	0.47	0.012	0.03	-2.58	2684	446
d	n-Heptane	0.54	451	1.2	5.72	0.47	0.011	0.02	-8.15	2239	358
e	n-Heptane	0.53	450	1.2	5.73	0.44	0.012	0.03	-28.14	1409	207
f	n-Heptane	1.00	348	1.0	7.19	0.25	0.008	0.03	28.93	3959	537
g	n-Heptane	0.51	362	1.0	6.90	0.33	0.012	0.04	42.18	3391	502

flame propagation, given by $\tau_c = \delta_l / u_l$ [24]. Shown in Fig. 7 are the variation of $\overline{\tau_{cl}}$ plotted as a function of Ma_b. It is not surprising that flames with higher Markstein numbers remain stable for longer time than the flames with lower Markstein numbers. A straight-line fit describes them well with a correlation of 0.86, and the correlation between $\overline{\tau_{cl}}$ and Ma_b can be written as

$$\overline{\tau_{cl}} = 358.1 + 6.14 Ma_b \tag{7}$$

Slightly less scatter in data is observed than data presented in Fig. 6.

In the present study, cell formations associated with the flame instability are observed for methane–air mixtures only at high pressures, while fully developed cellular methane–air flame is reported for large-scale unconfined gaseous explosions [17]. Shown in Fig. 8 are the flame radii plotted against time in the large-scale methane–air explosions reported in [17]. These experiments were designed to observe the effects of flame instability at atmospheric methane-air mixtures at 288 K. Also plotted in Fig. 8 are the flame radii against time data measured in the present experiments for an initial temperature of 300 K and an initial pressure of 0.1 MPa. Clearly, two regimes of flame propagation can be identified where in the initial stable regime the flame is stabilized by thermo-diffusion and flame stretch and the flame speed is related to the Markstein number and the flame stretch rate; and in the later phase of the flame propagation the flame is unstable and cellular and the flame speed might be well represented by a power law. For atmospheric methane–air flame propagation (with $u_l = 0.36$ m/s, $Ma_b = 21.7$, $\delta_l = 0.044$ mm and $\tau_c = 0.122$ ms [10]), no images are available to show the transition to the flame instability. However, for the onset of instability of atmospheric methane-air flame at 300 K, the estimated value of critical radius of 135 mm (using Eq. (6)) and the elapsed time of 60 ms (using Eq. (7)) are clearly marked by an "X" in Fig. 8. The estimated values seem to blend well with the experimental data from two different experiments conducted in two different length-scales.

Conclusions

1. Flame stretch affects the flame speed, and Markstein numbers are defined to account for the sensitivity of flame speed to such flame stretch. These numbers are correlated with the susceptibility to the development of flame instability.
2. A high value of Markstein number is stabilizing and able to counter the perturbation in flame fronts, and vice versa. Lower values of Markstein numbers are associated with early onset of instability at small flame radius in flame propagation.
3. Critical flame radius and the elapsed time for the onset of flame instability are linearly correlated with the Markstein number.

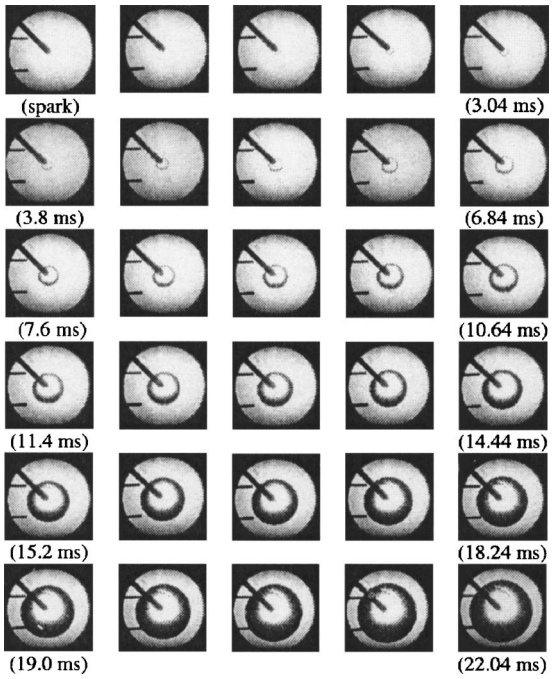

Fig. 1 Laminar flame propagation in a stoichiometric methane-air (ϕ=1.0) premixture at an initial temperature of 300 K and pressure of 0.1 MPa. First image corresponds to the spark ignition and the time interval between the images are 0.76 ms, and the size of the circular window is 150 mm in diameter.

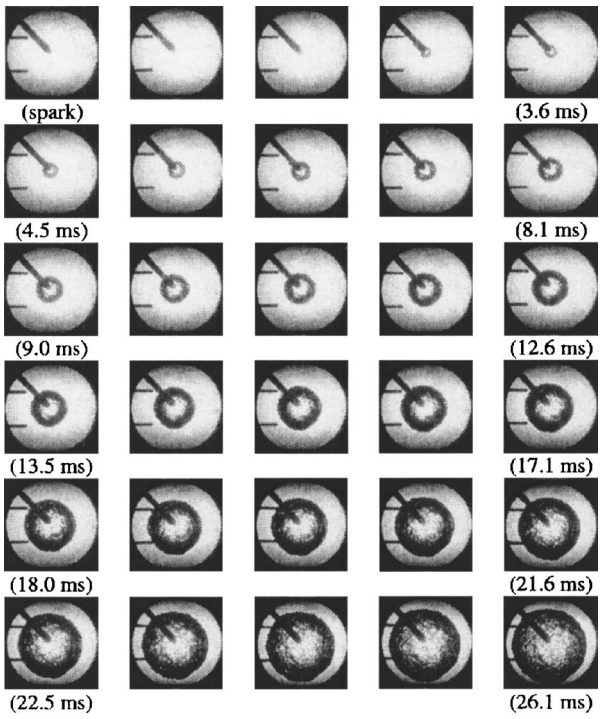

Fig. 2 Laminar flame propagation in a lean methane-air (ϕ =0.8) premixture at an initial temperature of 300 K and pressure of 0.5 MPa. First image corresponds to the spark ignition and the time intervals between the images are 0.9 ms, and the size of the circular window is 150 mm in diameter.

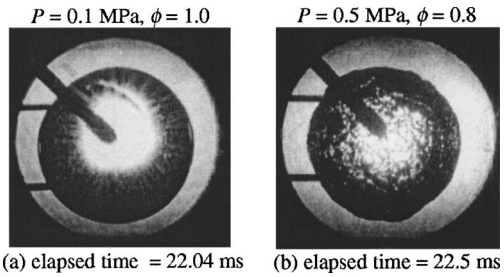

Fig. 3 Schlieren image of methane-air flames at 300 K, where flame is (*a*) not cellular, (*b*) cellular (size of the circular window is 150 mm in diameter)

Acknowledgment

The author acknowledges the financial assistance of the Commonwealth Scholarship Commission in the United Kingdom and many fruitful discussions with Prof. D. Bradley and Dr. R. Woolley.

Nomenclature

A = flame area
L_b = burned gas Markstein length
Ma_b = Markstein number, $\mathrm{Ma}_b = L_b/\delta_l$
P = initial pressure of the fuel-air premixture

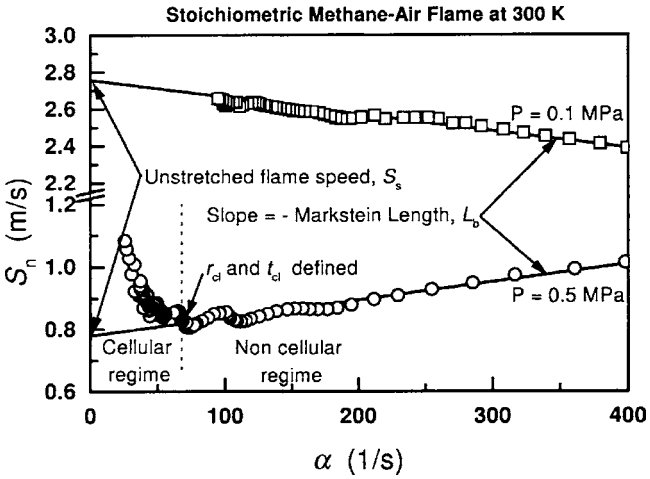

Fig. 4 Measured flame speeds at different flame stretch rates

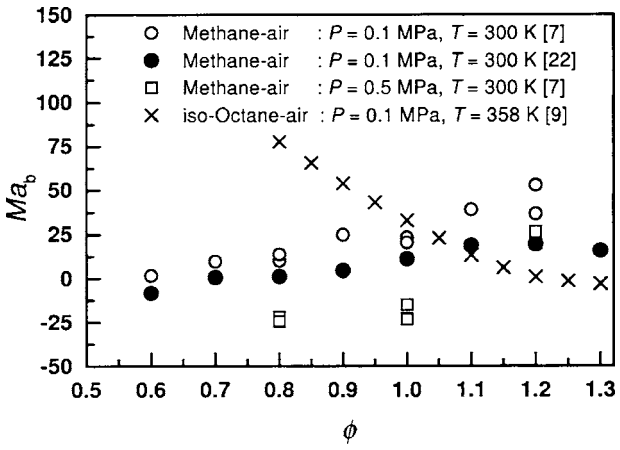

Fig. 5 Variations of Markstein number with equivalence ratio

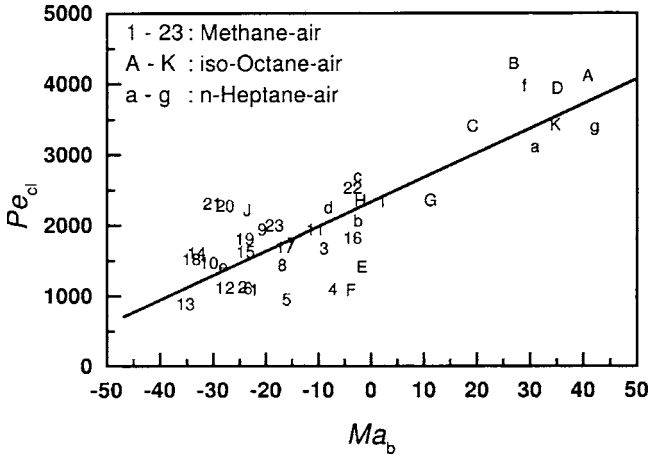

Fig. 6 Variations of Pe_{cl} with Ma_b for onset of the flame instability. Symbols correspond to initial conditions presented at Table 1

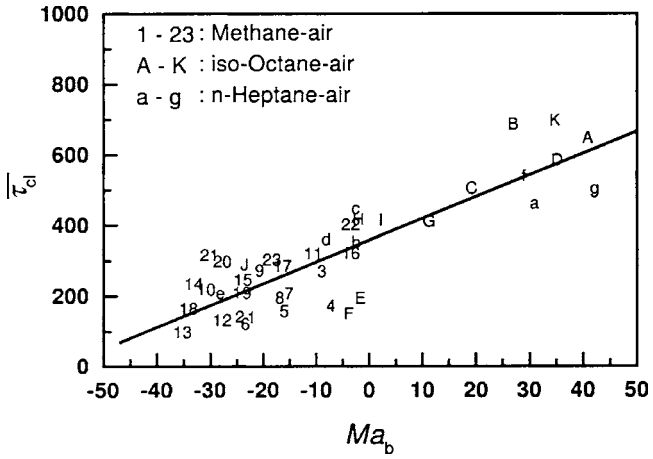

Fig. 7 Variation of dimensionless time, $\overline{\tau_{cl}}$, with Ma_b for onset of flame instability. Symbols correspond to initial conditions presented at Table 1

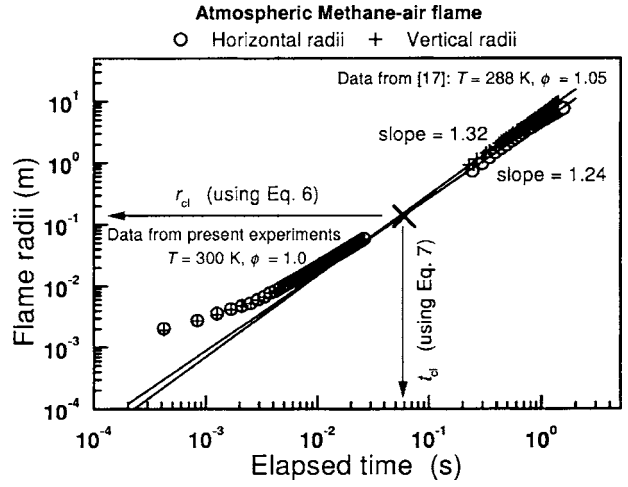

Fig. 8 Methane-air atmospheric flame propagation. Present work and that of [17]

Pe_{cl} = critical Peclet number for the onset of flame instability, $Pe_{cl}=r_{cl}/\delta_l$
r_{cl} = critical radius for onset of the flame instability
r_u = flame cold front radius, $r_u \cong r_{Sch}$
r_{Sch} = flame front radius observed by Schlieren photography
S_n = stretched laminar flame speed
S_s = unstretched laminar flame speed
t = elapsed time from ignition
t_{cl} = critical elapsed time for onset of the flame instability
T = initial temperature of the fuel-air premixture
u_l = nnstretched laminar burning velocity, $u_l=S_s(\rho_b/\rho_u)$
α = flame stretch rate, defined in Eq. (1)
δ_l = laminar flame thickness, $\delta_l=\nu/u_l$
ν = kinematic viscosity of the fuel-air premixture
ρ_b = burned gas density
ρ_u = unburned gas density
τ_c = chemical time of laminar flame, $\tau_c=\delta_l/u_l$
$\overline{\tau_{cl}}$ = dimensionless critical time for the onset of flame instability, $\overline{\tau_{cl}}=t_{cl}/\tau_c$
ϕ = equivalence ratio of the fuel-air premixture

References

[1] Law, C. K., and Sung, C. J., 2000, "Structure, Aerodynamics, and Geometry of Premixed Flamelets," Prog. Energy Combust. Sci., **26**, pp. 459–505.
[2] Bychkov, V. V., and Liberman, M. A., 2000, "Dynamics and Stability of Premixed Flames," Phys. Rep., **325**, pp. 115–237.
[3] Bradley, D., 2000, "Instabilities and Flame Speeds in Large Scale Premixed Gaseous Explosions," Philos. Trans. R. Soc. London, Ser. A, **357**, pp. 3567–3581.
[4] Williams, F. A., 1985, *Combustion Theory*, Addison-Wesley, Menlo Park, CA.
[5] Sivashinsky, G. I., 1990, "On the Intrinsic Dynamics of Premixed Flames," Philos. Trans. R. Soc. London, Ser. A, **332**, pp. 135–148.
[6] Coats, C. M., 1996, "Coherent Structures in Combustion," Prog. Energy Combust. Sci., **22**, pp. 427–509.
[7] Haq, M. Z., 1998, "Fundamental Studies of Premixed Combustion," Ph.D. thesis, The University of Leeds, Leeds, UK.
[8] Aung, K. T., Hasan, M. I., and Faeth, G. M., 1997, "Flame Stretch Interactions of Laminar Premixed Hydrogen/Air Flames at Normal Temperature and Pressure," Combust. Flame, **109**, pp. 1–24.
[9] Bradley, D., Hicks, R. A., Lawes, M., Sheppard, C. G. W., and Woolley, R., 1998, "The Measurement of Laminar Burning Velocities and Markstein Numbers for Iso-octane-Air and Iso-octane-n-Heptane-Air Mixtures at Elevated Temperatures and Pressures in an Explosion Bomb," Combust. Flame, **115**, pp. 126–144.
[10] Gu, X. J., Haq, M. Z., Lawes, M., and Woolley, R., 2000, "Laminar Burning Velocities and Markstein Lengths of Methane-Air Mixtures," Combust. Flame, **121**, pp. 41–58.
[11] Clavin, P., 1985, "Dynamic Behavior of Premixed Flame Fronts in Laminar and Turbulent Flows," Prog. Energy Combust. Sci., **11**, pp. 1–59.
[12] Bradley, D., Gaskell, P. H., and Gu, X. J., 1996, "Burning Velocities, Markstein Lengths, and Flame Quenching for Spherical Methane-Air Flames: A Computational Study," Combust. Flame, **104**, pp. 176–198.
[13] Zeldovich, Y. B., Barenblatt, G. I., Librovich, V. B., and Makhviladze, G. M., 1985, *The Mathematical Theory of Combustion*, Consultants Bureau, New York.
[14] Istratov, A. G., and Librovich, V. B., 1969, "On the stability of Gasdynamic Discontinuities Associated with Chemical Reactions. The Case of a Spherical Flame," Astronaut. Acta, **14**, pp. 453–467.
[15] Bradley, D., and Harper, C. M., 1994, "The Development of Instabilities in Laminar Explosion Flames," Combust. Flame, **99**, pp. 562–572.
[16] Bechtold, J. K., and Matalon, M., 1987, "Hydrodynamic and Diffusion Effects on the Stability of Spherically Expanding Flames," Combust. Flame, **67**, pp. 77–90.
[17] Lind, C. D., and Whitson, J. C., 1977, "Explosion Hazards Associated with Spill of Large Quantities of Hazardous Materials Phase II," Technical Report CG-D-85-77, Department of Transportation, U. S. Coast Guard.
[18] Makeev, V. I., Gostintsev, Y. A., Strogonov, V. V., Bokhon, Y. A., Chernushkin, Y. N., and Kulikov, V. N., 1984, "Combustion and Detonation of Hydrogen-Air Mixtures in Free Spaces," Combust., Explos. Shock Waves, **19**, pp. 16–18.
[19] Gostintsev, Y. A., Istratov, A. G., and Shulenin, Y. V., 1987, "Self-similar Propagation of a Free Turbulent Flame in Mixed Gas Mixtures," Combust.,

Explos. Shock Waves, **24**, pp. 563–569.
[20] Burcat, A., and McBride, B., 1997, "1997 Ideal Gas Thermodynamic Data for Combustion and Air-Pollution Use," Technical Report TAE-804, Technion—Israel Institute of Technology.
[21] Bechtold, J. K., and Matalon, M., 2001, "The Dependence of the Markstein Length on Stoichiometry," Combust. Flame, **127**, pp. 1906–1913.
[22] Hassan, M. I., Aung, K. T., and Faeth, G. M., 1998, "Measured and Predicted Properties of Laminar Premixed Methane/Air Flames at Various Pressures," Combust. Flame, **115**, pp. 539–550.
[23] Bradley, D., Cresswll, T. M., and Puttock, J. S., 2001, "Flame Acceleration Due to Flame-Induced Instabilities in Large-Scale Explosions," Combust. Flame, **124**, pp. 551–559.
[24] Poinsot, T., and Veynante, D., 2001, *Theoretical and Numerical Combustion*, Edwards, Philadelphia, PA.

Cooling of a Finned Cylinder by a Jet Flow of Air

F. Gori
e-mail: gori@uniroma2.it

M. Borgia

A. Doro Altan

M. Mascia

I. Petracci

Department of Mechanical Engineering,
University of Rome, "Tor Vergata," Via del Politecnico,
1-00133 Rome, Italy

A submerged slot jet of air is used to cool an externally finned cylinder, heated by electric current. The cylinder ensemble is made of a stainless steel finned tube and a Teflon bar core inside. Five thermocouples, pressed inside the steel tube by the Teflon bar, measure the wall temperature to determine local and mean convective heat transfer coefficients. The local Nusselt number has the maximum on the impinging point and the minimum on the rear point. The variation of local and mean Nusselt numbers with the distance from the slot exit is investigated. Empirical expressions are proposed to correlate the experimental data. The cooling of a finned cylinder with a jet flow realizes a higher heat transfer as compared to a smooth cylinder. [DOI: 10.1115/1.2098868]

Keywords: heat transfer, air flow, slot jet, externally finned cylinder

Introduction

The global efficiency of a jet flow as cooling system is due to the flow concentration and the limited fan expenses needed to move the smaller amount of fluid. Jet flow has been proposed as a cooling method to be used inside the engine of heavy trucks [1]. The specific interest of this application is to use external air, which enters throughout the fan of the vehicle, to cool the pipe where hot air, coming out of the compressor, is flowing to the intercooler. This is possible by using special nozzles, located after the fan, to converge the jet flow of air onto the hot-air tube. The jet flow increases the cooling performance but, due to the high temperature of the air at the outlet of the compressor, may be not enough to justify the presence of the nozzles. For this reason it has been proposed to use an externally finned tube, instead of the smooth tube.

Euro 4 emission regulations for the European heavy duty truck market will require development of high efficiency, low emission Diesel engines. To reach Euro 4 emission targets, several technical solutions have been proposed [2], which will have a strong impact on heat transfer requirements and on dynamic and static pressure loads on the heat exchangers. The increase of heat exchanger performances cannot solve the increased cooling requirements. It is also clear that there will be no more frontal surface available in the Euro 4 vehicles. Consequently, using conventional cooling systems, the cooling flow needs to be increased, with the result of a significant increase on the fan power consumption. Increase of the charge air boost pressure and consequently the charge air temperature will have a negative impact on the durability of the charge air coolers. Some preliminary experiments have been carried out at the Iveco Testing Laboratory, designed to test radiators, after-coolers, and fans [3].

The present paper describes further heat transfer experiments, carried out at the Heat Transfer and Energy Engineering Laboratory of the University of Rome, "Tor Vergata."

Literature Overview

Heat transfer between a finned cylinder and a cross-flow of air with dimensions much larger than the finned cylinder under test has been studied extensively in the literature to improve the cooling of airplane engines and fin-and-tube heat exchangers. This kind of flow condition is mentioned as full flow in the rest of the paper. The papers reported in the literature deal with the cooling of finned cylinders by a full flow of air. Because of the large number of papers only some of them are mentioned here [4–11]. The papers of the literature on full flow are relative to thermal and fluid dynamics conditions which are different from those experimented in the present paper and comparisons are not possible.

The present work employs an air flow with dimensions smaller than the impinged finned cylinder (but equal to the diameter of the nonfinned cylinder) and is referred as jet flow in the rest of the paper. A submerged jet flow of air consists of the flow into stagnant air. The fluid dynamics structure of the jet depends on the geometry of the nozzle and on the flow created by the wind tunnel. The two-dimensional structure of a jet flow consists of a developing and a developed region, as reported in [12,13].

The characteristics of the jet flow around a nonfinned cylinder depend on the relation between slot height, H, and cylinder diameter, D [14]. The ratio between heat transfer in jet and full flow, at several distances of the jet from the cooled cylinder, is investigated in [14] with the conclusions that, in case $D=H$, the maximum heat transfer can be reached at a distance $S/H=8$ and the convective heat transfer coefficient is higher than the full flow of about 20%. This conclusion, confirmed by the experiments [15], encouraged further experiments on finned cylinders to evaluate the improvements achievable using a combination of jet flow and fins.

Experiments

Experimental Apparatus. The experimental setup, generating the jet flow, is presented in Fig. 1.

The fan, with a power of 750 W, can move a maximum mass flow rate of 0.45 kg/s. The inlet duct of the fan has a circular cross section, with a diameter of 160 mm, and the exit duct has a square section, with the side of 135 mm. The fan lies on a base different from the rest of the wind tunnel in order to decrease the vibration level. The fan is followed by a settling chamber (made of plastic duct in order to reduce vibration) where the cross section is changed from square (at the fan exit) to circular with a diameter of 160 mm. After the settling chamber, an ensemble of honeycomb is located before the three metallic screens. After the third screen, the cross section of the wind tunnel is changed to a square one with a side of 106 mm. A converging duct is then used to convert the square cross section into a rectangular one, with height 17 mm and side 106 mm, followed by a rectangular slot, long enough to produce a slot jet flow in fully developed conditions.

The finned cylinder, represented in Fig. 2, is a commercial one.

The outside diameter of the tube (without the fins) is 17 mm while the thickness is 1 mm. The fins are on the outer surface in the form of a very thin helical metal ribbon, with fin pitch of 4 mm and fin height of 10 mm. The heater is spiraled on a threaded metallic bar, set inside the finned tube. The heating wire, covered by a ceramic layer, is heated by Joule effect, with the electric current given by the power supply. A brass cylinder is put

Contributed by the Heat Transfer Division of ASME for publication in the JOURNAL OF HEAT TRANSFER. Manuscript received February 18, 2004; final manuscript received March 18, 2005. Assoc. Editor: Phillip M. Ligrani.

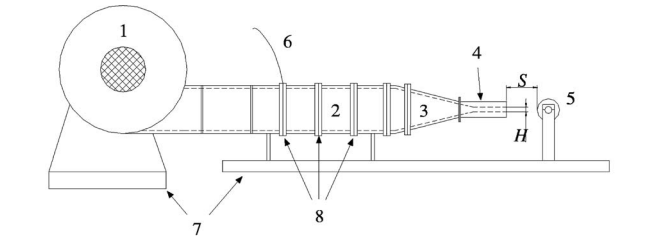

Fig. 1 Experimental setup

onto the heating wire in order to uniform the heat flux. The thermocouples are located on the middle transverse section of the finned tube, corresponding to the middle section of the rectangular slot, in order to have a two-dimensional problem. The exact location of the thermocouples, inside the finned tube, is obtained by positioning each one along a groove formed inside the Teflon tube, located between the brass cylinder and the finned tube (Fig. 3). In this way each thermocouple can be inserted and extracted from the finned tube.

The five thermocouples, made of Chromel and Constantan (type E), are positioned at five different angles from the impinging point of the jet, which is at zero degree. Figure 3 presents the thermocouples positions around the finned tube: TC2 is the thermocouple at the impingement point, TC3 at 90°, TC4 at 180°, TC5 at 235°, and TC6 at 315°. The system has been designed in order to allow the cylinder rotation around its axis. In this way, once the distance from the slot exit (S) is set, eight rotations of 45° allow us to measure, for each angular position, five temperatures. The first thermocouple (TC1, type J) measures the inlet air temperature and is located inside the wind tunnel, between the honeycomb and the first screen, not disturbing the air flow evolution. All the six temperature sensors have been made and calibrated in the laboratory.

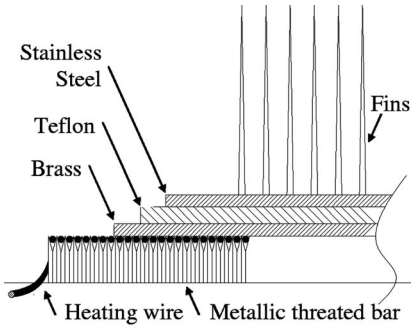

Fig. 2 Finned cylinder section

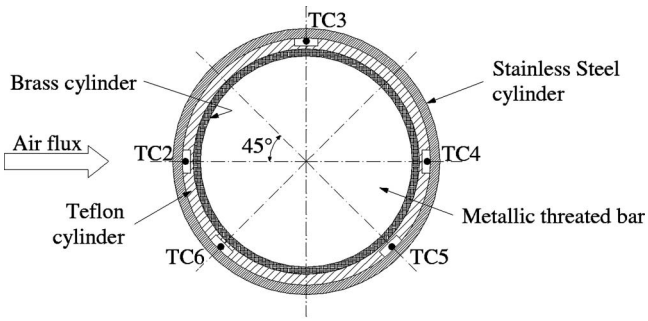

Fig. 3 Thermocouple positions

Table 1 Parameters to estimate temperature error sources

Error source (i)	Variable (X_i)	Bias (B_{Xi})		API
PT Thermometer	T_{PRT}	0.1 °C	B_T	API_T
DAQ system	ε	0.008% + 6μV		
Calibration: regression	T	0.05 °C		
Calibration: ITS-90	T	0.02 – 0.04 °C		

Table 2 Parameters to estimate velocity error sources

Error source (i)	Variable (X_i)	Bias (B_{Xi})		API
Pitot tube	u	1% ± 0.02 m/s	B_w	API_w
DAQ system	ε	0.05% + 5 mV		
Temperature	T	B_T		
Calibration	U_{calib}	B_{Ucalib}		

The average streamwise velocity (w) has been measured with a single wire hot-film anemometry to obtain a complete fluid dynamics map of the jet on the symmetric plane. The distance between the cylinder ensemble and the slot exit section is controlled by a micro-metric sledge operated by a computer-controlled motor.

Experimental Uncertainties. Uncertainty analysis has been carried out using the engineering method proposed in [16]. The errors are referred as *random* if they are varying during the experiment and valuable by the standard deviation of a representative measurements sample and *systematic* if they are static and assimilable to a mean value deviation. In the case of multiple samples per measurement, each measurement itself can be represented by the mean sample value and the uncertainty can be calculated using the *bias* (B) and the *average precision index* (API), which describe the fixed error and the sample standard deviation, respectively. Both are calculated on the basis of the sensitivity to the specific error source.

Error sources, introduced for each measured quantity defining several *cascade schemes*, are collected in Tables 1–3. Temperature uncertainty is affected by the PT thermometer[1] accuracy, by the thermocouples voltages acquired by the DAQ system, and by the calibration data interpolation (Table 1).

Velocity uncertainty includes Pitot tube,[2] DAQ system, temperature, and anemometer calibration data interpolation (Table 2).

The mean and local Nusselt numbers are evaluated taking into account the errors introduced by the convective heat transfer coefficients, while the diameter and the thermal conductivity contributions have been neglected (according to the materials and the dimensions provided by the suppliers). The forced convective heat transfer coefficient is defined as

$$h = Q_{fc}/(A\Delta T) \tag{1}$$

where Q_{fc} is the heat transfer by forced convection, A is the external surface of the finned cylinder, and ΔT is the temperature difference between cylinder and air jet.

Heat transfer due to natural convections, radiation, and axial and circumferential conduction have been neglected for the following reasons. Natural convection has some influence only at low Reynolds numbers. It has been evaluated by

$$Q_{nc} = h_{nc}A\Delta T \tag{2}$$

where the natural convection coefficient, given by

$$h_{nc} = 1.32(\Delta T D^{-1})^{0.25} \tag{3}$$

can be employed for air impinging on an horizontally displaced cylinder and for Rayleigh numbers in the range 10^3–10^9. The radiation contribution can be neglected by maintaining the temperature difference between cylinder and surrounding air under 6 °C. The axial thermal conduction is negligible on the middle cross section because of symmetry reasons also if the length of the

[1]Used to calibrate the thermocouples according to ITS90 standard.
[2]Used to calibrate the single hot-film anemometry probe.

Table 3 Parameters to estimate Nusselt and heat transfer error sources

Error source (i)	Variable (X_i)	Bias (B_{X_i})	API
Forced convection coefficient	h	B_{Nu}	API_{Nu}
Voltage difference	ΔV		
Electric current	I		
Electric resistance	R_{Shunt}		
Surface	A		
Temperature difference	ΔT		

Table 4 Instrumentation specifications

DAQ	Anemometry	Thermocouples/Cylinder
Data word length	16 bits/24 ch.	5,1/2 digit/20 ch.
Sampling frequency	33 kHz	48 kHz
Sampling range	0 – 10.24 V	± 300 mV
Resolution	2.5 mV	*NA*
Accuracy	±(0.05%+5mV)	±(0.008%+700μV)
Samples per scan	4096	50

Table 5 Air velocity uncertainty, δw

f (Hz)	Re	T (°C)	w (m/s)	B_U (m/s)	API_U (m/s)	$\delta w_{0.95}$ (%)
10	7,300	22.14	6.443	0.2571	0.0007	3.72
20	15,000	20.33	13.193	0.2581	0.0075	2.04
30	25,000	19.81	21.612	0.2549	0.0254	1.19
40	33,000	19.92	28.481	0.2540	0.0011	0.90

cylinder is greater than the slot width. The circumferential thermal conduction is equal to 1.2% of the total dissipated power because the difference between the temperature at 0° (impinging point) and at 180° (rear point) is variable between 1.7°C and 2.5°C for the powers applied and the air velocities.

The forced convection Nusselt number has been evaluated considering the dependences on the electrical quantities (voltage, current, and Shunt resistance) as reported in Table 3.

The instrumentation uncertainty has been taken into account with the main involved quantities reported in Table 4.

Tables 5–7 report the estimation of global uncertainty for air velocity, temperature, and Nusselt number (δw, δT, and δNu, respectively) in different operating conditions (fan rotation, reported as frequency of the controlling inverter, flow conditions, and distances from the slot exit).

The conclusion on the Nusselt number is a mean uncertainty of 6.4%.

Experimental Results

Experimental Analysis. In each experiment the temperature, velocity, and dissipated power are measured. The power (P) is used to evaluate the convective heat transfer, or Nusselt number, at each position of the thermocouples. The local Nusselt number is defined as

$$\mathrm{Nu}_{loc} = hD/k_a \tag{4}$$

where h is defined by the equation

$$P = \Delta V \cdot I = hA(T_i - T_a) \tag{5}$$

A is the surface of the cylinder not accounting the fins, T_a is the air temperature, T_i is the local temperature measured by the ith thermocouple, D is the diameter of the cylinder not accounting the fins, k_a is the air thermal conductivity, and ΔV and I are the voltage drop across the heater and the electric current, respectively. The final local Nusselt number expression is then

Table 6 Temperature uncertainty, δT

Re	Type/Location	S/H	T (°C)	B_T (°C)	API_T (°C)	$\delta T_{0.95}$ (%)
15,000	J / TC1	3.15	26.35	0.116	0.003	0.41
23,000	J / TC1	8	30.35	0.112	0.004	0.37
16,000	E / TC5 (235°)	8	32.27	0.113	0.003	0.34
16,000	E / TC4 (180°)	3.15	34.37	0.111	0.004	0.32
23,000	E / TC4 (180°)	1.59	38.42	0.110	0.004	0.27
23,000	E / TC5 (235°)	3.7	36.64	0.110	0.004	0.30

Table 7 Nusselt number uncertainty, δNu

Re	S/H	θ	Nu	B_{Nu}	API_{Nu}	$\delta \mathrm{Nu}_{0.95}$ (%)
16,000	8	180°	172.26	7.298	0.115	6.34
23,000	1.59	180°	177.65	7.301	0.121	6.34
16,000	1.59	90°	185.70	11.501	0.180	6.37
23,000	1.59	90°	212.02	12.101	0.184	6.38
23,000	1.59	360°	236.89	13.905	0.183	6.36

$$\mathrm{Nu}_{loc} = P/[\pi L_{cyl} k_a (T_i - T_a)] \tag{6}$$

where L_{cyl} is the length of the heated cylinder.

The corresponding local Nusselt number is presented in Fig. 4, versus the angular position, at a distance $S/H=8$ and several Reynolds numbers. The local Nusselt number has its maximum on the impinging point ($\theta=0°$) and its minimum on the rear point ($\theta=180°$), in agreement with laminar flow [17]. This trend is different from that measured in a turbulent flow [18], where a minimum value has been found at about 90°, similarly to the measurement in the jet cooling of smooth cylinders [19–21]. The local Nusselt number increases with the Reynolds number and is fairly symmetric.

The local Nusselt numbers are presented in Fig. 5 versus the dimensionless distances S/H for several Reynolds numbers and three angles, i.e., at the impinging point (Fig. 5(a)), at 90° (Fig. 5(b)), and at 180° (Fig. 5(c)).

Figure 5(a) shows that for Re=6000 the local Nusselt number has a maximum at $S/H=3.75$ and for Re=8000–10,000 the maximum is at $S/H=6$. The maximum value moves to $S/H=10$ for Re=13,000–19,000 and to $S/H=12$ for the highest Reynolds number experimented (Re=23,000). In conclusion, the maximum of the local Nusselt number moves to higher distance with the increase of the Reynolds number. The maximum variation of the local Nusselt number versus S/H (Fig. 5(a)), is 20% for Re=10,000 between $S/H=6$ (maximum) and $S/H=3.15$ (minimum).

At 90° from the impingement point (Fig. 5(b)), the maximum Nusselt number is at $S/H=6$ for Re=6000, at $S/H=8$ for Reynolds in the range Re=8000–13,000, and at $S/H=10$ for Re=19,000–23,000. The maximum variation of the local Nusselt number versus S/H (Fig. 5(b)) is 25% for Re=13,000 between $S/H=8$ (maximum) and $S/H=3.7$ (minimum).

At 180° from the impingement point (Fig. 5(c)), the maximum Nusselt number is at $S/H=6$ for Re=6000, at $S/H=8$ for Re=8000–13,000, at $S/H=10$ for Re=19,000, and at $S/H=12$ for Re=23,000. The maximum variation of the local Nusselt number versus S/H (Fig. 5(c)), is 20% for Re=19,000 between $S/H=10$ (maximum) and $S/H=1.59$ (minimum).

The variation of the local Nusselt number with the distance S/H is lower in the present experiments with a finned cylinder than in the experiments with a smooth cylinder [22]. The maximum variation of the local Nusselt number with the distance of the finned cylinder S/H is 25% for Re=13,000 between $S/H=8$ (maximum) and $S/H=3.7$ (minimum). For a smooth cylinder [22] the maximum variation of the local Nusselt number is 40.3% at the impinging point, 67.1% at 90°, and 79.6% at 180° for Re=24,000

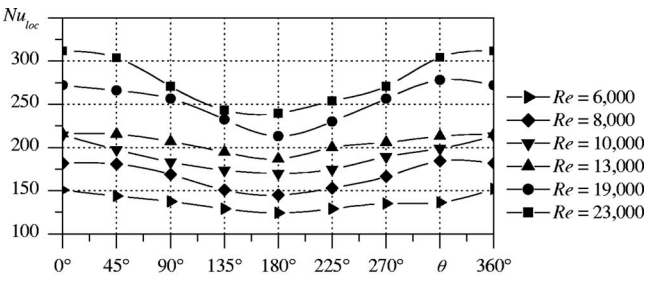

Fig. 4 Local Nusselt number at $S/H=8$

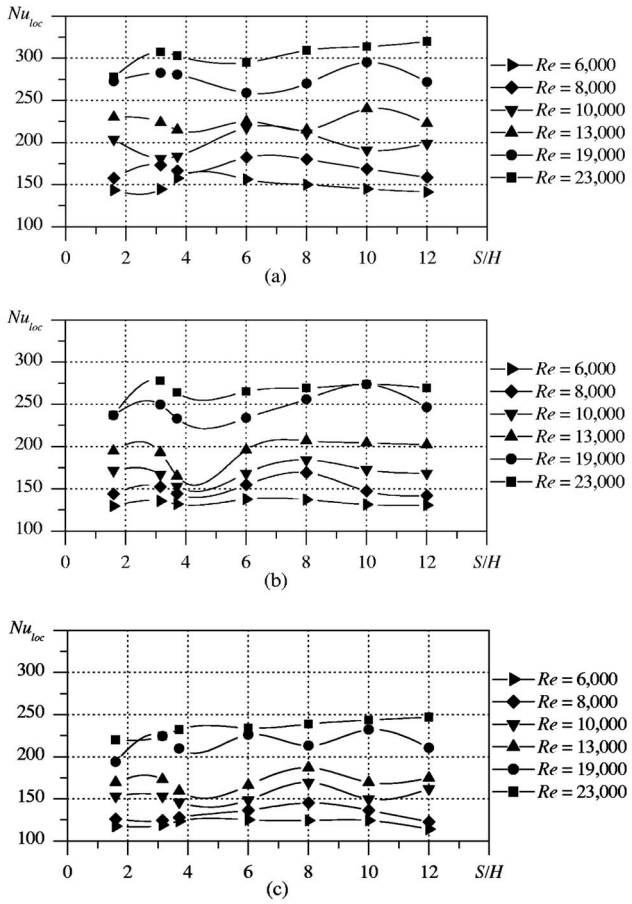

Fig. 5 Local Nusselt number versus S/H: (*a*) at the impingement point, (*b*) at 90° from the impingement point, and (*c*) at 180° from the impingement point

between $S/H=0.5$ (minimum) and $S/H=7$ (maximum).

The average Nusselt number, Nu_{av}, is evaluated with the following equation:

$$\mathrm{Nu}_{av} = h_{av} \cdot D/k_a \tag{7}$$

where h_{av}, the average convective heat transfer coefficient, is defined by

$$P = \Delta VI = h_{av}A(T_{av} - T_a) \tag{8}$$

T_{av} by

$$T_{av} = n^{-1}\Sigma_i T_i \tag{9}$$

and n is the number of temperature measurements along the circumference, equal to 8 for symmetry.

Figure 6 reports the average Nusselt numbers versus S/H for

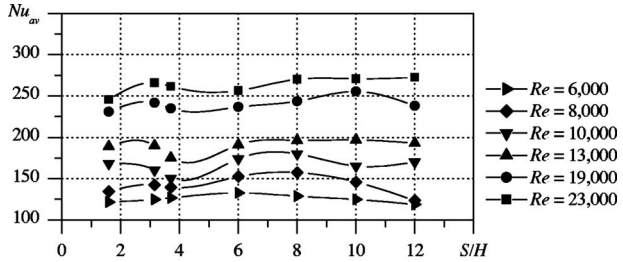

Fig. 6 Average Nusselt number versus S/H

Table 8 Coefficients of Eq. (10) and deviation from experimental data

S/H	a	b	Deviation (%)	
			Min	Max
1.59	1.601	0.507	0.11	5.52
3.15	1.211	0.539	0.07	2.20
3.7	1.283	0.530	0.99	6.47
6	2.553	0.462	0.18	1.94
8	1.930	0.495	0.71	3.13
10	1.041	0.558	0.33	3.90
12	0.760	0.589	0.19	3.84

Reynolds numbers in the range 6000–23,000. For the lowest Reynolds number, Re=6000, the increase of the Nusselt number with the distance from the slot exit is regular with a maximum at $S/H=6$. For Re=8000 the maximum of the Nusselt number moves to $S/H=8$. For Re=10,000 the maximum is around $S/H=8$ and for Re=13,000 the maximum is at $S/H=10$. For the highest Reynolds numbers experimented, i.e., Re=19,000 and Re=23,000, the maximum of the Nusselt number is measured at $S/H=10$ and at $S/H=12$, respectively. The maximum variation of the average Nusselt number with S/H (Fig. 6), is 27.4% for Re=8000 between $S/H=8$ (maximum) and $S/H=12$ (minimum).

The variation of the average Nusselt number with S/H in a finned cylinder is lower than in a smooth cylinder [23] where the maximum variation is 64.5% for Re=24,000 between $S/H=0.5$ (minimum) and $S/H=7$ (maximum).

In the experiments performed with smooth cylinders [22,23] the slot height is equal to the diameter of the smooth cylinder, as in the present experiments, where the diameter of the cylinder without fins is equal to the height of the slot. The fins enlarge the interaction between jet flow and cylinder smoothing out the influence of the jet flow.

Empirical Expressions

The average experimental Nusselt numbers have been correlated to the Reynolds number, at each distance S/H, by an expression similar to that proposed in [24]:

$$\mathrm{Nu}_m = a\mathrm{Re}^b \tag{10}$$

Table 8 reports the values of a and b for each distance S/H along to the maximum and minimum deviations of the experimental data from the predictions of Eq. (10). The maximum deviation is 6.5% at $S/H=3.7$ and 5.5% at $S/H=1.59$ but is lower than 4% everywhere else. Figure 7 reports the experimental average Nusselt numbers of this work and the values predicted by Eq. (10) versus the Reynolds number.

The dependence on the ratio S/H is taken into account by

$$\mathrm{Nu}_m = 1.33\mathrm{Re}^{0.52}(S/H)^{0.026} \tag{11}$$

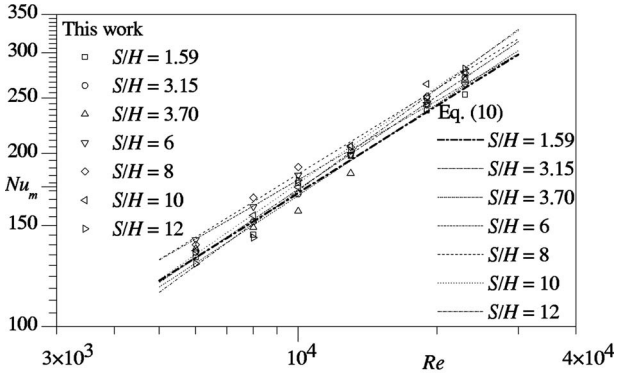

Fig. 7 Experimental average Nusselt numbers and predictions of Eq. (10)

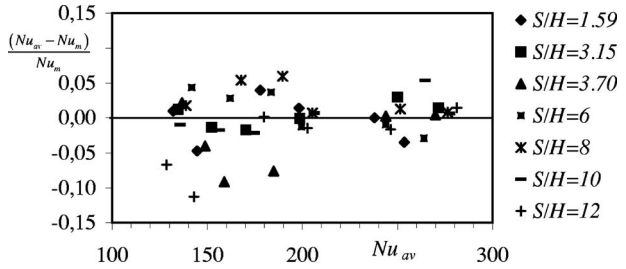

Fig. 8 Residual analysis using Eq. (11)

The residual analysis in the prediction of the experimental data with Eq. (11) is reported in Fig. 8 confirming a causal trend. A maximum deviation of 11.3%, in the prediction of the experimental data with Eq. (11) is obtained.

Finally, Fig. 9 reports the comparison between the experiments of this work with a finned cylinder and those of [23] with a smooth cylinder in similar geometric conditions, i.e., with the diameter of the cylinder equal to the slot height ($D=H$).

The increase of heat transfer due to the presence of the finned cylinder is quite evident.

The increase in the mean Nusselt number is evaluated using the predictions given by Eq. (10) of this work and the similar equation used in [23]. The results of this comparison are reported in Table 9. The maximum Nusselt number increase, about 74%, is obtained at the shorter distance S/H but the increase is always greater than 60% at greater distances.

Conclusions

The experiments on the cooling of a finned cylinder with a jet flow of air have shown that the local Nusselt number has the maximum on the impinging point and the minimum on the rear point. The trend of the local Nusselt number with the distance from the slot exit depends on the Reynolds number. Increasing the Reynolds number, the maximum of the local Nusselt number moves to longer distances from the slot exit. Similar conclusions are found for the average Nusselt number. Two empirical expressions are proposed to correlate the experimental data. The experimental average Nusselt numbers on a finned cylinder are higher than the Nusselt numbers on a smooth cylinder at the same Reynolds number and dimensionless distance from the slot exit. The variation of the local and average Nusselt numbers with the dimensionless distance of the finned cylinder from the slot exit is lower in a finned cylinder than in a smooth cylinder due to the presence of the fins which enlarge the dimensions of the impinged system "cylinder and fins" and smooth out the influence of the jet flow.

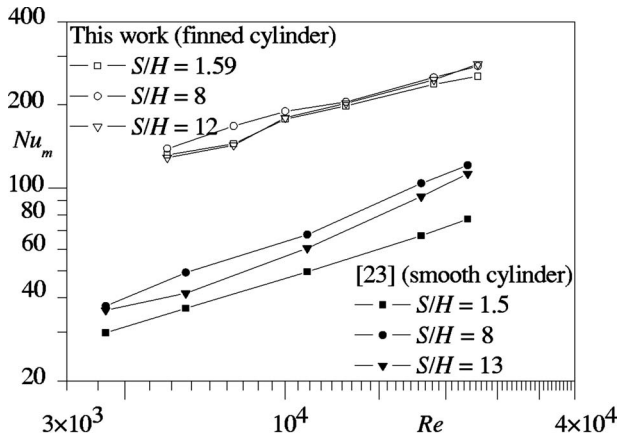

Fig. 9 Mean Nusselt numbers in finned and smooth cylinders

Table 9 Increase of mean Nusselt number in finned cylinder compared to smooth cylinder

	$S/H \approx 1.5$	$S/H = 8$	$12 < S/H < 13$
Minimum (%)	70.9	60.9	61.7
Average (%)	72.3	66.1	64.8
Maximum (%)	74.2	72.8	68.9

Acknowledgment

The present work has been supported by MIUR-COFIN.

Nomenclature

Latin

A = $\pi \cdot D$ surface of cylinder without fins
API = average precision index
B = bias
D = h, diameter of cylinder without fins
f = working frequency of fan power supply inverter
H = slot height
h = convective heat transfer coefficient
k = thermal conductivity
I = electric current
L = slot width
L_{cyl} = length of finned cylinder
n = number of thermocouples
NA = not available
Nu = $h \cdot D \cdot k^{-1}$, Nusselt number
P = dissipated electric power
Q = heat flux
R = electric resistance
Re = $w \cdot D \cdot \nu^{-1}$, Reynolds number
S = distance between slot and cylinder
T = temperature
U,u = streamwise velocities calibration
w = streamwise average velocity at slot exit
X = generic quantity

Greek

ε = electromotive force
ν = kinematics viscosity
θ = thermocouples angular position
ΔV = voltage difference across heating wire
ΔT = temperature difference

Subscripts

0.95 = interval of confidence of 95%
a = air
av = average
$calib$ = calibration
cyl = finned cylinder
fc = forced convection
i = generic position
loc = local
m = mean and empirical
nc = natural convection
PRT = Platinum resistance thermometer

References

[1] European Patent No. 00108568.7–2311, 2000, "Supercharged Internal-Combustion Engine;" IVECO FIAT SpA; Inventors: Gori Fabio, Pippione Eugenio e Scavarda Gianfranco, Bulletin 4/42, 13.10.2004.
[2] Valaszkai, L., and Jouannet, B., 2000, "Cooling System Optimization for Euro 4," EPA/02 Heavy Duty Trucks, SAE Technical Paper Series, 2000–01–0964.
[3] Gori, F., De Nigris, F., Pippione, E., and Scavarda, G., 2000, "Cooling of

Finned Cylinders by a Jet Flow of Air," IMECE, New Orleans.
[4] Schey, O. W., and Biermann, A. E., 1932, "Heat Dissipation from a Finned Cylinder at Different Fin-Plate/Air-Stream Angles," N. A. C. A. Technical Note No. 429, Washington.
[5] Brevoort, M. J., and Rollin, V. G., 1935, "Air Flow Around Finned Cylinders," N.A.C.A Report No. 555, Langley Field.
[6] Schey, O. W., and Ellenbrock, H. H., Jr., 1936, "Blower Cooling of Finned Cylinders," N.A.C.A Report No. 587, Langley Field.
[7] Biermann, A. E., 1937, "Heat Transfer From Cylinders Having Closely Spaced Fins," N.A.C.A. Technical Note No. 602, Washington.
[8] Ellenbrock, H. H., Jr., 1939, "Heat-Transfer Tests of a Steel Cylinder Barrel With Aluminum Fins," N.A.C.A. Technical Note, Washington.
[9] Ellenbrock, H. H., Jr., 1939, "Surface Heat-Transfer Coefficients of Finned Cylinders," N.A.C.A Report No. 676, Langley Field.
[10] Ellenbrock, H. H., Jr., and Mann, A. H., 1940, "Heat-Transfer Tests of a Steel Cylinder Barrel With Aluminum Fins of Optimum Proportion," N.A.C.A. Technical Note, Washington.
[11] Ellenbrock, H. H., Jr., 1940, "Heat-Transfer Tests of Two Steel Cylinder Barrels With Aluminum Fins Manufactured by Factory Production Method," N.A.C.A. Technical Note, Washington.
[12] Corrsin, S., 1943, "Investigation of Flow in an Axially Symmetrical Heated Jet of Air," N.A.C.A. Wartime Report-Series WR-94.
[13] Krothapalli, A., Baganoff, D., and Karamcheti, K., 1980, "Development and Structure of Rectangular Jet in a Multiple Jet Configuration," AIAA J., **18**(2), pp. 945–950.
[14] Schuh, H., and Persson, B., 1964, "Heat Transfer on Circular Cylinder Exposed to Free Jet Flow," Int. J. Heat Mass Transfer, **7**, pp. 1257–1271.
[15] Gori, F., and Coppa, P., 1998, "Circumferential Variation of Heat Transfer on Three Circular Cylinders Cooled by a Slot Jet of Air," Int. J. Heat Technol., **16**(2), pp. 63–69.
[16] Moffat, R. J., 1988, "Describing the Uncertainties in Experimental Results," Exp. Therm. Fluid Sci., **1**, pp. 3–17.
[17] Eckert, E., and Sohegen, S., 1952, "Distribution of Heat Transfer Coefficient Around Circular Cylinders at Reynolds Numbers 20–500," Trans. ASME, **74**, pp. 343–347.
[18] Adachi, T., Okamoto, S., and Adachi, M., 1979, "The Effect of Sound on the Rate of Heat Transfer From a Cylinder Placed Normal to an Air Stream," Bull. JSME, **22**, pp. 1407–1415.
[19] Gori, F., and Bossi, L., 2000, "On the Cooling Effect of an Air Jet Along the Surface of a Cylinder," Int. Commun. Heat Mass Transfer, **27**(5), pp. 667–676.
[20] Gori, F., and Bossi, L., 2002, "Cooling of Two Cylinders in a Row by a Slot Jet of Air," Int. J. Transp. Phenom., **4**, pp. 245–256.
[21] Gori, F., and Bossi, L., 2003, "Optimal Slot Height in the Jet Cooling of a Circular Cylinder," Appl. Therm. Eng., **23**(7), pp. 859–870.
[22] Gori, F., and Petracci, I., 2003, "Local Heat Transfer on a Circular Cylinder Impinged by a Submerged Slot Jet of Air," Eurotherm Seminar 74, March 23–26, pp. 63–69.
[23] Gori, F., and Petracci, I., 2003, "Heat Transfer Measurements Around a Circular Cylinder Impinged By a Slot Jet of Air and Numerical Simulations," IMECE, Washington.
[24] Hilpert, R., 1933, "Wärmeabgabe von geheitzen Drähten und Rohrer," Forsch. Geb. Ingenieurwes., **4**, pp. 215–224.